Fault Detection and Performance Analysis of Photovoltaic Installations

Mahmoud Dhimish

A thesis submitted to the University of Huddersfield in partial fulfilment of the requirements for the degree of Doctor of Philosophy

The University of Huddersfield

March 2018

Copyright Statement

i. The author of this thesis (including any appendices and/or schedules to this thesis) owns any copyright in it (the "Copyright") and s/he has given The University of Huddersfield the right to use such copyright for any administrative, promotional, educational and/or teaching purposes.

ii. Copies of this thesis, either in full or in extracts, may be made only in accordance with the regulations of the University Library. Details of these regulations may be obtained from the Librarian. This page must form part of any such copies made.

iii. The ownership of any patents, designs, trademarks and any and all other intellectual property rights except for the Copyright (the "Intellectual Property Rights") and any reproductions of copyright works, for example graphs and tables ("Reproductions"), which may be described in this thesis, may not be owned by the author and may be owned by third parties. Such Intellectual Property Rights and Reproductions cannot and must not be made available for use without the prior written permission of the owner(s) of the relevant Intellectual Property Rights and/or Reproductions.

Acknowledgments

I would like to express my heartfelt gratitude to my supervisors, Dr. Violeta Holmes, Dr. Bruce Mehrdadi, and Mr. Mark Dales for their guidance, support, and encouragement. Their sage advice, constructive criticism, and useful suggestions have assessed the completion of my PhD research. Above all, their energy and enthusiasm in research have greatly inspired me to contribute such a high-quality work for this thesis.

Appreciation goes to Mr. Dennis Town and Mr. Richard Midlam for their help and discussion on the implementation of the photovoltaic system. Thanks are also extended to the School of Computing and Engineering for providing their financial means and laboratory facilities.

I am greatly indebted to my father whose career in the engineering area has inspired the work contributed to this thesis, and to my mother whose prayer and advices have helped me sailing through this PhD study.

Most importantly, I would like to thank my wife Ghadeer. Her encouragement, support, quite patience and unwavering love were undeniably the bedrock upon which the past 2 years of my life have been built.

Finally, I would like to dedicate this thesis especially to my son Sam, born in June 2017.

Abstract

The cumulative global photovoltaic (PV) capacity has been growing exponentially around the world, especially due to the installation of grid connected photovoltaic (GCPV) plants. Fault detection and analysis are important for the efficiency, reliability and safety of solar photovoltaic (PV) systems. Even

This thesis reports the results of the research work conducted to invent novel fault detection algorithms and evaluate their deployment in multiple existing PV installation, and empirically validate their performance.

A major contribution of this thesis is the development of PV fault detection algorithms based on two indicators named power ratio (PR) and voltage ratio (VR). Both ratios are used to identify the type of the fault that occurs in the PV modules, in PV string, and/or in maximum power point tracking (MPPT) unit.

Three AI based algorithms were also used to detect faults in PV modules. The first algorithm uses six regions of the power and voltage ratio in order to detect faults in PV systems. The average detection accuracy for the algorithm is equal to 94.74%. However, Mamdani Fuzzy Logic system has been used to enhance the occurrence of fault detection in the PV installations which resulted in an increase to 99.12%.

The second proposed PV fault detection algorithm detects defective bypass diodes in PV modules using Mamdani Fuzzy Logic. Whereas, a third PV detection algorithm is based on artificial neural networks (ANN) networks. Four different ANN models have been modelled, which can be classified as follows:

- 2 inputs, 5 outputs using 1 hidden layer
- 2 inputs, 5 outputs using 2 hidden layers
- 2 inputs, 9 outputs using 1 hidden layer
- 2 inputs, 9 outputs using 2 hidden layers

The output results for the last ANN network had the highest overall fault detection accuracy of 92.1%.

In this thesis, the development of two hot spot mitigation techniques used in PV modules will be discussed. These techniques are capable of enhancing the output power of PV modules which are affected by hot spots and partial shading conditions. The detection of hot spots was captured using i5 FLIR thermal imaging camera.

Finally the thesis describes the impact of PV micro cracks on the output power of PV modules. A new statistical analysis approach using T-test and F-test was used to identify the significance impact of the cracks on the output power performance of the PV modules. This is developed using LabVIEW software.

Table of Contents

Copyright Statement ..... **i**

Acknowledgments ..... **ii**

Abstract ..... **iii**

List of Figures ..... **ix**

List of Tables ..... **xvii**

List of Abbreviations ..... **xix**

Chapter 1 Introduction **1**

1.1 Background and project motivation 2

1.2 Problem statement 5

1.3 Aim and objectives 7

1.4 Thesis contributions 8

1.5 Thesis outline 11

Chapter 2 Review of Photovoltaic Systems **13**

2.1 Operation of a solar cell 13

2.2 Solar cell theoretical curves modelling 15

2.3 Overview of existing photovoltaic monitoring systems 17

2.3.1 Monitoring PV and environmental parameters 18

2.3.2 Data acquisition system 20

2.4 Overview of Photovoltaic Faults 22

2.4.1 Impact of partial shading conditions on the PV output power performance 23

2.4.1.1 Enhancement of PV output power due to PS conditions using bypass diodes 25

2.4.1.2 The development of new PV array configuration systems 29

2.4.1.3 Advanced MPPT techniques for mitigating PS conditions affecting PV systems 33

2.4.2 Detecting faulty PV modules 37

2.4.2.1 Statistical and mathematical modelling techniques 37

2.4.2.2 Artificial Intelligence (AI) techniques in PV fault detection 43
2.4.3 Hot spots 48
2.4.4 PV micro cracks 54
2.5 Summary 62
Chapter 3 PV Monitoring System and Performance Analysis 63
3.1 Design of the Monitoring system 63
3.2 LabVIEW software application 72
3.2.1 Photovoltaic I-V and P-V theoretical curves modelling 72
3.2.2 Irradiance effect on PV theoretical curves 74
3.2.3 Temperature effect on PV theoretical curves 75
3.3 Factors impacting the performance of PV systems 76
3.3.1 PS conditions 76
3.3.2 Faulty PV modules 79
3.3.3 Faulty MPPT unit 81
3.3.4 Hot spots 82
3.3.5 PV micro cracks 83
3.3.6 PV array configuration 84
3.4 Summary 85
Chapter 4 Multiple PV Array Configurations 86
4.1 Modelling and simulation of a PV module 86
4.2 Calculation of the diagnostic indicators 88
4.2.1 Equivalent thermal voltage (*Vte*) 88
4.2.2 Fill Factor (FF) 89
4.2.3 PV module series resistance (R_s) 90
4.3 Simulation and data analysis for multiple PV array configurations 93
4.3.1 Examined PV array configurations 93
4.3.2 PV array configurations under STC 94

4.3.3 PV array configurations under PS condition – scenario 1 95
5.3.4 PV array configurations under PS condition – scenario 2 100
4.3.5 PV array configurations under faulty PV modules– scenario 3 105
4.4 Discussion 111
4.5 Summary 113
Chapter 5 Photovoltaic Fault Detection Techniques 114
5.1 Examined PV array configuration and fault classification 114
5.2 Novel fault detection algorithm 116
5.2.1 General PV fault detection algorithm 116
5.2.2 PV fault detection algorithm diagnosis rules 117
5.3 Results and discussion 123
5.3.1 Normal operation and sleep mode 123
5.3.2 PV faults caused by data acquisition system 123
5.3.3 Multiple PV faults occurring in the examined PV system 124
5.4 Evaluating the Proposed PV Fault Detection Algorithm Based on Array Aging 133
6.5 Summary 136
Chapter 6 PV Fault Detection using Artificial Intelligence System 138
6.1 PV fault detection using six layer detection approach 138
6.1.1 Overall six layer PV fault detection algorithm structure 138
6.1.2 Proposed Fuzzy Logic system 141
6.1.3 Evaluating the proposed six layer PV fault detection algorithm 145
6.2 Detecting defective bypass diodes in PV modules using Mamdani Fuzzy Logic system 154
6.2.1 Examined PV module characteristics 154
6.2.2 Inspection process 155
6.2.3 PV I-V curve analysis 156
6.2.4 Proposed PV bypass fault detection Fuzzy Logic system 163

6.2.5 Validation of the proposed PV bypass diode fault detection system using KC130GHT PV module 165
6.3 Comparing Mamdani Sugeno Fuzzy Logic and RBF ANN networks for PV fault detection .. 168
6.3.1 Examined PV system 168
6.3.2 Overall PV fault detection algorithm 169
6.3.3 Implementation of ANN networks 172
6.3.4 Implementation of Fuzzy Logic detection system 177
6.3.5 Performance evaluation for the proposed AI PV fault detection algorithms 181
6.3.5.1 Evaluating the proposed ANN networks 183
6.3.5.2 Evaluating the last ANN network using the second PV plant 186
6.3.5.3 Evaluating the proposed Fuzzy Logic systems 190
7.4 Summary 193
Chapter 7 PV Hot Spot and Micro Cracks 194
7.1 PV hot spots 194
7.1.1 Examined PV modules 194
7.1.2 Evaluating the PV I-V curve tracer and i5 FLIR thermal camera 196
7.1.3 Proposed hot spot mitigation techniques 198
7.1.4 Validating the proposed PV hot spot mitigation techniques 200
7.1.4.1 PV hot spot and I-V curve analysis 200
7.1.4.2 PV partial shading condition using the proposed hot spot mitigation techniques 204
7.1.5 Evaluating the 2nd proposed hot spot mitigation technique using a string of PV modules 207
7.1.6 Evaluating the 2nd proposed hot spot mitigation using a full day experiment 210
7.2 PV micro cracks 211
7.2.1 Electroluminescence setup and PV modules cracks 213
7.2.2 Statistical analysis approach 216
7.2.3 Results 218
7.2.3.1 Diagonal cracks 218

7.2.3.2 Parallel to busbars cracks 221
7.2.3.3 Perpendicular to busbars cracks 223
7.2.3.4 Multiple directions cracks 225
7.2.4 Discussion 227
7.3 Summary 228
Chapter 8 Summary, Conclusion and Recommendation for Further Work 229
8.1 Summary 229
8.2 Conclusion 231
8.3 Future work 233
References 234
Appendix A. Experimental PV Plants 244
1 Overview of the existing PV plant A 244
2 PV modules electrical characteristics 246
3 MPPT unit 246
4 DC/AC inverter 247
5 Temperature sensor 248
6 Davis weather station 248
7 PV plant A system architecture 249
8 Overview for PV plant B 251
9 PV modules electrical characteristics 252
10 DC/AC inverter unit 252
11 PV plant B system architecture 253
Appendix B. LabVIEW simulation code 255
Appendix C. MATLAB/Simulink models for multiple PV array configurations 257
Appendix D. ANN Output Confusion Matrix 260
Appendix E. ANN Network MATLAB Code 267

List of Figures

Figure 1.1 Top 10 countries in 2016 for annual installed PV capacity (International energy agency, 2016) 2
Figure 1.2 Fire hazard in a 383 kW PV array, in Bakersfield, California 2009 (Brooks, 2011) 3
Figure 2.1 Operation of a PV cell (Jenkins & Ekanayake, 2017) 13
Figure 2.2 (a) Simple equivalent circuit of an ideal solar cell, (b) Equivalent circuit of a solar cell with series and shunt resistance 15
Figure 2.3 (a) The I-V characteristics of an ideal solar cell, (b) The P-V characteristic for an ideal solar cell 16
Figure 2.4 (a) P-V curve under various G levels, (b) P-V curve under various T levels 17
Figure 2.5 Variable monitoring for a PV system. (a) Grid-connected PV system, (b) Stand-alone PV system (Madeti & Singh, 2017a) 19
Figure 2.6 (a) Examined site A and Site B, (b) Monitored parameters for the PV systems (Firth, Lomas, & Rees, 2010) 22
Figure 2.7 (a) Percentage of PS applied to a single PV module, (b) P-V curve of the PV module for each PS condition 23
Figure 2.8 (a) Six PV modules connected in series, (b) 25% PS affecting all PV modules 24
Figure 2.9 (a) Bypass diode connected in parallel with a PV module, (b) Series string of solar cells connected in an anti-parallel configuration with a bypass diode (Kukulka, 1997) 25
Figure 2.10 (a) Sectional view of solar cells according to the invention proposed by (Müller, 2002), (b) Circuit diagram of the solar cell and bypass diode according to the invention presented in (Sharps, 2008) 26
Figure 2.11 (a) Real image of SMT 6(60)P PV module, (b) PV module connection box, (c) PV module sub string connections to the bypass diodes 27
Figure 2.12 (a) Simulation results under STC for PV module shown previously in Figure 2.11, (b) LMPP and GMPP for 30% PS with 3 bypass diodes connected to the PV module 28
Figure 2.13 (a) Randomly tested solar irradiance levels, (b) Comparison of the five PV configuration output power (Wang & Hsu, 2011) 29
Figure 2.14 PS pattern affects a PV array. (a) TCT arrangement, (b) Su Do Ku arrangement, (c) Shade dispersion with Su Do Ku arrangement, (d) PV characteristics of the examined PV array including the GMPP (Rani, Ilango, & Nagamani, 2013) 30

Figure 2.15 GMPP (%) for the various configurations and arrangements under shading scenarios 1–4 with different irradiation levels (Belhaouas et al., 2017) 32
Figure 2.16 (a) Flowchart of a simple P&O algorithm (Femia et al., 2005), (b) Flowchart for IC algorithm (Lee, Bae, & Cho, 2006), (c) Flowchart of HC algorithm (F. Liu, Kang, Zhang, & Duan, 2008), (d) ANN configuration used to determine reference voltage at MPP (Kulaksız & Akkaya, 2012) 34
Figure 2.17 (a) Flow chart of the fault detection procedure proposed by (Chouder & Silvestre, 2010), (b) Examined PV systems used in (Gokmen, Karatepe, Celik, & Silvestre, 2012) 39
Figure 2.18 General schematic of the PV fault detection algorithm developed by (Bayrak, 2015) 41
Figure 2.19 Fuzzy Logic membership functions proposed in (Tadj, Benmouiza, Cheknane, & Silvestre, 2014) 43
Figure 2.20 (a) MLP ANN network, (b) RBF ANN network proposed in (Chine et al., 2016) 44
Figure 2.21 Input variables for the constructed fuzzy classifier proposed in (Belaout, Krim, & Mellit, 2016) 45
Figure 2.22 Measured PV module output current and voltage versus the estimated values obtained using the ANN-model proposed in (Mekki, Mellit, & Salhi, 2016) 46
Figure 2.23 PV fault detection topology using 10 PV strings presented by (Yi & Etemadi, 2017) 47
Figure 2.24 (a) Digital image of the lower part of a PV panel, (b) IR image of the back of the PV panel revealing a hot cell in reverse order as illustrated by the arrow (Kaplani, 2012) 48
Figure 2.25 (a) I-V curve of the examined PV module, (b) IR image of the PV module under G: 690 W/m^2, and T = 18 ^oC (Buerhop et al., 2012) 49
Figure 2.26 Proposed PV hot spot acceptance/rejection criteria developed by (Moretón, Lorenzo, & Narvarte, 2015) 50
Figure 2.27 I-V curve for no hot spot, one hot spot, and two hot spots affecting. (a) Opaque PV modules, (b) Semitransparent PV modules 50
Figure 2.28 IR image of 25% shading applied to a PV solar cell. (a) Before DMPPT, (b) After DMPPT (Solórzano & Egido, 2014) 51
Figure 2.29 (a) Bypassed sub panel string with one solar cell, (b) I-V curve characteristics (Kim & Krein, 2015) 52
Figure 2.30 (a) Schematic diagram of the proposed bypass strategy proposed by (Daliento, Di Napoli, Guerriero, & d'Alessandro, 2016), (b) Operation under sunny conditions, (c) Operation under shading conditions 53
Figure 2.31 PV micro cracks detecting using various detection techniques. (a) RUV, (b) STDWT, (c) Proposed PV micro crack detection technique developed by (Bin, Xianghao, & Shuai, 2011) 55

Figure 2.32 (a) ESPI technique proposed by (Wen & Yin, 2012), (b) ESPI image of polycrystalline silicon solar cell in temperature range of 32 ~ 32.4 ^{o}C 56
Figure 2.33 (a) Typical PL imaging setup developed by (Trupke, Bardos, Schubert, & Warta, 2006), (b) Example of PL image of a polycrystalline silicon solar cell, (c) New PL setup proposed by (Zhu, Juhl, Trupke, & Hameiri, 2017) 57
Figure 2.34 (a) A typical EL imaging setup developed by (Fuyuki & Kitiyanan, 2009), (b) Example of EL image of a polycrystalline solar cell, (c) EL image for a PV module taken by (Köntges et al., 2009), (d) power loss analysis per PV module based on number of crackes presented in (Köntges, Kunze, Kajari-Schröder, Breitenmoser, & Bjørneklett, 2011) 59
Figure 2.35 (a) Classification of crack orientations, (b) Relative occurrence of different crack orientation based on 27 examined PV modules 60
Figure 2.36 (a) Illuminated I-V curves for the crack-free cell and cells containing cracks, (b) Plot of the measured and simulated *Voc* as a function of D_c (Oh et al., 2016) 61
Figure 3.1 Overall designed PV monitoring system 64
Figure 3.2 Detailed monitoring system architecture 65
Figure 3.3 Vantage PRO2 monitoring device 66
Figure 3.4 Image of the monitoring screen for FLEXmax 80 MPPT device 67
Figure 3.5 Outback MATE 3 monitoring unit 67
Figure 3.6 LabVIEW code used to enable the connection with Arduino Ethernet shield 68
Figure 3.7 (a) Application Logo, (b) Application output results 69
Figure 3.8 Example of GUI developed using LabVIEW software (Mahmoud Dhimish, Holmes, & Dales, 2016) 70
Figure 3.9 (a) An example of web site that displays the status of the PV system, (b) An example of web site that displays the status of the weather station 71
Figure 3.10 PV solar module theoretical simulation using LabVIEW. (a) I-V curve simulation, (b) P-V curve simulation 73
Figure 3.11 Simulating the theoretical curves for the first PV plant module under various solar irradiance levels with PV module temperature of 25 ^{0}C. (a) I-V curve, (b) P-V curve 74
Figure 3.12 Simulating the theoretical curves for the first PV plant module under various PV module temperature and solar irradiance level is 1000 W/m^2. (a) I-V curve, (b) P-V curve 75
Figure 3.13 (a) PS percentage including opaque paper object, (b) Measured MPP using three PS conditions 77
Figure 3.14 P-V curve during PS conditions affecting three PV modules 78
Figure 3.15 Four series connected PV modules with central MPPT unit 79

Figure 3.16 (a) Measured vs. Theoretical output power, (b) Solar irradiance and average PV modules temperature, (c) FLEXmax 80 MPPT unit efficiency 80
Figure 3.17 (a) MPPT unit efficiency reduction, (b) MPPT unit input shut-down principle 82
Figure 3.18 Hot spotted solar cell in a PV module 83
Figure 3.19 Crack type. (a) Diagonal Crack ($+45^0$), (b) Diagonal Crack (-45^0), (c) Parallel to Busbars Crack, (d) Perpendicular to Busbars Crack, (e) Multiple Directions Crack 84
Figure 3.20 Summary of the proposed PV monitoring system 85
Figure 4.1 Photovoltaic modelling using MATLAB/Simulink. (a) Equivalent circuit of a PV module, (b) Simulating PV module under STC, (c) Photovoltaic I-V Curve, (d) Photovoltaic P-V Curve 87
Figure 4.2 Simulation of V_{te} under various solar irradiance levels, where the PV module temperature is at STC 89
Figure 4.3 (a) *FF* for the examined PV module, (b) *FF* variations during various solar irradiance levels, where the PV module temperature is at STC 90
Figure 4.4 Evaluating PV module R_s using various solar irradiance levels, where the PV module temperature is at STC 93
Figure 4.5 (a) Scenario 1 tested PS patterns, (b) MPP for PS pattern 1, (c) MPP for PS pattern 2 96
Figure 4.6 Simulated *FF*. (a) PS pattern 1, (b) PS pattern 2 98
Figure 4.7 Simulated *Vte*. (a) PS pattern 1, (b) PS pattern 2 99
Figure 4.8 (a) Scenario 2 tested PS patterns, (b) MPP for PS pattern 1, (c) MPP for PS pattern 2 101
Figure 4.9 Simulated FF. (a) PS pattern 1, (b) PS pattern 2 103
Figure 4.10 Simulated *Vte*. (a) PS pattern 1, (b) PS pattern 2 104
Figure 4.11 (a) Examined faulty PV conditions, (b) Output power for faulty pattern 1, (c) Output power for faulty pattern 2 106
Figure 4.12 Simulated *FF*. (a) Row level PV faulty condition, (b) Column level PV faulty condition 108
Figure 4.13 Simulated *Vte*. (a) Row level PV faulty condition, (b) Column level PV faulty condition 110
Figure 5.1 (a) Overall examined PV system architecture, (b) Different type of faults occurring in the examined PV plant 115
Figure 5.2 (a) General algorithm using statistical T-test technique, (b) T-test statistical confidence interval limits, (c) Activating the proposed PV fault detection algorithm 117
Figure 5.3 Threshold values for detecting faults in the PV system based on the PR ratio 120
Figure 5.4 DC side faulty regions based on the analysis of PR and VR 121
Figure 5.5 PV system theoretical and measured output power 124
Figure 5.6 PV system theoretical output power vs. measured output power under 10 different scenarios shown in Table 5.1 126

Figure 5.7 PR ratio for all PV strings 127
Figure 5.8 Detecting various faults using the proposed PV fault detection algorithm. (a) VR ratio for all PV strings, (b) Measured short circuit current 128
Figure 5.9 (a) PV array theoretical and measured output power, (b) first PV string PR and VR 130
Figure 5.10 (a) Second PV string PR and VR, (b) Third PV string PR and VR 132
Figure 5.11 Examined PV system 133
Figure 5.12 (a) PR variations for 3 faulty PV modules, (b) PR variations for all examined scenarios vs. detection limits which are explained in Table 6.3 135
Figure 5.13 Summary of the proposed PV fault detection algorithm in chapter 6 136
Figure 6.1 Detailed flowchart for the proposed PV fault detection algorithm 140
Figure 6.2 Fuzzy Logic classifier system design. (A) Voltage ratio input, (B) Power ratio input, (C) Fault detection output 142
Figure 6.3 (a) Mathematical calculations for the Fuzzy Logic system including VR and PR, (b) Examined PV system which comprises five series-connected PV modules (Mahmoud Dhimish, Holmes, Mehrdadi, & Dales, 2017a) 143
Figure 6.4 Fuzzy Logic system output surface comprising VR, PR and the fault detection output membership functions 144
Figure 6.5 Theoretical vs. Measured output power during 5 different days 145
Figure 6.6 Theoretical power vs. measured power for a PS condition affects the examined PV system 146
Figure 6.7 Theoretical curves vs. measured data. (a) Theoretical fault curve detection limits, (b) VR, PR, and the efficiency of the tested PV system 147
Figure 6.8 MPPT unit output power. (a) Examined partial shading condition, (b) P-V curve including the output LMPP and GMPP obtained by the MPPT unit 149
Figure 6.9 Theoretical detection limits vs. measured data for one faulty, two faulty, three faulty, and four faulty PV modules 150
Figure 6.10 Out of region samples processed by the Fuzzy Logic classification system 151
Figure 6.11 Theoretical detection limits vs. measured data before and after considering the age of the PV array. (a) Normal operation mode and partial shading, (b) One faulty PV module and partial shading, (c) Two faulty PV modules and partial shading, (d) Three faulty PV modules and partial shading 153
Figure 6.12 (a) Internal bypass connection for each PV module, (b) Junction box placed at the back of the PV module 154
Figure 6.13 (a) i5 FLIR camera, (b) PVA-1000s I-V curve tracer 155
Figure 6.14 (a) Real image of a PV module under 20% PS, (b) Real image of a PV module under 60% PS 156

Figure 6.15 (a) I-V curve characteristics under various PS conditions affecting the PV module, (b) P-V curve characteristics under various PS conditions affecting the PV module 157
Figure 6.16 (a) I-V curves under various conditions affecting the examined PV module, (b) Real image and thermography image of the examined PV module while disconnecting one bypass diode from the first PV string 159
Figure 6.17 I-V curve simulation under various partial shading conditions while disconnecting all bypass diodes from the examined PV module 162
Figure 6.18 Proposed fault detection system using Mamdani Fuzzy Logic system 163
Figure 6.19 (a) Input variables for the proposed Fuzzy Logic fault detection system, (b) output variable for the Fuzzy Logic fault detection system, (c) List of faults which can be detected using the PV fault detection system 164
Figure 6.20 Output results for 1 faulty bypass diode and 35% PS condition 166
Figure 6.21 Output results for 3 faulty bypass diodes & 60-70% partial shading “case scenario 2” 167
Figure 6.22 PV system used to evaluate the performance of various AI techniques 168
Figure 6.23 DC side numerical calculations at maximum and minimum operating points 170
Figure 6.24 Detailed PV fault detection approach 171
Figure 6.25 Adopted ANN networks. (A) 2 Inputs, 5 outputs using 1 hidden layer, (B) 2 Inputs, 5 outputs using 2 hidden layers, (C) 2 Inputs, 9 outputs using 1 hidden layer, (D) 2 Inputs, 9 outputs using 2 hidden layers 174
Figure 6.26 Dataset used to train and validate the ANN networks 176
Figure 6.27 Adopted Sugeno and Mamdani Fuzzy Logic systems 178
Figure 6.28 Fuzzy Logic systems classifier output surfaces. (a) Mamdani Fuzzy Logic system, (b) Sugeno Fuzzy Logic system 180
Figure 6.29 (a) Perturbation process made to test the PV system, (b) Theoretical output power vs. measured output power for all tested scenarios 182
Figure 7.1 Structure and instruments used to examine the hot spotted PV modules 195
Figure 7.2 I-V curve tracer output results for various irradiance levels 196
Figure 7.3 (a) Hot Spot detection using i5 FLIR thermal camera, (b) Output I-V curves using healthy PV module vs. hot spotted PV module 197
Figure 7.4 (a) The structure of the PV string for the examined PV module, (b) First hot spot mitigation technique, (c) Second proposed hot spot mitigation technique 199
Figure 7.5 (a) Output thermal images for the first hot spot mitigation technique, (b) Output thermal images for the second hot spot mitigation technique 201

Figure 7.6 Photovoltaic I-V curve analysis. (a) Before and after considering the hot spot mitigation techniques, G: 840 W/m^2, (b) Before and after considering the hot spot mitigation techniques, G: 507 W/m^2, (c) Before and after considering the hot spot mitigation techniques, G:177 W/m^2 203
Figure 7.7 Image of the tested PV module under shaded solar cell using opaque paper object 204
Figure 7.8 (a) Thermographic images of the shaded PV solar cell before and after the activation of the first hot spot mitigation technique, (b) Thermographic images of the shaded PV solar cell before and after the activation of the second hot spot mitigation technique 205
Figure 7.9 Photovoltaic output I-V curves. (a) Before and after activating the first hot spot mitigation technique, (b) before and after activating the second hot spot mitigation technique 206
Figure 7.10 Examined PV String Connection 207
Figure 7.11 (a) I-V curves for the examined PV modules under solar irradiance 760 W/m^2, (b) I-V curve for the entire PV array with and without the activation of the 2nd hot spot mitigation technique 208
Figure 7.12 (a) PV module theoretical circuit diagram, (b) PV module circuit diagram with hot spot mitigation technique, (c) IRFP260NPBF MOSFET Transistor 209
Figure 7.13 PV module I-V curve with and without MOSFET 210
Figure 7.14 (a) Measured PV output power, (b) PV cumulative energy 211
Figure 7.15 (a) 10 PV modules (SMT 6 (60) P); (b) 35 PV Modules (KC130 GHT-2); (c) Monitoring the examined PV systems using LabVIEW Software 212
Figure 7.16 Electroluminescence experimental setup 213
Figure 7.17 EL image of a single PV cell at different bias levels 214
Figure 7.18 EL images for various PV cracks. (a) Diagonal crack (+45^0); (b) Diagonal crack (-45^0); (c) Parallel to busbars crack; (d) Perpendicular to busbars crack; (e) Multiple directions crack 215
Figure 7.19 Crack type distribution among both examined PV systems (45 PV Modules) 215
Figure 7.20 Statistical approach used to identify whether the crack type has a significant impact on the output power performance of a photovoltaic module 217
Figure 7.21 (a) real-time long-term measured data for a diagonal crack affecting 1 and 5 solar cells, (b) Power ratio for a diagonal cracks affecting 1, 2, 3, 4 and 5 PV solar cells 220
Figure 7.22 (a) Real-time long-term measured data for a parallel to busbars crack affecting 1 and 4 solar cells, (b) Power ratio for parallel to busbars crack affecting 1, 2, 3 and 4 PV solar cells 222
Figure 7.23 (a) Real-time long-term measured data for a perpendicular to busbars crack affecting 1 and 4 solar cells, (b) Power ratio for a perpendicular to busbars crack affecting 1, 2, 3 and 4 (1-8 busbars) pv solar cells 224
Figure 7.24 (a) Real-time long-term measured data for a multiple directions cracks affecting 1, 3 and 5 solar cells; (b) Power ratio for multiple directions cracks affecting 1, 2, 3, 4 and 5 PV solar cells 226

Figure 7.25 Percentage of cracks for the examined PV modules, overall significant cracks percentage equals 60% out of 84% 227
Figure 8.1 Multiple PV systems connected through a multiple configuration box..... 233
Figure 1 (a) Davis weather station installed next to PV plant A, (b) Vantage PRO2 wireless weather station monitoring unit..... 249
Figure 2 (a) PV string connected to MPPT unit, (b) Three parallel PV strings connected to a single MPPT unit, (c) Three PV strings each connected to a MPPT unit..... 250
Figure 3 Second examined PV plant..... 251
Figure 4 PV plant B connection to the DC/AC inverter and UoH main grid 252
Figure 5 (a) PV configuration used in the PV system installed in 2006, (b) PV configuration used to validate the designed fault detection algorithms..... 253

List of Tables

Table 2.1 Variables to be measured according to British Standard BS IEC 61724 (Commission, 1998) .. 18
Table 2.2 Different characteristics of various solar radiation sensor types (Madeti & Singh, 2017a) 20
Table 2.3 Review of recent monitoring systems implemented in PV plants 21
Table 2.4 Comparison of P&O approaches 35
Table 2.5 Comparison of various PV fault detection algorithms 42
Table 4.1 Difference between estimated R_s and measured R_s 92
Table 4.2 Indicators values estimated for all examined PV array configurations 94
Table 4.3 Mathematical calculations of R_s for various PV array configurations 94
Table 4.4 Estimated R_s for one PV module only 95
Table 4.5 Estimated R_s for the examined PV array configurations under PS pattern 1 97
Table 4.6 Estimated R_s for the examined PV array configurations under PS pattern 2 97
Table 4.7 Estimated R_s for the examined PV array configurations under PS pattern 1 102
Table 4.8 Estimated R_s for the examined PV array configurations under PS pattern 2 102
Table 4.9 Estimated R_s for scenario 3: PV faulty conditions, row level 107
Table 4.10 Estimated R_s for scenario 3: PV faulty conditions, column level 107
Table 4.11 Change in the tested indicators for S and P configurations 111
Table 4.12 Change in the tested indicators for BL configuration 112
Table 4.13 Change in the tested indicators for SP and TCT configurations 112
Table 5.1 Diagnosis multiple faults in multiple strings locations 125
Table 5.2 Diagnosis multiple faults in multiple PV strings 129
Table 5.3 Theoretical threshold calculations using the examined older PV system shown in Figure 5.11 (Mahmoud Dhimish, Holmes, & Dales, 2017) 134
Table 6.1 Accuracy comparison between four different case scenarios 151
Table 6.2 PSCC results for the examined PV module while disconnecting all bypass diodes 162
Table 6.3 Various type of faults detected by the proposed machine learning techniques 172
Table 6.4 Fuzzy Logic input regions 178
Table 6.5 PV system under various faults 181
Table 6.6 Faults detected by the ANN networks 184
Table 6.7 PV system 2 under various faults 186
Table 7.1 Comparison between the first and second proposed hot spot mitigation technique using high, medium and low irradiance levels 202

Table 7.2 Statistical F-Test critical values for 99% confidence interval (p=0.01) (Miller & Miller, 2005) 217
Table 7.3 Statistical T-Test confidence interval (Miller & Miller, 2005) 217
Table 7.4 Diagonal cracks performance indicators 218
Table 7.5 Parallel to busbars cracks performance indicators 221
Table 7.6 Perpendicular to busbars cracks performance indicators 223
Table 7.7 Multiple directions cracks performance indicators 225
Table 1 KC130GHT-2 PV module electrical characteristics 252

List of Abbreviations

AI	Artificial Intelligence
ANN	Artificial Neural Network
BL	Bridge Linked
DA	Detection Accuracy
DAQ	Data Acquisition
EL	Electroluminescence
FF	Fill Factor
G	Sun irradiance (W/m^2)
GCPV	Grid Connected Photovoltaic
GMPP	Global Maximum Power Point
HC	Honey Comb
Impp	Current at Maximum Power Point (A)
IoT	Internet of Things
Isc	Short Circuit Current (A)
I-V	Current- Voltage
MLP	Multi-Layer Perceptron
LMPP	Local Maximum Power Point
MAE	Mean Absolute Error
MF	Membership Function
MPP	Maximum Power Point (W)
MPPT	Maximum Power Point Tracking
P	Parallel

PR	Power Ratio
PS	Partial Shading
PSCC	Percentage of Short Circuit Current
PV	Photovoltaic
PVD	Percentage of Voltage Drop
P-V	Power-Voltage
RBF	Radial Basis Function
RF	Radio Frequency
RMSE	Root Mean Squared Error
Rs	Series Resistance (Ω)
S	Series
SIR	Shading Identification Region
SP	Series Parallel
STC	Standard Test Condition
T	Temperature (^{0}C)
TCT	Total Cross Tied
VI	Virtual Instrumentation
Vmpp	Voltage at Maximum Power Point (V)
Voc	Open Circuit Voltage (V)
VR	Voltage Ratio
Vte	Thermal Voltage (V)

Chapter 1 Introduction

The main objective of this thesis is to present research work on the design and development of a novel PV fault detection and degradation analysis. PV fault detection algorithms have been widely used to detect various faults occurring in PV installations (Chine, Mellit, Pavan, & Kalogirou, 2014; Garoudja et al., 2017; Spataru, Sera, Kerekes, & Teodorescu, 2015). These algorithms relay on several parameters of PV installations such as voltage, current, power, and the series resistance of PV modules and depend on some environmental factors such as ambient temperature, and solar irradiance. However, the listed parameters are not always available in PV sites, thus, it is required to improve the existing PV detection algorithms in order to detect PV faults using fewer PV and environmental parameters.

Authors in (Moretón et al., 2015) studied the impact of PV hot spots on the performance of PV modules whereas few works such as (Daliento et al., 2016; Solórzano & Egido, 2014) suggested a suitable method to increase the output power of PV hot spotted solar cells. Up to date, there are few systems which have been industrialized and commercialized to improve the performance of hot spotted PV cells.

The analysis of PV micro cracks was inspected by (Köntges et al., 2011; Zhu et al., 2017) using electroluminescence (EL) imaging technique. However, the measured data were analysed using laboratory-based experiments, which did not contain a real-time long-term data measurements from an installed PV modules in various locations.

Firstly this thesis will describe the development of various PV fault detection algorithms which are divided into three main categories: mathematical and statistical analysis algorithms, Fuzzy Logic PV fault detection systems, and ANN based systems. All these algorithms depend only on the power and voltage ratios of the PV installations.

The second contribution of this work is the design of the novel PV hot spot mitigation techniques. The proposed techniques can be used to decrease the temperature of the PV hot spotted solar cells, and increase the generated power in the hot spotted solar cell in the affected PV modules.

Finally, the development of a novel statistical analysis approach, using T-test and F-test to analyse the impact of PV micro cracks on the output power of the PV modules, is described and compared with previous approaches. The proposed approach is able to identify whether a micro crack has a significant or insignificant impact on the PV module output power.

1.1 Background and project motivation

Photovoltaic (PV) energy has become one of the most important renewable energy resources, reaching a global accumulative installed capacity of approximately 75 GW in 2016, which is sufficient to supply 1.8% of the world's total electricity consumptions (International energy agency, 2016).

As shown in Figure 1.1, the United Kingdom is the fifth leading country for annual installed PV capacity. The significant growth of the PV market have led to substantial reductions in the price of PV modules.

According to the annual reports published by the UK department of business, energy & industrial strategy, the majority of PV installations are sub-4 kW retrofitted schemes, which increased by 35,188 from 2016 to total of 836,014 at the end of 2017. This growth generates approximately 82 MW.

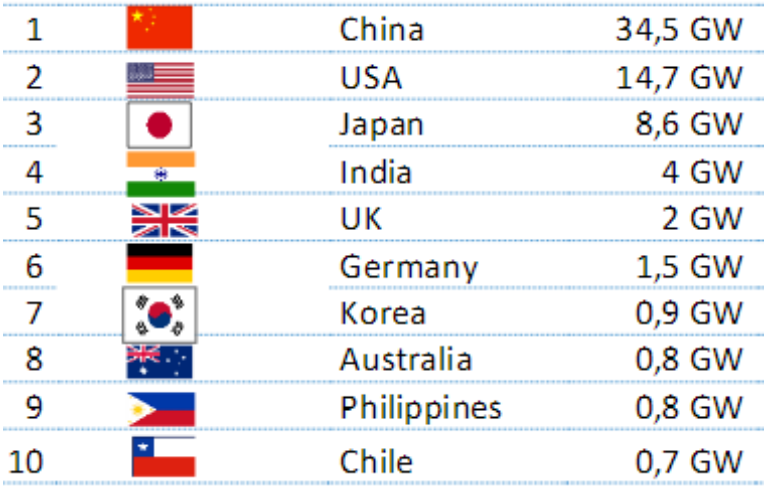

Figure 1.1 Top 10 countries in 2016 for annual installed PV capacity (International energy agency, 2016)

In the PV installations, fault detection analysis and protection are essential to prevent unexpected events in PV solar systems. Despite the fact that these systems have no moving parts and usually require low maintenance, they are still subject to various failures or faults along the PV arrays, power conditioning units, batteries, wiring, and utility interconnections (Zhao, 2015).

PV systems are scalable and modular technology can be used to build a PV power plant by connecting a large number of PV modules in multiple PV array configurations. Once PV modules are electrically connected, any fault among them can affect the entire system performance.

In large PV systems, it may become more difficult to detect or identify a fault effectively, which can remain hidden in the PV installation until the whole system breaks down.

Due to faults occurring in the PV arrays, several fire hazards have been reported in PV installations. On Sunday afternoon, April 5, 2009, smoke was seen rising from the roof of a store, home to a 383 kW PV array, in Bakersfield, California (Brooks, 2011).

The problem exposed by the Bakersfield Fire was that large inverters manufactured since 2005 employ ground-fault equipment that lifts the grounded conductor in the event of a ground fault. In practice, this is fine as long as it eliminates the only return path for the ground-fault currents. However, if a return path exists in the source-circuit conductors, a 30 kW array is capable of delivering approximately 100 amps of current, which is enough to burn the conductor (Brooks, 2011).

In July 2017, an investigation was launched into the fire risk posed by solar panels fitted to thousands of homes, schools, and businesses across the UK. The panels were investigated by the Building Research Establishment (BRE), a government fire safety contractor which was also testing building cladding in the wake of the Grenfell Tower disaster in west London (Ministry of Housing, Communities & Local Government, 2017). The investigation comes just days after 80 firefighters tackled a blaze at a new block of flats in Bow, east London, on 2 July, where the roof-mounted solar panels appear to have caught fire. The published report indicates that the fire is caused by a mismatch in PV modules. An internal investigation into another recent London tower block fire, in Thornton Heath in June 2017, indicated the blaze was caused by "an overheated solar panel".

Figure 1.2 Fire hazard in a 383 kW PV array, in Bakersfield, California 2009 (Brooks, 2011)

Nowadays, due to the growing capacity of PV systems, there has been an increase in the power conversion units, monitoring systems, communication equipment, and protection devices being added to PV installations. As a result massive PV data becomes available (both instantaneous and historical) (Zhao, 2015). Figure 1.3 shows an example of a typical gird-connected PV system (GCPV). Various PV data are available from weather station, PV arrays, PV inverters, and the utility grid.

The PV data are mainly used to evaluate the PV system performance and calculate the energy loss over long periods of time. Although fault detection has been developed using historical PV data, it requires a long processing time (at least few minutes). Hence, it is necessary to develop more responsive PV fault detection algorithms that can make better use of these readily available PV data.

In order to monitor the status of PV plants it is recommended to stream the data in real-time (few micro seconds). However, the data streaming depends on the capabilities of the microprocessors used in the PV system devices such as the maximum power point tacking units, and the inverters. In this thesis, the maximum power point tacking unit was used to measure all PV system parameters such as voltage, current, and power. The minimum time constant to stream measured data is 1 second, thus this time was selected as the sampling rate for all conducted experiments.

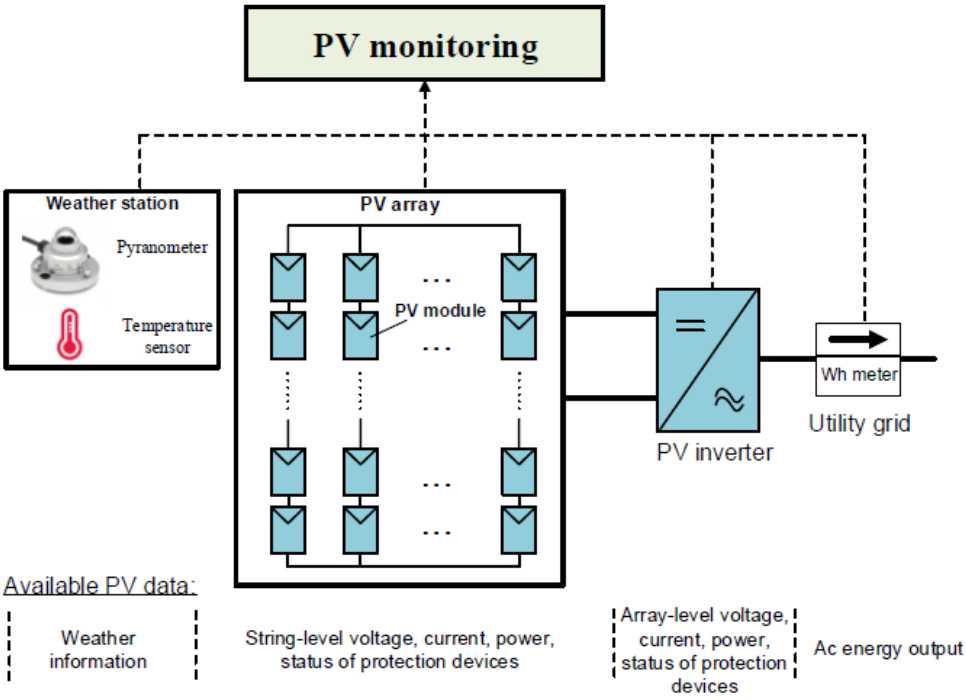

Figure 1.3 Large data are available in PV installations (Zhao, 2015)

1.2 Problem statement

A typical PV installation which includes 4 PV strings each consisting of 3 series-connected PV modules is shown in Figure 1.4. A central MPPT is used to maximize the output power of the entire PV systems.

Several types of fault could happen in this PV system, such as:

- Partial shading conditions
- Faulty PV module
- 2 Faulty PV modules
- Faulty PV string
- Faulty MPPT unit

These faults degrade the performance of the entire PV system, and decrease its generated output power. This thesis will outline novel detection algorithms which could be used to detect and locate various faults in PV plants and enhance the output power of hot spotted PV solar cells. Hot spotting is a reliability problem in PV panels, where a mismatched cell heats up significantly and degrades PV panel output power. High PV cell temperature due to hot spotting can damage the cell encapsulate and lead to secondary breakdown, where both cause permanent damage to the PV panel. An example of a PV hot spot is shown in Figure 1.5a.

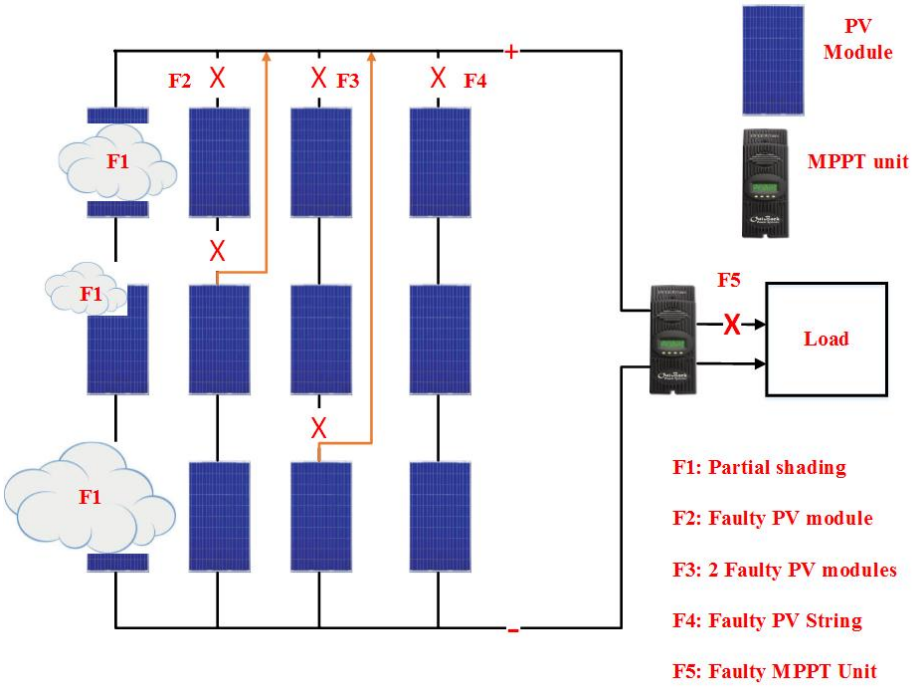

Figure 1.4 Schematic diagram of a PV system including various types of faults

Furthermore, PV micro cracks are one of the reasons that PV panels do not operate at their maximum power point. Figure 1.5b shows an example of PV micro cracks affecting a PV panel. The PV micro cracks, location, and size will be discussed in this thesis.

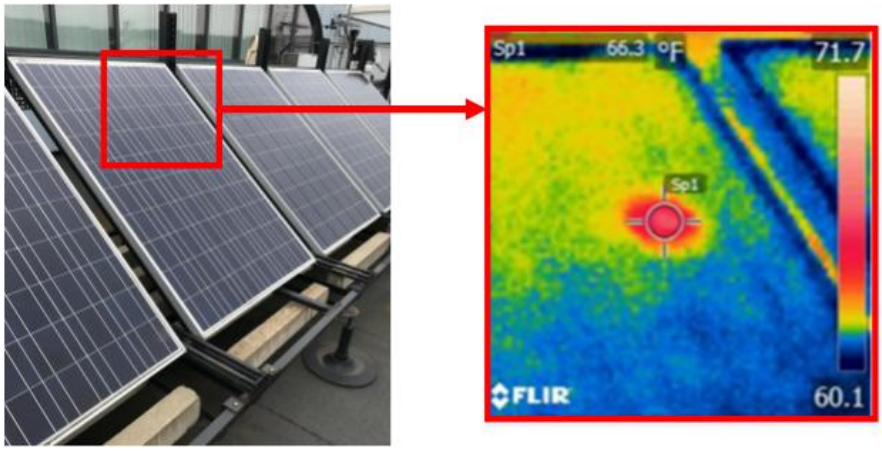

(a)

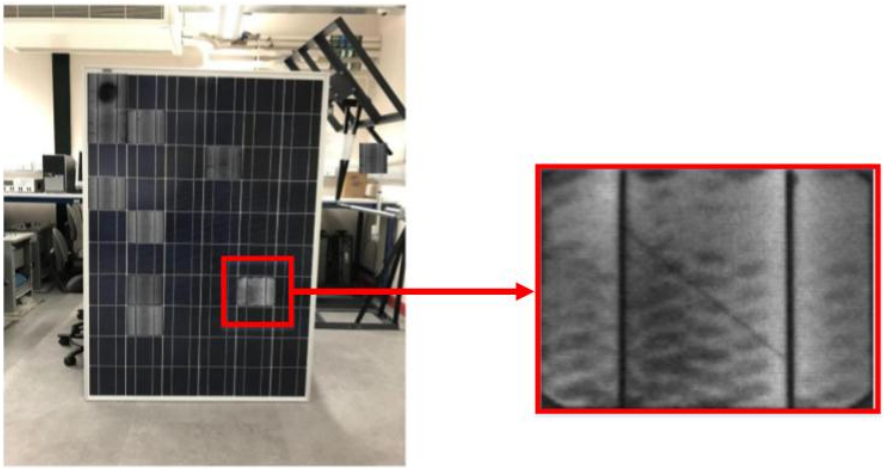

(b)

Figure 1.5 (a) Hot spotted PV solar cell, (b) PV micro cracks

1.3 Aim and objectives

The main aim of this research work is to design and implement PV fault detection algorithms which can detect multiple faults occurring in PV installations. In addition, a new hot spot mitigation technique will be devised which could be used with hot spotted PV modules. The impact of PV micro cracks based on statistical analysis approach is also to be considered.

There are six main objectives of this research, which are:

1. To create a monitoring systems based on internet of things (IoT) devices to monitor and analyse the performance of the PV systems installed at the University of Huddersfield. The IoT devices refers to a network of physical devices such as sensors, and PV modules that feature an internet protocol address for internet connectivity and the communication that occurs between these devices.
2. To model, analyse and compare the performance of multiple PV array configurations under various PS and faulty PV conditions
3. To develop a PV fault detection algorithm based on statistical analysis and mathematical techniques
4. To create a PV fault detection algorithm based on AI techniques such as Fuzzy Logic and ANN networks
5. To develop novel techniques which could be used to enhance the output power generated by hot spotted PV modules
6. To identify the impact of PV micro cracks on the generated power of PV modules

1.4 Thesis contributions

This thesis demonstrates several major research contributions and scientific advancements over the existing solutions. These contributions can be described as follows:

Contribution 1 (presented in chapter 5)

Developing a PV fault detection algorithm based on T-test statistical analysis technique as well as using the power ratio (PR) and voltage ratio (VR) in order to identify the type of the fault occurred in the PV plant. The PV detection algorithm has been validated using two PV plants installed at the University of Huddersfield. The first PV plant has a capacity of 2.2 kW, while the second PV plant capacity is 4.16 kW.

This contribution is published in the following journals:

i. Dhimish, M., & Holmes, V. (2016). Fault detection algorithm for grid-connected photovoltaic plants. Solar Energy, **137**, 236-245.
ii. Dhimish, M., Holmes, V., & Dales, M. (2017). Parallel fault detection algorithm for grid-connected photovoltaic plants. Renewable Energy, **113**, 94-111.
iii. Dhimish, M., Holmes, V., Mehrdadi, B., & Dales, M. (2017). Simultaneous fault detection algorithm for grid-connected photovoltaic plants. IET Renewable Power Generation, **11**, 1565-1575.

Contribution 2 (presented in chapter 6)

Developing three PV fault detection algorithms based on artificial intelligence (AI) techniques, as illustrated below:

1. The first algorithm uses six regions to detect faults in PV systems. This algorithm is based on PR and VR ratios, as well as a 3rd order polynomial functions. The average detection accuracy for the algorithm is equal to 94.74%. However, Mamdani Fuzzy Logic system was used to enhance the detection accuracy of the PV detection algorithm. The average detection accuracy increased to 99.12% after considering the Fuzzy Logic system.
2. The second PV fault detection algorithm is used to detect defective bypass diodes in PV modules. The algorithm is based on the analysis of three variables, percentage of voltage drop (PVD), percentage of open circuit voltage (POCV), and the percentage of short circuit current (PSCC). Mamdani Fuzzy Logic system has been used to detect up to 13 different faults associated with defective bypass diodes in PV modules. Several tests were used to confirm the ability of the proposed detection algorithm to detect defective bypass diodes in PV modules.

3. The third PV detection algorithm is based on ANN networks. Four different ANN models have been used and compared, which are classified as:
    - 2 inputs, 5outputs using 1 hidden layer
    - 2 inputs, 5 outputs using 2 hidden layers
    - 2 inputs, 9 outputs using 1 hidden layer
    - 2 inputs, 9 outputs using 2 hidden layers

The ANN networks have been developed using MATLAB/Simulink software. In conclusion, the last ANN network had the highest overall detection accuracy of 92.1%.

This contribution is published in the following journals:

i. Dhimish, M., Holmes, V., Mehrdadi, B., Dales, M., Chong, B., & Zhang, L. (2017). Seven indicators variations for multiple PV array configurations under partial shading and faulty PV conditions. Renewable Energy, **113**, 438-460.

ii. Dhimish, M., Holmes, V., Mehrdadi, B., & Dales, M. (2017). Diagnostic method for photovoltaic systems based on six layer detection algorithm. Electric Power Systems Research, **151**, 26-39.

iii. Dhimish, M., Holmes, V., Mehrdadi, B., Dales, M., & Mather, P. (2017). Detecting Defective Bypass Diodes in Photovoltaic Modules using Mamdani Fuzzy Logic System. Global Journal of Research In Engineering, **17**, 33-44.

iv. Dhimish, M., Holmes, V., Mehrdadi, B., Dales, M., & Mather, P. (2017). Photovoltaic fault detection algorithm based on theoretical curves modelling and fuzzy classification system. Energy, **140**, 276-290.

v. Dhimish, M., Holmes, V., Mehrdadi, B., & Dales, M. (2017). Multi-layer photovoltaic fault detection algorithm. High Voltage, **2**, 244-252.

vi. Dhimish, M., Holmes, V., Mehrdadi, B., & Dales, M. (2018). Comparing Mamdani Sugeno Fuzzy Logic and RBF ANN network for PV fault detection. Renewable Energy, **117**, 257-274.

Contribution 3 (presented in chapter 7)

Two hot spot mitigation techniques have been created for PV modules. The proposed techniques are capable of enhancing the output power of PV modules which are effected by hot spots and partial shading conditions. The proposed hot spot mitigation techniques use multiple MOSFTEs in the hot spotted PV module, while the detection of hot spots was captured using i5 FLIR thermal imaging camera.

In addition, develop a new statistical analysis approach using T-test and F-test to analyse the impact of PV micro cracks on the output power of the PV modules. The approach is developed using LabVIEW software. Forty-five PV modules with various types of cracks such as diagonal, parallel and perpendicular to busbars, and multiple directions crack have been examined. Before considering the statistical analysis approach, 84% of the examined PV modules showed a significant loss of the output power. However, the statistical approach has confirmed that this result is incorrect, since only 60% of the examine PV cracks suffered from the loss of power.

This contribution is published in the following journals:

i. Dhimish, M., Holmes, V., Mehrdadi, B., & Dales, M. (2017). The impact of cracks on photovoltaic power performance. Journal of Science: Advanced Materials and Devices, **2**, 199-209.

ii. Dhimish, M., Holmes, V., Dales, M., & Mehrdadi, B. (2017). Effect of micro cracks on photovoltaic output power: case study based on real time long term data measurements. Micro & Nano Letters, **12**, 803-807.

iii. Dhimish, M., Holmes, V., Mehrdadi, B., Dales, M., & Mather, P. (2017). Output Power Enhancement for Hot Spotted Polycrystalline Photovoltaic Solar Cells. IEEE Transactions on Device and Materials Reliability, **18**, 37-45.

iv. Dhimish, M., Holmes, V., Mehrdadi, B., Dales, M., & Mather, P. (2018). PV output power enhancement using two mitigation techniques for hot spots and partially shaded solar cells. Electric Power Systems Research, **158**, 15-25.

v. Dhimish, M., Holmes, V., Mather, P., & Sibley, M. (2018). Novel hot spot mitigation technique to enhance photovoltaic solar panels output power performance. Solar Energy Materials and Solar Cells, **179**, 72-79.

1.5 Thesis outline

The rest of the thesis is organised into nine chapters as follows:

Chapter 2:

The existing knowledge of PV characteristics which lead to the issue of partial shading, faulty PV modules, hot spots and micro cracks is reviewed in detail in this chapter. The theoretical model of a PV panel and its output voltage, current and power characteristics are also presented. In addition, PV monitoring systems and fault detection algorithms are be described.

Chapter 3:

This chapter describes the design and development of the monitoring system installed in the examined PV plants. The proposed monitoring unit uses the Virtual Instrumentation (VI) software via the Internet of Things (IoT) devices to monitor and analyse the performance of the PV systems under test. Additionally, five different factors which affect the output power of the PV systems will also be discussed.

Chapter 4:

The main goal of this chapter is to model, analyse and compare the performance of multiple PV array configurations under various PS and PV fault conditions. Five different PV array configurations have been tested including S, P, SP, TCT, and BL. Additionally, seven indicators have been compared during each examined scenario, where all tests have been carried out using MATLAB/Simulink software.

Chapter 5:

This chapter presents the development of the PV fault detection algorithm. The algorithm is based on T-test statistical analysis method and mathematical techniques. The proposed PV detection algorithm was validated using 3 PV strings each containing 3 series-connected PV modules and MPPT unit.

Chapter 6:

This chapter describe the use of artificial intelligence systems including Fuzzy Logic and artificial neural networks in PV fault detection. Several techniques are used to detect PV faults such as Mamdani Fuzzy Logic system, Sugeno Fuzzy Logic system, and radial basis function networks. The designed algorithms are evaluated using various PV systems including aged PV installation and different PV systems capacity.

Chapter 7:

This chapter presents the development of two techniques to enhance the output power of hot spotted PV solar cells. Both techniques were tested under various environmental conditions. Additionally, a statistical analysis approach using T-test and F-test are used to identify the impact of PV micro cracks on the output power of PV solar modules.

Chapter 8:

This chapter concludes the research with a summary of the achievement and contributions of this thesis, and presents the recommendations for further work.

Chapter 2 Review of Photovoltaic Systems

This chapter presents the background of the existing PV installations, theoretical curves modelling and an overview of recent monitoring systems deployed in PV systems. In addition, this chapter will cover various types of faults occurring in PV systems, as well as existing PV fault detection and classification techniques. The benefits and limitations of these existing techniques are also explored and assessed.

2.1 Operation of a solar cell

PV devices convert sunlight directly into electricity. There are a number of ways in which the PV effect can be exploited and some relatively new discoveries such as dye-sensitised (Upadhyaya, Senthilarasu, Hsu, & Kumar, 2013), organic polymer (Dou et al., 2013) and Perovskite PV cells (Zhou et al., 2014) using new materials show great promise. However, at present the commercially important PV technologies use solid semiconductor material to form a p-n (positive-negative) junction on to which light (solar energy) falls. Solar energy falling on the semiconductor material excites the flow of electrons that are pulled across the junction by the electric field created when the p-n junction is formed (Jenkins & Ekanayake, 2017). Finally, when the illuminated semiconductor p-n junction is connected to an external circuit, the flow of electrons across the junction creates a direct current (DC) electricity. A simple operation of a PV solar cell is shown in Figure 2.1.

As solar irradiance increases, more photons and electrons are released. The rise in the flow of electrons, increases the current flow generated by the PV solar cells. Hence, the short circuit current (I_{sc}) is directly proportional to the solar irradiance (G).

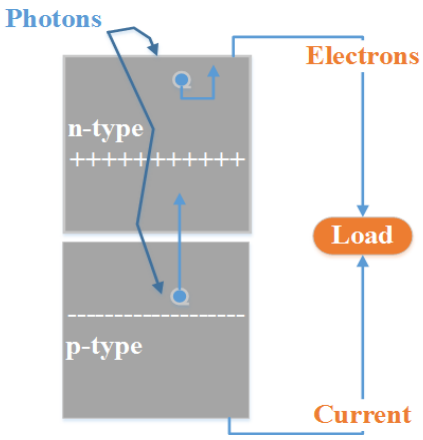

Figure 2.1 Operation of a PV cell (Jenkins & Ekanayake, 2017)

The open circuit voltage (V_{oc}) of the PV cell is determined by the electric field created in the depletion region of the p-n junction which is largely independent of the solar irradiance (McEvoy, Castaner, & Markvart, 2013). Thus, the operation of an ideal solar cell is described by Shockley solar cell Equation (2.1).

$$I = I_{ph} - I_o \left[e^{\frac{V}{V_T}} - 1 \right] \tag{2.1}$$

where I_{ph} is the photo-current that is directly proportional to the irradiance, I_o is the diode saturation current, V is the voltage across the terminals of the solar cell and V_T is the thermal voltage described by Equation (2.2).

$$V_T = \frac{K\,T}{q} \tag{2.2}$$

where K is Boltzmann's constant (1.38 x 10^{-23} J/kelvin), T is absolute temperature, q is the electron charge (1.602 x 10^{-19} C). The thermal voltage V_T at a room temperature of 300 Kelvin is equal to 0.026 V.

Equation (1.1) leads to the simple equivalent circuit of a solar cell, which is a current source in parallel with a diode, shown in Figure 2.2a.

The equivalent circuit can be extended to include shunt and series resistors to represent losses within the PV cell as shown in Figure 2.2b. The shunt resistor R_{sh} represents the leakage of current across the p-n junction around the edge of the cell and the effect of detects and impurities in the junction region. Furthermore, the series resistor R_s represents the resistance of the bulk semiconductor, the metallic contacts and connection of the contacts to the semiconductor material (McEvoy et al., 2013). Including the effect of these losses results in Equation (2.3), where n is the ideality factor which represents the combination of electrons and holes at defects in the junction region, n varies between 1 and 2.

$$I = I_{ph} - I_o \left[e^{\frac{q\,(V + R_S\,I)}{n\,K\,T}} - 1 \right] - \frac{V + R_S\,I}{R_{sh}} \tag{2.3}$$

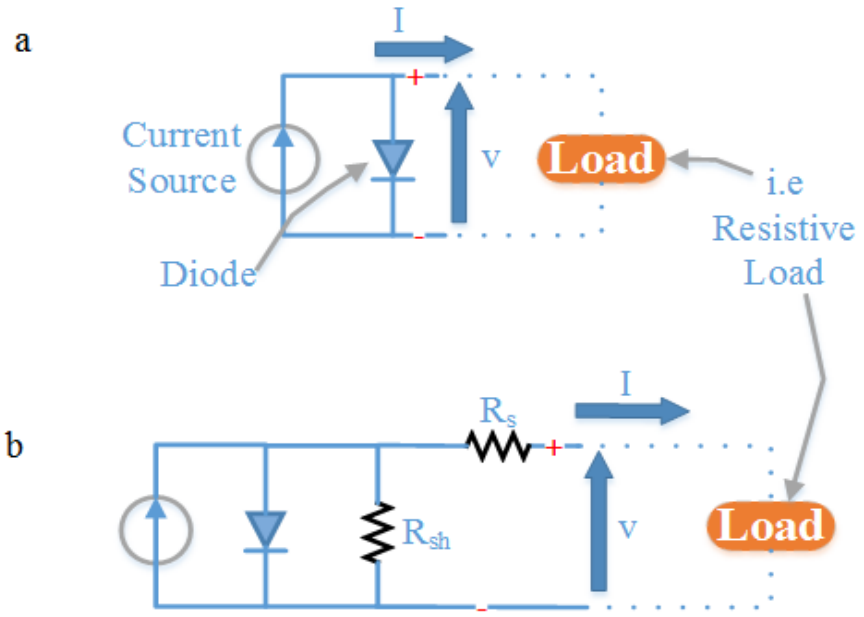

Figure 2.2 (a) Simple equivalent circuit of an ideal solar cell, (b) Equivalent circuit of a solar cell with series and shunt resistance

2.2 Solar cell theoretical curves modelling

There are two main curves which represent the characteristics of the voltage, current and power of the PV solar cell. The current-voltage (I-V) curve represents all possible current and voltage operating points for a PV cell. Similarly, the power-voltage (P-V) curve shows all possible operating points of the voltage and power generated by the PV cell.

Figure 2.3a and Figure 2.3b illustrate the theoretical output curves of a PV solar cell. As can be seen, the maximum current and voltage of the PV cell are equal to I_{sc} and V_{oc} respectively. The knee points, in both I-V and P-V curves, represent the maximum power point (MPP), where this point is the optimum output power produced by the PV cell which can be determined by choosing the ideal value of the connected load. The maximum power point is defined as the multiplication of the voltage and current at the MPP, where V_{mpp} and I_{mpp} are the voltage and current values at MPP that give the maximum operating output power. The unit of the MPP is Watt (W).

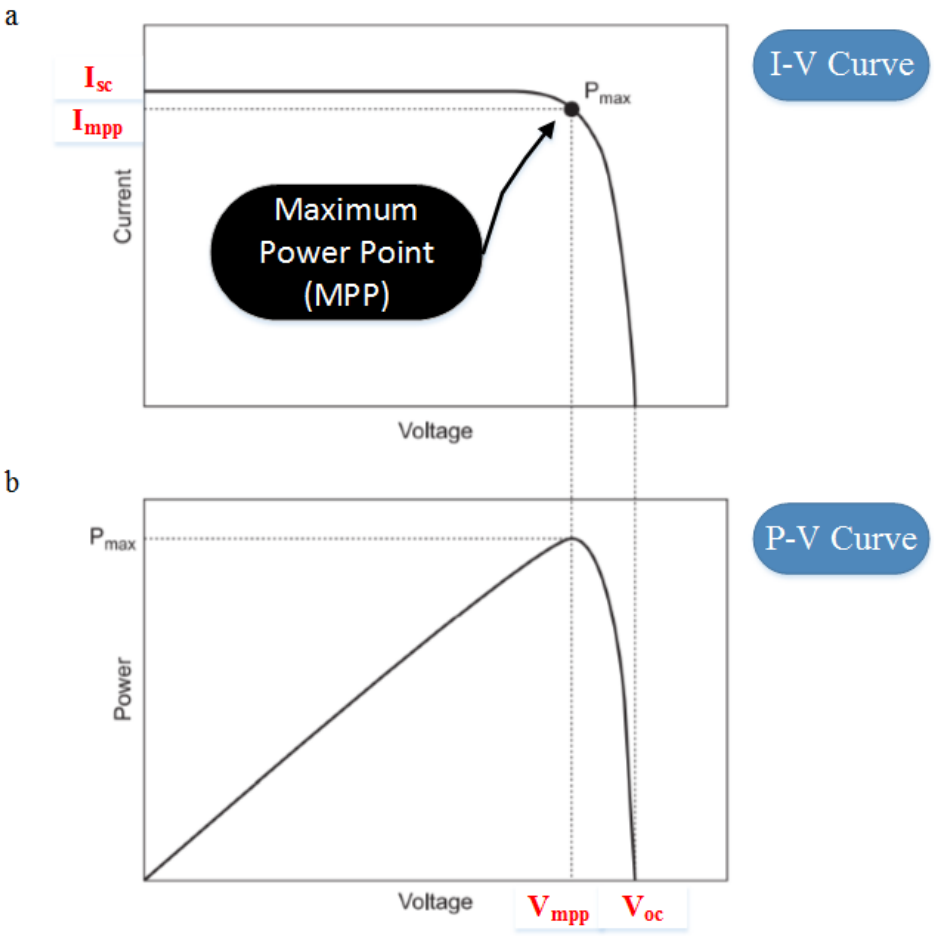

Figure 2.3 (a) The I-V characteristics of an ideal solar cell, (b) The P-V characteristic for an ideal solar cell

In fact, the I-V and P-V curves of the PV solar cell depend on the solar irradiance and the PV solar cell temperature. Figure 2.4a describes the behaviour a PV solar panel under various *G* levels and fixed solar cell temperature (25 ^{o}C). As the sun irradiance decreases, the output power produced by the PV panel decreases. MPP1, MPP2 and MPP3 are evaluated under three different irradiance levels: 1000 W/m^2, 700 W/m^2, and 500 W/m^2. In addition, the first case is called the standard test condition (STC) of any PV module at *G*: 1000 W/m^2 and *T*: 25 ^{o}C.

Furthermore, the behaviour of a PV panel under various temperature (*T*) levels and fixed solar irradiance is illustrated in Figure 2.4b. As the PV solar cell temperature increase, the output voltage and current also decrease. Thus, it will decrease the output power of the PV panel. Three various *T* levels are evaluated and compared in Figure 2.4b, where the *G* value is equal to 1000 W/m^2. The optimum MPP occurred in the first case, where the solar cell temperature is equal to 25 ^{o}C.

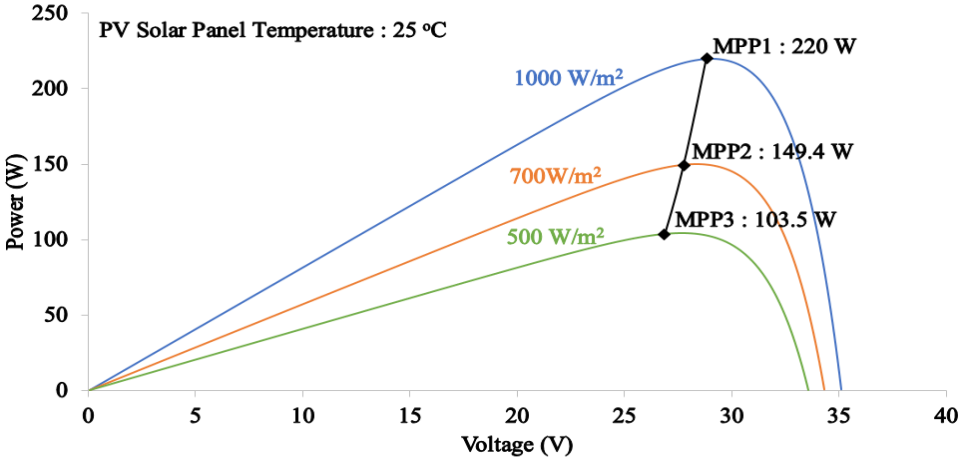

(a)

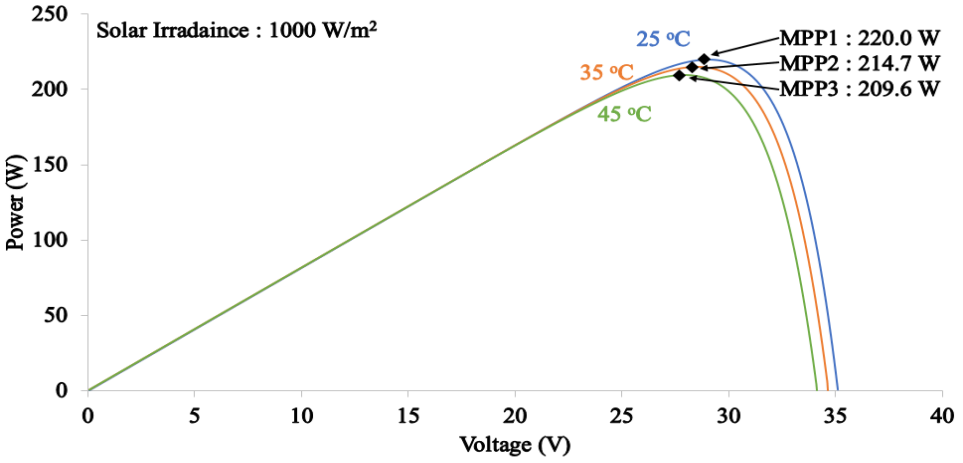

Figure 2.4 (a) P-V curve under various G levels, (b) P-V curve under various T levels

2.3 Overview of existing photovoltaic monitoring systems

In order to check the status and performance of a PV system, it is essential to implement a sustainable monitoring unit that is capable of monitoring, data logging and analysing number of parameters being measured in a PV plant. Therefore, a comprehensive review of various PV monitoring systems is presented in this section. This includes a detailed overview of all the major PV monitoring systems such as: sensors and their working principles, controllers used in data acquisition systems, data transmission methods, and data storage. The knowledge and understanding of all these aspects are crucial for the development of low cost, effective, and viable PV motoring systems for small and medium scale PV plants.

2.3.1 Monitoring PV and environmental parameters

The output power of a PV plant may decrease or increase drastically which leads to increased stress on the grid or sometimes causes power outage. Since PV achieves high penetration levels on utility grid, it is necessary to monitor the parameters for ensuring PV system reliability (von Appen, Braun, Stetz, Diwold, & Geibel, 2013). An important consideration in any PV monitoring system is the choice of parameters to be measured. These parameters are selected according to British Standard BS IEC 61724 (Commission, 1998). Based on the type of PV system configuration, a list of parameters is given in Table 1, which are distinguished as grid-connected and stand-alone PV system.

Two other PV parameters not listed in the BS IEC standard have been used; short circuit current, and open circuit voltage. Both parameters are used to identify the characteristics of the PV theoretical curves under partial shading and PV faulty conditions, both parameters are previously shown in Fig. 2.3.

Figure 2.5a and Figure 2.5b show the locations of different sensor of a typical grid-connected and stand-alone PV systems. The monitoring system consists of numerous sensors, which provide the data of different assets under various conditions. These data can be used by the operators in making decisions related to replacement, utilization and system reliability (Madeti & Singh, 2017a).

Table 2.1 Variables to be measured according to British Standard BS IEC 61724 (Commission, 1998)

PV system type	Parameters		
	Metrological	Electrical	
Grid-**connected**	1. Total solar irradiance, in the plane of PV array G_T 2. Ambient temperature 3. PV module temperature 4. Wind speed 5. Wind direction 6. Humidity 7. Barometric pressure	Photovoltaic: 1. Output voltage 2. Output current 3. Output power 4. Output energy	Utility grid: 1. Grid voltage 2. Current to utility grid 3. Power to utility grid 4. Power from utility grid 5. Utility grid impedance
Stand-alone			Load: 1. Output voltage 2. Output current 3. Output power

It is essential to measure the voltage and current in the PV system using voltage and current sensors. Generally, these sensors are embedded in the maximum power point tracking (MPPT) units which are connected to the PV modules.

Additionally, a large proportion of the solar radiation absorbed by the PV module does not reciprocate as electrical energy but leads to increase in the PV module temperature, and thus reduces its overall efficiency (Madeti & Singh, 2017a). One of the widely used temperature sensors is the thermocouple, since it can operate over wide temperature ranges (Bajzek, 2005). Another commonly used temperature sensor in PV systems is the resistance temperature detector (RTD). This type of temperature sensors has various advantages such as high stability, linearity and accuracy close to ± 0.1 ºC over a large range of temperatures (Webster & Eren, 2014).

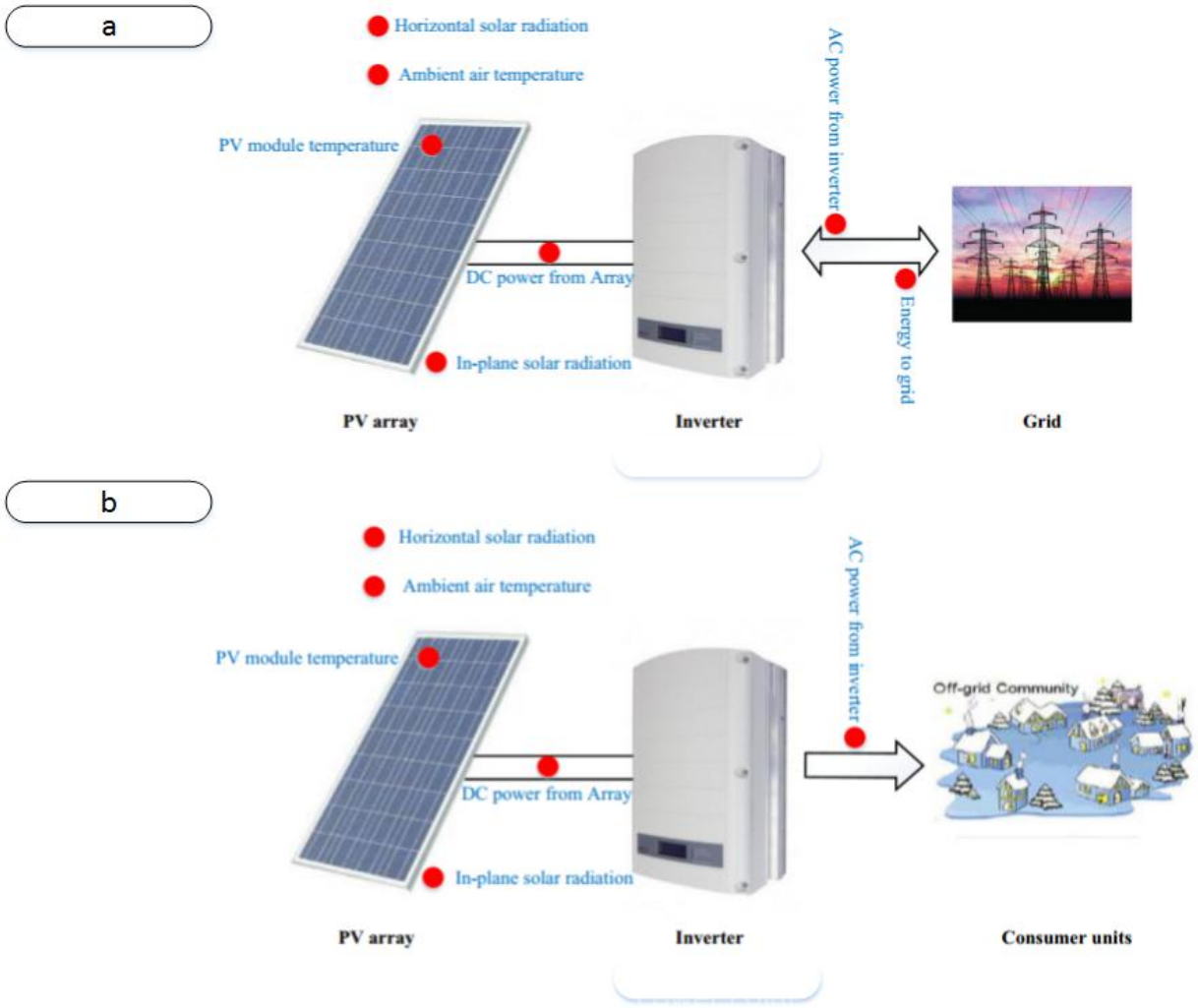

Figure 2.5 Variable monitoring for a PV system. (a) Grid-connected PV system, (b) Stand-alone PV system (Madeti & Singh, 2017a)

According to Table 2.1 and Figure 2.5, it is required to monitor the global solar radiation which is the sum of the diffused and reflected solar radiation. Nowadays, there are various types of sensors which convert the solar radiation into electrical current that can be measured by various means (Stoffel et al., 2000). Table 2.2 shows an overview of some of the current solar radiation sensors available on market.

Table 2.2 Different characteristics of various solar radiation sensor types (Madeti & Singh, 2017a)

Solar radiation sensor	Model number	Measurement range (W/m^2)	Temperature range (^oC)
Pyranometer	SP230-L	0 to 1750	-40 to +70
	LI200X-L	0 to 3000	-40 to +65
	LP02-L	0 to 2000	-40 to +80
	CMP6-L	0 to 2000	-40 to +80
	CMP11-L	0 to 4000	-40 to +80
	CMP22-L	0 to 4000	-20 to +50
Pyrheliometer	MS-56	0 to 4000	-30 to +80
	SHP1	0 to 4000	-30 to +60

2.3.2 Data acquisition system

Data acquisition (DAQ) systems play a vital role in the monitoring systems used in PV plants. Therefore, appropriate selection of a suitable DAQ system is an essential part of any PV system.

From a review of PV monitoring systems, summarized in Table 2.3, it is evident that there are several DAQ platforms used in data logging and monitoring the status of a PV systems, such as Virtual Instrumentation (VI) LabVIEW software, MATLAB/Simulink software and Web-based user interface applications.

Most recent monitoring units deployed in PV systems use wireless data transfer techniques such as XBee Pro, Bluetooth and radio frequency (RF) modules. Some monitoring units use a wired data transmission such as USB connection RS 485 proposed by (Hu et al., 2015) and Outback communication device manager.

Table 2.3 Review of recent monitoring systems implemented in PV plants

Year of the study	Research done by	Data transfer technology (wired)	Data transfer technology (wireless)	Used monitoring system
2015	(Shariff, Rahim, & Hew, 2015)	Not included	XBee Pro	LabVIEW
	(T. Hu, Zheng, Tan, Zhu, & Miao, 2015)	Not included	Wireless sensor network	Web-based user interface and Mobile phone application
2016	(Guerriero, Di Napoli, Vallone, d'Alessandro, & Daliento, 2016)	USB connection RS 485	Wireless sensor based on Microchip MiWi	Web-based user interface
	(Adhya, Saha, Das, Jana, & Saha, 2016)	Not included	SIM900 GPRS module	Web-based user interface and LCD monitoring device
	(Le, Tsai, & Lam, 2016)	STM32F4 discovery board	Bluetooth modules	MATLAB/Simulink
	(Touati, Al-Hitmi, Chowdhury, Hamad, & Gonzales, 2016)	Not included	XBee Pro	Web-based user interface and LabVIEW software
2017	(Kabalci & Kabalci, 2017)	Not included	XBee Pro	Visual Studio Net software development kit
	(Han, Jeong, Lee, & Kim, 2017)	Not included	Universal asynchronous receiver and transmitter (UART)	Power line communication (PLC) modules

2.4 Overview of Photovoltaic Faults

PV systems are subject to a variety of faults, including partial shading conditions impacting on the output power of the PV module, the maximum power point tracking units, PV hot spots, and PV micro cracks. The energy loss due to PV faults has been analysed and categorized in UK domestic PV systems and it was estimated that the annual energy loss is equal to 3.6% (Site A, first year of operation), 6.6% (Site A, second year of operation) and 18.9% (Site B, first year of operation) due to PV faults as described by (Firth et al., 2010). Both sites are shown in Figure 2.6a.

Monitoring systems were used in each site to record the performance of the PV modules. The monitored parameters in each site are shown in Figure 2.6b. Based on the analysis reported in (Firth et al., 2010), the largest energy loss was caused by sustained zero efficiency faults (when the monitored PV systems stopped generating power for long period). The second largest cause of energy loss was due to partial shading conditions affecting the PV modules. Therefore, in this section, PV faults and the suggested solutions from the literature will be discussed and evaluated.

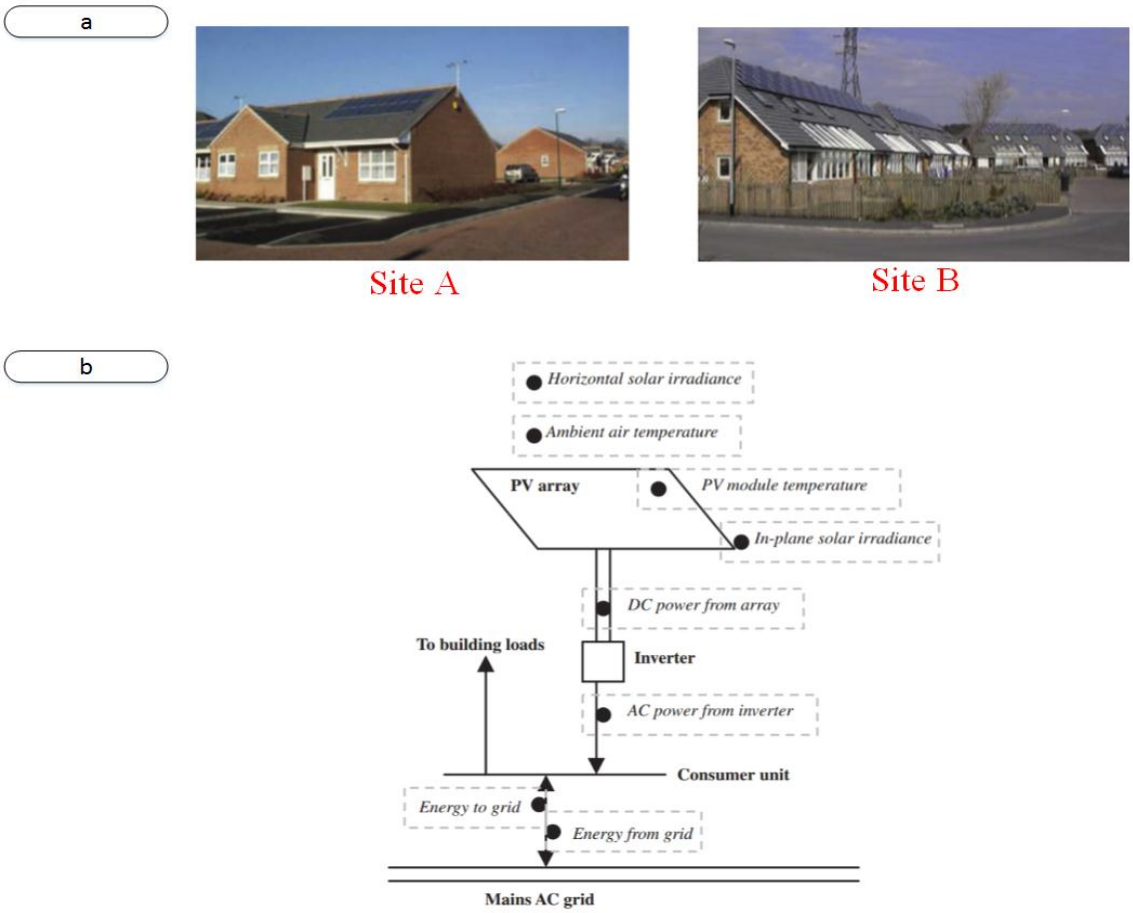

Figure 2.6 (a) Examined site A and Site B, (b) Monitored parameters for the PV systems (Firth, Lomas, & Rees, 2010)

2.4.1 Impact of partial shading conditions on the PV output power performance

Partial Shading (PS) conditions often occur in PV systems due to a number reasons, such as movement of the clouds, tall trees next to the PV installation, and some environmental conditions such as dust and snow. PS conditions cause losses in the PV system output power, hot spots effect, and system safety and reliability problems (Liu et al, 2015).

To study the impact of PS conditions, four different case scenarios have been simulated using a single PV module as shown in Figure 2.7a. The first case has been simulated during normal operation of the PV module (no PS), where the second, third, and fourth case are simulated under 10%, 50% and 75% PS. In all tested scenarios G and T are at STC (1000 W/m^2 and 25^{o}C).

Figure 2.7b illustrates the impact of PS conditions on a PV module using the theoretical P-V curve. It can be observed that, as the PS condition increases, the MPP of the PV module decreases. For example, the MPP of the PV module which is affected by 10% PS is equal to 196.9 W. However, by increasing the PS condition up to 75%, the MPP of the PV module decreases to 50.26 W (Gupta, 2016). The simulation results are not available in the article (Gupta, 2016). The results shown in Figure 2.7 are recreated using LabVIEW software to demonstrate the effect of PS conditions on the performance of PV modules.

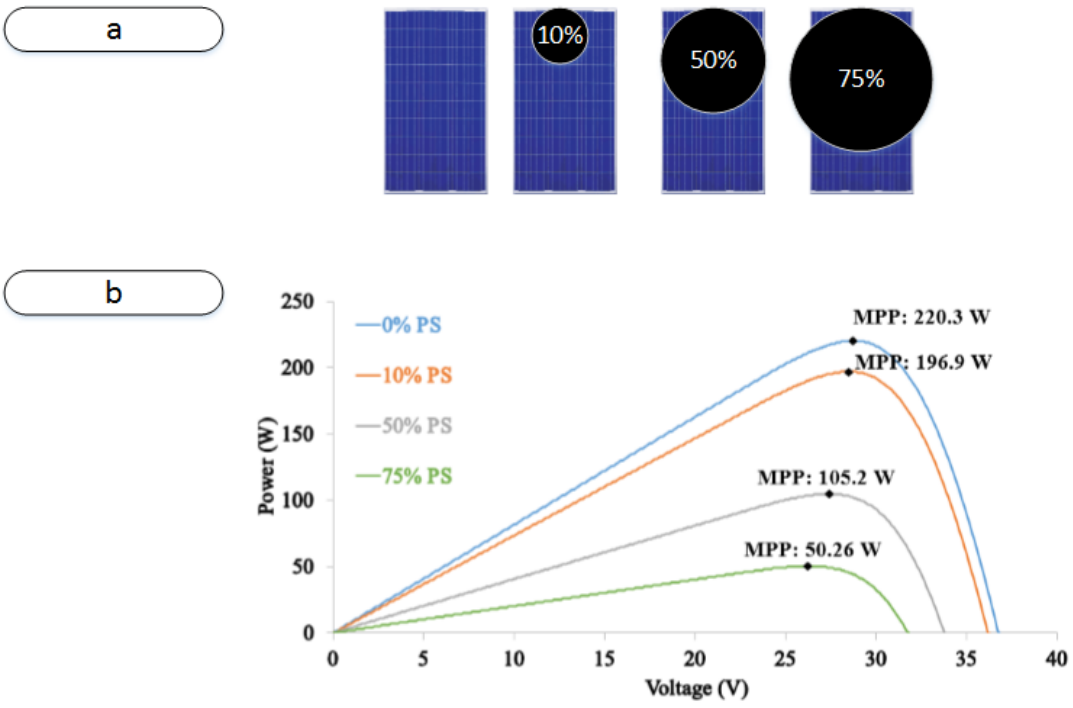

Figure 2.7 (a) Percentage of PS applied to a single PV module, (b) P-V curve of the PV module for each PS condition

Generally, in the UK private homes, PV systems are connected in an array of series PV modules (Firth et al., 2010; Freeman, Hellgardt, & Markides, 2017). The impact of PS conditions affecting this type of PV array configuration is simulated using six PV modules as shown in Figure 2.8a, where G and T are simulated at STC.

As illustrated in Figure 2.8b, at STC condition, the MPP is equal to 1322 W. However, a loss in the MPP is equal to 349.4 W during 25% PS affecting all PV modules. This large reduction in the output power of the PV system has been evaluated and enhanced by many techniques. A review of recent methods for enhancing the output power due to PS conditions affecting PV systems can be divided into three main categories:

A. MPP enhancement of PV systems due to PS conditions using bypass diodes
B. The development of new PV array configuration systems
C. Advanced MPPT techniques for mitigating PS conditions affecting PV systems

The simulation results are not available in the articles (Firth et al., 2010; Freeman, Hellgardt, & Markides, 2017), results shown in Figure 2.8 are recreated using LabVIEW software to demonstrate the effect of PS conditions on the performance of series connected PV modules.

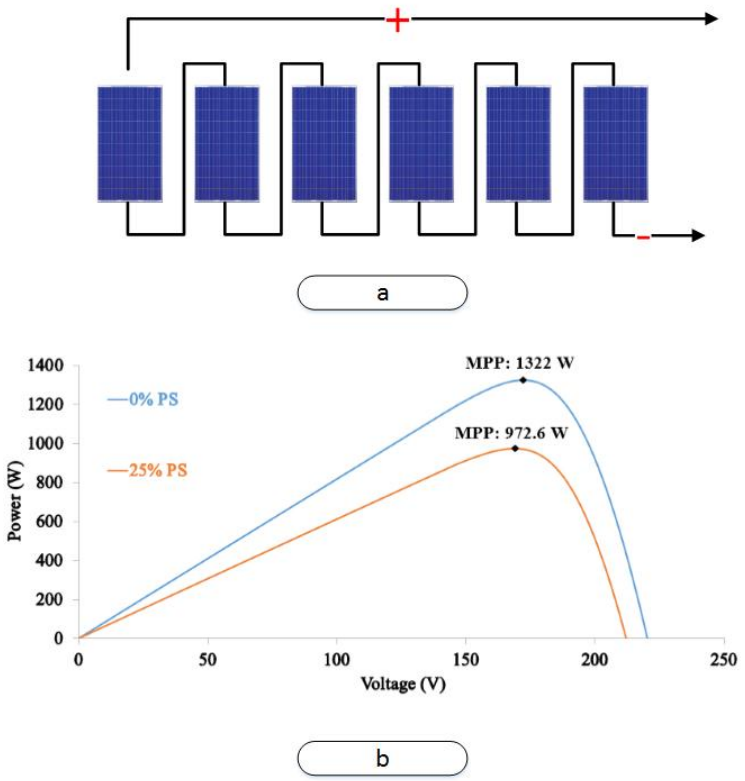

Figure 2.8 (a) Six PV modules connected in series, (b) 25% PS affecting all PV modules

2.4.1.1 Enhancement of PV output power due to PS conditions using bypass diodes

The effect of PS conditions in PV systems can be reduced and thus, increase the output power of the PV systems achieved using bypass diodes. A bypass diode is connected in parallel with each PV module, but with opposite polarity as shown in Figure 2.9a.

In 1984, a protection technique of PV modules was invented by (Lesk, 1984) using the parallel connection of bypass diodes across the PV modules. The patent shows that there is a huge improvement in the output power due to the reversely poled diode across each of the series connection PV solar cells in PS conditions. However, this protection technique was not developed on a full scale PV module which comprises multiple solar cells connected in series.

Moving to 1988, a protected solar cell including a monolithic bypass diode is formed by addition of an additional layer of semiconductive material having a type opposite to the outermost semiconductive layer of a solar cell was invented by (Cohen, 1988). The author of the patent claimed that the connectivity of bypass diodes across the PV solar cells increases its output power efficacy during PS conditions and some other environmental factors such as the change of sun irradiance and solar cell temperature variations.

The first PV module with integrated solar cell bypass diode was developed by (Kukulka, 1997). Each bypass diode is bonded to the solar cell for anti-parallel connection across the solar cell. As shown in Figure 2.9b, the bypass diode 10 and solar cell 12 are connected in an anti-parallel configuration such that the bypass diode is reverse biased when the solar cells are illuminated. Bypass diodes that have very low reverse currents are preferred to avoid reducing current in the solar cell during normal operation, which would reduce the efficiency of the PV module (Kukulka, 1997).

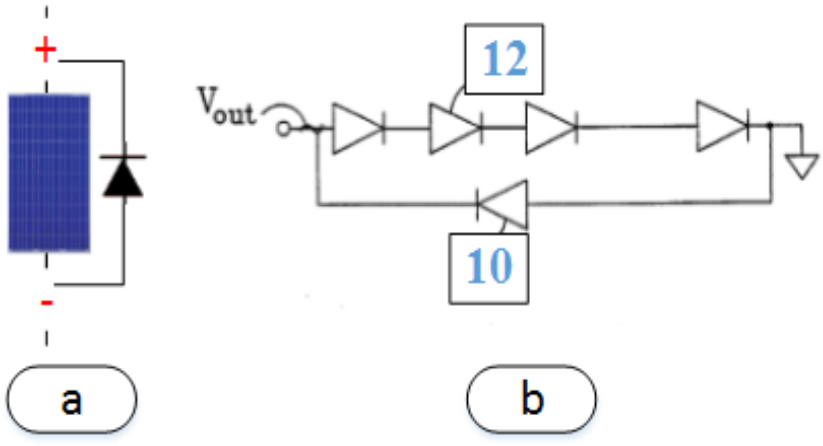

Figure 2.9 (a) Bypass diode connected in parallel with a PV module, (b) Series string of solar cells connected in an anti-parallel configuration with a bypass diode (Kukulka, 1997)

Another invention has been proposed by a German scientist (Müller, 2002). This invention relates to a production method for a solar cell which comprises an integrated bypass diode on the side facing away from the incident of light and which can be produced in simple manner by diffusion. Figure 2.10a shows a sectional view of the proposed method according to the invention.

The proposed method claimed that the blocking behavior of the bypass diodes can be optimized independent of the actual solar cell. The highest-possible breakdown voltage and a low forward voltage are sought that drive shaded solar cells in reverse direction. Thus increase the efficiency of the PV solar cells during PS conditions. In addition, this invention has a significant impact since the described procedure of the connectivity for the bypass diodes are integrated in the substrate material before the procedural steps to manufacture the photoelectric solar cell layers.

Later in 2008, a bypass diode is provided in the semiconductor structure with a region of first polarity of the solar cell connected with a region of second polarity of the bypass diode. This invention was developed by (Sharps, 2008). Figure 2.10b shows the circuit diagram of the proposed PV bypass diode structure. The cells A, B, and C are arranged in the same order and are electrically connected to a bypass diode.

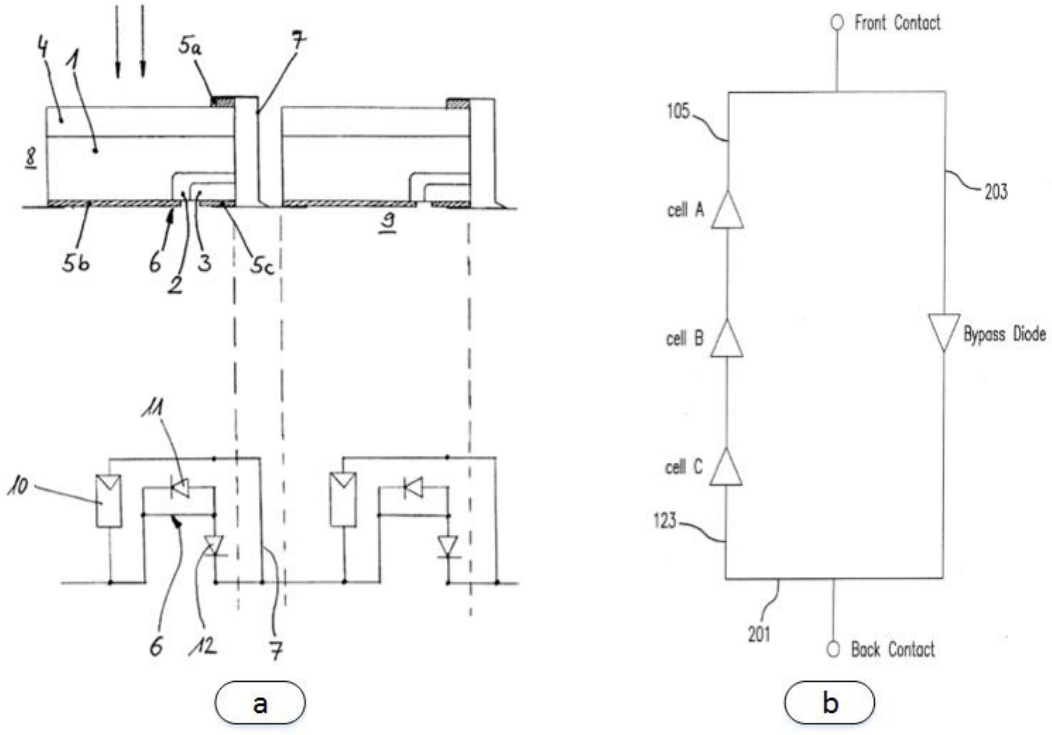

Figure 2.10 (a) Sectional view of solar cells according to the invention proposed by (Müller, 2002), (b) Circuit diagram of the solar cell and bypass diode according to the invention presented in (Sharps, 2008)

Most recently, a solar cell structure including a silicon carrier with a bypass diode is invented by (Ho & Suh, 2014). The proposed solar cell structure significantly increases the solar cell MPP. Additionally, it reduces material and manufacturing cost, and provides much more flexibility of the solar cell structures. Furthermore, a similar approach has been invented in 2017, where the main difference is the corner integration of the bypass diode interconnecting configuration for multiple solar cells instead of a single solar cell structure as described in (Hoang & Beyene, 2017).

Nowadays, PV modules manufactures include a multiple of bypass diodes within the PV module sub strings, as shown in Figure 2.11. Romag SMT 6(60) P PV module is an example of a PV module which contains three bypass diodes connected in parallel with the sub strings of the PV module. Figure 2.11a shows a real image of a PV module, while Figure 2.11b shows a connection box. The sub strings are connected to each bypass diode as illustrated in Figure 2.11c.

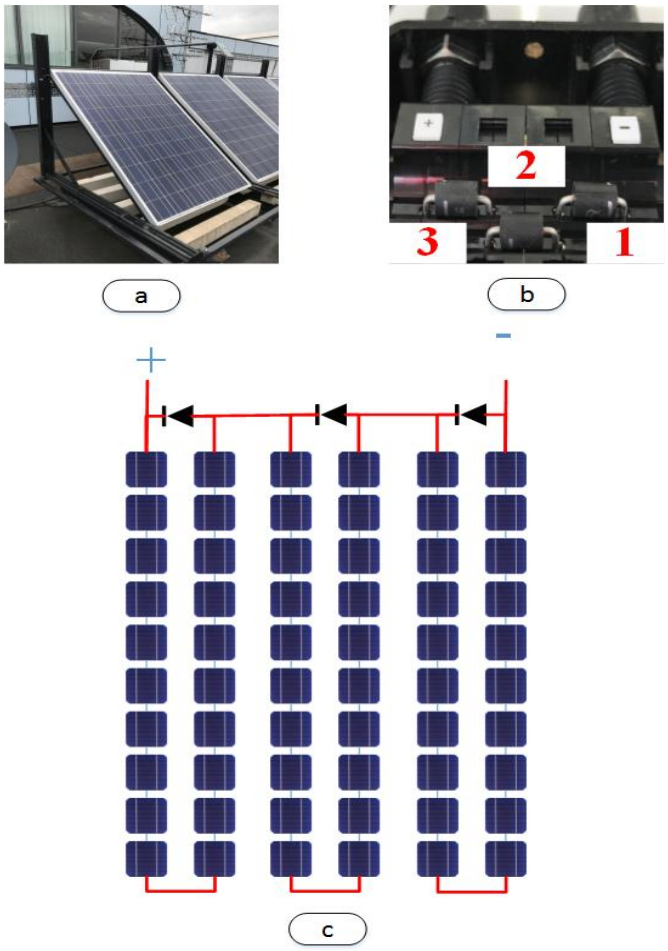

Figure 2.11 (a) Real image of SMT 6(60)P PV module, (b) PV module connection box, (c) PV module sub string connections to the bypass diodes

In order to understand better the impact of PS conditions in PV systems, the PV module shown in Figure 2.11a has been evaluated using two case scenarios: without and with bypass diodes connected to the PV panel. Figure 2.12a shows the simulation results for the PV module under STC and 30% PS condition. The MPP of the PV module without connecting any bypass diode is equal to 150.6 W, however, the MPP is increased to 169.7 W after connecting 3 bypass diodes to the PV module sub strings.

As can be seen in Figure 2.12b, while connecting bypass diodes to the PV module, the P-V curve shows multiple MPP peaks; that is, the curve comprises a global MPP (GMPP) and local MPP (LMPP). As a result, the PV module will remain running at the GMPP, therefore, more output power will be guaranteed from the PV module. However, in order to achieve this target, a global maximum power point tracking (GMPPT) technique must be used with the PV module. Figure 2.12 is recreated using LabVIEW software to demonstrate the effect of bypass diodes on the output power of a PV module.

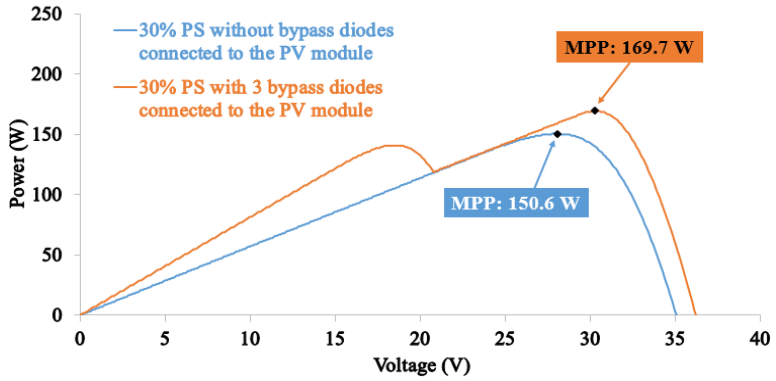

(a)

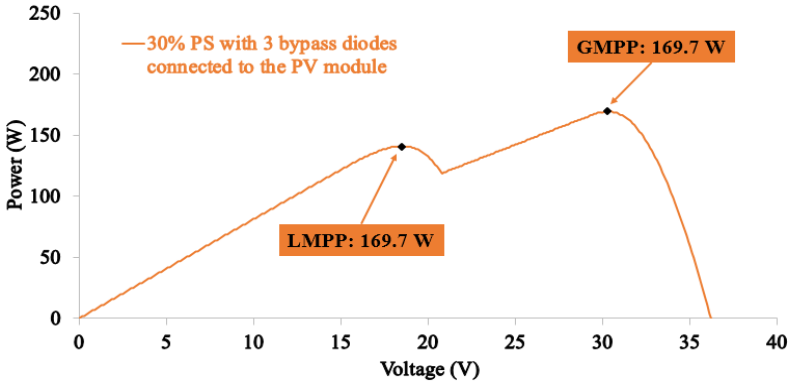

(b)

Figure 2.12 (a) Simulation results under STC for PV module shown previously in Figure 2.11, (b) LMPP and GMPP for 30% PS with 3 bypass diodes connected to the PV module

In conclusion, this section shows a significant improvement of the resulted MPP of the PV module which is affected by PS conditions. However, the application of the bypass diodes has been further investigated using multiple PV array configuration systems to enhance the output power of the PV module during PS conditions. This will be discussed in the following section.

2.4.1.2 The development of new PV array configuration systems

PV modules can be wired in different configurations. The impact of PS conditions affecting PV modules with different connection configurations has been investigated widely.

Five different PV connection configurations have been studied and compared by (Wang & Hsu, 2011), where the investigated PV configurations are: SS (simple series), SP (series-parallel), TCT (total-cross-tied), BL (bridge-linked) and HC (honey comb) configurations. A randomly generated solar irradiance has been applied on the five listed PV configurations, where the applied solar irradiance values are shown in Figure 2.13a. The average output power during all tested irradiance levels are reported in Figure 2.13b. In addition, PS conditions have been applied in each solar irradiance level with different PS percentage. It is found that in most PS conditions, the TCT configuration has a better performance over the other four configurations.

A detailed mathematical analysis of the TCT configuration under normal and PS conditions has been further investigated by (Mohammadnejad, Khalafi, & Ahmadi, 2016). Five different PS patterns have been tested on SP, BL, HC, and the TCT PV array configurations. Additionally, another test has been carried out using multiple PV array sizes such as 4x4, 5x4, 6x4 and 4x5 (Row x Column). The results show that TCT configuration has the least PV output power loss compared to all other tested PV array configurations.

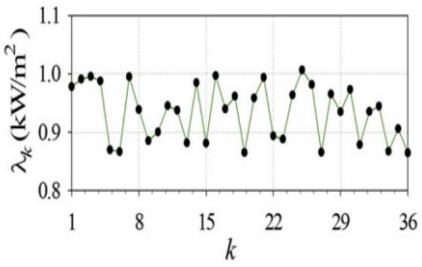

(a)

PV Configuration	Average Power (W)
SS	48.7
SP	48.8
TCT	49.2
BL	48.9
HC	49.1

(b)

Figure 2.13 (a) Randomly tested solar irradiance levels, (b) Comparison of the five PV configuration output power (Wang & Hsu, 2011)

In 2013, an approach developed by (Rani et al., 2013) used that same physical location of the modules in a TCT connected PV array. However, the arrangement of the PV modules is based on "Su Do Ku" puzzle pattern so as to distribute the PS shading over the entire PV array. The performance of the system is investigated for different shading patterns and the results show that positioning the modules of the array according to "Su Do Ku" puzzle pattern yields improved performance under partially shaded conditions.

Figure 2.14a shows the TCT arrangement of the PS affecting some PV modules in the entire PV array, where Figure 2.14b shows the "Su Do Ku" arrangement of the same PS conditions. However, the dispersion of the shading in the PV array due to the "Su Do Ku" arrangement is illustrated in Figure 2.14c. In figure 2.14d, it can be observed that applying the same shading pattern to the "Su Do Ku" PV arrangement, increases the generated PV output power from 4711 to 5045 W, which is 6.6% higher compared to the TCT arrangement.

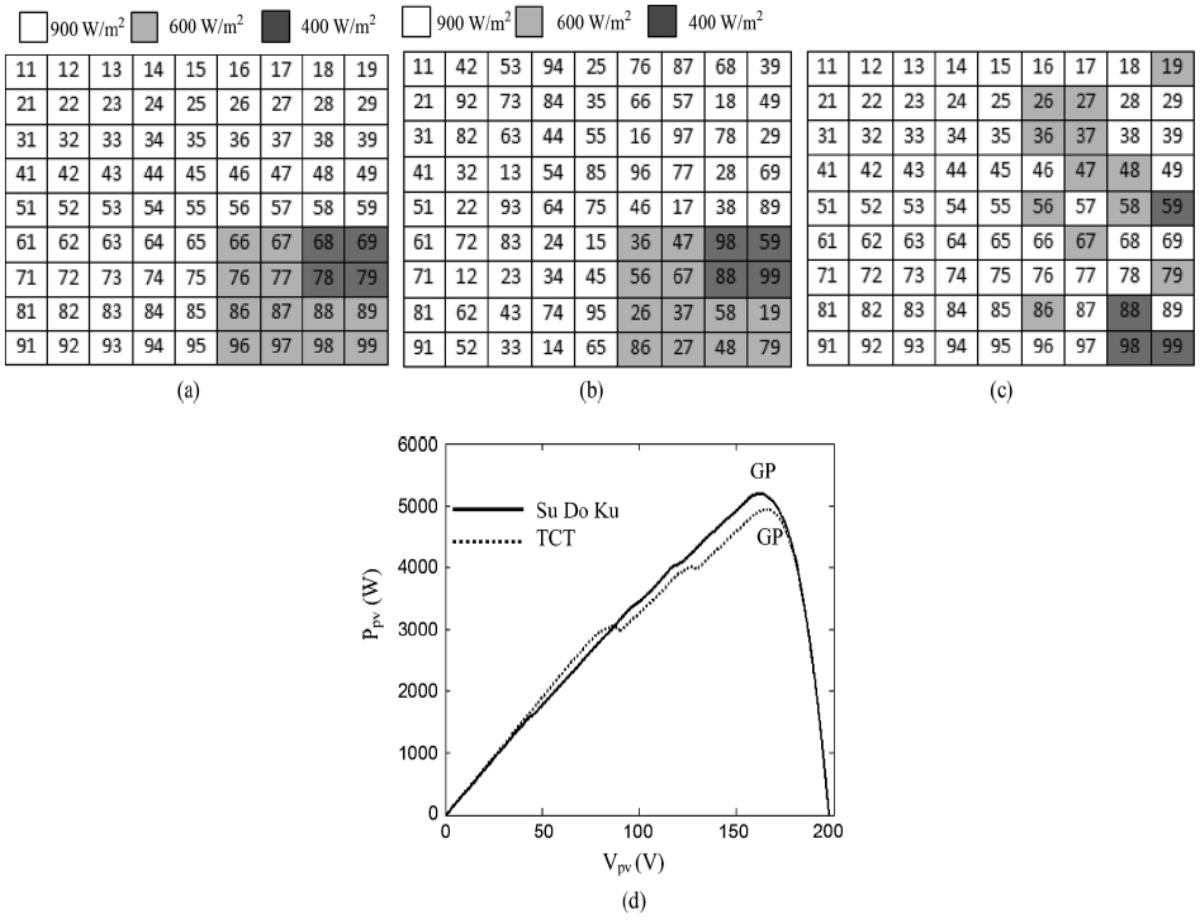

Figure 2.14 PS pattern affects a PV array. (a) TCT arrangement, (b) Su Do Ku arrangement, (c) Shade dispersion with Su Do Ku arrangement, (d) PV characteristics of the examined PV array including the GMPP (Rani, Ilango, & Nagamani, 2013)

Another configuration modification is the Electrical Array Reconfiguration (EAR) which consists of dynamically changing the electrical connections of PV modules. The main idea in the EAR approach is to adapt the PV arrays using a controllable switching matrix to select a configuration that reduces as much as possible the PS loss for a given shading pattern. This strategy requires a fully reconfigurable PV array and necessitates sensors and switches that increase system complexity and cost (Parlak, 2014; Tian, Mancilla–David, Ellis, Muljadi, & Jenkins, 2013).

Static reconfiguration of PV array is an alternative to EAR that achieves a balance between cost, complexity and PV efficiency. This approach relies on finding a PV module arrangement with a fixed predefined TCT configuration (Potnuru, Pattabiraman, Ganesan, & Chilakapati, 2015). Such arrangements and others discussed in (Deshkar, Dhale, Mukherjee, Babu, & Rajasekar, 2015; Rao, Ilango, & Nagamani, 2014) operate with an array having an equal number of rows and columns, and are restricted to adjusting the electrical connections of the PV modules which are in the same physical PV array row.

As a consequence, shading dispersion is limited and protection diodes power consumption is high. Similar approaches to change the PV module arrangement within a PV array under TCT and other configurations are discussed for example in (Celik, Karatepe, Silvestre, Gokmen, & Chouder, 2015; Yadav, Pachauri, & Chauhan, 2016). These arrangements still locate PV modules in the same column and are in fact almost identical to "Su Do Ku" approach shown previously in Figure 2.14. In addition, these new PS mitigation techniques have not taken into account the power dissipation of blocking and bypass diodes in the PV systems and, in most cases, have only been applied to small scale PV arrays (Vijayalekshmy, Bindu, & Iyer, 2016).

Most recently, a PS mitigation approach is developed by (Belhaouas et al., 2017) using three new physical PV array arrangements (shift-modified-cross tied linked (S-M-TCT), S-M-TCT + blocking diodes (BLK), and parallel shift-modified- cross tied linked (//S-M-TCT)). The arrangements are based on maximizing the distance between adjacent PV modules within a PV array by appropriately arranging modules in different rows and columns without changing the electrical connections. The new PV arrangements are shown to effectively obtain the following:

i. Eliminate multiple output power peaks
ii. Maximize output power of the PV system

Various shading scenarios have been conducted, and in conclusion, the proposed new PV arrangements generate higher output power compared to SP, TCT and "Su Do Ku" PV configurations as shown in Figure 2.15.

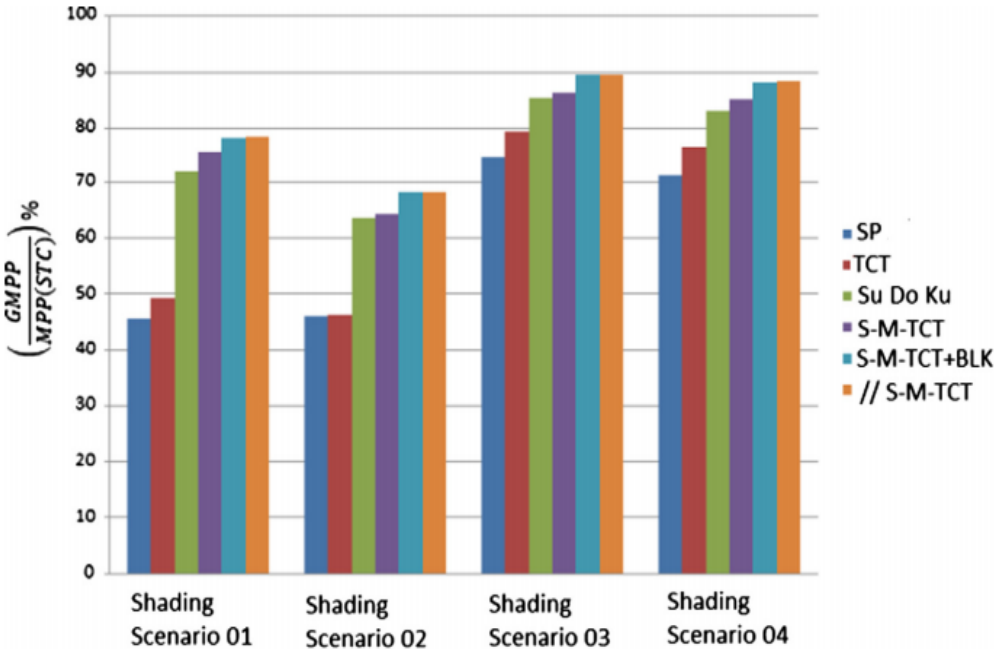

Figure 2.15 GMPP (%) for the various configurations and arrangements under shading scenarios 1–4 with different irradiation levels (Belhaouas et al., 2017)

An approach using MATLAB/Simulink software developed by (Yadav, Pachauri, Chauhan, Choudhury, & Singh, 2017) analysed the performance of TCT, series parallel - total cross-tied (SP-TCT), bridge link-total cross-tied (BL-TCT), bridge link- honey comb (BL-HC), Magic Square (MS) and MS puzzle pattern based reconfiguration like Re-arranged total-cross-tied (RTCT), Re-arranged series parallel- total-cross-tied (RSP-TCT), Re-arranged bridge link- total cross-tied (RBL-TCT) and Re-arranged bridge link-honey comb (RBL-HC).

The performance of all tested PV array configurations has been investigated using the P-V curve characteristics, power loss due to shading, fill factor, and shading dispersion effect on the MPP for various shading patterns such as:

1. Vertical shading
2. Horizontal shading
3. Diagonal shading

The main finding of this work is that the MPP of MS and RTCT configurations is at least 2279 W more than the TCT configuration. Also the mismatch power loss is 300 W less, and fill factor (FF) is 9.91 more than TCT configuration.

2.4.1.3 Advanced MPPT techniques for mitigating PS conditions affecting PV systems

The third mitigation technique for PS conditions affecting PV systems is the development of advanced MPPT techniques implemented in PV systems. Therefore, in this section a critical analysis on the conventional methods and soft computing techniques implemented for MPPT in PV systems will be briefly discussed.

In fact, MPPT is algorithm that includes in charge controllers used for extracting the maximum available power form PV modules under certain environmental and load conditions (Ram, Babu, & Rajasekar, 2017). One of the most popular methods used for MPPT in PV systems is Perturb and Observer (P&O) method. In this method, based on sensor inputs the PV power is calculated and the voltage perturbations are introduced to deduct the direction of tracking. According to the voltage perturbation the output power may either continuously rise or fall. Thus, the algorithm continuously keeps tracking the MPP via voltage perturbations. One of the earliest development of P&O technique is done by (Femia et al., 2005). Authors implemented the P&O algorithm in a DC-DC boost converter with a reference sampling time of 0.01 ms. However, the designed system seemed to be feasible under steady state conditions, but it greatly suffered during dynamic change in irradiation conditions. The proposed P&O is shown in Figure 2.16a.

The drawback of P&O in varying atmospheric conditions is well handled in methods proposed in (Abdelsalam, Massoud, Ahmed, & Enjeti, 2011; Ahmed & Salam, 2015), where the problem of steady state oscillations around MPP is reduced considerably. Table 2.4 summarizes the different P&O approaches developed for MPPT in PV systems. Another interesting method for maximising the output power of a PV module is the incremental conductance (IC). Usually, to track MPP using the IC method, three common steps are applied:

i. When $\frac{dP}{dV} = 0$, the error is zero and V_{mpp} can be achieved
ii. When $\frac{dP}{dV} > 0$, the MPP is dragged towards the left of the I-V curve (error is positive)
iii. When $\frac{dP}{dV} < 0$, the MPP is dragged towards the right of the I-V curve (error is negative)

The flowchart of a simple IC method is shown in Figure 2.16b. The researchers have followed many techniques to reduce the tracking error in IC method. An improved IC method with variable step size is introduced in (Li & Wang, 2009). The duty cycle generation is done based on Equation (2.4).

$$D(k) = D(k-1) \pm N * \left|\frac{P(k)-P(k-1)}{V(k)-V(k-1)}\right| \quad (2.4)$$

where k is the iteration value, P is the output power, V is the voltage, D is the duty cycle and N is the scaling factor that determines the accuracy of the MPP tracking.

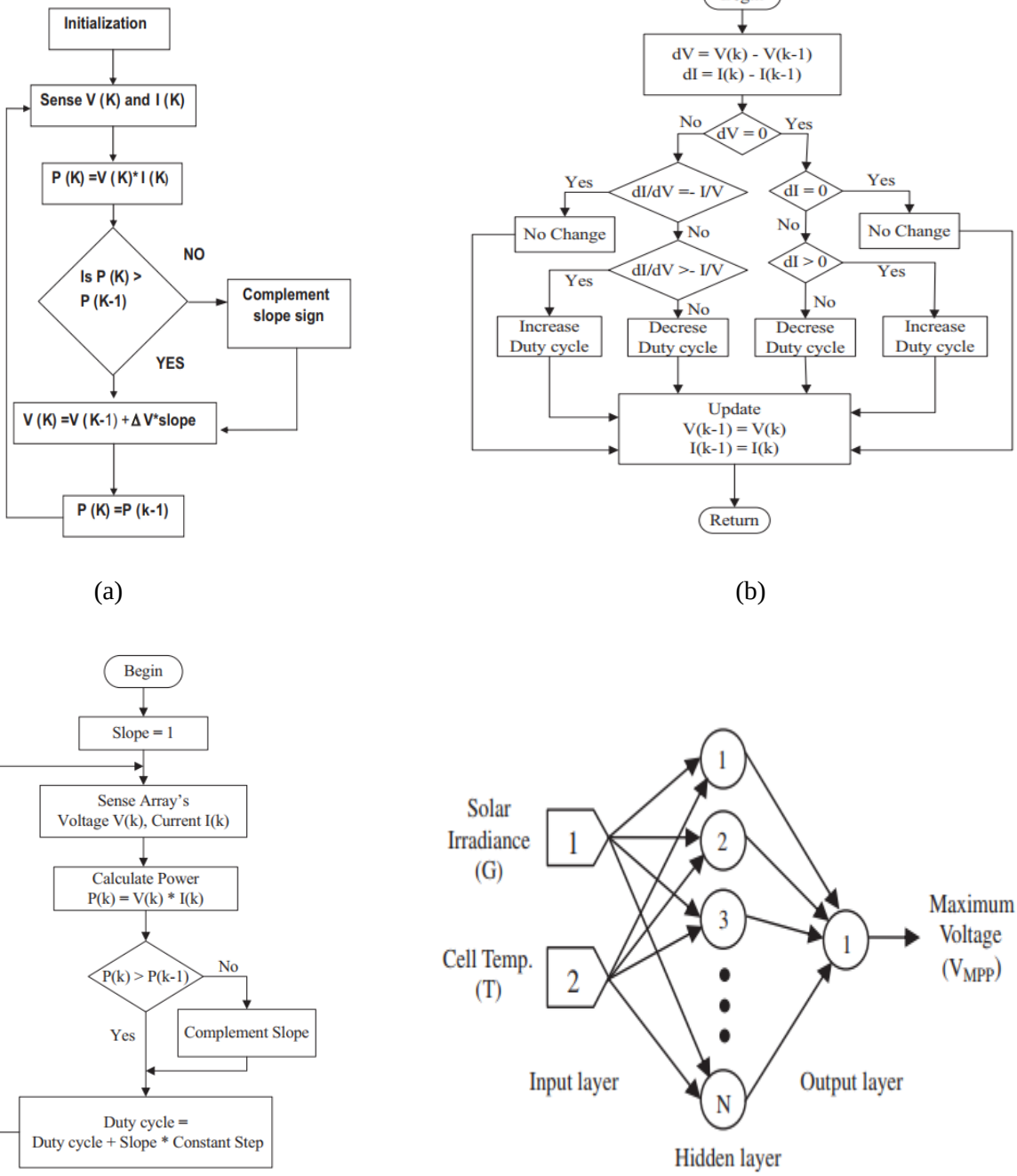

Figure 2.16 (a) Flowchart of a simple P&O algorithm (Femia et al., 2005), (b) Flowchart for IC algorithm (Lee, Bae, & Cho, 2006), (c) Flowchart of HC algorithm (F. Liu, Kang, Zhang, & Duan, 2008), (d) ANN configuration used to determine reference voltage at MPP (Kulaksız & Akkaya, 2012)

In (Radjai, Rahmani, Mekhilef, & Gaubert, 2014) the authors used fuzzy rules in combination with IC algorithm to continuously change the duty cycle values. The PV systems employed with IC algorithms are considered to be the best choice for low power applications since this method showed excellent performance for steady change in solar irradiance conditions (Radjai et al., 2014). However, this method fails to reach equilibrium state quickly and the converter duty cycle continues to oscillate around the MPP (Sivakumar, Kader, Kaliavaradhan, & Arutchelvi, 2015).

Table 2.4 Comparison of P&O approaches

Reference	Control variable	Converter type	Application	Description
(Femia, Petrone, Spagnuolo, & Vitelli, 2005)	Duty cycle	Boost converter	Grid-connected system	The author has analysed dynamic behavior of the system in boost converter and tested the system under various irradiation conditions.
(Ishaque, Salam, & Lauss, 2014)	Duty cycle	Buck-Boost converter	Stand-alone system	A PI controller is used to reduce the error in duty cycle. This ensures maximum power from PV array. The system can also be extended to grid connected systems.
(Kollimalla & Mishra, 2014)	PV Current	Boost converter	Stand-alone system	A new P&O based on short circuit current is proposed by using dSpace. The algorithm is tested under various irradiated conditions and varying output is obtained.
(Elgendy, Zahawi, & Atkinson, 2015)	Duty cycle	Buck converter	Stand-alone system	The P&O is implemented in 1080 W PV array. The efficiency of system is compared with three level operations and it is been proved that high perturbation has improved efficiency comparatively.
(Ahmed & Salam, 2015)	Duty cycle	Buck-Boost converter	Stand-alone system	The author has used this condition ($T_{r1} < \frac{\Delta P}{P} > T_{r2}$) to check the change in MPP values and the duty cycle is generated based on the boundary conditions to ensure proper MPP is reached effectively.

Hill Climbing (HC) method is one of the recommend MPPT techniques used in PV systems nowadays. It is widely used due to its simplicity and effectiveness. In this method, the voltage and current of the PV system is sensed and based on the calculated output power, the duty cycle of the converter is adjusted. The duty cycle is either incremented or decremented, so after a certain number of cycles, the converter is able to reach the MPP duty cycle (F. Liu et al., 2008). The flow chart of the HC method is shown in Figure 2.16c.

FLC-HC method presented in (Alajmi, Ahmed, Finney, & Williams, 2011) uses a Fuzzy Logic control (FLC) approach for controlling the duty cycle of the HC method. The new proposed controller improves the HC method by fuzzifying the rules of such techniques and eliminates their drawback. The proposed FLC-HC method offers fast and accurate converging to the MPP of stand-alone PV system. In each tested operating condition, the MPP is attained in a relatively short time and has a small oscillation in steady state. Moreover, when the weather conditions are changed, the FLC-HC algorithm forces the power to move directly to the new optimum point.

The major drawback of the HC and FLC-HC methods is that they fail to converge at 100% of the MPP; also the time taken to reach the steady state depends on the initial value of duty cycle and step size.

Most recently, some advanced MPPT techniques have been proposed and tested in PV systems. Artificial Neural Network (ANN) based MPPT algorithm is used to track the MPP of PV systems as presented by (Kulaksız & Akkaya, 2012). The approach uses a genetic algorithm (GA) optimized ANN based MPPT to maximize the MPP of a stand-alone PV system using boost converter. The major impact of this research is reducing the response time down to 0.06s due to varying the step size, and oscillations around the MPP.

Another interesting MPPT algorithm suggested by (Hassan et al., 2017). The algorithm is based on Neuro-Fuzzy wavelet based adaptive MPPT control. The proposed MPPT controller combines the reasoning capability of Fuzzy Logic, the learning capability of ANN networks and the localization properties of wavelets. The algorithm shows a superior performance comparing to P&O, IC and the FLC approaches. The efficiency of the technique is equal to 96.81% which is higher than the conventional FLC approach which has an efficiency of 83.66%.

In conclusion, this section shows that there are a variety of MPPT algorithms implemented in PV systems to track the MPP. The algorithms are based on different parameters such as duty cycle of the converters, PV output power, PV output current and PV output voltage. Some advanced techniques have been implemented such as FLC-HC and Neuro-fuzzy wavelet based adaptive MPPT control. However, up to date, there are few attempts to maximise the output power in PV systems for various PV array configurations (illustrated previously in section B).

2.4.2 Detecting faulty PV modules

Failures in PV arrays occur for several reasons such as line-to-line faults, arc faults and disconnection of PV modules in the PV strings. This section will demonstrate the recent fault detection algorithms which are implemented to detect faulty PV modules in PV strings. From the literature, it was identified that PV fault detection algorithms can be classified into two main categories: Statistical and mathematical modelling techniques, and machine learning techniques such as Fuzzy Logic and ANN networks.

2.4.2.1 Statistical and mathematical modelling techniques

Early in 2006, a modeling and fault diagnosis of a 3 kW PV system has been proposed by (Chao, Ho, & Wang, 2008). The proposed fault detection method will firstly create a set of fault matter-element of PV modules, and then a regular extended correction function will identify the fault type of the PV arrays by calculating the degrees of extended correction. The mathematical calculations used in this study are complex, since it depends on the variations of a vector element used in multi-dimensional matter-element. Thus, the correction function is not easy to recreate in larger PV system size (i.e. 10~15 kW).

In addition, the biggest limitation of the proposed fault detection algorithm is the lack of the capability of detecting PS conditions occurring in the PV system. However, this work was one of the earliest research that uses a mathematical expressions to identify the region of the fault occurring in a small scale size PV installation.

Later in 2010, authors (Chouder & Silvestre, 2010) proposed an automatic supervision and fault detection of a PV system based on power loss analysis. In this work, the fault detection algorithm used two indicators to identify the type of the fault occurring in the PV system. The first layer of the proposed fault detection algorithm is identifying whether the PV system has a fault. For that purpose Equation (2.5) has been introduced.

$$L_{c\_sim} = Y_r(G, T_c) - Y_{a\_sim}(G, T_c) \tag{2.5}$$

where L_{c_sim} is the captured losses, $Y_r(G, T_c)$ is the measured reference yield, and T_c is the PV module temperature.

After identifying the captured losses in the PV system, a statistical layer has been used as proposed by Equation (2.6).

$$L_{c\_sim} - 2\sigma < L_{c\_mes} < L_{c\_sim} + 2\sigma \tag{2.6}$$

where *Lc_mes* is the measured loss of the examined PV system.

Finally, if the fault signal of the statistical analysis is equal to 1, another layer is used to identify the type of the fault occurring in the PV system which are described in Figure 2.17a. In addition, R_c and R_v present the current and the voltage ratio of the PV system. This work proposes a simple fault detection algorithm for the PV systems. It cannot identify the number of faulty PV modules within the PV string, the location of the faulty PV modules in the PV string and PS conditions cannot be classified correctly. Since if the voltage ratio is greater than 1, multiple faults might occur such as aging, MPPT error and PS conditions.

Furthermore, a method of identifying faulty PV modules in a PV string has been proposed by (Gokmen et al., 2012). The PV fault detection algorithm uses the irradiance level, PV modules temperature, the number of PV modules in the examined PV string, and the output power of the PV string as an input for detecting whether the PV module is shorted or open circuited in the PV string. The proposed detection algorithm is tested on a series connected PV string which comprises 5 PV modules. The schematic of the tested PV system is shown in Figure 2.17b, where N (series connected PV modules) is equal to 5.

The main challenge of adapting this method into other PV systems is the calculation of the relative power from the PV string. In addition, the proposed fault detection algorithm is not capable of detecting PS conditions, and cannot be used with different PV configuration systems such as P, SP, and TCT.

Another interesting parameter based model PV fault detection algorithm is developed by (Y. Hu et al., 2013). In this work, all healthy PV modules are assumed to have the same parameters such as G, T and heat exchange coefficient U_{PV}. Additionally, the fault detection is categorized using Equation (2.7).

$$U_{PV} = \frac{G - P_{mpp}}{A_m\,(T_m - T_a)} \tag{2.7}$$

where G is solar irradiance in W/m^2, P_{mpp} is the maximum power point, A_m is the PV module area, T_m is the temperature of the PV module, and T_a is the ambient temperature.

The PV fault detection algorithm has been validated using a PV module which has a MPP equal to 0.8 W. Various experiments under different load conditions including MPP load, heavy load, light load and PS conditions have been conducted. The results indicate that Equation (1.7) can detect various faults during different load conditions connected to the PV module. However, the proposed Equation cannot be used in PV modules connected in S, PS, TCT or any other PV configuration, since it depends on the thermal heat of a single PV module and it requires the calculation of the area for a single PV module, which will be different in a PV string.

Another PV fault detection algorithm based on Equation (2.6) has been used by (Silvestre, Chouder, & Karatepe, 2013). The algorithm is capable of detecting possible faults such as PS conditions, one or more PV strings disconnected form the PV systems, and blocking diodes failure. However, the proposed algorithm cannot classify the type of the fault occurring in the PV system. In addition, the algorithm used is very similar to the PV fault detection approach previously described in (Chouder & Silvestre, 2010).

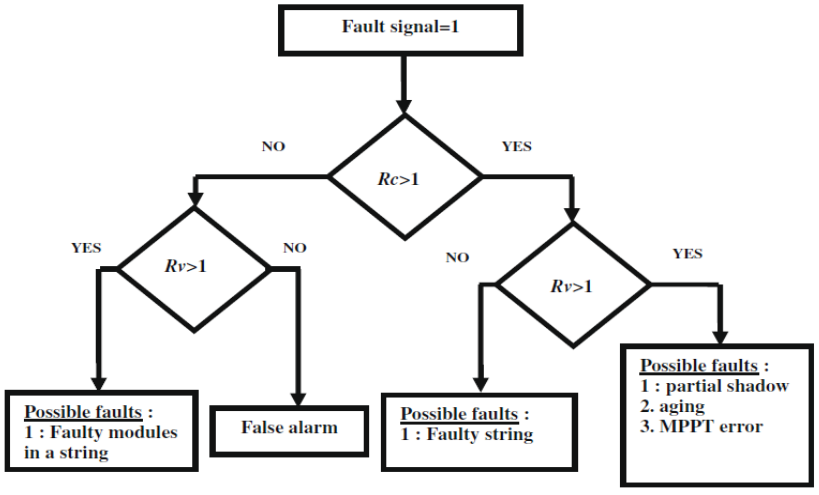

(a)

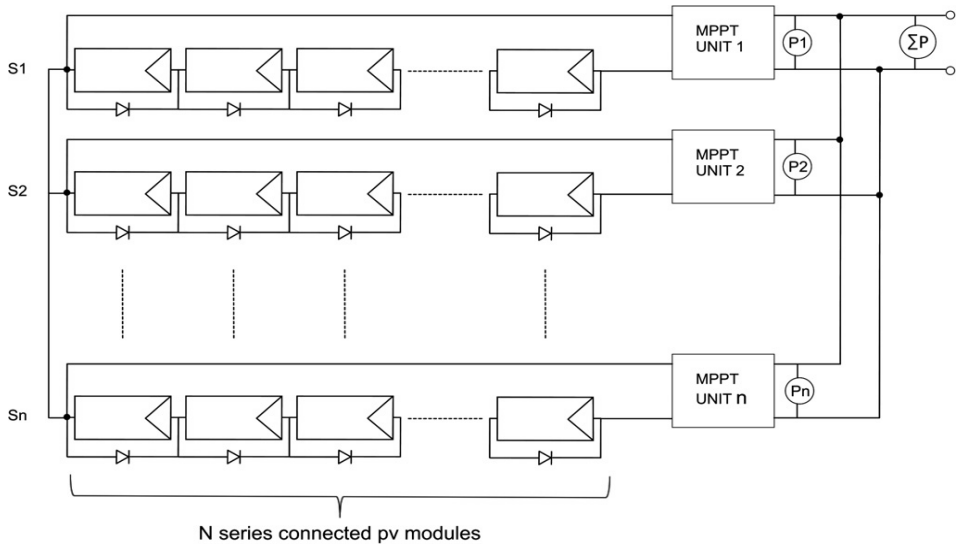

(b)

Figure 2.17 (a) Flow chart of the fault detection procedure proposed by (Chouder & Silvestre, 2010), (b) Examined PV systems used in (Gokmen, Karatepe, Celik, & Silvestre, 2012)

In (Solórzano & Egido, 2013) the authors proposed an automatic fault detection algorithm for PV system developed using MATLAB software. The algorithm can diagnose multiple faults in PV systems such as PS conditions, localized dirt, generalized dirt, possible hot spots, and module degradation and excessive losses in DC cables. Various mathematical calculations have been proposed using the variations of the PV output power, voltage, and current.

Although (Solórzano & Egido, 2013) proposed a suitable mathematical approach which can be widely used in PV systems, the algorithm cannot detect faulty PV modules (PV modules are disconnected in a PV string). Furthermore, the algorithm cannot distinguish between PS conditions and faulty PV strings in a PV system. These problems have been solved by (Chine et al., 2014). The new proposed PV detection algorithm can classify the type of the fault that has occurred in the DC and AC side of a PV system such as:

DC side

i. Faulty PV modules
ii. PS conditions
iii. MPPT error
iv. PV strings failure

AC side

i. Defect DC/AC inverter
ii. Hot DC/AC inverter
iii. Number of the faulty DC/AC inverter

In addition, the proposed algorithm uses the ratio of the voltage, current and power which is similar to the mathematical expression parameters used in (Solórzano & Egido, 2013). A new procedure for fault detection in grid-connected PV system based on the I_{mpp}, V_{mpp}, I_{sc}, and V_{oc} is proposed by (Silvestre, da Silva, Chouder, Guasch, & Karatepe, 2014). The algorithm is capable of detecting faulty PV strings and bypassed PV modules. The major limitation of the algorithm is that it cannot detect PS conditions, faulty PV modules, errors in MPPT units, and defects in DC/AC inverters.

The DC/DC converters are one of the failure sources in PV systems. In 2015, a fast switch fault detection method for boost converter used in a PV system is proposed by (Jamshidpour, Poure, & Saadate, 2015). The algorithm uses the signal provided by the current sensor dedicated to the control unit of the PV system. The results obtained show that a switch fault can be detected in less than one switching period of the boost converter, typically around 100 ms.

A further investigation on a remote isolated detection and control strategy for a PV based distributed system is developed by (Bayrak, 2015).The proposed method monitors and controls the grid, local load and the output of the PV inverter in real time with the communication of a circuit breaker. The proposed remote control system detects the changes in the currents of the circuit breakers, frequency, and the voltages by checking the defined threshold values at all electrical branches of the PV system. A general schematic of the proposed method is shown in Figure 2.18.

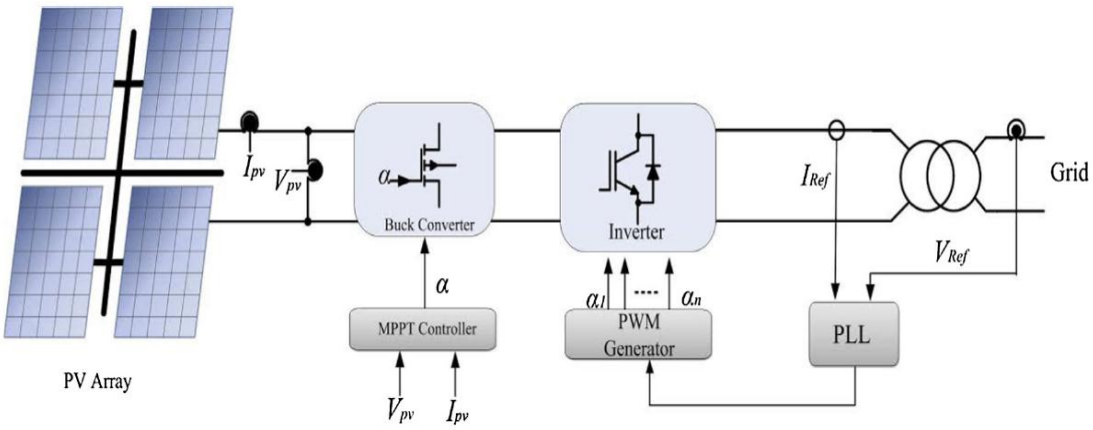

Figure 2.18 General schematic of the PV fault detection algorithm developed by (Bayrak, 2015)

Currently, various PV fault detection algorithms based on mathematical and statistical analysis techniques are used. Table 2.5 shows a comparison between five different approaches used in PV fault detection. As can be seen, the PV system output voltage and current are dominant in most recent fault detection methods. Furthermore, various statistical analysis techniques are used to identify the type of the fault in the PV plant, such as,

i. T-test: which uses the difference between the mean of the measured data and the theoretical output performance of the PV system

ii. Mean Absolute Error (MAE) and Root Mean Squared Error (RMSE)

iii. ± 2 standard deviation method

Lastly, in this section, the performance of various PV fault detection algorithms based on statistical analysis techniques and mathematical calculations have been discussed and compared. However, in the next section, the performance of various PV fault detection algorithms based on AI algorithm techniques are discussed.

Table 2.5 Comparison of various PV fault detection algorithms

Case Study		(Madeti & Singh, 2017b)	(Garoudja et al., 2017)	(Silvestre, Mora-López, Kichou, Sánchez-Pacheco, & Dominguez-Pumar, 2016)	(Ventura & Tina, 2016)
Year of the Study		2017	2017	2016	2016
Software used in the data analysis		Not used	Not used	MATLAB	PVSyst
PV system capacity		2.2 kWp	9.54 kWp	14.08 kWp	1 MWp
Fault Detection algorithm approach	Variables	PV output current and voltage	PV output current, and voltage	PV output voltage, current, and power	AC and DC power
	Statistical analysis technique	$\pm$ 2 standard deviation method	exponentially weighted moving average	Not used	MBE, RMSE and nRMSE
Type of the detected fault	PS conditions	×	√	×	√
	Faulty PV modules	√	√	√	×
	Faulty PV strings	√	√	√	×
	Error in MPPT	×	×	×	√
	Faulty DC/AC inverter	×	×	√	√

2.4.2.2 Artificial Intelligence (AI) techniques in PV fault detection

This section describes the use of AI algorithms in PV fault diagnosis. In 2011, (Karatepe & Hiyama, 2011) proposed a fault diagnosis method using several ANN networks in addition to an automatic control based module voltage terminal. The input layer of the proposed technique contains the solar irradiance, PV temperature, V_{mpp} and I_{mpp}. The proposed technique is capable of identifying the short circuited location of PV modules in one string. However, the technique cannot identify PS conditions, and fault PV strings.

Another PV fault detection approach which is capable of detecting three different solar irradiance levels in PV systems is proposed by (Tadj et al., 2014). The algorithm uses a Fuzzy Logic system to predict the cloud cover in the sky which can be classified as the following: cloudy, partial cloudy, and clear sky.

The membership functions are shown in Figure 2.19, where K_0 is the index by a partial shading to 0.2. This approach helps to detect possible faults occurring in the PV system without the need of any solar irradiance sensor. However, the approach does need a visible satellite based image of the cloud in order to define the clearness index parameter. Another limitation of the proposed approach that it does not identify whether the partial shading occurs because of a cloud, dust, helicopters, or haze affecting the PV modules.

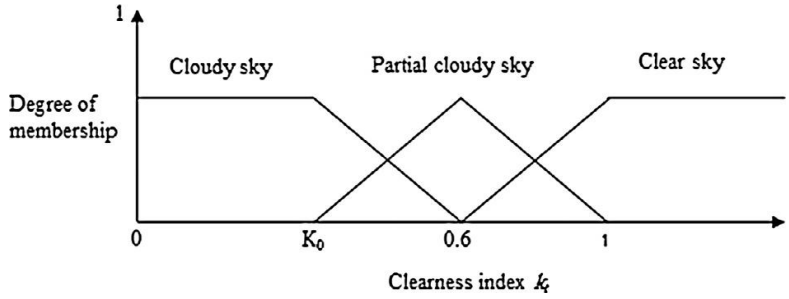

Figure 2.19 Fuzzy Logic membership functions proposed in (Tadj, Benmouiza, Cheknane, & Silvestre, 2014)

Another PV fault detection algorithm based on Neuro-Fuzzy fault classification system has been proposed by (Bonsignore, Davarifar, Rabhi, Tina, & Elhajjaji, 2014). The algorithm has been implemented using MATLAB/Simulink software. Six parameters have been used in order to implement the proposed algorithm which are I_{mpp}, V_{mpp}, V_{oc}, I_{sc}, *S1*, and *S2*, where *S1* and *S2* are calculated using Equation (2.8) and Equation (2.9) respectively:

$$S1 = \frac{I_{mpp} - I_{sc}}{V_{mpp} - V_{oc}} \tag{2.8}$$

$$S2 = \frac{0 - I_{mpp}}{V_{oc} - V_{mpp}} \tag{2.9}$$

The proposed Neuro-Fuzzy system is capable of detecting various faults in the PV system, such as, short circuited diode in a PV module, and PS conditions. The main limitation of the algorithm is the number of used variables in the fault classification, since the MPPT units used in PV plants cannot identify all required variables, especially the V_{oc} and I_{sc}.

Authors in (Chine et al., 2016) proposed a fault diagnosis technique for PV system based on ANN network. For a given set of working conditions such as solar irradiance and PV module's temperature, a number of attributes such as current, voltage, and number of peaks in the I-V curve of the PV string are calculated. Multilayer Perceptron (MLP) and Radial Basis Function (RBF) ANN networks have been used to detect PV fault. The output classification confusion matrix for both networks are shown in Figure 2.20, F4 is missing because it is associated with open circuit faults in any PV module that can be detected using a mathematical ratios presented in the article.

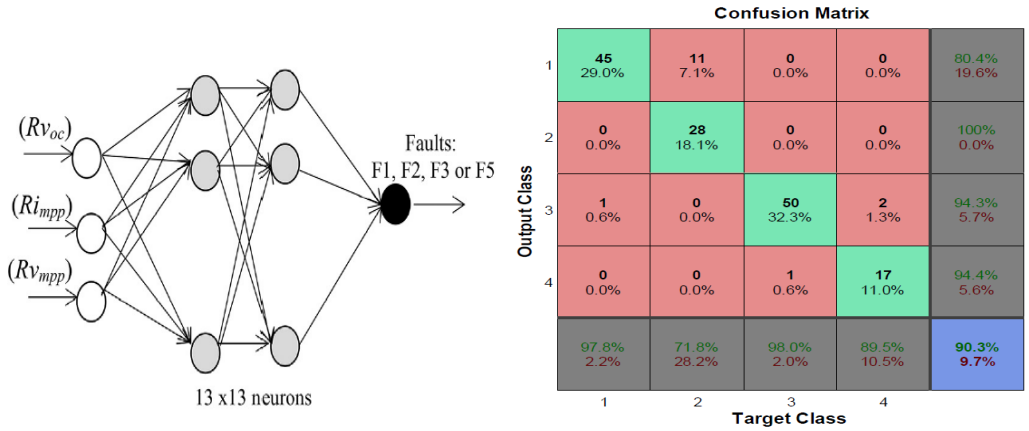

(a)

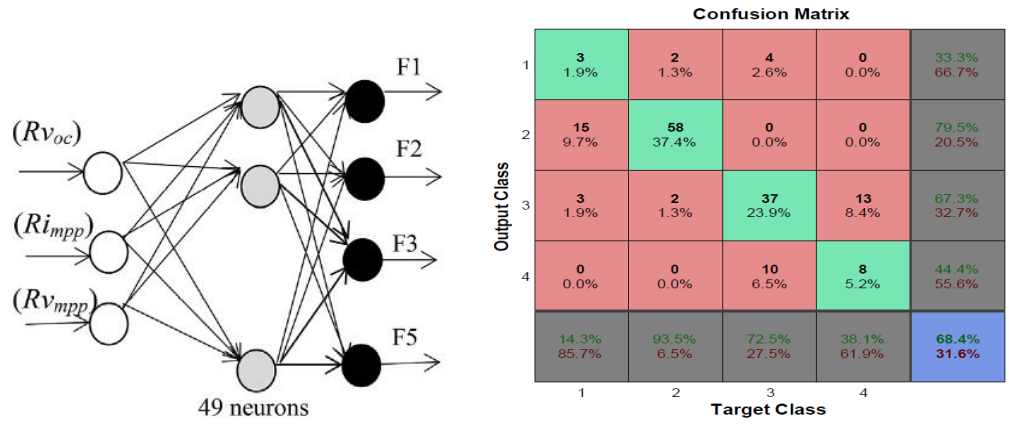

(b)

Figure 2.20 (a) MLP ANN network, (b) RBF ANN network proposed in (Chine et al., 2016)

The maximum accuracy achieved by the PV fault detection algorithm is equal to 90.3% using the MLP ANN network. As stated previously, the V_{oc} is not part of many MPPT units used in PV systems, therefore, this algorithm can only operate in PV systems which have a MPPT or a monitoring system that measures the value of the V_{oc}.

Another PV fault detection approach based on AI technique is proposed by (Belaout et al., 2016). The approach uses the values of V_{oc} and P_{mpp} as an inputs for the Fuzzy Logic system as shown in Figure 2.21, where the fuzzy classifier decides which fault occurred in the PV system according to the following rules:

i. If the fuzzy classifier output vector is equal to (g1, 0, 0), the faulty component is the bypass diode
ii. If the fuzzy classifier output vector is equal to (0, g2, 0), the faulty component is the blocking diode
iii. If the fuzzy classifier output vector is equal to (0, 0, g3), the faulty component is the series resistance
iv. If the fuzzy classifier output vector is equal to (0, 0, 0), no fault is detected
v. Otherwise, the PV system is affected by another fault type

Here, g is the discriminant function associated with the fuzzy rules.

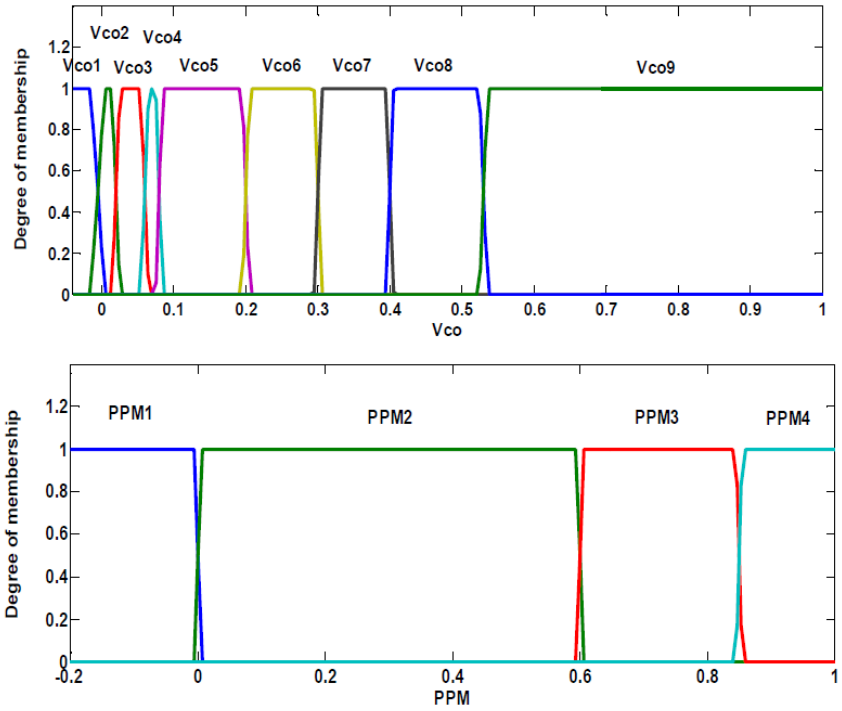

Figure 2.21 Input variables for the constructed fuzzy classifier proposed in (Belaout, Krim, & Mellit, 2016)

ANN based modelling and fault detection of PS conditions for PV modules is proposed by (Mekki et al., 2016). This approach uses MLP ANN network architecture which has only two input variables, solar irradiance and PV module temperature.

Figure 2.22 shows faulty state detection results under PS condition for the current and voltage, where 25 of the solar cells in the examined PV module which comprises 72 solar cells have been shaded. This approach can be generalized for a bigger PV array size, however, this has not been considered in the research. In Figure 2.22 the x-axis corresponds to the time in minutes.

Figure 2.22 demonstrates that when PS conditions affects a PV module, the measured current and voltage reduces comparing to the optimum (estimated) voltage and current conditions.

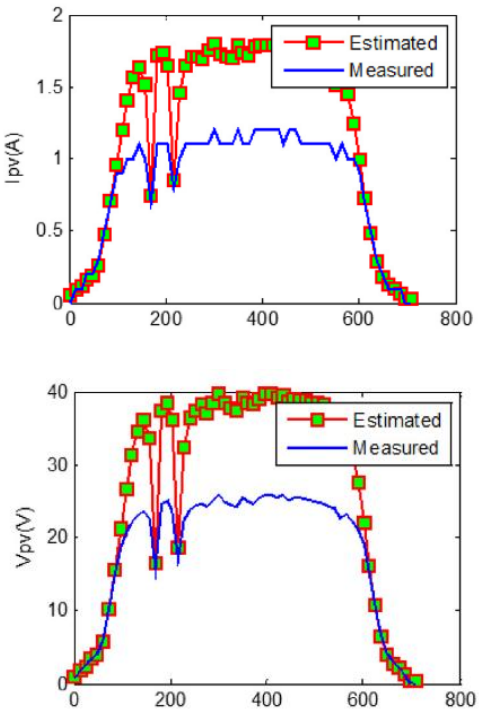

Figure 2.22 Measured PV module output current and voltage versus the estimated values obtained using the ANN-model proposed in (Mekki, Mellit, & Salhi, 2016)

Furthermore, a new fault detection technique based on multi-resolution signal decomposition and fuzzy interface systems is developed by (Yi & Etemadi, 2017). The proposed fault detection scheme is based on a pattern recognition approach that employs a multi resolution signal decomposition technique to extract the necessary features, based on which a fuzzy inference system determines if a fault has occurred. The control scheme of the proposed algorithm is shown in Figure 2.23.

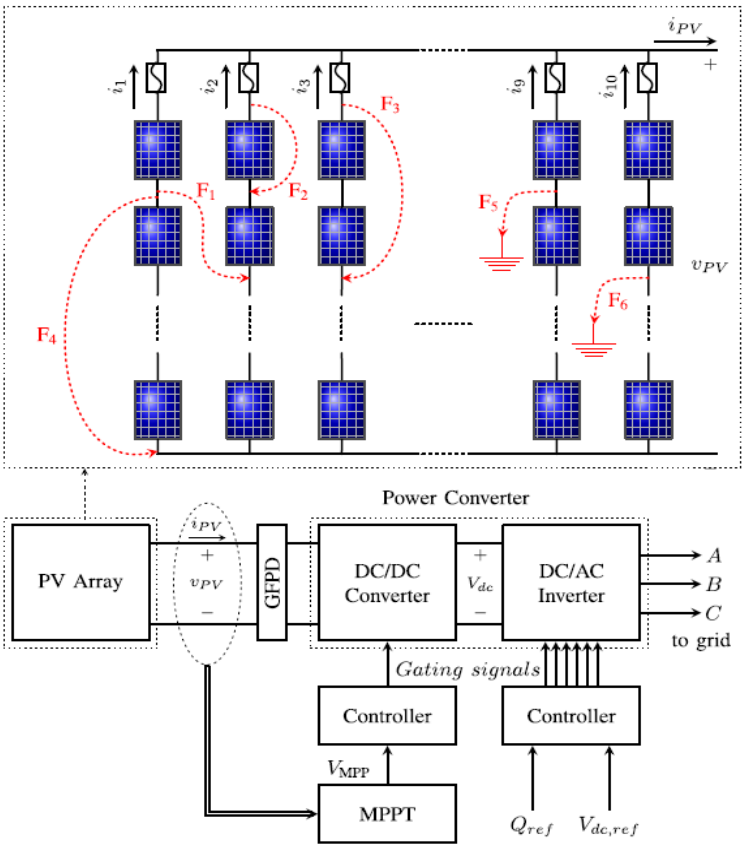

Figure 2.23 PV fault detection topology using 10 PV strings presented by (Yi & Etemadi, 2017)

Another intelligent PV fault diagnosis algorithm based on kernel extreme learning machine and I-V characteristics has been designed by (Chen et al., 2017). The proposed algorithm can be explained by the following:

i. Based on the key points and model parameters extracted from monitored I-V characteristic curves and environment conditions, an effective feature vector of seven dimensions is proposed as the input of the fault diagnosis model
ii. The emerging kernel based extreme learning machine (KELM), which features extremely fast learning speed and good generalization performance, is utilized to automatically establish the fault diagnosis model

The main limitation of the proposed algorithm is the capability of detecting faulty PV modules in the PV systems, and it cannot detect hot spots in the PV modules. Hot spots detection is another faulty condition which might occur in the PV modules. The next section describes hot spots detection and protection techniques.

2.4.3 Hot spots

A lack of maintenance in PV systems can cause hot spots due to localised or irregular dirt and PS conditions affecting the PV modules. Thus, it will cause permanent losses and reduce the reliability of the system. Hot spots are a well-known phenomenon, described as early as 1969 (Blake & Hanson, 1969), and still present in PV arrays.

Practically, PV hot spots occur when a cell, or group of cells, operates at reverse bias, dissipating power instead of delivering it and, therefore, operating at abnormally high temperatures. Even if the cell does not get damaged in the PV module, the exposure to high temperatures will result in a faster degradation of the material used for the PV modules encapsulation (Oreski & Wallner, 2005, 2009).

Infrared (IR) thermal cameras are a useful tool for detecting hot spots in PV systems. In (Kaplani, 2012), the author studied the degradation of PV systems caused by hot spots, and also developed an algorithm to automatically differentiate faulty and healthy PV cells. A sample of the digital and IR image is shown in Figure 2.24.

In (Buerhop et al., 2012), 260 PV modules were analysed by I-V curve as well as IR thermography to investigate the reliability of IR images under real time long term environmental conditions. One of the main findings of this research is the impact of faulty soldering in PV modules. According to the results shown in Figure 2.25a, the measured output power of the PV module is reduced by 11 W due to the hot spot affecting the PV module. Figure 2.25b shows the IR image of the examined PV module. This research does not focus on mitigating the hot spots in the PV modules.

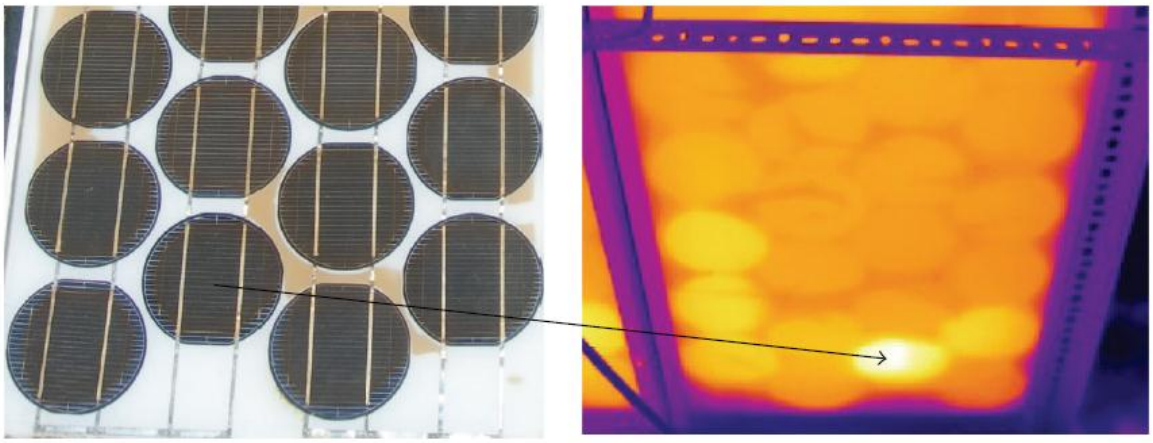

Figure 2.24 (a) Digital image of the lower part of a PV panel, (b) IR image of the back of the PV panel revealing a hot cell in reverse order as illustrated by the arrow (Kaplani, 2012)

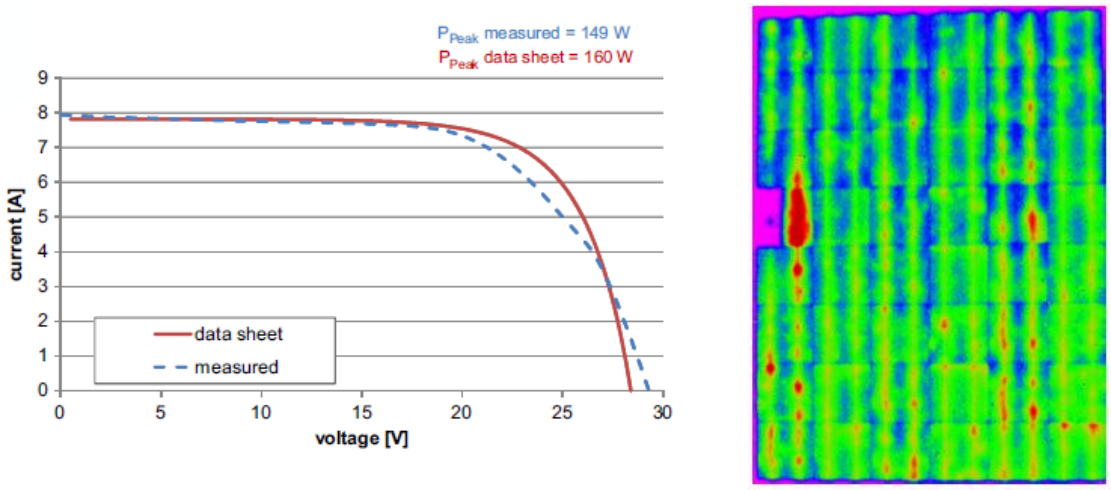

(a) (b)

Figure 2.25 (a) I-V curve of the examined PV module, (b) IR image of the PV module under G: 690 W/m^2, and T = 18 ^{o}C (Buerhop et al., 2012)

Another analysis carried out by (García, Marroyo, Lorenzo, Marcos, & Pérez, 2014) observed the degradation on PV plants affected by hot spots using I-V curves characteristics. The total number of PV modules affected by hot spots is equal to 1259, which is 5.7% of the total inspected PV modules (22088). In conclusion, this research shows that the maximum total output power loss due to PV hot spots is equal to 2.5%. However, the analysis does not propose a mitigation technique to enhance the output power performance of the hot spotted PV modules.

In 2015, an experimental observation on hot spots and a derived acceptance/rejection criteria was proposed by (Moretón et al., 2015). The experiments have been carried out using 200 affected PV modules by IR inspection camera. The end result based on various experimental observations is shown in Figure 2.26. This figure illustrates the application of the proposed acceptance/rejection criteria. The figure is divided into 4 regions:

i. Modules in region “A” are considered non-defective, because their hot spot temperature is not high
ii. Modules in region “B” are less straightforward, because these modules are possible candidates for a hot spot problem, but this problem has not evolved enough to imply a significant power loss. Therefore, these modules are not rejected, but they should be inspected again after one year. One year was recommended by the article authors, however, there is no scientific evidence from the article justifying why one year has been chosen as a maintenance period.
iii. Modules in region “C” and “D” are considered defective due to low power and lifetime threatening temperatures

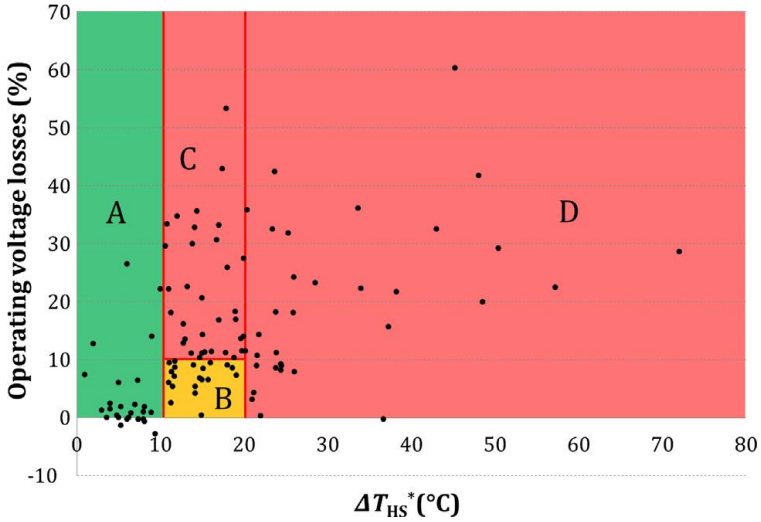

Figure 2.26 Proposed PV hot spot acceptance/rejection criteria developed by (Moretón, Lorenzo, & Narvarte, 2015)

A mathematical model proposed by (Rajput, Tiwari, & Sastry, 2016) has been developed to calculate solar cell temperature, hot spot temperature and PV module efficiency in opaque and semitransparent mono crystalline silicon PV module. The results have been validated experimentally, where opaque PV modules exhibits 2 to 3 ºC higher temperature in comparison to semitransparent PV modules for one as well as two hot spots. Figure 2.27 shows the I-V curve for three different cases: no hot spot, one hot spot and two hot spots in the PV module, for both opaque and semitransparent PV modules under the same outdoor environmental conditions.

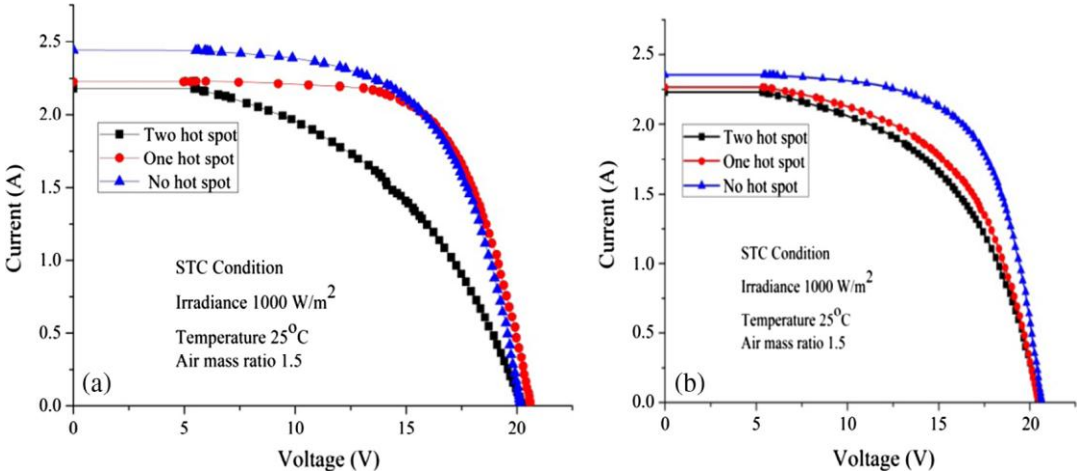

(a) (b)

Figure 2.27 I-V curve for no hot spot, one hot spot, and two hot spots affecting. (a) Opaque PV modules, (b) Semitransparent PV modules

So far, all previously mentioned hot spot detection algorithms/techniques have not considered the hot spot output power mitigation. However, a hot spot mitigation in PV arrays with distributed MPPT (DMPPT) has been proposed by (Solórzano & Egido, 2014). The proposed mitigation technique is based on the number of bypass diodes connected in each PV module. Further considerations have been taken into account:

i. The shaded cell has some margin until it works in reverse bias: from I_{mpp} to I_{sc}, related to the shunt or parallel resistance
ii. If the non-shaded cells reduce their current they are also increasing their voltage, so the power lost is not exactly equal to the current reduction and it depends on the slope of the I–V curve from V_{mpp} to V_{oc}, which is related to the series resistance of the cells

Figure 2.28 shows an experimental results of 25% shading applied to a PV solar cell. As can be seen, using the DMPPT technique reduces the temperature of the shaded solar cell up to 26.4 ºC compared to 34.4 ºC before considering the DMPPT technique.

A hot spot suppression technique is proposed by (Spanoche, Stewart, Hawley, & Opris, 2012). The suggested technique works with a model based MPPT algorithm to seek the best operating point to maximize the output power of the PV module, while limiting the rise of the temperature of the shaded solar cells. Theoretical and experimental results show that the power density dissipated in the shaded cell(s) is reduced by a factor of 4 when the operating conditions are determined by hot spot suppression technique.

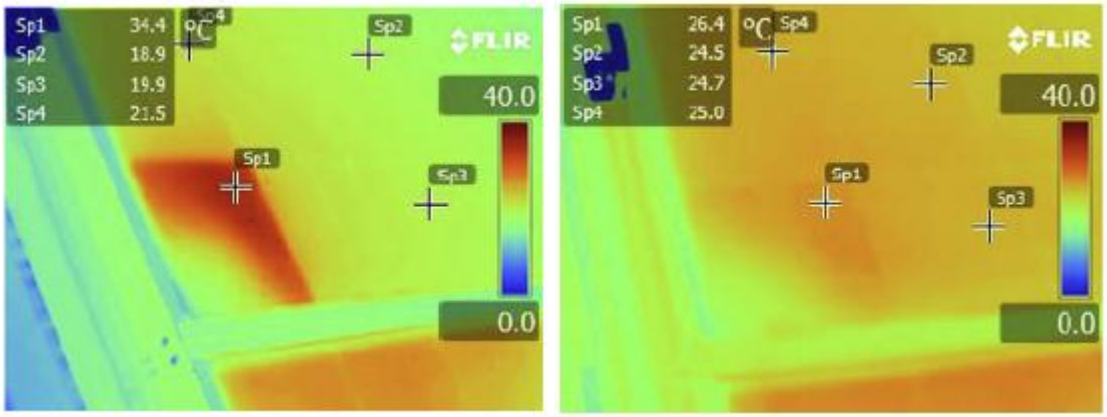

(a) (b)

Figure 2.28 IR image of 25% shading applied to a PV solar cell. (a) Before DMPPT, (b) After DMPPT (Solórzano & Egido, 2014)

Another technique for enhancing the output power of hot spotted PV modules is proposed by (Y. Hu, Cao, Ma, Finney, & Li, 2014). This technique uses the thermal images of the hot spotted PV module as an input for a mathematical model which extracts a quantitative information of the mismatch fault, which is then employed to regulate the MPPT control. The proposed model uses the main parameters such as I, V, T, and G to investigate the behavior of the PV module. Compared to the methods described previously, this research made the following improvements:

i. The temperature distribution under PV fault conditions is analysed by new electrical-thermal model
ii. The thermography-based temperature distribution analysis is effective in establishing parameter-based models and developing an optimized global MPPT algorithm in case of hot spotted PV solar cells

In 2015, a reexamination of PV hot spotting to show inadequacy of the bypass diodes used in PV panels is discussed in (Kim & Krein, 2015). The examined PS case is shown in Figure 2.29, where a leaf has fallen on PV cell 1 of a 24 cell sub string. The bypass diode is turned "on" based on the string current and bypass diodes passive behavior. Thus, the cell dissipate more than 20 times its rated MPP which can be illustrated as the following:

$$\frac{82\ W\ (Rated\ MPP\ as\ shown\ in\ Figure\ 2.29b)}{24\ (Number\ of\ sub\ string\ cells)} = 3.416\ W$$

$$76\ W\ (measured\ power\ shown\ in\ Figure\ 2.29b) \approx \mathbf{22}\ \times 3.416$$

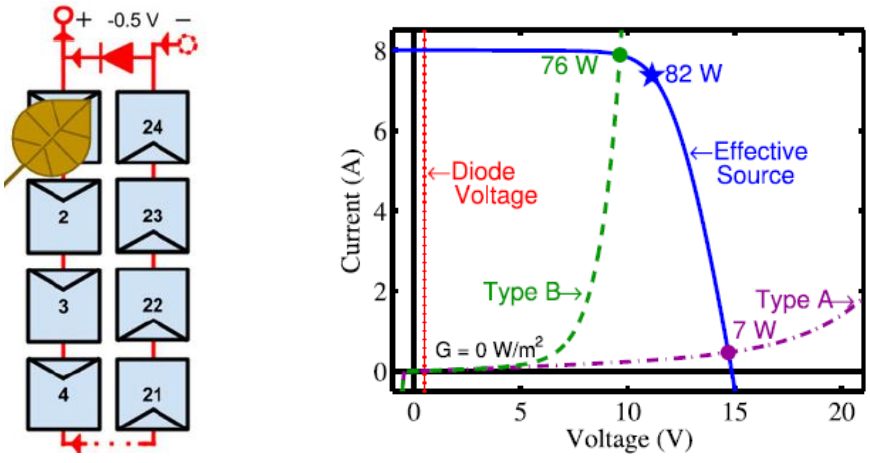

(a) (b)

Figure 2.29 (a) Bypassed sub panel string with one solar cell, (b) I-V curve characteristics (Kim & Krein, 2015)

A suitable solution for the sub string bypass diode connection has been reported in (Daliento et al., 2016), where a modified bypass circuit has been proposed to mitigate the hot spot reliability of PV solar cells. The approach relies on series-connected power MOSFET that subtracts part of the reverse voltage from the shaded solar cell. This is different from other active bypass circuits. The proposed solution does not require either a control logic or power supply and can be easily substituted to the standard bypass diode.

Figure 2.30a shows the schematic diagram of the connection for the MOSFET within the PV sub string. In sunny conditions (no shading) shown in Figure 2.30b, the diode is turned "off" and the power reduction of the sub panel due to the MOSFET is measured up to tens of milli watt. Figure 2.30c shows the working principles during one shaded solar cell in the PV sub string. The diode turns "on", and the current flowing through the MOSFET decreases and its operating point moves toward higher voltage.

This implies that the presence of the MOSFET reduces the power dissipation across the solar cell and, hence, its temperature; obviously the subtracted power is dissipated by the MOSFET, but the reliability concern is conveniently moved from the panel to an external device particularly suited for high temperature operation, which may in principle survive during the whole lifetime of the panel.

Although the proposed approach was not validated during hot spotted PV panels, it was validated during PS conditions. On the other hand, the measured enhancement in the PV output power was not reported during outdoor conditions.

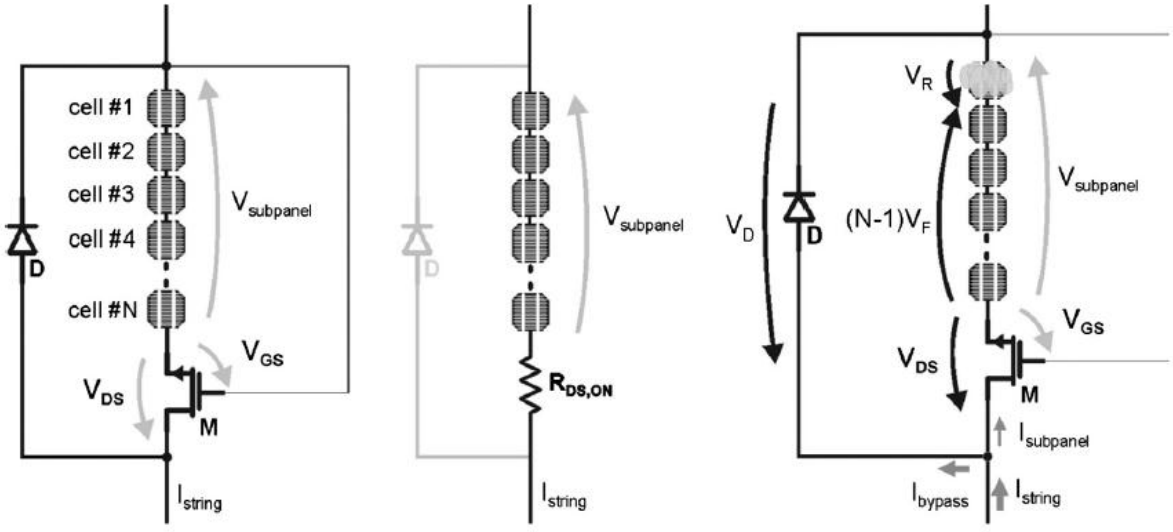

(a) (b) (c)

Figure 2.30 (a) Schematic diagram of the proposed bypass strategy proposed by (Daliento, Di Napoli, Guerriero, & d'Alessandro, 2016), (b) Operation under sunny conditions, (c) Operation under shading conditions

In this section, hot spot detection and possible mitigation techniques were discussed. Another important factor which might degrade the output power performance of PV modules is micro cracks, which will be explained in the next section.

2.4.4 PV micro cracks

Micro cracks in solar cells are a genuine problem for PV modules. They are hard to avoid and, up to now, the impact of PV micro cracks on the performance of the PV modules in various environmental conditions has not been reported. In order to examine micro cracks in PV modules, several methods have been proposed. Resonance ultrasonic vibrations (RUV) technique for crack detection in PV silicon wafers has been developed by (Belyaev et al., 2006; Dallas, Polupan, & Ostapenko, 2007). The technique uses ultrasonic vibrations of a tunable frequency and adjustable amplitude are applied to the silicon wafer by an external piezoelectric transducer in a frequency range of 20 to 90 kHz. The transducer contains a central hole allowing a reliable vacuum coupling between the wafer and transducer by applying 50-kPa negative pressure to the backside of the wafer.

RUV PV micro crack technique is sensitive to crack length and its location, and can be used to reject or accept wafers. However, it does not identify the exact location of the PV crack. A sample of a PV crack detected using RUV is shown in Figure 2.31a.

Optical transmission technique is another method used to detect micro cracks in PV modules. In optical transmission, the silicon wafer is placed above a broad-spectrum flashlight or laser diode and a charged coupled device (CCD) camera is used to detect the optical transmission through the wafer. The micro cracks inside the wafer affect the infrared portion of the light that passes through. The resolution of the CCD camera determines the minimum crack width that can be detected by this method (Abdelhamid, Singh, & Omar, 2014).

In (Yang, 2009) the author proposed a real time in-line scanning method, which is based on a short time discrete wavelet transform (STDWT), to determine reflective characteristics of PV micro cracks. Although the selection of a small window size increases the spatial resolution for the proposed system, it causes an irregular pattern of the PV micro crack detection, which makes the automatic detection hard to identify the type, and the size of the micro crack as shown in Figure 2.31b.

Another optical transmission technique which uses a general CCD camera with a laser diode as an automatic inspection for PV micro crack detection is proposed by (Bin et al., 2011). Although the proposed technique is useful in detecting the facial cracks, it fails to detect hidden cracks in awkward shaped plaques and cracks exhibiting snow-like point spread features as shown in Figure 2.31c.

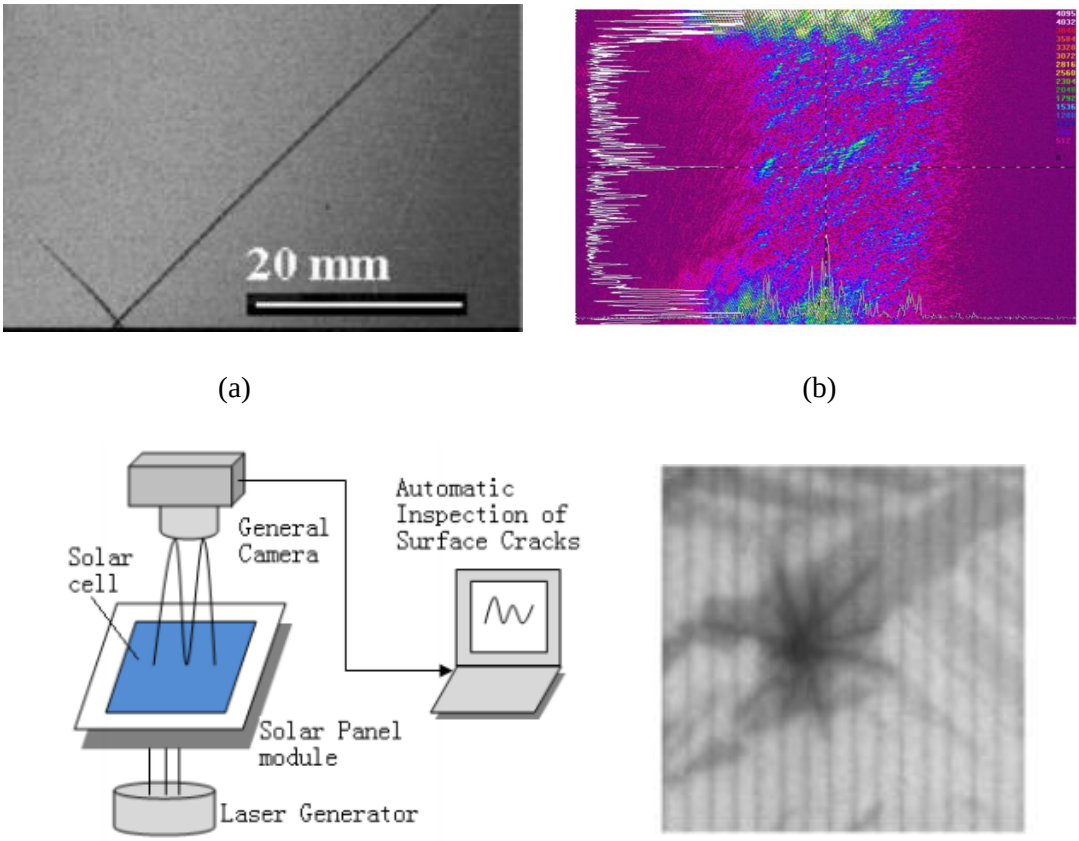

Figure 2.31 PV micro cracks detecting using various detection techniques. (a) RUV, (b) STDWT, (c) Proposed PV micro crack detection technique developed by (Bin, Xianghao, & Shuai, 2011)

(Wen & Yin, 2012) developed another technique called electronic speckle pattern interferometry (ESPI) which is used to detect PV solar cells micro cracks. In this method, speckle interference patterns are produced by real-time subtraction of sequential speckle images captured before and after an imposed deformation. This method depends on the variation of strain distribution due to thermal deformation in the solar cell, which is caused by discontinuities in material properties or the crystal lattice.

The ESPI image was taken from the back of the solar cells because ESPI is more suited to detect rough rather than smooth surfaces. This approach is used to detect both facial and sub facial cracks and can distinguish between crack and scratch. The overall system configuration of the ESPI method is shown in Figure 2.32a. ESPI image of a polycrystalline solar cell is shown in Figure 2.32b.

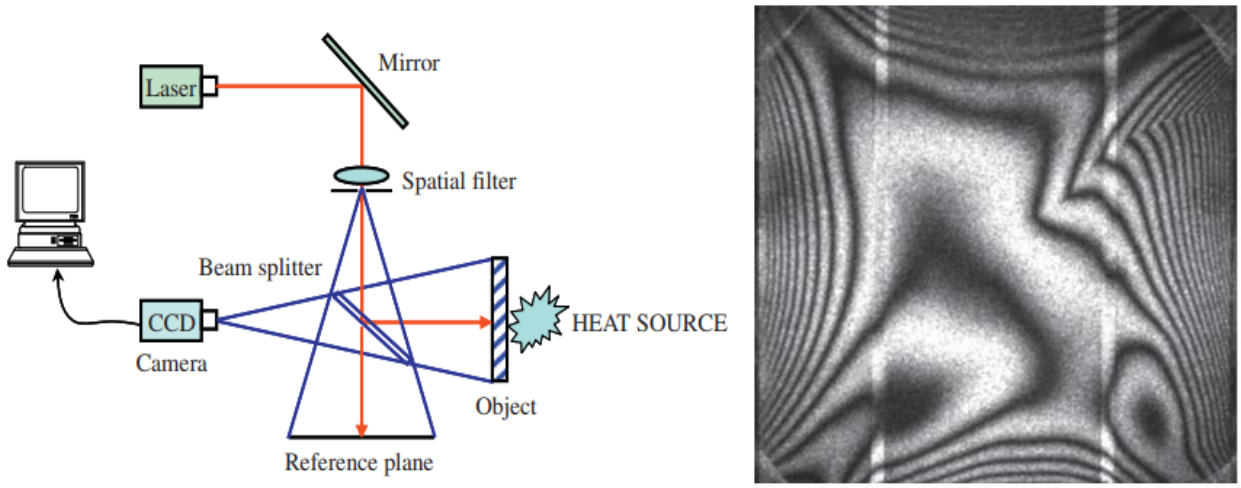

(a) (b)

Figure 2.32 (a) ESPI technique proposed by (Wen & Yin, 2012), (b) ESPI image of polycrystalline silicon solar cell in temperature range of 32 ~ 32.4 °C

The above mentioned PV micro cracks detection techniques are very efficient techniques for locating and detecting possible cracks occurring in the PV modules, however, these techniques cannot be applied for a finished full scale PV modules. Therefore, photoluminescence (PL) aiming technique was proposed to solve this problem, since it can be used to inspect micro cracks in silicon wafers and PV modules. Moreover, PL technique can be applied not only at the end of the PV solar cell's production, but also it can be slotted in during the process of production (Israil, Anwar, & Abdullah, 2013).

A typical PL imagine set-up has been firstly developed in 2006 by an Australian scientists (Trupke et al., 2006), the PL setup can be seen in Figure 2.33a. The PL image is the result of the electron-hole recombination, in which the electron is excited to the conduction band after absorption of photon. The electrons are emitted by means of a laser source. The PL image is detected using a CCD camera with a filter to remove the reflected and scattered laser light. An example of PL image for a PV solar cell is shown in Figure 2.33b.

Most recently, in 2017, the PL imaging technique was used by (Zhu et al., 2017). In this research, authors proposed a new PL setup that enables inhomogeneous illumination with arbitrary illumination patterns to determine various parameters of solar cells. Figure 2.33c shows the new PL setup which comprises ten different stages, where the first stage is the lamp and concave mirror, and the last stage contain the light sink.

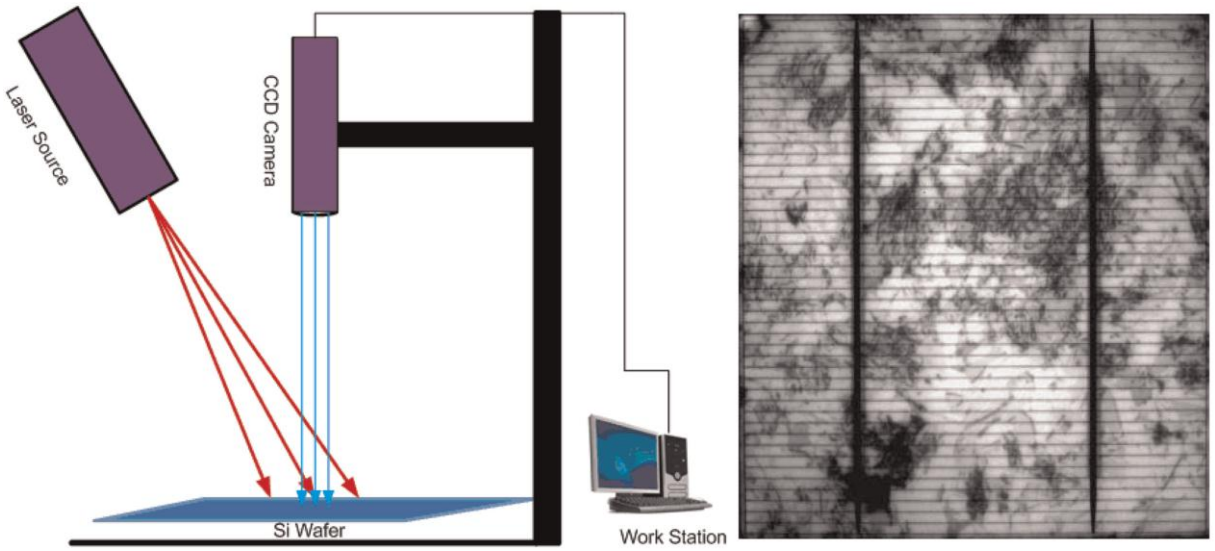

(a) (b)

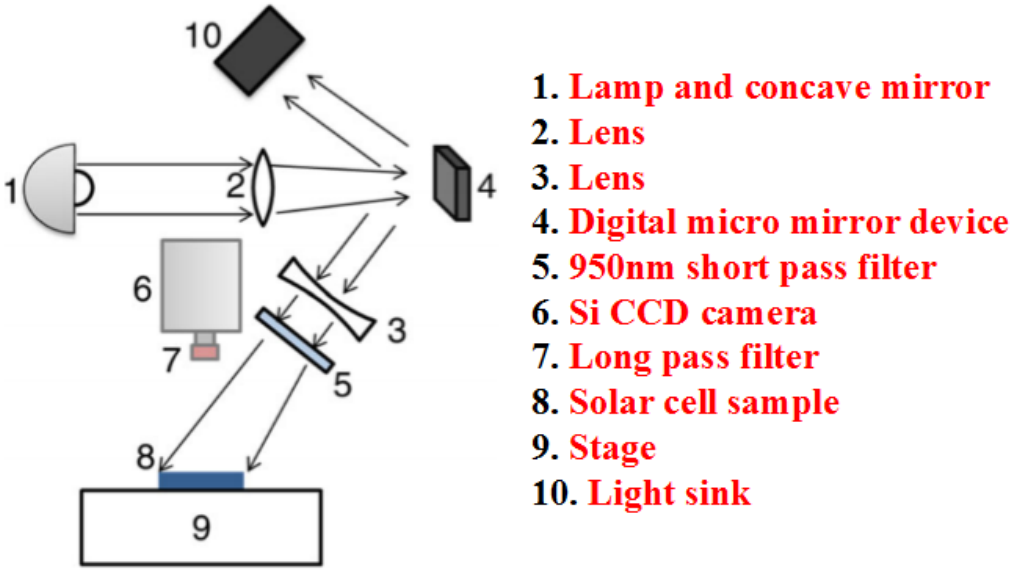

(c)

Figure 2.33 (a) Typical PL imaging setup developed by (Trupke, Bardos, Schubert, & Warta, 2006), (b) Example of PL image of a polycrystalline silicon solar cell, (c) New PL setup proposed by (Zhu, Juhl, Trupke, & Hameiri, 2017)

Electroluminescence (EL) aiming technique is another idea for the micro crack detection in PV solar cells. EL technique is the form of luminescence in which electrons are excited into the conduction band through the use of electrical current by connecting the solar cell in forward bias mode. This technique is very attractive, because it can be used not only with small solar cell sizes but also, it can be used with full scale PV modules (Israil et al., 2013).

A typical EL imaging setup can be seen in Figure 2.34a which was developed by (Fuyuki & Kitiyanan, 2009). The EL method requires the solar cells to be in the forward bias condition in order to emit infrared radiation. The EL ranges from 950 to 1250 nm with the peak occurring at approximately 1150 nm. Emission intensity is dependent on the density of defects in the silicon, with fewer defects resulting in more emitted photons. The EL system should be placed in a dark room, as the image of the cells is being taken by cooled CCD camera. An example of EL image for a solar cell is show in Figure 2.34b.

(Köntges et al., 2009) presented the use of EL imaging technique on a full scale PV module. Figure 2.34b shows the EL image of the examined PV module. This study was carried out to investigate a new EL image correction setup to increase the quality of the EL images. In addition, (Kontgers, Kunze, Kajari-Schroder, Breitenmoser, & Bjorneklett, 2010) studied the impact of micro cracks on the performance of PV modules using EL imaging method. This research proves that micro cracks do not reduce the power generation of a PV module by more than 2.5%, if the crack does not harm the electrical contact between the cell and fragments.

Same authors in (Köntges et al., 2011) have studied the impact of micro cracks on the PV module output power performance based on the number of cracked solar cells per PV module. The PV output power loss is approximately equal to 9.6% for a PV module which contains more than 25 micro cracks. In addition, the maximum power loss estimated for PV module with micro cracks between 10 and 15 is equal to 6.4%. Figure 2.34d shows the detailed power loss analysis for various number of cracked cells per module. In addition, authors stated that a defective cell with inactive cell area $A_{inactive}$ is in forward bias if the following Equation (2.10) is true.

$$\frac{A_{inactive}}{A_{total}} < \frac{I_{sc} - I_{mpp}}{I_{sc}} \tag{2.10}$$

where A_{total} is the total area of the solar cell, $A_{inactive}$ is the defective area in the examined solar cell.

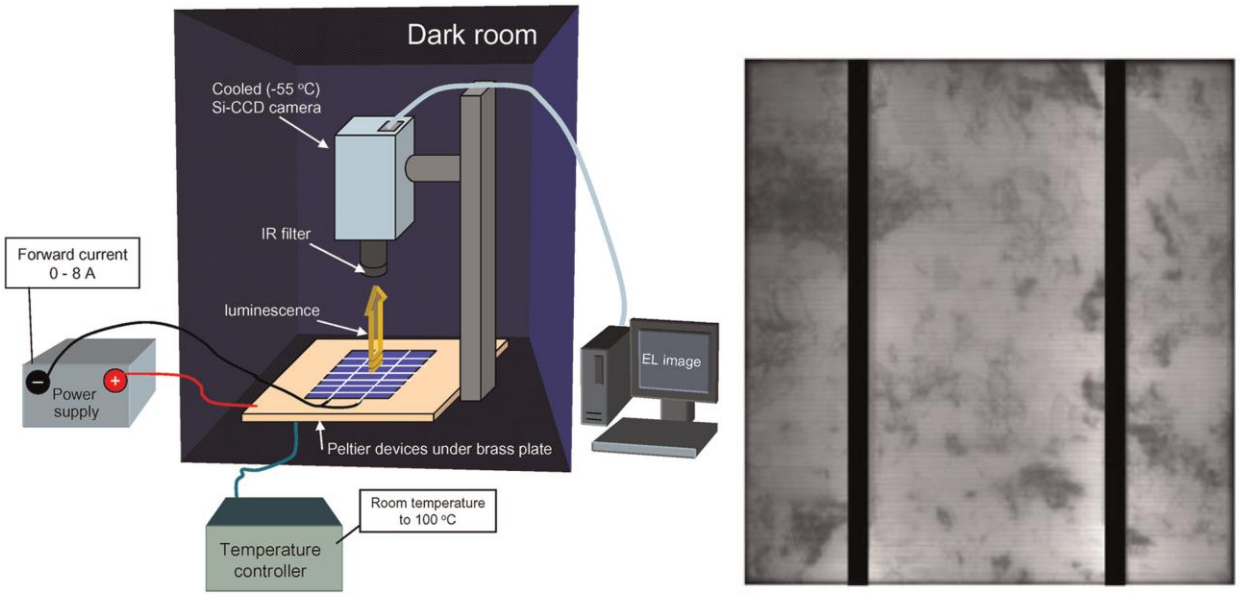

(a) (b)

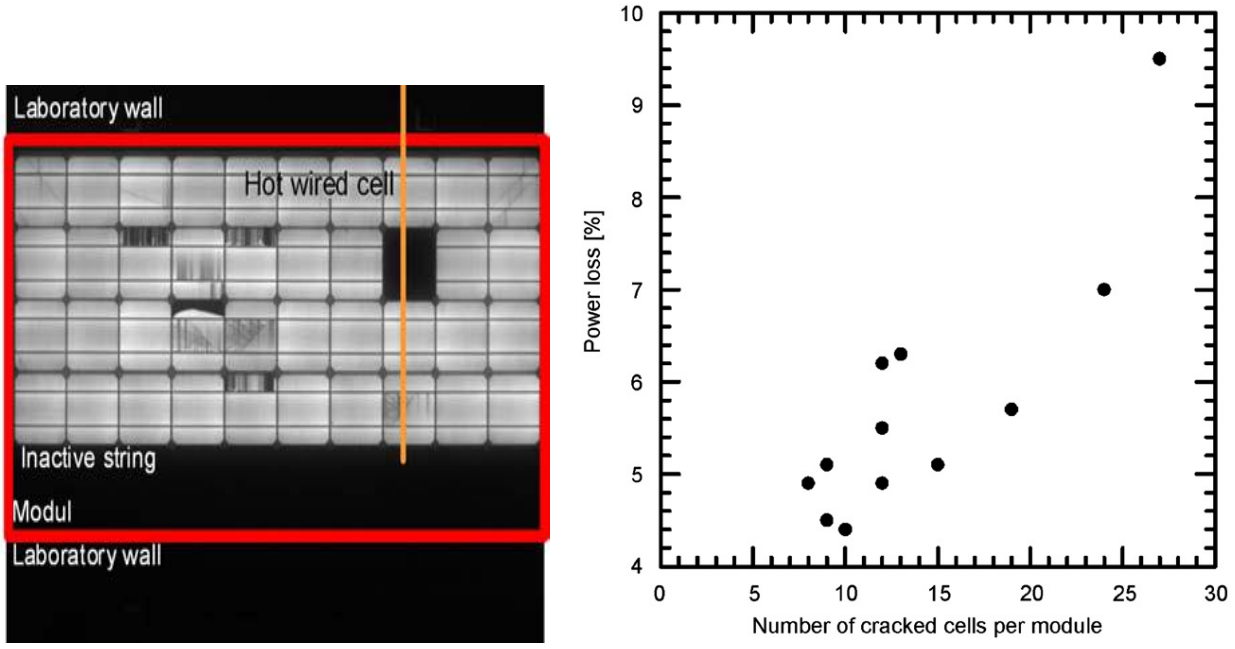

(c) (d)

Figure 2.34 (a) A typical EL imaging setup developed by (Fuyuki & Kitiyanan, 2009), (b) Example of EL image of a polycrystalline solar cell, (c) EL image for a PV module taken by (Köntges et al., 2009), (d) power loss analysis per PV module based on number of crackes presented in (Köntges, Kunze, Kajari-Schröder, Breitenmoser, & Bjørneklett, 2011)

A special and orientational distribution of micro cracks in crystalline PV modules was firstly presented by (Kajari-Schröder, Kunze, Eitner, & Köntges, 2011). PV micro cracks were classified into six sub categories shown in Figure 2.35a:

i. Dendritic
ii. Several
iii. $+45^0$
iv. -45^0
v. Parallel to busbars
vi. Perpendicular to busbars

The analysis has been carried out using 27 PV modules using EL imaging technique. The maximum cracks found in the PV modules are parallel to busbars with 50% relative occurrence, as shown in Figure 2.35b.

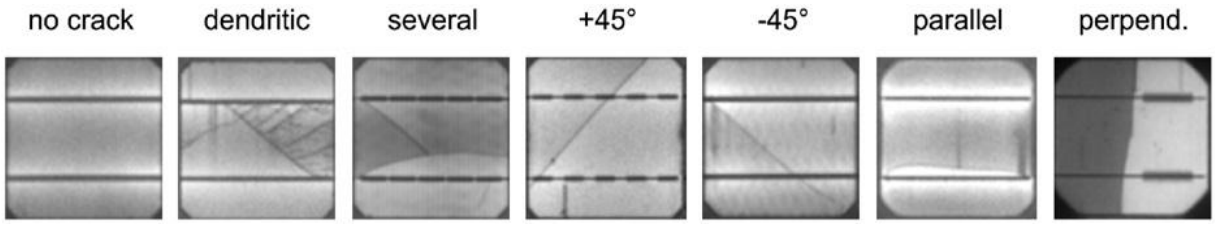

(a)

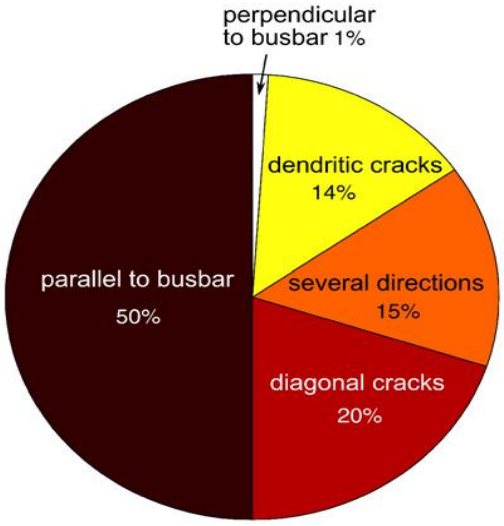

(b)

Figure 2.35 (a) Classification of crack orientations, (b) Relative occurrence of different crack orientation based on 27 examined PV modules

Furthermore, I-V curve analysis based on gallium arsenide (GaAs) PV solar cell on silicon substrate for crack-free and cracked PV solar cells has been investigated by (Oh et al., 2016). Figure 2.36a shows the illuminated I-V curves for various samples of PV solar cells with various crack sizes. As can be noticed the output voltage of the PV solar cells decreases when increasing the crack size. Figure 2.36b shows the variations of V_{oc} as a function of crack density D_c. The crack density defined as the total length of the crack liner per unit area, which was found to be in the range from 13.8 to 33.2 cm^{-1} in the investigated solar cell samples.

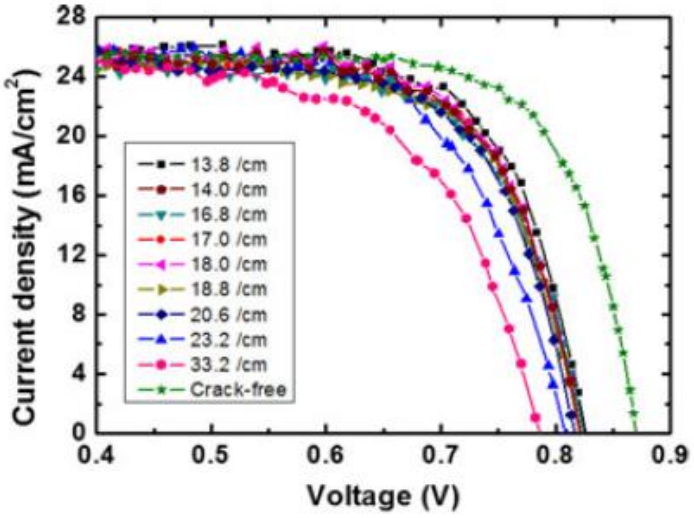

(a)

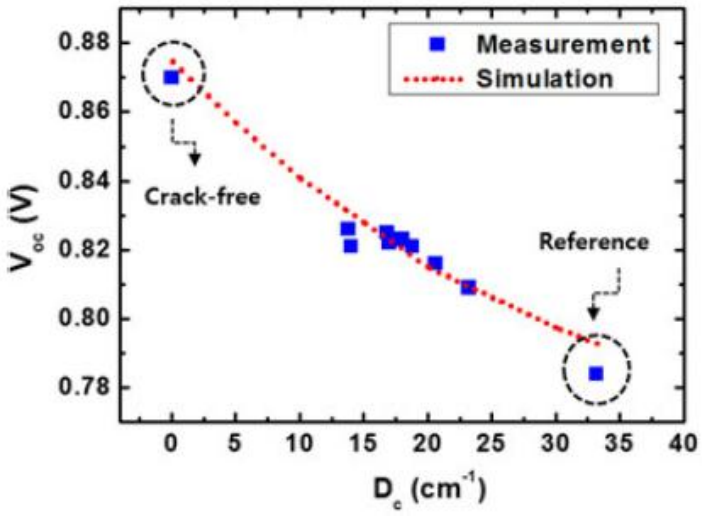

(b)

Figure 2.36 (a) Illuminated I-V curves for the crack-free cell and cells containing cracks, (b) Plot of the measured and simulated V_{oc} as a function of D_c (Oh et al., 2016)

2.5 Summary

In this chapter, the principles of operation for PV solar panels have been illustrated using the theoretical I-V and P-V curves. Furthermore, most recent PV monitoring and DAQ acquisition systems have been evaluated and compared.

As stated in this chapter, PV faults might lead to a significant reduction in the MPP produced from the PV plants. In UK domestic PV systems, the largest energy loss was caused by sustained zero efficiency faults (when the monitored PV systems stopped generating power for long period) (Firth et al., 2010). In order to detect this fault, several approaches have been investigated widely, basically, using the following two methods:

i. Statistical analysis techniques
ii. Artificial intelligence techniques such as Fuzzy Logic and ANN networks

However, there is a need to improve the developed techniques, since most of the proposed techniques required many measured parameters from the PV system, which leads to higher cost detection system and more complex PV system structures.

The second largest cause of energy loss in PV plants is PS conditions affecting the PV modules. The PV output power due to PS conditions can be improved using three main techniques:

i. The interconnection of bypass diodes in PV sub strings
ii. Developing new PV array configuration systems
iii. Enhancement of MPPT methods

Further research is required to combine these three techniques into one method in order to enhance the PV output power production. In addition, most MPPT proposed in the literature show that the detection of the MPP of the PV module could reach up to 99%. However, few MPPT technique are used with complex PV array configuration, thus, this field needs more investigation.

On the other hand, PV hot spots and micro cracks could decrease the output power production in PV panels. Up to date articles show that is not sufficient techniques, and algorithms which leads to a significant improvement in the PV output power.

In order to validate theoretical and simulation outcomes for enhancing PV fault detection algorithms, hot spot detection, micro crack analysis and the investigation of multiple PV array configurations, a number of experiments on two PV installations at the University of Huddersfield, which will be covered in the next chapter (Chapter 3).

Chapter 3 PV Monitoring System and Performance Analysis

One of the main aspects of any PV system is the monitoring unit used to log and analyse the performance of the PV installation. This chapter describes the design and development of the monitoring system installed in the examined PV plants. The proposed monitoring unit uses the Virtual Instrumentation (VI) software via the Internet of Things (IoT) devices to monitor and analyse the performance of the PV systems under test. Additionally, five different factors which affect the output power performance of the PV systems will also be discussed.

Part of this chapter has been published and presented in the Environment Friendly Energies & Applications (EFEA) conference, Serbia, 2016 (Mahmoud Dhimish et al., 2016; M. Dhimish et al., 2016).

3.1 Design of the Monitoring system

In this research, various monitoring platforms were used to assess the performance of the PV installations. Figure 3.1 illustrates the overall monitoring system design. The examined PV plants briefly described in Appendix A. FLEXmax 80 MPPT unit is used to track the MPP of the PV system, this unit has also been used to measure the voltage and the current of the PV system using the internal sensors in the device.

Liquid crystal display (LCD), mobile phone application, and Virtual Instrumentation (VI) LabVIEW software are used to monitor the data acquired from the PV installations. The weather station is connected wirelessly to Vantage PRO2 monitoring unit. Finally, LabVIEW software and Vantage PRO2 monitoring device are linked to a hyper Text Markup Language (HTML) code which generates a web site. This web site can be used to monitor the status of both PV system and weather station.

Various parameters could be monitored using the proposed monitoring system, such as:

i. PV system output voltage, current, and power
ii. PV modules temperature
iii. Solar irradiance, ambient temperature, humidity, and wind speed

The designed monitoring system could also be used to log the measured environmental and PV system data using LabVIEW software.

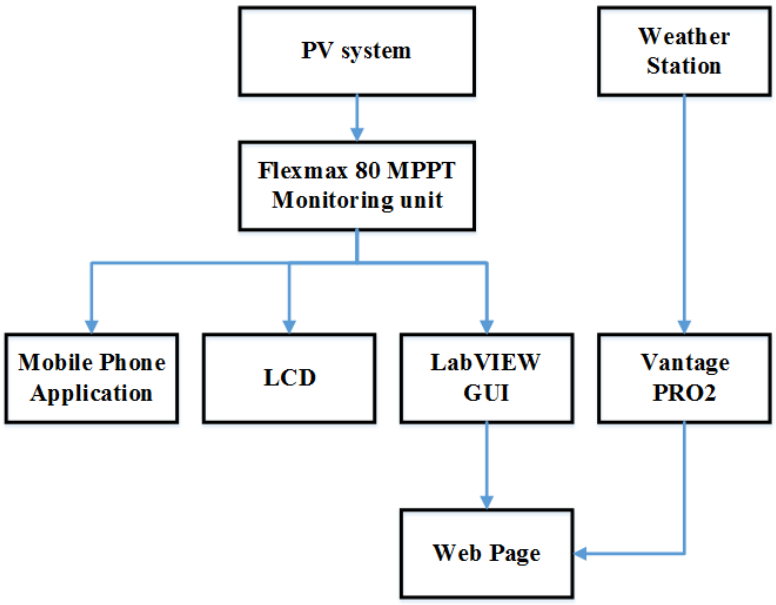

Figure 3.1 Overall designed PV monitoring system

Figure 3.2 presents the detailed architecture of the monitoring system used in the PV installations. As can be noticed, the designed monitoring system comprises eight monitoring subsystems, which can be classified as follows:

1. Remote monitoring using Vantage PRO2 monitoring device:

Vantage PRO2 (Davis, 2017b) is a monitoring device that can communicate with Davis weather station console using radio frequency (RF) transmission (wireless link). The device has some features such as: transmission distance up to 300 meters, saving data on a USB memory stick, and it can easily be plugged into a PC and then analyse the measured data received from the weather station.

Figure 3.3 shows the display screen of this monitoring unit. Each label presents a different feature in the monitoring unit. This device displays the graph of logged data over the past 24 days, months or years, all without using a PC. However, in this research, Vantage PRO2 to a PC running LabVIEW software in order to monitor, and analyse the environmental conditions affecting the examined PV installations.

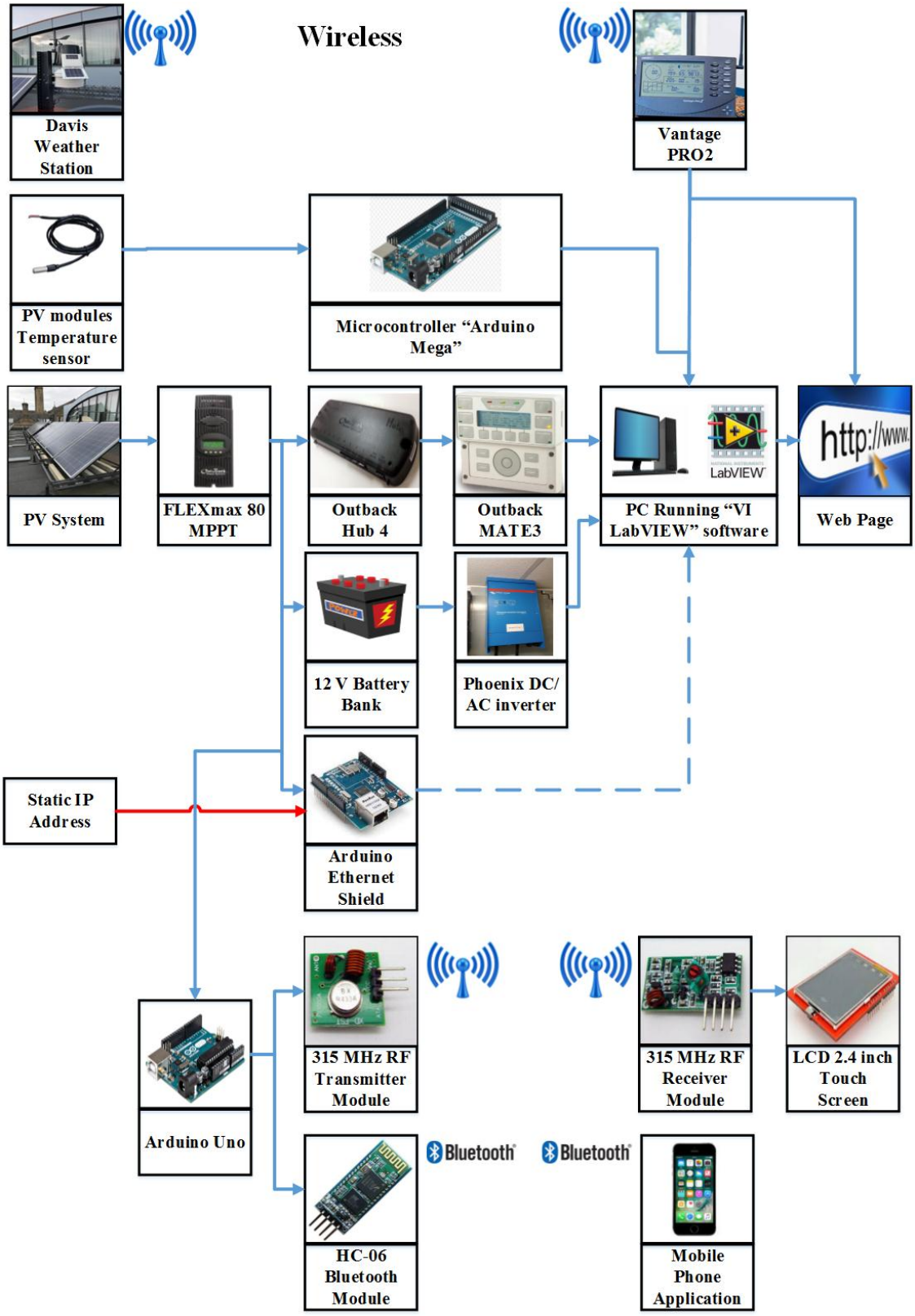

Figure 3.2 Detailed monitoring system architecture

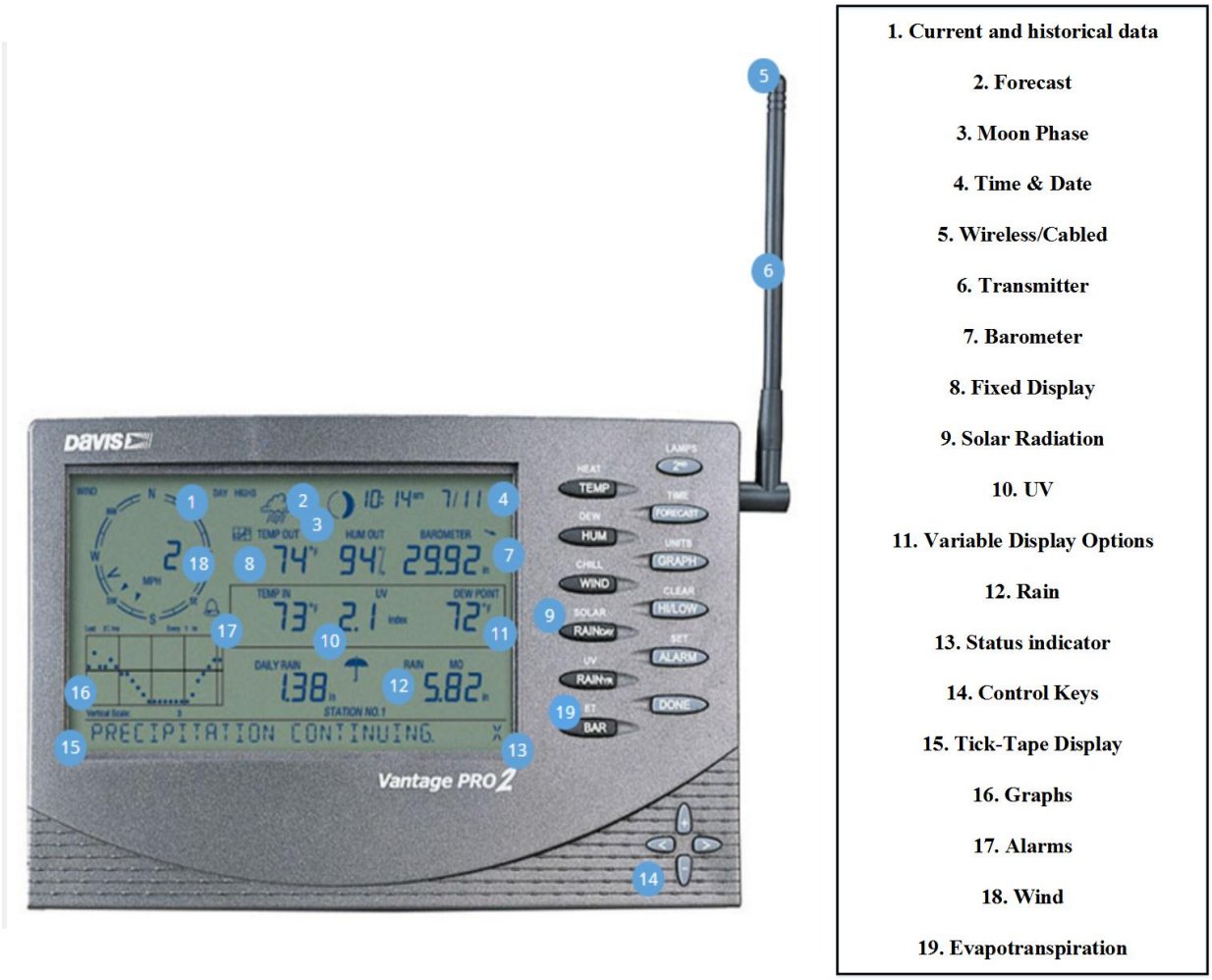

1. Current and historical data
2. Forecast
3. Moon Phase
4. Time & Date
5. Wireless/Cabled
6. Transmitter
7. Barometer
8. Fixed Display
9. Solar Radiation
10. UV
11. Variable Display Options
12. Rain
13. Status indicator
14. Control Keys
15. Tick-Tape Display
16. Graphs
17. Alarms
18. Wind
19. Evapotranspiration

Figure 3.3 Vantage PRO2 monitoring device

2. Local monitoring unit using FLEXmax 80 MPPT unit:

The first stage for monitoring the performance of the PV system consists of FLEXmax 80 MPPT. This device allows the user to monitor the data such as, the input voltage, input current, output voltage, output current, and the battery status. FLEXmax 80 device is capable of logging the data of the PV system up to 128 days using its internal memory chip.

This device can also be connected using USB or Ethernet cable to a micro controller such as (Arduino) or the Outback Hub 4 connection device (this Hub is manufactured by Outback to support the connection between FLEXmax 80 MPPT and PC user interface). Figure 3.4 shows an image of the monitoring screen for FLEXmax 80 MPPT device.

Figure 3.4 Image of the monitoring screen for FLEXmax 80 MPPT device

3. Local monitoring unit using Outback MATE3:

Another local monitoring unit used in the system is Outback MATE3 (Power, 2015). This device has the capability to display and control the data from the PV system on the PC.

This device is connected via Ethernet cable to the communication Hub (Outback Hub 4). A full schematic of this monitoring unit is presented in Figure 3.5.

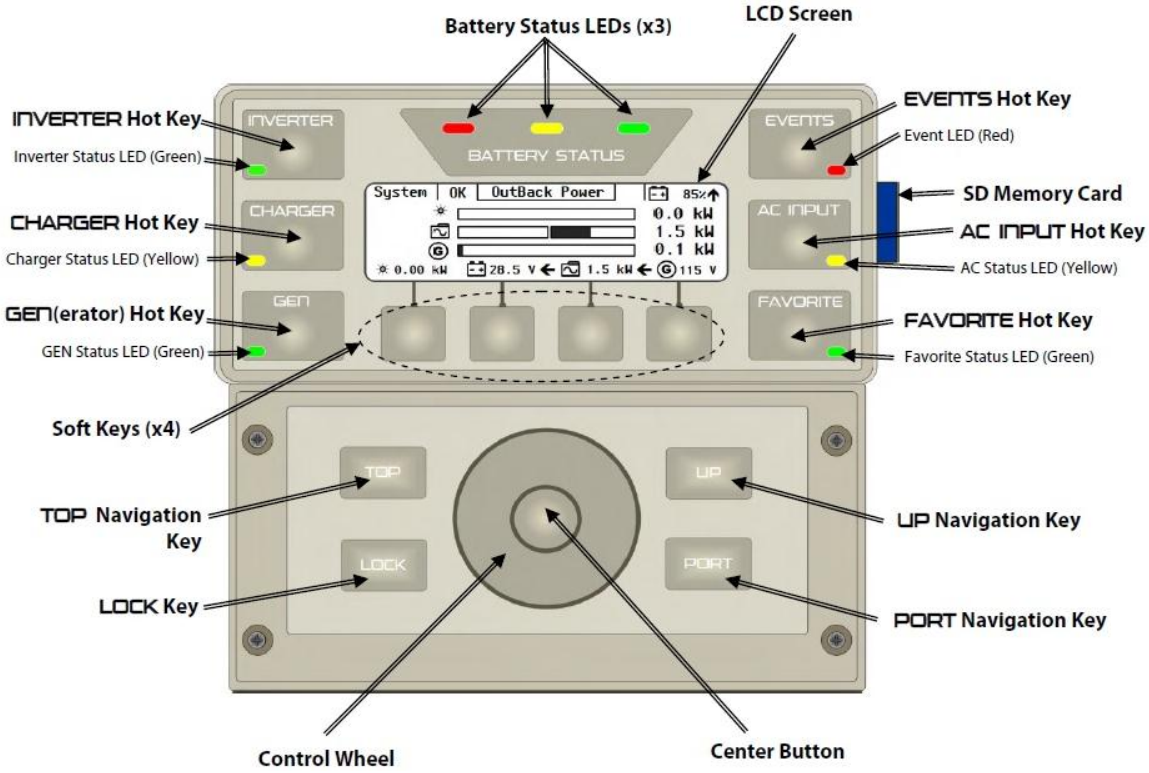

Figure 3.5 Outback MATE 3 monitoring unit

4. Remote monitoring using Arduino Ethernet shield:

The Arduino Ethernet shield connects Arduino microcontroller to the internet using a static IP address. This shield is based on the Wiznet W5100 Ethernet chip which provides a network stack capable of both Transmission Control Protocol (TCT) and User Datagram Protocol (UDP).

This shield has been used to send the data from the FLEXmax80 MPPT unit to PC/Server. The entire data are received by LabVIEW software. Figure 3.6 presents the LabVIEW block diagram code which enables the connection between the Ethernet shield with LabVIEW Graphical User Interface (GUI) (M. Dhimish et al., 2016).

Three analogue input pins have been used to receive the data from the PV module voltage, current and temperature. TCP protocol has been used to enable the connection between the shield with LabVIEW. Finally, the interval between the measurements is equal to 10 ms.

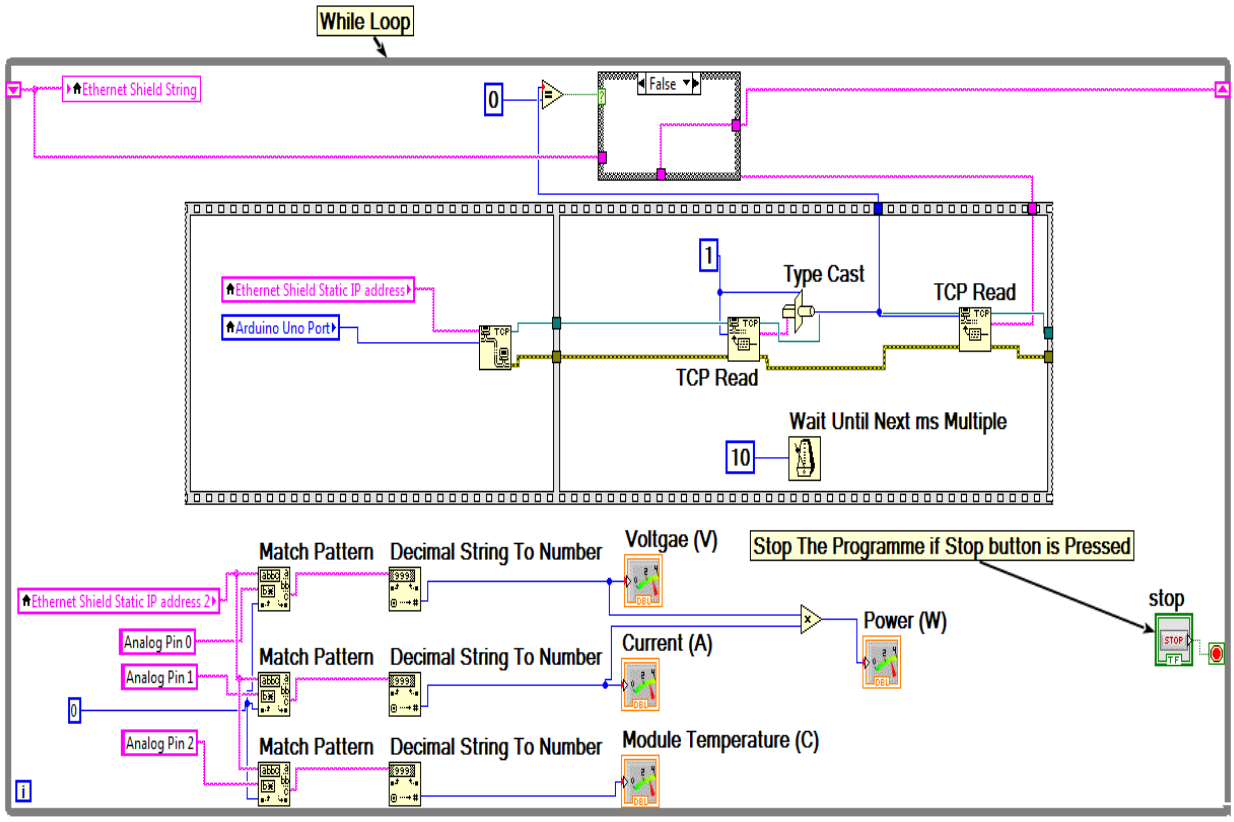

Figure 3.6 LabVIEW code used to enable the connection with Arduino Ethernet shield

5. Remote monitoring using radio frequency (RF) transceiver:

Another remote monitoring unit has been designed to monitor the performance of the PV system using RF transceiver. The data will be sent and monitored using a LCD touch screen. The data include PV system voltage, current and output power. The touch screen is refreshed at a frequency of 1 Hz. This unit also incorporate a password access control feature.

6. Remote monitoring using Bluetooth Module:

Most mobile phones have integrated Bluetooth technology so it was decided to create a simple mobile phone application to allow users to view the live measured PV data. By using the MIT app inventor tool, an android mobile phone application was created. A Bluetooth module transmits measured data to the mobile device running the android app. Figure 3.7 shows a typical logo and the received data on the mobile phone. The output data of the mobile phone application include the PV module temperature, voltage, current, power, and solar irradiance.

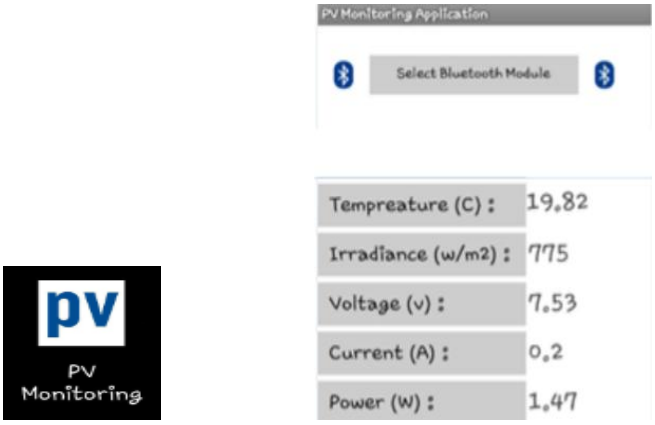

(a) (b)

Figure 3.7 (a) Application Logo, (b) Application output results

7. GUI using VI LabVIEW software:

LabVIEW software offers three main features for the user of the PV system:

1. Operates as a GUI to monitor the status of examined PV installation
2. Works as a logging system. Each measured parameter from the PV installation can be saved over a period of time (i.e. 1 day, 1 month, and 1 year ….etc.)
3. Links the GUI to a web page using HTML code

Figure 3.8 shows one example of a GUI developed using LabVIEW. The front panel of the LabVIEW code consists of four main parts: "A" presents the status of the weather station. Outback Hub 4 and MATE3 data stream status is shown in part "B". The third part "C", shows the PV system output power performance using three MPPT units and the voltage level of the battery bank. At the bottom of the front panel the data stream can be monitored using historical chart, which is presented in "D".

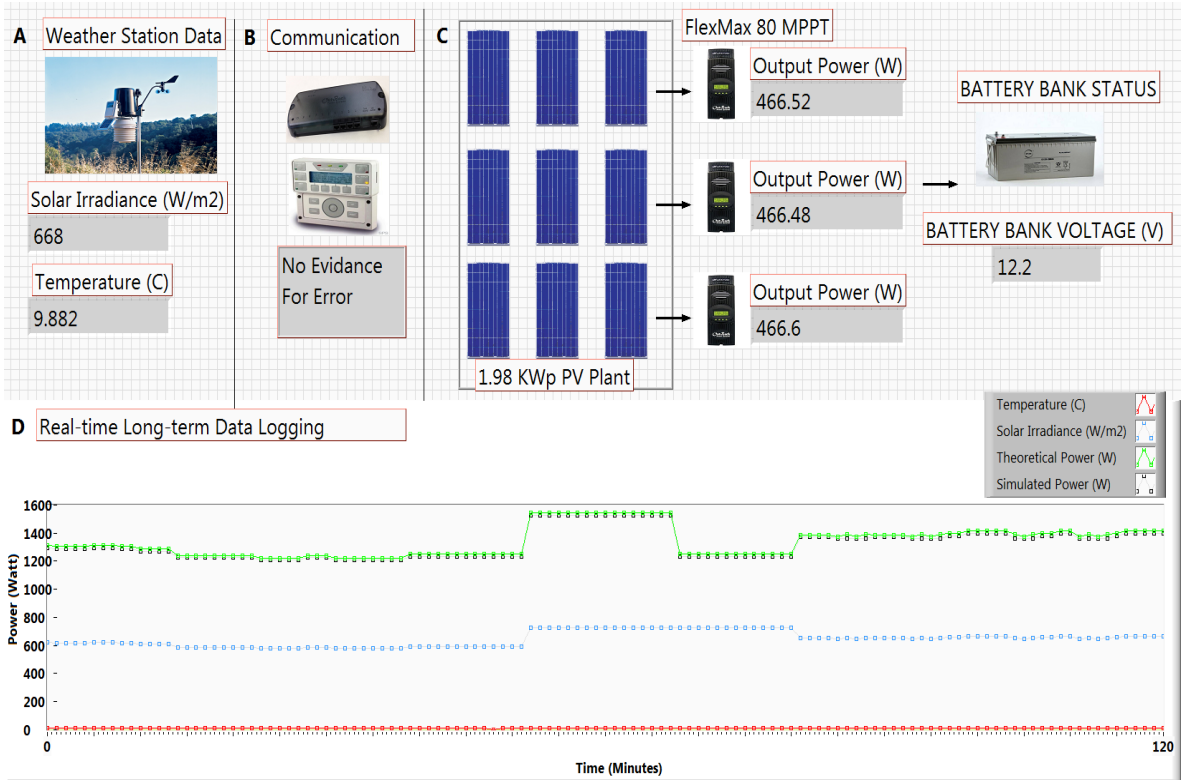

Figure 3.8 Example of GUI developed using LabVIEW software (Mahmoud Dhimish, Holmes, & Dales, 2016)

8. Remote monitoring using web site:

Using HTML code and Dreamweaver software, it is possible to create a web site that is linked to the LabVIEW software. In addition, it is possible to link the GUI of the LabVIEW software to a web site using a tool offered by LabVIEW called web publishing tool (Mahmoud Dhimish et al., 2016).

Two examples of LabVIEW GUI front panel are shown in Figure 3.9. Figure 3.9(a) demonstrates the status of PV plant A, where Figure 3.9(b) presents the status of the weather station.

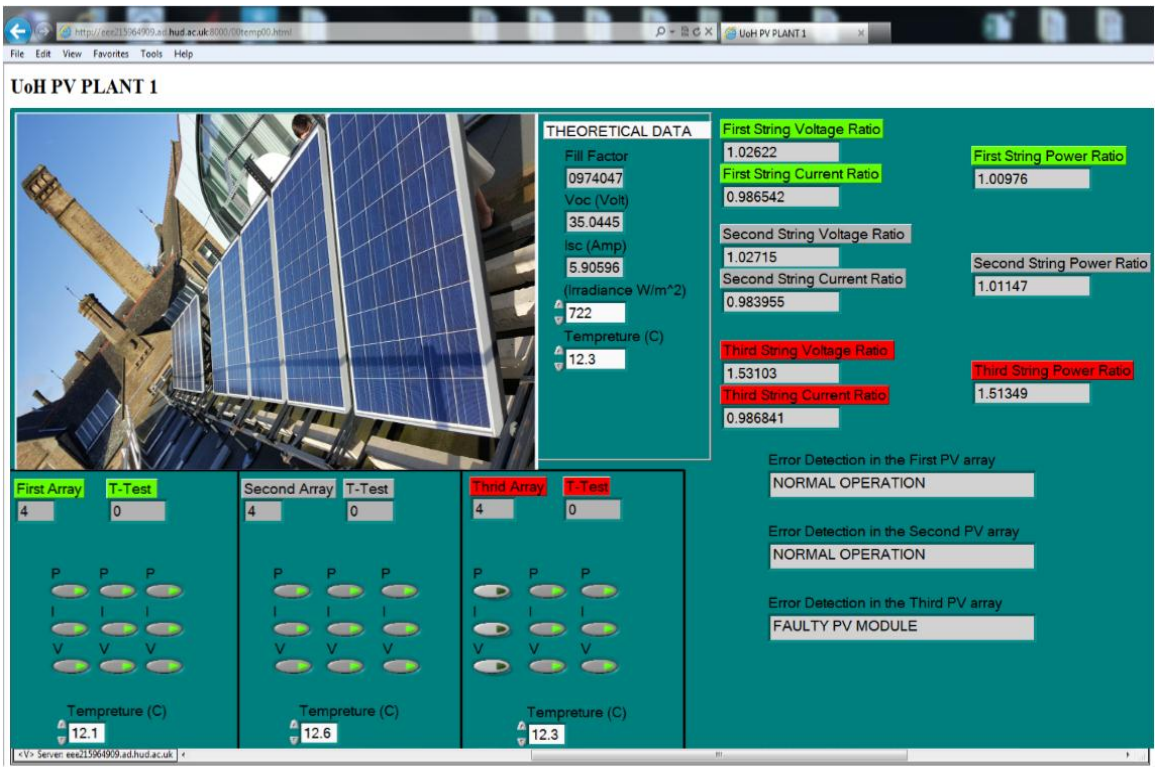

(a)

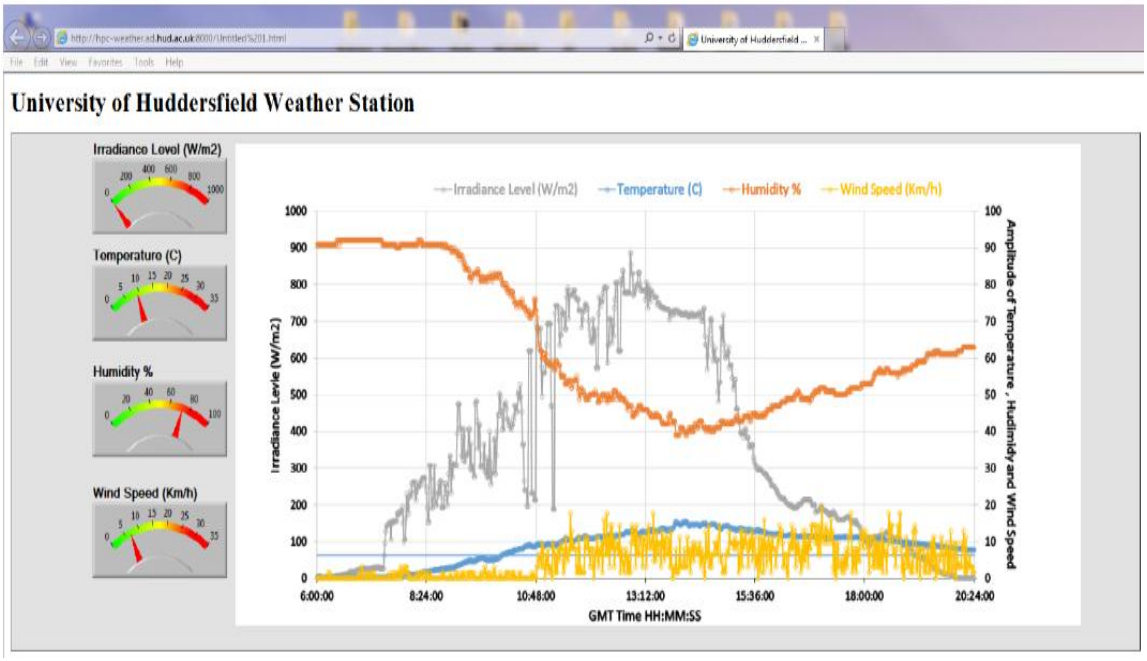

(b)

Figure 3.9 (a) An example of web site that displays the status of the PV system, (b) An example of web site that displays the status of the weather station

3.2 LabVIEW software application

As mentioned previously, LabVIEW software is used to monitor, analyse, and log the PV measured data. In addition, LabVIEW software has been used to simulate the I-V and P-V theoretical curves for a PV module as well as a PV string. In this section, the theoretical curves of a single and string of PV modules will be described. The solar irradiance and PV modules temperature effect will also be presented.

3.2.1 Photovoltaic I-V and P-V theoretical curves modelling

In this research, two PV installations have been used. Each contains a different PV module characteristics. The first tested PV plant (PV plant A) contains a PV modules with a peak power of 220 W_p, and the second PV plant (PV plant B) contains 32 PV modules each with a peak power equals to 130 W_p.

The theoretical I-V and P-V curves have been simulated using LabVIEW software. Figures 3.10a and 3.10b show the simulation curves of the first PV plant module under STC conditions. As can be seen, the simulation requires a number of PV parameters including:

1. Voltage at maximum power point (V_{mpp})
2. Current at maximum power point (I_{mpp})
3. Open circuit voltage (V_{oc})
4. Short circuit current (I_{sc})
5. Series resistance (R_s)
6. Shunt resistance (R_{sh})

These parameters need to be at STC conditions for the simulated PV module, which are available in the manufacturer PV datasheet.

Next, by using the mathematical equations described earlier by Equations (2.1 – 2.3), it is possible to simulate I-V and P-V curves of the PV module. In order to simulate the PV module under various environmental conditions, solar irradiance and PV module temperature are required.

Figure 3.10 shows a horizontal and vertical red line across the I-V and P-V curve. These lines locate the MPP of the PV module. The output of the simulated curves gives the user the values of V_{mpp}, I_{mpp}, P_{mpp}, I_{sc} and V_{oc}. Appendix B shows the simulated results of the second PV plant module under STC conditions.

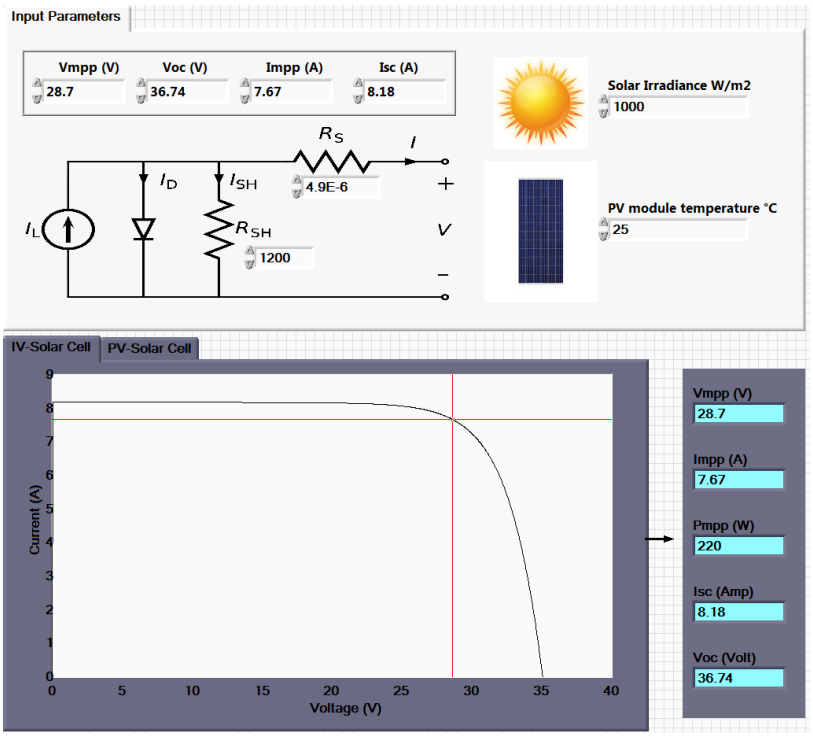

(a)

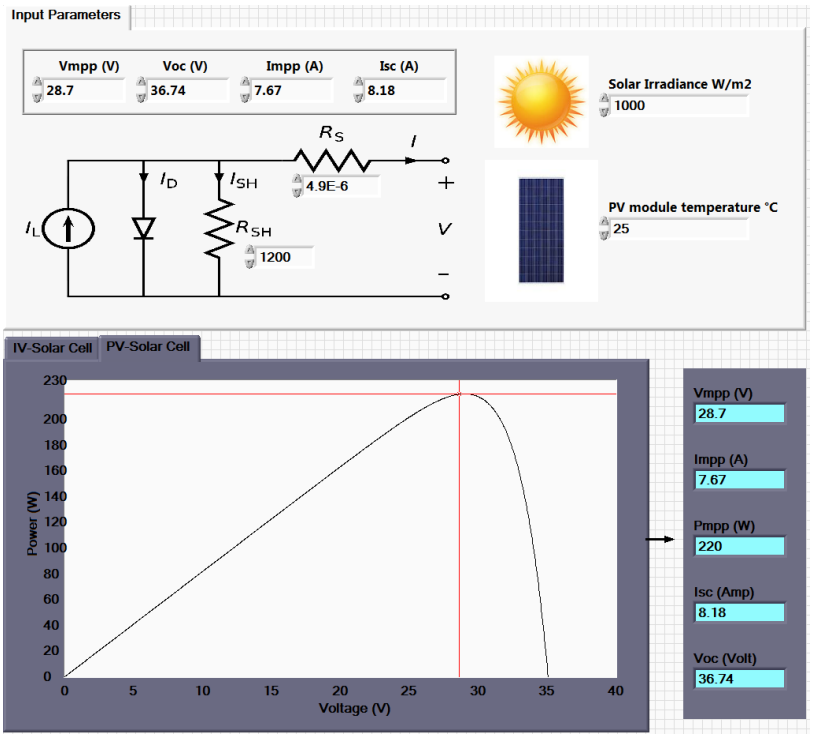

(b)

Figure 3.10 PV solar module theoretical simulation using LabVIEW. (a) I-V curve simulation, (b) P-V curve simulation

3.2.2 Irradiance effect on PV theoretical curves

In this section, the impact of solar irradiance on the theoretical curves (I-V and P-V) will be described using the analysis of the first PV plant module. As shown in Figures 3.11a and 3.11b, three solar irradiance levels have been simulated (750, 550, and 350 W/m^2), the PV module temperature is at SCT (25 ^{0}C).

I-V and P-V curves show that while decreasing the solar irradiance, the value of V_{oc} and I_{sc} is decreased. In addition, the output power of the PV module is also decreased. As an example, the P_{mpp} at 750 W/m2 is equal to 161 W. However, P_{mpp} is equal to 115 W and 70.2 W at 550 W/m^2 and 350 W/m^2 respectively.

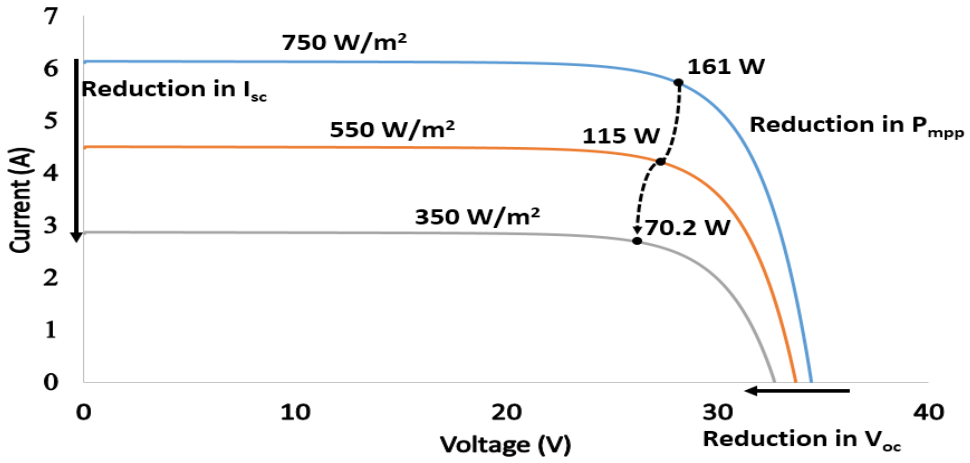

(a)

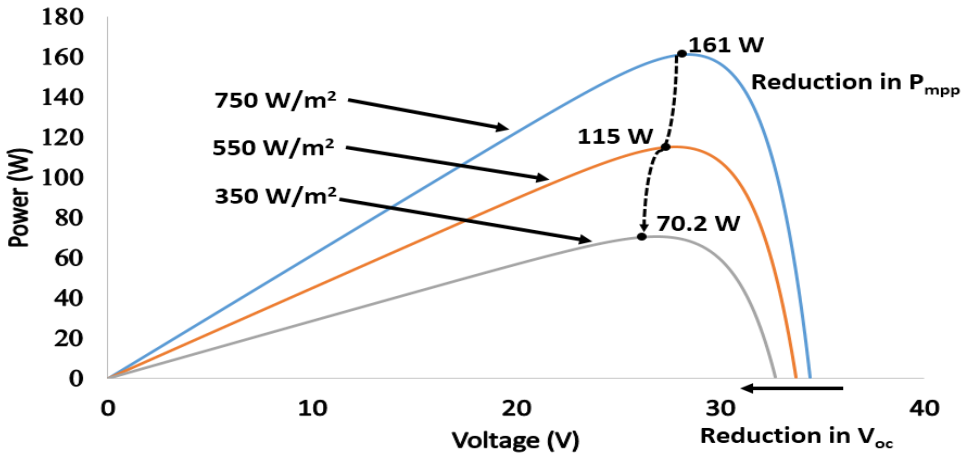

(b)

Figure 3.11 Simulating the theoretical curves for the first PV plant module under various solar irradiance levels with PV module temperature of 25 ^{0}C. (a) I-V curve, (b) P-V curve

3.2.3 Temperature effect on PV theoretical curves

The impact of the PV module temperature will be discussed in this section. Figure 3.11 shows both the I-V and P-V curve of a PV module under various PV module temperature, while the solar irradiance is at STC (1000 W/m^2).

Figure 3.12a shows that while increasing the PV module temperature, the I_{sc} remains constant. However, there is a reduction in the V_{oc}. Furthermore, PV output power increases while decreasing the PV module temperature. Figure 3.12b illustrates the difference between the PV output power during three different PV module temperature conditions (10, 20 and 30 ^{0}C).

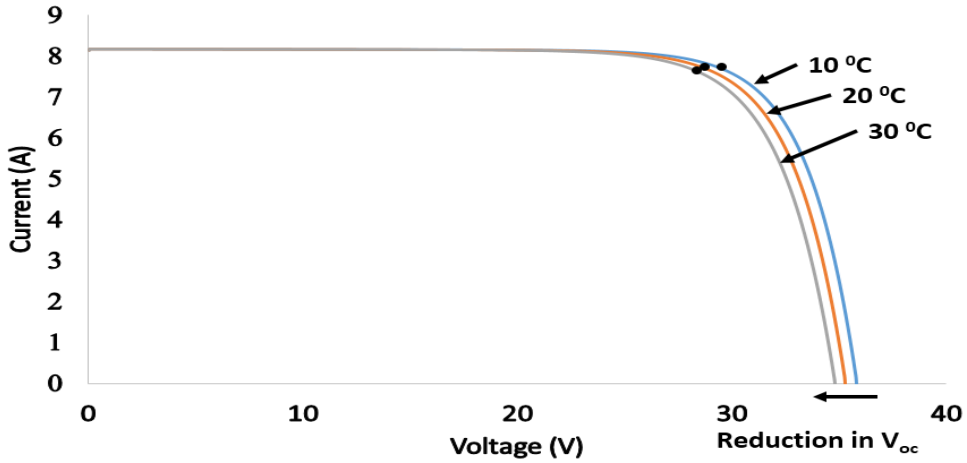

(a)

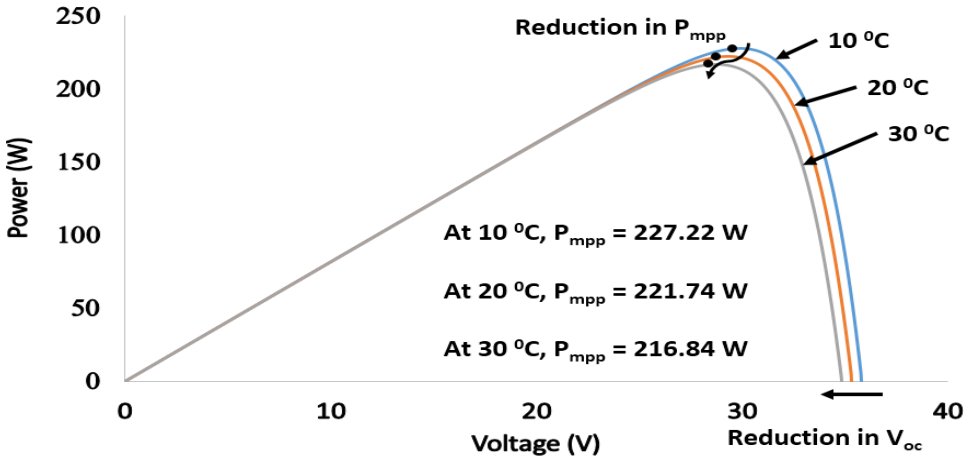

(b)

Figure 3.12 Simulating the theoretical curves for the first PV plant module under various PV module temperature and solar irradiance level is 1000 W/m^2. (a) I-V curve, (b) P-V curve

3.3 Factors impacting the performance of PV systems

There are several factors which impact the performance of the PV systems such as, PS conditions, hot spots, micro cracks, dust, wind speed, humidity, faulty PV modules, MPPT unit efficiency, DC/AC inverter efficiency etc.

In this section, factors which have been analysed and evaluated during the period of the research will be addressed. This section will illustrate the behaviour of the examined PV modules under each studied factor.

3.3.1 PS conditions

PS conditions decrease the output power of the PV modules. In this section, two case scenarios will be presented to describe the performance of PV modules under various PS conditions.

1. Standalone PV module:

This case will analyse the performance of a standalone PV module in the PV plant A, under 3 different PS conditions of 10%, 30%, and 50% using the P-V curve analysis. The PS conditions percentage are described in Figure 3.13a. An opaque paper has been used to cover the PV module in order to produce a PS on the examined PV module. The PV module is connected to FLEXmax 80 MPPT unit to track the MPP of the tested PV panel.

Three PS conditions have been tested (10%, 30% and 50%). The results of the output power are presented in the P-V curve shown in Figure 3.13b. The values obtained are described as follows:

1. 10% PS, PV module P_{mpp} = 208.2 W
2. 30% PS, PV module P_{mpp} = 169.7 W
3. 50% PS, PV module P_{mpp} = 141.5 W

This case shows that the output power decreases as the PS increases. The P-V curve has been simulated using LabVIEW, where the MPPs have been measured during the PS conditions.

Further investigation on PS conditions and a proper detection algorithm will be presented in chapter 5, in order to explain how to detect PS conditions in PV modules based on the ratio of the power and voltage of the PV modules.

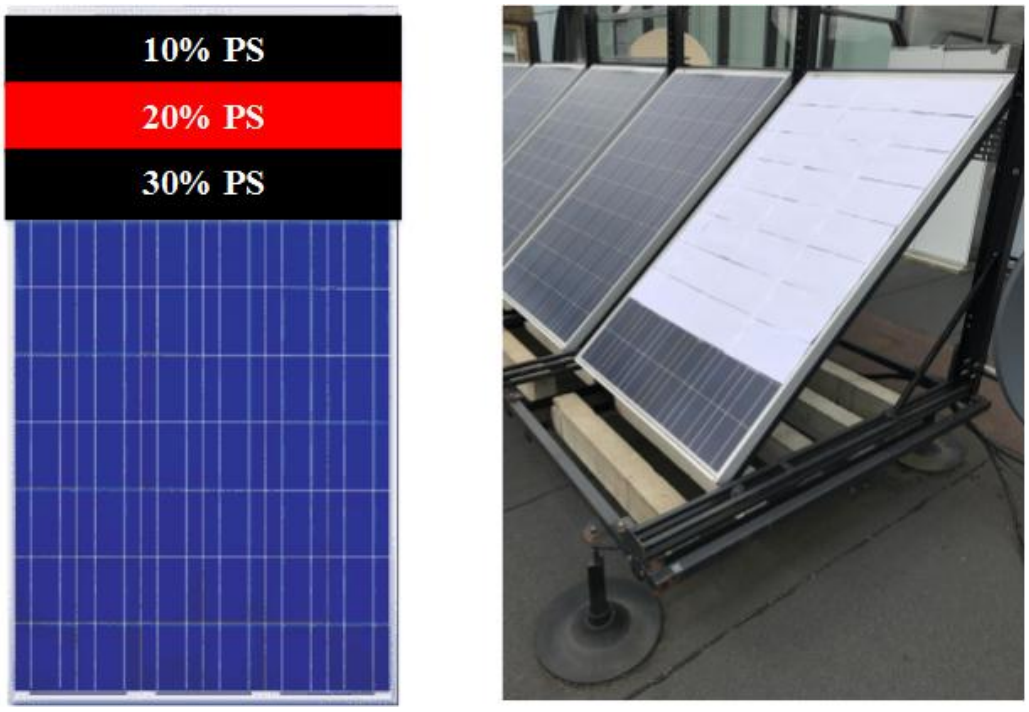

(a)

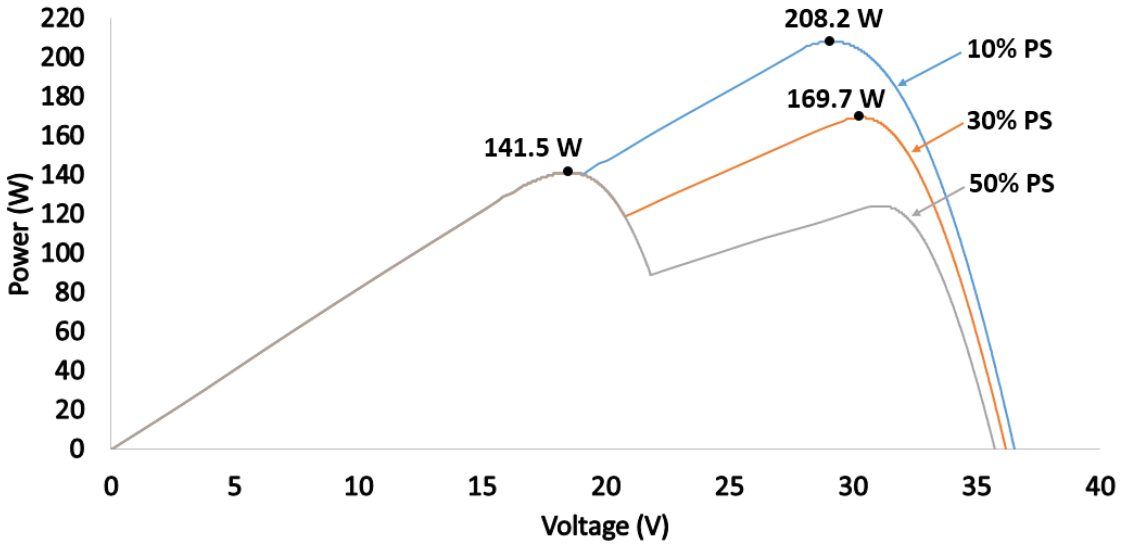

(b)

Figure 3.13 (a) PS percentage including opaque paper object, (b) Measured MPP using three PS conditions

2. PV string:

This section describes the performance of a PV string that comprises 3 PV modules connected in series during PS conditions. Three different scenarios have been examined:

1. All PV modules affected by the same PS condition (20% PS)
2. Two PV modules are affected by 20% PS, while the third is affected by 40% PS
3. Each of the examined PV modules affected by a different PS condition:
    - 1st PV module is affected by 20% PS
    - 2nd PV module is affected by 40% PS
    - 3rd PV module is affected by 60% PS

Figure 3.14 shows the P-V curve which is simulated using LabVIEW software. Subsequently, the MPPs for each tested scenario is measured during different PS conditions. In scenario 1, where all PV modules are subjected to 20% PS, the MPP is equal to 570.8 W. Increasing the PS affecting the third PV module to 40%, the MPP reduces to 510 W. In last scenario when all PV modules have different shading conditions, the MPP is equal to 450.2 W.

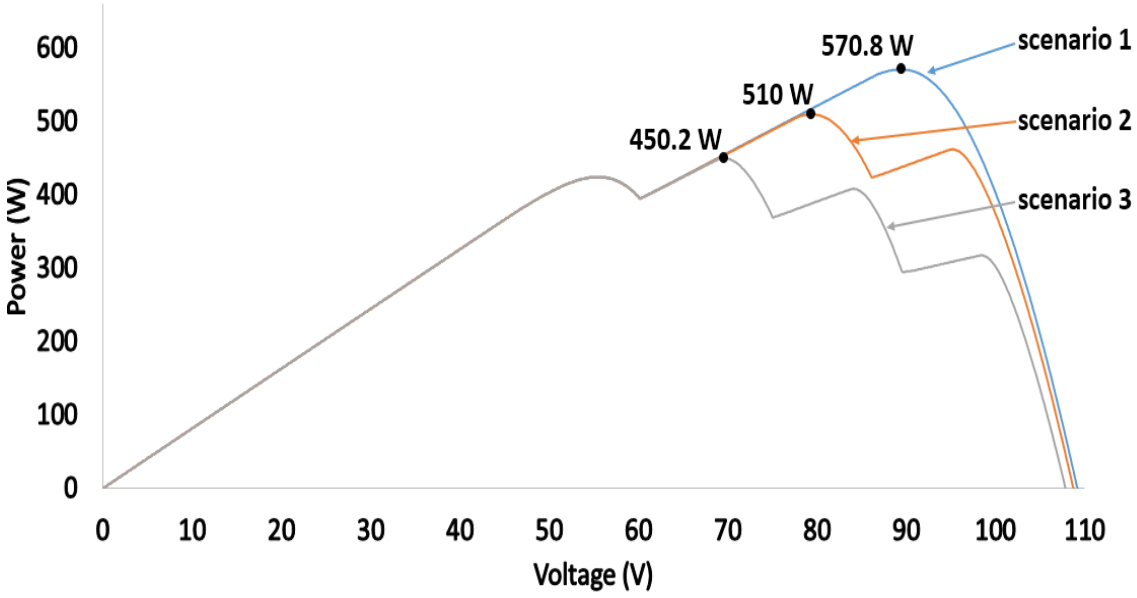

Figure 3.14 P-V curve during PS conditions affecting three PV modules

3.3.2 Faulty PV modules

The second factor which impacts the performance of PV system output power production, is the faulty PV modules. In this thesis, a faulty PV module corresponds to a short-circuited PV module. In other words, the PV module is completely disconnected/removed from the PV string.

In order to describe the performance of a PV string during faulty PV modules, four series connected PV modules were examined. The experiment setup is shown in Figure 3.15. This experiment was conducted in real environmental conditions, where G: 612-626 W/m^2, and T: 16-16.9 ^{0}C. Both G and T are shown in Figure 3.16b.

In normal operation mode, where there is not any faulty PV module in the PV string, the output power of the PV string is approximately 320 W_p. However, while disconnecting one, two and three PV modules from the PV string, the output power is equal to:

i. Disconnecting 1 PV module, P ≈ 235 W_p
ii. Disconnecting 2 PV modules, P ≈ 158 W_p
iii. Disconnecting 3 PV modules, P ≈ 78 W_p

As can be noticed, the output power decrease while increasing the number of faulty PV modules. Figure 3.16a shows the output power of the examined tests, where the efficiency of the MPPT unit is reported in Figure 3.16c.

Since there is a significant reduction in the output power due to the faulty PV modules in the PV plants, it is indeed important to implement and develop a fault detection system which can monitor and locate the faulty PV modules in PV strings. Faulty PV modules in PV strings could be detected using various ways, which will be described in the chapter 5.

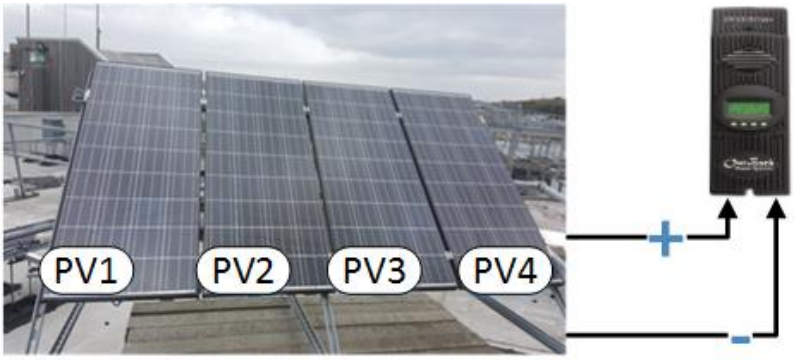

Figure 3.15 Four series connected PV modules with central MPPT unit

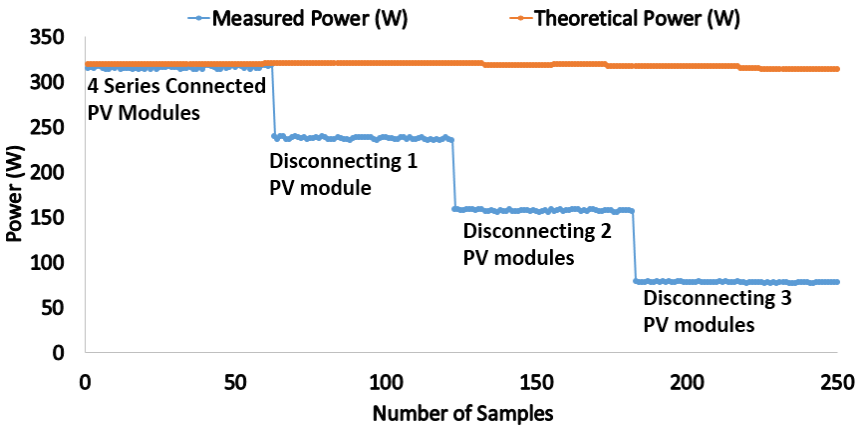

(a)

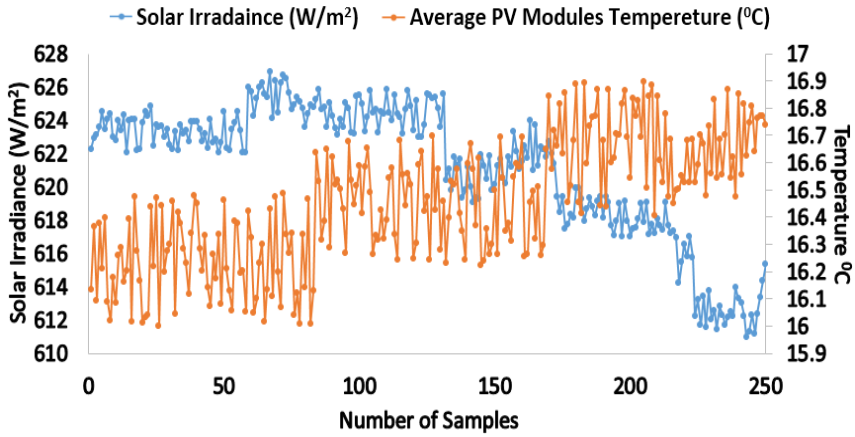

(b)

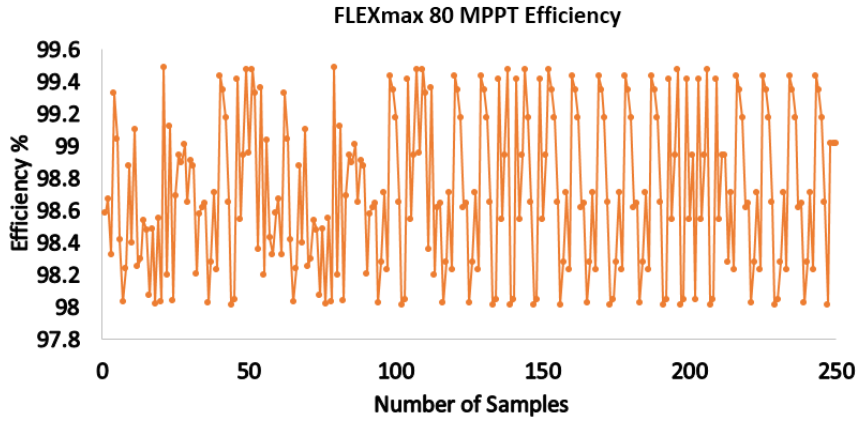

(c)

Figure 3.16 (a) Measured vs. Theoretical output power, (b) Solar irradiance and average PV modules temperature, (c) FLEXmax 80 MPPT unit efficiency

3.3.3 Faulty MPPT unit

There are two possible faults associated with MPPT units used in PV installations. These faults are described below:

1. MPPT efficiency

The efficiency of MPPT units plays a crucial role in providing the maximum output power from the PV modules. The MPPT unit efficiency could be decreased due to several reasons, such as:

i. Fast fluctuations in the solar irradiance affecting the PV modules
ii. Increase/decrease in the PV modules temperature

These factors rapidly increase or decrease the output power from the PV modules. Thus, it requires a fast change in the duty cycle of the MPPT unit to track the new MPP of the PV modules. Figure 3.17a shows an example for two MPPs obtained using the MPPT unit. MPP1 is at the optimum point, where the maximum power is equal to 130 W. The MPPT unit efficiency reduces, and its MPP is equal to 127.7 W. This reduction in the efficiency of the MPPT units could be improved by applying new MPPT techniques as was discussed earlier in the literature review chapter.

2. MPPT unit disconnection

The second type of fault occurs in MPPT units when the PV installation input voltage or input current exceeds the operating threshold. Thus, the MPPT unit will completely shut down. Figure 3.17b shows an example for FLEXmax 80 MPPT unit connected to 2 different voltage ratings:

1. When the input voltage is below the operating threshold (150 VDC), the MPPT unit still in operates and tracks the MPP
2. When the input voltage exceeds the limits (150 VDC), the MPPT unit shut down

A suitable fault detection system has been developed to identify this type of fault which will be described in chapter 5.

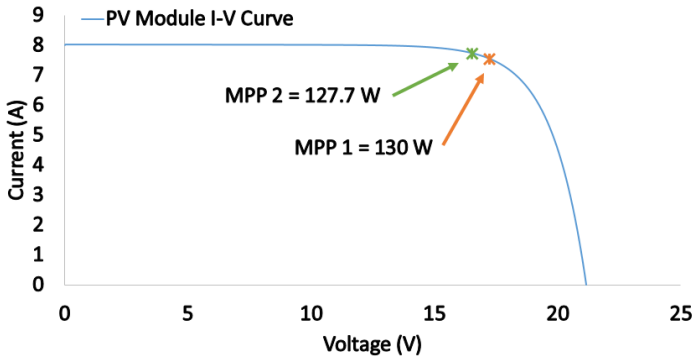

(a)

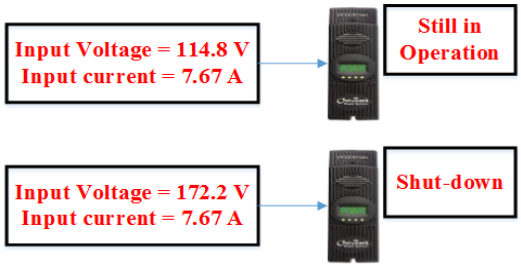

(b)

Figure 3.17 (a) MPPT unit efficiency reduction, (b) MPPT unit input shut-down principle

3.3.4 Hot spots

Another factor which impacts on the performance of PV modules is hot spots. Hot spotted solar cells reduce the output power produced by the PV modules. Therefore, PV hot spots detection and mitigation technique is indeed important to have in PV plants. Figure 3.18 shows an example of a hot spotted PV solar cell which was found in one of the examined PV modules in PV plant A. The hot spot was captured using i5 FLIR thermal imaging camera, which has the following specification:

- Thermal image quality 100 x 100 pixels
- Field of view 21^0(H) x 21^0(V)
- Thermal sensitivity 0.5 ^{0}C

This hot spot reduces the PV output power up to 5.19 W. This permanent power loss could be minimized by developing a new PV hot spot mitigating technique, which will reduce the impact of the hot spots on the performance of PV modules. The proposed hot spot mitigation technique developed in this research will be explained in chapter 7.

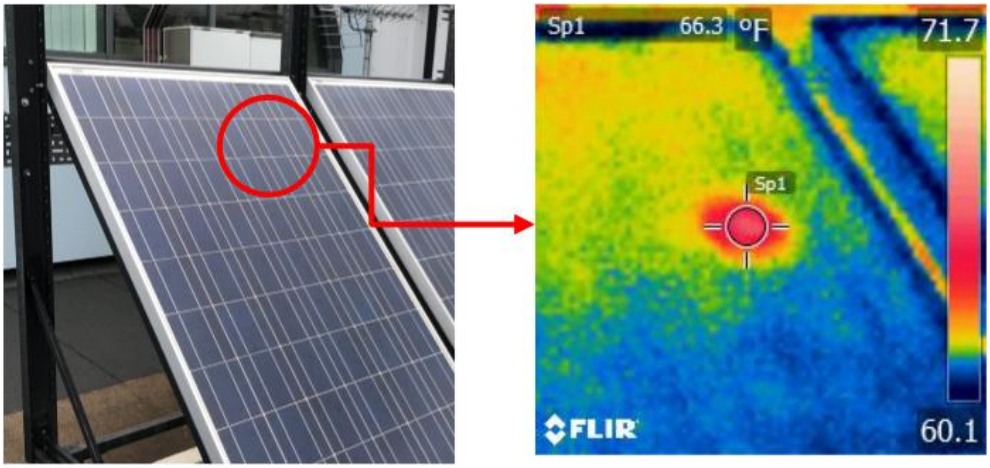

Figure 3.18 Hot spotted solar cell in a PV module

3.3.5 PV micro cracks

The last factor, which will be studied in this research is PV micro cracks. PV micro cracks occur in PV modules due to the following reasons:

i. Environmental Conditions:
   - Solar radiation
   - Temperature variations
   - Humidity
   - Wind speed

ii. PV module defects:
   - Manufacturing defects in PV module martials
   - Manufacturing defects during packing and shipping the PV modules

PV micro cracks permanently reduce the PV output power. However, this output power reduction depends on the PV crack type and size. From the results obtained in this research, it was found that multiple directions crack which affects 5 solar cells reduce the efficiency of the PV module down to 92.19%. Therefore, a statistical analysis approach was developed in order to examine the impact of five different types of PV cracks which can be seen in Figure 3.19.

The statistical analysis approach was also used to test whether the PV crack significantly reduces the PV output power or not. In addition, a comparison between the crack type, size and location was also conducted. This investigation of PV micro cracks will be described in chapter 7.

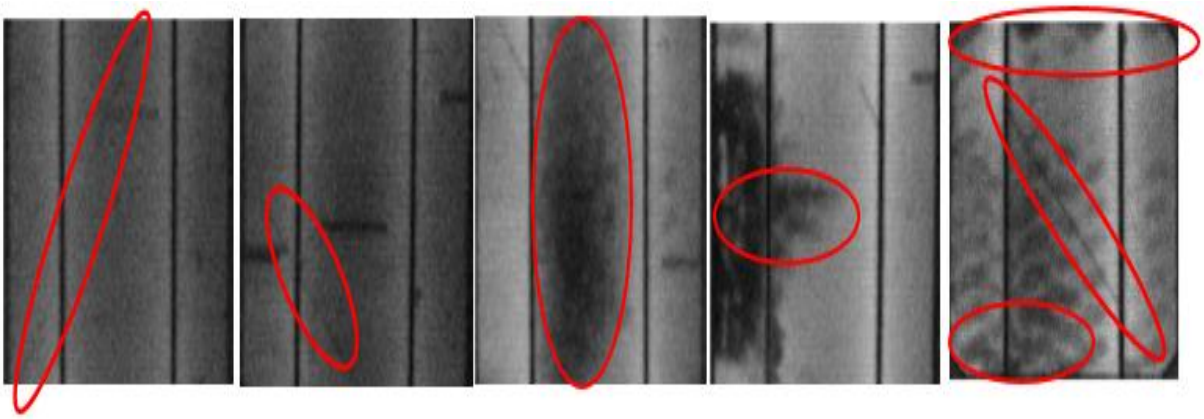

Figure 3.19 Crack type. (a) Diagonal Crack ($+45^0$), (b) Diagonal Crack (-45^0), (c) Parallel to Busbars Crack, (d) Perpendicular to Busbars Crack, (e) Multiple Directions Crack

3.3.6 PV array configuration

PV modules can be connected in different PV array configuration. During normal operation mode (no PS affecting the PV modules), the performance for most PV array configurations are the same including the output power, voltage and current of the PV system. However, during PS conditions, the PV array configuration could increase or decrease the PV output power depending on the shading pattern on the PV modules and the location of the affected PV modules. Therefore, in this research we examined the behaviour of five different PV array configurations has been examined, including:

1. Series (S)
2. Parallel (P)
3. Series-Parallel (SP)
4. Total-Cross-Tied (TCT)
5. Bridge-Linked (BL)

The PV array configurations have been examined under various PS patterns, and faulty PV modules. Seven different indicators have been measured during each examined case. As a results, it was found that the TCT configuration has the highest output power among all tested PV configurations. This will be described in the next chapter (chapter 4).

3.4 Summary

This chapter described a monitoring system designed to monitor the status of the existing PV modules at the University of Huddersfield. Eight different monitoring techniques have been demonstrated and can be summarized in Figure 3.20.

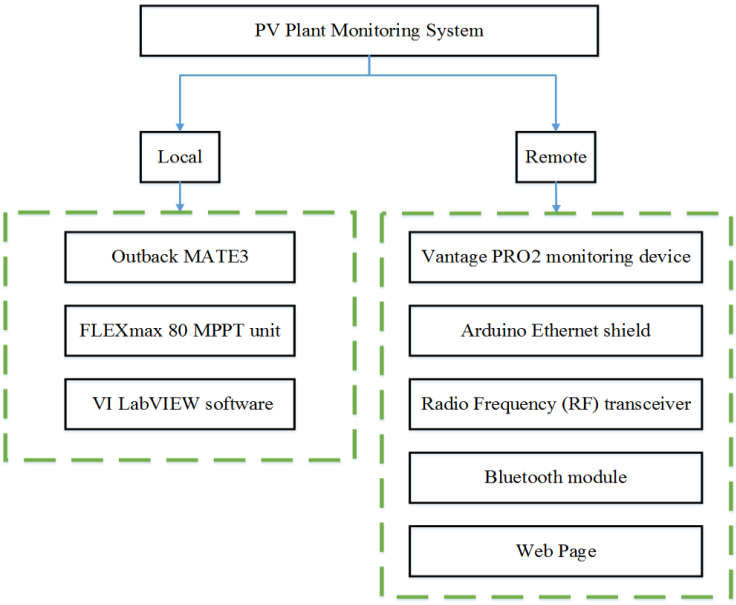

Figure 3.20 Summary of the proposed PV monitoring system

Furthermore, LabVIEW software structure was explained. It was shown that the main purpose of the LabVIEW software is to monitor, analyse and log the PV measured data, as well as perform the theoretical curves of the examined PV modules under various environmental conditions.

The last section has presented six different factors impacting the performance of PV systems, including:

1. PS conditions
2. Faulty PV modules
3. Faulty MPPT unit
4. Hot spots
5. PV micro cracks
6. PV array configuration

Each of the mentioned factors will be described in the following chapters. The last factor (PV array configuration) will be described in the next chapter.

Chapter 4 Multiple PV Array Configurations

The main goal of this chapter is to model, analyse and compare the performance of multiple PV array configurations under various PS and PV faulty conditions. Five different PV array configurations have been tested including S, P, SP, TCT, and BL. Additionally, seven indicators have been compared during each examined case scenario, where all tests have been carried out using MATLAB/Simulink software.

This chapter is based on work carried out with collaboration of the institute of communication and power networks, Leeds University and published as a journal article in (Mahmoud Dhimish, Holmes, Mehrdadi, Dales, Chong, et al., 2017).

4.1 Modelling and simulation of a PV module

MATLAB/Simulink software has been used to model, simulate and analyse the performance of the examined PV modules including multiple PV array configurations systems. Figure 4.1a shows the equivalent circuit of a PV module. The voltage and current characteristics of the PV module is obtained using Equation (4.1) (McEvoy et al., 2013).

$$I = I_{ph} - I_o\left(e^{\frac{V+IR_s}{N_s V_t}} - 1\right) - \left(\frac{V+IR_s}{R_{sh}}\right) \quad (4.1)$$

where I_{ph} is the photo-generated current at STC , I_o is the dark saturation current at STC, R_s is the module series resistance, R_{sh} is the panel parallel resistance, N_s is the number of series cells in the PV module and V_t is the thermal voltage and it can be calculated using Equation (4.2) (McEvoy et al., 2013).

$$V_t = \frac{A\,k\,T}{q} \quad (4.2)$$

where A is the diode ideality factor, k is Boltzmann's constant, T is the module temperature in kelvin and q is the charge an electron.

The simulation of the PV module under STC conditions is shown in Figure 4.1b. Figure 4.1c and Figure 4.1d show respectively the I-V and P-V curves of the examined PV module under three different irradiance conditions: 1000 W/m^2, 500 W/m^2, and 100 W/m^2. The PV module parameters such as I_{sc}, V_{oc}, P_{mpp}, V_{mpp}, and I_{mpp} have been taken from Table 3.1.

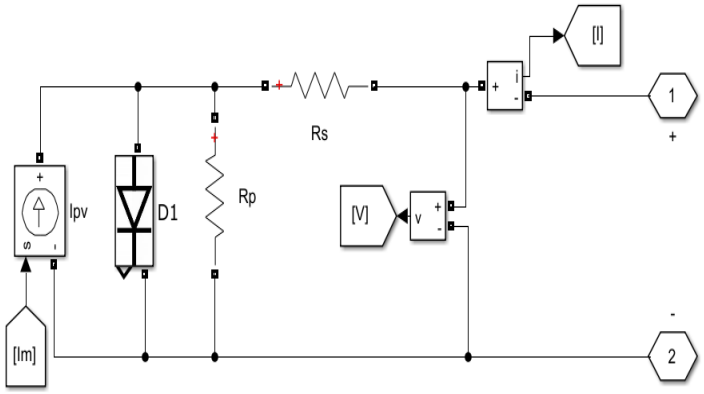

(a)

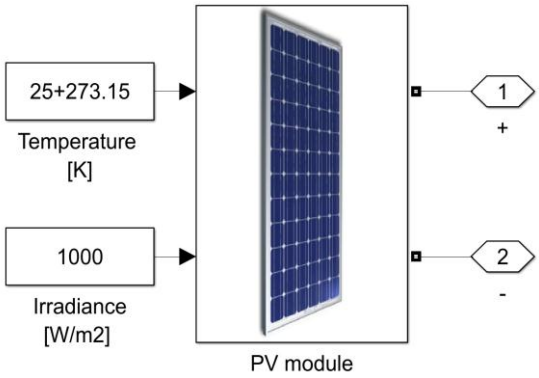

(b)

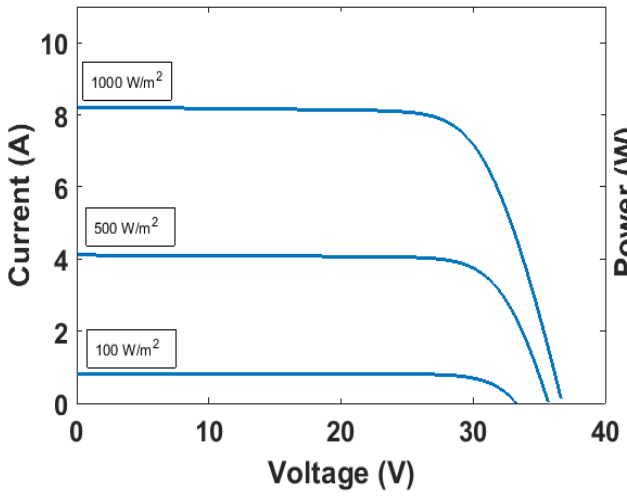

(c)

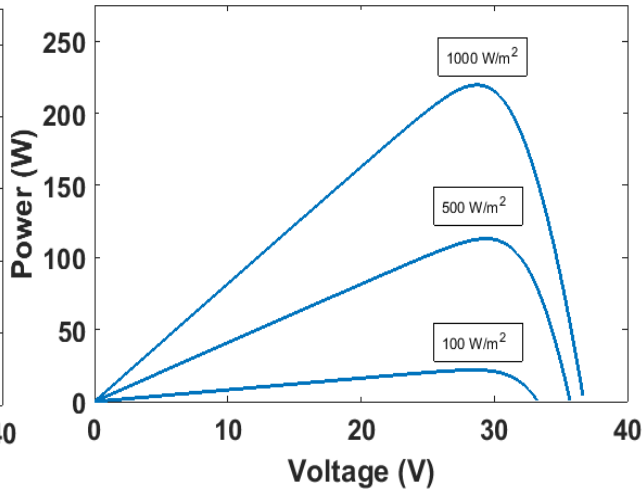

(d)

Figure 4.1 Photovoltaic modelling using MATLAB/Simulink. (a) Equivalent circuit of a PV module, (b) Simulating PV module under STC, (c) Photovoltaic I-V Curve, (d) Photovoltaic P-V Curve

4.2 Calculation of the diagnostic indicators

In order to compare the examined PV array configurations. Firstly, it is required to identify the main indicators which will be studied and compared during the examined tests. As mentioned earlier, seven indicators including: V_{mpp}, V_{oc}, I_{mpp}, I_{sc} and P_{mpp} will be simulated. And three new diagnostic indicators, equivalent thermal voltage (V_{te}), Fill Factor (FF) and PV series resistance (R_s) which will be described in this section.

4.2.1 Equivalent thermal voltage (V_{te})

In a previous work (Silvestre, Boronat, & Chouder, 2009; Spataru et al., 2015) the estimation of the thermal voltage of a PV model under partial shading conditions has been expressed by Equation (4.3).

$$V_{te} = \frac{(2V_{mpp} - V_{oc})(I_{sc} - I_{mpp})}{I_{mpp} - (I_{sc} - I_{mpp}) \ln(\frac{I_{sc} - I_{mpp}}{I_{sc}})} \tag{4.3}$$

where V_{mpp} is voltage at maximum power point, I_{mpp} presents the current at the maximum power point, V_{oc} is the open circuit voltage, and I_{sc} is the short circuit current estimated by the I-V or P-V curve of the PV module.

A second commonly used method to estimate the thermal voltage is to evaluate the change of the diode ideality factor A of the PV module (Sera, Teodorescu, & Rodriguez, 2008). This method can be calculated using (4.4).

$$V_{te} = \frac{N_s\, A\, k\, T}{q} \tag{4.4}$$

where N_s is the number of solar cells connected in series, k is the Boltzmann constant, T is the junction temperature in kelvin and q is equal to the charge of an electron.

In this research, the first method based on Equation (4.3) was used to estimate the thermal voltage. It does not require the estimation of the ideality factor for the PV modules. The ideality factor cannot be estimated using the MPPT units provided in the PV systems.

In order to investigate the V_{te} variations, the PV module shown previously in Figure 4.1b has been simulated under various irradiance levels (100 – 1000 W/m^2), where the PV module temperature is at STC. Figure 4.2 shows the simulation results of the V_{te}. It is evident that there is a reduction in the V_{te} between 100 – 300 W/m^2. After 300 W/m^2 the V_{te} starts to increase. This increase could be used as an indication of the increase of the PV solar irradiance.

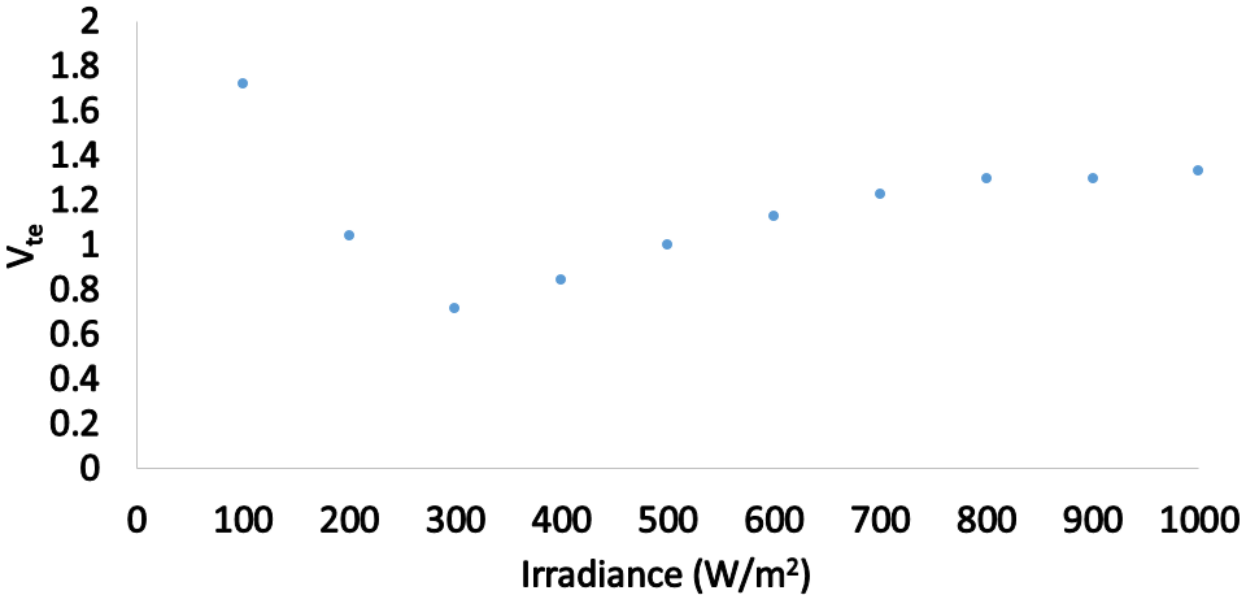

Figure 4.2 Simulation of V_{te} under various solar irradiance levels, where the PV module temperature is at STC

4.2.2 Fill Factor (FF)

The fill factor (*FF*) is a generic diagnostic indicator which is sensitive to power losses due to shading and faulty conditions occurring in PV systems (Spataru et al., 2015). FF is sufficiently robust to the irradiance change and the temperature levels. *FF* can be calculated using Equation (4.5).

$$FF = \frac{I_{mpp}\, V_{mpp}}{I_{sc}\, V_{oc}} \tag{4.5}$$

The fill factor is a good indicator since it depends on the voltage and current changes in the PV modules. Figure 4.3a shows the I-V curve of the examined PV module, and the parameters used in the calculation of the FF indicator are also shown.

At STC condition, the PV module FF can be evaluated as the following:

$$FF = \frac{I_{mpp}\, V_{mpp}}{I_{sc}\, V_{oc}} = \frac{7.67 \times 28.7}{8.18 \times 36.74} = 73.25\%$$

Figure 4.3b shows the variations of the *FF* under various irradiance levels (100~1000 W/m^2), where the PV module temperature is at STC. The *FF* does not follow a specific pattern (decrease or increase). However, the *FF* shows that the PV module under normal operation conditions is between 71% and 74%. Therefore, if the simulated *FF* is below or above the thresholds, this indicates that the PV module is under faulty conditions (PV module might be affected by a hot spot, micro crack, or increase/decrease in the PV module temperature).

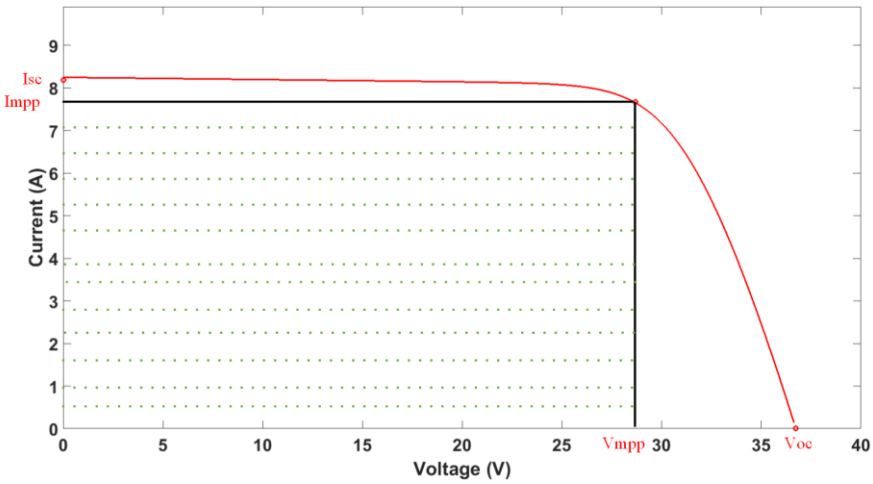

(a)

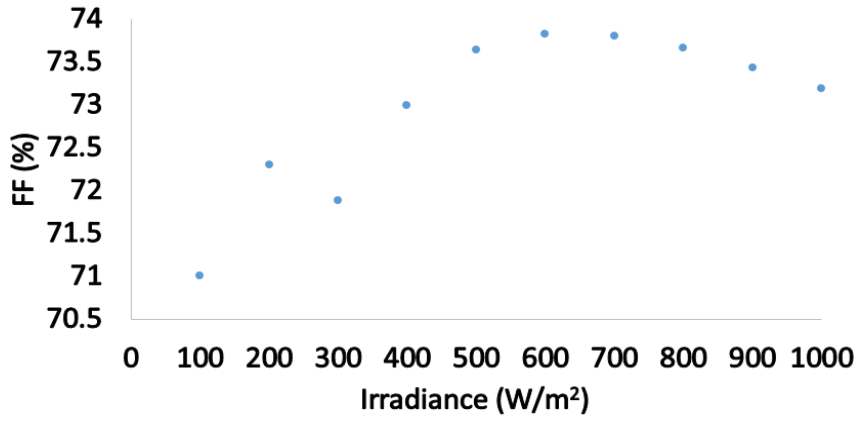

(b)

Figure 4.3 (a) *FF* for the examined PV module, (b) *FF* variations during various solar irradiance levels, where the PV module temperature is at STC

4.2.3 PV module series resistance (R_s)

Method 1:

One commonly used method to estimate R_s is to evaluate the derivative of the voltage with respect to the current at the V_{oc}. The expression to approximate the R_s for a PV module is described by Equation (4.6).

$$R_{s,e} = -\frac{dV}{dI}\Big|_{V \approx V_{oc}} = -\frac{V_2 - V_1}{I_2 - I_1}\Big|_{V \approx V_{oc}} \quad (4.6)$$

where V_2, V_1, I_2 and I_1 are the voltage and the current points estimated near to V_{oc}.

The value of the series resistance estimated by the derivative may vary with the irradiance and the temperature conditions. In (Sera, Mathe, Kerekes, Teodorescu, & Rodriguez, 2011), authors proposed a method to translate the value of the estimated R_s to STC in order to mitigate the effect of the irradiance (G) and PV module temperature (T). The final expression is illustrated by Equation (4.7).

$$R_s = R_{s,e} + \frac{V_{te}}{I_{sc}} \left(\frac{G}{G_{STC}} \times \frac{T_{STC}}{T} - 1\right) \tag{4.7}$$

where G_{STC} is equal to 1000 W/m^2 and T_{STC} is equal to 25 ^{o}C.

The estimation of R_s requires the voltage and the current measurements of at least two points of the I-V curve close to the V_{oc}. This method also requires the value of the irradiance and the PV modules temperatures to perform the estimation of the series resistance value.

Method 2:

Another method of estimating the series resistance of a PV module is to evaluate the derivative of the voltage with respect to the current at the short circuit and maximum power point. Such point is characterised by a current lower, and closer to I_{mpp} and it is denominated as Q. This method was proposed by (Sera et al., 2011). There are two options to calculate Q using Equations (4.8 & 4.9).

$$Q1 = I_{sc,e} - (0.75 \times I_{mpp}) \tag{4.8}$$

$$Q2 = I_{sc,e} - (0.60 \times I_{mpp}) \tag{4.9}$$

where the value of $I_{sc,e}$ is the estimated short circuit current and can be evaluated using (20).

$$I_{sc,e} = \frac{I_{sc}}{K_1} \tag{4.10}$$

where K_1 is the ratio between I_{mpp} and I_{sc} and it is assumed as constant value of 0.92.

The last expression for estimating the value of the series resistance is expressed by (4.11).

$$R_s = -\frac{dV}{dI}\Big|_{I \approx Q} = -\frac{V_2 - V_1}{I_2 - I_1}\Big|_{I \approx Q} \tag{4.11}$$

The evaluation of the series resistance requires at least two points of the I-V curve for the PV module. Furthermore, it is required to measure:

1. I_{mpp}
2. I_{sc}

Figure 4.4 shows the value of the series resistance estimated using method 1 and method 2. The estimated values of the R_s is compared with the measured R_s (Outdoor measurements using a PV module in PV plant A). Therefore, the difference between the measured values and the estimated values can be expressed by Equation (4.12).

$$Difference = Estimated\ R_s - Measured\ R_s \tag{4.12}$$

Table 4.1 illustrates the comparison between the estimated R_s and measured R_s using method 1 at V_{oc}, and method 2 at Q1 and Q2. The minimum average difference of 1.71% is obtained using method 1. Therefore, in this chapter, method 1 is used for the estimation of R_s.

Table 4.1 Difference between estimated R_s and measured R_s

Irradiance level (W/m^2)	Measured R_s (Ω)	Estimated R_s (Ω) using method 1		Estimated R_s (Ω) using method 2, Q1		Estimated R_s (Ω) using method 2, Q2	
		R_s (Ω)	Difference	R_s (Ω)	Difference	R_s (Ω)	Difference
1000	0.48484	0.51	0.0277	0.53	0.0477	0.58	0.0977
900	0.537836	0.54	0.0077	0.59	0.0577	0.59	0.0577
800	0.567762	0.58	0.0177	0.62	0.0577	0.70	0.1377
700	0.623004	0.63	0.0147	0.68	0.0587	0.68	0.0647
600	0.698996	0.70	0.0077	0.60	-0.092	0.81	0.1177
500	0.789787	0.80	0.0147	0.83	0.0480	0.93	0.1447
400	0.934482	0.95	0.0177	0.98	0.0477	1.1	0.1977
300	1.172762	1.2	0.0277	1.2	0.0617	1.3	0.1377
200	1.688184	1.7	0.0177	1.7	0.0417	1.8	0.1277
100	3.240672	3.2	0.0177	3.2	0.0407	3.3	0.0977
		Average Difference (%)		**Average Difference (%)**		**Average Difference (%)**	
		1.71		**3.69**		**11.81**	

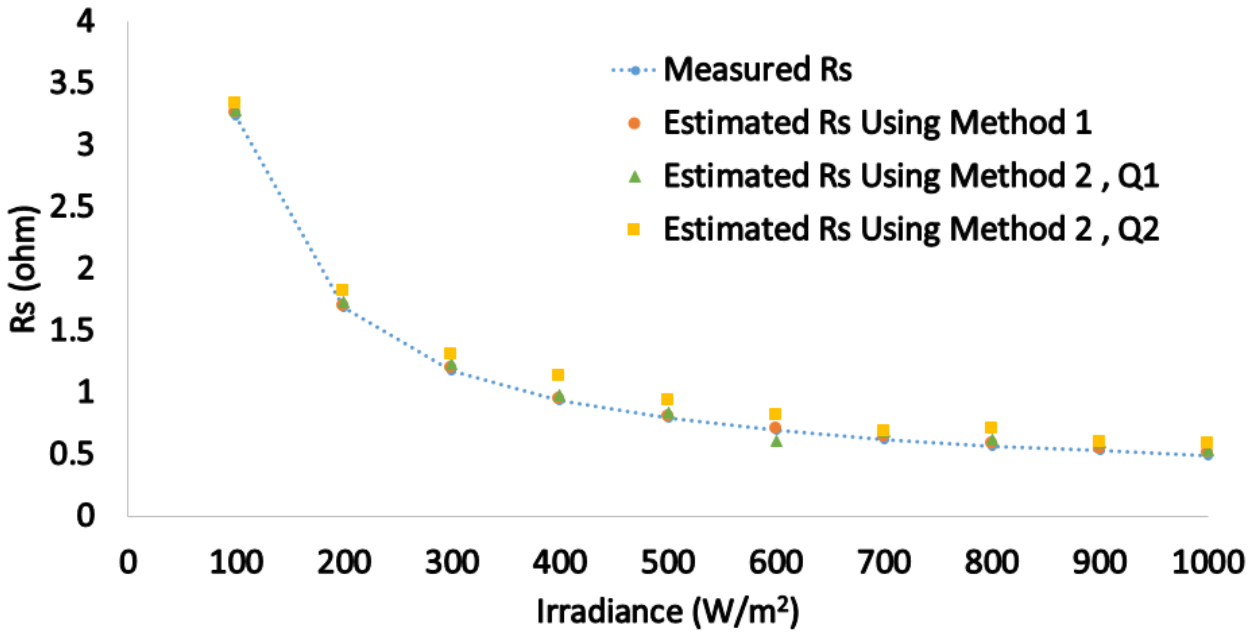

Figure 4.4 Evaluating PV module R_s using various solar irradiance levels, where the PV module temperature is at STC

4.3 Simulation and data analysis for multiple PV array configurations

This section describes the modelling and analysis of the examined multiple PV array configurations. In order to test the multiple PV array configurations, 24 PV modules were used. The PV module temperature was fixed at the standard test condition (STC) 25 ^{o}C.

4.3.1 Examined PV array configurations

Five PV array configurations were used in order to examine the difference between each PV array configuration under normal operation, partial shading, and faulty PV conditions. The examined PV array configurations are listed below:

1. S
2. P
3. SP
4. TCT
5. BL

MATLAB/Simulink software is used to create the examined PV array configurations. Appendix C contains all MATLAB/Simulink software models which are used to configure the PV modules. Furthermore, during the simulation all indicators: V_{mpp}, V_{oc}, I_{mpp}, I_{sc}, P_{mpp}, R_s, FF and V_{te} have been logged in a spreadsheet to evaluate the performance for each PV array configuration separately.

4.3.2 PV array configurations under STC

This section presents the variations of the simulated indicators at STC conditions applied to the PV array configurations. Table 4.2 shows the value of the indicators which have been simulated for the examined PV array configurations. The main outcomes from the obtained results can be expressed by the following:

1. Series configuration: the dominant indicator is the value of the V_{oc}, V_{mp}, and the value of the thermal voltage.
2. Parallel configuration: I_{sc}, I_{mpp}, and the thermal voltage have the least values across all other PV configurations.
3. SP, TCT and BL configurations have similar results across all indicators.
4. At STC, the FF for all PV configurations is approximately equal to 73.2%.

Table 4.2 Indicators values estimated for all examined PV array configurations

PV configuration	I_{sc} (A)	V_{oc} (V)	I_{mpp} (A)	V_{mpp} (V)	P_{mpp} (W)	R_s (Ω)	V_{te} (V)	FF (%)
S	8.177	881.2	7.538	700.3	5279	12.1	36.2	73.2
P	196.2	36.74	181.4	29.1	5279	0.02	1.4	73.2
SP	32.71	220.3	30.26	174.4	5279	0.7	8.5	73.2
TCT	32.71	220.3	30.33	174	5278	0.7	8.3	73.2
BL	32.71	220.3	30.33	174	5278	0.7	8.3	73.2

Furthermore, the evaluation of the series resistance across one PV module in the examined PV array configurations can be calculated according to the mathematical expressions listed in Table 4.3.

Table 4.3 Mathematical calculations of R_s for various PV array configurations

PV array configuration	Mathematical expression for estimating the value of R_s for one PV module in the PV array configuration	
S	$\frac{R_{s\,(Obtained\ from\ the\ I-V\ Curve)}}{24_{(total\ PV\ module\ in\ the\ PV\ array\ configuration)}}$	(4.13)
P	$R_{s\,(Obtained\ from\ the\ I-V\ Curve)} \times 24_{(total\ PV\ module\ in\ the\ PV\ array\ configuration)}$	(4.14)
SP, TCT and BL	$\frac{R_{s\,(Obtained\ from\ the\ I-V\ Curve)} \times 4\ _{(number\ of\ PV\ columns)}}{6\ _{(number\ of\ PV\ modules\ in\ one\ PV\ row\ "PV\ String")}}$	(4.15)

Using the Equations (4.13 – 4.15), the estimation of R_s for a single PV module in the PV array configurations is shown in Table 4.4. There is a slight difference between the measured R_s at STC and the estimated R_s. However, the average difference between the measured R_s and the calculated R_s among all tested PV array configurations is equal to 2.2%.

Table 4.4 Estimated R_s for one PV module only

PV configuration	R_s (Ω)	Calculated R_s for one PV module (Ω)	Measured R_s for one PV module at STC (Ω)	Difference in the estimation of R_s (%)
S	12.18	0.5	0.48	2.2
P	0.020	0.4	0.48	-0.2
SP	0.75	0.5	0.48	2
TCT	0.75	0.5	0.48	2
BL	0.75	0.5	0.48	2

4.3.3 PV array configurations under PS condition – scenario 1

In this section, the PV array configurations will be evaluated using uniform and non-uniform PS patterns which affects a row of PV modules (row-level PS condition). Figure 4.5a shows the simulated shading patterns affecting the PV array (Mahmoud Dhimish, Holmes, Mehrdadi, Dales, Chong, et al., 2017).

The first PS pattern is applied on a row of PV modules at irradiance level equal to 500 W/m^2 (uniform shading). However, the second PS pattern consists of various non-uniform irradiance levels (200, 400, 600 and 800 W/m^2).

The MPP obtained from the examined PV array configurations under shading pattern 1 is reported in Figure 4.5b. The P configuration shows the maximum output power compared to all other examined PV array configurations. The configurations S, SP, TCT and BL generate the same MPP in each case.

Figure 4.5c shows that P configuration has the largest MPP among all other PV array configurations under PS pattern 2. TCT and BL come second best choice whereas the S configuration has the lowest performance, despite the fact that P configuration has the highest MPP.

However, P configuration is practically not useful in real PV systems, since has low voltage ratings and high current rating. These ratings are not suitable with DC/AC inverters which are commonly used in PV installations.

Partial Shading Pattern 1

500 W/m^2	500 W/m^2	500 W/m^2	500 W/m^2
1000 W/m^2	1000 W/m^2	1000 W/m^2	1000 W/m^2
1000 W/m^2	1000 W/m^2	1000 W/m^2	1000 W/m^2
1000 W/m^2	1000 W/m^2	1000 W/m^2	1000 W/m^2
1000 W/m^2	1000 W/m^2	1000 W/m^2	1000 W/m^2
1000 W/m^2	1000 W/m^2	1000 W/m^2	1000 W/m^2

Case 1:First Row 500W/m^2

Case 2:First and Second Rows 500W/m^2

Case 3:First, Second and Third Rows 500W/m^2

Case 4:First, Second, Third and Fourth Rows 500W/m^2

Case 5:First, Second, Third, Fourth and Fifth Rows 500W/m^2

Partial Shading Pattern 2

200 W/m^2	400 W/m^2	600 W/m^2	800 W/m^2
1000 W/m^2	1000 W/m^2	1000 W/m^2	1000 W/m^2
1000 W/m^2	1000 W/m^2	1000 W/m^2	1000 W/m^2
1000 W/m^2	1000 W/m^2	1000 W/m^2	1000 W/m^2
1000 W/m^2	1000 W/m^2	1000 W/m^2	1000 W/m^2
1000 W/m^2	1000 W/m^2	1000 W/m^2	1000 W/m^2

Case 1:First Row unevenly shaded (pattern 2)

Case 2:First and Second Rows unevenly shaded (pattern 2)

Case 3:First, Second and Third Rows unevenly shaded (pattern 2)

Case 4:First, Second, Third and Fourth Rows unevenly shaded (pattern 2)

Case 5:First, Second, Third, Fourth and Fifth Rows unevenly shaded (pattern 2)

(a)

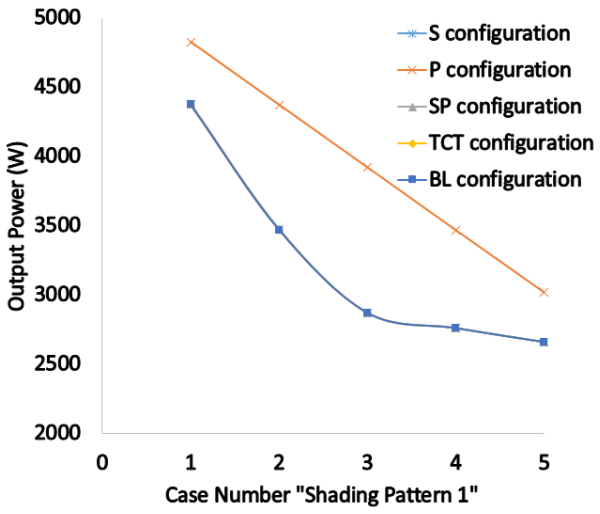

(b)

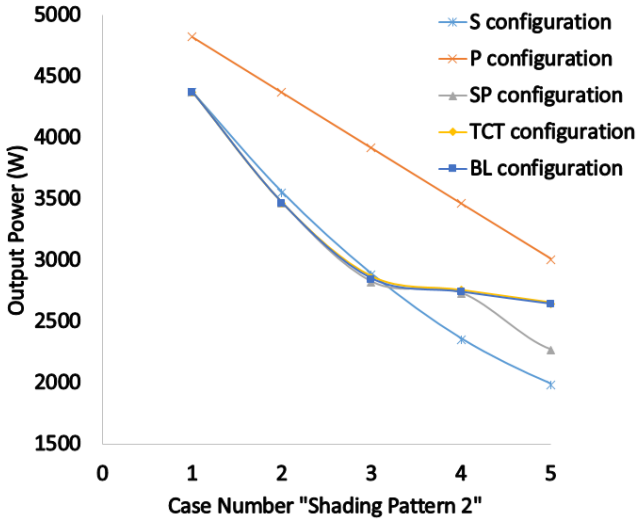

(c)

Figure 4.5 (a) Scenario 1 tested PS patterns, (b) MPP for PS pattern 1, (c) MPP for PS pattern 2

For PS pattern 1 and 2, the series resistance of the examined PV array was estimated using method 1 described previously in section 5.2.3. Table 4.5 and Table 4.6 show the estimated R_s for PS pattern 1 and PS pattern 2 respectively. The estimated R_s for the S configuration is increased by approximate by 1.13-1.8 Ω. Additionally, the estimated R_s for SP, TCT and BL configurations is increased by approximately 0.07 Ω. There is a very small amount of change in the R_s obtained for P configuration, the increase is only equal to 0.002 Ω.

Table 4.5 Estimated R_s for the examined PV array configurations under PS pattern 1

Case #	Estimated R_s (Ω) for Shading Pattern 1				
	S	P	SP	TCT	BL
Case 1	13.3	0.022	0.82	0.82	0.82
Case 2	14.4	0.023	0.89	0.89	0.89
Case 3	15.6	0.025	0.96	0.96	0.96
Case 4	16.7	0.027	1	1	1
Case 5	17.8	0.029	1.1	1.1	1.1

Table 4.6 Estimated R_s for the examined PV array configurations under PS pattern 2

Case #	Estimated R_s (Ω) for Shading Pattern 2				
	S	P	SP	TCT	BL
Case 1	14	0.022	0.84	0.82	0.83
Case 2	15.9	0.023	0.92	0.89	0.90
Case 3	17.7	0.025	0.99	0.96	0.97
Case 4	19.6	0.027	1	1	1
Case 5	21.4	0.029	1.1	1.1	1.1

The *FF* indicator was also calculated for each examined PS pattern. Figure 4.6a and Figure 4.6b illustrate the *FF* variations for the examined PV array configurations under PS pattern 1 and PS pattern 2 respectively. The P configuration shows that the *FF* has a value close to 73% the highest among all tested case scenarios. However, a reduction in the *FF* was obtained across all other PV array configurations (Mahmoud Dhimish, Holmes, Mehrdadi, Dales, Chong, et al., 2017).

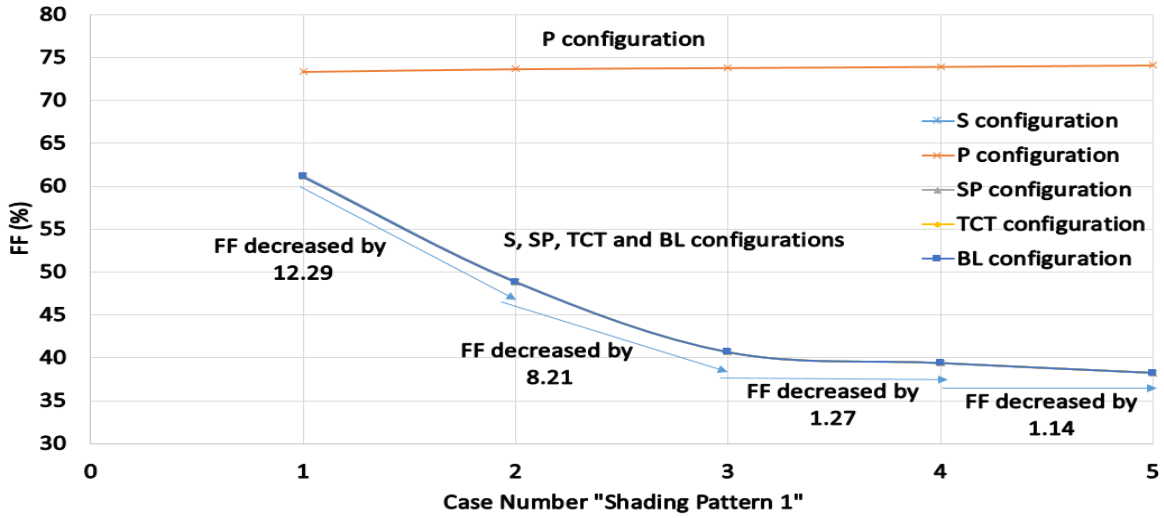

(a)

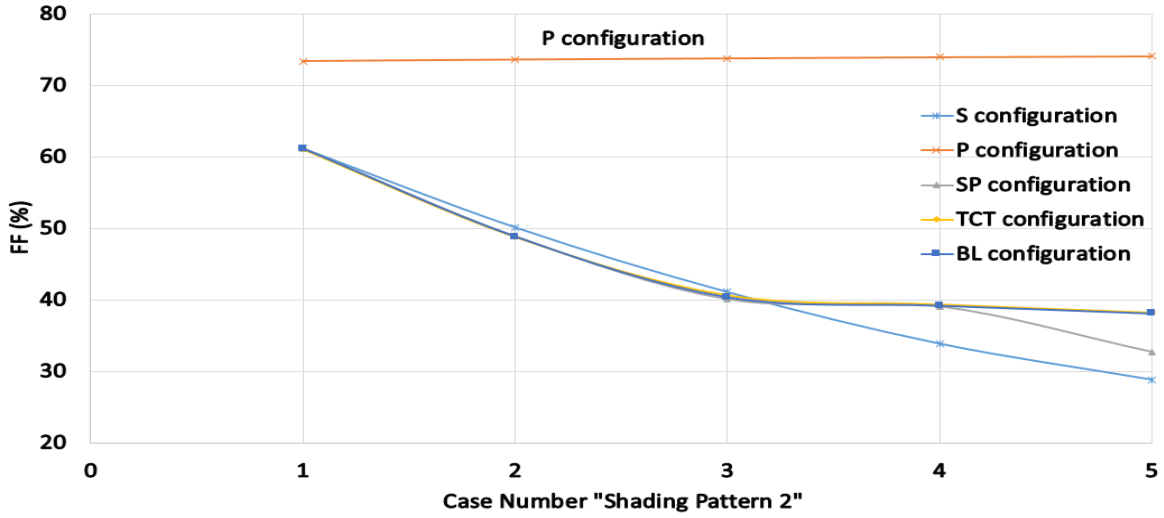

(b)

Figure 4.6 Simulated *FF*. (a) PS pattern 1, (b) PS pattern 2

The last indicator, V_{te} was also simulated during both PS patterns as shown in Figure 4.7a and 4.7b. The threshold values of the V_{te} is taken from Table 4.2. It is evident that the V_{te} for P configuration is approximately 1.44V, which is exactly the same as the P configuration V_{te} threshold.

S, SP, TCT and BL PV array configurations show that the value of V_{te} is lower than the value of V_{te} threshold in low partial shading conditions for reduction in irradiance < 6000 W/m^2. However, in most

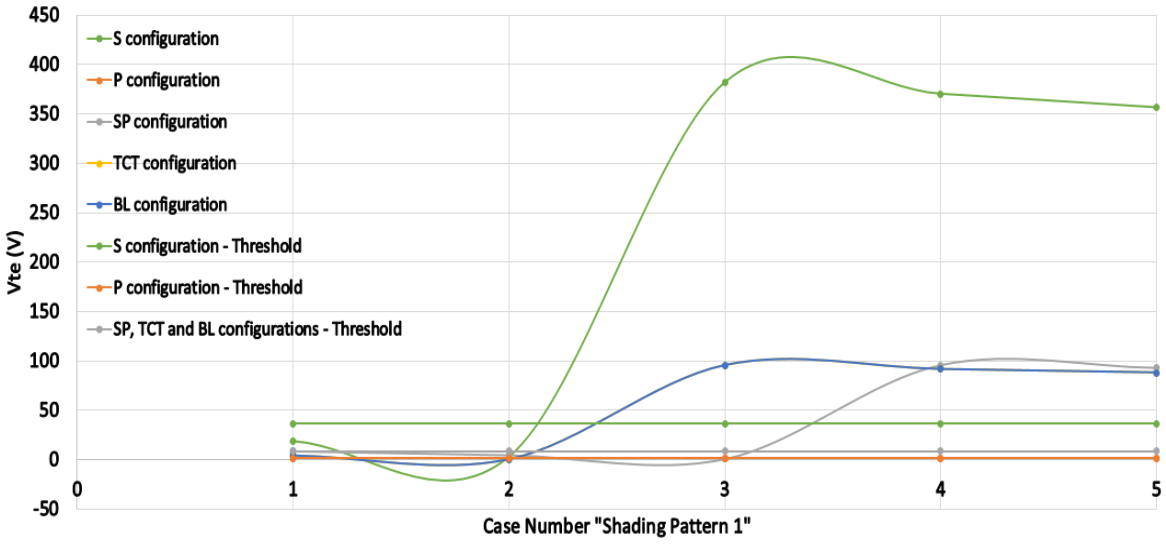

(a)

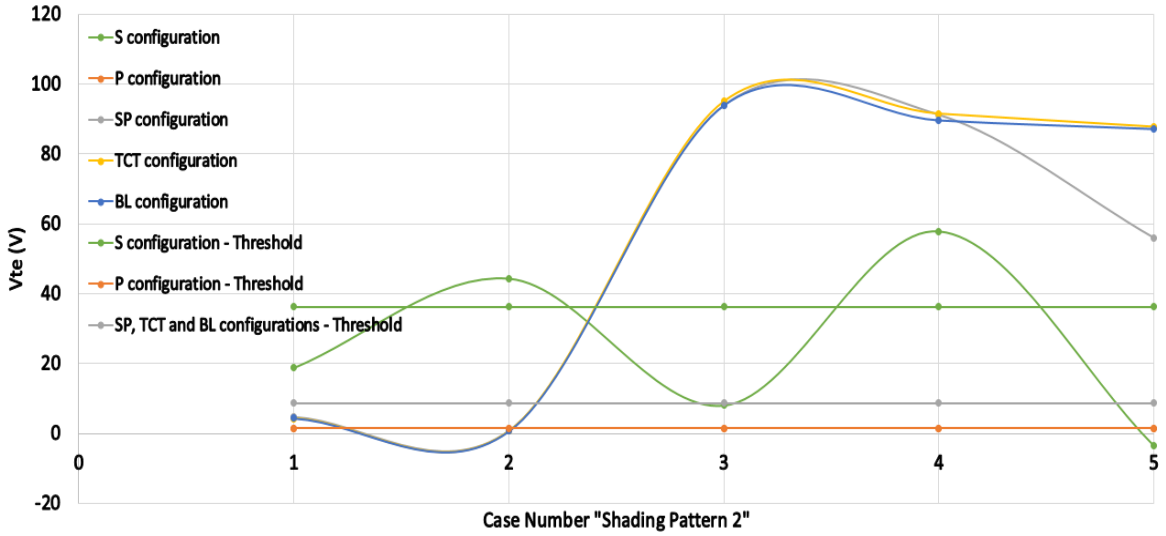

(b)

Figure 4.7 Simulated V_{te}. (a) PS pattern 1, (b) PS pattern 2

partial shading conditions examined in this section, the value of the V_{te} obtained is greater than the value of V_{te} threshold for reduction in the irradiance ≥ 6000 W/m^2.

This section presents the performance of the examined PV array configurations under a row-level PS patterns, the results obtained could be illustrated by the following:

- R_s is a good indicator to predict PS conditions for S, SP, TCT and BL PV array configurations. However, R_s is not a useful indicator for P configuration since it does not change significantly during the variations in the PS conditions affecting the PV system.
- FF has a significant drop in its value while increasing the PS conditions in the S, SP, TCT and BL configurations. This is not a proper indicator to be used with P configuration since it does not change among all tested PS conditions.
- When the reduction in the irradiance is greater than 6000 W/m^2, the value of the V_{te} in most PS conditions affecting row-level of PV modules is greater than the value of V_{te} threshold for S, SP, TCT and BL PV array configurations. However, P configuration shows that the value of the V_{te} almost equal to the value of V_{te} threshold.

5.3.4 PV array configurations under PS condition – scenario 2

In the previous section, the PV array configurations are tested under row-level PS conditions. However, this section will describes the performance of the PV array configurations under PS conditions affecting a column of PV modules (column-level).

Figure 4.8a shows the examined PS conditions. The first PS pattern is applied on a column of PV modules at irradiance level equal to 500 W/m^2. However, the second shading pattern consists of various irradiance levels (100, 200, 500, 600, 800 and 900 W/m^2) applied to six PV modules.

Figure 4.8b shows the MPP obtained in each PV array under PS pattern 1. P, SP, TCT and BL configurations show approximately the same MPP. Furthermore, S configuration generates the minimum output power for PS pattern 1. The MPP obtained from PS pattern 2 is shown in Figure 4.8c. The optimum simulated MPP obtained for P configuration is the highest and that for S configuration remains the worst PV array configuration.

Table 4.7 shows the estimated R_s for each PV array for PS pattern 1. As can be seen, R_s estimated for the S configuration is increasing by approximately 1.68 Ω. Whereas the estimated series resistance for SP, TCT, and BL configurations is increasing by approximately 0.12 Ω. However, the P configuration remains at nearly constant resistance between 0.02 – 0.03 Ω.

For the second shading pattern (non-uniform irradiance) the estimated R_s for SP, TCT and BL configurations is increasing by 0.3 Ω. P configuration remains at the same R_s which is between 0.02 – 0.03 Ω. Similarly, the estimated series resistance for S configuration has increased by 4.4 Ω while increasing the PS conditions. The results are shown in Table 4.8.

Partial Shading Pattern 1

500 W/m²	1000 W/m²	1000 W/m²	1000 W/m²
500 W/m²	1000 W/m²	1000 W/m²	1000 W/m²
500 W/m²	1000 W/m²	1000 W/m²	1000 W/m²
500 W/m²	1000 W/m²	1000 W/m²	1000 W/m²
500 W/m²	1000 W/m²	1000 W/m²	1000 W/m²
500 W/m²	1000 W/m²	1000 W/m²	1000 W/m²

Case 1:First Column 500W/m²

Case 2:First and Second Columns 500W/m²

Case 3:First, Second and Third Columns 500W/m²

Case4:First, Second, Third and Fourth Columns 500W/m²

Partial Shading Pattern 2

100 W/m²	1000 W/m²	1000 W/m²	1000 W/m²
200 W/m²	1000 W/m²	1000 W/m²	1000 W/m²
500 W/m²	1000 W/m²	1000 W/m²	1000 W/m²
600 W/m²	1000 W/m²	1000 W/m²	1000 W/m²
800 W/m²	1000 W/m²	1000 W/m²	1000 W/m²
900 W/m²	1000 W/m²	1000 W/m²	1000 W/m²

Case 1:First Column unevenly shaded

Case 2:First and Second Columns unevenly shaded

Case 3:First, Second and Third Columns unevenly shaded

Case 4:First, Second, Third and Fourth Columns unevenly shaded

(a)

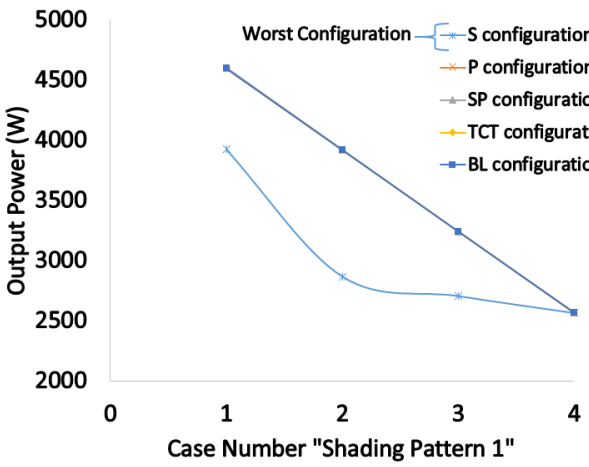

(b)

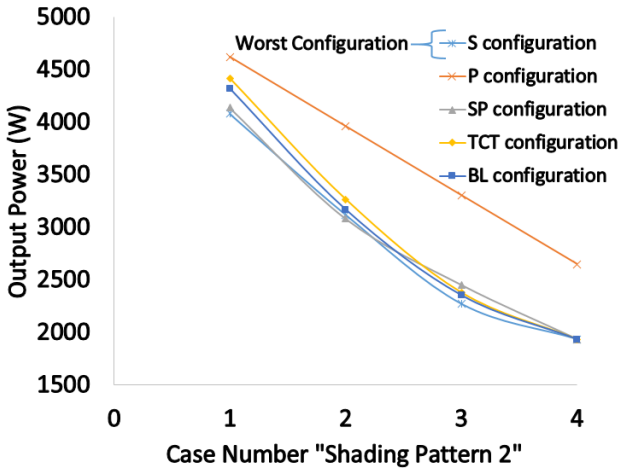

(c)

Figure 4.8 (a) Scenario 2 tested PS patterns, (b) MPP for PS pattern 1, (c) MPP for PS pattern 2

Table 4.7 Estimated R_s for the examined PV array configurations under PS pattern 1

Case #	Estimated R_s (Ω) for Shading Pattern 1				
	S	P	SP	TCT	BL
Case 1	13.8	0.022	0.81	0.81	0.81
Case 2	15.5	0.025	0.89	0.89	0.89
Case 3	17.2	0.028	1	1	1
Case 4	18.9	0.033	1.1	1.1	1.1

Table 4.8 Estimated R_s for the examined PV array configurations under PS pattern 2

Case #	Estimated R_s (Ω) for Shading Pattern 2				
	S	P	SP	TCT	BL
Case 1	16.8	0.022	0.83	0.81	0.82
Case 2	21.3	0.025	0.96	0.91	0.92
Case 3	25.7	0.028	1.1	1.1	1.1
Case 4	30	0.032	1.8	1.8	1.8

Figure 4.9a and Figure 4.9b illustrates the *FF* variations among the examined PV array configurations for PS pattern 1 and PS pattern 2 respectively. PS pattern 1 shows that P, SP, TCT and BL configurations have a value of *FF* approximate to 74% among all tested cases. However, a reduction in the *FF* was only obtained across the S configuration. PS pattern 2 (non-uniform shading) shows a different results comparing to shading pattern 1 (uniform shading), these results could be illustrated as the following:

- The estimated *FF* for the P configuration under non-uniform and uniform shading patterns are exactly equal
- There is a large reduction in the *FF* for S, SP, TCT and BL configurations in the non-uniform PS pattern conditions
- Figure 4.9b shows that the value of the *FF* for the S configuration at case 4 is equal to 74% because in this particular shading case, the percentage of shading among all PV modules is equal. However, according to case 4 in Figure 4.9b, the FF for S configuration is equal to 32%

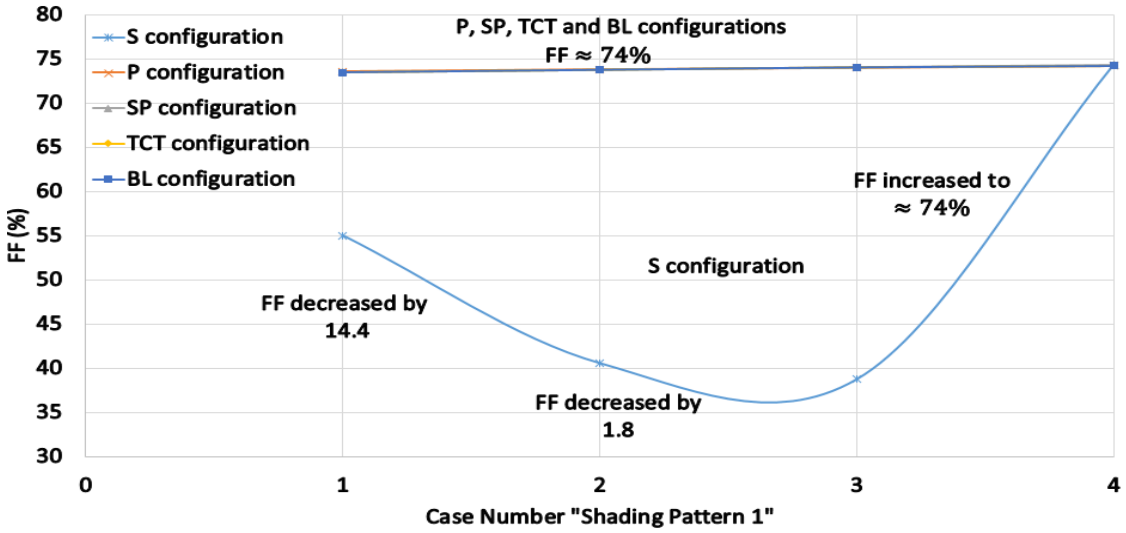

(a)

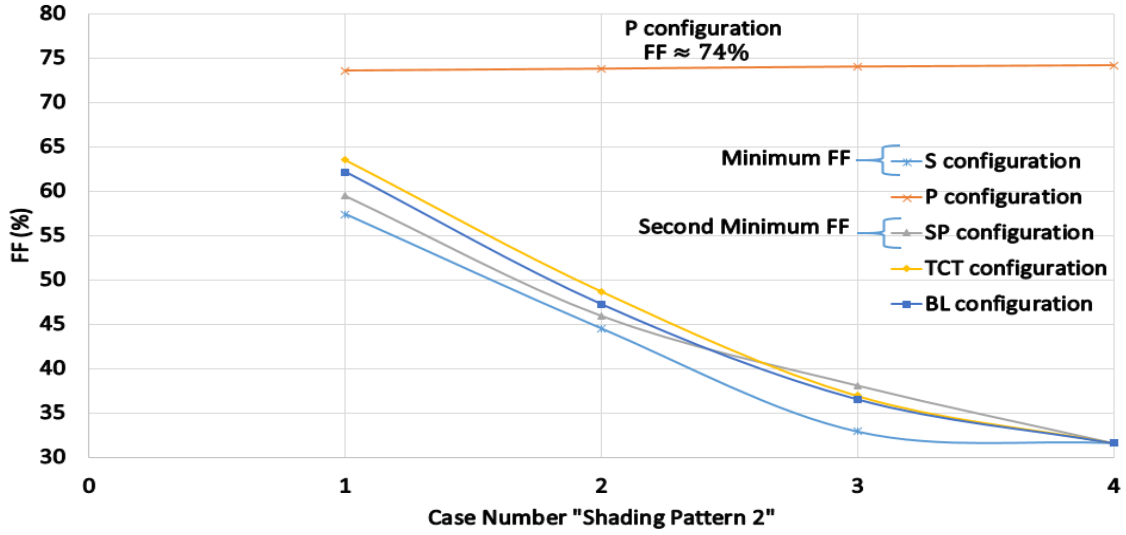

(b)

Figure 4.9 Simulated FF. (a) PS pattern 1, (b) PS pattern 2

The simulated V_{te} for PS pattern1 and PS pattern 2 are shown in Figure 4.10a and 5.10b respectively. The threshold values of the V_{te} is taken from Table 4.2. It is evident that the V_{te} for P configuration is approximately equal to 1.44V, which is exactly the same as the P configuration V_{te} threshold.

The simulated values of the V_{te} for SP, TCT and BL configurations are exactly the same as the V_{te} threshold during PS pattern 1. However, the estimated V_{te} for S configuration is greater than the value of the V_{te} threshold when the reduction in irradiance ≥ 6000 W/m^2 (Mahmoud Dhimish, Holmes, Mehrdadi, Dales, Chong, et al., 2017).

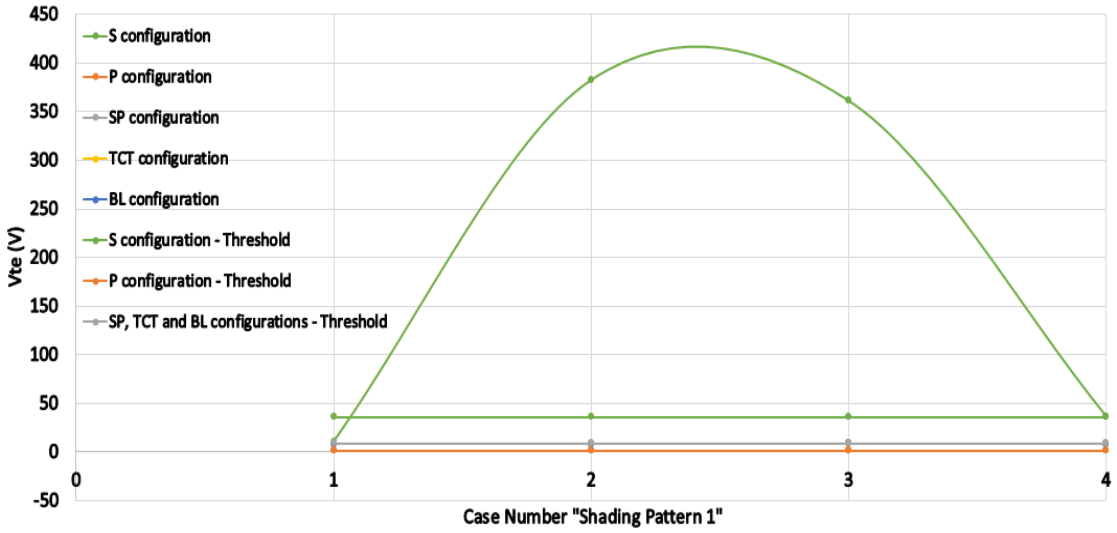

(a)

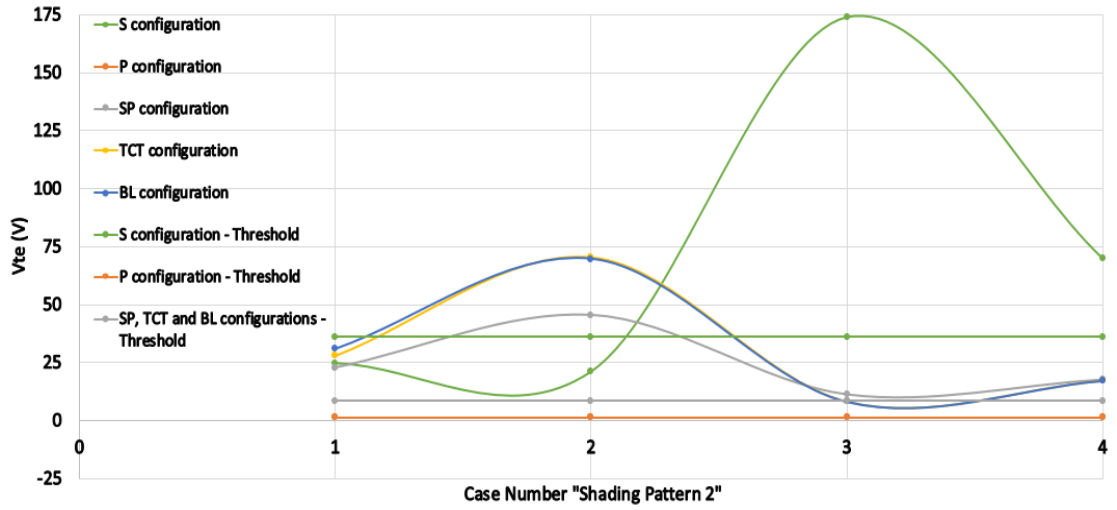

(b)

Figure 4.10 Simulated V_{te}. (a) PS pattern 1, (b) PS pattern 2

Figure 4.10b shows that the simulated V_{te} is exactly the same as the V_{te} threshold for PS pattern 2. SP, TCT and BL configurations prove that when the reduction in the irradiance is greater than 2900 W/m^2 the simulated value of V_{te} is always greater than V_{te} threshold. Moreover, V_{te} for S configuration remains greater than V_{te} threshold when the reduction in irradiance $\geq$ 6000 W/m^2.

This section described the performance of the examined PV array configurations under uniform and non-uniform PS affecting a column of PV modules. The main findings could be deducted as:

1. Under uniform PS patterns, the output power for P, SP, TCT and BL configurations are exactly the same. However, the S configuration shows the least output power among all PV array configurations
2. Under non-uniform PS patterns, the optimum output power was estimated to be the highest for the parallel configuration
3. R_s is a good indicator for detecting/predicting PS shading conditions for S, SP, TCT and BL configurations. The value of the R_s changes significantly when increasing the PS conditions applied to the PV configurations
4. The *FF* indicator could be used to predict PS conditions for SP, TCT, and BL configurations only under non-uniform irradiance conditions. Furthermore, there is a large drop in the value of *FF* for the S configuration under uniform and non-uniform irradiance levels
5. The value of the V_{te} could be used for detecting PS conditions for S, SP, TCT and BL configurations under non-uniform PS conditions

4.3.5 PV array configurations under faulty PV modules– scenario 3

In this section, the PV array configurations will be evaluated under faulty PV modules. Two faulty scenarios were used to examine the output performance for each PV array configuration. Figure 4.11a illustrates both faulty patterns which can be described by the following:

1. Row level: six different scenarios were tested to examine the impact of faulty PV modules which are disconnected from a row of PV modules on the output power of the PV configurations
2. Column level: four different scenarios were tested to examine the impact of faulty PV modules which are disconnected from a column of PV modules on the output power of the PV configurations

Figure 4.11b and Figure 4.11c show that the configurations S and P provide the highest MPP among all PV array configurations. The second maximum output power is achieved by the SP configuration. However, lower output power is estimated for the TCT configuration among all examined PV faulty conditions.

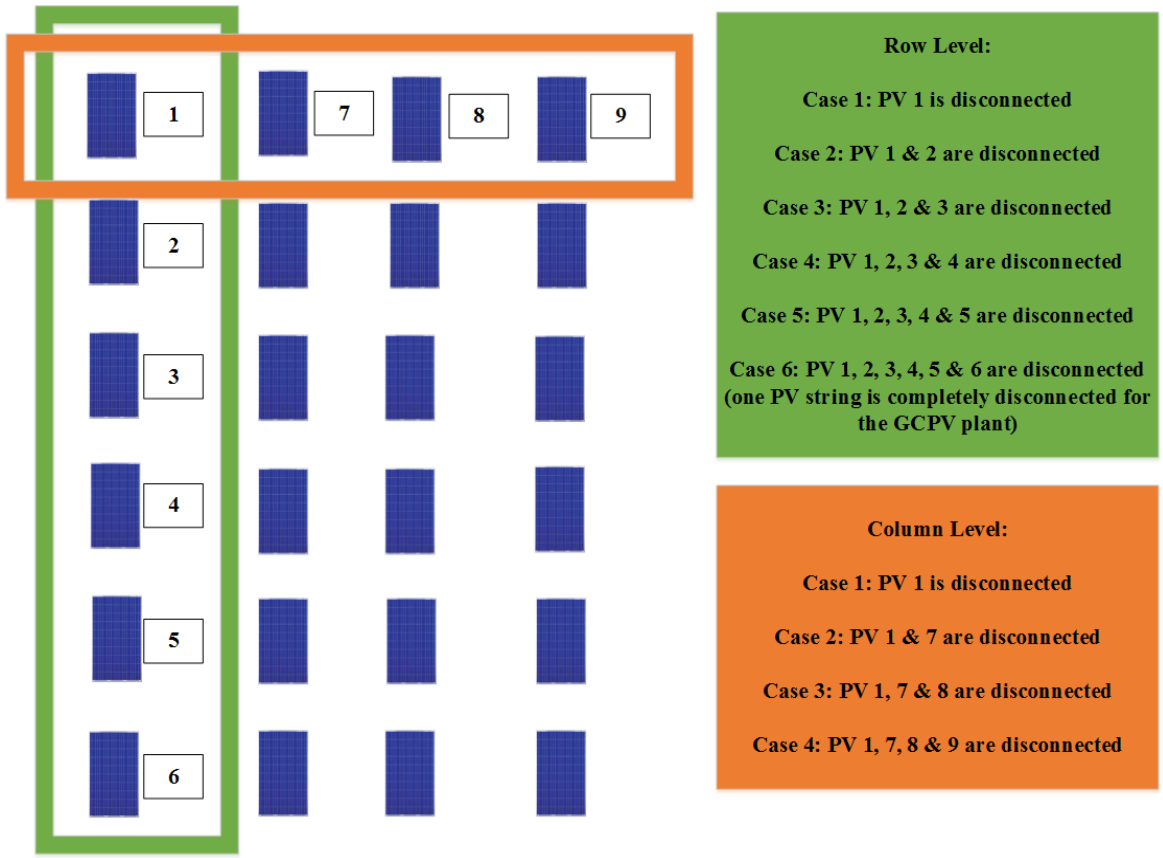

(a)

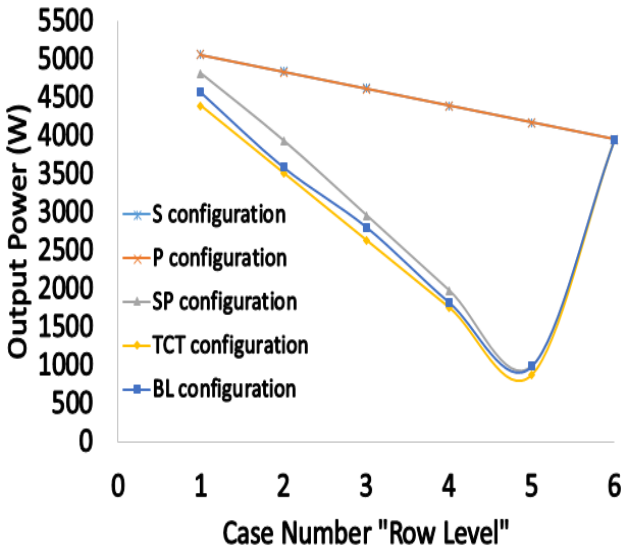

(b)

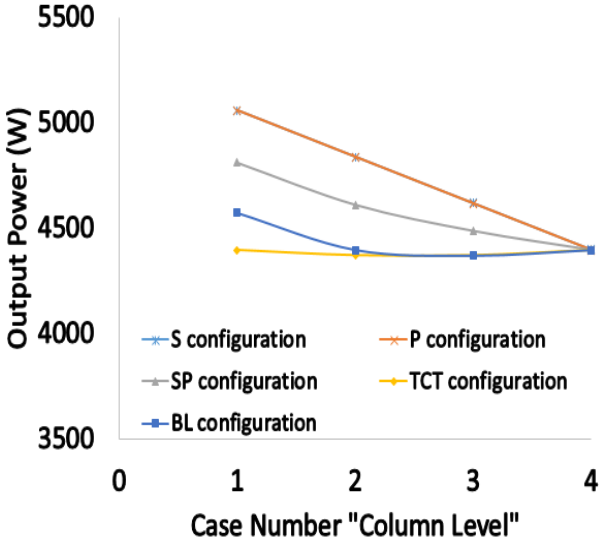

(c)

Figure 4.11 (a) Examined faulty PV conditions, (b) Output power for faulty pattern 1, (c) Output power for faulty pattern 2

The simulated R_s for the row level PV faulty conditions are illustrated in Table 4.9. The S configuration shows that R_s is decreasing by 0.49 Ω while disconnecting one PV module. This result is approximately equal to the measured value of R_s of one PV module (0.48484 Ω) under STC. The simulated R_s for the P configuration is approximately equal to 0.02 Ω.

Table 4.10 shows the simulated R_s for the column level PV faulty conditions. It is evident that the value of R_s for the S and SP configurations decreases when the number of faulty PV modules increases. The simulated R_s for TCT and BL increase for the first three faulty PV conditions. However, R_s is equal to 0.63 Ω when disconnecting entire PV column from the SP, TCT and BL array configurations.

Table 4.9 Estimated R_s for scenario 3: PV faulty conditions, row level

Case #	Estimated R_s (Ω) for Shading Pattern 1				
	S	P	SP	TCT	BL
Case 1	11.5	0.022	0.80	0.63	0.82
Case 2	11	0.023	1	0.50	0.59
Case 3	10.5	0.024	0.88	0.37	0.59
Case 4	10	0.025	0.59	0.25	0.33
Case 5	9.5	0.026	0.29	0.12	0.29
Case 6	9	0.028	1	1	1

Table 4.10 Estimated R_s for scenario 3: PV faulty conditions, column level

Case #	Estimated R_s (Ω) for Shading Pattern 2				
	S	P	SP	TCT	BL
Case 1	11.5	0.022	0.80	0.63	0.82
Case 2	11	0.023	0.76	0.88	0.91
Case 3	10.5	0.024	0.69	1.1	1.1
Case 4	10	0.025	0.63	0.63	0.63

Figures 5.12a and 5.12b illustrate the *FF* variations among the tested PV array configurations during faulty PV conditions: row level and column level respectively. The row faulty PV conditions show that S, P, and TCT configurations have *FF* value approximately 73.2% for all tested scenarios. However, a reduction in the *FF* was only evident in the SP and BL configurations.

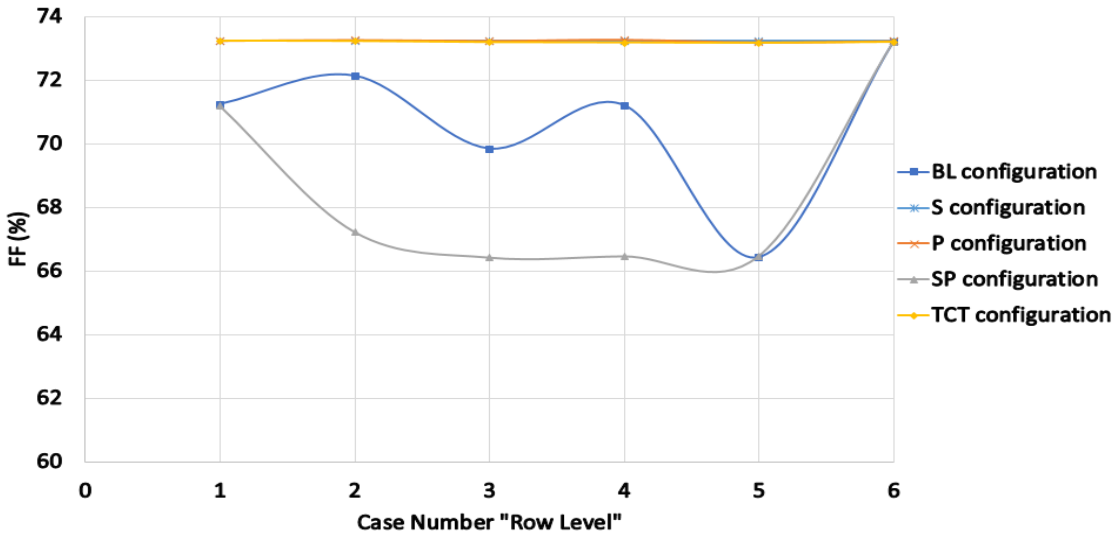

(a)

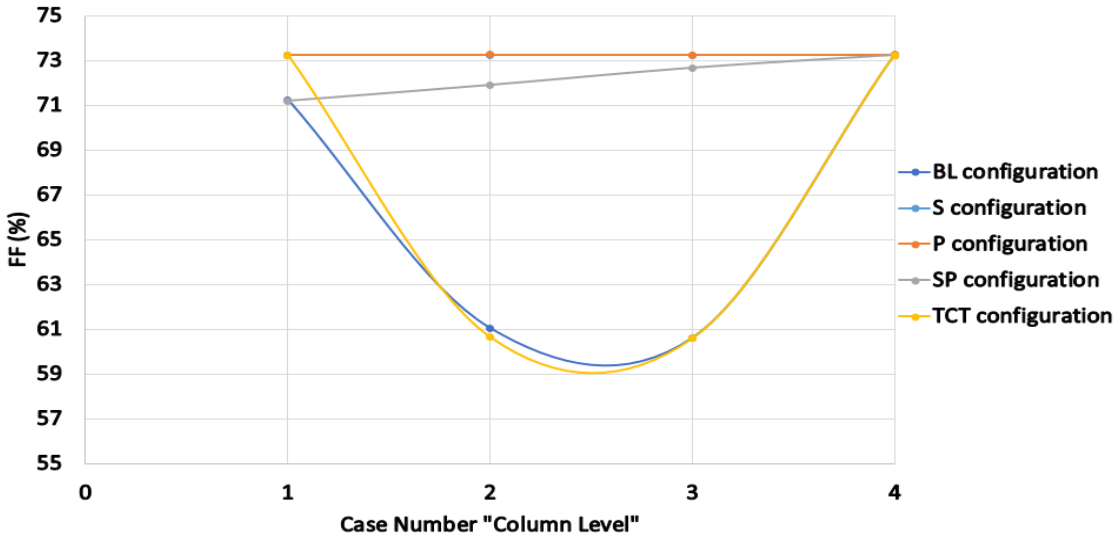

(b)

Figure 4.12 Simulated *FF*. (a) Row level PV faulty condition, (b) Column level PV faulty condition

The column faulty PV conditions show that the *FF* for the S and P configuration remains at 73.2%. Furthermore, there is a huge reduction in the estimated *FF* for both TCT and BL configurations. The only case which shows an increase in the simulated values of the *FF* is obtained for the SP configuration.

As shown in Figure 4.12a at case 6 (Faulty PV string) the estimated value of the *FF* across all PV array configurations is equal to 73.2%. Similar results, obtained for case 4 (faulty column) are shown in Figure 4.12b.

The simulated V_{te} for each PV array configuration under faulty PV modules conditions (row level and column level) are shown in Figures 5.13a and 5.13b respectively. Figure 4.13a shows that V_{te} for P configuration is equal to 1.36V. This is approximately equal to P configuration V_{te} threshold: 1.44V.

The simulated value of the V_{te} for S, SP, TCT and BL configurations is decreased while increasing the number of faulty PV modules due to the decrease in the V_{mpp}. Despite the decreasing V_{oc}, the value of V_{mpp} is multiplied by a factor of 2, therefore, V_{te} is also decreasing. This result can be expressed by the following:

$$V_{te} \downarrow = \frac{(2V_{mpp} \downarrow\downarrow - V_{oc} \downarrow)(I_{sc} - I_{mpp})}{I_{mpp} - (I_{sc} - I_{mpp}) \ln(\frac{I_{sc} - I_{mpp}}{I_{sc}})}$$

Different results are obtained for case 6 in Figure 4.13a when a faulty PV string occurred in each PV configuration. The value of V_{te} for the SP, TCT and BL is increased because the value of the I_{sc} and I_{mpp} is decreased:

$$V_{te} \uparrow = \frac{(2V_{mpp} \downarrow\downarrow - V_{oc} \downarrow)(I_{sc} \downarrow - I_{mpp} \downarrow)}{I_{mpp\downarrow} - (I_{sc} \downarrow - I_{mpp} \downarrow) \ln\left(\frac{I_{sc} \downarrow - I_{mpp\downarrow}}{I_{sc} \downarrow}\right)}$$

The denominator is decreasing more than the numerator. Similar results are obtained for the estimated V_{te} in the column-level faulty PV conditions as shown in Figure 4.13b.

The main findings of this section can be listed as follows:

- When the number of faulty PV modules in increases, R_s is decreases in S, SP TCT and BL configurations
- The *FF* for the S and P configurations in faulty PV conditions remains at 73.2%

- The simulated value of V_{te} for S, SP, TCT and BL configurations is decreased when increasing the number of faulty PV modules. However, in case of the faulty PV string occurring in the PV configurations, the value of the V_{te} is increased only in SP, TCT and BL
- P configuration remains relatively insensitive for the *FF* variations and V_{te}

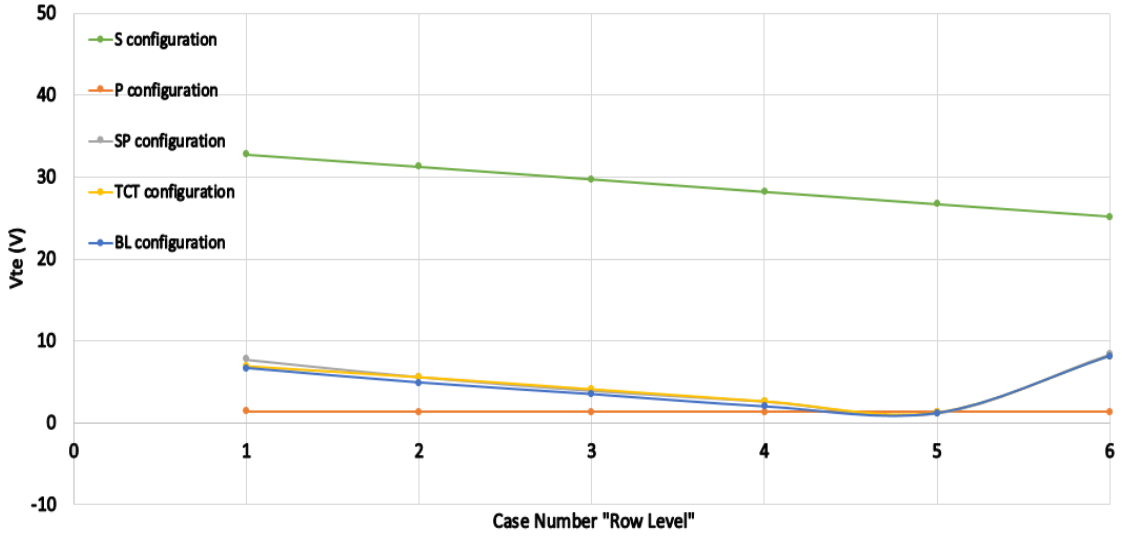

(a)

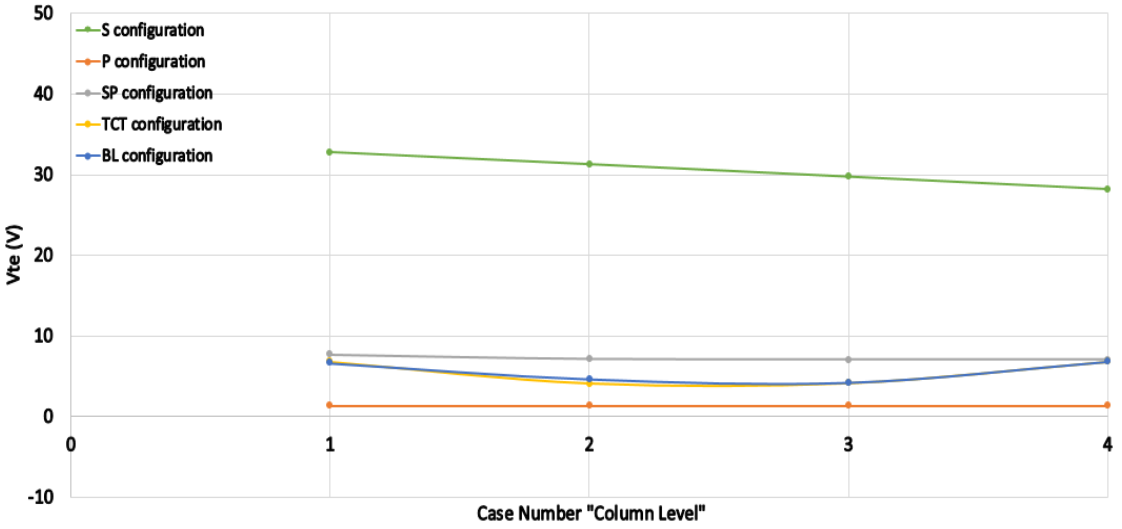

(b)

Figure 4.13 Simulated V_{te}. (a) Row level PV faulty condition, (b) Column level PV faulty condition

4.4 Discussion

Five different PV array configurations were simulated using MATLAB/Simulink software under various PS and faulty PV conditions. Seven parameters were obtained under each examined shading and PV faulty scenario.

Table 4.11, Table 4.12, and Table 4.13 show the variations for all examined indicators used in the simulation. Three different symbols are used to show whether the value of the indicator has an "↓" decrease, "↑" increase, "–" no change in its value and ↓↑ decrease or increase in the value of the indicator (Mahmoud Dhimish, Holmes, Mehrdadi, Dales, Chong, et al., 2017).

Table 4.11, Table 4.12, and Table 4.13 provide the main parameters that could be used for estimating/predicting PS conditions in all PV array configurations. The results described in these tables could be used to create a generic algorithm for detecting PS conditions and faulty PV modules in multiple PV array configurations. Also it can be used to create a reconfigurable PV array system which improves the power generation of PV installations.

Table 4.11 Change in the tested indicators for S and P configurations

Scenario	PV array configurations													
	S							P						
	I_{sc}	I_{mpp}	V_{oc}	V_{mpp}	R_s	FF	V_{te}	I_{sc}	I_{mpp}	V_{oc}	V_{mpp}	R_s	FF	V_{te}
Increasing uniform shading on PV row	-	↓	↓	↓↑	↑	↓	↓↑	↓	↓	↓	↓	-	-	-
Increasing non-uniform shading on PV row	-	↓	↓	↓↑	↑	↓	↓↑	↓	↓	↓	↓	-	-	-
Increasing uniform shading on PV column	-	↓	↓	↓↑	↑	↓↑	↓↑	↓	↓	↓	↓	-	-	-
Increasing non-uniform shading on PV column	-	↓	↓	↓↑	↑	↓	↓	↓	↓	↓	↓	-	-	-
Increasing faulty PV modules in PV row	-	-	↓	↓	↓	-	↓	↓	↓	-	-	↑	-	↓
Increasing faulty PV modules in PV column	-	-	↓	↓	↓	-	↓	↓	↓	-	-	↑	-	↓

Table 4.13 Change in the tested indicators for SP and TCT configurations

Scenario	PV array configurations													
	SP							TCT						
	I_{sc}	I_{mpp}	V_{oc}	V_{mpp}	R_s	FF	V_{te}	I_{sc}	I_{mpp}	V_{oc}	V_{mpp}	R_s	FF	V_{te}
Increasing uniform shading on PV row	-	↓	↓	↓↑	↑	↓↑	↑	-	↓	↓	↓↑	↑	↓	↓↑
Increasing non-uniform shading on PV row	-	↓	↓	↓↑	↑	↓	↓↑	-	↓	↓	↓↑	↑	↓	↓↑
Increasing uniform shading on PV column	-	↓	↓	↓	↑	-	-	↓	↓	↓	↓↑	↑	-	-
Increasing non-uniform shading on PV column	-	↓	↓	↓	↑	↓	↓↑	↓	↓	↓	↓↑	↑	↓	↓↑
Increasing faulty PV modules in PV row	-	-	↓	↓	↓↑	↓	↓	-	-	↓	↓	↓	-	↓
Increasing faulty PV modules in PV column	-	-	↓	↓	↓	↑	↓	-	-	↓	↓	↓	↓	↓

Table 4.12 Change in the tested indicators for BL configuration

Scenario	PV array configuration						
	BL						
	I_{sc}	I_{mpp}	V_{oc}	V_{mpp}	R_s	FF	V_{te}
Increasing uniform shading on PV row	-	↓	↓	↓↑	↑	↓	↓↑
Increasing non-uniform shading on PV row	-	↓	↓	↓↑	↑	↓	↓↑
Increasing uniform shading on PV column	↓	↓	↓	↓	↑	-	-
Increasing non-uniform shading on PV column	↓	↓	↓	↓↑	↑	↓	↓↑
Increasing faulty PV modules in PV row	-	-	↓	↓	↓	↓↑	↓
Increasing faulty PV modules in PV column	-	-	↓	↓	↓↑	↓	↓

4.5 Summary

In this chapter, the simulation and modelling for five different PV array configurations have been described:

1. Series (S)
2. Parallel (P)
3. Series-parallel (SP)
4. Total-cross-tied (TCT)
5. Bridge linked (BL)

The PV array configurations have been simulated under various PS and faulty PV conditions. The performance of seven indicators have been studied. These indicators are:

1. Short circuit current (I_{sc})
2. Current at maximum power point (I_{mpp})
3. Open circuit voltage (V_{oc})
4. Voltage at maximum power point (V_{mpp})
5. Series resistance (R_s)
6. Fill factor (FF)
7. Thermal voltage (V_{te})

All simulated results in this chapter have been carried out using MATLAB/Simulink software.

As a result, the TCT configuration has the highest output power during all examined PS conditions. In addition, TCT configuration generates the highest output power among all PV faulty case scenarios. The second best choice is the BL configuration, whereas the S configuration has the lowest output power comparing to all other examined configurations.

The next chapter will demonstrate various PV fault detection algorithms which can be used in various PV array configurations. Moreover, the proposed PV fault detection algorithms are based on either a statistical analysis method or/and mathematical analysis techniques.

Chapter 5 Photovoltaic Fault Detection Techniques

In this chapter, a PV fault detection algorithm based on statistical analysis and mathematical models will be presented. The algorithm has been validated using PV plant A described earlier in chapter 3.

The algorithm, data analysis, and the results of this chapter have been published in the following journal articles (Mahmoud Dhimish & Holmes, 2016; Mahmoud Dhimish, Holmes, & Dales, 2017; Mahmoud Dhimish, Holmes, Mehrdadi, & Dales, 2017d).

5.1 Examined PV array configuration and fault classification

In this chapter, PV plant 1 has been used to validate the developed PV fault detection algorithm. During the experiment, the PV modules were organized in 3 PV strings and each string is made up of 3 series-connected PV modules.

Each PV string is connected to a FLEXmax MPPT unit, which has an output efficiency not less than 98.5%. In order to enable or disable the connection of any PV module during the experiment, a connection/switching unit was used.

Vantage Pro monitoring unit is used to receive the global solar irradiance measured by a Davis Weather Station which includes a pyranometer. The pyranometer is placed at the same tilt and azimuth angle as the PV installation.

Hub 4 communication manager is used to facilitate the acquisition of module temperatures using the Davis external temperature sensor, and the electrical data for each photovoltaic string. Finally, LabVIEW software is used to implement the data logging and monitoring functions of the tested PV system. Figure 5.1a illustrates the overall system architecture of the examined PV system (Mahmoud Dhimish, Holmes, & Dales, 2017).

Since multiple faults can occur in PV systems, the proposed PV fault detection algorithm uses the following classification:

1. Faults in the data acquisition
2. Faults in the DC side of the PV system

Figure 5.1b shows possible faults which can be categorised by the fault detection algorithm.

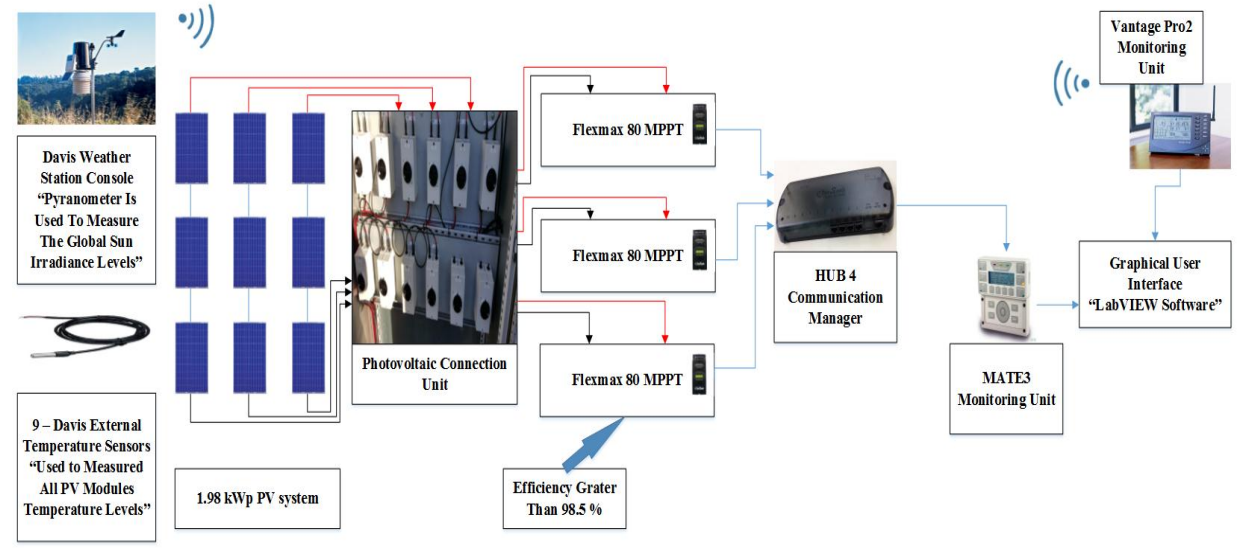

(a)

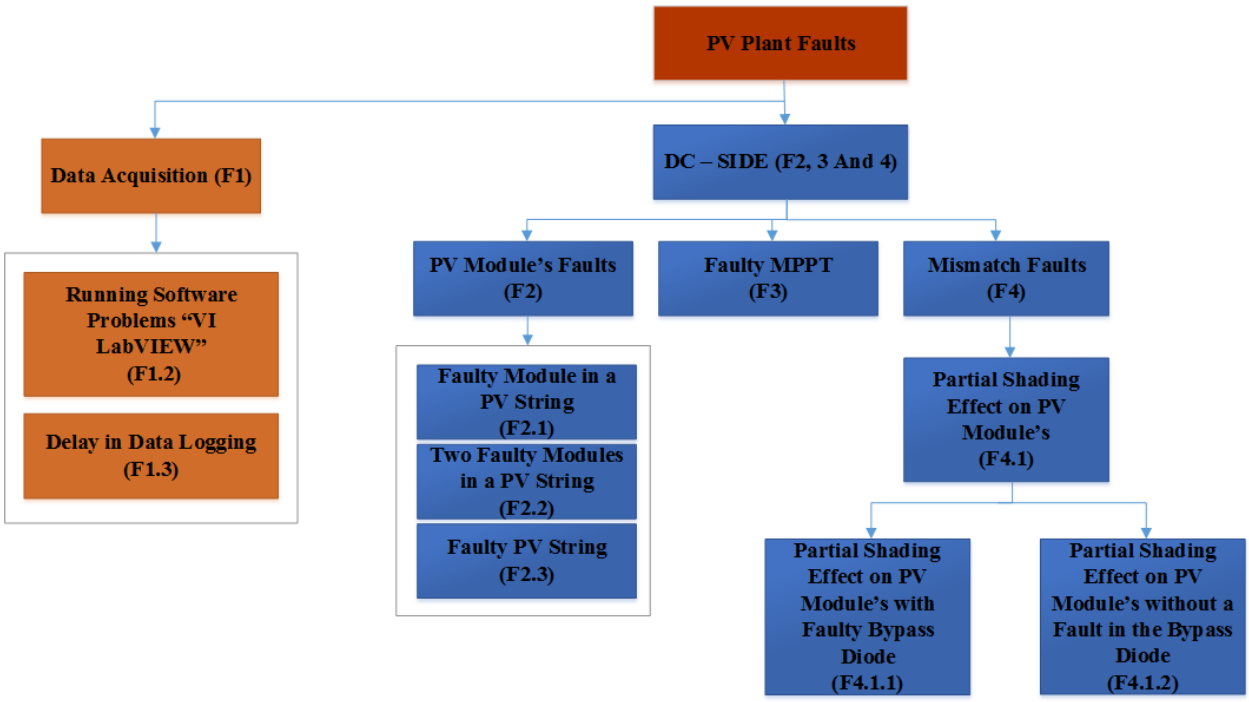

(b)

Figure 5.1 (a) Overall examined PV system architecture, (b) Different type of faults occurring in the examined PV plant

5.2 Novel fault detection algorithm

5.2.1 General PV fault detection algorithm

The main objective of the fault detection algorithm is to detect and determine when and where a fault has occurred in the PV system. The algorithm uses the climate data collected by the Davis weather station and the internal sensors of the MPPT units. Furthermore, LabVIEW software simulates the theoretical I-V curve of the PV system as shown in Figure 5.2a.

The T-test statistical analysis method is used to compare the theoretical and measured output power of the PV system. The T-test is evaluated using (5.1) (Mahmoud Dhimish, Holmes, & Dales, 2017).

$$T = \frac{(\bar{x} - \mu)\sqrt{n}}{s} \tag{5.1}$$

where $\overline{x}$ is the mean of the samples, μ is the population mean, n is the sample size and s is the standard deviation of the entire data.

The real-time measurements are taken by averaging 60 samples taken at one minute intervals. The results obtained for power, voltage and current are calculated at one minute intervals for each sample set. To determine whether the T-test analysis is significant, a threshold value of 2.68 was used as shown in Figure 5.2b.

This value has been used since it is the theoretical threshold of the T-test for a confidence interval equal to 99%. However, the threshold could be chosen as 1.64 if the values of the simulated power by the PV system has low degree of accuracy (in case MPPT unit is not used with the PV plant).

To determine the value of the T-test, firstly the PV power simulation (theoretical power) is compared with the output measured power. Then the value of the T-test is taken from Figure 5.2b based on the confidence limit needed in the simulation.

In the proposed algorithm, the confidence limit and the number of samples that have been used are equal to 99% and 60 respectively. Finally, if the T-test value is above the threshold 2.68, therefore, a fault has been detected in the PV system, which means that the proposed fault detection algorithm is activated as shown in Figure 5.2c.

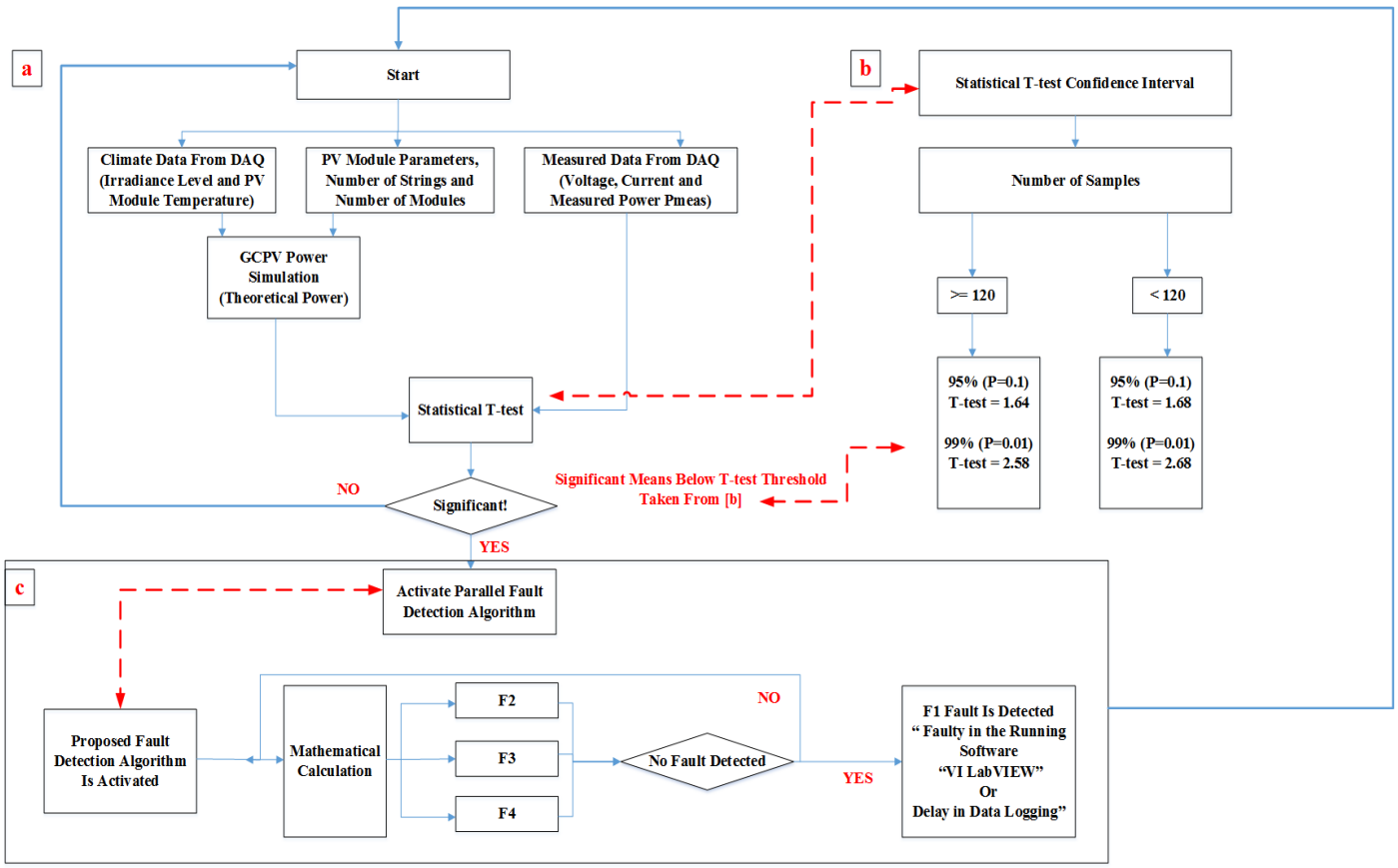

Figure 5.2 (a) General algorithm using statistical T-test technique, (b) T-test statistical confidence interval limits, (c) Activating the proposed PV fault detection algorithm

5.2.2 PV fault detection algorithm diagnosis rules

In order to determine the type of a fault that has occurred in the PV plant, two ratios have been identified, power ratio (PR) and voltage ratio (VR). These have been used to categorise the region of the fault because both ratios have the following features:

1. Both ratios are changeable during the faulty conditions in the PV plant
2. When disconnecting a PV module in a series PV string, the VR will decrease significantly
3. When the power ratio is equal to zero, the voltage ratio can still have a value regarding the voltage open circuit of the PV modules

The power and voltage ratios are given by the following expressions:

$$PR = \frac{P_{theoretical}}{P_{measured}} \tag{5.2}$$

$$VR = \frac{V_{theoretical}}{V_{measured}} \tag{5.3}$$

where $P_{theoretical}$ is the theoretical output power generated by the GCPV system, $P_{measured}$ is the measured output power from PV string, $V_{theoretical}$ is the theoretical output voltage generated by the GCPV system and $V_{measured}$ is the measured output DC voltage from PV string.

Based on the analysis of the power ratio for the PV system, numerical calculations for the DC side fault rules are shown in Figure 5.3. Since the internal sensors of the MPPT have a minimum efficiency of 98.5%, the power ratios are calculated at 1.5% error tolerance of the theoretical power which presents the maximum error condition for the examined PV system (Mahmoud Dhimish, Holmes, Mehrdadi, & Dales, 2017d). The values are calculated according to the set of conditions shown in Figure 5.3.

The maximum and minimum PR and VR ratios are expressed by (5.4 – 5.7) which contain the tolerance rate of the MPPT unit and the total number of PV modules in the PV string.

$$PR\ min = \frac{\frac{P_{theoretical}}{number\ of\ PV\ strings}}{\frac{P_{measured}}{number\ of\ PV\ strings} - n\,P_0} \tag{5.4}$$

$$PR\ max = \frac{\frac{P_{theoretical}}{number\ of\ PV\ strings}}{\left(\frac{P_{measured}}{number\ of\ PV\ strings} - n\,P_0\right) \times MPPT\ Tolerance\ Rate} \tag{5.5}$$

$$VR\ min = \frac{V_{theoretical}}{V_{measured} - n\,V_0} \tag{5.6}$$

$$VR\ max = \frac{V_{theoretical}}{(V_{measured} - n\,V_0) \times MPPT\ Tolerance\ Rate} \tag{5.7}$$

where n is the number of faulty PV modules and P_0 is the peak power of the PV module at STC (220 W_p).

The number of faulty PV modules are expressed by the number of PV modules in the examined PV string. For example, if the PV string comprises 3 photovoltaic modules connected in series, therefore, n = 3. Additionally, the peak power can be found in the data sheet of the examined PV module.

The selection of the PR ratio regions shown in Figure 5.3 is based on Equations (5.4) and (5.5) as follows:

Normal operation mode:

$$\text{PR min} = \frac{\frac{P_{theoretical}}{\text{number of PV strings}}}{\frac{P_{measured}}{\text{number of PV strings}} - n P_0} = \frac{\frac{1982}{3}}{\frac{1982}{3} - 0(220.2)} = \frac{660.6}{660.6 - 0} = 1$$

$$\text{PR max} = \frac{\frac{P_{theoretical}}{\text{number of PV strings}}}{\left(\frac{P_{measured}}{\text{number of PV strings}} - n P_0\right) \times \text{MPPT Tolerance Rate}} =$$

$$\frac{\frac{1982}{3}}{\left(\frac{1982}{3} - 0(220.2)\right)\times 98.5\%} = \frac{660.6}{(660.6 - 0)\times 98.5\%} = 1.015228$$

1 Faulty PV module:

$$\text{PR min} = \frac{\frac{P_{theoretical}}{\text{number of PV strings}}}{\frac{P_{measured}}{\text{number of PV strings}} - n P_0} = \frac{\frac{1982}{3}}{\frac{1982}{3} - 1(220.2)} = \frac{660.6}{660.6 - 220.2} = 1.5$$

$$\text{PR max} = \frac{\frac{P_{theoretical}}{\text{number of PV strings}}}{\left(\frac{P_{measured}}{\text{number of PV strings}} - n P_0\right) \times \text{MPPT Tolerance Rate}} =$$

$$\frac{\frac{1982}{3}}{\left(\frac{1982}{3} - 1(220.2)\right)\times 98.5\%} = \frac{660.6}{(660.6 - 220.2)\times 98.5\%} = 1.5233$$

2 Faulty PV modules:

$$\text{PR min} = \frac{\frac{P_{theoretical}}{\text{number of PV strings}}}{\frac{P_{measured}}{\text{number of PV strings}} - n P_0} = \frac{\frac{1982}{3}}{\frac{1982}{3} - 2(220.2)} = \frac{660.6}{660.6 - 440.4} = 3$$

$$\text{PR max} = \frac{\frac{P_{theoretical}}{\text{number of PV strings}}}{\left(\frac{P_{measured}}{\text{number of PV strings}} - n P_0\right) \times \text{MPPT Tolerance Rate}} =$$

$$\frac{\frac{1982}{3}}{\left(\frac{1982}{3} - 2(220.2)\right)\times 98.5\%} = \frac{660.6}{(660.6 - 440.4)\times 98.5\%} = 3.0466$$

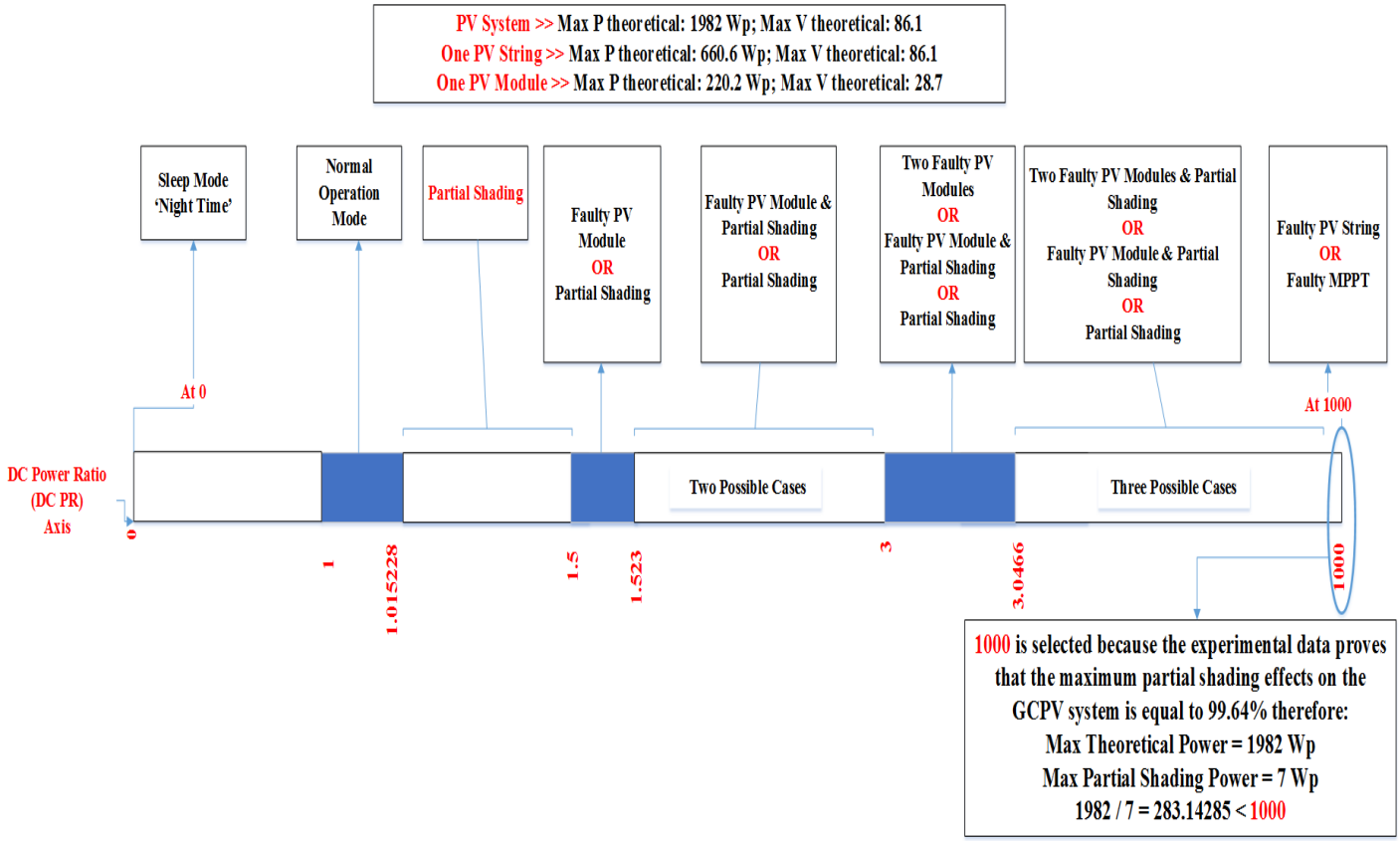

Figure 5.3 Threshold values for detecting faults in the PV system based on the PR ratio

As shown in Figure 5.3, the type of the fault in the regions cannot be classified. For example: when the PR is between 1.523 and 3, two possible faults might occur in the PV system:

1. Faulty PV module and PS condition
2. PS condition

To distinguish between which fault occurred in the PV system, VR ratio has been used. Figure 5.4 illustrates the relationship between the power ratio and voltage ratio. The faults can be detected according to the following set of conditions (Mahmoud Dhimish, Holmes, Mehrdadi, & Dales, 2017d):

1. Sleep mode will start during the night when PR=0
2. If $1.015 \geq PR \geq 1$: it means that the PV system operates at the normal operation mode
3. If $1.52 \geq PR \geq 1.5$: in this case, two categories of faults are identified. If $1.5233 \geq VR \geq 1.5$: It indicates that there is a faulty PV module in the string, otherwise, a partial shading condition has occurred in the PV string
4. If $3 > PR > 1.52$: in this case if the VR is between 1.5 and 1.5233, a faulty PV module and a partial shading effect on the PV string. However, if the VR is outside the range of 1.5233 – 1.5, partial shading is the only condition affecting the PV string

5. If 1000 > PR ≥ 3: this case can determine various faults such as: Faulty PV module with PS affecting the PV string, partial shading on the PV string, two faulty modules in the PV string, two faulty modules in the PV string and partial shading
6. If PR = 1000, where the PV plant has a failure in a PV string or a failure in a MPPT unit

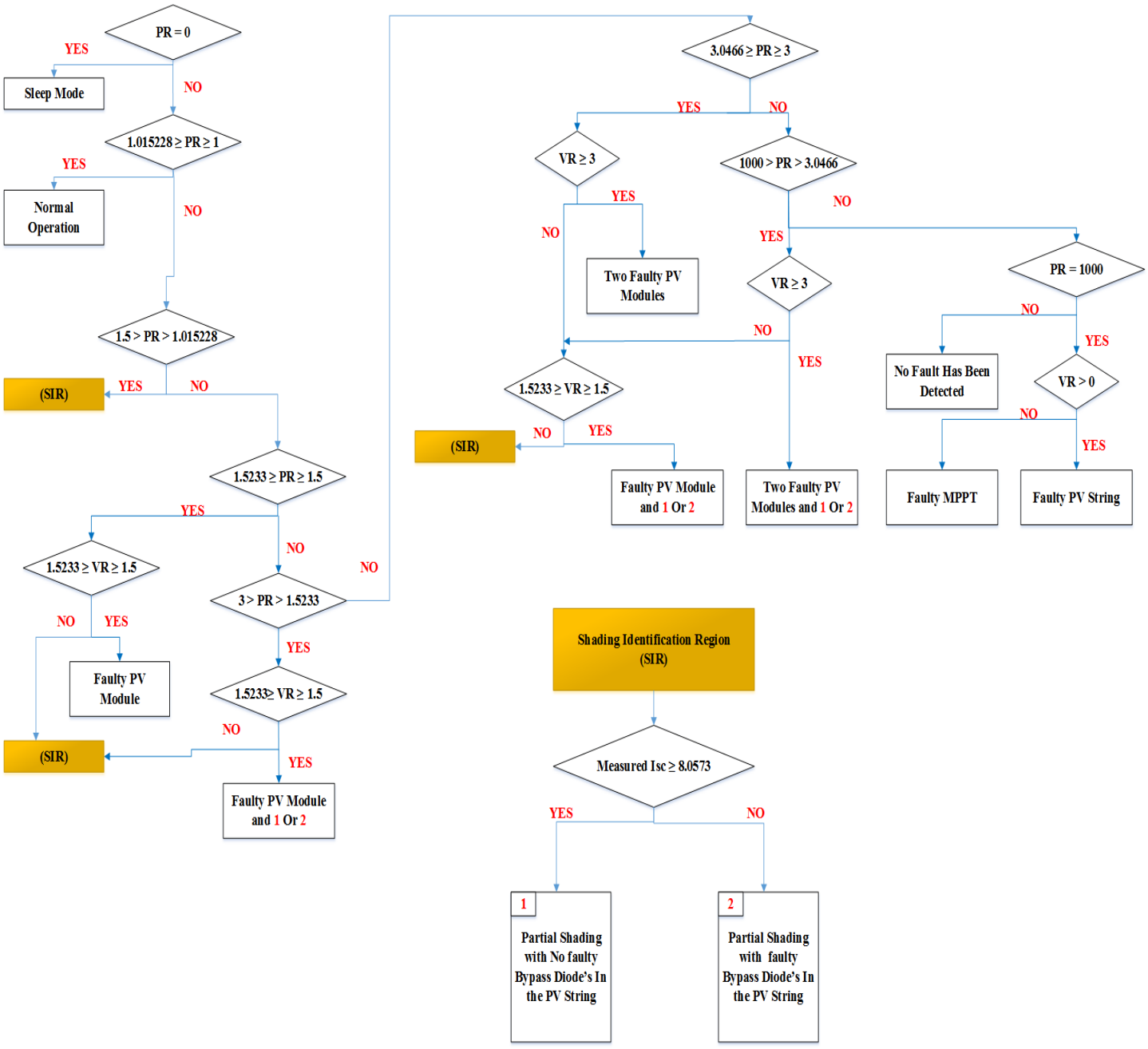

Figure 5.4 DC side faulty regions based on the analysis of PR and VR

The selection of the VR ratio regions shown in Figure 5.4 is based on Equations (5.6) and (5.7) as follows:

Normal operation mode:

$$\text{VR min} = \frac{V_{theoretical}}{V_{measured} - n\,V_0} = \frac{86.1}{86.1 - 0(28.7)} = 1$$

$$\text{VR max} = \frac{V_{theoretical}}{(V_{measured} - n\,V_0) \times \text{MPPT Tolerance Rate}} = \frac{86.1}{(86.1 - 0(28.7)) \times 98.5\%} = 1.015228$$

1 Faulty PV module:

$$\text{VR min} = \frac{V_{theoretical}}{V_{measured} - n\,V_0} = \frac{86.1}{86.1 - 1(28.7)} = 1.5$$

$$\text{VR max} = \frac{V_{theoretical}}{(V_{measured} - n\,V_0) \times \text{MPPT Tolerance Rate}} = \frac{86.1}{(86.1 - 1(28.7)) \times 98.5\%} = 1.5233$$

2 Faulty PV modules:

$$\text{VR min} = \frac{V_{theoretical}}{V_{measured} - n\,V_0} = \frac{86.1}{86.1 - 2(28.7)} = 3$$

$$\text{VR max} = \frac{V_{theoretical}}{(V_{measured} - n\,V_0) \times \text{MPPT Tolerance Rate}} = \frac{86.1}{(86.1 - 2(28.7)) \times 98.5\%} = 3.0466$$

The decisions to identify the faulty cases are illustrated in Figure 5.4. For example, when the power ratio is equal to 1.5, the algorithm has to decide the fault type based on the calculated VR. Therefore, if the voltage ratio is between 1.5 and 1.5233, faulty PV module is detected in the PV system otherwise, PS has occurred in the PV system.

As shown in Figure 5.4, the PV fault detection algorithm is capable of detecting the fault associated with bypass diodes in the examined PV modules. Since the I_{sc} of the tested PV modules is equal to 8.18 A, and by applying the tolerance rate of the MPPT internal current sensor, the minimum measured I_{sc} is equal to:

$$\text{Minimum measured } I_{sc} = (I_{sc})\ 8.18 \text{ x (MPPT minimum accuracy) } 98.5\% = 8.057 \text{ A}$$

Therefore, during all PV conditions without faulty bypass diodes associated with the PV module, the measured I_{sc} must be in the range of 8.18 – 8.057 A. This is acknowledged by shading identification region (SIR) in Figure 5.4.

5.3 Results and discussion

In this section, the performance of the proposed PV fault detection algorithm will be validated using various faulty conditions affecting the examined PV system. The acquired data for various days have been considered. The time zone for all measurements is GMT, taken in Huddersfield, UK.

5.3.1 Normal operation and sleep mode

The Normal operation and sleep mode for the tested PV system are shown in Figure 5.5. Starting from 6:00 and ending at 6:21, the PV system is in sleep mode where the PV modules have not yet received any solar irradiance to generate output power. However, between the time 6:22 and 19:41, the PV system is in the normal operation mode. The measured power is very close to the theoretical output power simulated using LabVIEW software.

According to the achieved results of this test, the average efficiency for the MPPT unit is equal to 98.89%.

5.3.2 PV faults caused by data acquisition system

There are multiple faults which might occur in the PV system due to the data acquisition units such as:

- Running LabVIEW software: errors in loading graphs and saving data
- Delay in Data Logging: delay in the readings obtained by the internal sensors of the MPPT unit

As shown in Figure 5.5, the VI LabVIEW software stopped logging the measured and theoretical data between 13:27 and 13:55. This type of fault might occur in the running software due to the multiple functions which the software handles at the same time. It is therefore required to create a structural code before the data collection stage.

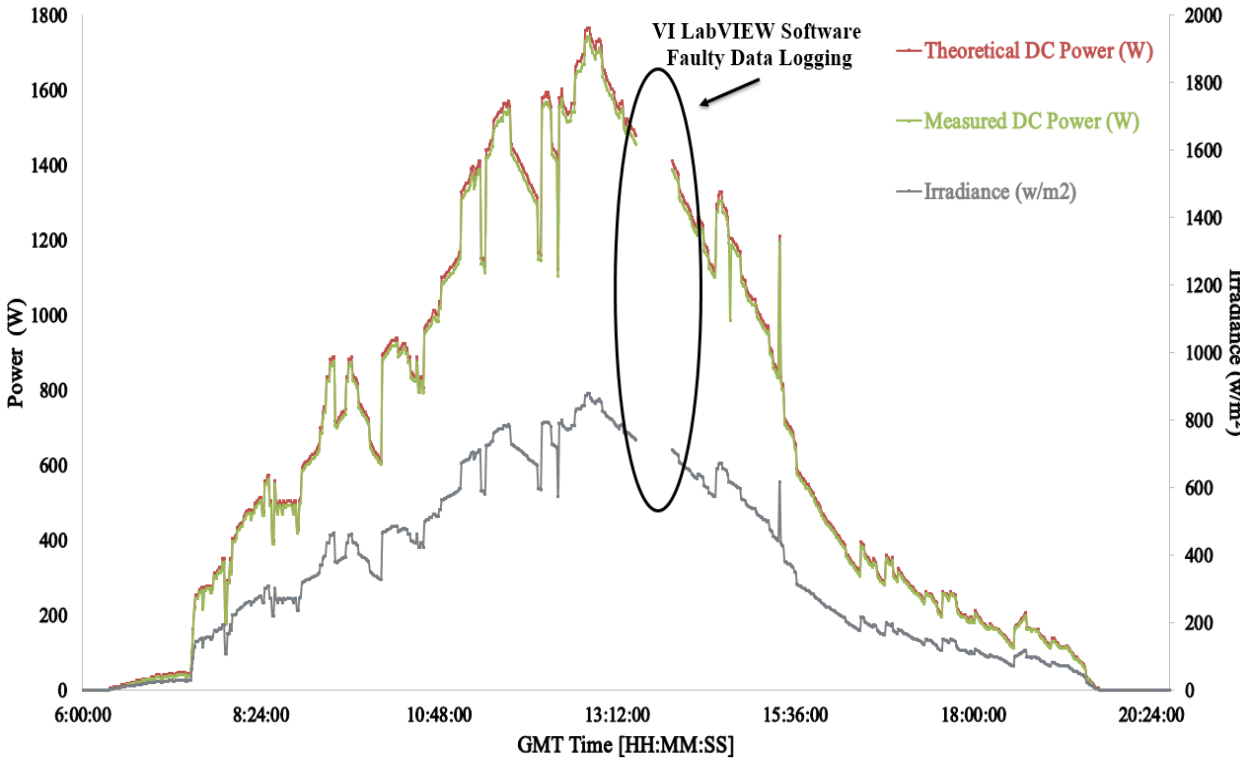

Figure 5.5 PV system theoretical and measured output power

5.3.3 Multiple PV faults occurring in the examined PV system

In order to test the ability of the fault detection algorithm, described previously in section 5.2, a number of experiments were conducted over a period of two days. Each day contains multiple faults introduced to the PV system.

A. <u>Day 1:</u>

In this day, multiple PV faults have been conducted. Table 5.1 shows the start and end time for each conducted experiment. Ten different scenarios were tested sequentially, between 6:00 and 20:24. Various faults have been tested such as:

- Faulty PV module in a PV string
- Two faulty PV modules in a PV string
- 30% Partial shading and faulty PV module without faults in the bypass diode
- Faulty MPPT unit
- Faulty PV string

Figure 5.6 show the theoretical and measured output power of the PV system under all conducted tests shown in Table 5.1. The PV system is at sleep mode between the times 6:00 – 6:20 and 19:41 – 20:24. The output power during these case scenarios is equal to zero, since there is no solar irradiance absorbed by the solar cells. The power ratio and voltage ratio during the tests are shown in Figure 5.7 and Figure 5.8a respectively.

Table 5.1 Diagnosis multiple faults in multiple strings locations

Case Number	Start Time	End Time	First PV String	Second PV String	Third PV String
1	6:00	6:20	sleep mode	sleep mode	sleep mode
2	6:21	10:00	normal operation	normal operation	normal operation
3	10:00	11:00	faulty PV module	normal operation	normal operation
4	11:00	12:00	normal operation	two faulty PV modules	faulty PV module
5	12:00	13:00	normal operation	normal operation	30% partial shading and faulty PV module without fault in bypass diode in the PV string
6	13:00	14:00	normal operation	normal operation	30% partial shading and faulty PV module and faulty bypass diode in the PV string
7	14:00	15:00	faulty MPPT	normal operation	normal operation
8	15:00	16:00	faulty MPPT	faulty PV string	normal operation
9	16:00	19:41	normal operation	normal operation	normal operation
10	19:41	20:24	sleep mode	sleep mode	sleep mode

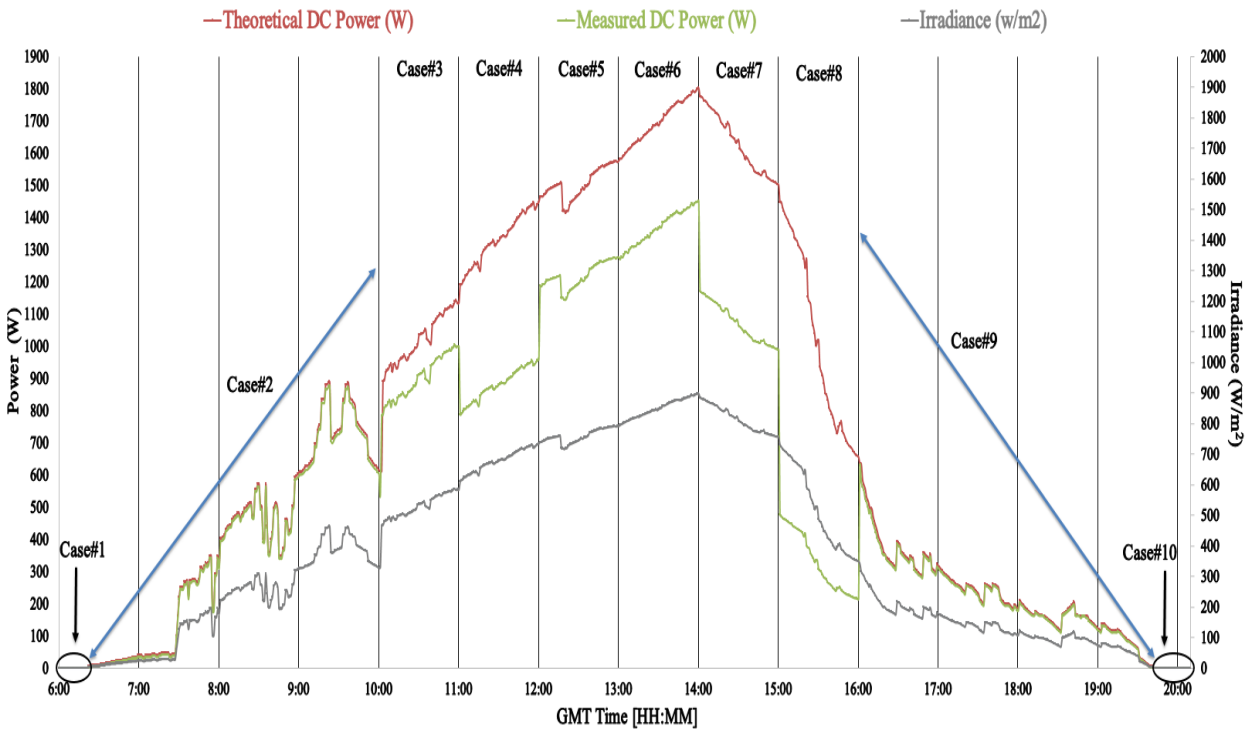

Figure 5.6 PV system theoretical output power vs. measured output power under 10 different scenarios shown in Table 5.1

As shown in Figure 5.6, starting from 6:21, the PV system starts to generate output power after the sleep mode is finished. The PV system operates in a normal operation mode until 10:00 (case scenario 2), where the PR and the VR ratio of this scenario are equal to 1.012 and 1.18 respectively as shown in Figure 5.7 and Figure 5.8a.

One faulty PV module is introduced in the first PV string between 10:00 and 11:00. The power ratio and voltage ratio for this particular scenario are equal to 1.511 and 1.502 respectively.

Two faulty PV modules in the second PV string are tested between 11:00 and 12:00. In this case, the power ratio for the second PV string is equal to 3.021, while the first and third PV strings operate in normal operation mode.

By disconnecting one PV module and applying a 30% partial shading by placing an opaque paper on the third PV string as shown in Figure 5.6, between 12:00 and 14:00, the power ratio is equal to 2.36. Additionally, the measured short circuit current is used to detect possible faults in the bypass diode in the PV string.

Figure 5.8b shows the variations of the measured short circuit current for the PV system. As described earlier in section 5.2, the theoretical upper and lower limits for the short circuit current are equal to 8.18A and 8.0571A respectively.

A faulty bypass diode is detected by the PV fault detection algorithm between 13:00 and 14:00. In this case, the measured short circuit current lies between 5.6 A and 5.9 A as shown in Figure 5.8b.

The only difference between a faulty MPPT unit and faulty PV string is that the voltage ratio ratio maintains a value greater than 1 during the disconnection of a PV string. Faulty MPPT and faulty PV string conditions are tested between 14:00 and 16:00 in different PV strings.

The voltage ratio and power ratio for a faulty MPPT are equal to 1000 for the first PV string as shown in Figure 5.7 and Figure 5.8a. However, the PR and VR ratios for the faulty PV string tested between 15:00 and 16:00 on the second PV string is equal to 1000 and 1.003 respectively.

From 16:00 until 20:24 no faults occurred in the PV system and the sleep mode of the system starts when the power ratio and voltage ratio is equal to zero at 19:41.

The results obtained for various test conditions indicate that PV fault detection algorithm has a high detection capability, there is no evidence of any errors in the detecting algorithm while conducting different fault case scenarios at different PV locations. The time and the type of fault are recognized by the algorithm.

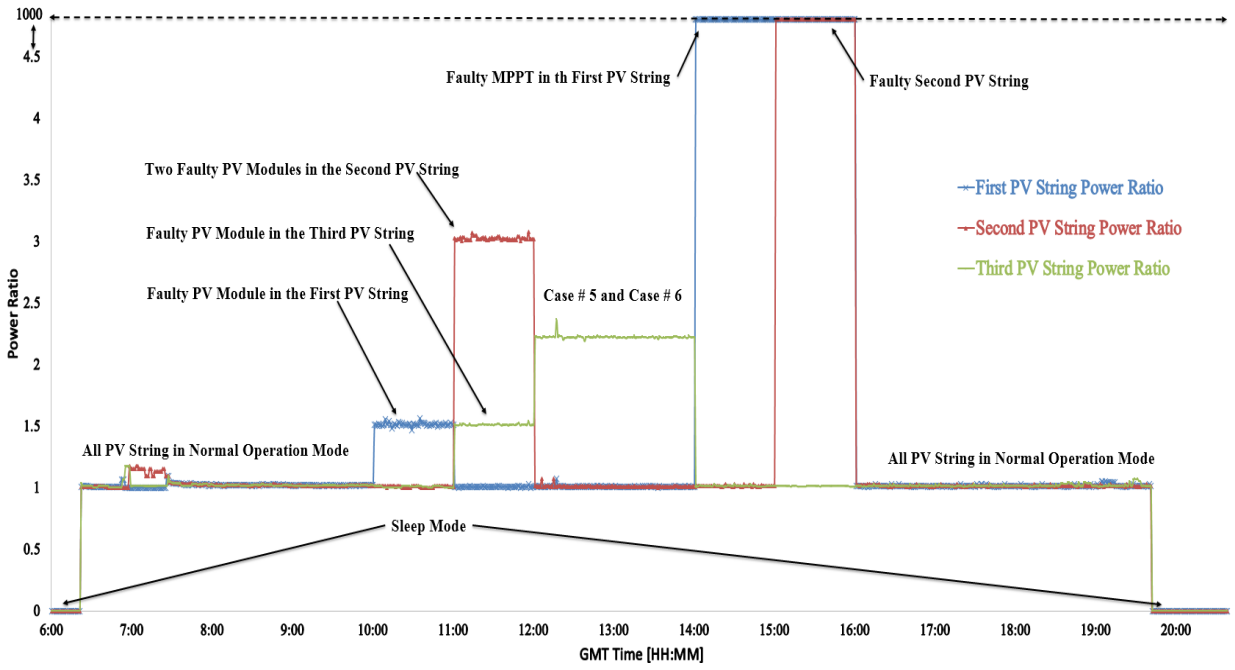

Figure 5.7 PR ratio for all PV strings

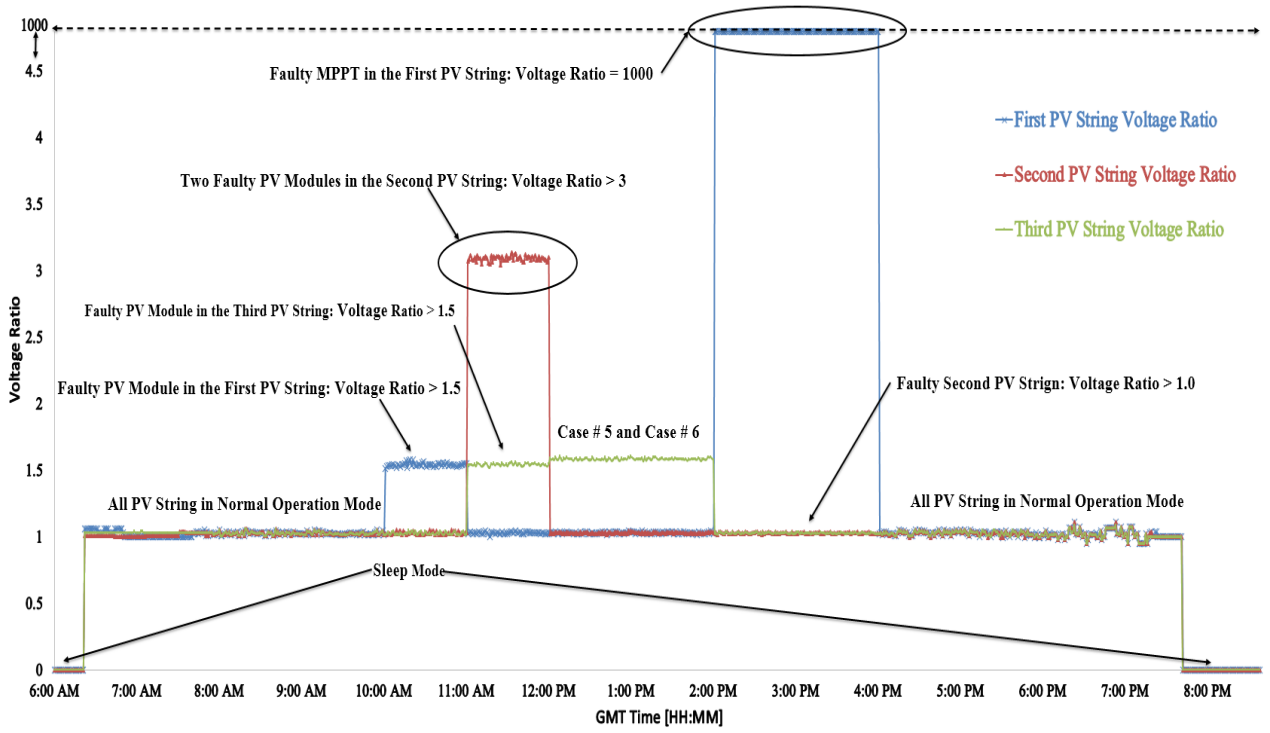

(a)

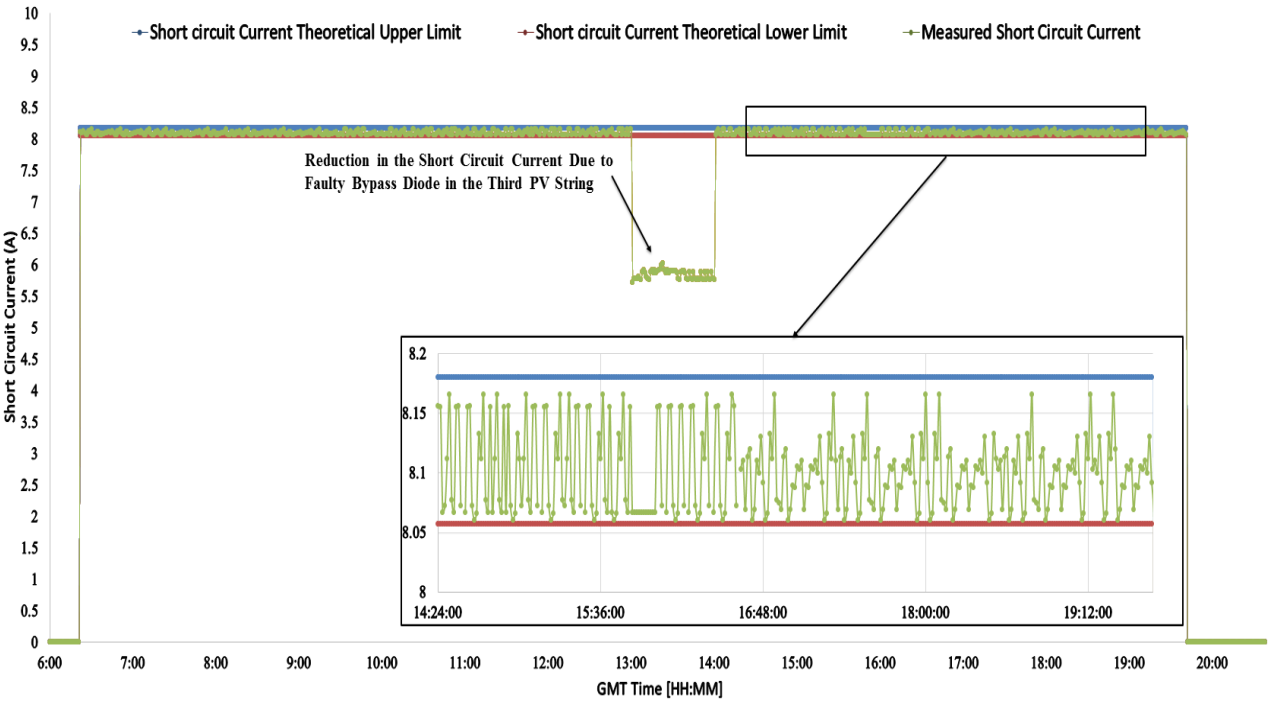

(b)

Figure 5.8 Detecting various faults using the proposed PV fault detection algorithm. (a) VR ratio for all PV strings, (b) Measured short circuit current

A. Day 2:

This test is conducted to confirm the ability of the PV fault detection algorithm to detect multiple faults associated with different PV strings locations.

Table 5.2 shows the starting and ending time of each experiment on the examined strings in the PV plant. Eight different time periods were examined, starting and ending at 4:48am – 21:36pm respectively.

Figure 5.9a shows the theoretical vs. measured output power for the PV system whilst Figures 5.9b, 5.10a and 5.10b describe the resultant power and voltage ratios for each tested PV string.

There is a rapid change in the irradiance level during the test time period, and this is shown in Figure 5.9a. Starting from 4:48:00, all PV strings were in sleep mode, voltage ratio and power ratio are equal to zero. At 5:39:18 the PV strings started working in normal operation mode. One faulty PV module has been detected in the third PV string at 9:58:18.

Table 5.2 Diagnosis multiple faults in multiple PV strings

Case Number	Start Time	End Time	First PV String Shown in Figure 5.9a	Second PV String Shown in Figure 5.10a	Third PV String Shown in Figure 5.10b
1	4:48:00	5:39:18	Sleep Mode	Sleep Mode	Sleep Mode
2	5:39:18	9:59:18	Normal Operation	Normal Operation	Normal Operation
3	9:59:18	11:29:18	Normal Operation	60% Partial Shading	One Faulty PV
4	11:29:18	13:06:18	40% Partial Shading	Normal Operation	Two Faulty PV
5	13:06:18	15:51:18	40% Partial Shading	Faulty PV String	Normal Operation
6	15:51:18	17:25:18	One Faulty PV and 40% Partial Shading	Normal Operation	Faulty MPPT
7	17:25:18	19:35:19	Normal Operation	Normal Operation	Normal Operation
8	19:35:19	21:36:00	Sleep Mode	Sleep Mode	Sleep Mode

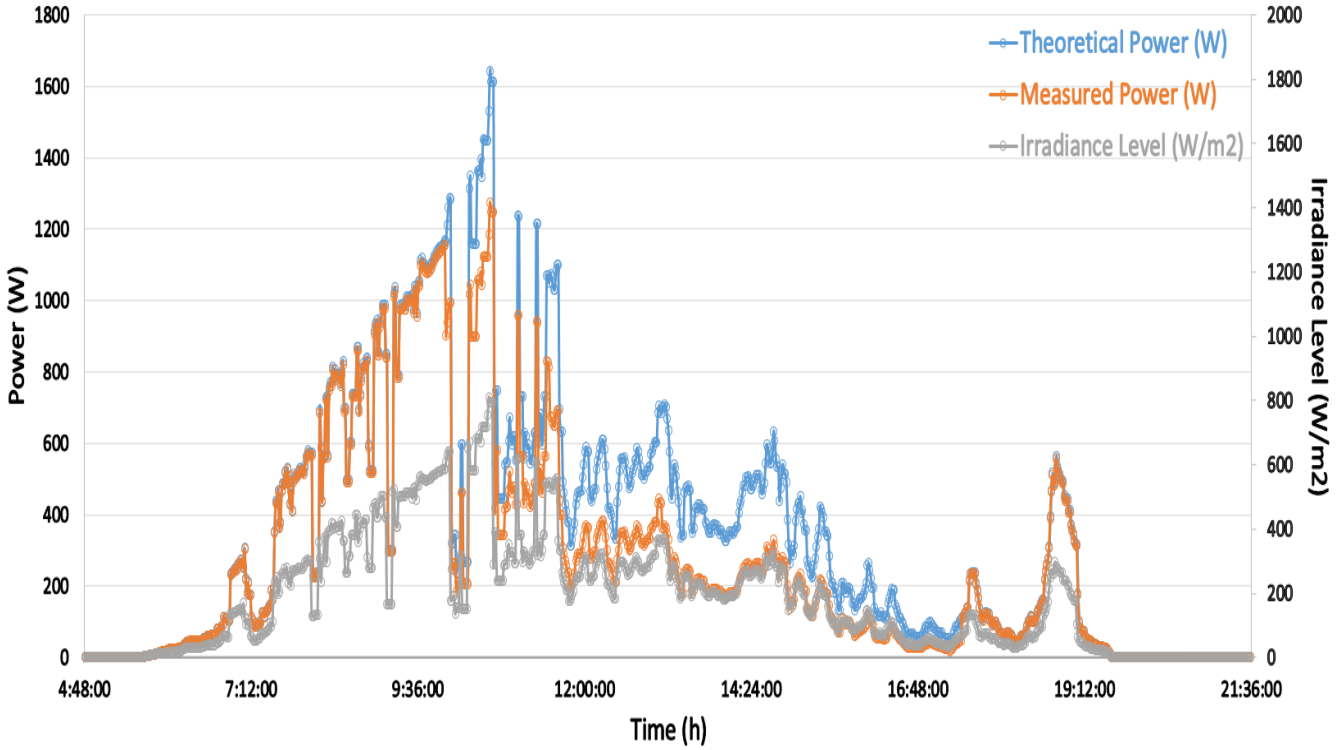

(a)

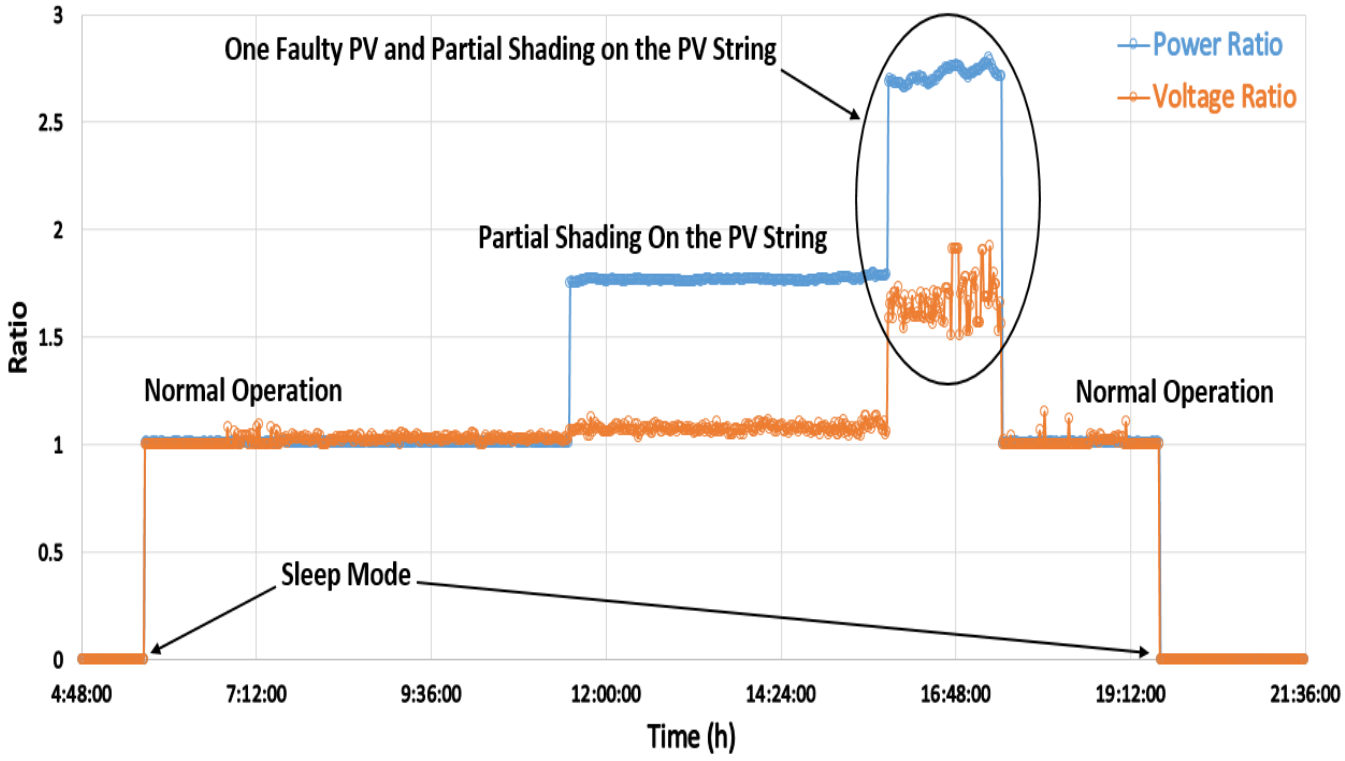

(b)

Figure 5.9 (a) PV array theoretical and measured output power, (b) first PV string PR and VR

After 1.5 hour, two faulty PV modules are detected in the third PV string and 40% partial shading detected in the first PV String. The power ratio and voltage ratio for both tests are shown in Figure 5.10b and Figure 5.10b respectively.

Starting at 13:06:17, one faulty PV module is detected in the second PV string as shown in Figure 5.10a, power ratio region 1. At the same time period, PS and normal operation mode are determined by the detection algorithm in the first PV string and third PV string respectively.

Furthermore, faulty PV string is detected at 13:06:17 in the second PV string. The VR ratio for the test is between 1 and 1.04. However, the power ratio is equal to 1000 as shown in Figure 5.10a, power ratio region 2.

Faulty maximum power point tracking unit is detected in the third PV string at 15:51:18. According to Figure 5.10b, power ratio region 2, the voltage ratio and power ratio is equal to 1000. At the same period of time, faulty PV module and 40% partial shading is detected in the first PV string. The voltage ratio is between 1.5 and 2. However, the power ratio is always greater than 2.5.

During the time 17:25:18 – 19:35:18, the PV fault detection algorithm indicates that the PV plant is working probably without any faults. The entire system is back to sleep mode at 19:35:18, where VR = PR = 0.

In this test, the fault detection algorithm shows a significant success in detecting many possible failure that may occur in the PV plant. The time and the region of the fault are detected by the algorithm, as well as the type of the fault.

It was also demonstrated that the detection algorithm can achieve a high accuracy rate in detecting failures under a rapid change in the irradiance level as shown in Figure 5.9a.

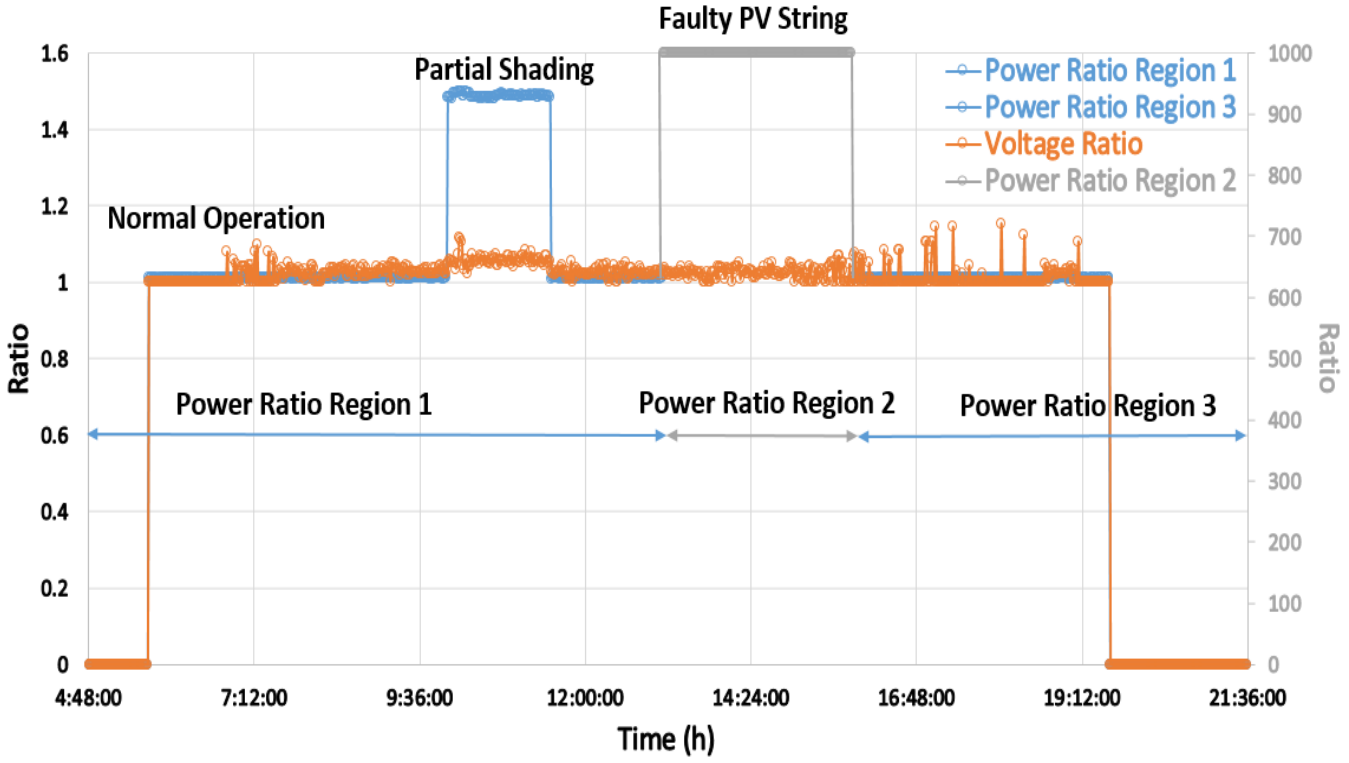

(a)

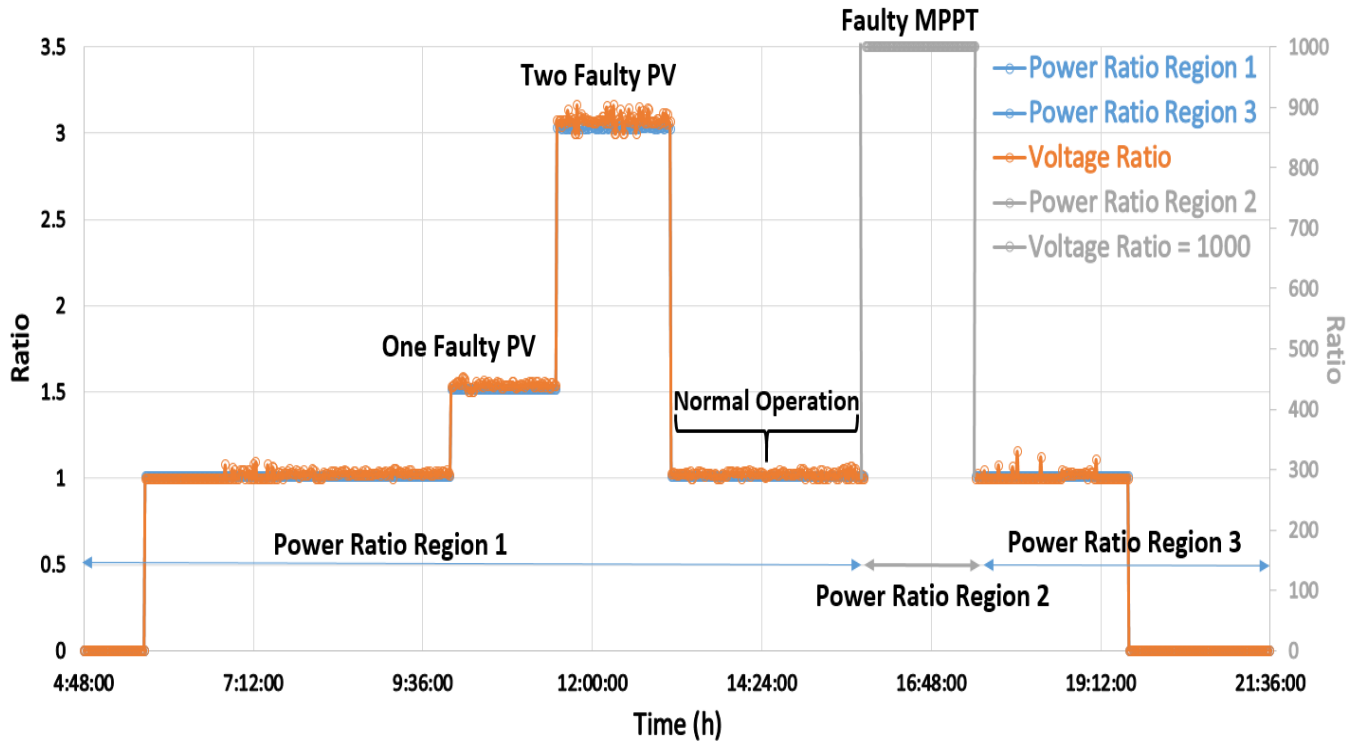

(b)

Figure 5.10 (a) Second PV string PR and VR, (b) Third PV string PR and VR

5.4 Evaluating the Proposed PV Fault Detection Algorithm Based on Array Aging

Since the examined PV modules used in the previous sections are new (installed 3 years ago), the proposed PV detection algorithm was evaluated using an older PV system shown in Figure 5.11, where the total PV system capacity is equal to 0.52 kWp (Mahmoud Dhimish, Holmes, & Dales, 2017). The MPPT unit and DC/AC inverter have been explained in Appendix A.

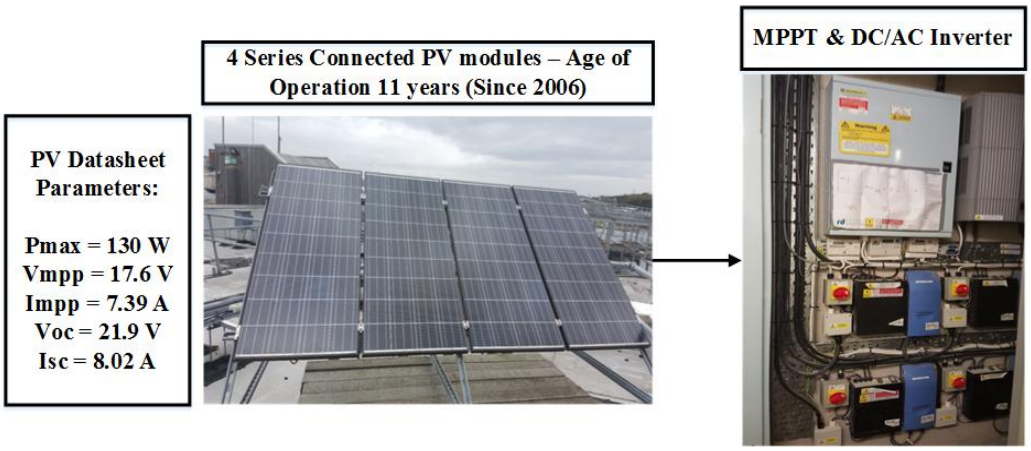

Figure 5.11 Examined PV system

The PV modules were installed at the University of Huddersfield 11 years ago. Table 5.3 shows the theoretical PR fault detection limits calculated using Equations (5.4) and (5.5) for various scenarios before considering the age of the PV installation.

Figure 5.12a shows the measured PR while disconnecting 3 PV modules (3 PV modules are inactive). Using the detection limits obtained from Equations (5.4) and (5.5), most of the measured PR samples do not lie between the detection limits since Equations (5.4) and (5.5) do not contain the degradation rate of the PV array due to the PV array age. Therefore, it is required to use Equation (5.8) to estimate the new detection limits which includes the degradation rate for the PV installation, where the new detection limits are presented in Table 6.3.

In principle, the degradation rate for PV modules stands for the percentage of output power loss compared to the data sheet of the PV modules. There are various mechanisms lead to PV degradation such as dirt/dust, humidity fluctuations, wind speed fluctuations, and manufacturing defects.

$$\mathrm{PR} = \frac{\mathrm{P_{theoretical}}}{\mathrm{P_{measured}} \times \mathrm{MPPT\ efficiency} \times (\,100 - \mathrm{PV\ Degredation\ Rate}\,)} \tag{5.8}$$

Table 5.3 Theoretical threshold calculations using the examined older PV system shown in Figure 5.11 (Mahmoud Dhimish, Holmes, & Dales, 2017)

Examined Case Scenario	Theoretical Thresholds Calculations Using (5.4 and 5.5) Before Considering the PV Array Age of Installation	Theoretical Thresholds Calculations Using (5.8) After Considering the PV Array Age of Installation
Normal Operation mode	$\text{PRmin} = \frac{130 \times 4}{130 \times 4} = 1$ $\text{PRmax} = \frac{130 \times 4}{130 \times 4 \times 98.5\%} = 1.015$	$\text{PRmin} = \frac{130 \times 4}{130 \times 4} = 1$ $\text{PRmax} = \frac{130 \times 4}{130 \times 4 \times 98.5\% \times (100 - 7.37)\%} = 1.096$
Faulty PV module	$\text{PRmin} = \frac{130 \times 4}{130 \times 3} = 1.3$ $\text{PRmax} = \frac{130 \times 4}{130 \times 3 \times 98.5\%} = 1.35$	$\text{PRmin} = \frac{130 \times 4}{130 \times 3} = 1.3$ $\text{PRmax} = \frac{130 \times 4}{130 \times 3 \times 98.5\% \times (100 - 7.37)\%} = 1.46$
2 Faulty PV modules	$\text{PRmin} = \frac{130 \times 4}{130 \times 2} = 2$ $\text{PRmax} = \frac{130 \times 4}{130 \times 2 \times 98.5\%} = 2.03$	$\text{PRmin} = \frac{130 \times 4}{130 \times 2} = 2$ $\text{PRmax} = \frac{130 \times 4}{130 \times 2 \times 98.5\% \times (100 - 7.37)\%} = 2.19$
3 Faulty PV modules	$\text{PRmin} = \frac{130 \times 4}{130 \times 1} = 4$ $\text{PRmax} = \frac{130 \times 4}{130 \times 1 \times 98.5\%} = 4.06$	$\text{PRmin} = \frac{130 \times 4}{130 \times 1} = 4$ $\text{PRmax} = \frac{130 \times 4}{130 \times 1 \times 98.5\% \times (100 - 7.37)\%} = 4.38$

Figure 5.12b shows the measured PR values for several tests, such as 3 faulty PV modules, two faulty PV modules and one faulty PV module. The theoretical thresholds are calculated at a degradation rate equal to 7.37%. This rate is selected to ensure all measured data lies within the detection region of the power ratio as illustrated in Table 5.3.

In conclusion, PV degradation rate is a complex problem in PV systems, because it depends on multiple factors such as humidity, wind, dust, and partial shading. These factors are unpredictable and subject to the location of the PV systems and the weather conditions.

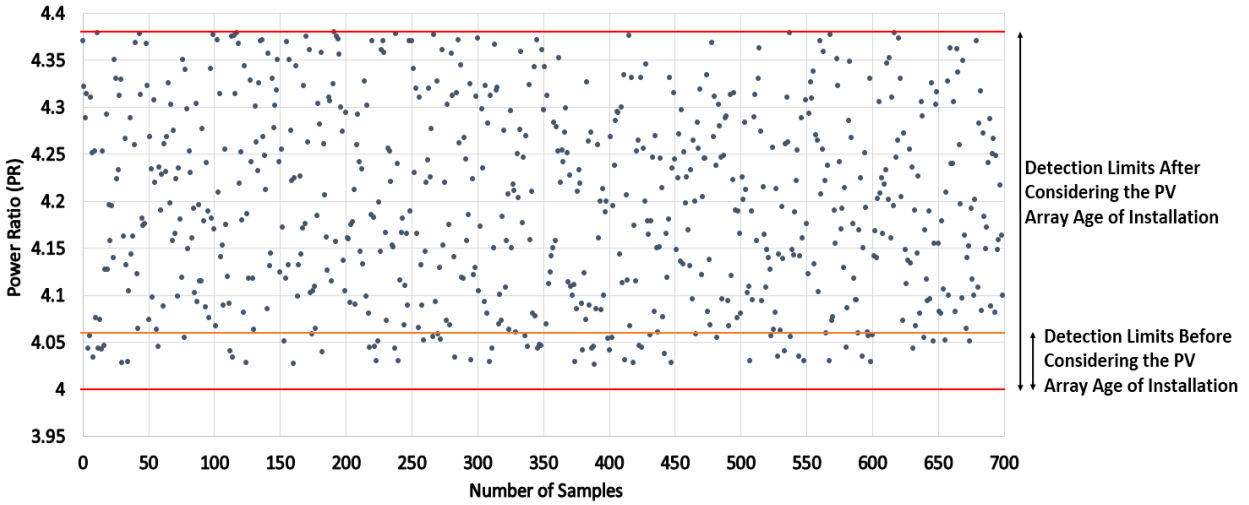

(a)

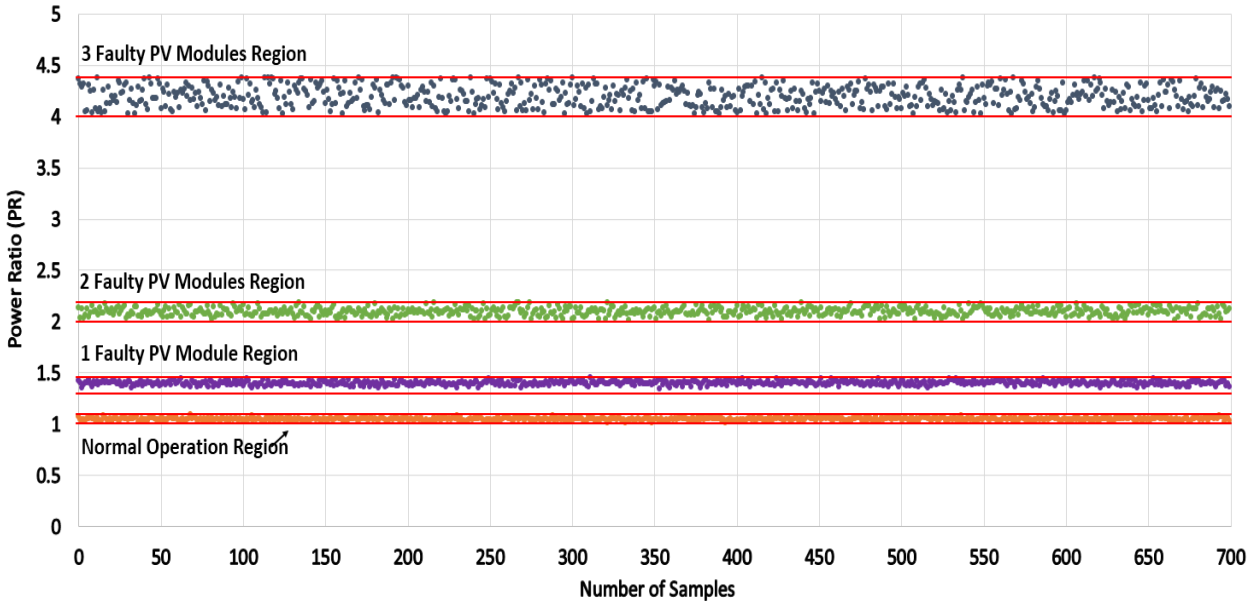

(b)

Figure 5.12 (a) PR variations for 3 faulty PV modules, (b) PR variations for all examined scenarios vs. detection limits which are explained in Table 6.3

6.5 Summary

In this chapter, the development of a PV fault detection algorithm was presented. The algorithm uses T-test statistical analysis technique to detect faults in the PV system. However, in order to identify the type of the fault occurred in the PV plant, I defined two new indicators named power ratio (PR) and voltage ratio (VR).

Both ratios are used to determine the type of fault, time and the region of the fault occurring in the PV system. A summary of the PV fault detection thresholds is shown in Figure 5.13.

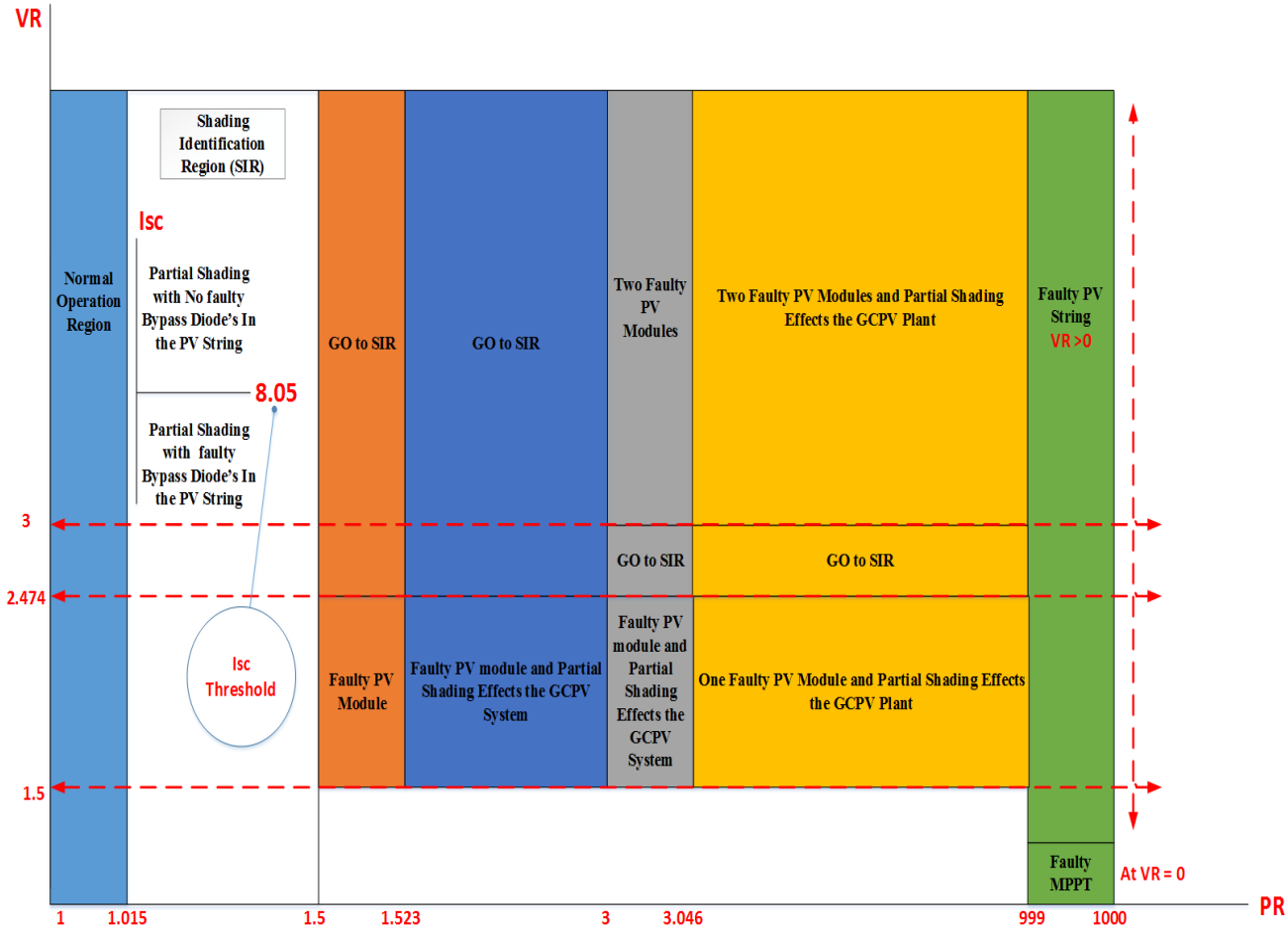

Figure 5.13 Summary of the proposed PV fault detection algorithm in chapter 6

The main advantages of the proposed fault detection algorithm are:

- The algorithm is easy to implement, since it depends only on the voltage and the power of the photovoltaic system which can easily be measured in most PV installations

- The algorithm uses simple statistical analysis technique (T-test) which depends on a simple statistical calculations such as the standard deviation and number of samples

- The proposed algorithm uses two main equations to create a set of rules for detecting faults in the PV system. Both equations require the voltage and the power measurements, therefore, it is simple to recreate and adapt both equations in other PV systems

- Multiple faults can be detected using the proposed algorithm, which suggests the algorithm is realistic and reliable to be used in PV systems. All faults that can be detected using the proposed algorithm are shown in section 5.1

- The PV fault detection algorithm can be adopted with aged PV modules by using Equation (5.8)

In the next chapter, the proposed PV fault detection algorithm will be enhanced using artificial intelligence systems such as Fuzzy Logic and artificial neural networks. In addition, the proposed PV fault detection algorithm will be improved by detecting multiple faults associated with the bypass diodes in the PV modules.

Chapter 6 PV Fault Detection using Artificial Intelligence System

This chapter demonstrates the use of artificial intelligence systems including Fuzzy Logic and artificial neural networks in PV fault detection. Several techniques are used to detect PV faults such as Mamdani Fuzzy Logic system, Sugeno Fuzzy Logic system, and radial basis function networks.

The data presented in this chapter have been published in the following journal articles (Mahmoud Dhimish, Holmes, Mehrdadi, & Dales, 2017a, 2017c; Mahmoud Dhimish, Holmes, Mehrdadi, Dales, & Mather, 2017b).

6.1 PV fault detection using six layer detection approach

6.1.1 Overall six layer PV fault detection algorithm structure

In this section, the development of a PV fault detection algorithm which allows the detection of multiple faults occurring in the PV plant will be demonstrated. The algorithm is based on the analysis of the PR and VR described earlier in chapter 5.

Figure 6.1 shows the overall structure of the PV fault detection algorithm. The first layer passes the measured irradiance and PV module's temperature to the LabVIEW software in order to simulate the theoretical voltage, current, and power of the tested PV plant.

To determine if a fault has occurred in an examined PV system, the PR and VR have been used. Both PR and VR can be summarized as by Equations (6.1) and (6.2).

$$PR = \frac{P_{G,T}}{P_{G,T} - nP_0} \tag{6.1}$$

$$VR = \frac{V_{G,T}}{V_{G,T} - nV_0} \tag{6.2}$$

where $P_{G,T}$ is the theoretical output power generated by the PV system at specific G (irradiance) and T (module temperature) values, n is the number of PV modules, $V_{G,T}$ is the theoretical output voltage and both $V_{0,}$ P_o are the maximum operating voltage and power at STC (G: 1000 w/m^2, T: 25 °C) respectively.

The number of PV modules in the examined PV string is represented by n. For example, if a PV string comprises five photovoltaic modules connected in series, then, n = 5.

In reality, the internal sensors used to measure the voltage and current for a PV system have efficiencies of less than 100%. This tolerance rate must therefore be considered in the power ratio and voltage ratio calculations. In this section, low and high limits are used as an indicator for the minimum and maximum operating points of the voltage and power for the examined PV systems. The difference between the high and low limit can be explained as follows:

1. High limit: where the maximum operating accuracy of the sensors is applied (normally its 100%). The high limit for both PR and VR ratios are expressed by Equations (6.1) and (6.2)

2. Low limit: where the minimum efficiency (minimum tolerance rate) for the voltage and current sensors is applied. PR and VR low limits are represented in Equations (6.3) and (6.4)

$$PR\ Low\ limit = \frac{P_{G,T}}{(P_{G,T} - nP_0)\eta_{sensor}} \tag{6.3}$$

$$VR\ Low\ limit = \frac{V_{G,T}}{(V_{G,T} - nV_0)\eta_{sensor1}} \tag{6.4}$$

where η_{sensor} is the accuracy of both the voltage and current sensor, while, $\eta_{sensor1}$ is the accuracy of the voltage sensor:

$$\eta_{sensor} = \eta_{sensor1}(Voltage\ Sensor\ accuracy) + \eta_{sensor2}(Current\ Sensor\ accuracy) \tag{6.5}$$

The power ratio and voltage ratio high and low detection limits are evaluated for the examined PV system using various irradiance levels, as described in the third layer in Figure 6.1. For this particular layer, the analysis of the PR vs. VR curves can be seen in the example shown next to layer 5, Figure 6.1. This example shows the high and low detection limits for two case scenarios: one faulty PV module and two faulty PV modules, where both curves are created using 3rd order polynomial functions (Mahmoud Dhimish, Holmes, Mehrdadi, & Dales, 2017c).

The purpose of the 3rd order polynomial curves is to generate a regression function which describes the performance of the curves which are created by the theoretical points using LabVIEW software. 3rd order was selected because it matches 4th, 5th, and 6th polynomial order with a minimum tested coefficient of determination (R^2) 99%, so for simplicity for the output variables, the 3rd order was used. The coefficient of determination is a measure of the global fit of the polynomial model, where its value varies between 0 – 100%. The better fit model results with higher coefficient of determination (close to 100%).

Layer 5 shows the measured data vs. the 3rd order polynomial curves simulated by LabVIEW software. The measured PR and measured VR can be evaluated using the following formula:

$$Measured\ PR\ \times\ Measured\ VR = \frac{P_{G,T}}{P_{MEASURED}} \times \frac{V_{G,T}}{V_{MEASURED}} \tag{6.6}$$

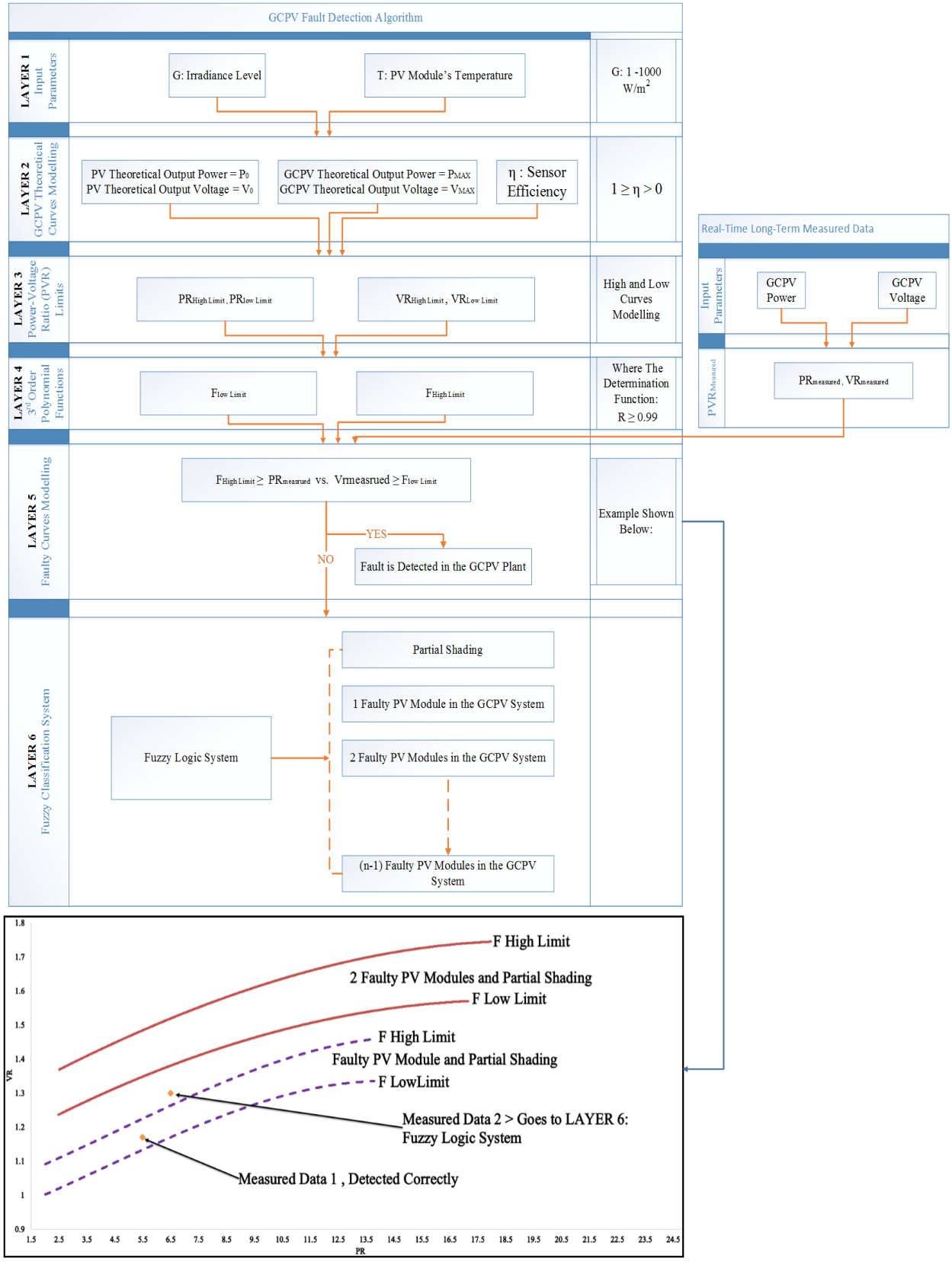

Figure 6.1 Detailed flowchart for the proposed PV fault detection algorithm

If the measured PR and VR is out of range:

$$F\ High\ limit > Measured\ PR\ \times Measured\ VR > F\ low\ limit \tag{6.7}$$

The fault detection algorithm cannot identify the type of the fault that has occurred in the PV plant. However, it can predict two possible faulty conditions which might have occurred in the PV system. As shown in Figure 6.1, layer 5, the measured data 2 indicates two possible faulty conditions: Faulty PV module and partial shading effects on the PV system, and two faulty PV modules and partial shading effects on the PV system. Therefore, out of region samples are processed by a Fuzzy Logic classifier as shown in Figure 6.1, layer 6. The structure of the Fuzzy Logic will be described in the next sub section.

6.1.2 Proposed Fuzzy Logic system

Fuzzy Logic system was selected as a proposed solution to enhance the PV fault detection algorithm. Practically, the Fuzzy Logic system is chosen due to its tolerant of imprecise data, as well as it can be built on top of operating control system without using any training data set, therefore it is enough to adjust the inputs/outputs of the system and resonate the fuzzy rules to enhance the detection.

The main purpose for proposing a Fuzzy Logic system in the PV fault detection algorithm is to detect measured points which cannot be classified by the high and low detection limits shown in Figure 6.1. Thus, it will increase the overall detection accuracy for the PV fault detection. As described in the previous section, the measured data which lie out of the detection limits are processed by a Fuzzy Logic system. The overall design of the fuzzy system is shown in Figure 6.2.

The Fuzzy Logic system consists of two inputs: voltage ratio and power ratio which are described by (A) and (B) in Figure 6.2 respectively. The membership function for each input is divided into five fuzzy sets described as: PS (partial shading condition), 1 (one faulty PV module), 2 (two faulty PV modules), 3 (three faulty PV modules), and 4 (four faulty PV modules).

The calculation of each membership function for voltage ratio, and power ratio are reported in Figure 6.3a. The membership functions are based on the mathematical calculation of the examined PV plant. The examined PV system which is used to evaluate the performance of the fault detection algorithm is shown in Figure 6.3b, which consists of 5 series connected PV modules (Mahmoud Dhimish, Holmes, Mehrdadi, & Dales, 2017a).

Both Fuzzy Logic system inputs voltage ratio and power ratio are evaluated at the maximum power and voltage of the PV system which are equal to 1100 W_p and 143.5 V. Additionally, the mathematical calculations includes the PS conditions which might affect the performance of the entire PV system.

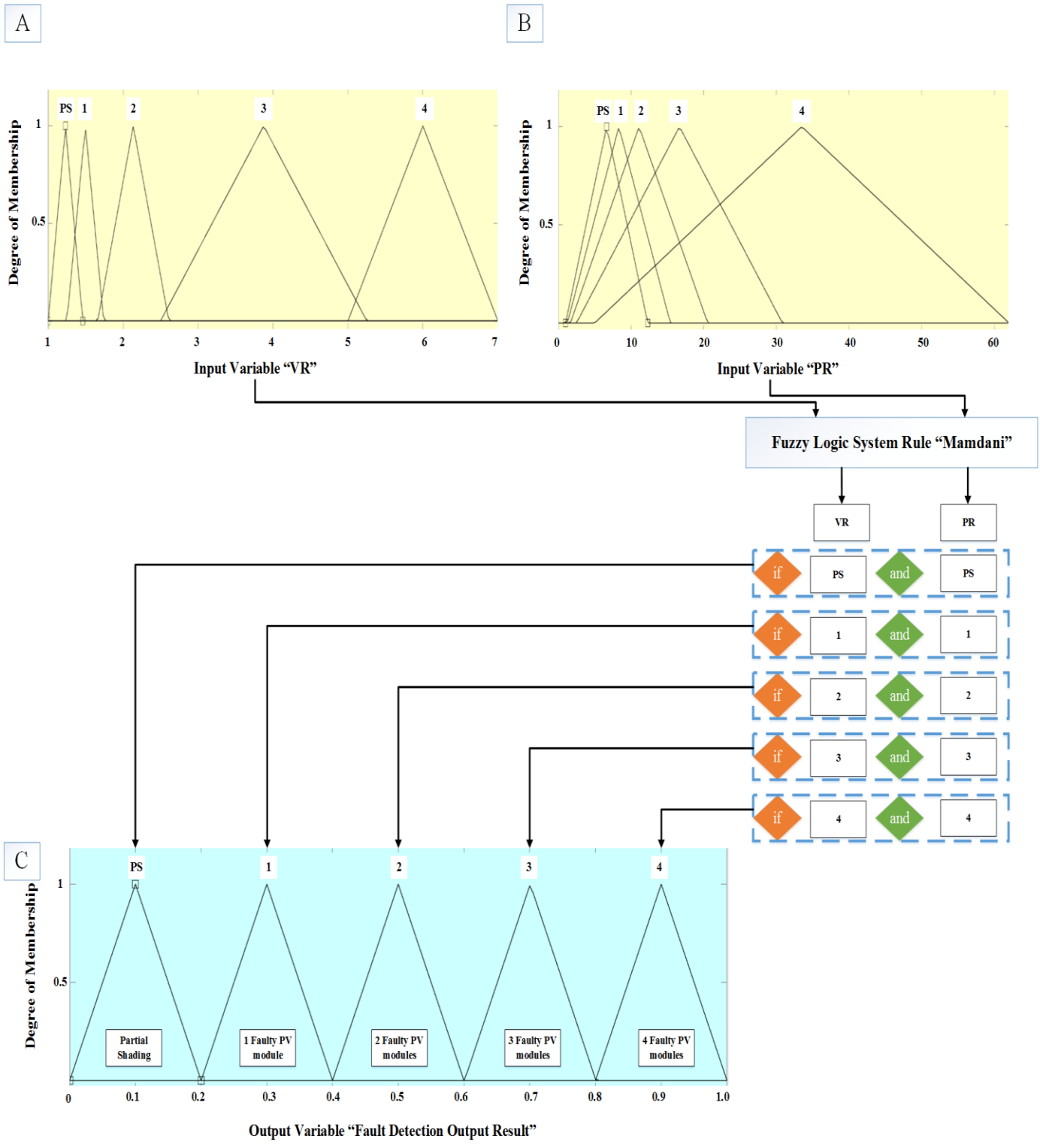

Figure 6.2 Fuzzy Logic classifier system design. (A) Voltage ratio input, (B) Power ratio input, (C) Fault detection output

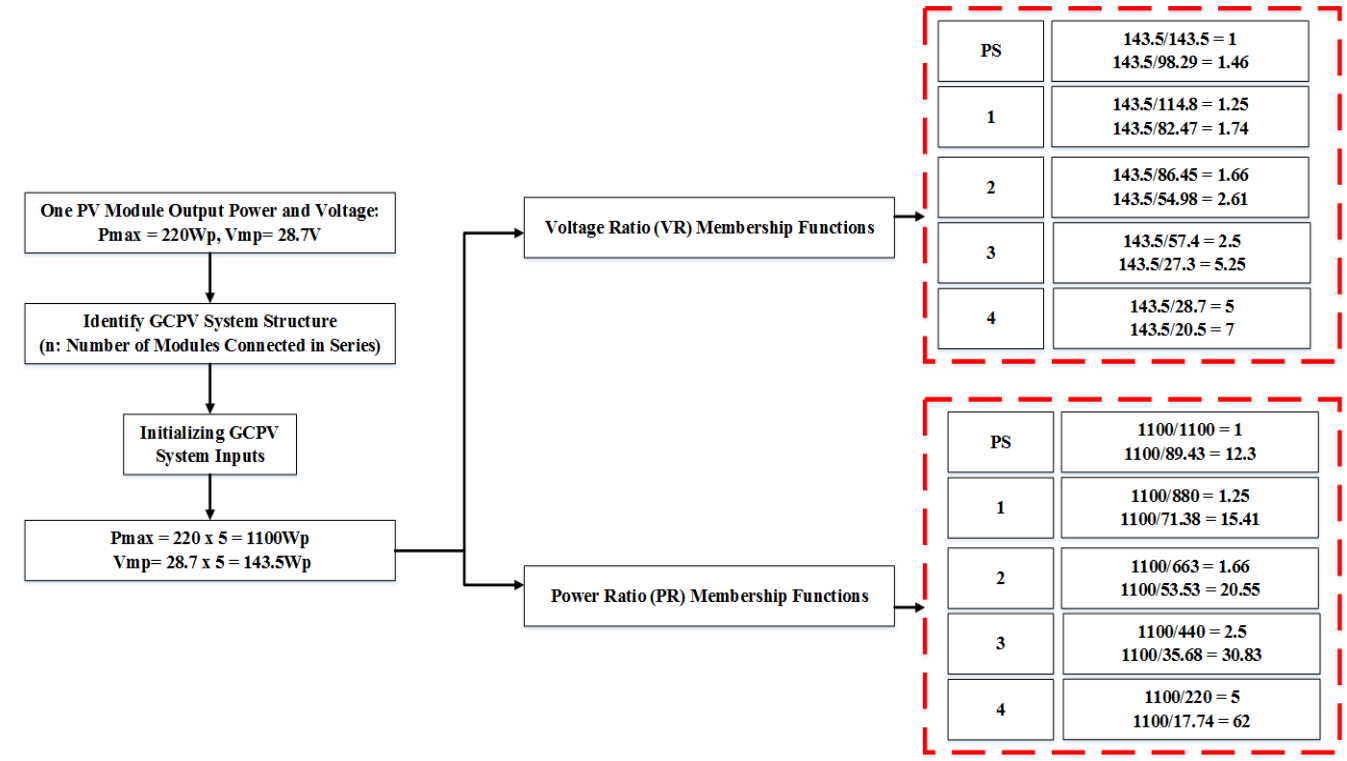

(a)

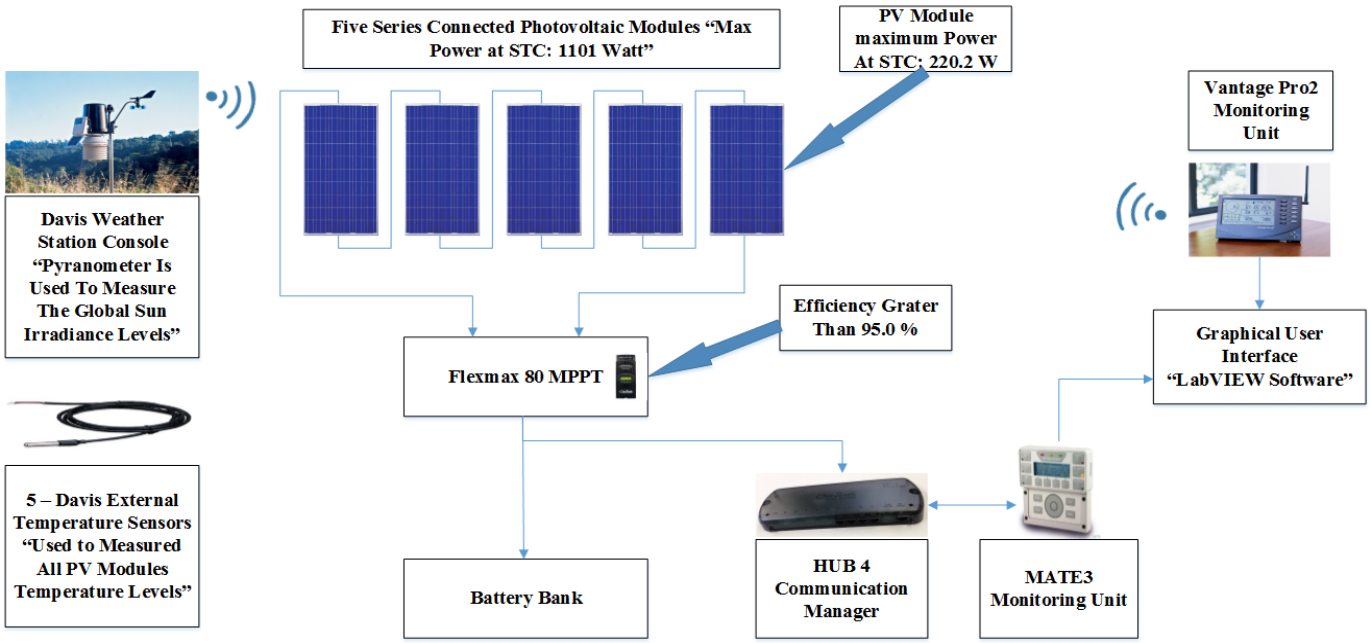

(b)

Figure 6.3 (a) Mathematical calculations for the Fuzzy Logic system including VR and PR, (b) Examined PV system which comprises five series-connected PV modules (Mahmoud Dhimish, Holmes, Mehrdadi, & Dales, 2017a)

The Fuzzy Logic system applies the approach of Mamdani method (min-max) managed by the Fuzzy Logic system rule. The Fuzzy Logic system rules are based on: if-then statement. Each case scenario is presented after the Fuzzy Logic system rule as shown in Figure 6.2.

The output membership functions are divided into 5 sets: PS (0 - 0.2), faulty PV module (0.2 – 0.4), two faulty PV modules (0.4 – 0.6), three faulty PV modules (0.6 – 0.8) and four faulty PV modules (0.8 – 1.0).

Furthermore, the output surface for the Fuzzy Logic system is plotted and presented by a 3D fitting curve shown in Figure 6.4, where the x-axis represents the power ratio, y-axis presents voltage ratio and the fault detection output classification is on the z-axis.

In order to generalize the proposed Fuzzy Logic system, it is required to input the values of the voltage and the power to the fuzzy interface system, and then, the faulty region could be calculated using the Equations (35) and (36) for the variations of the power and voltage respectively.

The output detection membership function could be extended up to the value of the PV modules connected in series in each PV string separately and this extension in the membership function can be evaluated within the region of 0 to 1 as the following: 1 / number of series PV modules in the PV string.

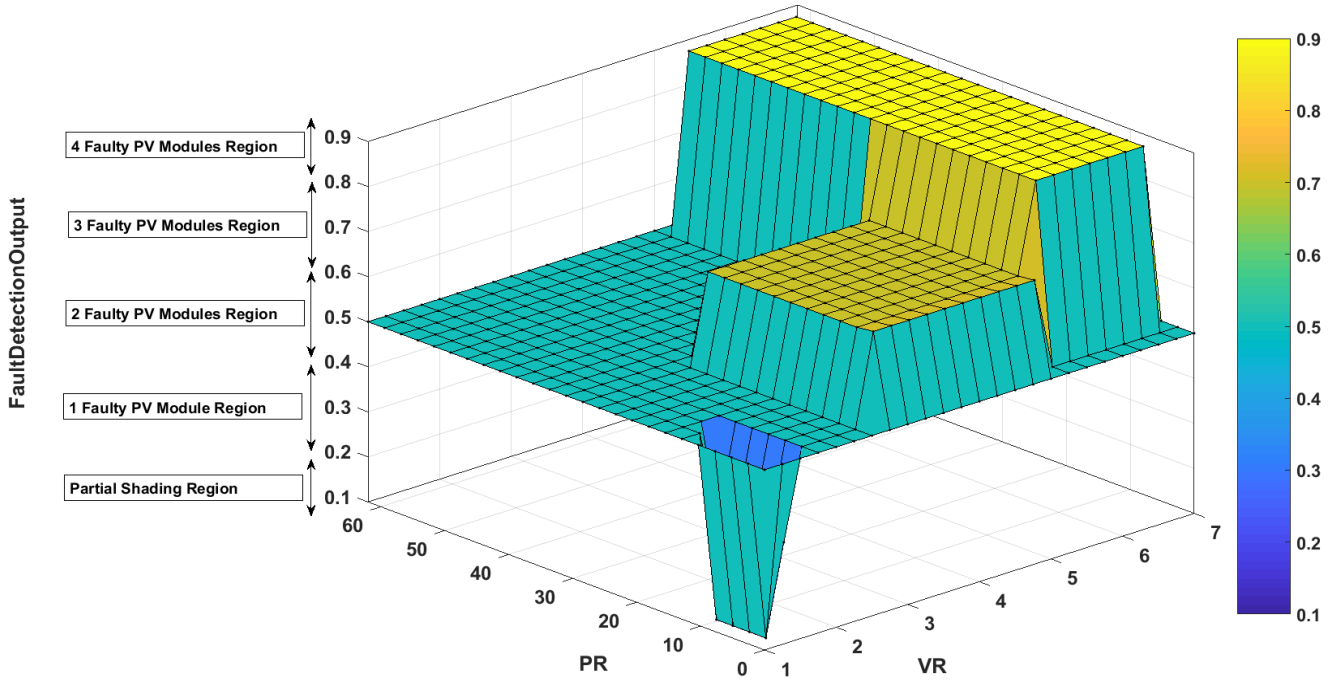

Figure 6.4 Fuzzy Logic system output surface comprising VR, PR and the fault detection output membership functions

6.1.3 Evaluating the proposed six layer PV fault detection algorithm

The proposed six layer PV fault detection algorithm has been validated using a PV plant which comprises five series-connected PV modules shown in Figure 6.3b. The Fault detection algorithm is validated experimentally over a period of 5 days.

In each day, the PV system was perturbed with different fault type. The theoretical and measured output power are shown in Figure 6.5, and can be explained as follows:

1. Day1: Normal operation mode and partial shading effects the PV plant (no fault occurred in any of the tested PV modules
2. Day2: One faulty PV module and partial shading affect the PV plant
3. Day3: Two faulty PV modules and partial shading affect the PV plant
4. Day4: Three faulty PV modules and partial shading affect the PV plant
5. Day5: Four faulty PV modules and partial shading affect the PV plant

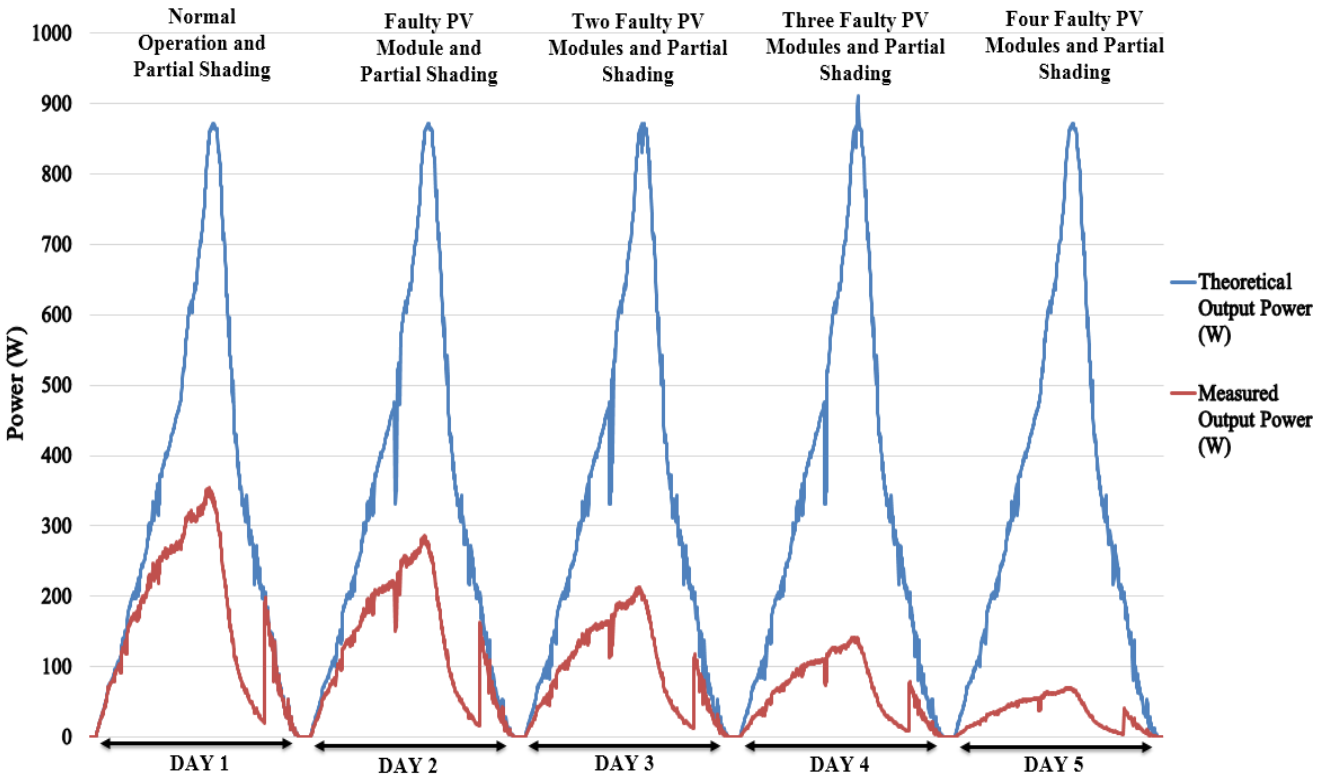

Figure 6.5 Theoretical vs. Measured output power during 5 different days

A. Evaluating the proposed theoretical curves modelling which uses 3rd order polynomial functions:

In this section, the performance of the fault detection algorithm (theoretical curves modelling) is verified using normal operation mode and partial shading effects the PV system. Figure 6.6 describes the theoretical simulation vs. the real-time long-term data measurement.

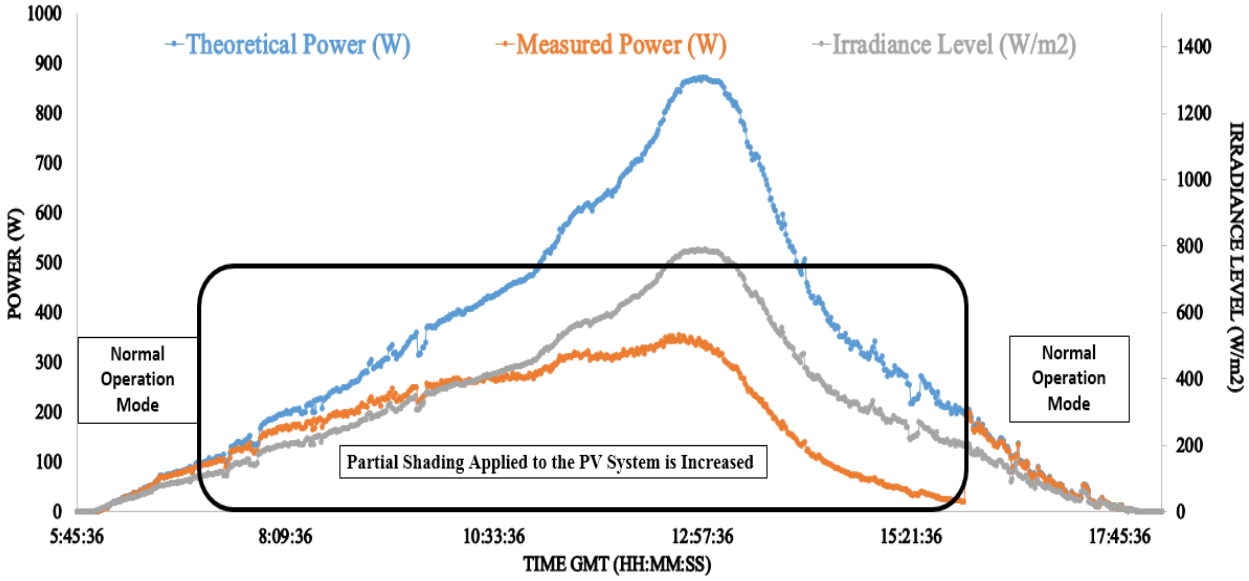

Figure 6.6 Theoretical power vs. measured power for a PS condition affects the examined PV system

In order to apply a PS condition to the PV modules an opaque paper object has been used. PS was applied to all PV modules with the same shading percentage. PS condition is increased during the test.

Figure 6.7a shows the entire measured data vs. the theoretical detection limits which are discussed previously in section 6.1. Most of the measured data lie within the high and low theoretical detection limits which are simulated using 3rd order polynomial function. The high and low detection limit functions are also illustrated in the Figure 6.7a.

PR and VR ratios for this particular test are shown in Figure 6.7b. Since the PS condition applied to the PV system is increasing, the VR and PR ratios are increasing slightly during the test. Moreover, Figure 6.7b shows the efficiency of the PV plant during the experiment. The efficiency is evaluated using (6.8).

$$\text{Efficiency} = \frac{\text{Measured Output Power}}{\text{Theoretical Power}} \tag{6.8}$$

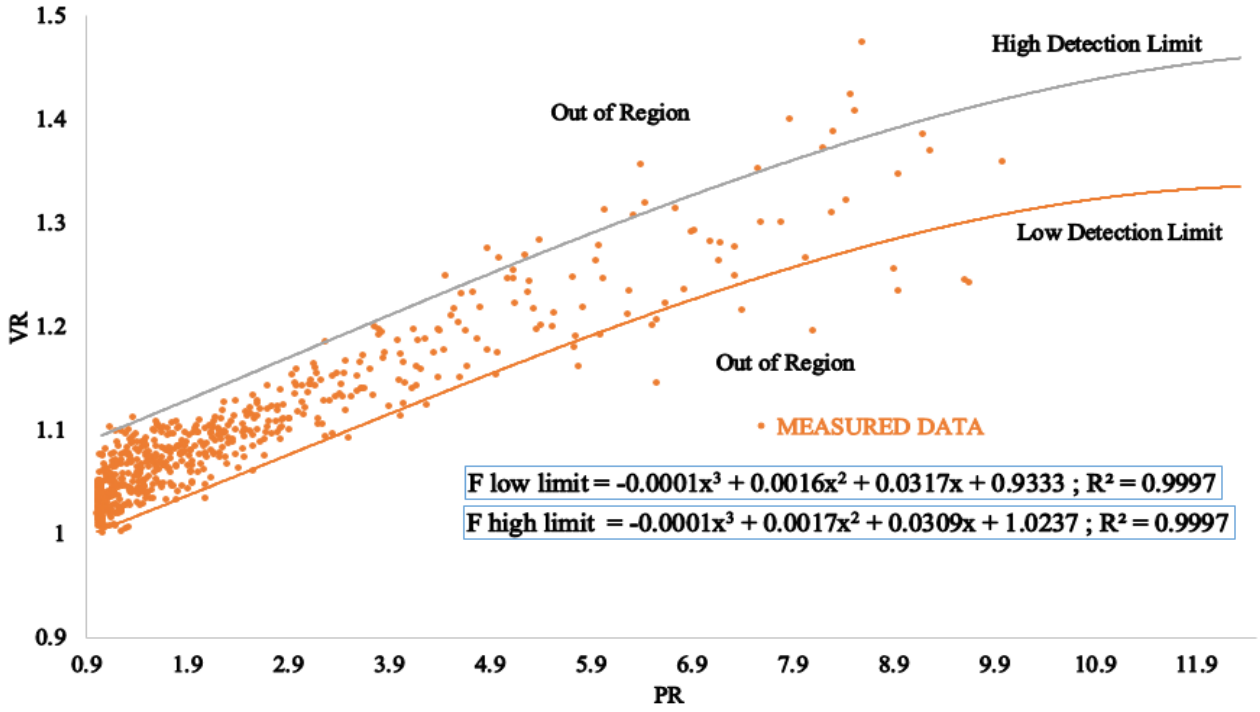

(a)

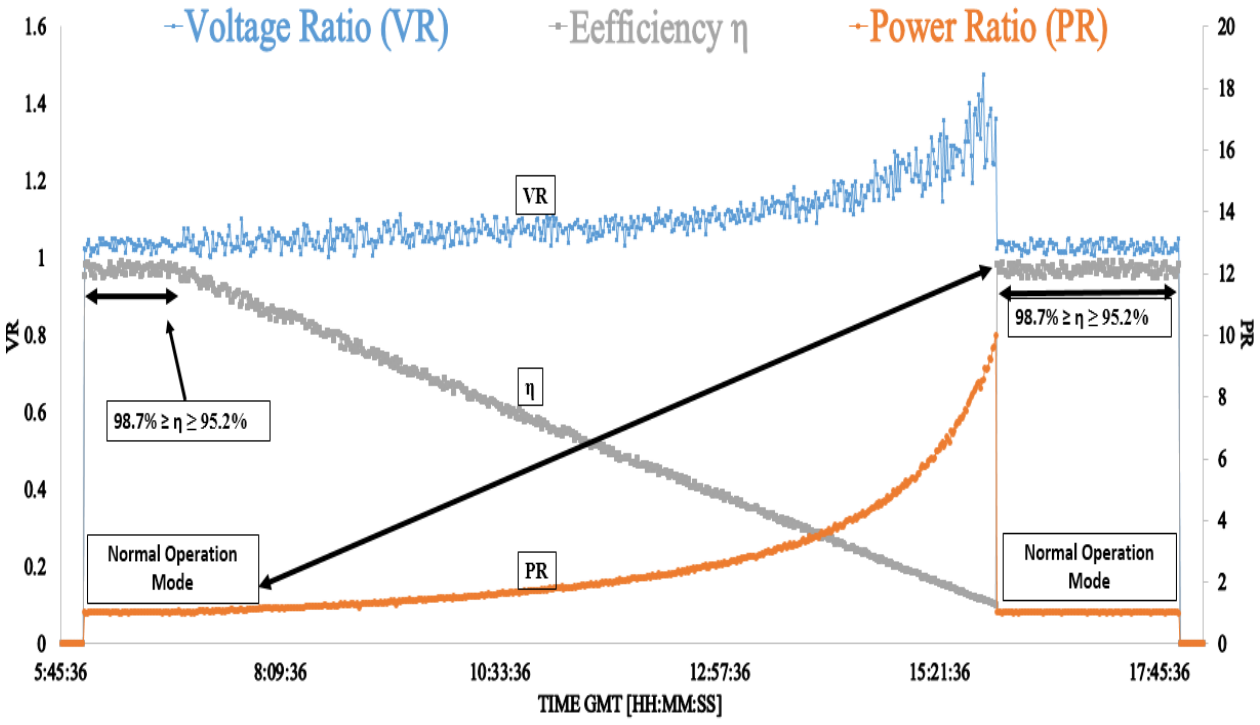

(b)

Figure 6.7 Theoretical curves vs. measured data. (a) Theoretical fault curve detection limits, (b) VR, PR, and the efficiency of the tested PV system

From Figure 6.7b, the efficiency of the tested PV system decreased while increasing the PS applied to the PV modules. The detection accuracy (DA) for the proposed PV detection algorithm is calculated using (6.9).

$$\text{Detection accuracy (DA)} = \frac{\text{Total Number of Samples} - \text{Out of Region Samples}}{\text{Total Number of Samples}} \quad (6.9)$$

Using (6.9), based on the experimental test shown in Figure 6.7b, the proposed algorithm has a detection accuracy equal to:

$$\text{Detection accuracy} = \frac{720 - 37}{720} = 0.9486 = 94.86\%$$

In this test, the theoretical curve modelling fault detection algorithm shows a significant success for detecting partial shading conditions applied to the PV plant. The detection accuracy rate could be increased using a Fuzzy Logic classification system. Therefore, out of region samples (samples which are away from the high and low detection limits) are processed by the Fuzzy Logic system.

In this section, the MPPT unit is used to locate and acquire the output power at the global maximum power point (GMPP), therefore, all local maximum power points (LMPP) are not considered in the fault detection algorithm (Mahmoud Dhimish, Holmes, Mehrdadi, Dales, & Mather, 2017b).

Figure 6.8a illustrates one examined case scenario which shows the percentage of the partial shading on each tested PV modules. The output P-V curve of the PV system is shown in Figure 6.8b. It is shown that the MPPT unit locates all LMPP and GMPP, however, the output of the MPPT unit is at the GMPP.

In order to detect all LMPPs and the GMPP obtained by the MPPT unit, it is required to further investigate MPPT techniques which is not one of the targets of the proposed PV fault detection algorithm.

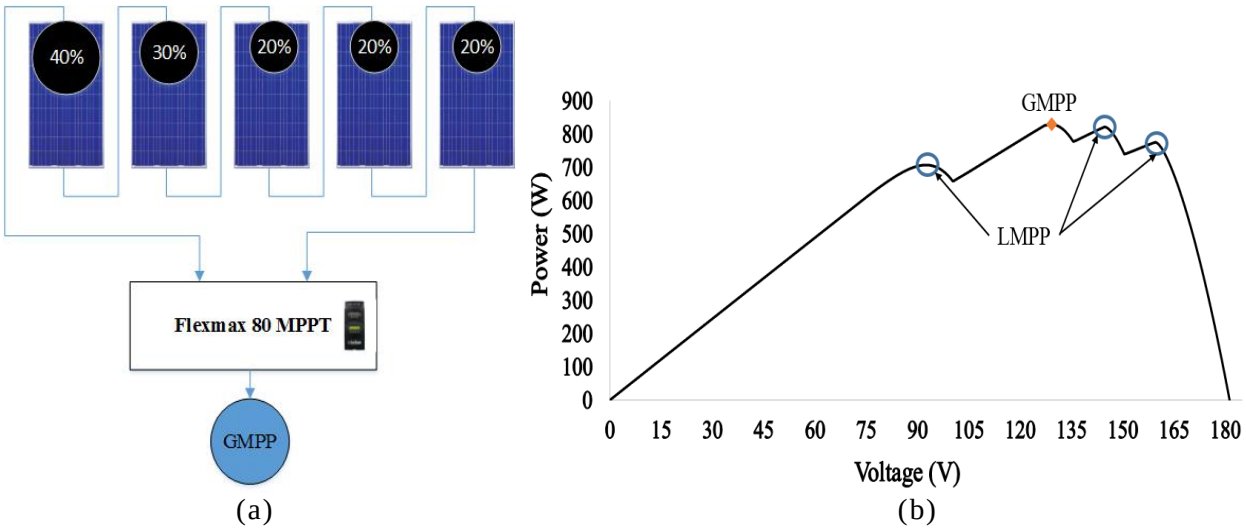

Figure 6.8 MPPT unit output power. (a) Examined partial shading condition, (b) P-V curve including the output LMPP and GMPP obtained by the MPPT unit

B. Evaluating the proposed Fuzzy Logic system

This section is created to confirm the ability of the PV fault detection algorithm to detect faulty PV modules occurring in the PV system using the theoretical curve modelling algorithm and Fuzzy Logic classification system. Four different case scenarios have been tested:

A. Faulty PV module with partial shading condition
B. Two faulty PV modules with partial shading condition
C. Three faulty PV modules with partial shading condition
D. Four faulty PV module and partial shading condition

Each case scenario is examined during a time period of a full day as shown previously in Figure 6.5 (Day 2, 3, 4 and 5). The total number of the samples for each day are equal to 720.

Figure 6.9 shows the theoretical curve limits vs. real-time long-term measured data. 3rd order polynomial functions of the theoretical high and low limits are plotted, while the minimum determination factor (R^2) is equal to 99.59% (Mahmoud Dhimish, Holmes, Mehrdadi, Dales, & Mather, 2017b).

The measured data for each test are plotted and compared with the theoretical curve limits. Most of the measured data among the 4 day test period lies within the high and low detection limits of the theoretical curves. However, in each day, several out of region samples have been detected as shown in Figure 6.9.

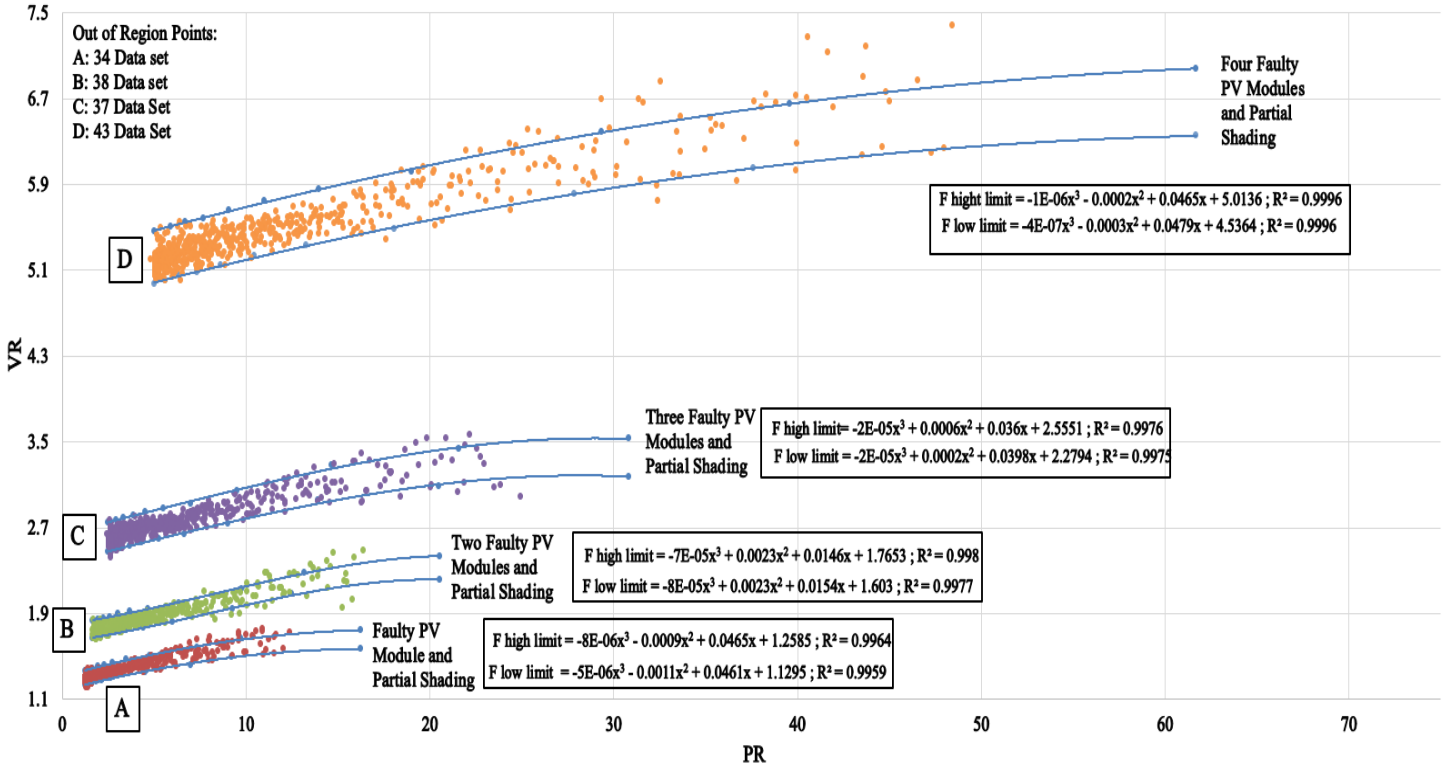

Figure 6.9 Theoretical detection limits vs. measured data for one faulty, two faulty, three faulty, and four faulty PV modules

The detection accuracy (DA) for each case scenario is calculated using (6.9) and described in Table 6.1. The minimum and maximum detection accuracy are equal to 94.03% and 95.27%, respectively, before considering the Fuzzy Logic classification system.

For each examined case scenario including the test illustrated in section A, out of region samples have been processed by the Fuzzy Logic classification system. Figure 6.10 describes the performance of the Fuzzy Logic system during each test:

- Test 1: PS
- Test 2: One faulty PV module and PS
- Test 3: Two faulty PV modules and PS
- Test 4: Three faulty PV modules and PS
- Test 5: Four faulty PV modules and PS

Table 6.1 Accuracy comparison between four different case scenarios

Test Number	Case Scenario	Without Fuzzy Classifier		Including Fuzzy Classifier	
		Out of Region Samples	Detection Accuracy (DA %)	Out of Region Samples	Detection Accuracy (DA %)
Test 1 - PS (described in section 6.1.3 (A))	Partial shading affects the GCPV system	37	94.86	5	99.31
Test 2 - One faulty PV module and PS (presented as A in Figure 6.9)	Faulty PV module and partial shading	34	95.27	7	99.03
Test 3 - Two faulty PV modules and PS (presented as B in Figure 6.9)	Two faulty PV module and partial shading	38	94.72	8	98.80
Test 4 - Three faulty PV modules and PS (presented as C in Figure 6.9)	Three faulty PV module and partial shading	37	94.86	5	99.31
Test 5 - Four faulty PV modules and PS (presented as D in Figure 6.9)	Four faulty PV module and partial shading	43	94.03	6	99.16

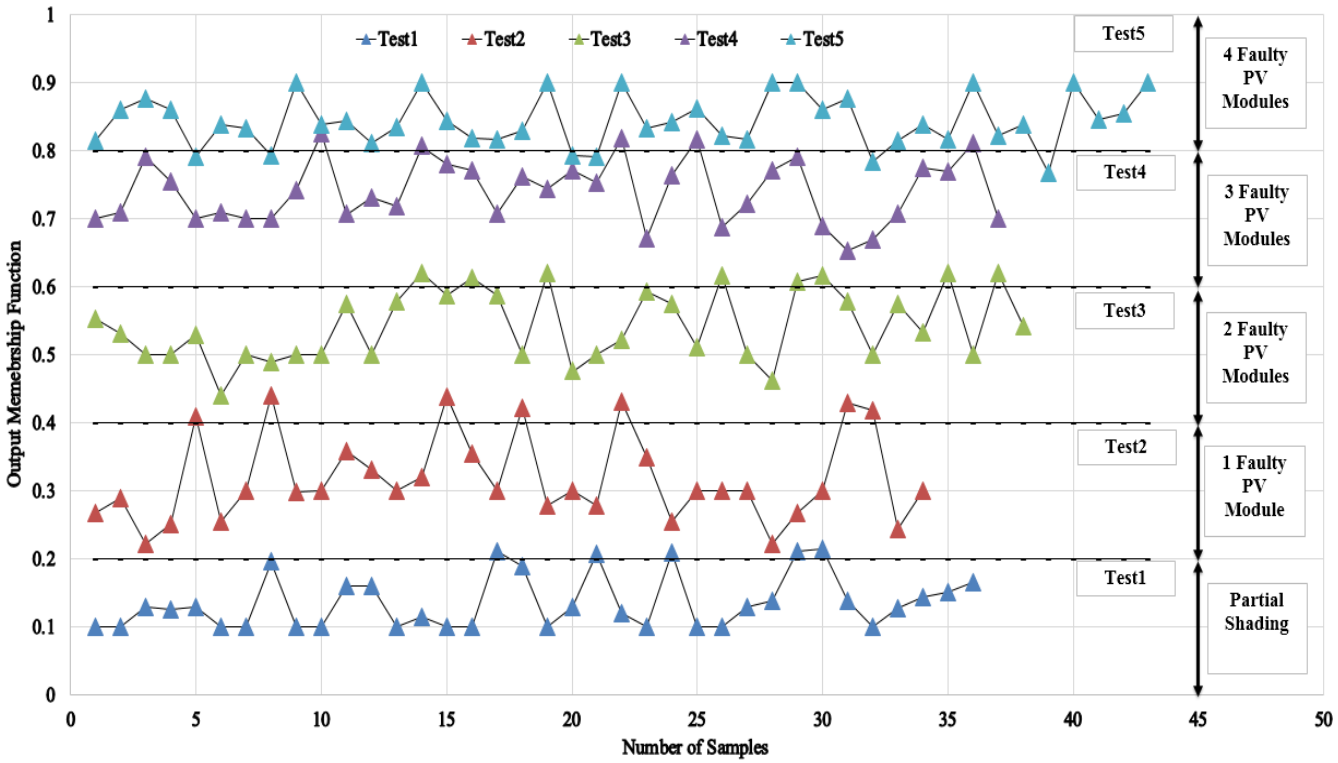

Figure 6.10 Out of region samples processed by the Fuzzy Logic classification system

From Figure 6.10, it is evident that most of the samples are categorized correctly by the fuzzy classifier. For example, before considering the Fuzzy Logic system, the detection accuracy for test 2 is equal to 95.27% while the DA increased up to 99.03% after taking into account the Fuzzy Logic classification system.

This result is due to the detection of the out of region samples. The results for this test is shown in Figure 6.10, only 7 out of 34 processed samples are detected incorrectly, while 27 samples have been detected correctly within an output membership function between 0.2 and 0.4.

Table 6.1 shows number of out of region samples and the detection accuracy for each test separately. The detection accuracy increased up to at least 98.8% after considering the Fuzzy Logic system.

In this section, the evaluation for the PV fault detection algorithm and the Fuzzy Logic system are discussed and evaluated using various experiments. From the obtained results, it is confirmed that the fault detection algorithm is suitable for detecting faulty conditions in PV systems accurately.

C. Evaluating the proposed theoretical curves based on PV array ages:

In this section, the evaluation of the 3rd order polynomial curves modelling are explained using the PV system described in section 6.4. The PV plant is presented in Appendix A, and the PV plant has an accumulative degradation rate of 7.37% (Mahmoud Dhimish, Holmes, Mehrdadi, & Dales, 2017a).

For various experiments, including: normal operation mode and PS, one faulty PV modules and PS, two fault PV modules and PS, and three faulty PV modules and PS, the results are shown in Figure 6.11.

The average detection accuracy of the proposed fault detection limits is approximately equal to 94% comparing to 51% before considering the PV degradation rate. In fact, this experiment assumes that all out of region samples are due to the degradation of the PV plant. However, there are some other factors that might affect the accuracy of the measured data, such as the dirt/dust, humidity fluctuations, wind speed, snow, and partial shading caused by birds, helicopters, and trees.

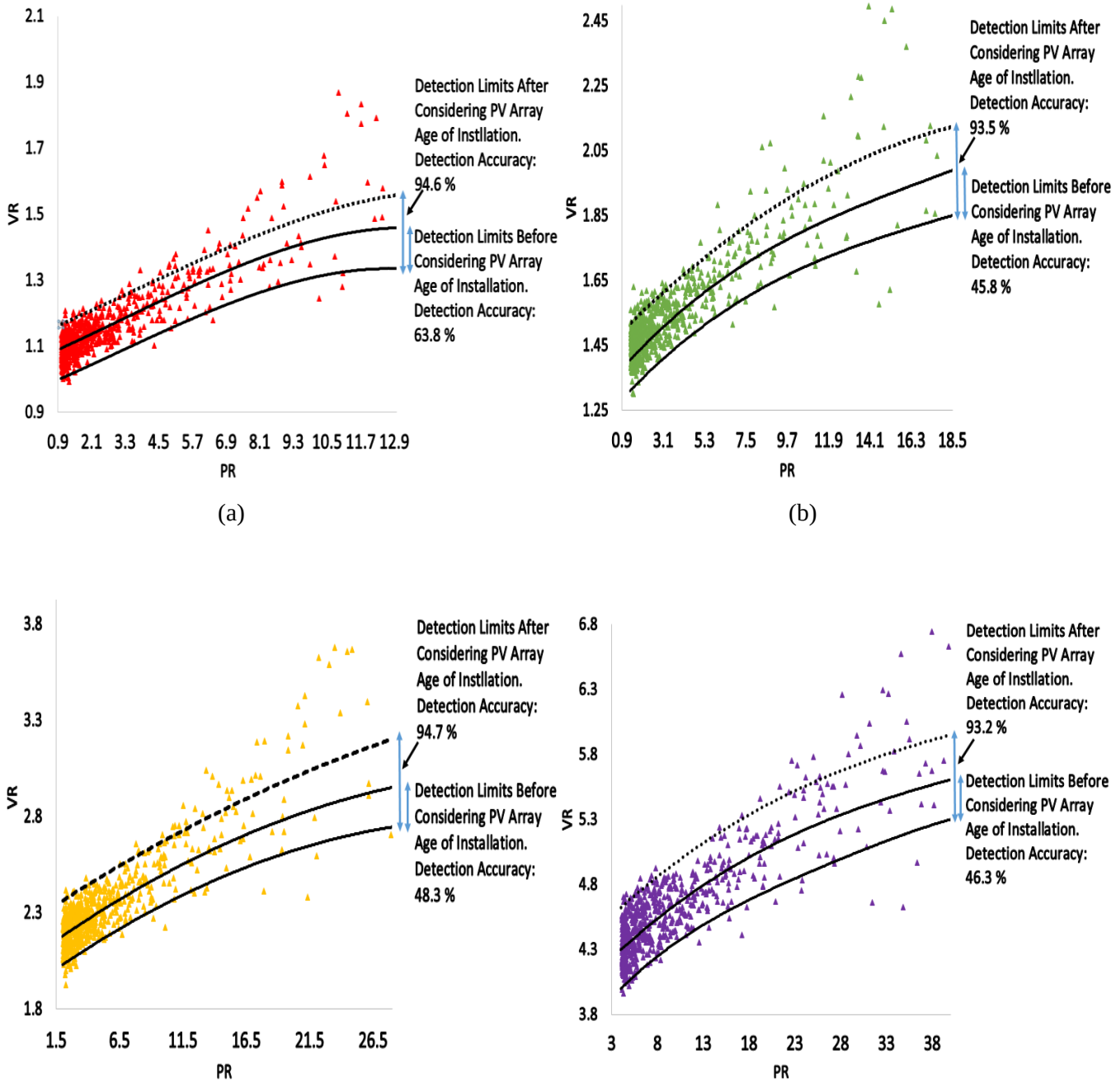

Figure 6.11 Theoretical detection limits vs. measured data before and after considering the age of the PV array. (a) Normal operation mode and partial shading, (b) One faulty PV module and partial shading, (c) Two faulty PV modules and partial shading, (d) Three faulty PV modules and partial shading

6.2 Detecting defective bypass diodes in PV modules using Mamdani Fuzzy Logic system

This section will demonstrate the design of a PV fault detection algorithm which is capable of detecting defective bypass diodes in the PV modules. The algorithm is based on the analysis of three variables: percentage of voltage drop (PVD), percentage of open circuit voltage (POCV), and the percentage of short circuit current (PSCC) (Mahmoud Dhimish, Holmes, Mehrdadi, Dales, & Mather, 2017a).

Mamdani Fuzzy Logic system is used to detect up to 13 different faults associated with the defective bypass diodes in PV modules.

6.2.1 Examined PV module characteristics

The PV modules used in this section are those previously explained in chapter 3. The PV modules comprise three bypass diodes connected in parallel to each PV solar cell string. Figure 6.12a shows the connection of the bypass diodes in the examined PV modules. In addition, Figure 6.12b shows the junction box placed at the back of the PV module.

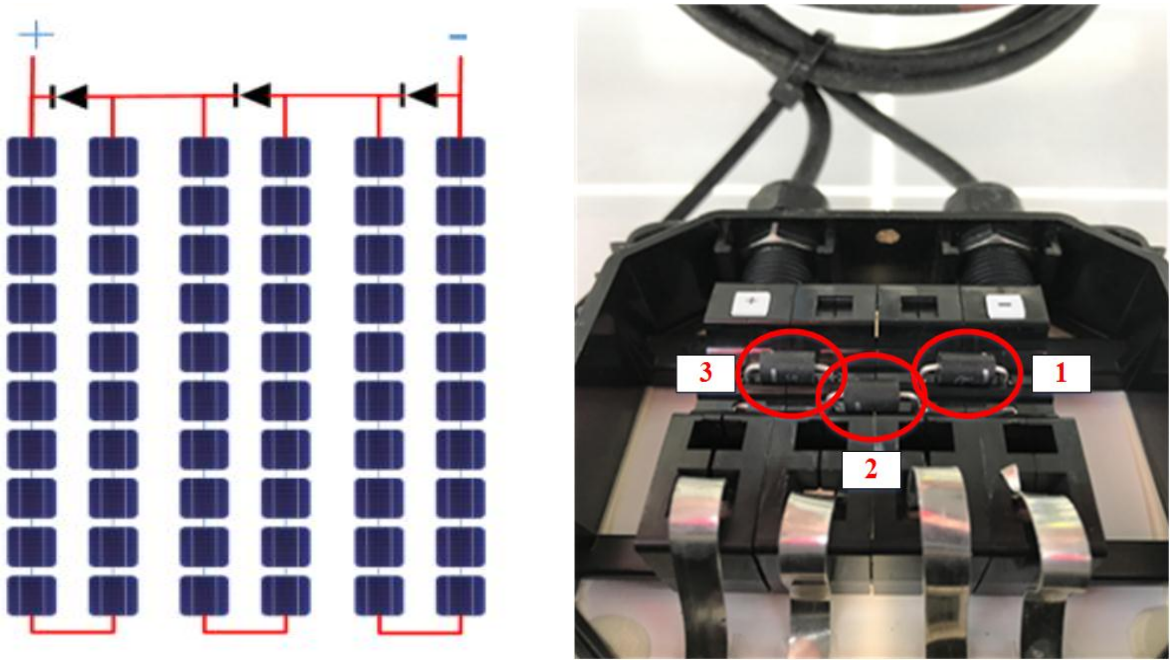

(a) (b)

Figure 6.12 (a) Internal bypass connection for each PV module, (b) Junction box placed at the back of the PV module

6.2.2 Inspection process

The investigation of the temperature variations during partial shading and faulty bypass diodes (bypass diode disconnected from the PV modules) have been captured using i5 FLIR thermal camera. This camera has the following specification:

- Thermal image quality: 100x100 pixels
- Field of view: 21^0 (H) x 21^0(V)
- Thermal sensitivity: 0.5 ^{0}C

The PV module I-V curves are captured using PVA-1000s I-V curve tracer. The I-V curve measurement provides I_{sc}, V_{oc}, I_{mpp}, V_{mpp}, and P_{mpp}. This unit has the following specification:

- Voltage Resolution: 25 mV
- Current Resolution: 2 mA
- Irradiance Accuracy: ±2%, 0 to 1500 W/m^2
- PV Cell Temperature Accuracy: ±2%, -10 to +65 ^{0}C

The i5 FLIR camera and the I-V curve tracer are shown in Figure 2.13.

(a) (b)

Figure 6.13 (a) i5 FLIR camera, (b) PVA-1000s I-V curve tracer

6.2.3 PV I-V curve analysis

In this section, the analysis of the PV I-V curve will be demonstrated using two case studies:

A. I-V curve characteristics under partial shading conditions

The first test will explain the impact of PS conditions on the I-V curve for a standalone PV module. The PV module was covered by an opaque paper in order to examine various PS conditions. Figure 6.14a show the image of the opaque object covering the examined PV module.

Multiple experiments have been conducted under various PS conditions, starting from 10% and ending up with 90%. Three thermal images of the examined PV module under PS conditions (10%, 30%, and 60%) are shown in Figure 6.14. All experiments were performed while there is no defective bypass diodes connected in the tested PV module (Mahmoud Dhimish, Holmes, Mehrdadi, Dales, & Mather, 2017a).

Figure 6.15a and Figure 6.15b show the experiment output for the I-V and P-V curves for all tested PS conditions. As can be seen, while increasing the percentage of shading the V_{oc} of the PV module decreases. However, the I_{sc} remains at the same theoretical threshold 8.18 A.

(a) (b)

Figure 6.14 (a) Real image of a PV module under 20% PS, (b) Real image of a PV module under 60% PS

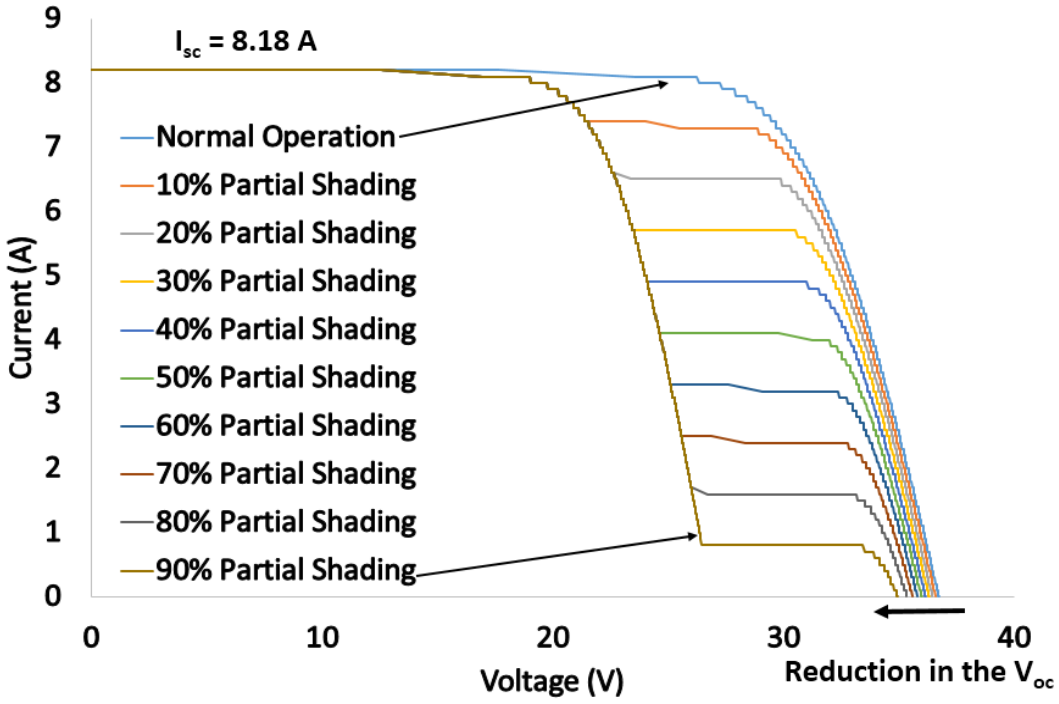

(a)

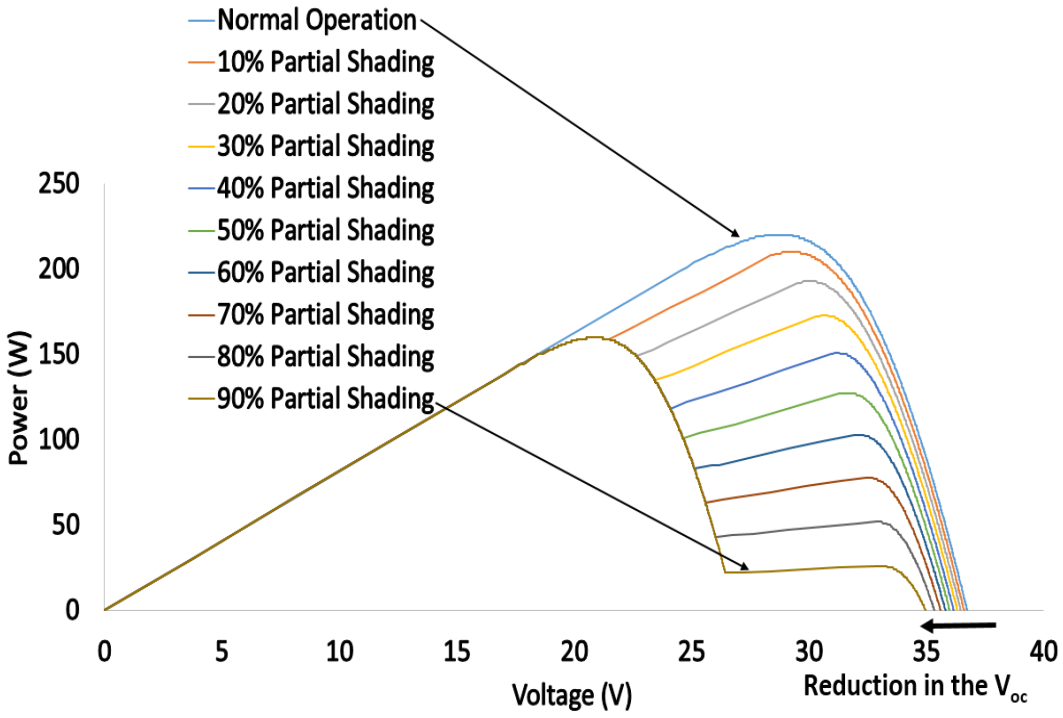

(b)

Figure 6.15 (a) I-V curve characteristics under various PS conditions affecting the PV module, (b) P-V curve characteristics under various PS conditions affecting the PV module

B. I-V curve characteristics under 90% partial shading condition and faulty bypass diodes

This test was experimentally evaluated while disconnecting one, two, and three bypass diodes in the PV module under 90% partial shading condition (worst case scenario). As shown in Figure 6.16a, during 90% partial shading and no disconnection of PV module bypass diodes, the PV module I-V curve started to drop its I_{sc} at 17.5 V; this drop as V_{drop} in the I-V curve.

However, the first drop in the I-V curve while disconnecting one bypass diode is equal to 15 V. Faster drop is associated with 90% partial shading and 2 faulty bypass diodes in the PV module, which is between 10.5 and 17.5 V.

The last case is when all PV module bypass diodes were completely removed during 90% partial shading condition. In this case, the drop in the I_{sc} is obtained at the start of the I-V curve (at 0~2.87 V). This loss in the current will affect the output power of the PV module significantly. The output power obtained in each case scenario is presented as follows:

- No fault in the bypass diodes:
    - P_{mpp} = 159.8 W
- Disconnecting 1 bypass diode:
    - P_{mpp} = 141.5 W
- Disconnecting 2 bypass didoes:
    - P_{mpp} = 104.8 W
- Disconnecting all bypass didoes:
    - P_{mpp} = 18.84 W

While disconnecting the bypass diodes from this PV module during PS conditions, the PV module output power will decrease. This phenomenon occurs due to the impact of the reverse-bias feature of the bypass diodes.

Furthermore, Figure 6.16b shows that while disconnecting one bypass diode from the examined PV module, the temperature rises in the PV string associated with the faulty bypass diode location. The increase of the PV string temperature will decrease the PV output power.

According to Figure 6.16b, the increase of the PV string temperature is equal to:

Increase in the PV string temperature = 18.8 ^{0}C (PV string without bypass diode) – 17 ^{0}C (adjacent PV strings with bypass diodes) = 1.8 ^{0}C

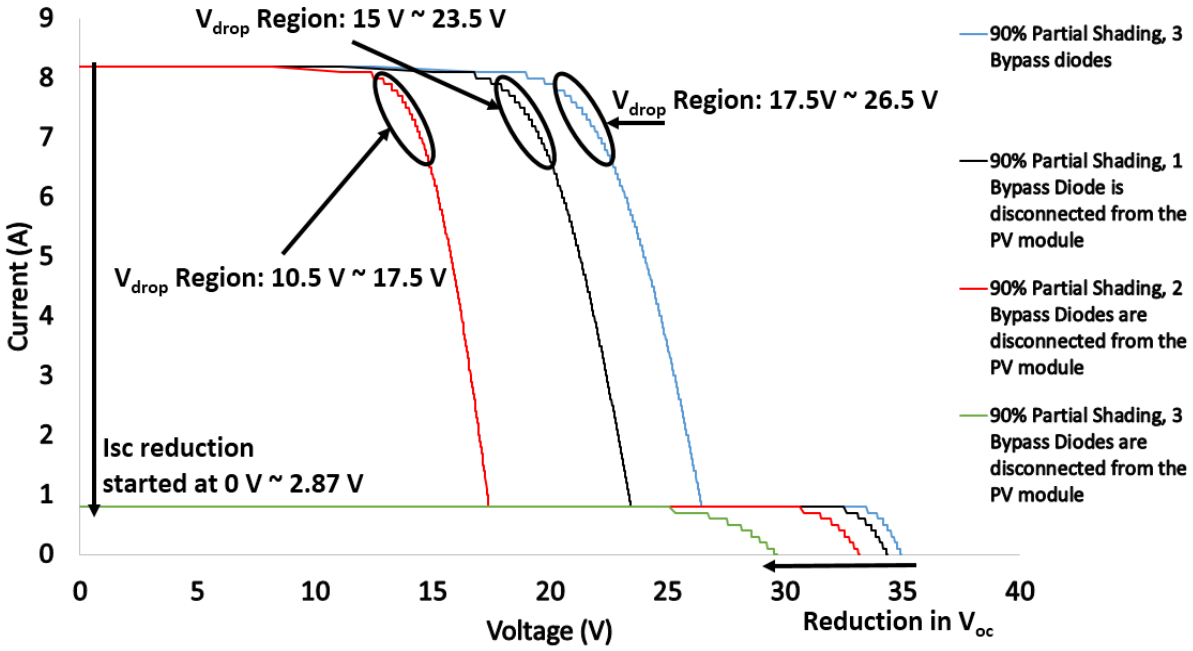

(a)

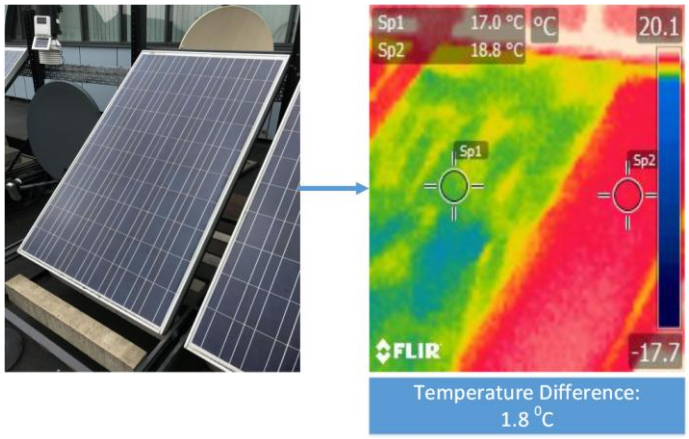

(b)

Figure 6.16 (a) I-V curves under various conditions affecting the examined PV module, (b) Real image and thermography image of the examined PV module while disconnecting one bypass diode from the first PV string

Since the voltage drop (V_{drop}) has been measured during worst case scenario at each I_{sc} level of the examined I-V curves, it has been found that the V_{drop} in each examined case can be classified as the following:

- No fault in the bypass diodes:
    - V_{drop} Region: 17.5 ~ 26.5 V
- Disconnecting 1 bypass diode:
    - V_{drop} Region: 15 ~ 23.5 V
- Disconnecting 2 bypass didoes:
    - V_{drop} Region: 10.5 ~ 17.5 V
- Disconnecting all bypass didoes:
    - V_{drop} Region: 0 ~ 2.87 V

In order to generalize the findings of the V_{drop}, the percentage of V_{mpp} has been compared with the V_{drop} values, which can be formalized as Equation (6.10) by the percentage of voltage drop (PVD).

$$Percentage\ of\ Voltage\ Drop\ (PVD) = \frac{V_{drop}}{V_{mpp}} \times 100 \tag{6.10}$$

The following calculations show the percentage of voltage drop based on (6.10) which is validated using the examined I-V curve shown in Figure 6.16a.

No fault in the bypass diodes:

$$\text{PVD} = \frac{17.5 \sim 26.5}{28.7} \times 100 = 61.0\% \sim 92.3\%$$

Disconnecting 1 bypass diode:

$$\text{PVD} = \frac{15 \sim 23.5}{28.7} \times 100 = 52.2\% \sim 81.9\%$$

Disconnecting 2 bypass didoes:

$$\text{PVD} = \frac{10.5 \sim 17.5}{28.7} \times 100 = 36.5\% \sim 61\%$$

Disconnecting all bypass didoes:

$$\text{PVD} = \frac{0 \sim 2.87}{28.7} \times 100 = 0\% \sim 10\%$$

The regions of the PVD are overlapping. However, in the last region, when disconnecting all bypass diodes from the PV module, the PVD is between 0 and 10%. This region does not overlap with all other regions. Therefore, In order to increase the detection accuracy of the first three case scenarios, the percentage of open voltage circuit (POCV) is used. The POCV is calculated using (6.11).

$$Percentage\ of\ open\ voltage\ circuit\ (POCV) = \frac{Measured\ Voc}{Theoretical\ Voc} \times 100 \qquad (6.11)$$

From the results obtained previously in Figure 6.16a, the POCV for each tested case scenario has been calculated as the following:

No fault in the bypass diode:

$$\text{POCV} = \frac{36.74 \sim 35}{36.74} \times 100 = 100\% \sim 95.3\%$$

Disconnecting 1 bypass diode:

$$\text{POCV} = \frac{36.74 \sim 33.5}{36.74} \times 100 = 100\% \sim 91.2\%$$

Disconnecting 2 bypass diode:

$$\text{POCV} = \frac{36.74 \sim 32.1}{36.74} \times 100 = 100\% \sim 87.3\%$$

Since I_{sc} is another variable which could be used to examine the faulty bypass diodes in PV modules, the percentage of short circuit current (PSCC) has been used to estimate the shading percentage which affects the PV module. PSCC can be calculated using Equation (6.12).

$$Percentage\ of\ Short\ Circuit\ Current\ (PSCC) = \frac{Measured\ Isc}{Theoretical\ Isc} \times 100 \qquad (6.12)$$

The PSCC is equal to 1 in the first 3 cases (no fault in the bypass diodes, disconnecting 1 bypass diode, and disconnecting 2 bypass diodes). However, the PSCC was evaluated using partial shading conditions between 0% up to 90% while disconnecting all bypass diodes in the examined PV module. The PSCC results are shown in Table 6.2, where the I-V curve simulation is presented in Figure 6.17.

The results show that the percentage of PSCC depends on the percentage of shading affecting the PV module. An increase of the PS condition results in a decrease in the PSCC percentage.

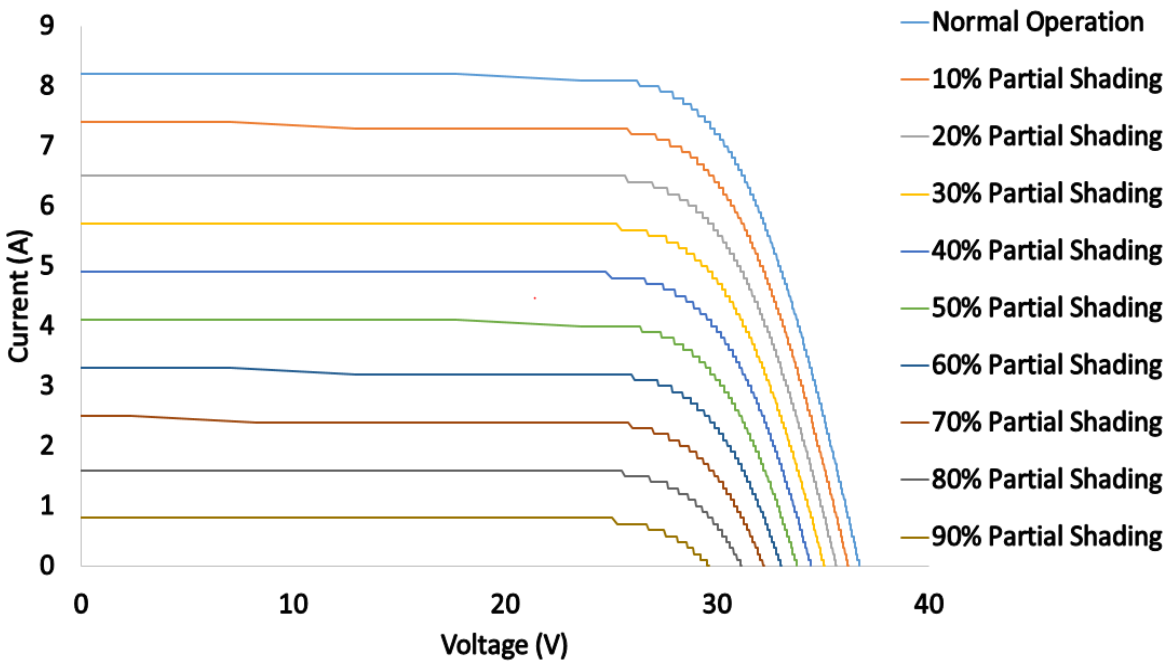

Figure 6.17 I-V curve simulation under various partial shading conditions while disconnecting all bypass diodes from the examined PV module

Table 6.2 PSCC results for the examined PV module while disconnecting all bypass diodes

Shading Percentage %	Measured I_{sc} (A)	PSCC %
Normal Operation	8.18	100
10%	7.37	90
20%	6.55	80
30%	5.73	70
40%	4.91	60
50%	4.09	50
60%	3.28	40
70%	2.46	30
80%	1.64	20
90%	820 mA	10

6.2.4 Proposed PV bypass fault detection Fuzzy Logic system

In this section, the proposed PV bypass diode fault detection system will be presented. The detection system is based on the variations of the I-V curve presented in the previous section (V_{drop}, I-V curve V_{oc}, and I-V curve I_{sc}).

Next, Mamdani Fuzzy Logic system is used to detect the faults in the examined PV module. Subsequently, the fuzzy system is based on three inputs: PVD, POCV, and PSCC. The overall structure of the fault detection systems in shown in Figure 6.18.

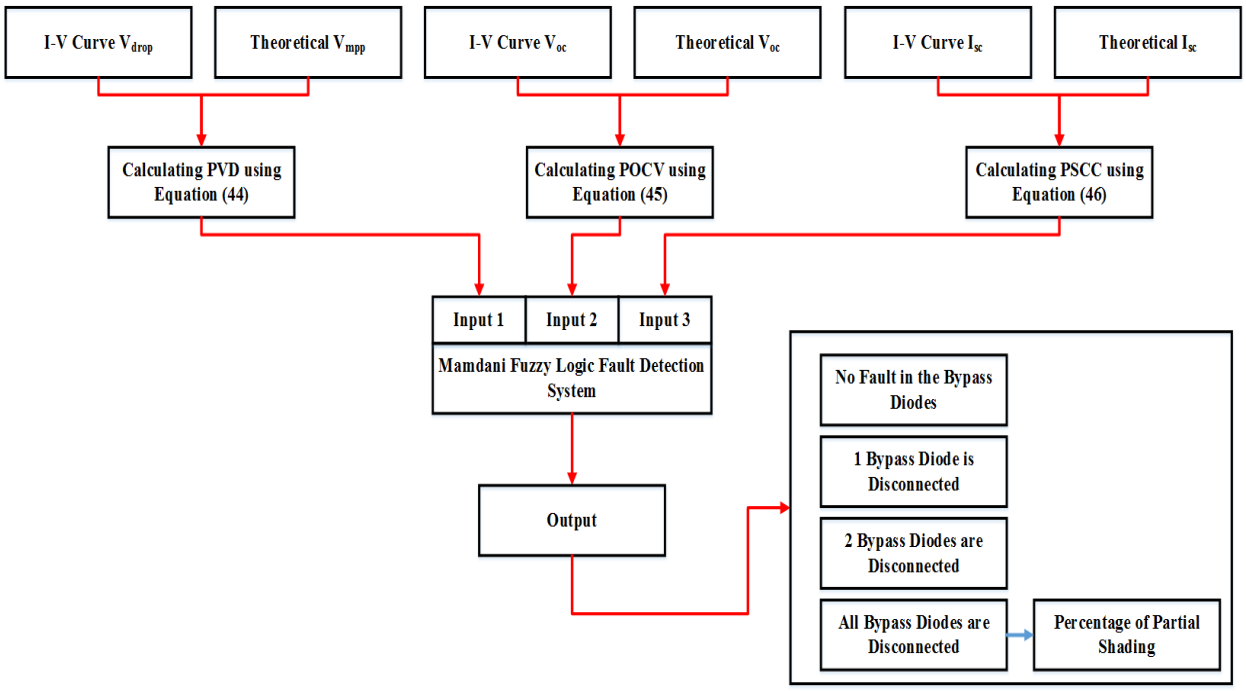

Figure 6.18 Proposed fault detection system using Mamdani Fuzzy Logic system

All inputs are processed by the Fuzzy Logic system based on the membership functions shown in Figure 6.19a, where all the percentages are discussed previously in section 6.2.3.

The output of the Fuzzy Logic system is capable of classifying 13 different types of fault associated with PV bypass diodes and PS conditions. Figure 6.19b illustrates the output membership function used in the Mamdani Fuzzy Logic system. The list of the faults which can be detected by the proposed algorithm is shown in Figure 6.19c (Mahmoud Dhimish, Holmes, Mehrdadi, Dales, & Mather, 2017a).

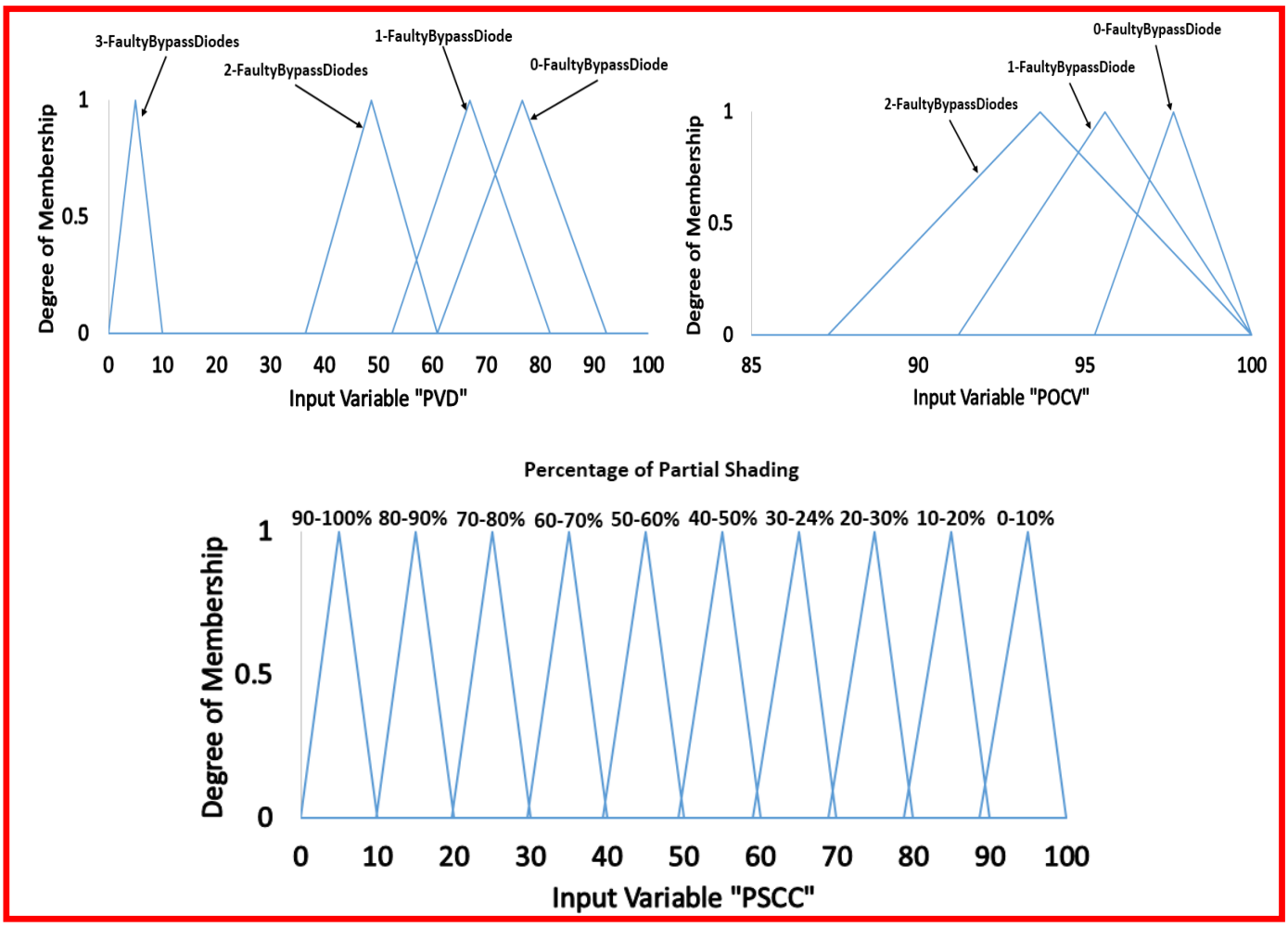

(a)

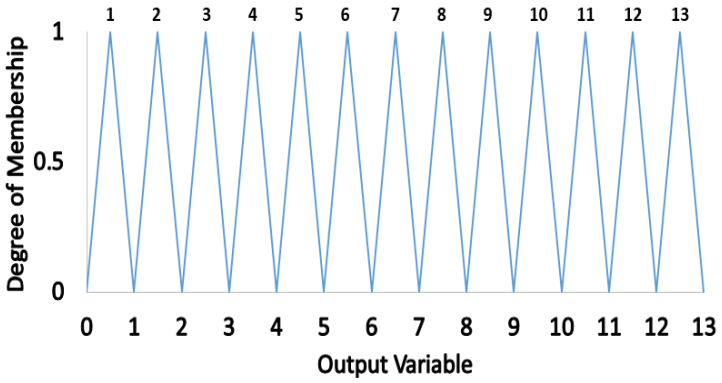

(b)

1 >> No Faults in the Bypass Diodes
2 >> 1 Fualty Bypass Diode
3 >> 2 Faulty Bypass Diodes
4 >> 3 Faulty Bypass Diodes & 0-10% Partial Shading
5 >> 3 Faulty Bypass Diodes & 10-20% Partial Shading
6 >> 3 Faulty Bypass Diodes & 20-30% Partial Shading
7 >> 3 Faulty Bypass Diodes & 30-40% Partial Shading
8 >> 3 Faulty Bypass Diodes & 40-50% Partial Shading
9 >> 3 Faulty Bypass Diodes & 50-60% Partial Shading
10 >> 3 Faulty Bypass Diodes & 60-70% Partial Shading
11 >> 3 Faulty Bypass Diodes & 70-80% Partial Shading
12 >> 3 Faulty Bypass Diodes & 80-90% Partial Shading
13 >> 3 Faulty Bypass Diodes & 90-100% Partial Shading

(c)

Figure 6.19 (a) Input variables for the proposed Fuzzy Logic fault detection system, (b) output variable for the Fuzzy Logic fault detection system, (c) List of faults which can be detected using the PV fault detection system

The Fuzzy Logic system rule are based on: if, and statement. All selected rules in the Fuzzy Logic system can be described by the following:

1. If (PVD is 0-FaultyBypassDiode) and (POCV is 0-FaultyBypassDiode) then (Output is 1) (1)
2. If (PVD is 1-FaultyBypassDiode) and (POCV is 1-FaultyBypassDiode) then (Output is 2) (1)
3. If (PVD is 2-FaultyBypassDiodes) and (POCV is 2-FaultyBypassDiodes) then (Output is 3) (1)
4. If (PVD is 3-FaultyBypassDiodes) and (PSCC is 0-10%PartialShading) then (Output is 4) (1)
5. If (PVD is 3-FaultyBypassDiodes) and (PSCC is 10-20%PartialShading) then (Output is 5) (1)
6. If (PVD is 3-FaultyBypassDiodes) and (PSCC is 20-30%PartialShading) then (Output is 6) (1)
7. If (PVD is 3-FaultyBypassDiodes) and (PSCC is 30-40%PartialShading) then (Output is 7) (1)
8. If (PVD is 3-FaultyBypassDiodes) and (PSCC is 40-50%PartialShading) then (Output is 8) (1)
9. If (PVD is 3-FaultyBypassDiodes) and (PSCC is 50-60%PartialShading) then (Output is 9) (1)
10. If (PVD is 3-FaultyBypassDiodes) and (PSCC is 60-70%PartialShading) then (Output is 10) (1)
11. If (PVD is 3-FaultyBypassDiodes) and (PSCC is 70-80%PartialShading) then (Output is 11) (1)
12. If (PVD is 3-FaultyBypassDiodes) and (PSCC is 80-90%PartialShading) then (Output is 12) (1)
13. If (PVD is 3-FaultyBypassDiodes) and (PSCC is 90-100%PartialShading) then (Output is 13) (1)

The Fuzzy Logic system depends on the variations of the I-V curve, where the simulated results obtained in the previous section depend on a PV module which has specific operating characteristics. Therefore, the main challenge of the Fuzzy Logic system, is whether the rules and classification could be used in other PV modules. In the next section, the fuzzy system will be evaluated using a different PV module, with different operating conditions.

6.2.5 Validation of the proposed PV bypass diode fault detection system using KC130GHT PV module

In this section, the proposed PV bypass diode fault detection based on Mamdani Fuzzy Logic system will be evaluated using KC130GHT PV module. The PV module and its electrical characteristics are shown previously in Figure 5.11.

A. PV module under one defective bypass diode and 35% PS condition

This test was evaluated when the PV module has one defective bypass diode (one bypass diode was removed from the PV module). V_{drop}, V_{oc}, and I_{sc} of the PV module are shown in Figure 6.20.

The percentage PVD, POCV, PSCC are equal to 58.52%, 99.08% and 100% respectively. Next, these percentages are processed by the Fuzzy Logic system. As shown in Figure 6.20, the output of the fuzzy system is equal to 1.91, which is between the regions "1-2". This region indicates that there is one defective bypass diode in the PV module. The classifications of all regions are previously described in Figure 6.19c.

In conclusion, this test was performed by the Fuzzy Logic, and it has successfully detected the defective bypass diode in the PV module.

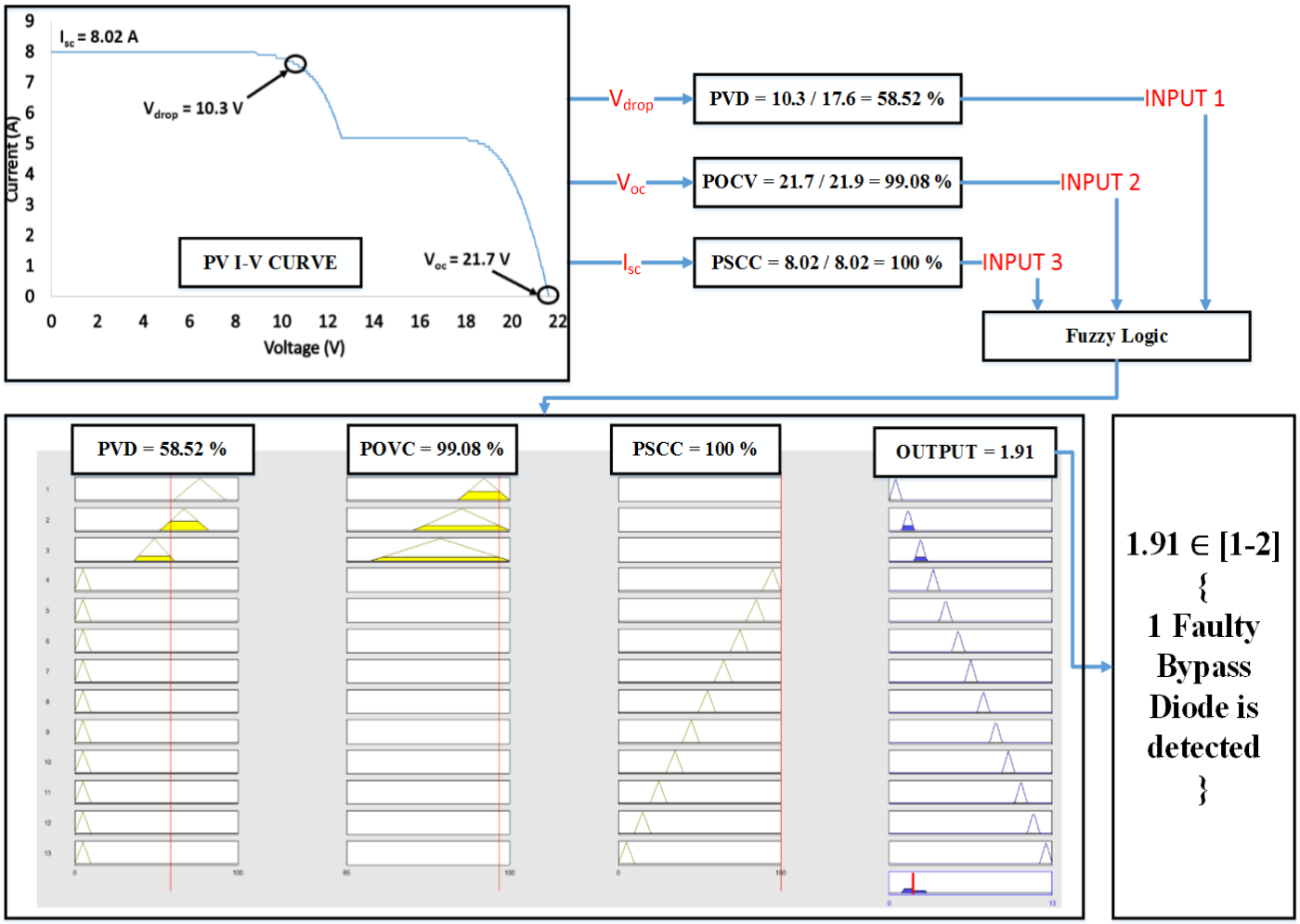

Figure 6.20 Output results for 1 faulty bypass diode and 35% PS condition

B. PV module under three defective bypass diodes and 65% PS condition

The second test was performed when the PV module has three defective bypass diodes (all bypass diodes have been removed from the PV module). This test was also evaluated while covering 65% of the PV module using an opaque paper.

The output performance of the PV module parameters is shown in Figure 2.21. The theoretical I_{sc} dropped down to 2.81A after 0.3V. The percentages of PVD, POCV and PSCC are equal to 1.70%, 91.32%, and 35.04%.

The output of the fuzzy system is equal to 9.5, which is between the regions "9-10". This region indicates that there are three faulty bypass diodes and 60-70% partial shading affects the PV module.

This test also confirms the ability of the proposed Fuzzy Logic system to detect defective bypass diodes in the PV module.

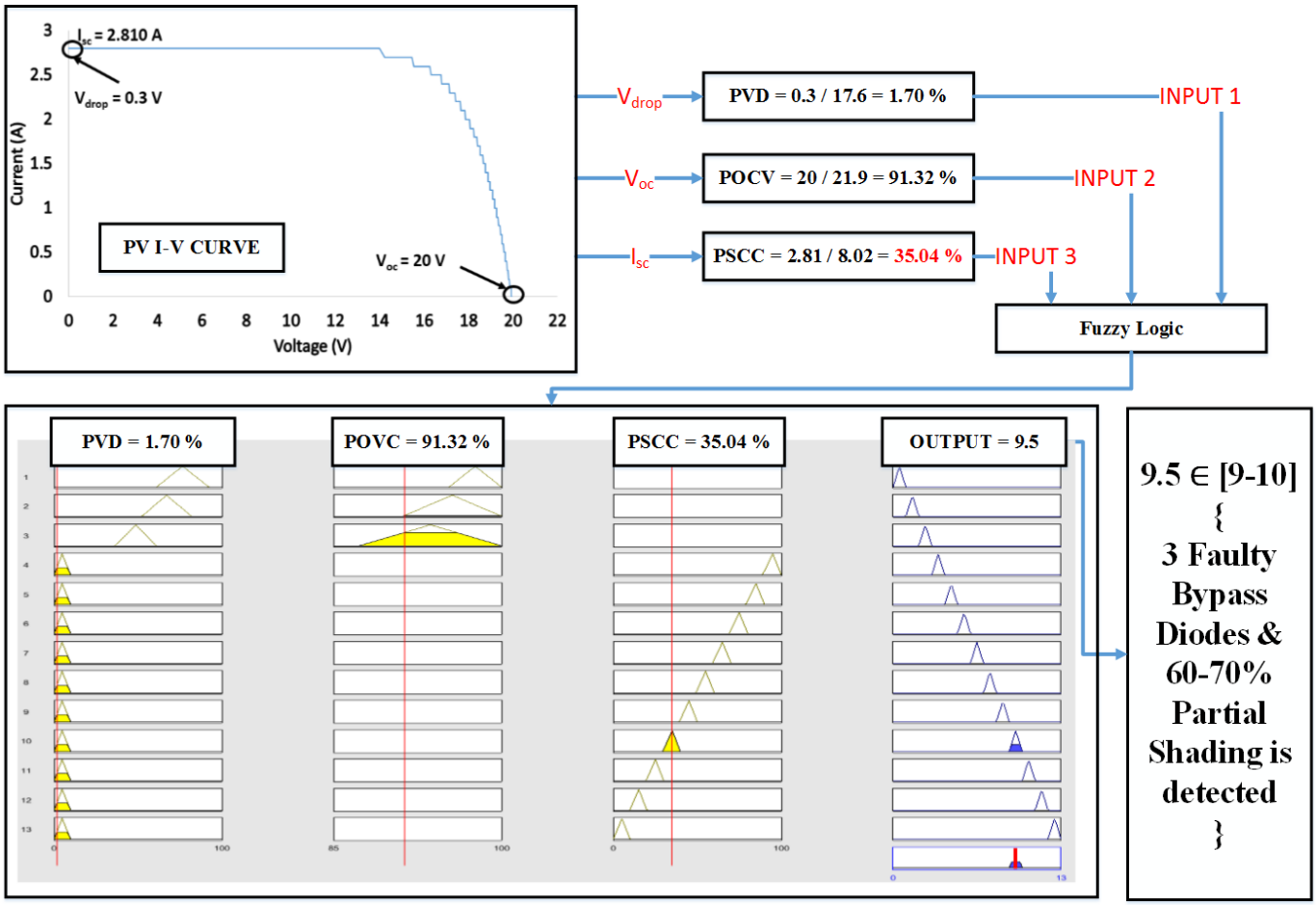

Figure 6.21 Output results for 3 faulty bypass diodes & 60-70% partial shading "case scenario 2"

6.3 Comparing Mamdani Sugeno Fuzzy Logic and RBF ANN networks for PV fault detection

In the previous sections (sections 6.1 and 6.2), Mamdani Fuzzy Logic system based on the min-max membership functions was used to detect possible faults in PV plants. However, in this section, the detection of PV faults will be evaluated using various AI techniques such as Mamdani Fuzzy Logic, Sugeno Fuzzy Logic, and four different radial basis function (RBF) ANN networks.

6.3.1 Examined PV system

The PV system architecture used to evaluate the performance of the AI techniques consists of a PV string which comprise five PV modules connected in series. The PV system overall design is shown in Figure 6.22 (Mahmoud Dhimish, Holmes, Mehrdadi, & Dales, 2018).

The PV module electrical characteristics are previously shown in Table 3.1. The MPPT unit is already discussed in Appendix A.

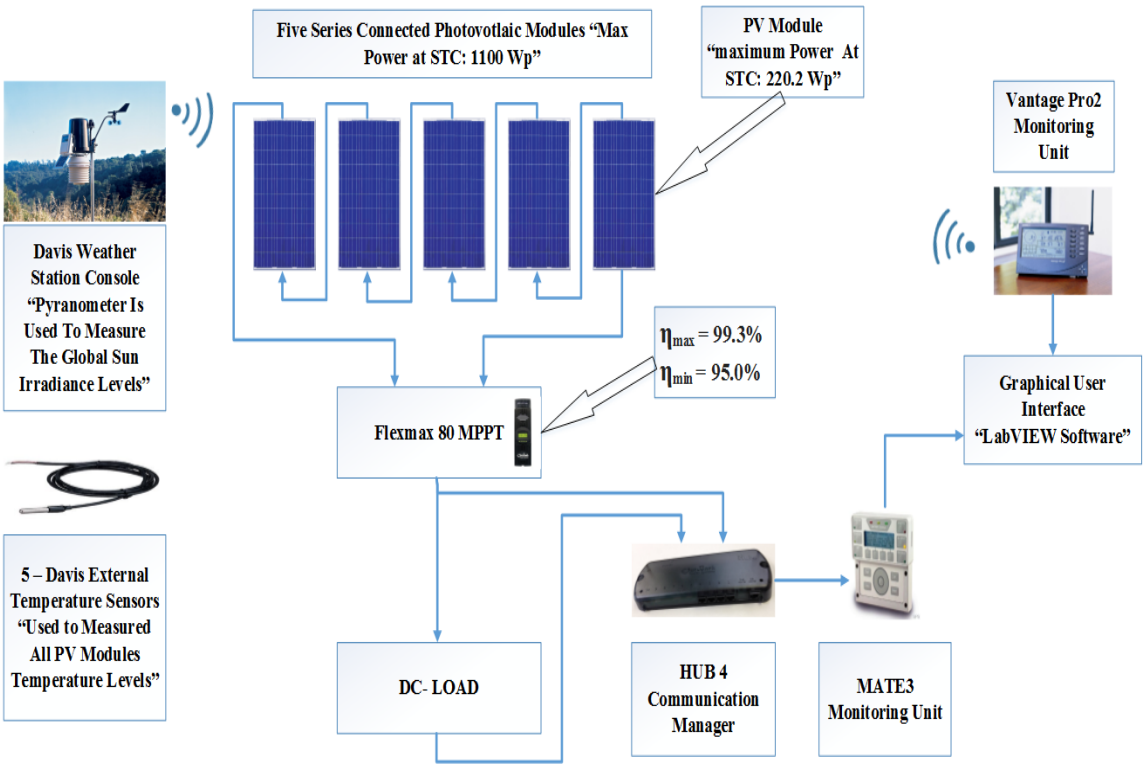

Figure 6.22 PV system used to evaluate the performance of various AI techniques

6.3.2 Overall PV fault detection algorithm

The implementation of the fault detection algorithm is based on power and voltage ratios, which are calculated using Equations (6.1) and (6.2) respectively.

Since the internal sensors of the MPPT have a conversion error rate of 5% as shown in Figure 6.22, the power ratios are calculated at 5% error tolerance of the theoretical power which presents the maximum error conditions for the tested PV system. Therefore, the maximum and minimum power and voltage ratios are expressed by the following formulas which contains the tolerance rate of the MPPT unit:

$$\text{PR min} = \frac{P_{theoretical}}{P_{measured}} \tag{6.13}$$

$$\text{PR max} = \frac{P_{theoretical}}{P_{measured} \times \text{MPPT Tolerance Rate}} \tag{6.14}$$

$$\text{VR min} = \frac{V_{theoretical}}{V_{measured}} \tag{6.15}$$

$$\text{VR max} = \frac{V_{theoretical}}{V_{measured} \times \text{MPPT Tolerance Rate}} \tag{6.16}$$

The normal operation mode region of the examined PV plant at STC is shown as case 1 in Figure 6.23, the values of the PR are calculated using Equations (6.13) and (6.14) as follows:

$$\text{Normal Operation Mode, PR min} = \frac{P_{theoretical}}{P_{measured}} = \frac{1100}{1100} = 1$$

$$\text{Normal Operation Mode, PR max} = \frac{P_{theoretical}}{P_{measured} \times \text{MPPT Tolerance Rate}} = \frac{1100}{1100 \times 95\%} = 1.053$$

As can be noticed from case 2 in Figure 6.23, the maximum partial shading condition detected by the irradiance sensor is equal to 97.3%, therefore, the maximum PR is calculated as the following:

$$\text{Fault Detection Algorithm Maximum PR} = \frac{P_{theoretical}}{P_{measured} \times \text{MPPT Tolerance Rate}} = \frac{1100}{23.66 \times 95\%} \approx 50$$

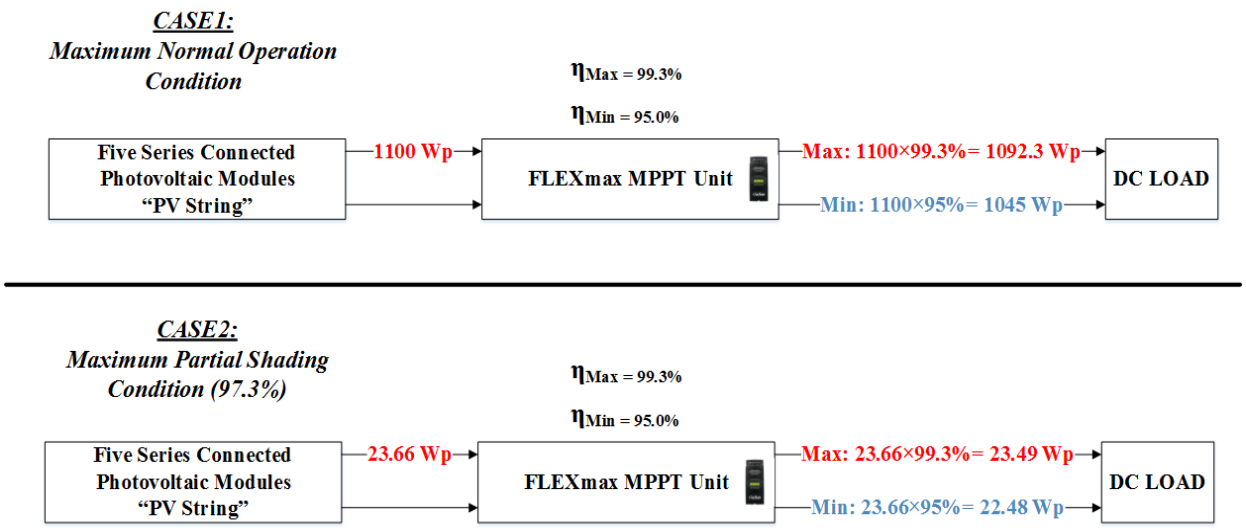

Figure 6.23 DC side numerical calculations at maximum and minimum operating points

The value of the maximum PR is important because if the PR is greater than 50, then the fault detection algorithm can specify whether a fault occurred in the MPPT unit or there is a complete disconnection of a PV string from the entire PV system. In order to detect which type of fault occurred when PR > 50, the value of the voltage ratio has been considered:

1. If VR ≥ 0, then a faulty PV string is detected
2. If VR = 0, then a faulty MPPT unit is detected

Furthermore, if the value of the PR does not lie within the normal operation mode region and it is not higher than the PR max threshold (PR ≥ 50), then the value of the PR and VR is passed to the second part of the fault detection algorithm which consists of two different machine learning techniques as shown in Figure 6.24.

The first technique is the artificial neural network (ANN). In order to select the most suitable ANN model structure, four different ANN models have been developed:

- 2 Inputs, 5 outputs using 1 hidden layers
- 2 Inputs, 5 outputs using 2 hidden layers
- 2 Inputs, 9 outputs using 1 hidden layers
- 2 Inputs, 9 outputs using 2 hidden layers

An illustration on the selection of the variables and ANN model structure is covered in the next sub section (7.3.3).

The second machine learning technique used to detect faults in the PV system is the Fuzzy Logic. Two different Fuzzy Logic systems have been implemented:

- Mamdani-type Fuzzy Logic system interface
- Sugeno-type Fuzzy Logic system interface

Table 6.3 Shows the types of the fault which can be detected using both proposed machine learning techniques.

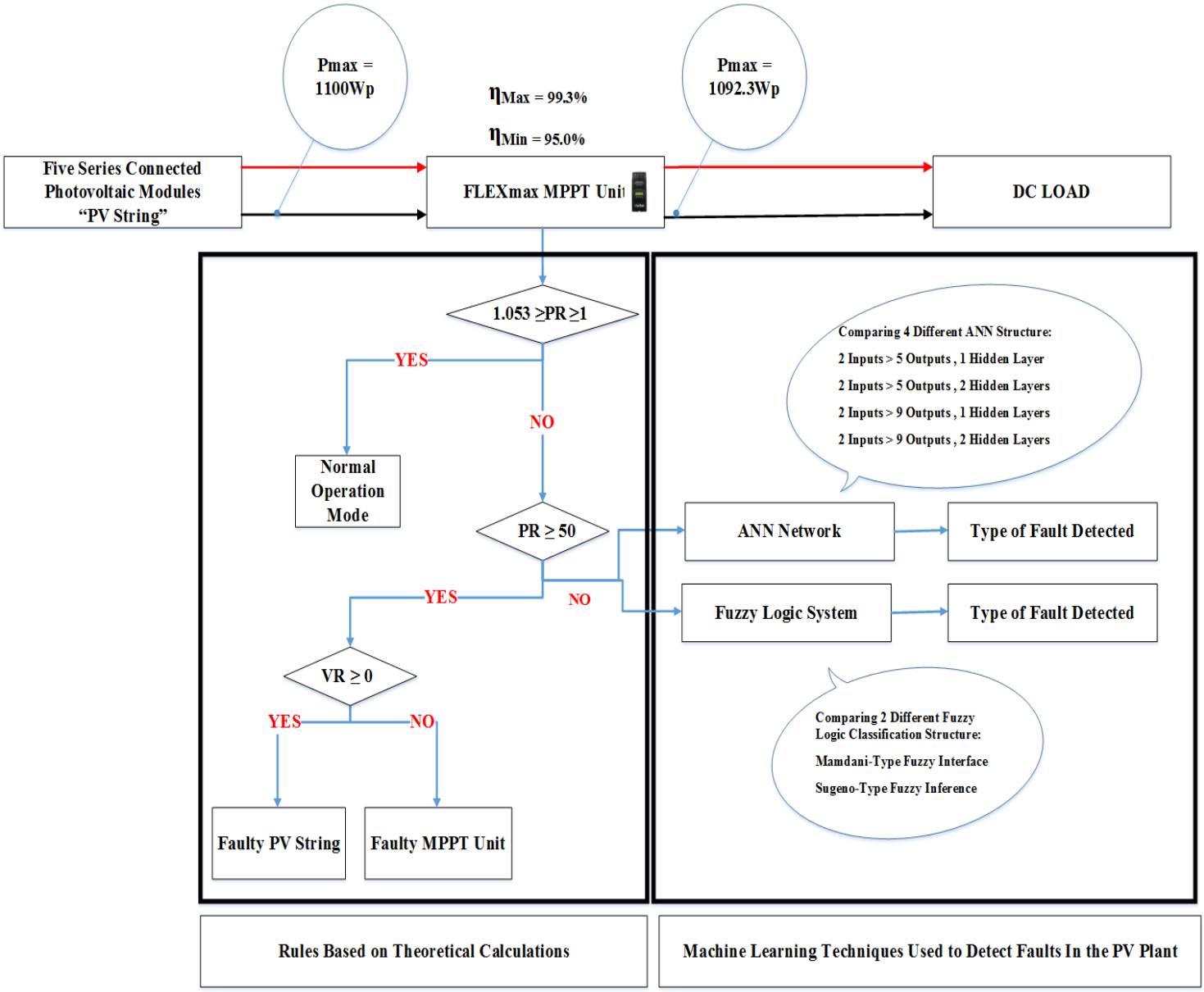

Figure 6.24 Detailed PV fault detection approach

Table 6.3 Various type of faults detected by the proposed machine learning techniques

Type of Fault	Symbol
Normal operation and PS affects the PV system	F1
One faulty PV module	F2
Two faulty PV modules	F3
Three faulty PV modules	F4
Four faulty PV modules	F5
One faulty PV module and PS affects the PV system	F6
Two faulty PV modules and PS affects the PV system	F7
Three faulty PV modules and PS affects the PV system	F8
Four faulty PV modules and PS affects the PV system	F9
Faulty PV string	F10
Faulty MPPT unit	F11

6.3.3 Implementation of ANN networks

The main objective of the ANN model is to detect PV faults. The ANN model has been developed as follows:

- Selection of input and output variables
- Data set normalization
- Selection of network structure
- Network training
- Network test

The input parameters used to configure all tested ANN models are VR and PR ratios. The data set (input variables) are normalized within the range of -1 and +1 using Equation (6.17).

$$y = \frac{(y_{max} - y_{min})(x - x_{min})}{(x_{max} - x_{min})} + y_{min} \quad (6.17)$$

where $x_{min-max} \in \{x_{min}, x_{max}\}$, $y_{min-max} \in \{y_{min}, y_{max}\}$ and x is the original data value and y is the corresponding normalized value with $y_{min} = -1$ and $y_{max} = +1$.

In order to select the most efficient architecture for the ANN model, a comparison between four different ANN models has been performed where the structure of all tested ANN networks is the Radial Basis Function (RBF) as shown in Figure 6.25.

ANN models A and B are using 2 inputs (voltage and power ratio) and five outputs, where the hidden layers are equal to one and two respectively. The purpose of increasing the hidden layers is to increase the computational performance of the ANN network, thus increasing the detection accuracy (DA) of the ANN model. The faults are illustrated in Table 6.3.

From the research conducted using several days' measurements (will be described in section 6.3.5), the comparison between model A and model B shows that both models have a low detection accuracy where the maximum achieved detection accuracy is equal to 77.7%. Therefore, this challenge was solved by adding new types of faults for the ANN network that allow the ANN model to detect faulty PV modules only (No PS on the entire PV plant).

ANN models C and D are using 2 inputs (voltage, and power ratio) and nine outputs, where the hidden layers are equal to one and two respectively. The faults which can be detected using both ANN models presented in Table 6.3.

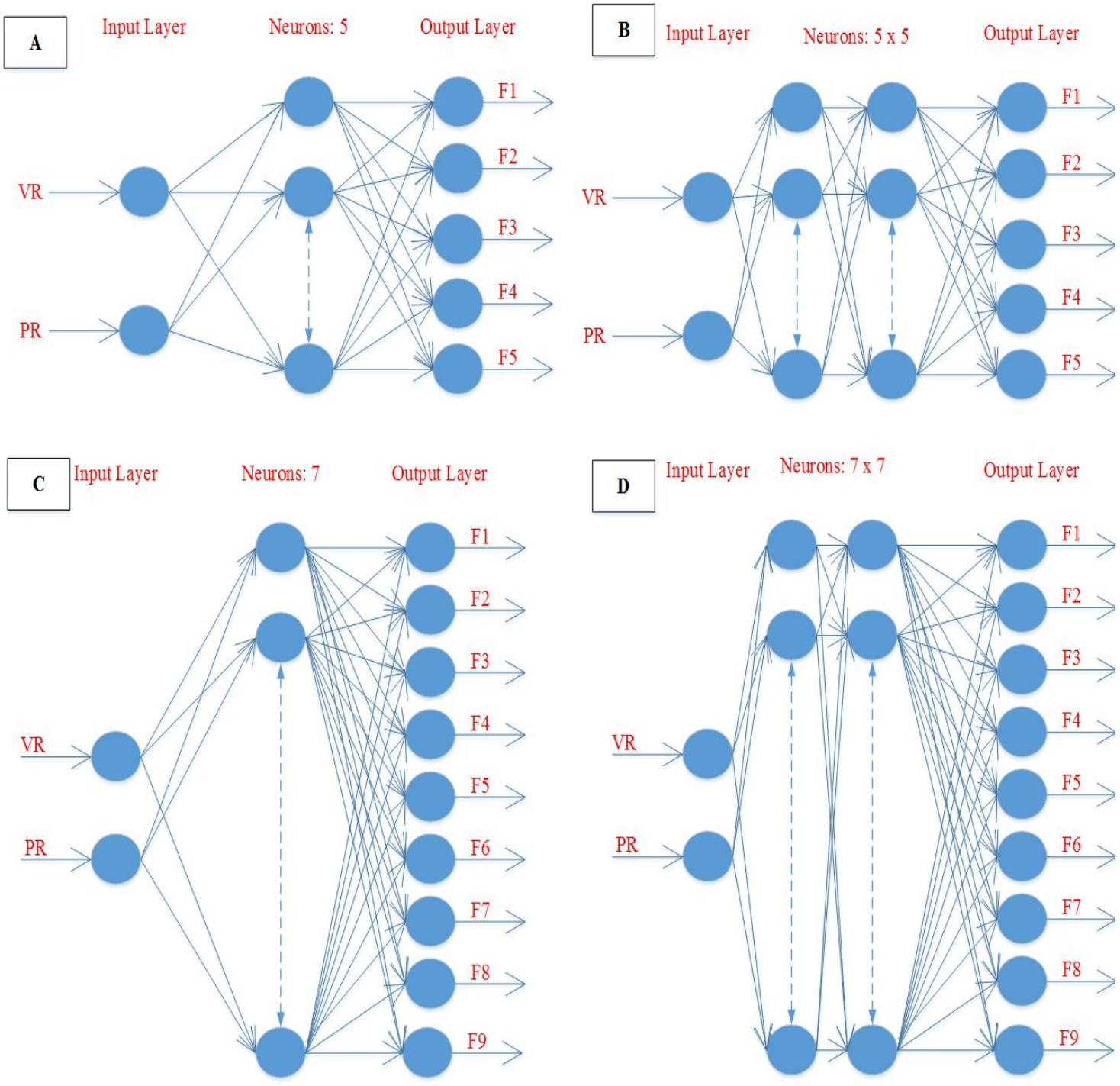

Figure 6.25 Adopted ANN networks. (A) 2 Inputs, 5 outputs using 1 hidden layer, (B) 2 Inputs, 5 outputs using 2 hidden layers, (C) 2 Inputs, 9 outputs using 1 hidden layer, (D) 2 Inputs, 9 outputs using 2 hidden layers

In this section, the data sets have been recorded from the experimental setup shown in Figure 6.22. The data set used to train, validate, and test the ANN networks contains 6480 measurements logged in 9 days (each day consists of 720 sample) as shown in Figure 6.26.

During the experiment, the PV modules' temperature is between 15.3 – 16.7 ºC. The values of the voltage ratio and power ratio have been logged. Each day has a different fault applied to the PV systems which can be simplified by the following:

- Day 1: Partial shading conditions affecting the PV system
- Day 2: One PV module has been disconnected from the PV system
- Day 3: Two PV modules have been disconnected from the PV system
- Day 4: Three PV modules have been disconnected from the PV system
- Day 5: Four PV modules have been disconnected from the PV system
- Day 6: One PV module has been disconnected and PS applied to all other PV modules
- Day 7: Two PV modules have been disconnected and PS applied to all other PV modules
- Day 8: Three PV modules have been disconnected and PS applied to all other PV modules
- Day 9: Four PV modules have been disconnected and PS applied to all only existing PV module

The obtained measurements are divided into three subsets:

1. 70% of the data are used to train the ANN networks
2. 10% of samples are used to validate the ANN network. This data set is not used in the training process
3. 20% of samples are used to test the actual ANN network detection accuracy

The implementation of the ANN network has been developed using MATLAB/Simulink software. ALL results obtained from the ANN networks will be discussed in the next section. The maximum obtained detection accuracy among all tested ANN models is equal to 92.1%. This result is achieved using the last ANN network which consists of 2 inputs, 9 outputs using 2 hidden layers.

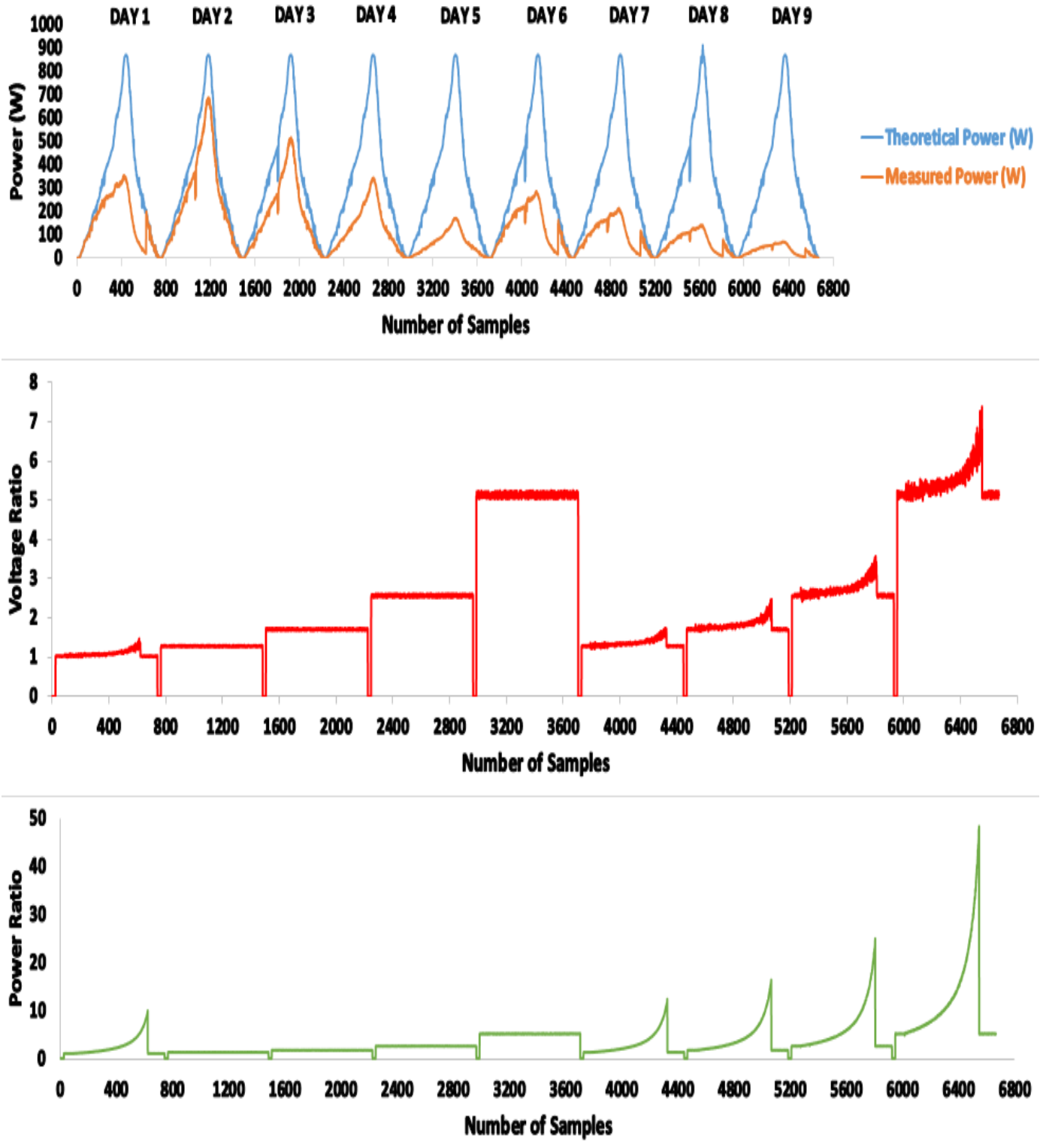

Figure 6.26 Dataset used to train and validate the ANN networks

6.3.4 Implementation of Fuzzy Logic detection system

The second machine learning technique used to detect faults in the PV system is the Fuzzy Logic. In order to select the most efficient model for the Fuzzy Logic system fault detection interface, a comparison between two fuzzy models widely utilized for the classification of faults has been performed: Mamdani Fuzzy Logic and Sugeno type fuzzy system (Mahmoud Dhimish et al., 2018).

Mamdani Fuzzy Logic systems are commonly suited to human input interface. However, the Sugeno fuzzy systems are well established using a linear weighted mathematical expressions. The main advantages for both Fuzzy Logic systems are illustrated by the following:

- Sugeno:
    - Computationally efficient
    - Works with linear techniques
    - It works well with optimization methods and adaptive techniques
- Mamdani:
    - It is intuitive
    - It has widespread acceptance
    - It is suited to human input systems interface

Both implemented Fuzzy Logic systems are shown in Figure 6.27. The voltage, and power ratio is used as input variables for the Fuzzy Logic classification system. The VR and PR regions are illustrated in Table 6.4. As can be seen, ten different regions have been selected, where region 1 is the low partial shading (PS) condition. Whereas, region 4 is used for a faulty PV module with high PS condition (50% ~ 97.3% PS). The minimum and maximum limits for each region of the voltage ratio and power ratio are also shown in Table 6.4, the defuzzification process for the input rules is the centroid type.

All measurements for the theoretical voltage and power ratios have been taken from a MATLAB/Simulink model which is designed the same as the examined PV system presented in Figure 6.22 with the consideration of all PV parameters.

There is a difference in the implementation of the ANN and Fuzzy Logic systems with respect to analysis of acquired data from the sensors (i.e. irradiance sensor). To train the ANN networks for detecting PV faults, it is necessary to classify the measured data. For example, the partial shading conditions samples shown in Figure 6.26 are not categorized as low or high partial shading regions. Thus, it is not applicable to divide the partial shading into two regions. Whereas, in a Fuzzy Logic system, it is applicable to differentiate between these regions (high and low partial shading regions) which are used in a set of rules incorporated within the fuzzy inference system as shown in Figure 6.27.

Table 6.4 Fuzzy Logic input regions

Scenario	Partial Shading %	Min Voltage (V)	Max Voltage (V)	Min Power (W)	Max Power (W)	Fuzzy Classification System Region
Partial Shading (PS)	0 - 49%	1	1.2	1	2.4	1
	50 - 97.3%	1.1	1.4	2.1	28	2
Faulty PV Module and PS	0 - 49%	1.26	1.5	1.3	3	3
	50 - 97.3%	1.34	1.7	2.7	35	4
2 Faulty PV Module and PS	0 - 49%	1.67	1.95	1.8	4	5
	50 - 97.3%	1.76	2.26	3.5	47	6
3 Faulty PV Module and PS	0 - 49%	2.52	2.93	2.5	5.9	7
	50 - 97.3%	2.65	3.4	5.3	70	8
4 Faulty PV Module and PS	0 - 49%	5	5.9	5	12	9
	50 - 97.3%	5.3	6.8	10.6	141	10

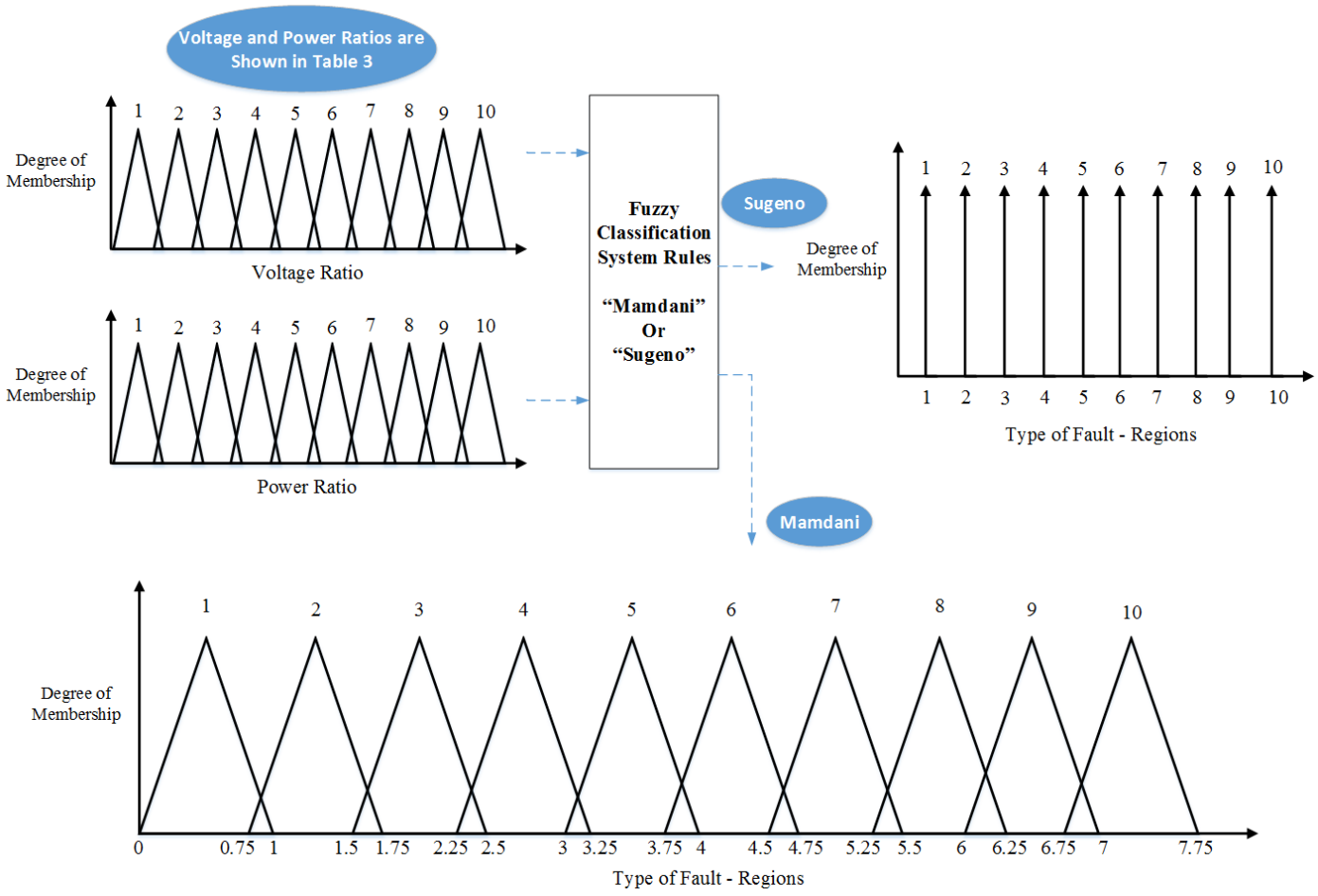

Figure 6.27 Adopted Sugeno and Mamdani Fuzzy Logic systems

After identifying the input variables VR and PR regions, it is required to set the rules for the Fuzzy Logic system interface. As shown in Figure 6.27, Mamdani Fuzzy Logic system consists of ten different membership functions (MF) which are described by the following:

- MF1: Low PS affecting the PV system
- MF2: High PS affecting the PV system
- MF3: One faulty PV module and low PS affecting the PV system
- MF4: One faulty PV module and high PS affecting the PV system
- MF5: Two faulty PV modules and low PS affecting the PV system
- MF6: Two faulty PV modules and high PS affecting the PV system
- MF7: Three faulty PV modules and low PS affecting the PV system
- MF8: Three faulty PV modules and high PS affecting the PV system
- MF9: Four faulty PV modules and low PS affecting the PV system
- MF10: Four faulty PV modules and high PS affecting the PV system

The Mamdani based system architecture is using the Max-Min composition technique with a centroid type defuzzification process.

Similarly, the Fuzzy Logic rules obtained for the Sugeno type Fuzzy Logic interface are equal to 10 as shown in Figure 6.27. Each rule presents the same rule as described in the Mamdani Fuzzy Logic system. The Sugeno based system architecture is using the Max-Min composition technique with a centroid type defuzzification process.

It is worth pointing out that a high number of Fuzzy Logic rules ensure both completeness and appropriate resolution of the fault detection accuracy. However, a high number of fuzzy rules may lead to an over parameterized system, thus reducing generalization capability and accuracy of detection of the type of the fault occurring in the examined PV system.

Therefore, the number of fuzzy rules depends on the number of input variables, system performance, the execution time and the membership functions. In this section, ten Fuzzy Logic rules were decided upon according to a sensitivity analysis made by varying the number and type of the rule. A satisfactory level of performance was obtained after a tuning process, i.e. starting from faulty PV module only and progressively modifying the fuzzy system to detect all possible faults that may occur in the PV plant according to the faults types listed in Table 6.3.

Both Fuzzy Logic systems rules are based on: if-then statement. The fuzzy rules are listed as the follows:

- 1. If (Voltage-Ratio is 1) and (Power-Ratio is 1) then (Type-of-Fault-Detected is 1) (1)
- 2. If (Voltage-Ratio is 2) and (Power-Ratio is 2) then (Type-of-Fault-Detected is 2) (1)
- 3. If (Voltage-Ratio is 3) and (Power-Ratio is 3) then (Type-of-Fault-Detected is 3) (1)
- 4. If (Voltage-Ratio is 4) and (Power-Ratio is 4) then (Type-of-Fault-Detected is 4) (1)
- 5. If (Voltage-Ratio is 5) and (Power-Ratio is 5) then (Type-of-Fault-Detected is 5) (1)
- 6. If (Voltage-Ratio is 6) and (Power-Ratio is 6) then (Type-of-Fault-Detected is 6) (1)
- 7. If (Voltage-Ratio is 7) and (Power-Ratio is 7) then (Type-of-Fault-Detected is 7) (1)
- 8. If (Voltage-Ratio is 8) and (Power-Ratio is 8) then (Type-of-Fault-Detected is 8) (1)
- 9. If (Voltage-Ratio is 9) and (Power-Ratio is 9) then (Type-of-Fault-Detected is 9) (1)
- 10. If (Voltage-Ratio is 10) and (Power-Ratio is 10) then (Type-of-Fault-Detected is 10) (1)

The output surfaces for Mamdani and Sugeno systems are plotted and represented by a 3D curves as shown in Figures 6.28a and 6.28b respectively. Where the x-axis presents the PR ratio, y-axis presents the VR ratio, and the fault detection output is on the z-axis.

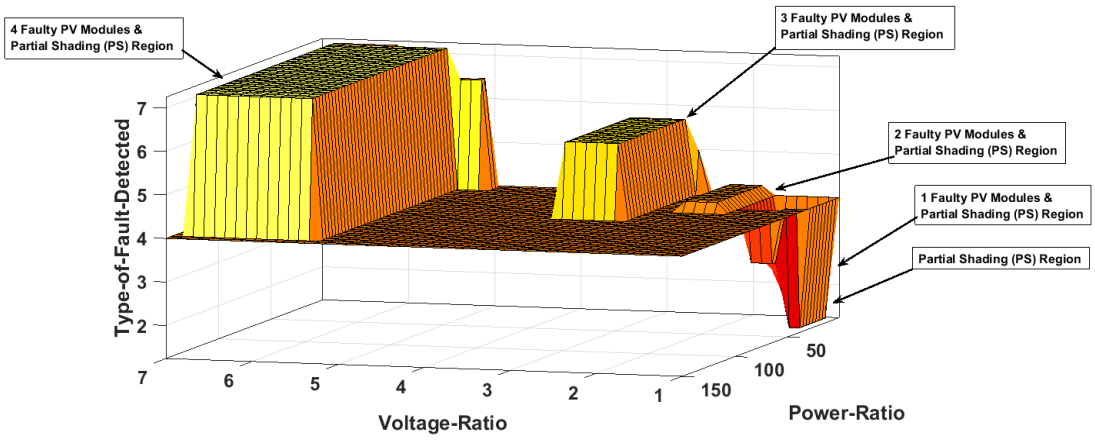

(a)

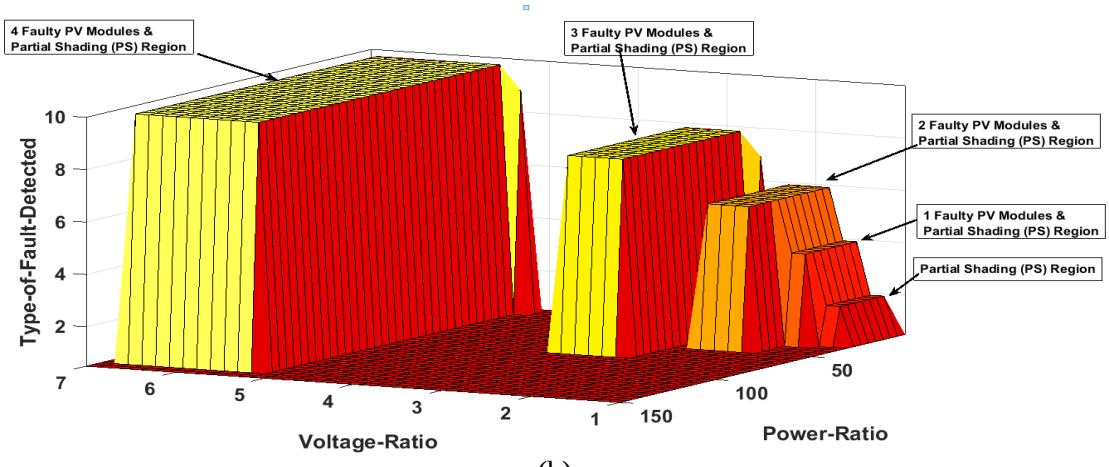

(b)

Figure 6.28 Fuzzy Logic systems classifier output surfaces. (a) Mamdani Fuzzy Logic system, (b) Sugeno Fuzzy Logic system

6.3.5 Performance evaluation for the proposed AI PV fault detection algorithms

In order to test the effectiveness of the proposed fault detection algorithm, a number of experiments were conducted. Furthermore, the data used for training the ANN networks previously shown in Figure 6.26 are not used in the evaluation process. Table 6.4 shows a full day experimental scenarios which are applied to the PV plant, where the perturbation process made to the PV system is shown in Figure 6.29a. Each scenario lasts for an hour and it contains a different condition applied to the PV system.

As can be seen, the data samples for both sleep and normal operation modes are not included in the evaluation process of the machine learning techniques, since both scenarios can be detected using the mathematical regions explained in Figure 6.24. All other samples are used to evaluate the ANN networks, where all samples are independent of the ANN networks training data.

Table 6.5 PV system under various faults

Scenario #	Start time	End time	Condition applied to the PV system	Number of samples applied to the ANN network
1	5:45	5:57	Sleep mode	-
2	5:58	6:59	Normal operation mode	-
3	7:00	7:59	20% partial shading	60
4	8:00	8:59	Faulty PV module and 20% partial shading	60
5	9:00	9:59	Faulty PV module and 40% partial shading	60
6	10:00	10:59	Normal operation mode	-
7	11:00	11:59	2 Faulty PV modules and 30% partial shading	60
8	12:00	12:59	30% partial shading	60
9	13:00	13:59	4 Faulty PV modules only	60
10	14:00	14:59	3 Faulty PV modules and 20% partial shading	60
11	15:00	15:59	3 Faulty PV modules only	60
12	16:00	17:57	Normal operation mode	-
13	17:58	19:00	Sleep mode	-
				Sum: 480

Scenarios 3-5 and 7-11 are evaluated by the ANN network and the Fuzzy Logic systems, where the total number of samples for the faulty conditions is equal to 480. A comparison between the theoretical output power vs. measured output power of the PV system during the tested faulty conditions is shown in Figure 6.29b.

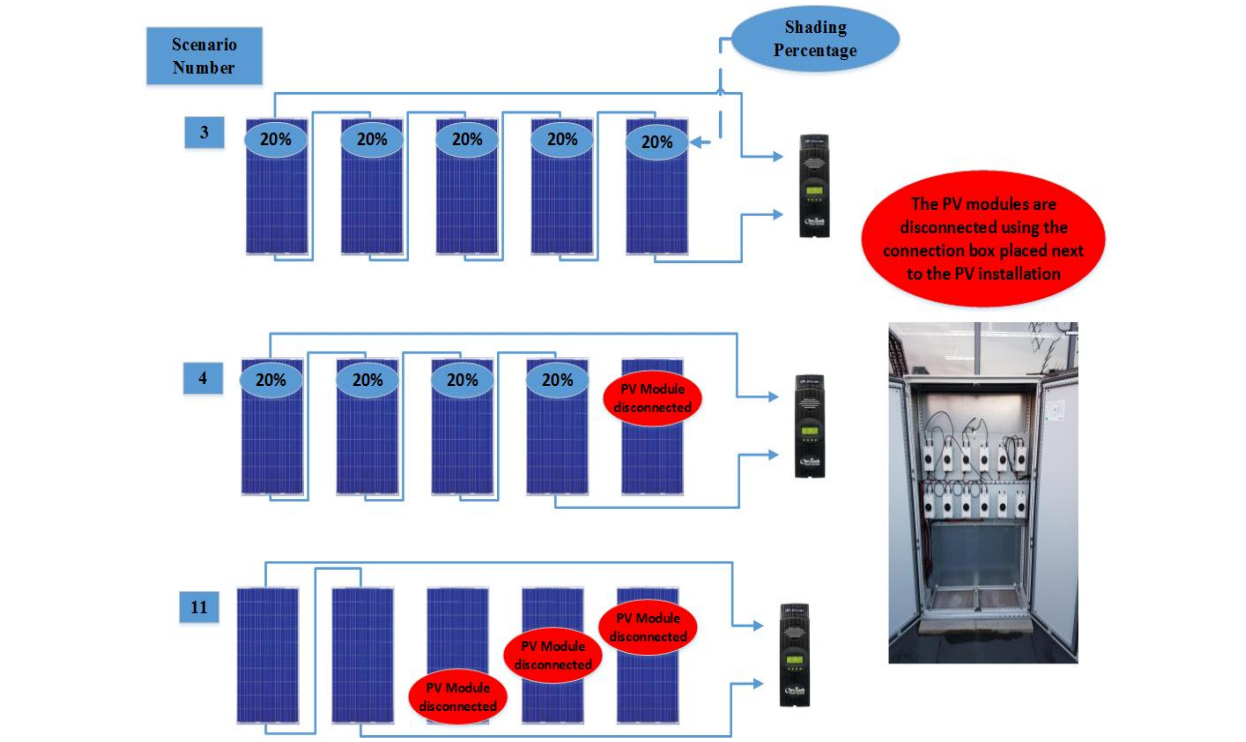

(a)

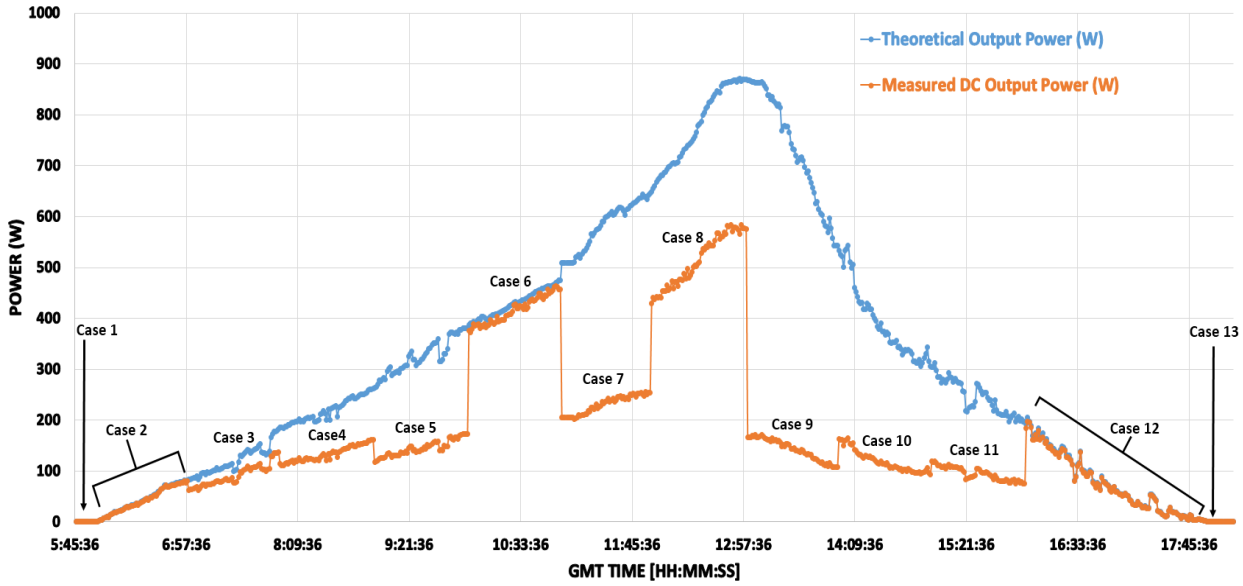

(b)

Figure 6.29 (a) Perturbation process made to test the PV system, (b) Theoretical output power vs. measured output power for all tested scenarios

6.3.5.1 Evaluating the proposed ANN networks

In order to verify the performance of the proposed ANN networks, the voltage and power ratios of 480 samples illustrated in Table 6.5 have been used as an input for each ANN network shown previously in Figure 6.25. The obtained results using each ANN network are shown in Figures 6.30 and 6.31.

The cells of each matrix with red and green colors present the percentage of faults correctly and not correctly classified by the ANN network respectively. The fault classification number, fault type and number of samples for each examined ANN network are shown in Table 6.6. The grey blocks represents the total percentage of the detection accuracy in the column and row respectively.

In order to understand how to read the confusion matrices shown in Figure 6.30, the first confusion matrix (Figure 6.30a) will be explained. In this figure, the first five diagonal cells show the number and percentage of correct classifications by the trained network. For example, 118 samples for F1 (fault type, shown in Table 6.6), are correctly classified. This corresponds to 24.6% of all tested samples (480 sample). Similarly, 30 samples are correctly classified as F2, this corresponds to 6.3% of all 480 samples.

In row 1, one sample is incorrectly classified as F1 although it is actually classified as F3, this corresponds to 0.2% of all 480 samples. Similarly, 2 samples of F5 are incorrectly classified as F1 and this corresponds to 0.4% of all 480 samples. Furthermore, in row 2, 30 samples are correctly classified as being F2, this corresponds to 6.3% of all 480 samples.

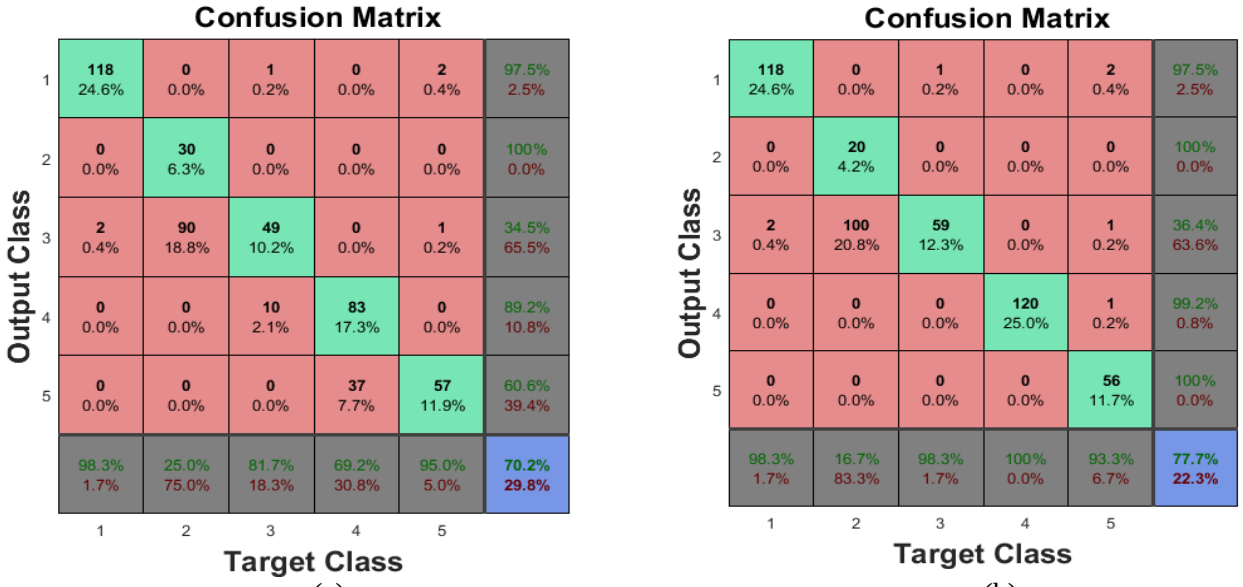

(a) (b)

Figure 6.30 Classification confusion matrices for the examined ANN networks. (a) 2 Inputs, 5 outputs using 1 hidden layer, (b) 2 Inputs, 5 outputs using 2 hidden layers,

Out of 121 sample which correspond to row 1, 97.5% are correct and 2.5% are wrong. Out of 120 samples corresponds to column 1, 98.3% are correct and 1.7% are classified incorrectly. For row 2, all samples have been classified correctly, 100%. However, for column 2, out of 120 samples, 25% are correct and 75% are incorrect.

The overall detection accuracy of the confusion matrix could be calculated using the diagonal cells as the following:

$$1^{st} \text{ cell } (24.6\%) + 2^{nd} \text{ cell } (6.3\%) + 3^{rd} \text{ cell } (10.2\%) + 4^{th} \text{ cell } (17.3\%) + 5^{th} \text{ cell } (11.9\%) = 70.2\%$$

70.2% corresponds to the percentage of correctly classified samples (out of all tested samples, 480 sample). And 29.8% correspond to incorrectly classified samples.

From the obtained results in Figure 6.30a, the minimum detection accuracy is associated with column 2, where 75% of the samples are incorrectly classified. This situation occurred when 3 faulty PV modules and PS affecting the PV module (F3) is classified as F2.

Similar results are obtained with the second ANN network (contains 2 outputs and 2 hidden layers) shown in Figure 6.30b. The percentage of the error in identifying F3 is increased to 83.3%, shown in column 2. However, the overall detection accuracy of the second ANN network is increased to 77.7% comparing to 70.2% obtained by the first ANN network. This increase in the detection accuracy is due to the second hidden layer which enables more training and validation for the trained samples of the ANN network before the testing phase (Mahmoud Dhimish et al., 2018).

Table 6.6 Faults detected by the ANN networks

ANN network	Fault number	Type of the fault	Number of samples
ANN network 1 and 2 as shown in Figures 6.31a and 6.31b respectively	F1	PS affecting the PV system	120
	F2	1 Faulty PV module & PS affecting the PV module	120
	F3	2 Faulty PV modules & PS affecting the PV module	60
	F4	3 Faulty PV modules & PS affecting the PV module	120
	F5	4 Faulty PV modules & PS affecting the PV module	60
ANN network 3 and 4 as shown in Figures 6.31c and 6.31d respectively	F1	PS affecting the PV system	120
	F2	1 Faulty PV module	0
	F3	2 Faulty PV modules	0
	F4	3 Faulty PV modules	60
	F5	4 Faulty PV modules	60
	F6	1 Faulty PV module & PS affecting the PV module	120
	F7	2 Faulty PV modules & PS affecting the PV module	60
	F8	3 Faulty PV modules & PS affecting the PV module	60
	F9	4 Faulty PV modules & PS affecting the PV module	0

As can be noticed, ANN networks one and two have low overall detection accuracy. As mentioned earlier in section 6.3.3, this challenge was solved by adding new type of faults for the ANN network that allows the ANN model to detect faulty PV modules only (no PS on the entire PV plant).

Figure 6.31a describes the output classification confusion matrix of the third ANN network (contains 9 outputs and 1 hidden layer). The overall detection accuracy of the ANN network is equal to 87.5% where the highest error is associated with F7 (row 7). This fault is related to the samples of F7 which are classified as F8. This situation occurred when two faulty PV modules with high PS condition is detected by the ANN network as three faulty PV modules with low PS condition affecting the entire PV system.

The last ANN network contains 2 inputs, 9 outputs and 2 hidden layers has the highest overall detection accuracy which is equal to 92.1%. This ANN network detects accurately 442 samples out of 480 samples, this results is shown in Figure 6.31b.

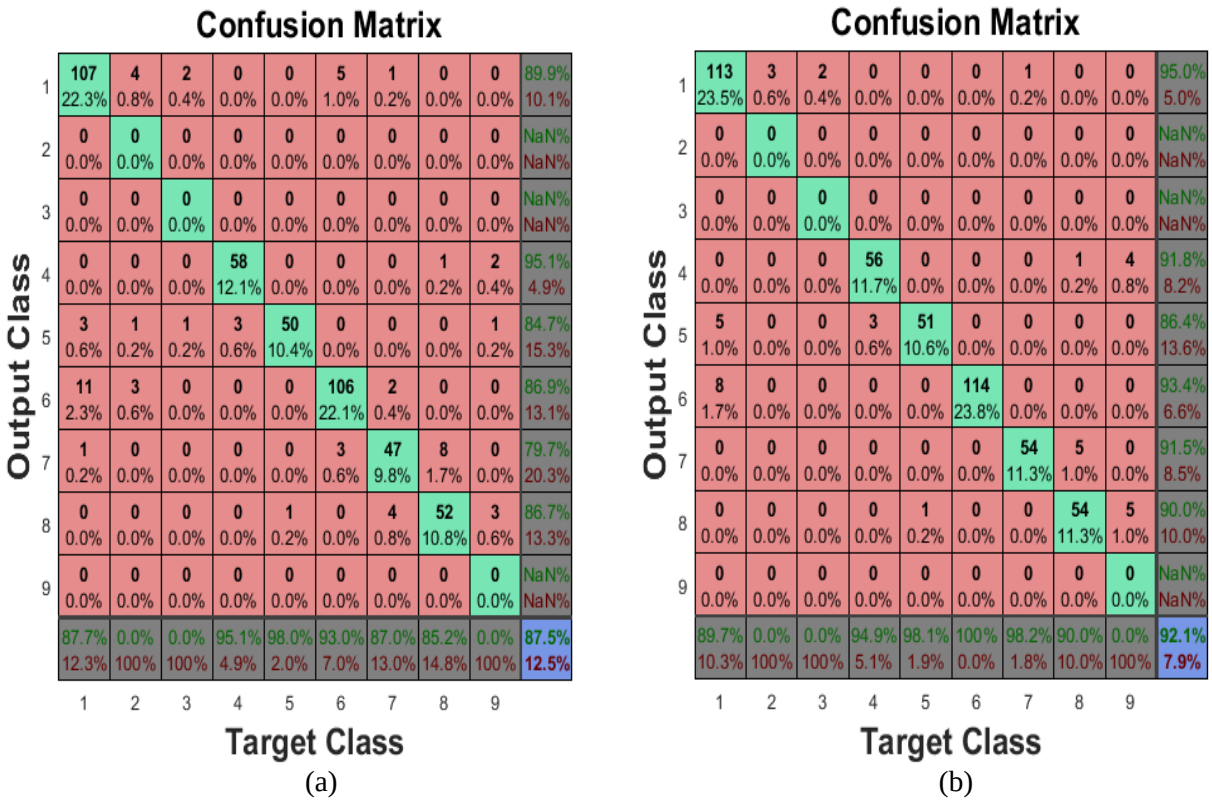

(a) (b)

Figure 6.31 Classification confusion matrices for the examined ANN networks. (a) 2 Inputs, 9 outputs using 1 hidden layer, (b) 2 Inputs, 9 outputs using 2 hidden layer

6.3.5.2 Evaluating the last ANN network using the second PV plant

In the previous section, the ANN detection algorithm has been evaluated using various ANN models, where the last model containing 2 inputs, 9 outputs using 2 hidden layers has the maximum detection accuracy. The ANN network attained the highest detection accuracy using 7 neurons. Appendix D shows the results of the ANN network using 2 to 9 neurons. In addition, Appendix E shows the MATLAB code of the ANN model (Mahmoud Dhimish et al., 2018).

Since the last ANN model achieved the highest detection accuracy, this ANN model will be evaluated using the second PV plant installed at the University of Huddersfield. Various types of faults have been examined. The list of faults is shown in Table 6.7. The theoretical output power vs. the measured output power of the PV plant is shown in Figure 6.32.

Table 6.7 PV system 2 under various faults

Scenario #	Start time	End time	Condition applied to the PV system	Number of samples applied to the ANN network
1	5:45	5:57	Sleep mode	-
2	5:58	6:59	Normal operation mode	-
3	7:00	7:59	30% partial shading	60
4	8:00	8:59	1 faulty PV module	60
5	9:00	9:59	2 Faulty PV modules	60
6	10:00	10:59	Normal operation mode	-
7	11:00	11:59	1 faulty PV module and 90% partial shading	60
8	12:00	12:59	2 faulty PV modules and 10% partial shading	60
9	13:00	13:59	3 faulty PV modules and 20% partial shading	60
10	14:00	14:59	4 faulty PV modules and 20% partial shading	60
11	16:00	17:57	Normal operation mode	-
12	17:58	19:00	Sleep mode	-
				Sum: 420

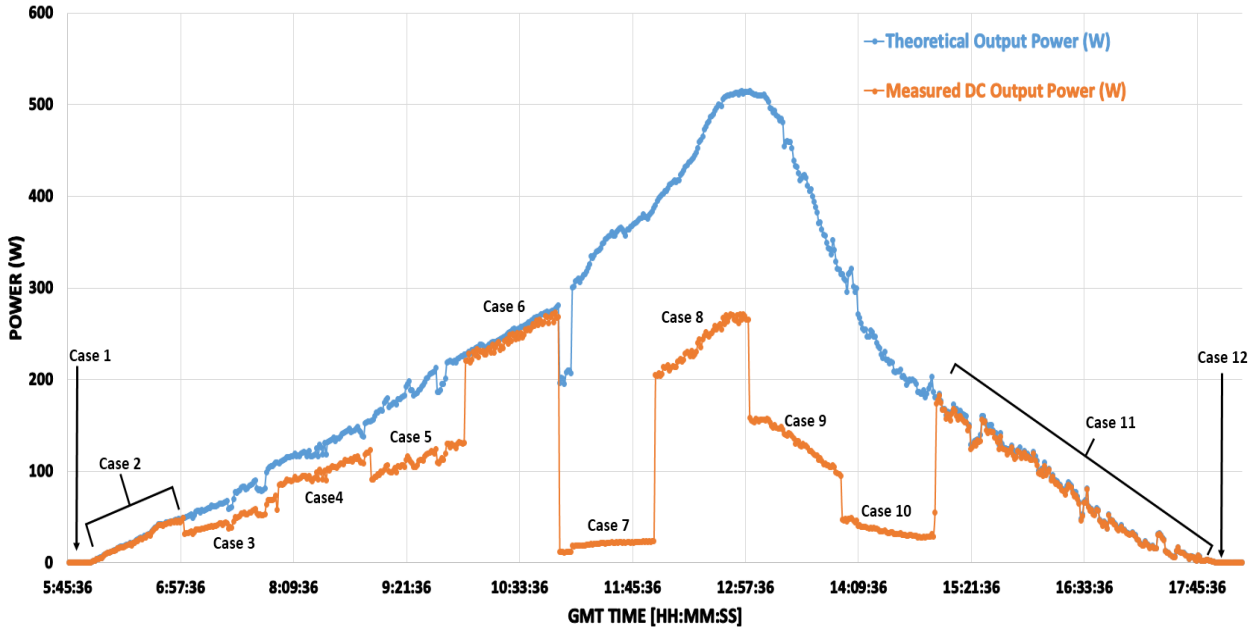

Figure 6.32 Theoretical output power vs. measured output power for all tested scenarios

The ANN network output confusion matrix are shown in Figures 6.33 and 6.34. The presented ANN confusion matrix are evaluated using various neurons numbers. As can be noticed, the detection accuracy achieved by all examined neurons is relatively high. Still the highest detection accuracy is achieved by the ANN network that has 7 neurons (Detection accuracy 91.9%).

This outcome matches the results shown in the previous section. However, the detection accuracy dropped by 0.2%:

92.1% - 91.9% = 0.2%

In conclusion, this section confirms the high accuracy of the proposed ANN network using the evaluation of the last ANN model on a different PV plant. There is still a drop in the detection accuracy of the proposed ANN model. The reason for the drop in the detection accuracy is the percentage of the tolerance associated with the voltage and current sensors used in the PV site. This will affect the measured data, and will decrease the overall detection accuracy of the ANN network.

The best ANN network with 8 neurons achieved the maximum detection accuracy. However, it is also possible to use an ANN network with less or more neurons, because as evident from the conducted results shown in Figures (6.33) and (6.64), the minimum achievable fault detection accuracy is equal to 88.8%.

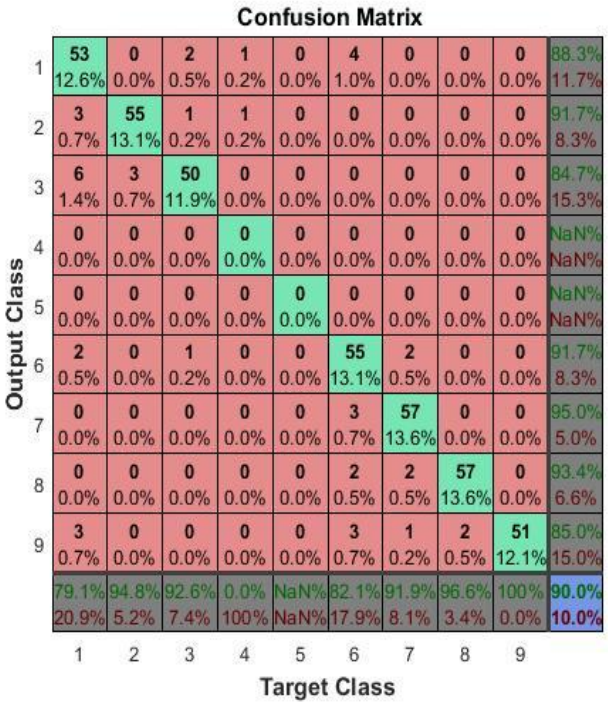

(a)

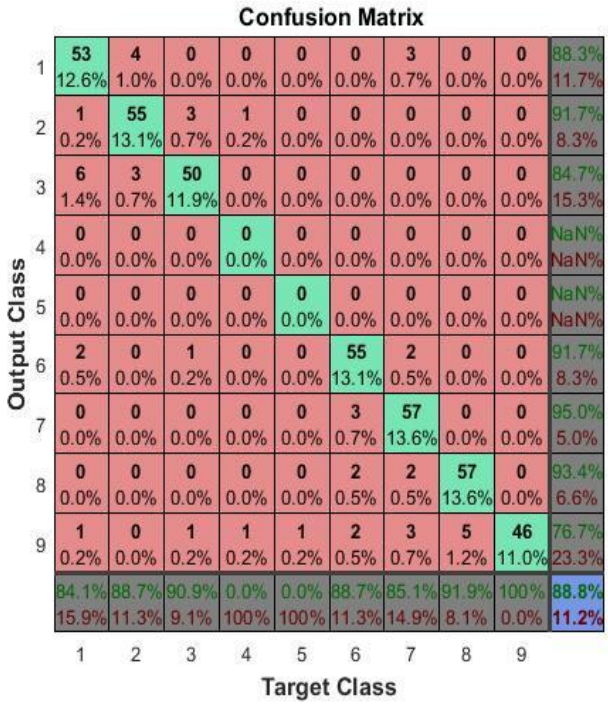

(b)

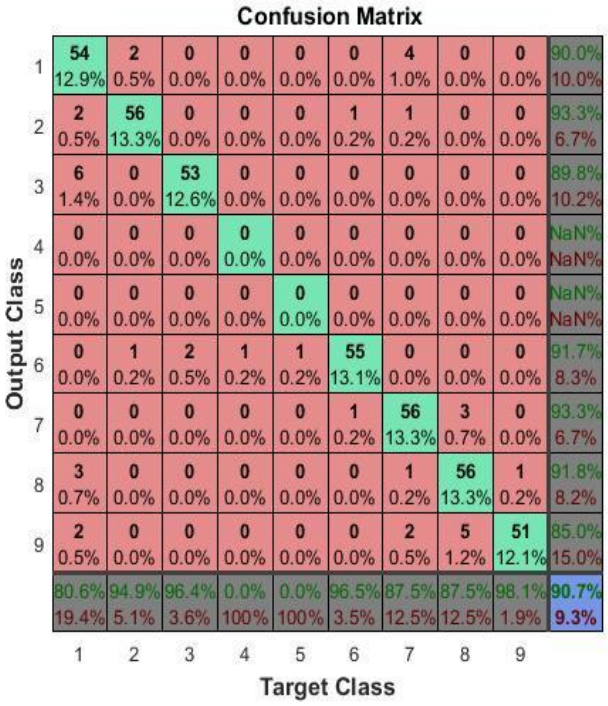

(c)

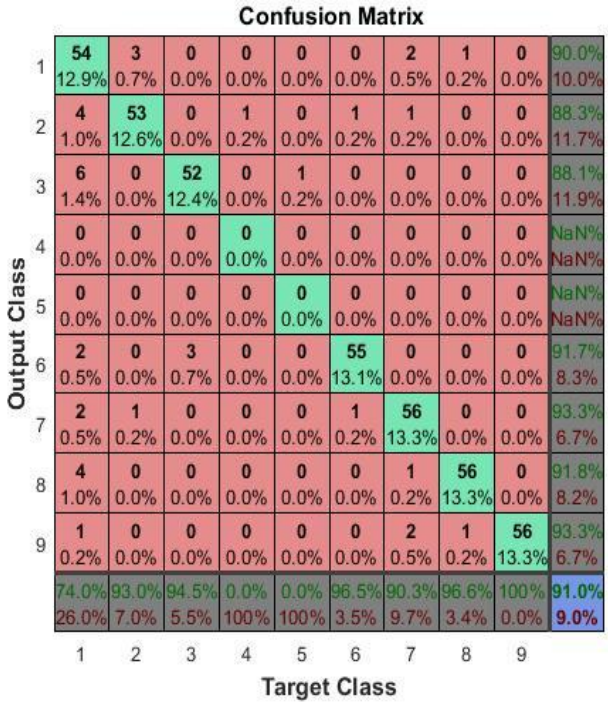

(d)

Figure 6.33 Classification confusion matrices for the examined ANN network. (a) 2 neurons, (b) 3 neurons, (c) 4 neurons, (d) 5 neurons

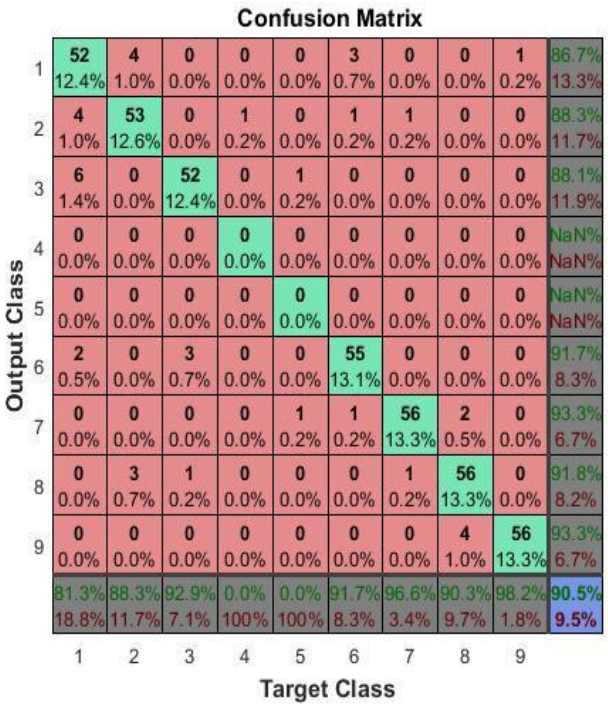

(a)

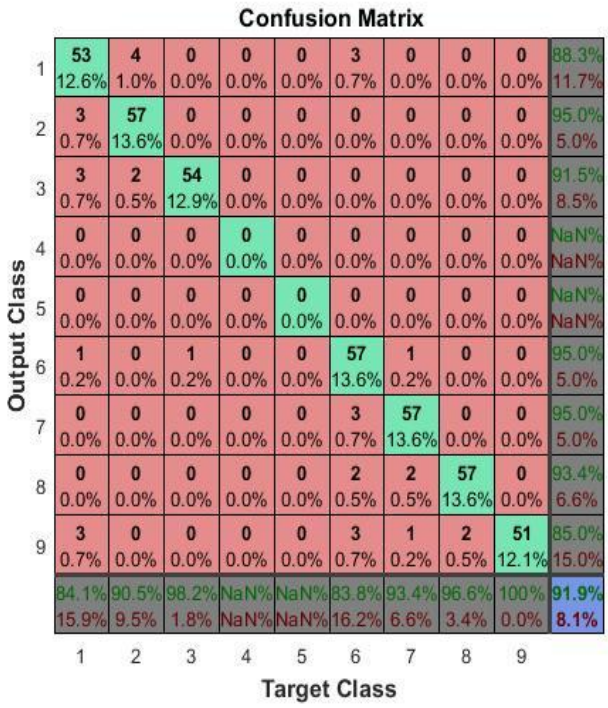

(b)

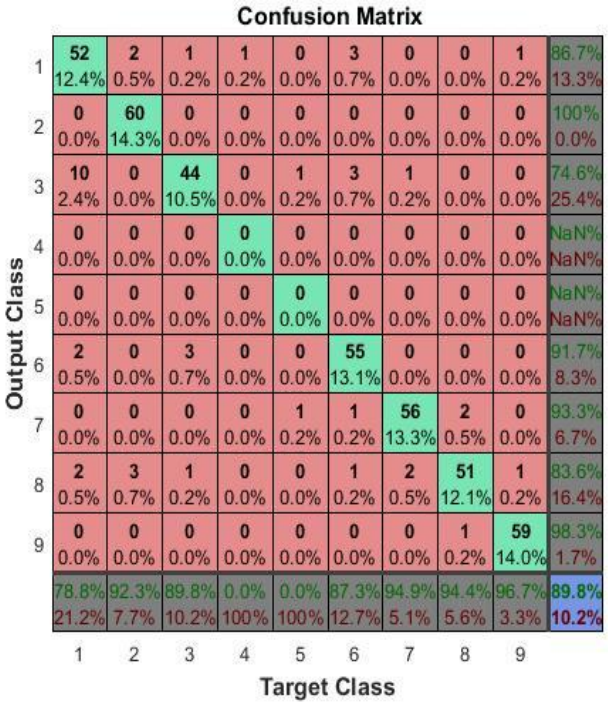

(c)

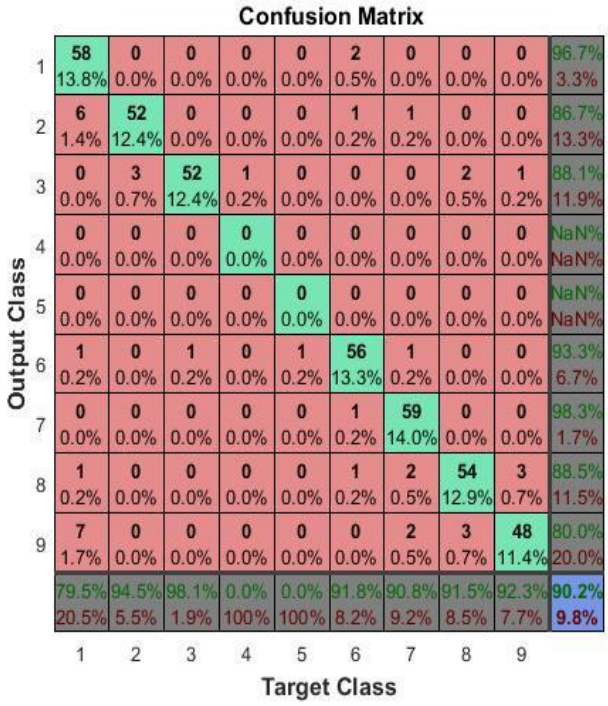

(d)

Figure 6.34 Classification confusion matrices for the examined ANN network. (a) 6 neurons, (b) 7 neurons, (c) 8 neurons, (d) 9 neurons

6.3.5.3 Evaluating the proposed Fuzzy Logic systems

In order to test the effectiveness of the proposed Fuzzy Logic systems (Mamdani and Sugeno), the faulty samples shown previously in Table 6.5 have been processed in each fuzzy system.

- **Mamdani Fuzzy Logic system:**

Figure 6.35a shows the output membership function vs. the faulty samples (480) processed by Mamdani Fuzzy Logic system. Each faulty PV condition is labelled on the figure. As an example, case 3 presents 20% partial shading condition affecting the PV module. For this particular PV faulty scenario, the output of the fuzzy system is equal to 0.5, which is the region of PS condition illustrated in Figure 6.35b.

Similarly, cases 4 and 5 present a faulty PV module with 20% and 40% PS respectively. Both cases are within the same membership function region due to the low PS condition affecting the PV modules, this situation is labeled as case 4 and case 5 in both Figures 6.34a and 6.34b.

Figure 6.34 shows that all tested faulty conditions are accurately detected by Mamdani Fuzzy Logic system. However, between case 7 and case 8 there is a small amount of error in detecting the region of the fault, the same result occurring between case 8 and case 9.

This situation occurs due to the high number of faulty regions identified by the fuzzy system. Additionally, voltage and power ratios strongly depend on the performance of the voltage and current sensors used to detect the change in the PV parameters (voltage, current and power). Therefore, the Fuzzy Logic system might need extra seconds to start detecting the exact fault occurring in the PV installation.

- **Sugeno Fuzzy Logic system:**

Figure 6.36a shows the output membership function vs. the faulty samples for Sugeno Fuzzy Logic system. Each faulty PV condition is labelled on the figure. As an example, case 7 presents two faulty PV modules and low partial shading condition affecting the PV plant. For this particular PV faulty scenario, the output of the fuzzy system is equal to 5, which is the region of PS condition illustrated in Figure 6.36b.

Similarly, cases 10 and 11 represent three faulty PV modules with 20% and 0% PS respectively. Both cases are within the same membership function region due to the low PS condition affecting the PV modules. This situation is labeled as case 10 and case 11 in both Figures 6.35a and 6.35b.

From the obtained results by the Sugeno Fuzzy Logic system, all examined faulty conditions are accurately detected. However, between case 7 and case 8 there is a small amount of error in detecting the region of the fault.

This section presents the performance of the Fuzzy Logic systems developed for detecting faulty conditions in the tested PV system. Both Fuzzy Logic systems show accurate results in detecting various faults comparing to the results obtained by the ANN network, which has a maximum detection accuracy equals to 92.1%.

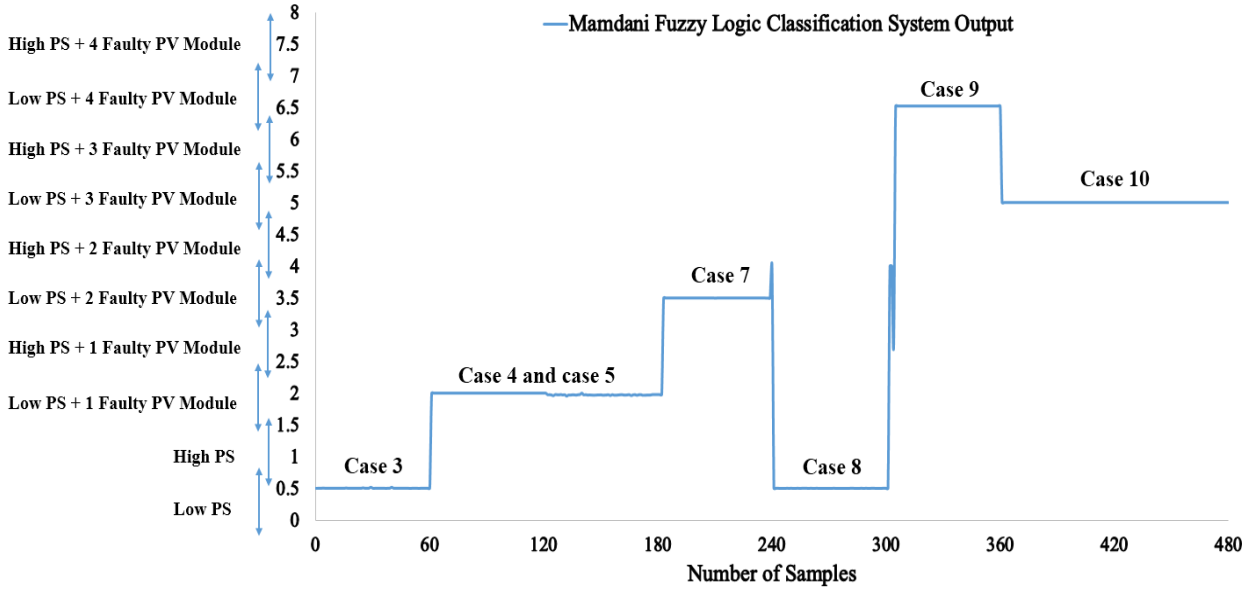

(a)

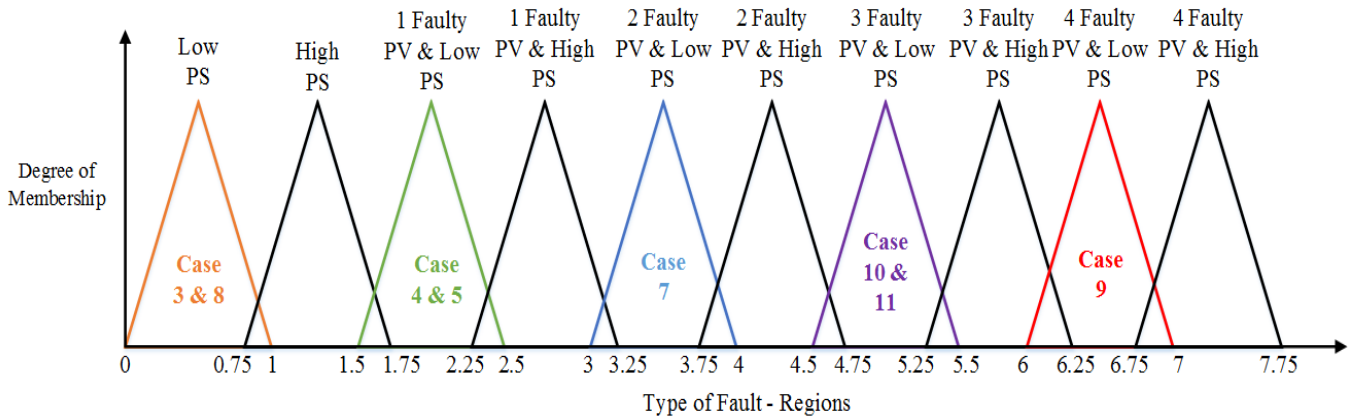

(b)

Figure 6.35 Output results using Mamdani Fuzzy Logic system. (a) Membership functions vs. number of samples, (b) Membership functions explained previously in section 6.3.4 vs. type of fault

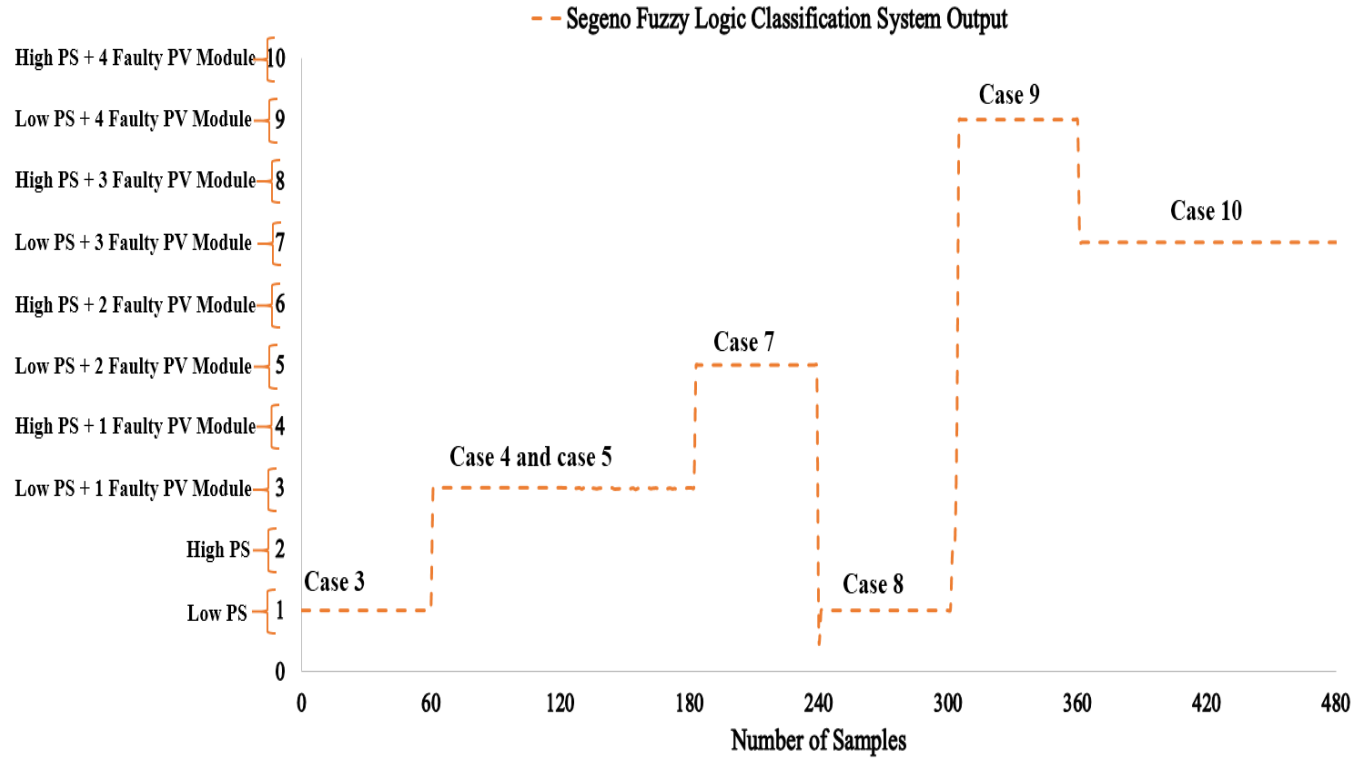

(a)

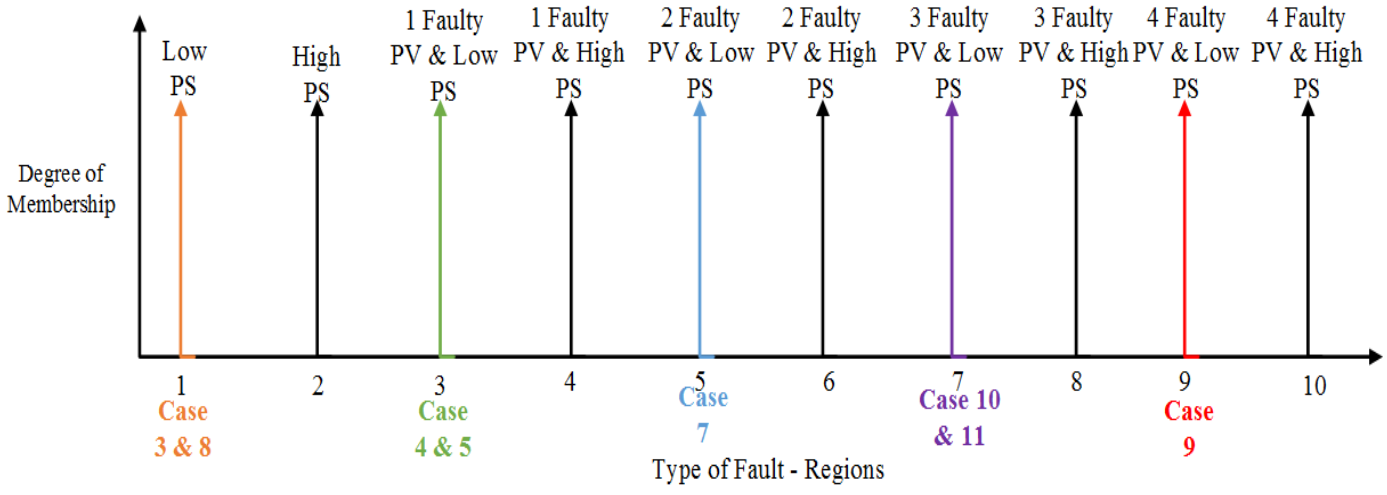

(b)

Figure 6.36 Output results obtained using Sugeno Fuzzy Logic system. (a) Membership functions vs. number of samples, (b) Membership function explained previously in section 6.3.4 vs. type of fault

7.4 Summary

This chapter describes the development of multiple PV fault detection methods using AI techniques including Mamdani Fuzzy Logic, Sugeno Fuzzy Logic, and artificial neural networks. Several methods have been studied and analysed using various PV array structure.

A summary for the proposed methods is shown in Figure 6.37.

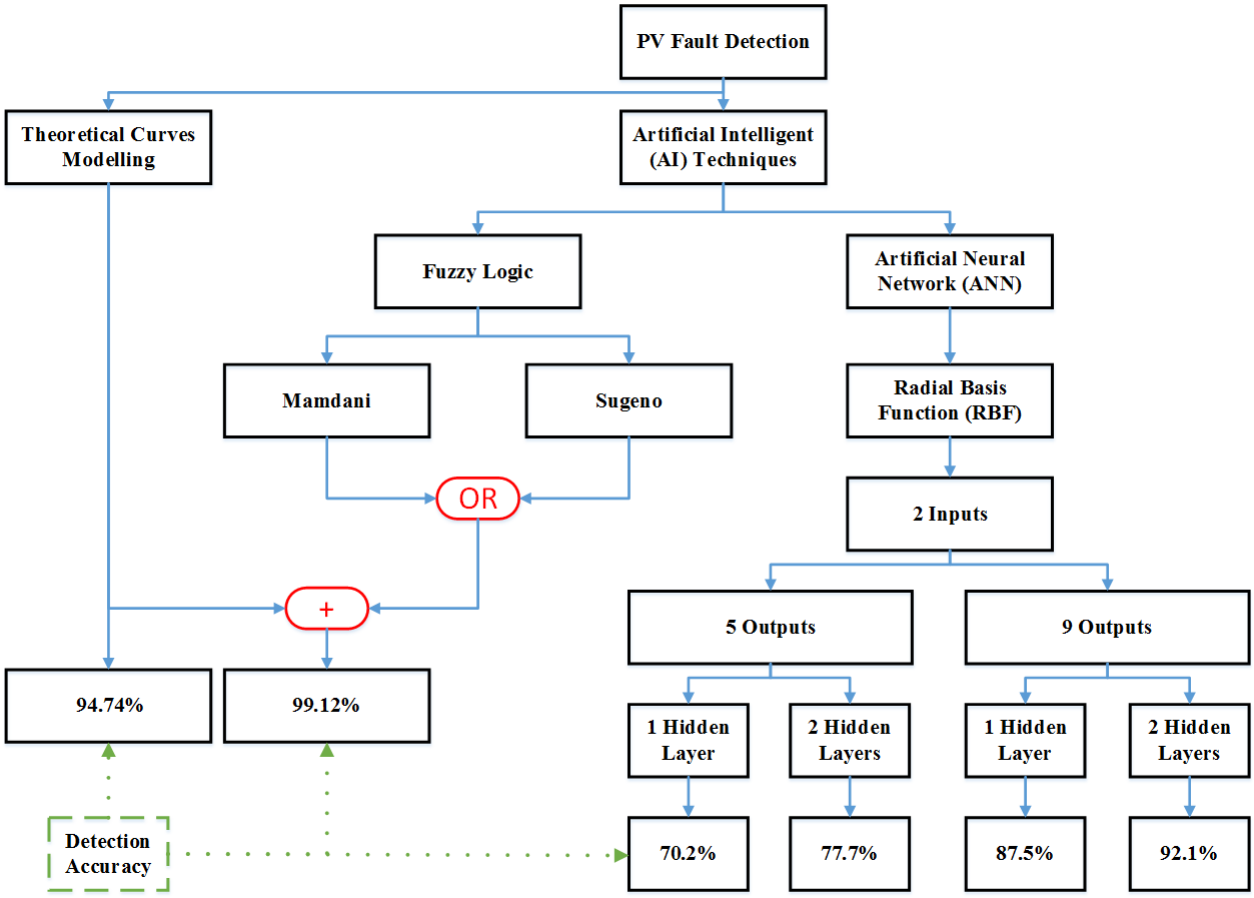

Figure 6.37 Overall proposed PV fault detection algorithms

The Fuzzy Logic system increases the detection accuracy of PV fault detection algorithm from 94.74% to 99.12%. On the other hand, four ANN networks have been compared where the highest detection accuracy (92.1%) is achieved using the last ANN network (2 inputs, 9 outputs using 2 hidden layers).

In the next chapter, the output power of PV hot spotted solar cells will be enhanced using two techniques. Additionally, the analysis of PV micro cracks including diagonal, parallel to busbars, and perpendicular to busbars cracks will be discussed.

Chapter 7 PV Hot Spot and Micro Cracks

In chapters 5 and 6, the fault detection algorithms based on various techniques have been introduced. However, there are different types of faults occurring in PV systems, which cannot be identified by previously discussed algorithms such as hot spots and micro cracks. There is not enough scientific evidence for the faults causing hot spots. However, the authors (R. Moreton et al., 2015) demonstrated that dust and humidity are two reasons which cause hot spots in PV modules. In addition, (K. Kim & P. Krein, 2015) confirmed that the fluctuations of the temperature cause hot spots in PV modules. Some preliminary work has been completed to address hot spots and micro cracks issues.

This chapter focuses on the development of novel techniques to enhance the output power performance of hot spotted PV solar cells. Additionally, a statistical analysis approach for identifying the impact of PV micro cracks on the output power of PV modules will be described.

This data presented in this chapter have been published in the following articles (M Dhimish et al., 2017; M Dhimish et al., 2017a; M Dhimish et al., 2017b).

7.1 PV hot spots

Hot spotting is a reliability problem in photovoltaic (PV) panels where a mismatched cell heats up significantly and degrades PV panel output power performance. High PV cell temperature due to hot spotting can damage the cell encapsulate and lead to second breakdown, where both cause permanent damage to the PV panel. Therefore, in this section a comparison between two hot spot mitigation techniques is performed using a simple, costless and reliable method.

7.1.1 Examined PV modules

PV modules installed in PV plant A, described in Appendix A will be used to examine and evaluate the performance of the proposed hot spot mitigation techniques. In order to inspect the PV modules, i5 FLIR thermal image camera has been used (INSRUMENTS, 2013). In addition, I-V curve analysis for the tested PV modules is carried out using I-V curve tracer.

I-V curve tracer was also used to plot the I-V curve of the examined PV modules under various experimental conditions. The main specification, including the voltage resolution, and current resolution can be seen in Figure 7.1. As can be noticed, the error in the measured PV voltage, PV current, solar irradiance and PV module temperature is very limited due to the high accuracy of the I-V tracer (Solmetric, 2016). The overall structure of the proposed PV inspection method is shown in Figure 7.1.

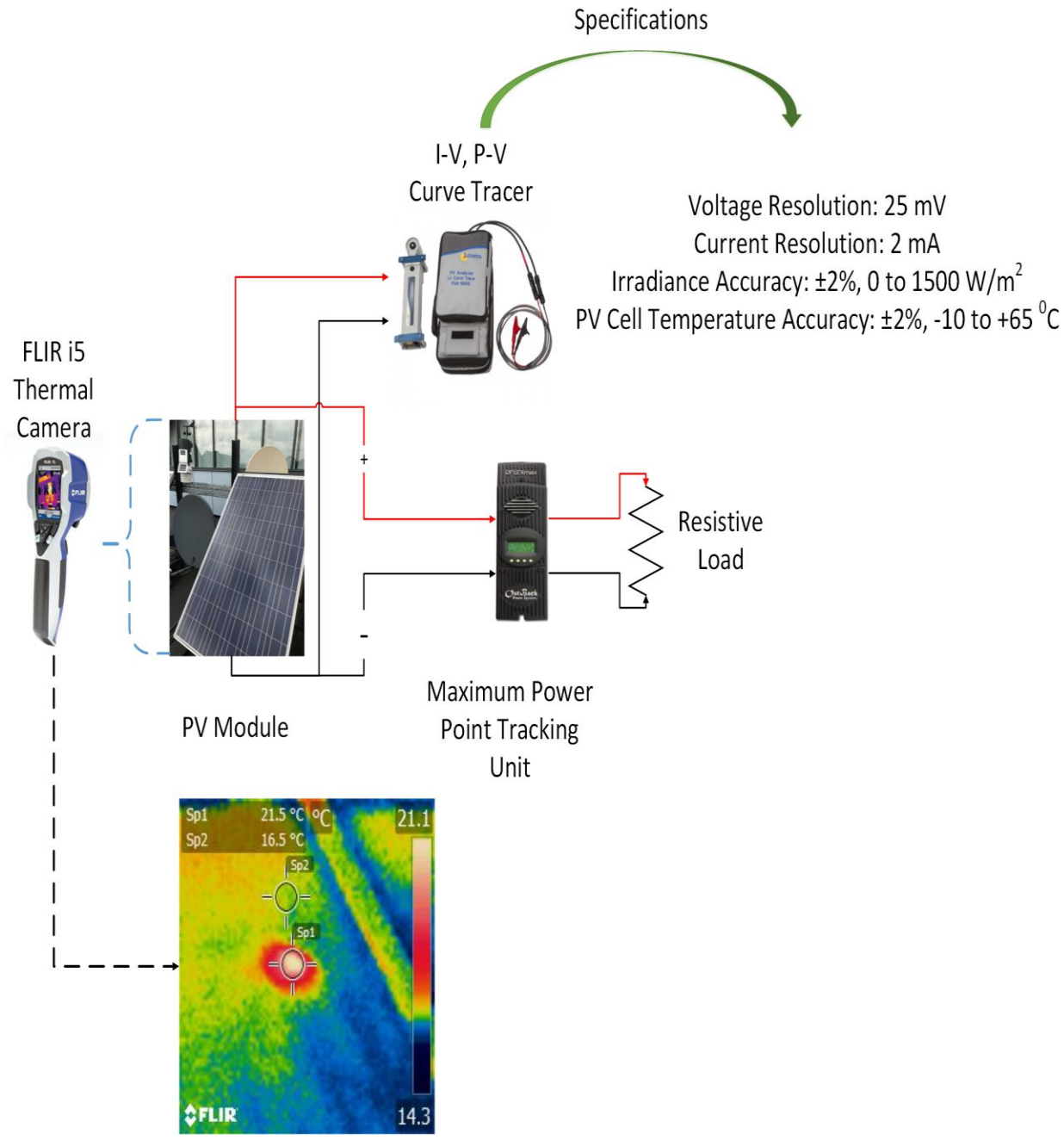

Figure 7.1 Structure and instruments used to examine the hot spotted PV modules

7.1.2 Evaluating the PV I-V curve tracer and i5 FLIR thermal camera

In this section, the output results of the I-V curve tracer shown in Figure 7.1 will be evaluated using various environmental conditions affecting a PV module.

Figure 7.2 shows three different I-V curves obtained under high, medium, and low irradiance levels. The theoretical MPP and measured MPP at each environmental condition are shown in Figure 7.2. The accuracy of the I-V curve tracer is equal to:

- High irradiance level: (185.60 / 186.382) x 100 = 99.58%
- Medium irradiance level: (107.79 / 108.299) x 100 = 99.53%
- Low irradiance level: (30.409 / 30.5991) x 100 = 99.38%

As can be noticed, the accuracy of the measured MPP and I-V curves is nearly equal to the theoretical data, where the average accuracy in the measured data is equal to 99.5%.

The investigation of the hot spots in the examined PV system was carried out using FLIR i5 thermal camera as shown in Figure 7.1. This camera has a thermal sensitivity equal to 0.5 ^{0}C, where its specification is described earlier in section 7.1.1.

A test was carried out using a PV module affected by one hot spotted solar cell. The thermal image of the examined PV module is shown in Figure 7.3a. The temperature of the hot spotted solar cell is equal to 21.1 ^{0}C. However, the temperature of the adjacent solar cells is 16.4 ^{0}C.

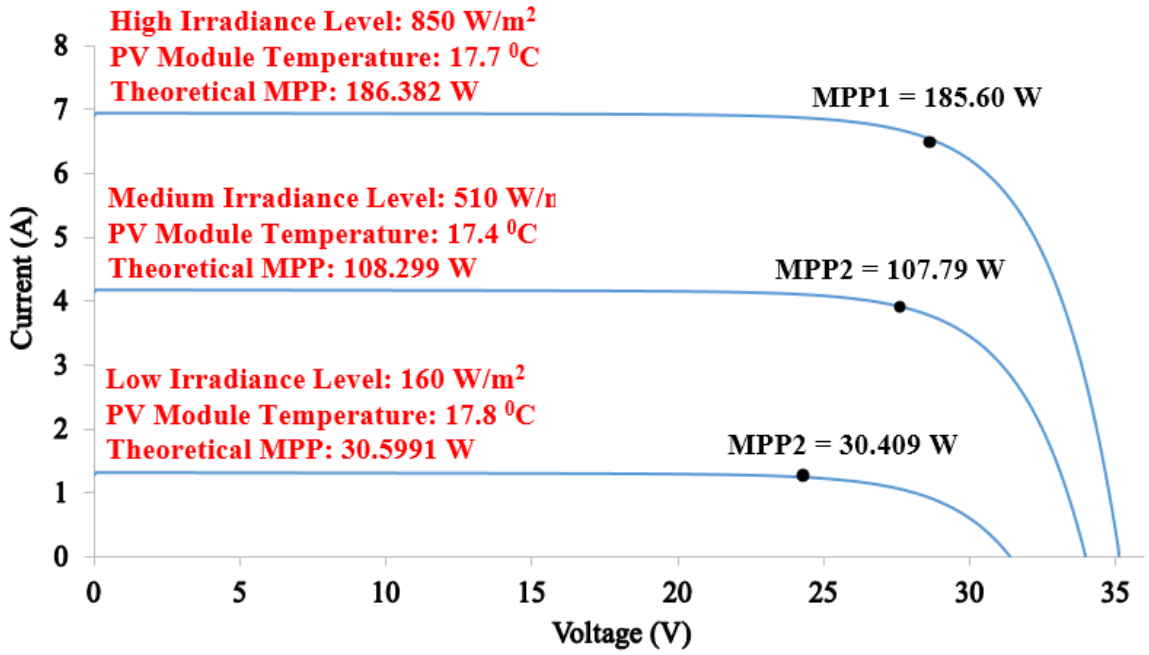

Figure 7.2 I-V curve tracer output results for various irradiance levels

The I-V curve of the hot spotted PV module is compared with healthy PV module (PV module without hot spots). The result is shown in Figure 3.8b. The MPP for a PV module without hot spots is equal to 121.61 W. However, the MPP for hot spotted PV module is equal to 115.83 W. Therefore, the power loss due to the hot spot in the examined PV module is equal to 5.78 W.

This experiment was conducted under 621 W/m^2 solar irradiance and the PV modules temperature is approximately equal to 18.2 ^{0}C. According to the measured data in Figure 7.2, the average accuracy of the I-V curve tracer is equal to 99.5%. Therefore, the measured data illustrated in Figure 7.3b have an error in the measurements equal to ±0.5%.

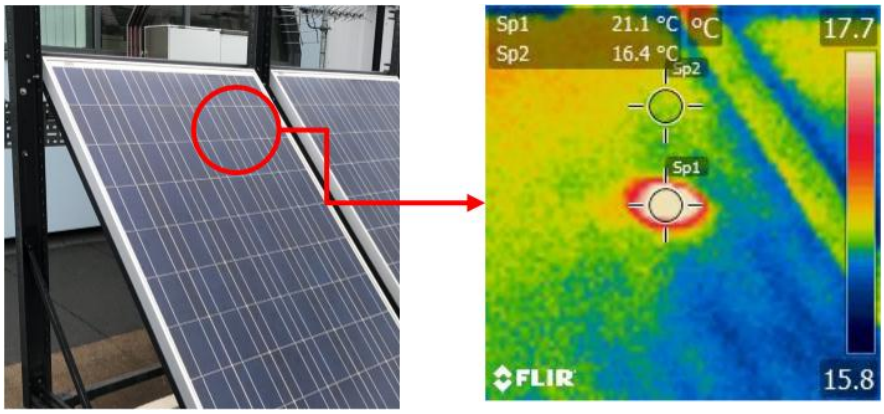

(a)

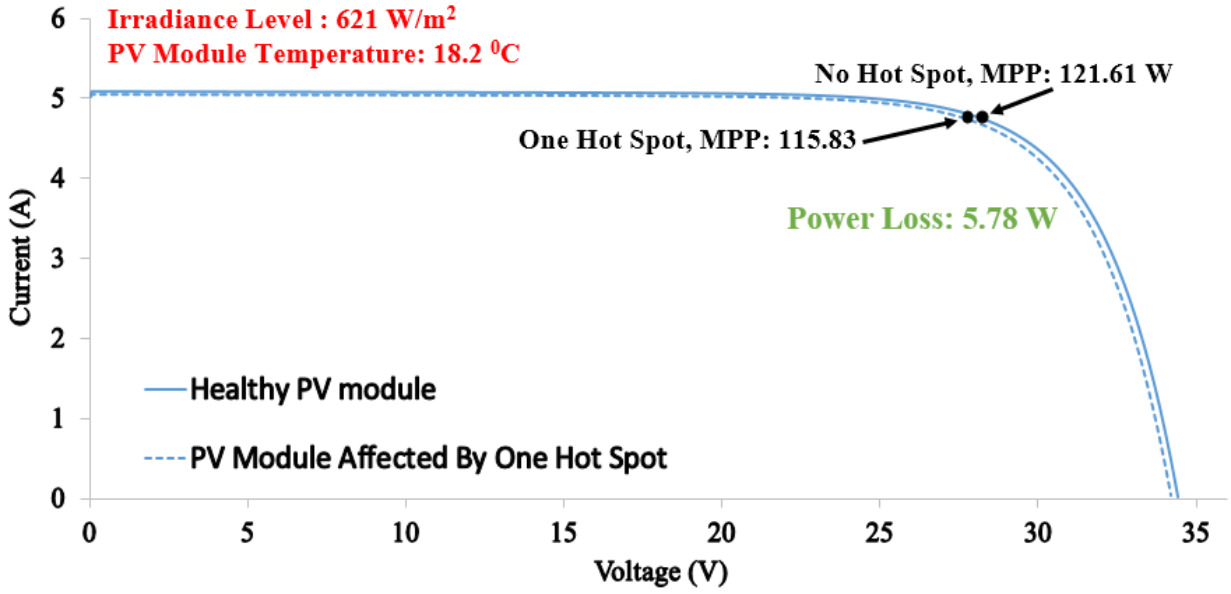

(b)

Figure 7.3 (a) Hot Spot detection using i5 FLIR thermal camera, (b) Output I-V curves using healthy PV module vs. hot spotted PV module

7.1.3 Proposed hot spot mitigation techniques

The first proposed hot spot mitigation technique is connected to each PV string in the PV module. The tested PV module bypass diodes shown in Figure 7.4a will be replaced by six MOSFETs as shown in Figure 7.4b.

Two MOSFETs were connected to each PV string in the PV module. Switch 1 is in series with the PV string and is normally "on"; it opens when a hot spot condition is detected to prevent further hot spotting. While, switch 2 is in parallel with the PV string and it is normally in "open" mode, it turns "on" to allow a bypass current path when the PV string is open circuited.

Another hot spot mitigation technique was used with the PV module instead of the connection for each MOSFET to the PV strings as shown in Figure 7.4c. The same concept has been applied, where switch 1 is in series with the PV module is normally "on"; it opens when a hot spot condition is detected to prevent further hot spotting. Switch 2 is in parallel with the PV module and is normally "open"; it turns "on" to allow a bypass current path when the PV string is open circuited.

As can be noticed, the proposed PV hot spot mitigation techniques are simple to implement, since it only required to add additional MOSFETs for the hot spotted PV module.

Power MOSFETs IRFZ44V (IRFZ44V, 2013) were used to implement and test the suggested hot spot mitigation techniques. The MOSFETs drain-to-source breakdown voltage is equal to 60 V, and the voltage drop in drain-to-source is as low as 50 mV. Hence, the selection of the MOSFETs plays an important role in the mitigation techniques. Therefore, the following MOSFET criteria must be met:

- Low drain-to-source voltage drop: better results in the I-V curve
- Fast switching speed: to enable fast drop in the temperature of the hot spotted solar cell
- Low on-resistance: low resistance means more current passes through the PV string
- High operating temperature
- Cost effective

The cost of the used MOSFETs is equal to £0.85. Therefore, the total cost for the first and second proposed techniques using 3 PV modules is equal to £18 and £5.10 respectively.

It is worthy to note that both proposed mitigation techniques should be placed with the hot spotted PV solar module after it has been inspected by the thermal imaging. This is one of the disadvantages of the proposed mitigation techniques. In the next section, the validation and comparison between both presented hot spot mitigation techniques will be described.

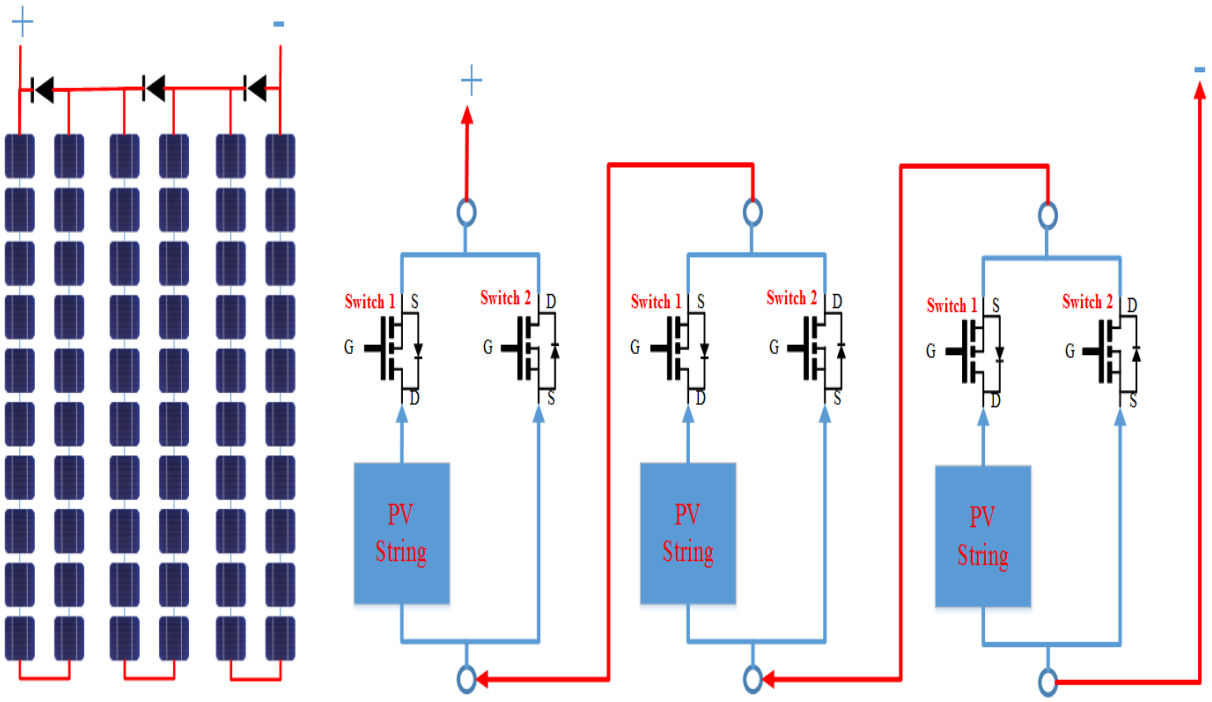

(a) (b)

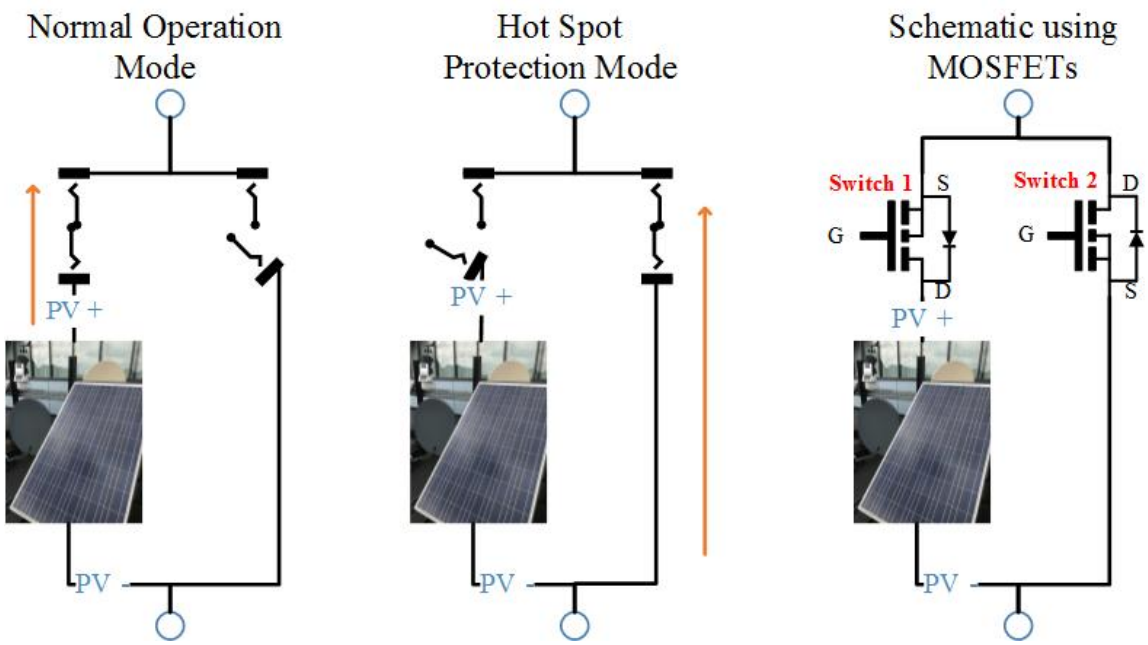

Figure 7.4 (a) The structure of the PV string for the examined PV module, (b) First hot spot mitigation technique, (c) Second proposed hot spot mitigation technique

7.1.4 Validating the proposed PV hot spot mitigation techniques

In this section the validation for both proposed hot spot mitigation techniques will be done using two case studies. The first will focus on the I-V curve analysis. Whilst the second case study will focus on partial shading condition enhancement.

7.1.4.1 PV hot spot and I-V curve analysis

There are several stages that have been assessed during the operation of the proposed hot spotting mitigation techniques. These stages are described as follows:

Hot spot mitigation technique 1:

The results obtained by the first mitigation technique are shown in Figure 7.5a. The results can be described by the following:

- Before the activation, the temperature of the hot spotted PV solar cell is equal to 21.1 ^{0}C, while the adjacent (reference) solar cell temperature is equal to 16.4 ^{0}C.
- 1 minute after the activation, the temperature of the hot spotted PV solar cell reduced to 20.4 ^{0}C, the difference between the hot spotted PV solar cell and the reference solar cell temperature is equal to 4 ^{0}C.
- 2 minutes after the activation: the maximum temperature for the hot spotted PV solar cell is reduced to 19.5 ^{0}C, compared to 21.1 ^{0}C before the activation of the mitigation technique.

Hot spot mitigation technique2:

The results obtained by the first mitigation technique are shown in Figure 7.4b. The results can be described by the following:

- Before the activation, the temperature of the hot spotted PV solar cell is equal to 21.5 ^{0}C, while the adjacent (reference) solar cell temperature is equal to 16.5 ^{0}C.
- 1 minute after the activation: the temperature of the hot spotted PV solar cell reduced to 19.1 ^{0}C, the difference between the hot spotted PV solar cell and the reference solar cell temperature is equal to 2.6 ^{0}C.
- 2 minutes after the activation: the maximum temperature for the hot spotted PV solar cell is reduced to 18.3 ^{0}C, compared to 21.5 ^{0}C before the activation of the mitigation technique.

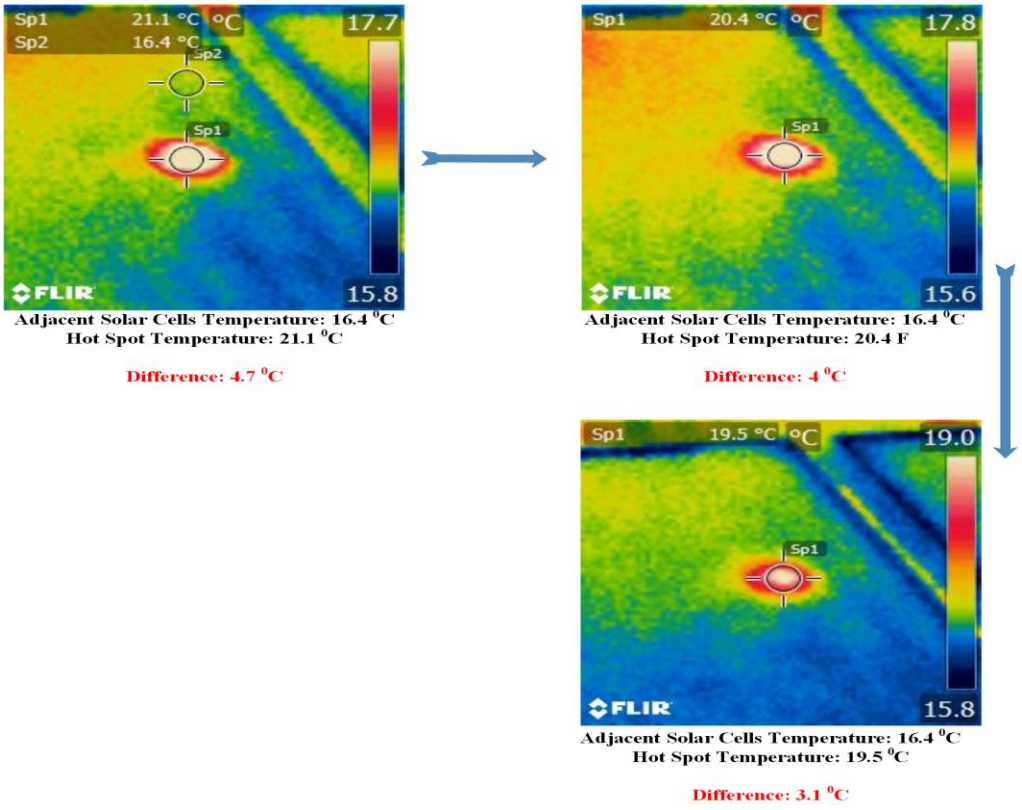

(a)

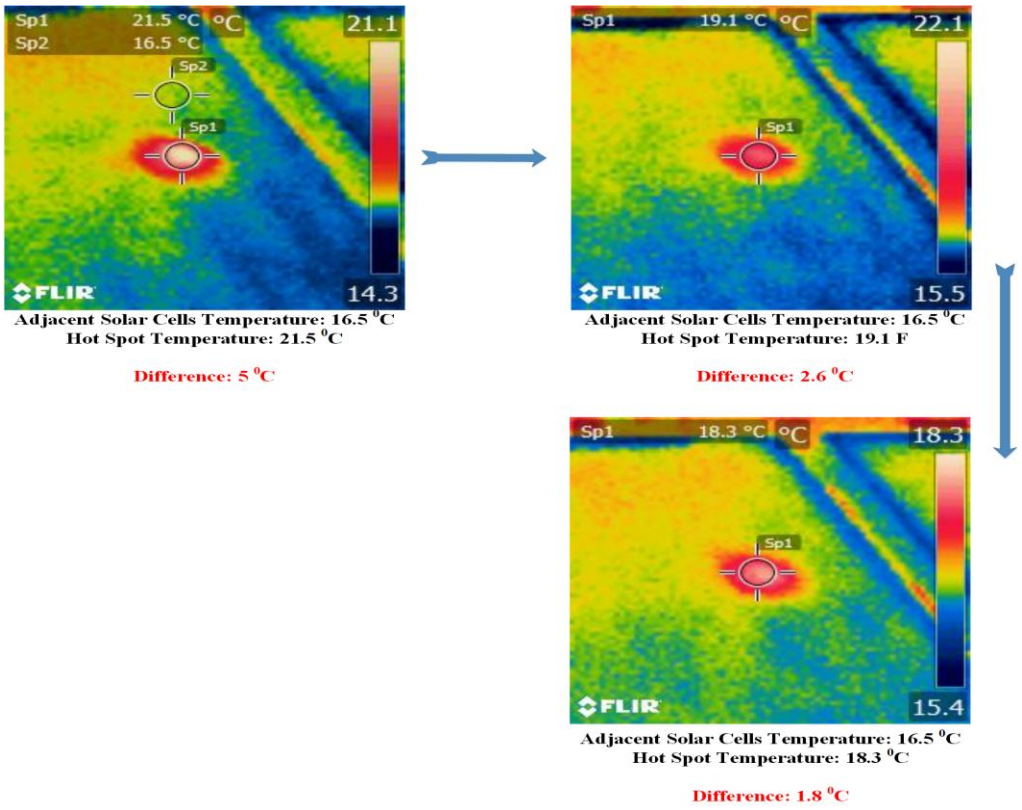

(b)

Figure 7.5 (a) Output thermal images for the first hot spot mitigation technique, (b) Output thermal images for the second hot spot mitigation technique

The main reason for the proposed hot spotting mitigation techniques is to improve the output power performance of the examined hot spotted PV module. The value of the power before and after the activation for each proposed technique was monitored in three different irradiance levels: high irradiance level: 840 W/m^2, medium irradiance level: 507 W/m^2 and low irradiance level: 177 W/m^2, while in all tested scenarios, the PV temperature is approximately equal to 16.2 ^{o}C.

Figure 7.6a shows the output I-V curve of the PV module at high irradiance level. The measured output power after the activation of the 1st proposed technique has a power loss equals to 3.94 W compared to 5.19 W with no mitigation technique installed in the PV module. However, power loss is minimized while activating the 2nd hot spot mitigation technique (P_{loss} = 1.23 W).

The output I-V curves of the examined PV module under medium and low irradiance levels are shown in Figures 7.6b and 7.6c respectively. The output results show a significant improvement in the output power using the 2nd mitigation technique compared to the 1st technique. Table 7.1 demonstrates a comparison between the output results for each examined irradiance level.

In conclusion, this section shows the validation and the enhancement of the temperature and the output power generated by the PV module using both proposed hot spot mitigation techniques. Technique 2 has a better output power performance compared to the 1st proposed mitigation technique.

Table 7.1 Comparison between the first and second proposed hot spot mitigation technique using high, medium and low irradiance levels

Irradiance (W/m^2)	Theoretical Power (W)	Case Scenario	Voltage (V)	Current (A)	Power (W)	P_{loss} (W)	Efficiency (%)
High 840	186.4	No mitigation	27.19	6.66	181.18	5.19	97.2
		1st Technique	27.49	6.63	182.44	3.94	97.88
		2nd Technique	28.33	6.53	185.15	1.23	99.33
Medium 507	108.2	No mitigation	26.00	4.02	104.54	3.63	96.64
		1st Technique	26.23	4.00	105.15	3.02	97.20
		2nd Technique	27.21	3.94	107.26	0.91	99.15
Low 177	34.4	No mitigation	23.73	1.39	33.02	1.37	95.99
		1st Technique	24.24	1.38	33.49	0.91	97.33
		2nd Technique	24.94	1.36	34.01	0.39	98.85

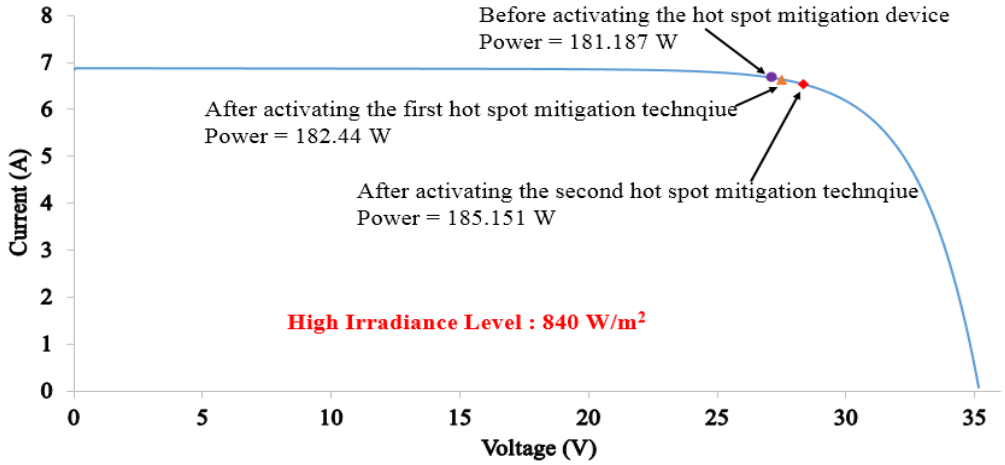

(a)

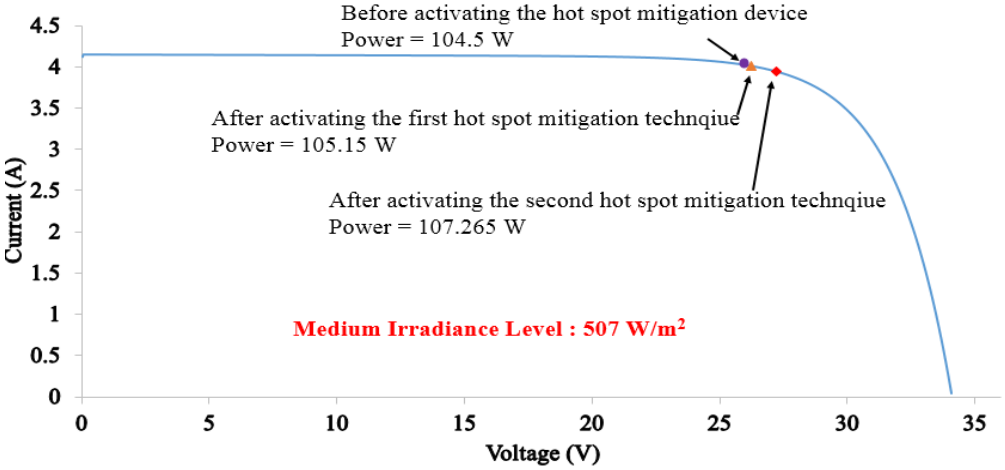

(b)

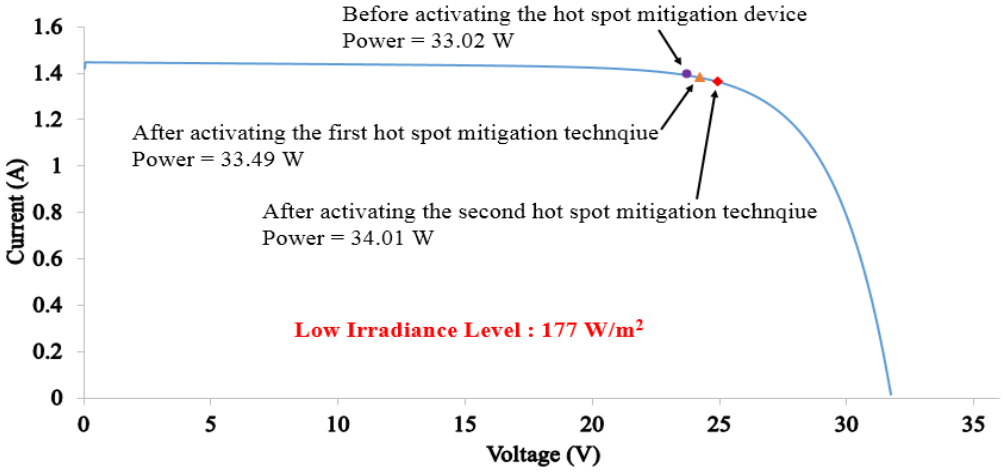

(c)

Figure 7.6 Photovoltaic I-V curve analysis. (a) Before and after considering the hot spot mitigation techniques, G: 840 W/m^2, (b) Before and after considering the hot spot mitigation techniques, G: 507 W/m^2, (c) Before and after considering the hot spot mitigation techniques, G:177 W/m^2

7.1.4.2 PV partial shading condition using the proposed hot spot mitigation techniques

The main purpose of this section is to demonstrate the ability of the proposed hot spot mitigation techniques to increase the output power of a PV module during partial shading conditions affecting a PV module.

In order to test the ability of the proposed hot spot mitigation techniques, another experimental test has been carried out on a PV module with partially shaded solar cell. Figure 7.7 shows an image of the examined PV module under shaded solar cell using opaque paper. The PV module was experimented on under an irradiance level equal to 784 W/m^2.

Figure 7.7 Image of the tested PV module under shaded solar cell using opaque paper object

The first test was carried out using the activation of the first proposed hot spot mitigation technique. Figure 7.8a shows the thermography image of the shaded solar cell before and after the activation of the 1st hot spot mitigation technique.

Before the activation, the temperature of the shaded solar cell is equal to 19.2 ^{0}C. The solar cell temperature decreases to a minimum value of 17.7 ^{0}C after the activation of the hot spot mitigation technique. This decrease in the value of the temperature will guarantee an increase in the output power produced by the PV module. As illustrated in Figure 7.9a, the output power before and after the activation is equal to 171.787 W and 172.508 W respectively. Thus, the total increase in the output power is equal to 0.721 W.

The second test used the activating of the second proposed hot spot mitigation technique. Figure 7.8b shows the thermal images of the shaded solar cell before and after activating the mitigation technique. The difference in the temperature of the shaded solar cell is equal to:

(No mitigation) 21.7 ^{0}C – (After activating the 2nd hot spot mitigation technique) 18.5 ^{0}C = 3.1^{0}C

This decrease in the temperature of the shaded solar cell guarantee an increase of the measured maximum power point of the PV module. Figure 7.9b describes that the total increase in the output measured power is equal to 1.689 W after the activation of the proposed second hot spot mitigation technique.

In conclusion, this section demonstrates that both proposed hot spot mitigation techniques are useful in case a partial shading condition has occurred in the PV module. An enhancement of the temperature and output power of the PV module is guaranteed. The second proposed hot spot mitigation technique shows better performance compared to the 1st technique.

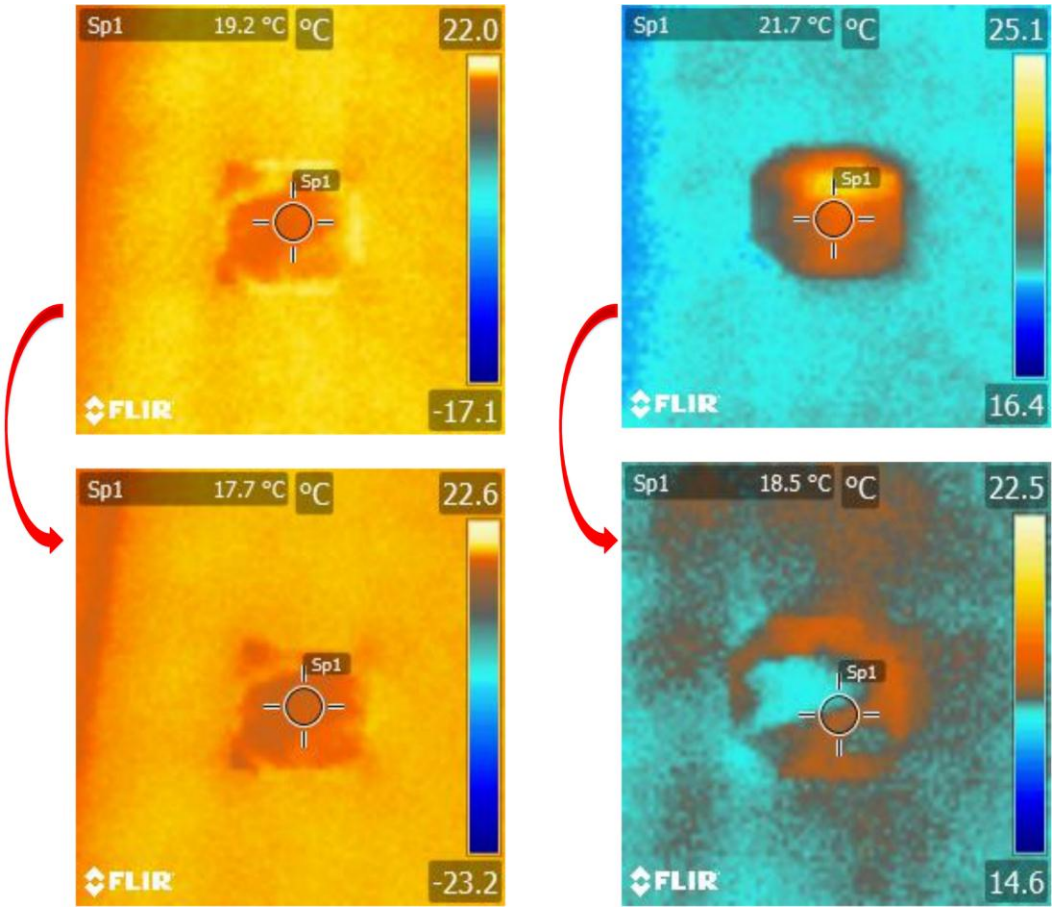

(a) (b)

Figure 7.8 (a) Thermographic images of the shaded PV solar cell before and after the activation of the first hot spot mitigation technique, (b) Thermographic images of the shaded PV solar cell before and after the activation of the second hot spot mitigation technique

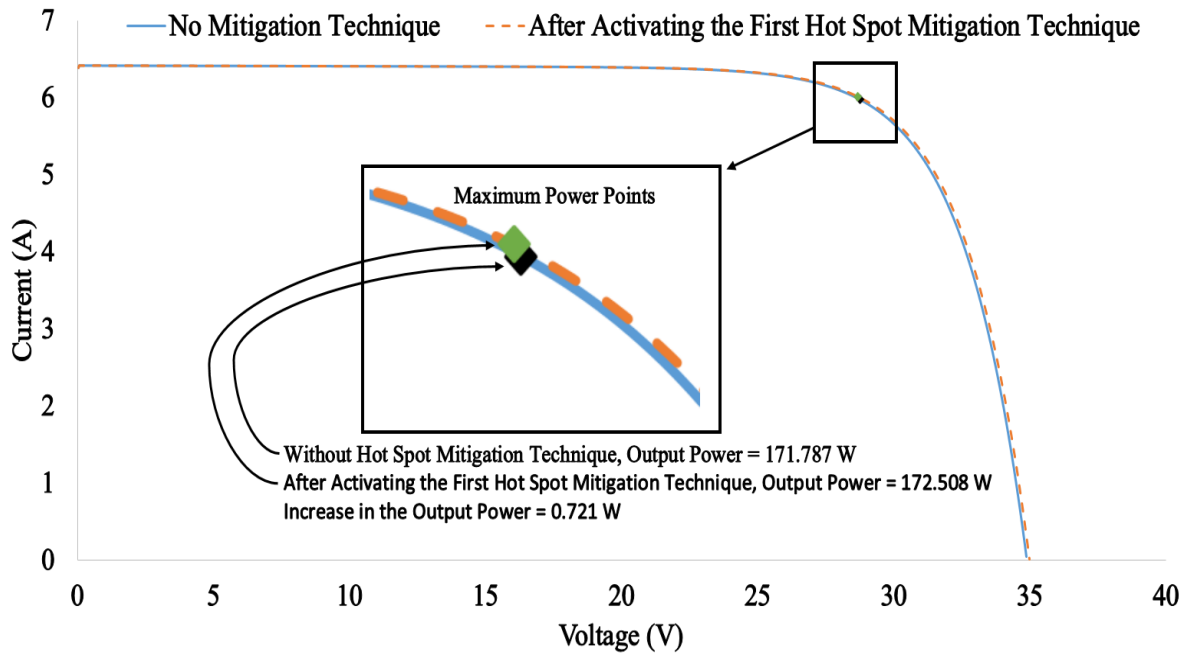

(a)

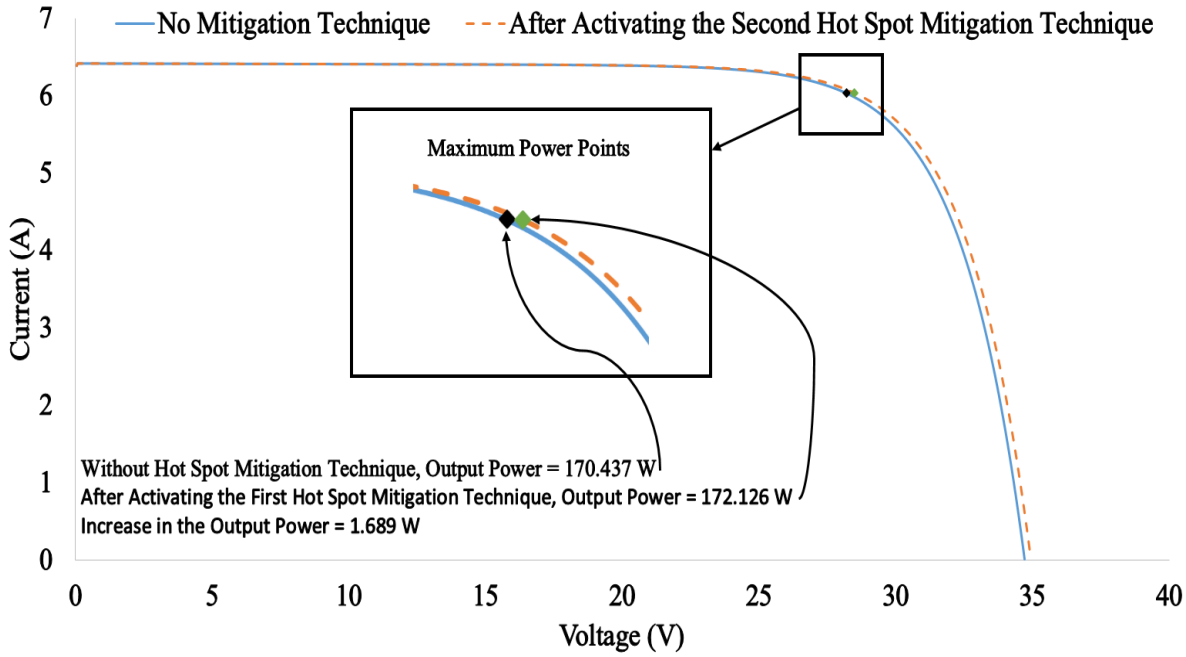

(b)

Figure 7.9 Photovoltaic output I-V curves. (a) Before and after activating the first hot spot mitigation technique, (b) before and after activating the second hot spot mitigation technique

7.1.5 Evaluating the 2nd proposed hot spot mitigation technique using a string of PV modules

In the previous section, the 2nd PV hot spot mitigation technique shows a better enhancement in the PV output power compared to the 1st technique. In this section, the proposed 2nd hot spot protection mitigation technique will be activated while connecting the PV module which is affected by a hot spot in series with two PV modules as shown in Figure 7.10.

Figure 7.10 shows that the I-V curve tracer has three output I-V curves, where I-V curve 1 is associated to the hot spotted PV module. The duration for activating the hot spot mitigation technique is equal to 2 minutes. This short period ensures that the I-V curves and measured output power for each examined PV module do not change rapidly due to the impact of the thermal effect of the PV module which are not directly related to the hot spot itself.

Figure 7.11a shows the I-V curves for each examined PV module with and without the hot spot mitigation technique. As can be seen, the second and third PV module I-V curves which are presented by I-V curve 2 and I-V curve 3, respectively, do not change during the experiment. However, the I-V curve 1 changes after the activation of the hot spot mitigation technique.

The output power after activating the mitigation technique for the hot spotted PV module is equal to 164.39 W, while without activating the hot mitigation technique, the output power is equal to 160.85 W. Figure 7.11b shows the I-V curves with and without the activation of the hot spot mitigation technique for the entire PV string. The total increase of the measured power is equal to 3.57 W.

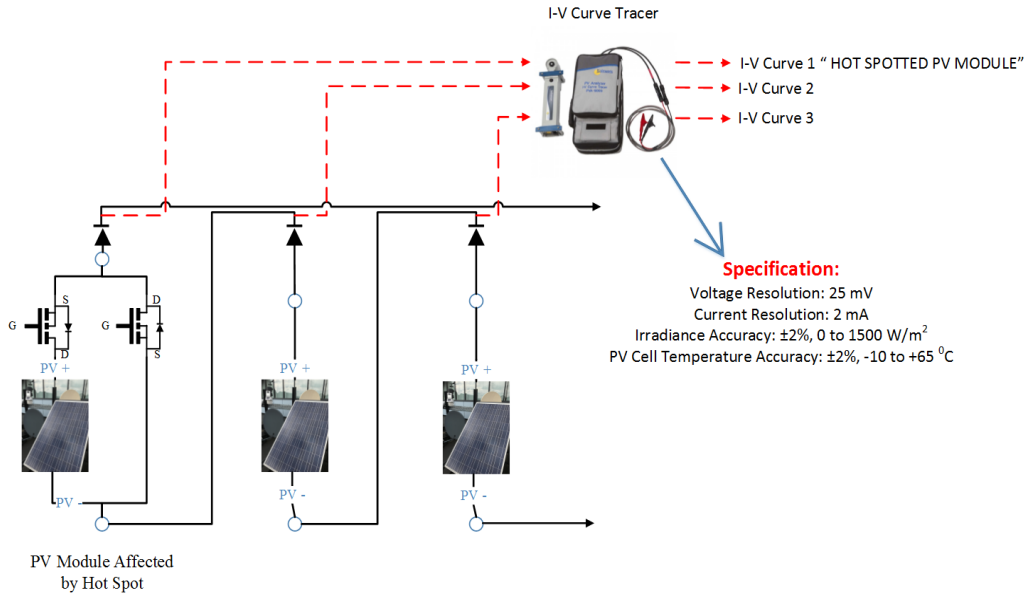

Figure 7.10 Examined PV String Connection

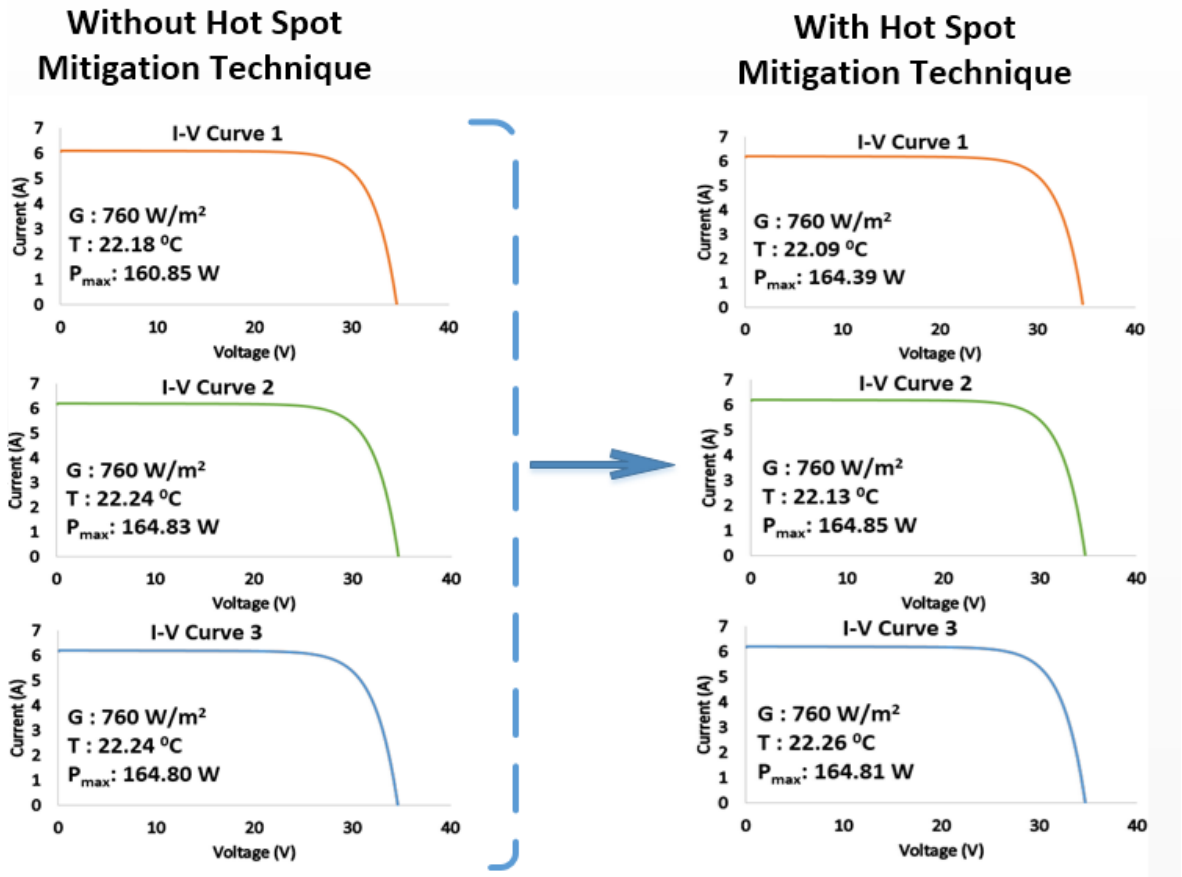

(a)

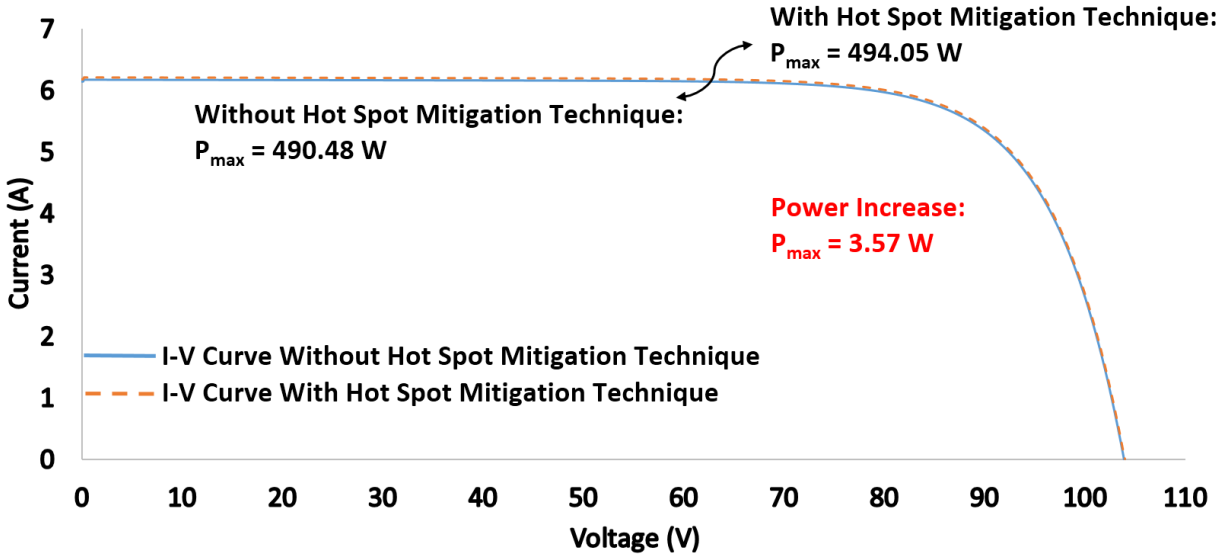

(b)

Figure 7.11 (a) I-V curves for the examined PV modules under solar irradiance 760 W/m^2, (b) I-V curve for the entire PV array with and without the activation of the 2nd hot spot mitigation technique

In fact, MOSFETs add additional series loss due to their operation, this loss is due to "MOSFET Drain to Source ON Resistance ($R_{ds(on)}$)". Therefore, it is extremely important to select for the hot spot mitigation technique a suitable MOSFET which has low $R_{ds(on)}$.

Figure 7.12a show the theoretical circuit diagram of a PV module. The PV module has an extra series resistance due to the MOSFET connection which is described in Figure 7.12b.

In this section, IRFP260NPBF MOSFET Transistor has been used(IRFP260NPBF, 2013) which has an $R_{ds(on)}$ of 40 mΩ. The cost of the MOSFET is approximately £2.15. A real image of the MOSFET is shown in Figure 7.12c.

Due to the additional series loss of the MOSFET, the I-V curve under STC has been conducted for the examined PV module. Figure 7.13 proves that the maximum power without MOSFET under STC is equal to 220 W. However, after the connection of the MOSFET, the maximum power is equal to 219.72W, thus the power loss is 0.28 W per PV module.

This loss is very small compared to the measured power loss of a hot spotted PV module, which is found to be 3.6 W. Therefore, this technique provides a simple and reliable solution to mitigate hot spots in PV plants. In addition, the mitigation technique including MOSFETs can only be added to the hot spotted PV modules. However, it is required to localize the hot spotted PV modules using thermal image technique or any other suitable method.

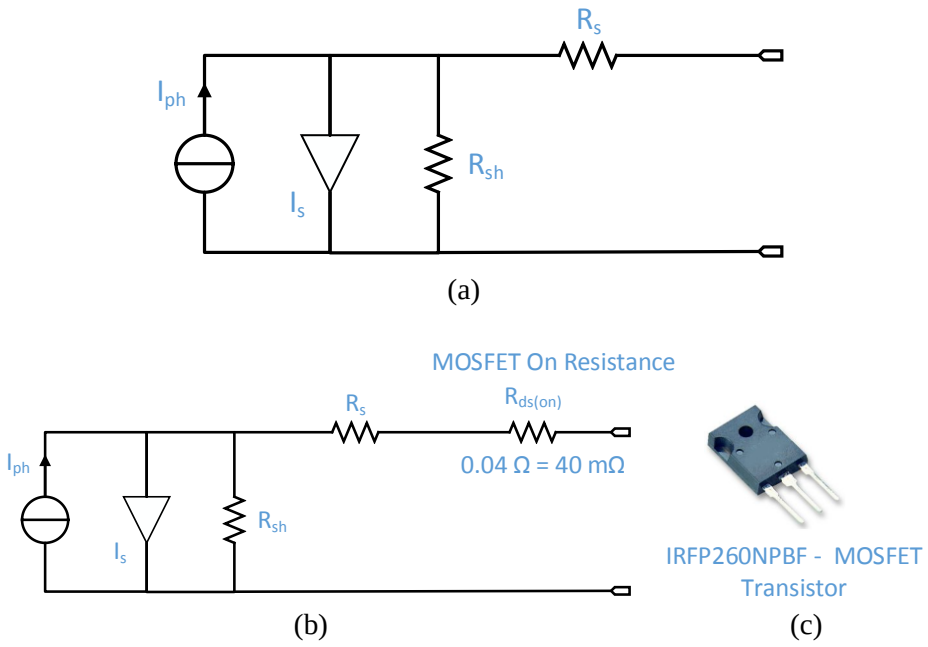

Figure 7.12 (a) PV module theoretical circuit diagram, (b) PV module circuit diagram with hot spot mitigation technique, (c) IRFP260NPBF MOSFET Transistor

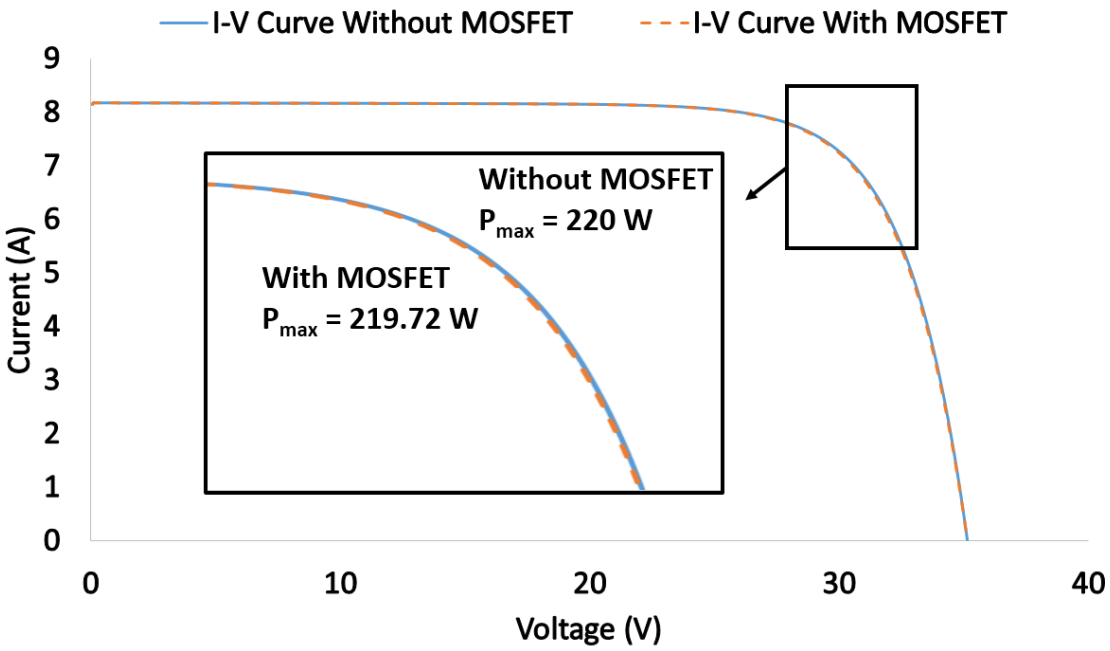

Figure 7.13 PV module I-V curve with and without MOSFET

7.1.6 Evaluating the 2nd proposed hot spot mitigation using a full day experiment

In order to judge the appropriateness of the proposed hot spot mitigation technique, the evaluation of the PV module with and without the mitigation technique was assessed. Figure 7.14a shows the measured PV power. As can be seen, the mitigation technique is activated every 3 hours, each lasts for 2 minutes, and therefore in this period the output measured power generated from the PV module is zero. However, the PV module is back at its optimum power level when switching "off" the hot spot protection mode. The average power without and with the hot spot mitigation technique is equal to 73.6 Wp and 76.4 Wp respectively. Thus, the average increase in the PV power for a period of full day is equal to 2.8 Wp.

Similarly, Figure 7.14b shows the cumulative energy of the PV module with and without the hot spot mitigation technique. The cumulative energy of the PV module without the hot spot mitigation technique equals to 1.12 kWh. However, there is an increase of 0.03 kWh after using the hot spot mitigation technique.

In conclusion, hot spots occur in PV modules due to various reasons such as the fluctuations of the PV temperature, humidity variations, and wind speed. In addition, manufacturing defects result a hot spot in PV solar cells. In this section, it was evident that the proposed hot spot mitigation technique enhanced the overall performance of a PV module with a total increase in the output energy 0.03 kWh per day (estimated yearly increase 0.03 x 365 = 10.95 kWh).

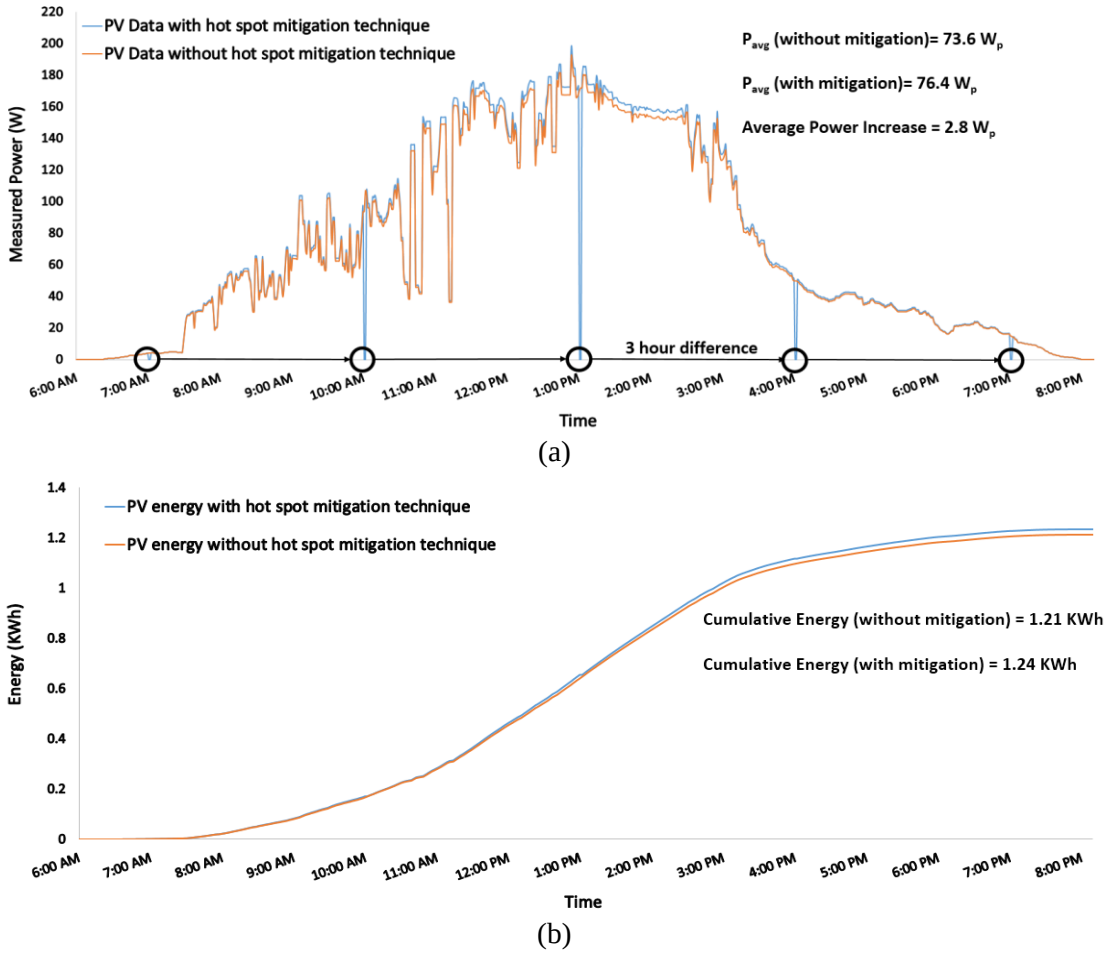

Figure 7.14 (a) Measured PV output power, (b) PV cumulative energy

7.2 PV micro cracks

This section will focus on the impact of PV micro cracks on the performance of PV modules. Both tested PV plants (shown in chapter 3) will be used to inspect micro cracks and the degradation impact on the output power of PV modules. The first PV plant consists of 10 PV modules with an optimum power 200 W_p. The second PV plant consists of 35 PV modules with 130 W_p each. Parts of the examined PV plants are shown in Figures 7.15a and 7.15b.

As presented in Figure 7.15c, a controlling unit is designed to allow the user to connect any PV module to a FLEXmax 80 MPPT. In order to facilitate a real-time monitoring for each PV module, Vantage Pro monitoring unit is used to receive the global solar irradiance measured by Davis weather station which includes pyranometer. Hub 4 communication manager is used to facilitate acquisition of modules temperature using Davis external temperature sensor, and the electrical data for each photovoltaic module. LabVIEW software is used to implement the data logging and monitoring functions of the examined PV modules.

(a)

(b)

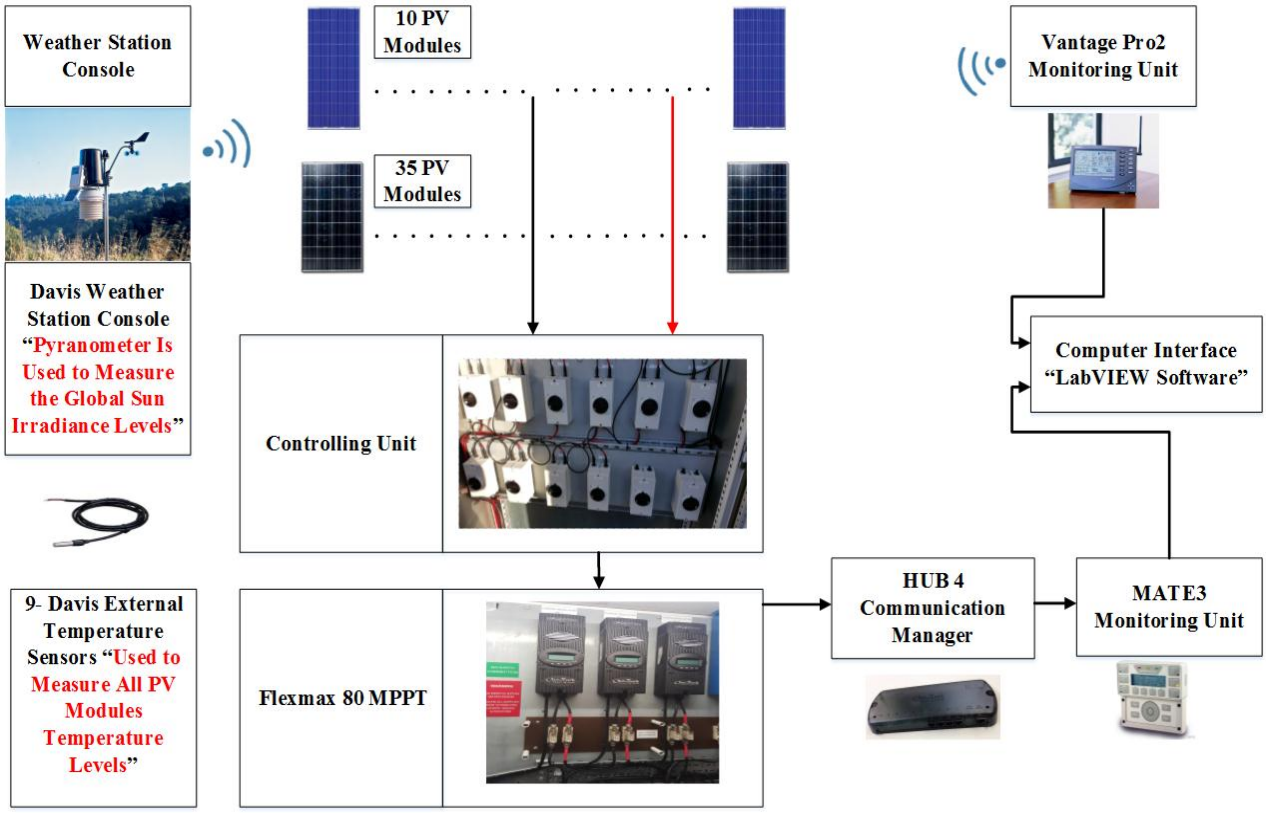

(c)

Figure 7.15 (a) 10 PV modules (SMT 6 (60) P); (b) 35 PV Modules (KC130 GHT-2); (c) Monitoring the examined PV systems using LabVIEW Software

7.2.1 Electroluminescence setup and PV modules cracks

The electroluminescence (EL) setup is shown in Figure 7.16. The system is comprised of a light-tight black-box with housed inside is a digital camera and a sample holder. The digital camera is equipped with a standard F-mount 18–55 mm lens. To allow for detection in the near infrared, the IR filter was removed and replaced with a full spectrum window of equal optical path length.

To capture PV micro cracks, Nikon D40 camera was used, but in principle any digital camera with similar grade CCD or CMOS sensor and where the IR filter can be removed would serve the purpose. The bias was applied and the resultant current and the voltage are measured by a voltage and current sensors which are connected to the personal computer (PC).

In order to reduce noise and increase the accuracy, all EL images are processed by removing background noise and erroneous pixels. Firstly a background image is taken under the same conditions as the EL images but without forward biasing the cell. This background image is subtracted from each EL image in order to reduce noise. The images are cropped to the appropriate size and in the case of the high resolution imaging system cell images are compiled together to form an image of the entire module. Additionally, to increase the accuracy and the vision of the EL image, each PV module cell is captured separately because the EL image was captured using low cost camera – this is the only limitation in the used EL imaging setup.

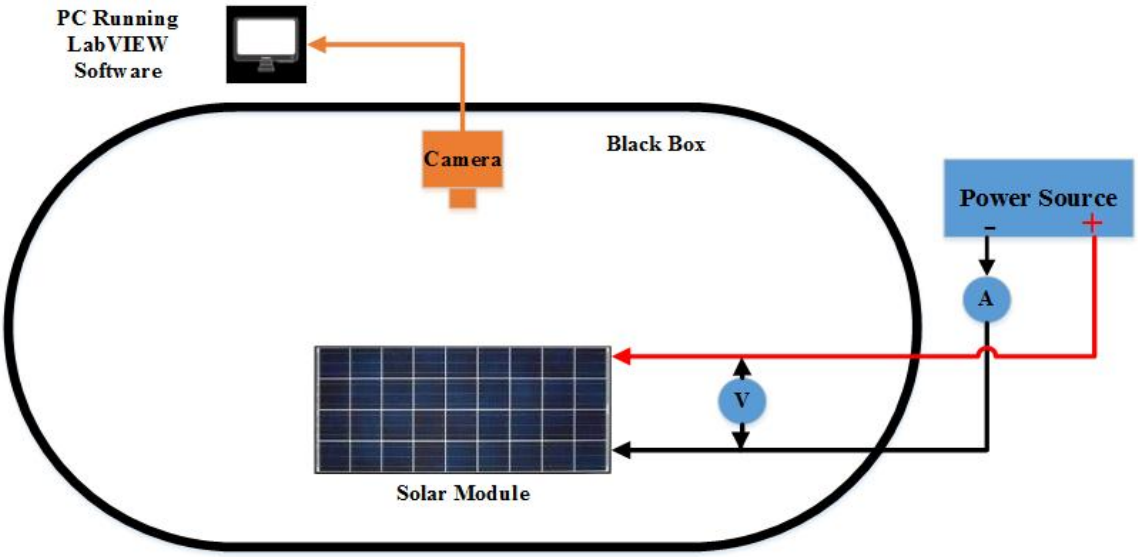

Figure 7.16 Electroluminescence experimental setup

To identify the bias voltage and the current which must be used to examine the PV module, the PV module main electrical characteristics must be identified. For example, the electrical characteristics for PV modules of PV plant B are shown in Table 3.1.

The PV cells of the examined PV module was biased at various levels. The current bias ranges from a forward current of about 10% of the module I_{sc} to just over 110% I_{sc}.

Figure 7.17 show EL image of a single PV cell at different bias levels. As can be seen, at low current levels, the solar cell has much lower intensity compared to a high bias level. However, the solar cell features become more prominent at higher bias levels which could potentially be related to the series resistance across the PV cells.

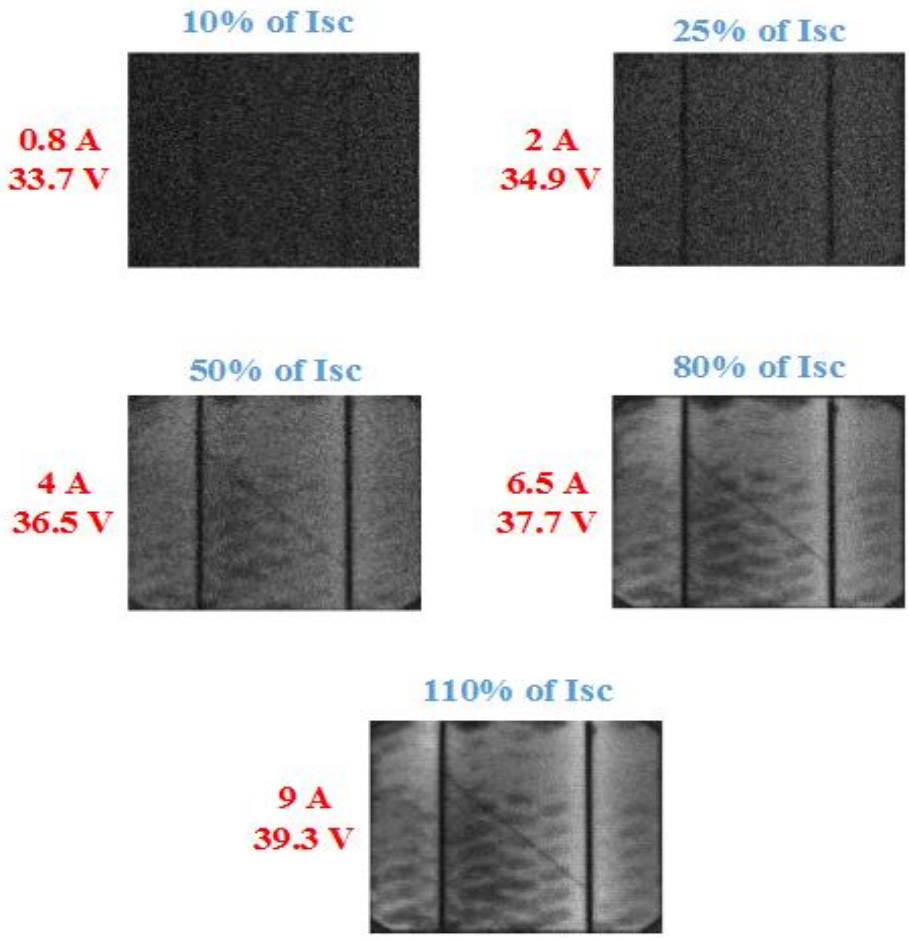

Figure 7.17 EL image of a single PV cell at different bias levels

Broken cells are sorted according to the type of crack. Figure 7.18 shows all examined crack types which are classified as the following: diagonal (+45^0), diagonal (- 45^0), parallel to busbars, perpendicular to busbars, Multiple directions crack.

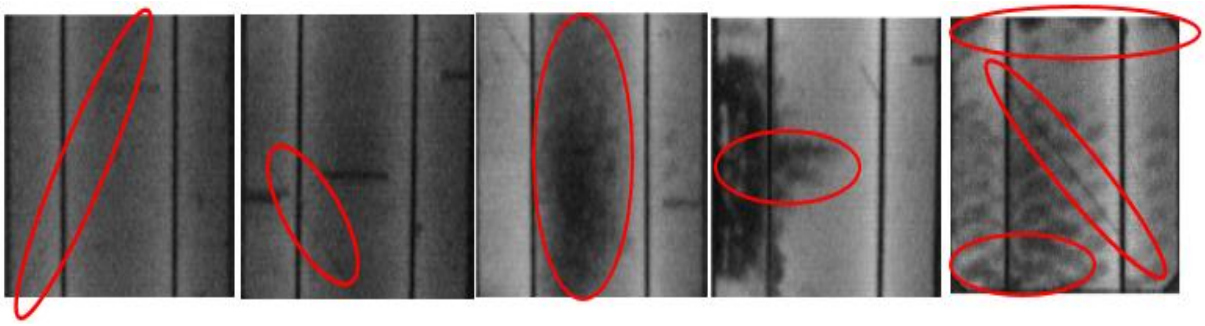

(a) (b) (c) (d) (e)

Figure 7.18 EL images for various PV cracks. (a) Diagonal crack (+45^0); (b) Diagonal crack (-45^0); (c) Parallel to busbars crack; (d) Perpendicular to busbars crack; (e) Multiple directions crack

Broken cells are sorted according to the type of the crack. Based on the EL images taken from 45 different PV modules, it was found that the distribution for a cell to be cracked is shown in Figure 7.19.

Only 15% of the total PV modules have no cracks. However, 84% of the PV modules contains at least one type of the crack: diagonal (26%), parallel to busbars (20%), and perpendicular to busbars (8%) or multiple directions crack (28%).

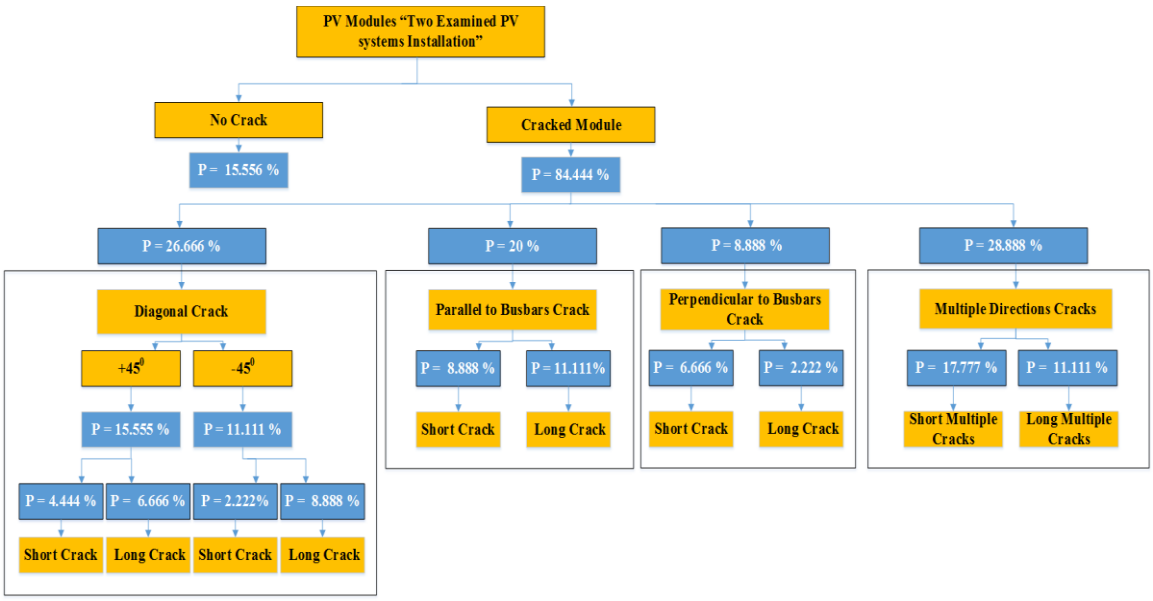

Figure 7.19 Crack type distribution among both examined PV systems (45 PV Modules)

7.2.2 Statistical analysis approach

A statistical analysis approach is used to determine whether the PV crack has a significant impact on the total generated output power performance or not. Two statistical methods are used, T-test and F-test. The first method (T-test) is used to compare the simulated theoretical power with the measured PV output power. T-test can be evaluated using (7.1) where $\overline{x}$ is the mean of the samples, μ is the population mean, n is the sample size and SD is the standard deviation of the entire data (Miller & Miller, 2005).

The confidence interval for all measured samples is equal to 99%. Statistically speaking, the crack does not have a significant impact on the output power performance if the T-test value is significant, which means that the T-test value is less than or equal to 2.58 as shown in Table 7.2 (Miller & Miller, 2005).

If the T-test value is not significant, another statistical method/layer is used to compare the output measured power from the cracked PV module with a PV module that has 0% of cracks. This layer is used to confirm that the output generated power of the cracked PV module has a significant impact (Real Damage) on the total generated output power performance of the examined photovoltaic module.

The overall statistical approach is shown in Figure 7.20. The F-test is calculated using (7.2). The explained variance is calculated using between groups mean square value, the unexplained variance is calculated using within groups mean square value.

Table 7.3 illustrates the expected output results from F-test using 99% (P=0.01) confidence interval. In this work, an infinite number of samples (total measured samples > 120) is used to determine whether the F-test value is significant (F-test ≤ 6.635) or not significant (F-test > 6.635).

$$T = \frac{(\overline{x} - \mu)\sqrt{n}}{SD} \tag{7.1}$$

$$F = \frac{\text{Explained Variance}}{\text{Unexplained Variance}} \tag{7.2}$$

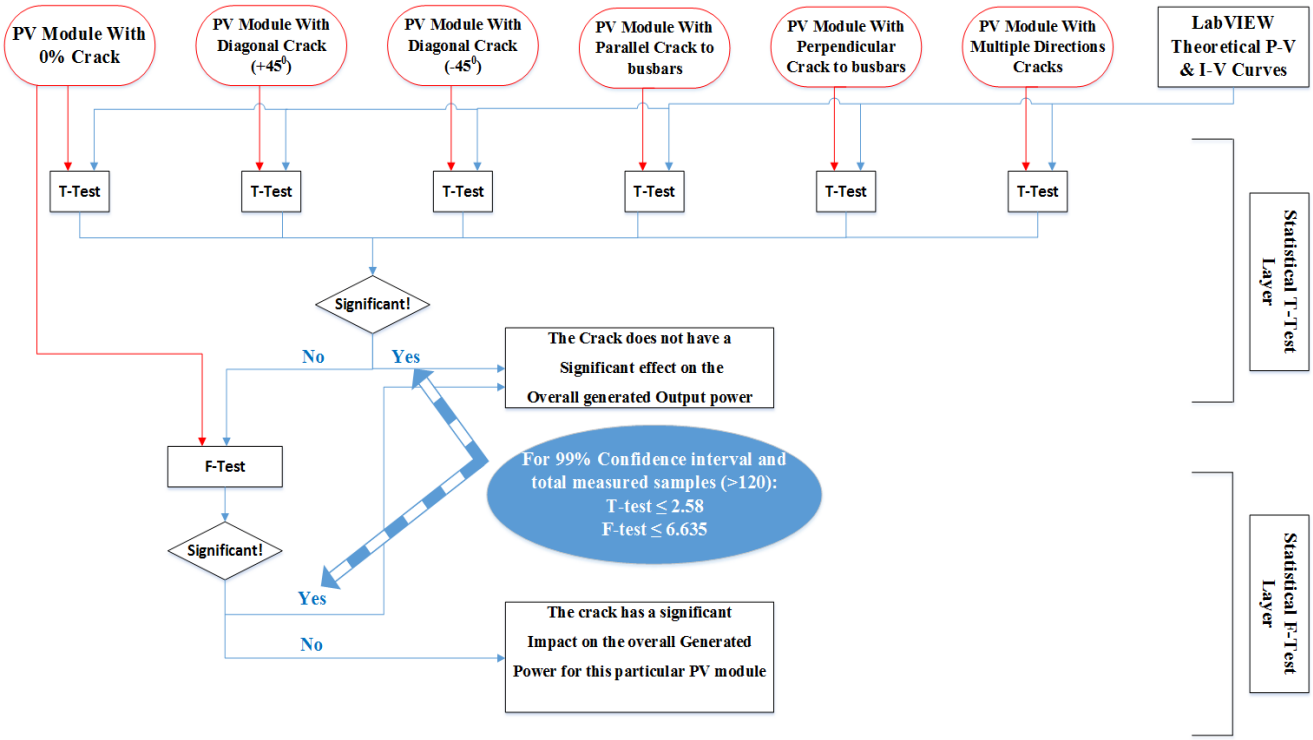

Figure 7.20 Statistical approach used to identify whether the crack type has a significant impact on the output power performance of a photovoltaic module

Table 7.3 Statistical T-Test confidence interval (Miller & Miller, 2005)

Value of t for Confidence Interval of Critical Value |t| for P Values of Number of Degrees of Freedom	90 % (P=0.1)	95% (P=0.05)	99% (P=0.01)
1	6.31	12.71	63.66
20	1.72	2.09	2.85
50	1.68	2.01	2.68
∞	1.64	1.96	2.58

Table 7.2 Statistical F-Test critical values for 99% confidence interval (p=0.01) (Miller & Miller, 2005)

Degree of Freedom (Measured Samples)	Output F-test For a Significant Results
1	4052.181
120	4.787
∞	6.635

7.2.3 Results

According to the statistical approach explained previously in Figure 7.20, T-test and F-test methods are significant based on a threshold values. Therefore, I have divided all crack-types into two main categories, Short: crack effects one solar cell in a PV module; Long: crack effects two or more solar cells in a PV module.

Furthermore, fitted line regression is used for the entire measured PV crack-type data. A fitted regression represents a mathematical regression equation for the PV measured data. I have selected the fitted regression lines to illustrate the relationship between a predictor variable (Measured PV Power) and a response variable (Irradiance Level) and to evaluate whether the model fits the data.

If the measured PV power data is very close to the fitted line regression model, there is a significant relationship between the predictor with the response variable

7.2.3.1 Diagonal cracks

The measured data which has been extracted from both diagonal crack categories indicate that there is a huge similarity in the measured output power performance for all examined PV modules containing $+45^0$ and -45^0 diagonal crack. Therefore, both categories are classified as one.

Using the statistical analysis approach, the result of the T-test values for all examined PV modules (12 PV modules) containing diagonal cracks are shown in Table 7.4. Since the T-test value for a diagonal crack affecting 1 or 2 solar cells is less than 99% of the confidence interval threshold (2.58), the output power performance for the PV module is statistically not significant: No evidence for a real damage in the PV module. The F-test for a diagonal crack affecting 1 or 2 solar cells is equal to 4.55 and 5.67 respectively. The mathematical expressions for the fitted line regression are illustrated in Table 7.4.

Table 7.4 Diagonal cracks performance indicators

Diagonal Crack	Number of Effected Solar Cells	Approximate Area Broken (mm)	T-test Value	Significant/Not Significant Effect on the PV Power Performance	Fitted Line Regression Equation
Short $+45^0$ OR Short -45^0	1	1 mm^2 – 83 mm^2	0.40 - 0.66	**Not Significant**	$P_{TH} = 0.1424 + 1.001\ P_{Meas}$
Long $+45^0$ OR Long -45^0	2	85.85 mm^2 – 169.7 mm^2	1.22 – 1.86	**Not Significant**	$P_{TH} = 0.2875 + 1.003\ P_{Meas}$
	3	172.7 mm^2 - 256.6 mm^2	2.51 - 2.71	Significant	$P_{TH} = 0.5125 + 1.006\ P_{Meas}$
	4	257. 5 mm^2 - 344.4 mm^2	2.65 – 2.70	Significant	$P_{TH} = 0.7034 + 1.008\ P_{Meas}$
	5	345.1 mm^2 – 424.3 mm^2	3.12 – 3.35	Significant	$P_{TH} = 1.151 + 1.013\ P_{Meas}$

Measured data for a full day were used to estimate the output power performance for a diagonal crack which affects 1 and 5 solar cells; the results are presented in Figure 7.21a. The theoretical simulated output power, which is calculated using LabVIEW software has a standard deviation equals to 61.46 which is very close to the standard deviation for a diagonal crack that affects 1 solar cell (SD=61.38).

However, a diagonal crack that affects 5 solar cells has a huge reduction in the output power performance of the PV module where the standard deviation is equal to 60.99.

Figure 7.21b shows the power ratio for the examined diagonal cracks effects 1, 2, 3, 4 and 5 solar cells. The power ratio of the PV module affected by diagonal cracks can be classified as the following:

- Diagonal crack affects 1 solar cell = 99.64%
- Diagonal crack affects 2 solar cells = 99.23%
- Diagonal crack affects 3 solar cells = 98.61%
- Diagonal crack affects 4 solar cells = 98.09%
- Diagonal crack affects 5 solar cells = 96.83%

As can be seen, more diagonal cracks in the PV module resulting more degradation in the generated output power.

The power ratio is estimated using (7.3).

$$\text{Power ratio} = \frac{\text{Meaured Output Power}}{\text{Theoretical Output Power}} \times 100\% \qquad (7.3)$$

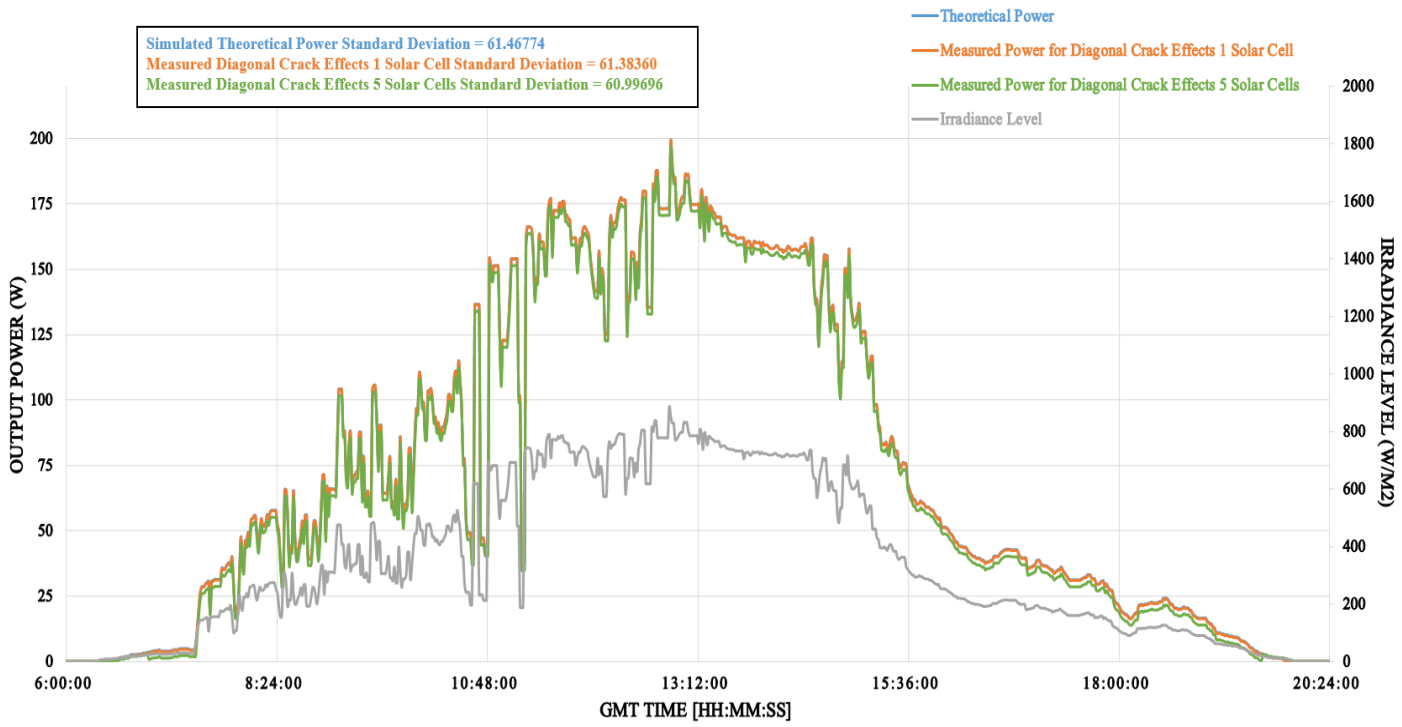

(a)

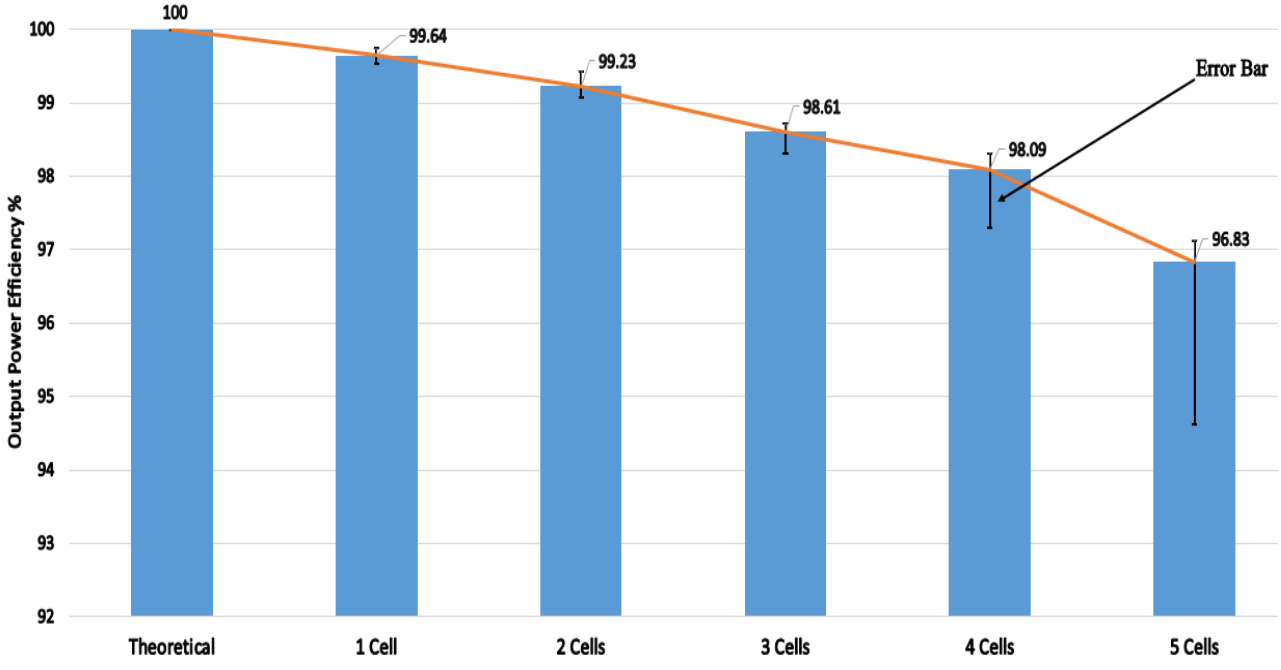

(b)

Figure 7.21 (a) real-time long-term measured data for a diagonal crack affecting 1 and 5 solar cells, (b) Power ratio for a diagonal cracks affecting 1, 2, 3, 4 and 5 PV solar cells

7.2.3.2 Parallel to busbars cracks

As shown previously in Figure 7.19, parallel to the busbars cracks have a percentage of occurrence 20% (9 PV modules out of 45 examined PV modules) and they are listed as the following:

- 8% (4 PV modules): Short Crack Effect
- 11% (5 PV modules): Long Crack Effect

Not all cracks parallel to busbars cracks have a significant impact/reduction on the output power performance of the PV modules. As shown in Table 7.5, parallel to busbars cracks effecting one solar cell statistically indicates that there is no real damage in the PV module. The result is confirmed by the T-test value which is less than the threshold value 2.58.

Parallel to busbars cracks affecting two solar cells with approximate broken area less than 82mm^2 have no significant impact on the amount of power generated by the PV module. Additionally, Table 7.5 shows the mathematical equations for the measured fitted line regression which describes the relationship between the theoretical and measured output power.

Figure 7.22a presents the measured data for a parallel to busbars crack affecting one and four solar cells. The standard deviation for the theoretical simulated power is 62.01 which is very close to the standard deviation for a parallel to busbars crack affects one solar cell (61.8).

However, parallel to busbars crack affecting five solar cells has a huge reduction in the output power performance of the PV module while the standard deviation is equal to 61.09.

Figure 7.22b shows the power ratio for the examined parallel to busbars cracks effecting 1, 2, 3 and 4 solar cells. The reduction of power estimated for a parallel to busbars crack effects one solar cell is between 0.75% - 0.97%. However, the estimated reduction of power for a parallel to busbars crack effecting three and four solar cells is between 2.39% - 3.0% and 3.67% - 4.55% respectively.

Table 7.5 Parallel to busbars cracks performance indicators

Crack Type		Number of Affected Solar Cells	Approximate Area Broken (mm)	T-test Value	Significant/Not Significant Effect on the PV Power Performance	Fitted Line Regression Equation
Parallel To Busbars	Short	1	1 mm^2 – 59.2 mm^2	0.78 – 1.13	**Not Significant**	$P_{TH} = 0.3002 + 1.001\ P_{Meas}$
	Long	2	63 mm^2 – 81 mm^2	1.42 – 1.87	**Not Significant**	$P_{TH} = 0.3990 + 1.004\ P_{Meas}$
			82 mm^2 – 121 mm^2	2.62 – 2.74	Significant	$P_{TH} = 0.6923 + 1.008\ P_{Meas}$
		3	122 mm^2 – 177 mm^2	4.04 – 4.81	Significant	$P_{TH} = 0.9218 + 1.010\ P_{Meas}$
		4	177.3 mm^2 – 239.7 mm^2	4.39 – 5.66	Significant	$P_{TH} = 1.3590 + 1.016\ P_{Meas}$

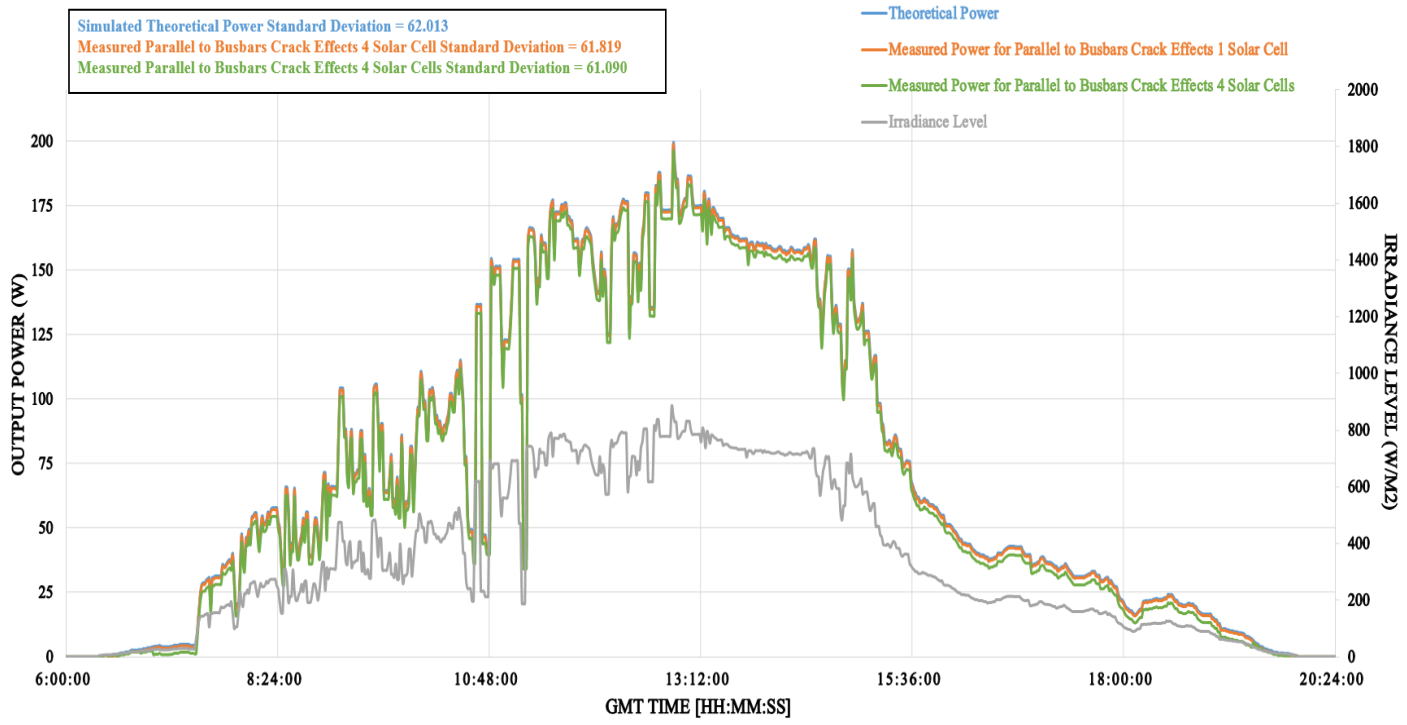

(a)

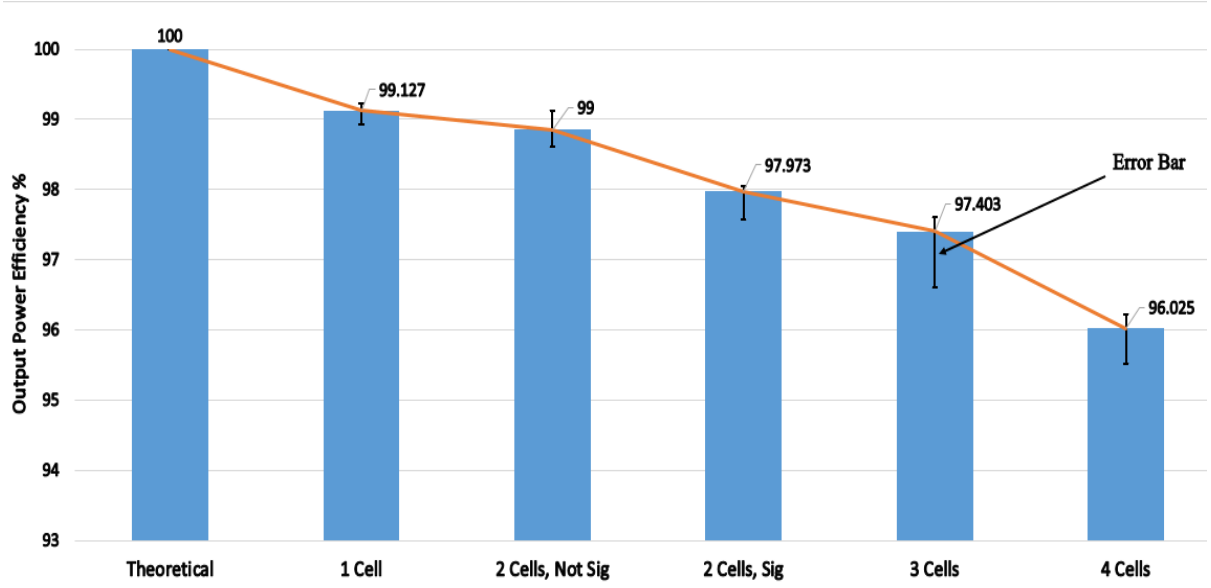

(b)

Figure 7.22 (a) Real-time long-term measured data for a parallel to busbars crack affecting 1 and 4 solar cells, (b) Power ratio for parallel to busbars crack affecting 1, 2, 3 and 4 PV solar cells

7.2.3.3 Perpendicular to busbars cracks

Perpendicular to busbars cracks usually do not occur in PV modules. In the results obtained from the examined PV modules, only 4 PV modules from 45 have been classified as having a perpendicular to busbars cracks PV modules.

The results of the examined PV modules are shown in Table 7.6. Perpendicular to busbars cracks affecting 1, 2, and 3 busbars statistically considered as non-significant PV micro cracks. Because the T-test is below the threshold value.

The output power measured for a perpendicular to busbars cracks affecting one and four solar cells is shown in Figure 7.23a. The difference between the theoretical standard deviation and a perpendicular to busbars cracks affects 4 solar cells is equal to 1.014.

Figure 7.23b shows the measured power ratio for a perpendicular to busbars affects 1, 2, 3, and 4 solar cells (1-8 Busbars). The results show that perpendicular to busbars cracks affects 8 busbars has a largest reduction in power ratio is equal to 95.591%.

However, the power ratio for perpendicular to busbars cracks affects 1, 2, 3, and 4 busbars at least equal to 98%.

Table 7.6 Perpendicular to busbars cracks performance indicators

Crack Type		Number of Effected Solar Cells	Number of Effected Busbars	Approximate Area Broken (mm)	T-test Value	Significant/Not Significant Effect on the PV Power Performance	Fitted Line Regression Equation
Perpendicular To Busbars	Short	1	1	1 mm^2 – 16.2 mm^2	0.65 – 0.82	**Not Significant**	$P_{TH} = 0.0927 + 1.001\ P_{Meas}$
			2	16.3 mm^2 – 60 mm^2	0.92 – 1.31	**Not Significant**	$P_{TH} = 0.1524 + 1.002\ P_{Meas}$
	Long	2	3	61.3 mm^2 – 78.5 mm^2	1.43 – 1.96	**Not Significant**	$P_{TH} = 0.3604 + 1.004\ P_{Meas}$
			4	79.4 mm^2 – 120 mm^2	2.52 – 2.77	Significant	$P_{TH} = 0.4678 + 1.005\ P_{Meas}$
		3	5	120.5 mm^2 – 137.4 mm^2	2.83 – 2.94	Significant	$P_{TH} = 0.7397 + 1.008\ P_{Meas}$
			6	138 mm^2 – 179.8 mm^2	2.79 – 3.11	Significant	$P_{TH} = 0.9265 + 1.010\ P_{Meas}$
		4	7	181.5 mm^2 – 195 mm^2	3.02 – 3.27	Significant	$P_{TH} = 1.0790 + 1.012\ P_{Meas}$
			8	196.2 mm^2 – 240.2 mm^2	3.10 – 3.55	Significant	$P_{TH} = 1.4590 + 1.018\ P_{Meas}$

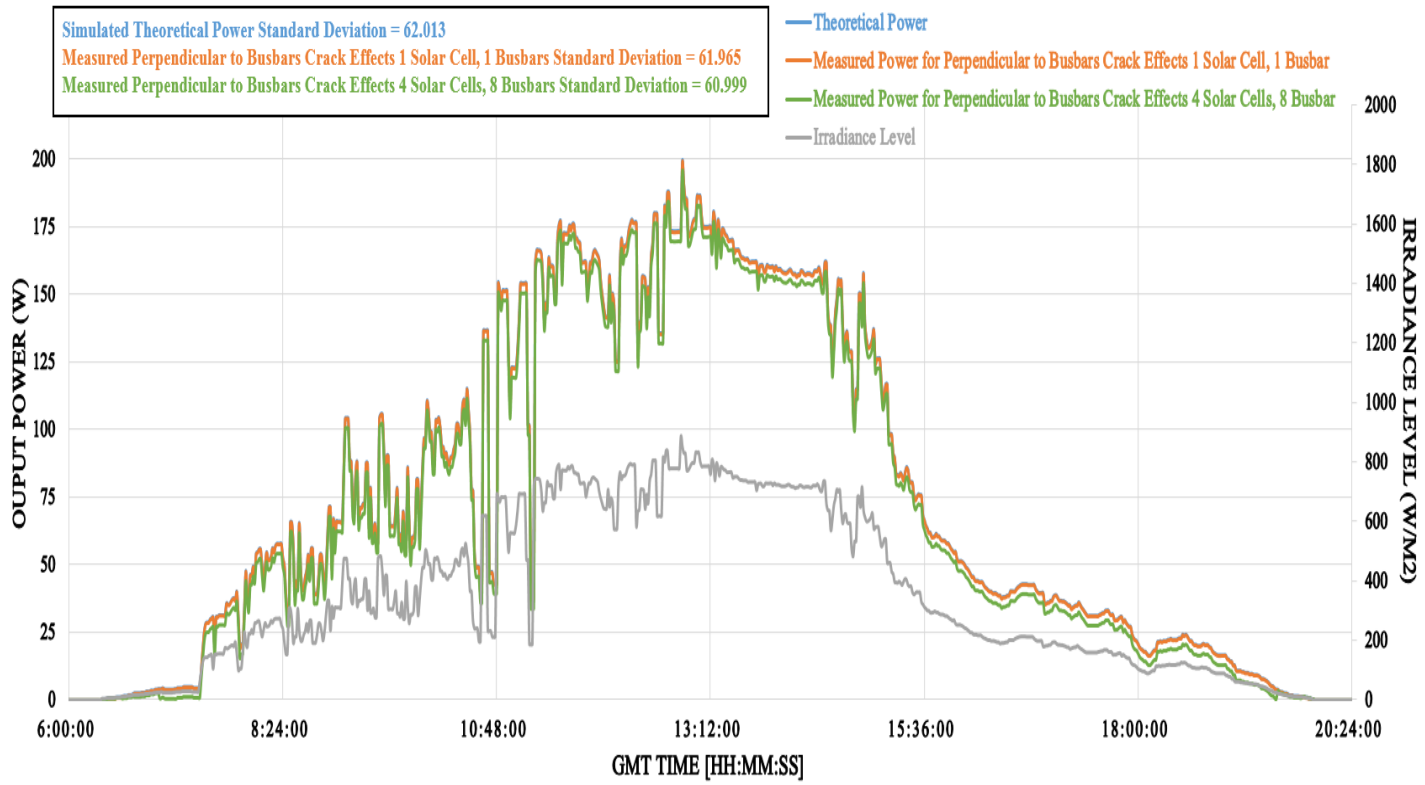

(a)

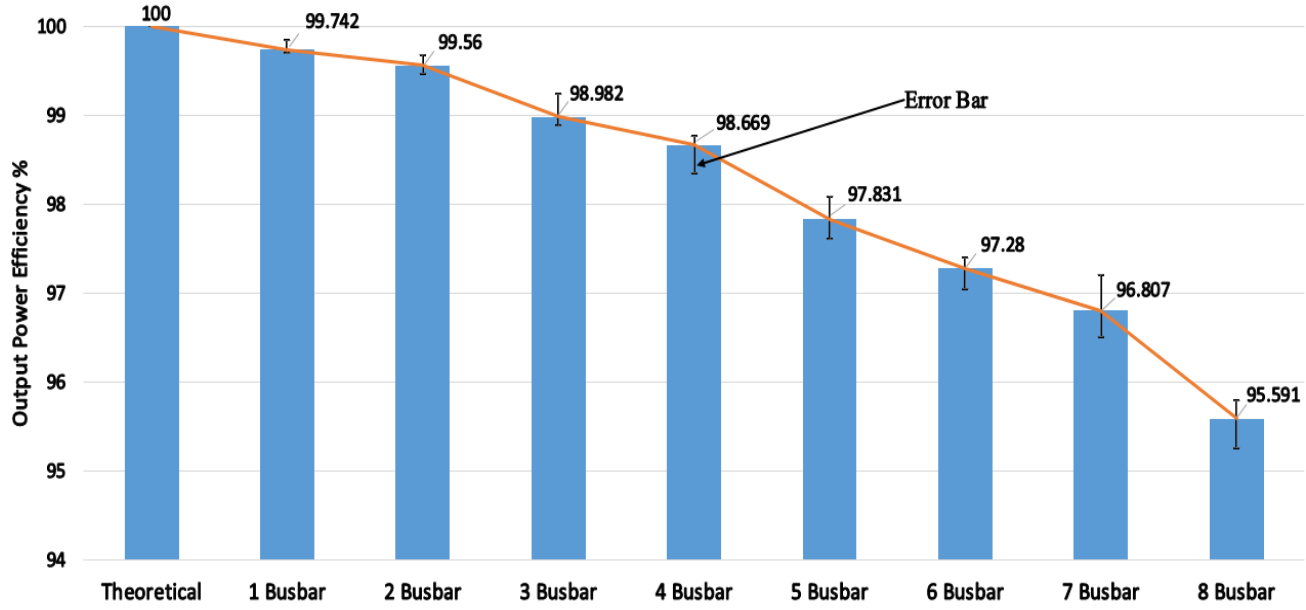

(b)

Figure 7.23 (a) Real-time long-term measured data for a perpendicular to busbars crack affecting 1 and 4 solar cells, (b) Power ratio for a perpendicular to busbars crack affecting 1, 2, 3 and 4 (1-8 busbars) pv solar cells

7.2.3.4 Multiple directions cracks

Multiple directions cracks have the highest degradation rates in the measured output power comparing to all other PV micro cracks-types.

The results of the PV modules affected by multiple directions cracks are shown in Table 7.7. Multiple directions cracks affecting 1 solar cell with approximate area broken between 1 to 45 mm^2 is statistically not significant, since the T-test is between 2.06 and 2.44.

However, all other multiple directions cracks affects PV solar cells are do have a significant degradation on the output power of the PV module.

Figure 7.24a shows the output power for three different PV modules affected by multiple directions cracks. As can be seen, the output power measured for a PV module affected by multiple directions cracks on 5 solar cells has the highest loss compared to all other measured data.

Figure 7.24b summaries the power ratio for the multiple directions cracks affecting 1, 2, 3, 4, and 5 solar cells. The power ratio decreases as the number of affected PV solar cells increases.

The highest degradation is when the power ratio is equal to 92.19% obtained for multiple directions cracks affecting 5 solar cells.

Table 7.7 Multiple directions cracks performance indicators

	Number of Affected Solar Cells	Approximate Area Broken (mm)	T-test Value	Significant/Not Significant Effect on the PV Power Performance	Fitted Line Regression Equation
Multiple Directions Crack	1	1 mm^2 – 45 mm^2	2.06 – 2.44	**Not Significant**	$P_{TH} = 0.3679 + 1.004\ P_{Meas}$
		46.2 mm^2 – 1000 mm^2	2.68 – 2.88	Significant	$P_{TH} = 0.5330 + 1.005\ P_{Meas}$
	2	100 mm^2 – 3700 mm^2	3.25 – 3.33	Significant	$P_{TH} = 1.028 + 1.012\ P_{Meas}$
	3	170 mm^2 – 5000 mm^2	4.70 – 4.88	Significant	$P_{TH} = 1.554 + 1.019\ P_{Meas}$
	4	223 mm^2 – 8200 mm^2	6.17 – 6.31	Significant	$P_{TH} = 2.015 + 1.027\ P_{Meas}$
	5	400 mm^2 – 9800 mm^2	7.30 – 7.52	Significant	$P_{TH} = 2.577 + 1.033\ P_{Meas}$

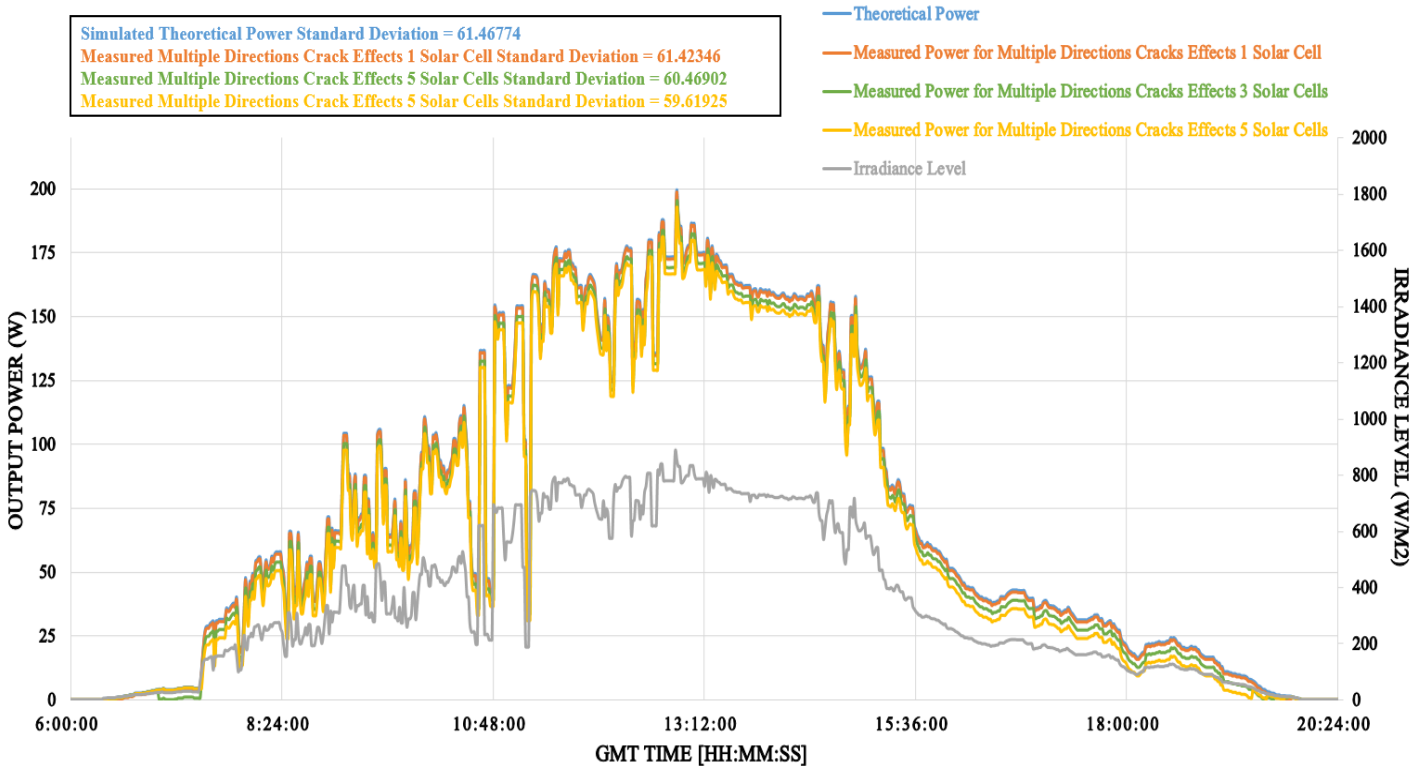

(a)

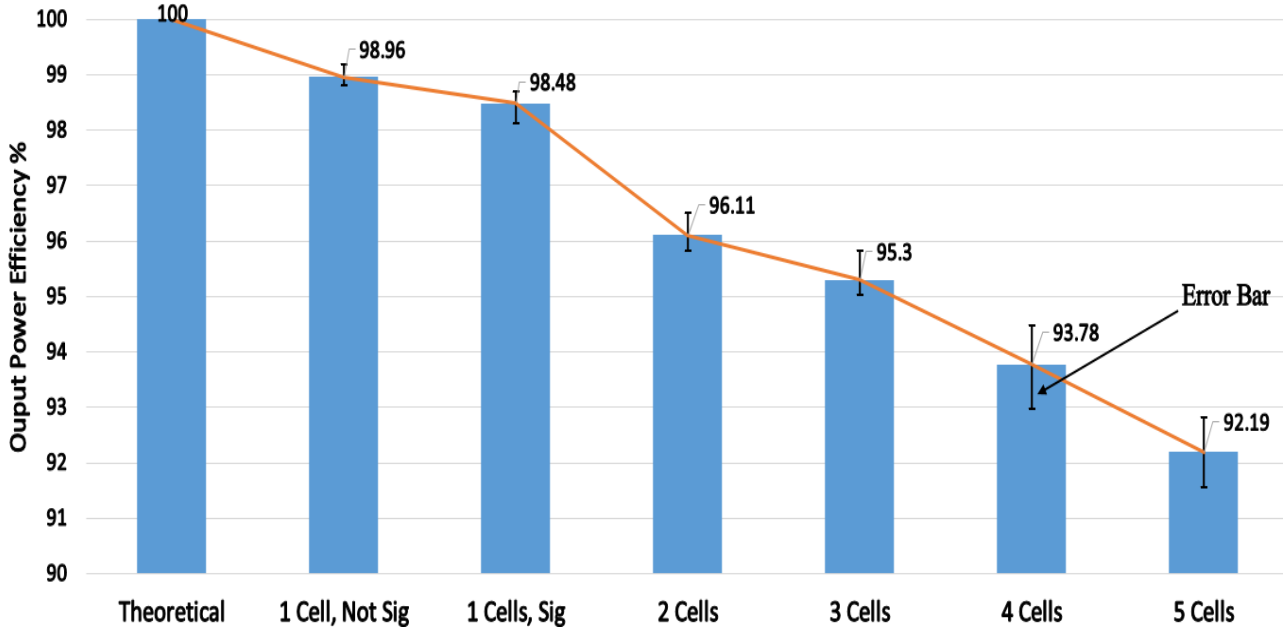

(b)

Figure 7.24 (a) Real-time long-term measured data for a multiple directions cracks affecting 1, 3 and 5 solar cells; (b) Power ratio for multiple directions cracks affecting 1, 2, 3, 4 and 5 PV solar cells

7.2.4 Discussion

The observed modules have 38 PV modules with various crack-types. The probability of occurrence for each crack-type is previously shown in Figure 7.19. Before considering the statistical analysis approach, it is hypothetically true to say that 84.4% have a significant impact on the output power performance.

However, the statistical approach has confirmed that this is incorrect, because only 60% have a significant impact on the output power performance for all examined PV modules. The results are summarized in Figure 7.25.

This result can be investigated further more by applying the same statistical approach to various PV systems. The only difference might be the confidence interval limits (99%, 95% and 90%) due to the various accuracy rates for the instrumentation used in the PV systems such as the voltage, current and temperature sensors.

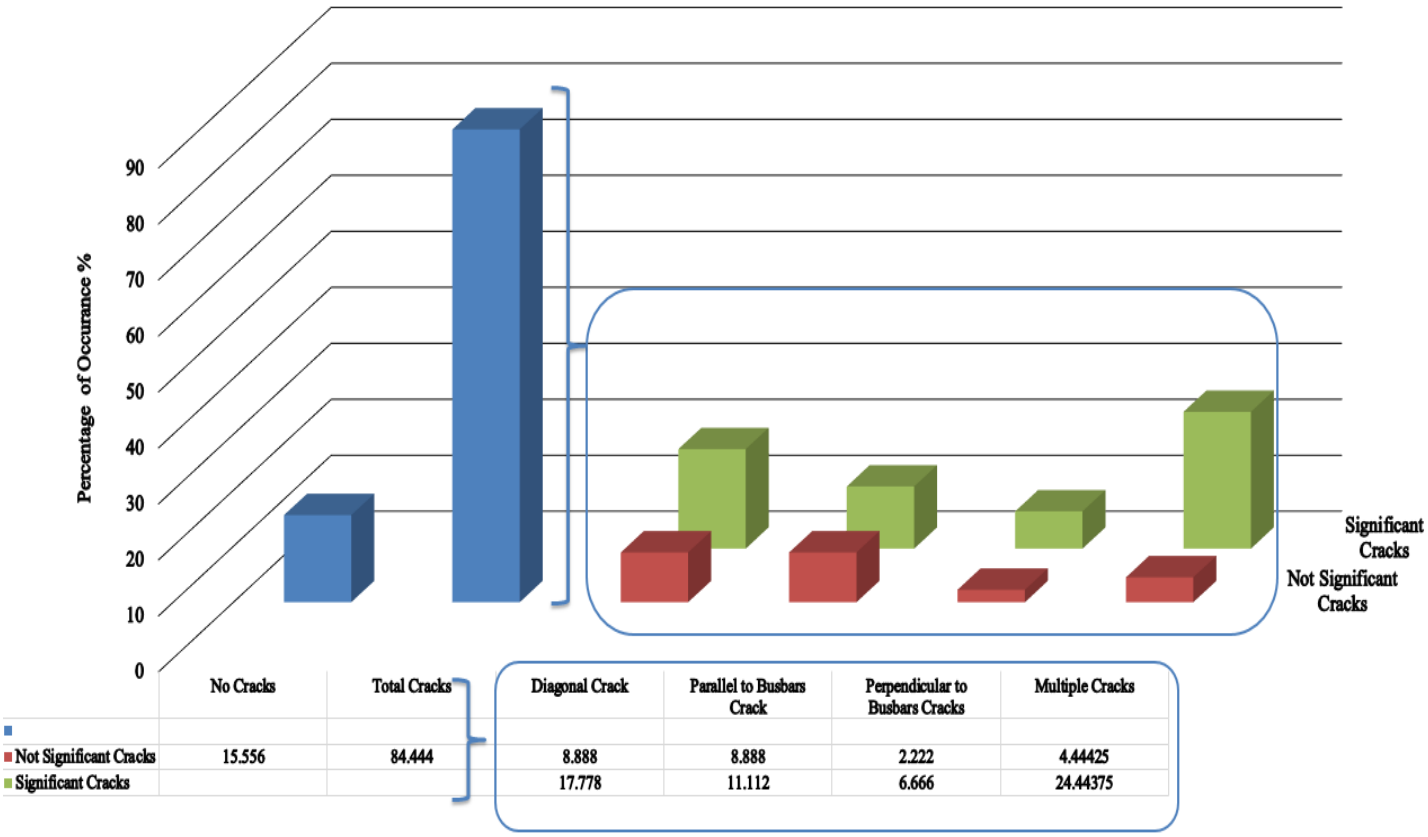

Figure 7.25 Percentage of cracks for the examined PV modules, overall significant cracks percentage equals 60% out of 84%

7.3 Summary

In this chapter the demonstration of two hot spot mitigation techniques was discussed. The offered techniques are capable to enhance the output power of PV modules which are effected by hot spots and partial shading conditions. The proposed hot spot mitigation techniques use multiple MOSFETs in the affected PV module, while the detection of hot spots was captured using i5 FLIR thermal imaging camera.

Several experiments have been conducted during various environmental conditions, where the PV module I-V curve was evaluated in each observed test to analyze the output power performance before and after the activation of both proposed hot spot mitigation techniques.

One PV module affected by a hot spot was tested. After activating the first mitigation technique the output power of the PV module increased by 1.25 W in high irradiance levels, 0.61 W in medium irradiance level and 0.46 W in low irradiance level. The same experiment has been evaluated using the 2nd proposed hot spot mitigation technique, while the output power increased by 3.96 W in high irradiance level, 2.72 W in medium irradiance level and 0.98 W in low irradiance level.

Both proposed hot spot mitigation techniques were applied on a shaded PV module. The temperature was reduced and output power of the PV module enhanced using both techniques. However, the second mitigation technique shows a better performance comparing to the first.

The second part of this chapter focuses on the impact of PV micro cracks on the output power of the PV modules. A new statistical approach using T-test and F-test was used to identify the significant of the cracks on the output power performance of the PV modules. The approach is developed using LabVIEW software. 45 PV modules with various crack-type such as diagonal, parallel to busbars, perpendicular to busbars and multiple directions crack have been examined.

Before considering the statistical analysis approach, 84% of the examined PV modules have a significant impact on the output power performance. However, the statistical approach has confirmed that this result is incorrect, since only 60% of the examine PV cracks have a significant impact on the output power performance.

Next chapter will describe the conclusions of this thesis and the future work.

Chapter 8 Summary, Conclusion and Recommendation for Further Work

In this chapter, a summary of the main findings will be presented. In addition, some conclusions are drawn on the work undertaken in this research and the main contributions are presented. Also some potential suggestions are outlined for future work.

8.1 Summary

There were several goals for this research which can be listed as follows:

1. Create a monitoring systems based on internet of things (IoT) devices to monitor and analyse the performance of the PV systems installed at the University of Huddersfield
2. Model, analyse and compare the performance of multiple PV array configurations systems under various PS and faulty PV conditions
3. Development of a PV fault detection algorithm based on statistical analysis and mathematical techniques
4. Create a PV fault detection algorithm based on AI techniques such as Fuzzy Logic and ANN networks
5. Development of novel techniques which could be used to enhance the output power generated by hot spotted PV modules
6. Identification of the impact of PV micro cracks on the generated power of PV modules

These goals have been achieved successfully by implementing multiple algorithms which have been validated using two PV plants installed at the University of Huddersfield. This thesis presented detailed description of the major contributions made in this work, which are summarised as follows:

- The design of a PV monitoring system based on IoT devices was proposed in chapter 4. The PV monitoring system comprises various local and remote monitoring platforms. The designed system was evaluated on two different PV plants.

- The simulation and modelling for five different PV array configurations have been presented in chapter 5. The PV configurations including: series, parallel, series-parallel, total-cross-tied, and bridge-linked. The PV configurations were compared using the variations of seven indicators.

The analysis of these indicators can be further used in various PV plants, and it can be used to enhance the PV plants configuration based on faulty PV and partial shading conditions.

- In chapter 6, the development of a PV fault detection algorithm was presented. This novel algorithm is capable of detecting various faults in PV plants such as:

    - Normal operation mode
    - Partial shading conditions affecting the PV system with no faulty bypass diodes in the PV system
    - Partial shading conditions affecting the PV system with faulty bypass diodes in the PV system
    - Faulty PV modules, where the PV modules are disconnected from the PV string
    - Faulty PV modules and partial shading affecting the PV system
    - Faulty PV string
    - Faulty MPPT unit

- As stated in chapter 2, there are few AI techniques deployed in PV fault detection. Therefore, chapter 7 presents the use of multiple AI techniques in order to detect faults in PV plants. The AI techniques can be summarized as follows:

    - The first algorithm used six layers to detect faults in PV systems. The average detection accuracy for the algorithm is equal to 94.74%. However, Mamdani Fuzzy Logic system was used to improve the detection accuracy of the proposed PV detection algorithm. The average detection accuracy increased to 99.12% after considering the Fuzzy Logic system

    - The second designed PV fault detection algorithm is used to detect defective bypass diodes in PV modules. This algorithm was developed using Mamdani Fuzzy Logic system and it can detect up to 13 different faults associated with defective bypass diodes in PV modules. This algorithm was validated on two different PV plants

    - The last PV detection algorithm proved that the ANN network containing 2 inputs, 9 outputs using 2 hidden layers and 7 neurones had the highest overall detection accuracy. This ANN network was evaluated on two PV plants, where the maximum detection accuracy is equal to 92.1% and 91.9% respectively

- The development of two hot spot mitigation techniques used in PV modules are presented in chapter 8. The offered techniques are capable to enhance the output power of PV modules which are effected by hot spots and partial shading conditions. One PV module affected by a hot spot was tested. After activating the first mitigation technique the output power of the PV module increased by 1.25 W in high irradiance levels, 0.61 W in medium irradiance level and 0.46 W in low irradiance level. Same experiment has been evaluated using the 2nd proposed technique, while the output power increased by 3.96 W in high irradiance level, 2.72 W in medium irradiance level and 0.98 W in low irradiance level

  The second part of chapter 8 focuses on the impact of PV micro cracks on the output power of PV modules. A new statistical approach using T-test and F-test was used to identify the significant impact of the cracks on the output power performance of the PV modules. Before considering the statistical analysis approach, 84% of the examined PV modules have a significant loss in the output power. However, the statistical approach confirmed that this result is incorrect, since only 60% of the examined PV cracks have a significant loss in the output power performance

8.2 Conclusion

Photovoltaic systems can be configured in several ways such as series (S), parallel (P), series-parallel (SP), total-cross-tied (TCT), and bridge-linked (BL) connection. In this research, it was found that the TCT configuration has the maximum output power among all above listed PV configurations. In addition, it was found that the TCT configuration has the least loss in the power when faulty conditions arise in the PV system (faulty conditions such as partial shading, faulty PV modules, and faulty PV strings). Furthermore, the second best configuration is the BL, whereas the series (S) configuration has the lowest output power.

In the PV systems several faulty conditions could exist such as faulty PV modules, partial shading conditions, faulty PV strings, and faulty maximum power point tracking units. In this thesis, the development of a fast, reliable, and accurate PV fault detection algorithm is presented. The algorithm depends on two variables; power ratio and voltage ratio. It was evident from the conducted experiments that these variables can be used to locate possible faults in new and old PV systems. The maximum detection accuracy of this technique is 94.74%.

To improve the accuracy of the PV fault detection, Fuzzy Logic AI technique was used to increase the overall detection accuracy of the power, voltage ratio algorithm up to 99.12%. Mamdani and Sugeno fuzzy systems were tested, and it was found that both had identical performance.

In addition, Artificial Neural Network (ANN) technique was developed to detect faults in PV systems based on previously logged data. The main findings show that ANN networks with two hidden layers yield better performance compared with one hidden layer. To compare the detection accuracy, various ANN neurons were tested. It was found that an ANN networks with 2 hidden layers, containing 8 neurons achieve the highest detection accuracy of 92.1%.

It can be concluded these AI based algorithms can detect faults in photovoltaic systems such as faulty PV modules, partial shading conditions, faulty PV strings, and faulty maximum power point tracking units.

However, there are other types of faults found in PV systems which cannot be identified using the presented algorithms, these are hot spots, micro cracks, and PV line-to-line faults, which will be addressed in the future work. Some preliminary work has been completed to address hot spots and micro cracks issues.

Two PV hot spot mitigation techniques were developed. The best performing hot spot mitigation technique contains 2 MOSFETs connected with the hot spotted PV module. The conducted experiments show that the difference between the hot spotted PV module temperature, before and after the activation of this technique, is equal to 21.5 ^{0}C and 18.3 ^{0}C respectively. Moreover, the suggested hot spot mitigation technique increases the daily yield output power of the hot spotted PV modules up to 0.03 kWh (estimated yearly increase 0.03 x 365 = 10.95 kWh).

Electroluminescence (EL) imaging technique can be used to identify micro cracks in PV modules. It was found that multiple directions cracks decrease the output power of PV modules up to 8%, whereas diagonal cracks decrease PV output power by 4%.

8.3 Future work

The PV detection techniques proposed in chapters 6 and 7 could be enhanced using a generic PV fault detection algorithm which can be used in various PV array configurations, size, and location. The PV fault detection algorithms are implemented using LabVIEW software. In the future, it is intended to incorporate the algorithms into microcontroller units.

In addition, the algorithm used to detect defective bypass diodes in PV modules could be enhanced by using the analysis of the series resistance (R_s) and shunt resistance (R_{sh}). The Fuzzy Logic system could be also improved by adding the R_s and R_{sh} as new inputs in the Mamdani Fuzzy Logic system interface, thus it will increase the overall detection accuracy for the algorithm.

This thesis do not contain any details on how to increase the output power of adjacent PV installations. This could be established by selecting the most suitable configuration such as series, parallel, total-cross-tied, in order to enhance the performance of the PV array under partial shading conditions. Figure 8.1 shows the connection box, which can be placed next to the adjacent PV systems. The connection box enables the re-configuration of the PV modules, thus increase the total energy yield.

In future, it is also intended to develop a new technological solution to predict the energy of PV systems. This is possible by predicting the PV temperature and solar irradiance based on historic weather data patterns. The outcomes of this research will be used for analytical performance analysis, failure analysis as well as performance pattern generation to enable network operators to plan energy injection to the grid.

Figure 8.1 Multiple PV systems connected through a multiple configuration box

References

Abdelhamid, M., Singh, R., & Omar, M. (2014). Review of microcrack detection techniques for silicon solar cells. *IEEE Journal of Photovoltaics*, *4*(1), 514-524.

Abdelsalam, A. K., Massoud, A. M., Ahmed, S., & Enjeti, P. N. (2011). High-performance adaptive perturb and observe MPPT technique for photovoltaic-based microgrids. *IEEE transactions on power electronics*, *26*(4), 1010-1021.

Adhya, S., Saha, D., Das, A., Jana, J., & Saha, H. (2016). *An IoT based smart solar photovoltaic remote monitoring and control unit.* Paper presented at the Control, Instrumentation, Energy & Communication (CIEC), 2016 2nd International Conference on.

International energy agency. (2016). Snapshot of global photovoltaic markets. Argentina: International energy agency

Ahmed, J., & Salam, Z. (2015). An improved perturb and observe (P&O) maximum power point tracking (MPPT) algorithm for higher efficiency. *Applied Energy*, *150*, 97-108.

Alajmi, B. N., Ahmed, K. H., Finney, S. J., & Williams, B. W. (2011). Fuzzy-logic-control approach of a modified hill-climbing method for maximum power point in microgrid standalone photovoltaic system. *IEEE transactions on power electronics*, *26*(4), 1022-1030.

Bajzek, T. J. (2005). Thermocouples: a sensor for measuring temperature. *IEEE Instrumentation & Measurement Magazine*, *8*(1), 35-40.

Bayrak, G. (2015). A remote islanding detection and control strategy for photovoltaic-based distributed generation systems. *Energy conversion and management*, *96*, 228-241.

Belaout, A., Krim, F., & Mellit, A. (2016). *Neuro-fuzzy classifier for fault detection and classification in photovoltaic module.* Paper presented at the Modelling, Identification and Control (ICMIC), 2016 8th International Conference on.

Belhaouas, N., Cheikh, M.-S. A., Agathoklis, P., Oularbi, M.-R., Amrouche, B., Sedraoui, K., & Djilali, N. (2017). PV array power output maximization under partial shading using new shifted PV array arrangements. *Applied Energy*, *187*, 326-337.

Belyaev, A., Polupan, O., Dallas, W., Ostapenko, S., Hess, D., & Wohlgemuth, J. (2006). Crack detection and analyses using resonance ultrasonic vibrations in full-size crystalline silicon wafers. *Applied Physics Letters*, *88*(11), 111907.

Bin, L., Xianghao, H., & Shuai, F. (2011). *Automatic inspection of surface crack in solar cell images.* Paper presented at the Control and Decision Conference (CCDC), 2011 Chinese.

Blake, F., & Hanson, K. (1969). *The hot-spot failure mode for solar arrays.* Paper presented at the Proceedings of the 4th Intersociety Energy Conversion Engineering Conference.

Bonsignore, L., Davarifar, M., Rabhi, A., Tina, G. M., & Elhajjaji, A. (2014). Neuro-fuzzy fault detection method for photovoltaic systems. *Energy Procedia, 62*, 431-441.

Brooks, B. (2011). The Bakersfield Fire: A Lesson in Ground-Fault Protection. from https://solarprofessional.com/articles/design-installation/the-bakersfield-fire-a-lesson-in-ground-fault-protection#.WcpmIcZrxph

Buerhop, C., Schlegel, D., Niess, M., Vodermayer, C., Weißmann, R., & Brabec, C. (2012). Reliability of IR-imaging of PV-plants under operating conditions. *Solar Energy Materials and Solar Cells, 107*, 154-164.

Celik, B., Karatepe, E., Silvestre, S., Gokmen, N., & Chouder, A. (2015). Analysis of spatial fixed PV arrays configurations to maximize energy harvesting in BIPV applications. *Renewable Energy, 75*, 534-540.

Chao, K.-H., Ho, S.-H., & Wang, M.-H. (2008). Modeling and fault diagnosis of a photovoltaic system. *Electric Power Systems Research, 78*(1), 97-105.

Chen, Z., Wu, L., Cheng, S., Lin, P., Wu, Y., & Lin, W. (2017). Intelligent fault diagnosis of photovoltaic arrays based on optimized kernel extreme learning machine and IV characteristics. *Applied Energy*.

Chine, W., Mellit, A., Lughi, V., Malek, A., Sulligoi, G., & Pavan, A. M. (2016). A novel fault diagnosis technique for photovoltaic systems based on artificial neural networks. *Renewable Energy, 90*, 501-512.

Chine, W., Mellit, A., Pavan, A. M., & Kalogirou, S. (2014). Fault detection method for grid-connected photovoltaic plants. *Renewable Energy, 66*, 99-110.

Chouder, A., & Silvestre, S. (2010). Automatic supervision and fault detection of PV systems based on power losses analysis. *Energy conversion and management, 51*(10), 1929-1937.

Cohen, M. J. (1988). Monolithic solar cell and bypass diode system: US Patents.

Commission, I. (1998). International Standard IEC 61724: Photovoltaic System Performance Monitoring—Guidelines for Measurements, Data Exchange and Analysis. *IEC*.

Daliento, S., Di Napoli, F., Guerriero, P., & d'Alessandro, V. (2016). A modified bypass circuit for improved hot spot reliability of solar panels subject to partial shading. *Solar Energy, 134*, 211-218.

Dallas, W., Polupan, O., & Ostapenko, S. (2007). Resonance ultrasonic vibrations for crack detection in photovoltaic silicon wafers. *Measurement Science and Technology, 18*(3), 852.

Davis, United kingdom. (2016). Temperature Probe with RJ Connector. Retrieved from https://www.davisnet.com/product/temperature-probe-with-rj-connector/.

Davis, United Kingdom (2017). Davis Weather Station. Retrieved from http://www.davisweather.co.uk/

Davis, United Kingdom (2017). VANTAGE PRO2. Retrieved from https://www.davisnet.com/solution/vantage-pro2/

Deshkar, S. N., Dhale, S. B., Mukherjee, J. S., Babu, T. S., & Rajasekar, N. (2015). Solar PV array reconfiguration under partial shading conditions for maximum power extraction using genetic algorithm. *Renewable and Sustainable Energy Reviews, 43*, 102-110.

Dhimish, M., & Holmes, V. (2016). Fault detection algorithm for grid-connected photovoltaic plants. *Solar Energy, 137*, 236-245.

Dhimish, M., Holmes, V., & Dales, M. (2016). *Grid-connected PV virtual instrument system (GCPV-VIS) for detecting photovoltaic failure.* Paper presented at the Environment Friendly Energies and Applications (EFEA), 2016 4th International Symposium on.

Dhimish, M., Holmes, V., & Dales, M. (2017). Parallel fault detection algorithm for grid-connected photovoltaic plants. *Renewable Energy, 113*, 94-111.

Dhimish, M., Holmes, V., Dales, M., Mather, P., Sibley, M., Chong, B., & Zhang, L. (2017). *The impact of cracks on the performance of photovoltaic modules.* Paper presented at the PowerTech, 2017 IEEE Manchester.

Dhimish, M., Holmes, V., Dales, M., & Mehrdadi, B. (2017). The effect of micro cracks on photovoltaic output power: case study based on real time long term data measurements. *Micro & Nano Letters*.

Dhimish, M., Holmes, V., & Mehrdadi, B. (2016, 14-16 Sept. 2016). *Grid-connected PV monitoring system (GCPV-MS).* Paper presented at the 2016 4th International Symposium on Environmental Friendly Energies and Applications (EFEA).

Dhimish, M., Holmes, V., Mehrdadi, B., & Dales, M. (2017a). Diagnostic method for photovoltaic systems based on six layer detection algorithm. *Electric Power Systems Research, 151*, 26-39.

Dhimish, M., Holmes, V., Mehrdadi, B., & Dales, M. (2017b). The Impact of Cracks on Photovoltaic Power Performance. *Journal of Science: Advanced Materials and Devices*.

Dhimish, M., Holmes, V., Mehrdadi, B., & Dales, M. (2017c). Multi-Layer Photovoltaic Fault Detection Algorithm. *High Voltage*.

Dhimish, M., Holmes, V., Mehrdadi, B., & Dales, M. (2017d). Simultaneous fault detection algorithm for grid-connected photovoltaic plants. *IET Renewable Power Generation*.

Dhimish, M., Holmes, V., Mehrdadi, B., & Dales, M. (2018). Comparing Mamdani Sugeno Fuzzy Logic and RBF ANN network for PV fault detection. *Renewable Energy, 117*, 257-274.

Dhimish, M., Holmes, V., Mehrdadi, B., Dales, M., Chong, B., & Zhang, L. (2017). Seven indicators variations for multiple PV array configurations under partial shading and faulty PV conditions. *Renewable Energy*.

Dhimish, M., Holmes, V., Mehrdadi, B., Dales, M., & Mather, P. (2017a). Detecting Defective Bypass Diodes in Photovoltaic Modules using Mamdani Fuzzy Logic System. *Global Journal of Research In Engineering*.

Dhimish, M., Holmes, V., Mehrdadi, B., Dales, M., & Mather, P. (2017b). Photovoltaic fault detection algorithm based on theoretical curves modelling and fuzzy classification system. *Energy*.

Dou, L., You, J., Hong, Z., Xu, Z., Li, G., Street, R. A., & Yang, Y. (2013). 25th anniversary article: a decade of organic/polymeric photovoltaic research. *Advanced materials, 25*(46), 6642-6671.

Elgendy, M. A., Zahawi, B., & Atkinson, D. J. (2015). Operating characteristics of the P&O algorithm at high perturbation frequencies for standalone PV systems. *IEEE Transactions on Energy conversion, 30*(1), 189-198.

Victron Energy. (2017). Inverters. Retrieved from https://www.victronenergy.com/inverters.

Femia, N., Petrone, G., Spagnuolo, G., & Vitelli, M. (2005). Optimization of perturb and observe maximum power point tracking method. *IEEE transactions on power electronics, 20*(4), 963-973.

Firth, S. K., Lomas, K. J., & Rees, S. J. (2010). A simple model of PV system performance and its use in fault detection. *Solar Energy, 84*(4), 624-635.

Freeman, J., Hellgardt, K., & Markides, C. N. (2017). Working fluid selection and electrical performance optimisation of a domestic solar-ORC combined heat and power system for year-round operation in the UK. *Applied Energy, 186*, 291-303.

Fuyuki, T., & Kitiyanan, A. (2009). Photographic diagnosis of crystalline silicon solar cells utilizing electroluminescence. *Applied Physics A: Materials Science & Processing, 96*(1), 189-196.

García, M., Marroyo, L., Lorenzo, E., Marcos, J., & Pérez, M. (2014). Observed degradation in photovoltaic plants affected by hot-spots. *Progress in Photovoltaics: Research and applications, 22*(12), 1292-1301.

Garoudja, E., Harrou, F., Sun, Y., Kara, K., Chouder, A., & Silvestre, S. (2017). Statistical fault detection in photovoltaic systems. *Solar Energy, 150*, 485-499.

Gokmen, N., Karatepe, E., Celik, B., & Silvestre, S. (2012). Simple diagnostic approach for determining of faulted PV modules in string based PV arrays. *Solar Energy, 86*(11), 3364-3377.

Ministry of Housing, Communities & Local Government. (2017). Grenfell Tower. Retrieved from https://www.gov.uk/government/collections/grenfell-tower.

Guerriero, P., Di Napoli, F., Vallone, G., d'Alessandro, V., & Daliento, S. (2016). Monitoring and diagnostics of PV plants by a wireless self-powered sensor for individual panels. *IEEE Journal of Photovoltaics, 6*(1), 286-294.

Gupta, A. (2016). *Solar Photovoltaics Engineering. A Power Quality Analysis Using Matlab Simulation Case Studies*: Anchor Academic Publishing.

Han, J., Jeong, J.-D., Lee, I., & Kim, S.-H. (2017). *Low-cost monitoring of photovoltaic systems at panel level in residential homes based on power line communication.* Paper presented at the Consumer Electronics (ICCE), 2017 IEEE International Conference on.

Hassan, S. Z., Li, H., Kamal, T., Arifoğlu, U., Mumtaz, S., & Khan, L. (2017). Neuro-Fuzzy Wavelet Based Adaptive MPPT Algorithm for Photovoltaic Systems. *Energies, 10*(3), 394.

Ho, F. F., & Suh, C. H. (2014). Solar cell structure including a silicon carrier containing a by-pass diode: US Patents.

Hoang, B., & Beyene, S. G. (2017). Integral corner bypass diode interconnecting configuration for multiple solar cells: US Patents.

Hu, T., Zheng, M., Tan, J., Zhu, L., & Miao, W. (2015). Intelligent photovoltaic monitoring based on solar irradiance big data and wireless sensor networks. *Ad Hoc Networks, 35*, 127-136.

Hu, Y., Cao, W., Ma, J., Finney, S. J., & Li, D. (2014). Identifying PV module mismatch faults by a thermography-based temperature distribution analysis. *IEEE Transactions on Device and Materials Reliability, 14*(4), 951-960.

Hu, Y., Gao, B., Song, X., Tian, G. Y., Li, K., & He, X. (2013). Photovoltaic fault detection using a parameter based model. *Solar Energy, 96*, 96-102.

FLIR. (2013). FLIR i3 / i5 / i7. Retrieved from http://www.flir.co.uk/instruments/display/?id=65813.

HEXFET ® Power MOSFET. (2013). IRFZ44V. Retrieved from https://www.infineon.com/dgdl/irfz44v.pdf?fileId=5546d462533600a40153563b4cd12212.

Ishaque, K., Salam, Z., & Lauss, G. (2014). The performance of perturb and observe and incremental conductance maximum power point tracking method under dynamic weather conditions. *Applied Energy, 119*, 228-236.

Israil, M., Anwar, S. A., & Abdullah, M. Z. (2013). Automatic detection of micro-crack in solar wafers and cells: a review. *Transactions of the Institute of Measurement and Control, 35*(5), 606-618.

Jamshidpour, E., Poure, P., & Saadate, S. (2015). Photovoltaic systems reliability improvement by real-time FPGA-based switch failure diagnosis and fault-tolerant DC–DC converter. *IEEE Transactions on Industrial Electronics, 62*(11), 7247-7255.

Jenkins, N., & Ekanayake, J. (2017). *Renewable Energy Engineering*: Cambridge University Press.

Kabalci, E., & Kabalci, Y. (2017). *Remote monitoring system design for photovoltaic panels.* Paper presented at the Advanced Topics in Electrical Engineering (ATEE), 2017 10th International Symposium on.

Kajari-Schröder, S., Kunze, I., Eitner, U., & Köntges, M. (2011). Spatial and orientational distribution of cracks in crystalline photovoltaic modules generated by mechanical load tests. *Solar Energy Materials and Solar Cells, 95*(11), 3054-3059.

Kaplani, E. (2012). Detection of degradation effects in field-aged c-Si solar cells through IR thermography and digital image processing. *International Journal of Photoenergy, 2012*.

Karatepe, E., & Hiyama, T. (2011). *Controlling of artificial neural network for fault diagnosis of photovoltaic array.* Paper presented at the Intelligent System Application to Power Systems (ISAP), 2011 16th International Conference on.

Kim, K. A., & Krein, P. T. (2015). Reexamination of photovoltaic hot spotting to show inadequacy of the bypass diode. *IEEE Journal of Photovoltaics, 5*(5), 1435-1441.

Kollimalla, S. K., & Mishra, M. K. (2014). A novel adaptive P&O MPPT algorithm considering sudden changes in the irradiance. *IEEE Transactions on Energy conversion, 29*(3), 602-610.

Kontgers, M., Kunze, I., Kajari-Schroder, S., Breitenmoser, X., & Bjorneklett, B. (2010). *Quantifying the risk of power loss in PV modules due to micro cracks.* Paper presented at the 25th European Photovoltaic Solar Energy Conference, Valencia, Spain.

Köntges, M., Kunze, I., Kajari-Schröder, S., Breitenmoser, X., & Bjørneklett, B. (2011). The risk of power loss in crystalline silicon based photovoltaic modules due to micro-cracks. *Solar Energy Materials and Solar Cells, 95*(4), 1131-1137.

Köntges, M., Siebert, M., Hinken, D., Eitner, U., Bothe, K., & Potthof, T. (2009). *Quantitative analysis of PV-modules by electroluminescence images for quality control.* Paper presented at the 24th European Photovoltaic Solar Energy Conference, Hamburg, Germany.

Kukulka, J. R. (1997). Solar cell with integrated bypass diode and method: US Patents.

Kulaksız, A. A., & Akkaya, R. (2012). A genetic algorithm optimized ANN-based MPPT algorithm for a stand-alone PV system with induction motor drive. *Solar Energy, 86*(9), 2366-2375.

Le, P. T., Tsai, H.-L., & Lam, T. H. (2016). A wireless visualization monitoring, evaluation system for commercial photovoltaic modules solely in MATLAB/Simulink environment. *Solar Energy, 140*, 1-11.

Lesk, I. A. (1984). Protected photovoltaic module: US Patents.

Li, J., & Wang, H. (2009). *A novel stand-alone PV generation system based on variable step size INC MPPT and SVPWM control.* Paper presented at the Power Electronics and Motion Control Conference, 2009. IPEMC'09. IEEE 6th International.

Liu, F., Kang, Y., Zhang, Y., & Duan, S. (2008). *Comparison of P&O and hill climbing MPPT methods for grid-connected PV converter.* Paper presented at the Industrial Electronics and Applications, 2008. ICIEA 2008. 3rd IEEE Conference on.

Liu, Y.-H., Chen, J.-H., & Huang, J.-W. (2015). A review of maximum power point tracking techniques for use in partially shaded conditions. *Renewable and Sustainable Energy Reviews, 41*, 436-453.

Madeti, S. R., & Singh, S. (2017a). Monitoring system for photovoltaic plants: A review. *Renewable and Sustainable Energy Reviews, 67*, 1180-1207.

Madeti, S. R., & Singh, S. (2017b). Online fault detection and the economic analysis of grid-connected photovoltaic systems. *Energy*.

McEvoy, A., Castaner, L., & Markvart, T. (2013). *Solar Cells: Materials, Manufacture and Operation* (2nd ed.). GB: Academic Press.

Mekki, H., Mellit, A., & Salhi, H. (2016). Artificial neural network-based modelling and fault detection of partial shaded photovoltaic modules. *Simulation Modelling Practice and Theory, 67*, 1-13.

Miller, J. N., & Miller, J. C. (2005). *Statistics and chemometrics for analytical chemistry*: Pearson Education.

Mohammadnejad, S., Khalafi, A., & Ahmadi, S. M. (2016). Mathematical analysis of total-cross-tied photovoltaic array under partial shading condition and its comparison with other configurations. *Solar Energy, 133*, 501-511.

Moretón, R., Lorenzo, E., & Narvarte, L. (2015). Experimental observations on hot-spots and derived acceptance/rejection criteria. *Solar Energy, 118*, 28-40.

Müller, R. (2002). Solar cell comprising a bypass diode: Google Patents.

Oh, S., Jun, D. H., Shin, K. W., Choi, I., Jung, S. H., Choi, J., . . . Yoon, E. (2016). Control of Crack Formation for the Fabrication of Crack-Free and Self-Isolated High-Efficiency Gallium Arsenide Photovoltaic Cells on Silicon Substrate. *IEEE Journal of Photovoltaics, 6*(4), 1031-1035.

Oreski, G., & Wallner, G. (2005). Aging mechanisms of polymeric films for PV encapsulation. *Solar Energy, 79*(6), 612-617.

Oreski, G., & Wallner, G. (2009). Evaluation of the aging behavior of ethylene copolymer films for solar applications under accelerated weathering conditions. *Solar Energy, 83*(7), 1040-1047.

Parlak, K. Ş. (2014). PV array reconfiguration method under partial shading conditions. *International Journal of Electrical Power & Energy Systems, 63*, 713-721.

Potnuru, S. R., Pattabiraman, D., Ganesan, S. I., & Chilakapati, N. (2015). Positioning of PV panels for reduction in line losses and mismatch losses in PV array. *Renewable Energy, 78*, 264-275.

Outback Power (2015). MATE3. Retrieved from http://www.outbackpower.com/outback-products/manage-the-system/mate3-system-display-and-controller/item/mate3

Outback Power (2017). FLEXmax 60/80. Retrieved from http://www.outbackpower.com/outback-products/make-the-power/flexmax-series-charge-controllers/item/flexmax-6080

Radjai, T., Rahmani, L., Mekhilef, S., & Gaubert, J. P. (2014). Implementation of a modified incremental conductance MPPT algorithm with direct control based on a fuzzy duty cycle change estimator using dSPACE. *Solar Energy, 110*, 325-337.

Rajput, P., Tiwari, G., & Sastry, O. (2016). Thermal modelling and experimental validation of hot spot in crystalline silicon photovoltaic modules for real outdoor condition. *Solar Energy, 139*, 569-580.

Ram, J. P., Babu, T. S., & Rajasekar, N. (2017). A comprehensive review on solar PV maximum power point tracking techniques. *Renewable and Sustainable Energy Reviews, 67*, 826-847.

Rani, B. I., Ilango, G. S., & Nagamani, C. (2013). Enhanced power generation from PV array under partial shading conditions by shade dispersion using Su Do Ku configuration. *IEEE Transactions on Sustainable Energy, 4*(3), 594-601.

Rao, P. S., Ilango, G. S., & Nagamani, C. (2014). Maximum power from PV arrays using a fixed configuration under different shading conditions. *IEEE Journal of Photovoltaics, 4*(2), 679-686.

Romag, United Kingdom (2017). Solar Panel Kits. Retrieved from http://www.romag.co.uk/solar/solar-kits/

Sera, D., Mathe, L., Kerekes, T., Teodorescu, R., & Rodriguez, P. (2011). *A low-disturbance diagnostic function integrated in the PV arrays' MPPT algorithm.* Paper presented at the IECON 2011-37th Annual Conference on IEEE Industrial Electronics Society.

Sera, D., Teodorescu, R., & Rodriguez, P. (2008). *Photovoltaic module diagnostics by series resistance monitoring and temperature and rated power estimation.* Paper presented at the Industrial Electronics, 2008. IECON 2008. 34th Annual Conference of IEEE.

Shariff, F., Rahim, N. A., & Hew, W. P. (2015). Zigbee-based data acquisition system for online monitoring of grid-connected photovoltaic system. *Expert Systems with Applications, 42*(3), 1730-1742.

Sharps, P. R. (2008). Inverted metamorphic solar cell with bypass diode: Google Patents.

Silvestre, S., Boronat, A., & Chouder, A. (2009). Study of bypass diodes configuration on PV modules. *Applied Energy, 86*(9), 1632-1640.

Silvestre, S., Chouder, A., & Karatepe, E. (2013). Automatic fault detection in grid connected PV systems. *Solar Energy, 94*, 119-127.

Silvestre, S., da Silva, M. A., Chouder, A., Guasch, D., & Karatepe, E. (2014). New procedure for fault detection in grid connected PV systems based on the evaluation of current and voltage indicators. *Energy conversion and management, 86*, 241-249.

Silvestre, S., Mora-López, L., Kichou, S., Sánchez-Pacheco, F., & Dominguez-Pumar, M. (2016). Remote supervision and fault detection on OPC monitored PV systems. *Solar Energy, 137*, 424-433.

Sivakumar, P., Kader, A. A., Kaliavaradhan, Y., & Arutchelvi, M. (2015). Analysis and enhancement of PV efficiency with incremental conductance MPPT technique under non-linear loading conditions. *Renewable Energy, 81*, 543-550.

Solmetric, United States (2016). PV Analyzer I-V Curve Tracers. Retrieved from http://www.solmetric.com/pvanalyzermatrix.html

Solórzano, J., & Egido, M. (2013). Automatic fault diagnosis in PV systems with distributed MPPT. *Energy conversion and management, 76*, 925-934.

Solórzano, J., & Egido, M. (2014). Hot-spot mitigation in PV arrays with distributed MPPT (DMPPT). *Solar Energy, 101*, 131-137.

Spanoche, S. A., Stewart, J. D., Hawley, S. L., & Opris, I. E. (2012). *Model-based method for partially shaded PV modules hot spot suppression.* Paper presented at the Photovoltaic Specialists Conference (PVSC), Volume 2, 2012 IEEE 38th.

Spataru, S., Sera, D., Kerekes, T., & Teodorescu, R. (2015). Diagnostic method for photovoltaic systems based on light I–V measurements. *Solar Energy*, *119*, 29-44.

Stoffel, T., Reda, I., Myers, D., Renne, D., Wilcox, S., & Treadwell, J. (2000). Current issues in terrestrial solar radiation instrumentation for energy, climate, and space applications. *Metrologia, 37*(5), 399.

Tadj, M., Benmouiza, K., Cheknane, A., & Silvestre, S. (2014). Improving the performance of PV systems by faults detection using GISTEL approach. *Energy conversion and management*, *80*, 298-304.

Tian, H., Mancilla–David, F., Ellis, K., Muljadi, E., & Jenkins, P. (2013). Determination of the optimal configuration for a photovoltaic array depending on the shading condition. *Solar Energy, 95*, 1-12.

Touati, F., Al-Hitmi, M., Chowdhury, N. A., Hamad, J. A., & Gonzales, A. J. S. P. (2016). Investigation of solar PV performance under Doha weather using a customized measurement and monitoring system. *Renewable Energy, 89*, 564-577.

Trupke, T., Bardos, R., Schubert, M., & Warta, W. (2006). Photoluminescence imaging of silicon wafers. *Applied Physics Letters, 89*(4), 044107.

Upadhyaya, H. M., Senthilarasu, S., Hsu, M.-H., & Kumar, D. K. (2013). Recent progress and the status of dye-sensitised solar cell (DSSC) technology with state-of-the-art conversion efficiencies. *Solar Energy Materials and Solar Cells, 119*, 291-295.

Ventura, C., & Tina, G. M. (2016). Utility scale photovoltaic plant indices and models for on-line monitoring and fault detection purposes. *Electric Power Systems Research, 136*, 43-56.

Vijayalekshmy, S., Bindu, G., & Iyer, S. R. (2016). A novel Zig-Zag scheme for power enhancement of partially shaded solar arrays. *Solar Energy, 135*, 92-102.

von Appen, J., Braun, M., Stetz, T., Diwold, K., & Geibel, D. (2013). Time in the sun: the challenge of high PV penetration in the German electric grid. *IEEE power and energy magazine, 11*(2), 55-64.

Wang, Y.-J., & Hsu, P.-C. (2011). An investigation on partial shading of PV modules with different connection configurations of PV cells. *Energy, 36*(5), 3069-3078.

Webster, J. G., & Eren, H. (2014). *Measurement, instrumentation, and sensors handbook: spatial, mechanical, thermal, and radiation measurement* (Vol. 1): CRC press.

Wen, T.-K., & Yin, C.-C. (2012). Crack detection in photovoltaic cells by interferometric analysis of electronic speckle patterns. *Solar Energy Materials and Solar Cells, 98*, 216-223.

Yadav, A. S., Pachauri, R. K., & Chauhan, Y. K. (2016). Comprehensive investigation of PV arrays with puzzle shade dispersion for improved performance. *Solar Energy, 129*, 256-285.

Yadav, A. S., Pachauri, R. K., Chauhan, Y. K., Choudhury, S., & Singh, R. (2017). Performance enhancement of partially shaded PV array using novel shade dispersion effect on magic-square puzzle configuration. *Solar Energy, 144*, 780-797.

Yang, W.-R. (2009). *Short-time discrete wavelet transform for wafer microcrack detection.* Paper presented at the Industrial Electronics, 2009. ISIE 2009. IEEE International Symposium on.

Yi, Z., & Etemadi, A. H. (2017). Fault Detection for Photovoltaic Systems Based on Multi-Resolution Signal Decomposition and Fuzzy Inference Systems. *IEEE Transactions on Smart Grid, 8*(3), 1274-1283.

Zhao, Y. (2015). *FAULT DETECTION, CLASSIFICATION AND PROTECTION IN SOLAR PHOTOVOLTAIC ARRAYS.* Northeastern University Boston, Massachusetts.

Zhou, H., Chen, Q., Li, G., Luo, S., Song, T.-b., Duan, H.-S., . . . Yang, Y. (2014). Interface engineering of highly efficient perovskite solar cells. *Science, 345*(6196), 542-546.

Zhu, Y., Juhl, M. K., Trupke, T., & Hameiri, Z. (2017). Photoluminescence Imaging of Silicon Wafers and Solar Cells With Spatially Inhomogeneous Illumination. *IEEE Journal of Photovoltaics*.

Appendix A. Experimental PV Plants

Appendix A provides details for two PV systems installed at the University of Huddersfield (UoH). The first PV system has been installed and configured as part of this research. Furthermore, the second PV system installed at UoH in 2006. The PV systems configuration, PV modules electrical characteristics, and the equipment such as irradiance sensors, and temperature sensors are also explained.

1 Overview of the existing PV plant A

The first mounted PV plant consists of ten SMT 6 (60) P polycrystalline silicon PV modules, each with a nominal output power of 220 W_p. Figure 2a shows an image of the installed PV modules, where the tilt angle is equal to 42^0. This PV plant has been fully funded by the department of Computing and Engineering UoH in 2014.

Each PV module contains three bypass diodes, the interconnection of the bypass in a PV module sub strings are shown in Figure 1. The purpose of the bypass didoes is to maximise the output power of the PV modules during PS conditions. Figure 2b shows an image of the bypass diodes connected to a PV module.

Figure 2c shows the connection box which is placed next to the PV system. The purpose of the connection box is to configure the PV plant. For example, the examined PV modules could be connected in series, parallel, or series-parallel PV array configurations.

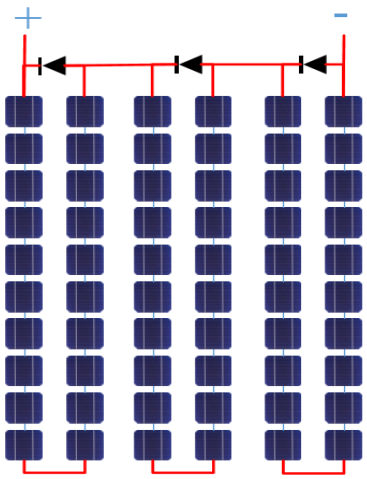

Figure 1 Interconnection of the bypass diodes in each examined PV module

(a)

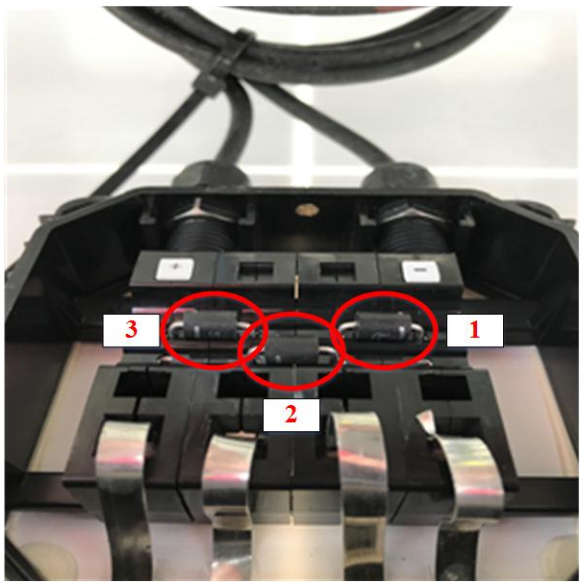

(b)

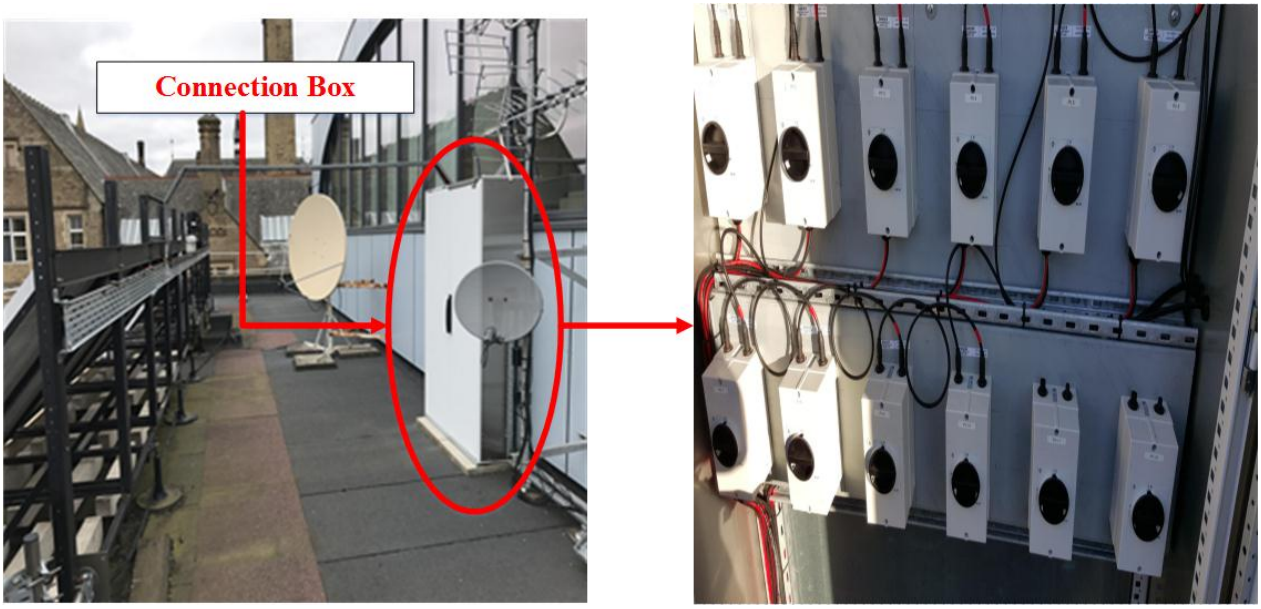

(c)

Figure 2 (a) Image of PV plant A, (b) Bypass diodes connected to the PV module, (c) Connection box

2 PV modules electrical characteristics

The SMT6 (60) P PV modules manufactured by Romag (Romag, 2017) have been used in this PV plant. The electrical characteristics of the PV panels are shown in Table 1. All listed values for the PV electrical characteristics is under STC (G: 1000 W/m^2, and T: 25 ^{0}C).

Table 1 SMT6 (60) P PV module electrical characteristics

PV module electrical characteristics	Value
Peak Power	220 W
Voltage at maximum power point (V_{mpp})	28.7 V
Current at maximum power point (I_{mpp})	7.67 A
Open Circuit Voltage (V_{OC})	36.74 V
Short Circuit Current (I_{sc})	8.24 A
Number of cells connected in series	60
Number of cells connected in parallel	1

3 MPPT unit

In order to operate PV plant A at its maximum output power, FLEXmax 80 MPPT units shown in Figure 3 have been used. The specification of the MPPT are described as follows (Power, 2017):

i. Maximum output current: 80 A
ii. Maximum PV open circuit voltage: 150 V
iii. Peak efficiency greater than 98%
iv. Full output power in ambient temperature as high as 40 ^{0}C

Figure 0 FLEXmax 80 MPPT unit

4 DC/AC inverter

Phoenix DC/AC inverter manufactured by Victron Energy (Energy, 2017) was used to convert the DC power stored in a battery bank to an AC load. Figure 3.4a shows the inverter used and its basic installation diagram. The inverter has an input voltage range of 9.5 – 17 V, output voltage: 230 VAC ± 2%, Frequency of 50 Hz ± 0.1%, continuous output power at 25 ^{0}C of 2000 VA, and maximum conversion efficiency of 92%.

PV plant A is connected to a 12V battery bank, then it is connected to the inverter as shown in Figure 4. This inverter has a RS-485 port which can be converted to RS-232. A RS-232 to USB conversion cable is also required to connect the inverter to a PC user interface.

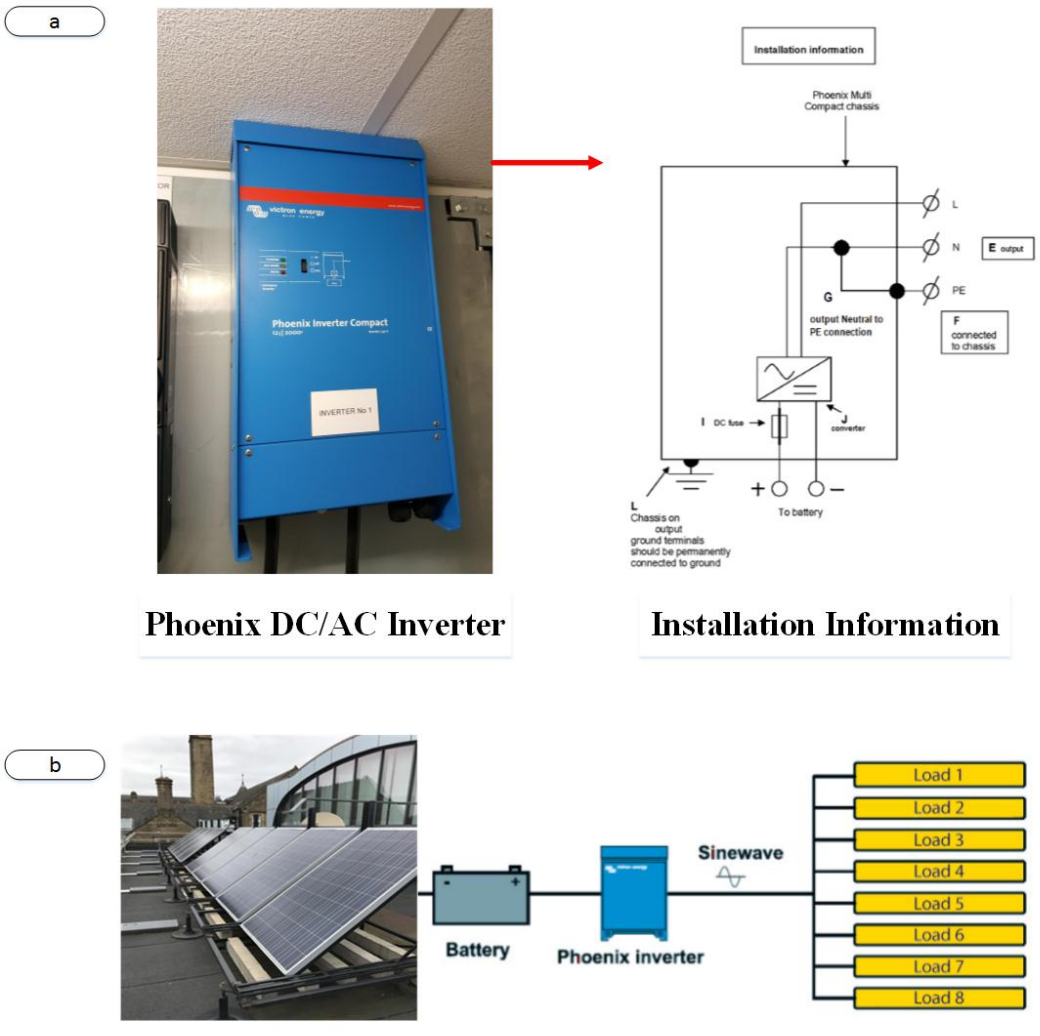

Figure 4 (a) Phoenix inverter installation information, (b) Connection of PV plant A to an AC load

5 Temperature sensor

In order to examine the PV modules surface temperature, Davis temperature sensors probes have been connected at the back of each PV module as shown in Figure 5. This probe measures temperature range as low as -40 ^{0}C and as high as 65 ^{0}C (Davis, 2016).

PV module temperature measurements is crucial, in order to predict the PV panel I-V and P-V curve. However, the irradiance level is also needed in the prediction process. Therefore, next section will demonstrate the weather station which has been used to measure the irradiance level of the PV modules.

Figure 5 Davis temperature sensor probe connected to a PV module

6 Davis weather station

Davis weather station (Davis, 2017a) has been installed next to the PV system. The weather station comprises various sensors which measures the following environmental conditions:

i. Wind speed, range: 2 to 150 mile per hour (mph)
ii. Wind direction
iii. Temperature, range: -40 ^{0}C to 65 ^{0}C
iv. Relative humidity, range: 0% to 100%
v. Rainfall in mm or inches
vi. Solar irradiance, range: 0 W/m^2 to 2000 W/m^2

Figure 6a shows an image of the installed weather station. This weather station is wirelessly connected to a monitoring unit called Vantage PRO2 as shown in Figure 6b, which can be connected to a personal computer (PC) to monitor and log the above listed environment parameters.

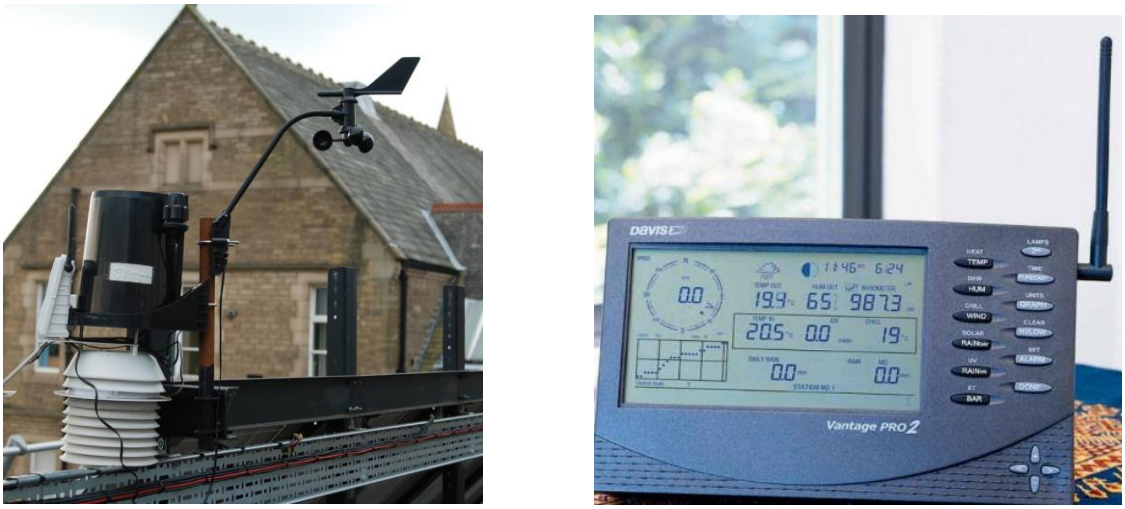

(a) (b)

Figure 1 (a) Davis weather station installed next to PV plant A, (b) Vantage PRO2 wireless weather station monitoring unit

7 PV plant A system architecture

As shown earlier in Figure 2c, the connection box allows the reconfiguration of the PV modules. In this section, three configuration topologies will be presented.

The first PV configuration topology shown in Figure 7a contains one PV string connected to a MPPT unit. The MPPT unit should not exceed the V_{oc} of the PV system. Therefore, this PV configuration is often not used, because while increasing the number of PV modules, the PV system V_{oc} will increase, which results in a complete shut down for the MPPT unit.

The second PV configuration is shown in Figure 7b. This configuration comprise multiple PV strings in parallel with a central MPPT unit. The input V_{oc} for the MPPT unit is equal to V_{oc} of one PV string, while the current is the sum of the PV strings output currents.

In the last PV configuration illustrated in Figure 7c each PV string is connected to a MPPT unit, and the DC load is shared across all MPPT units. This PV topology is more expensive than the second PV configuration, because it requires more MPPT units installed at the PV installation. However, during PS conditions, it guarantees more output power compared to the second PV configuration.

For all PV configuration topologies, the current and voltage of the PV system was measured using the internal sensors in the MPPT unit. The monitoring system used in the PV plants will be discussed in the next chapter.

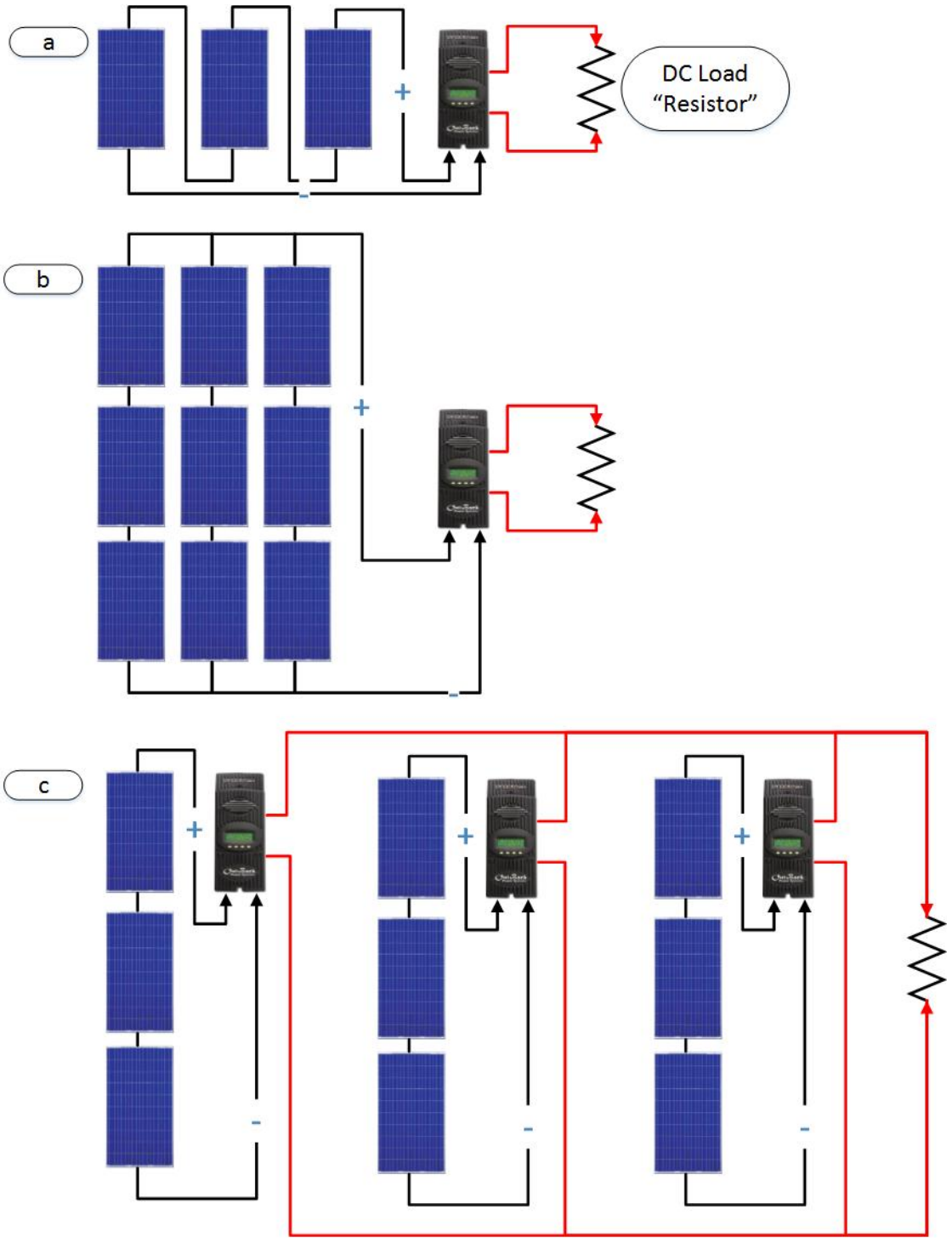

Figure 2 (a) PV string connected to MPPT unit, (b) Three parallel PV strings connected to a single MPPT unit, (c) Three PV strings each connected to a MPPT unit

8 Overview for PV plant B

The second mounted PV plant consists of thirty two multicrystal PV modules installed on the roof of the school of music at the UoH. Each PV module has a nominal output power of 130 Wp. Figure 8 shows an image of the installed PV modules, where the tilt angle is equal to 42^0. This PV plant is in operation since 2006.

The PV modules of this PV system does not contain any bypass diodes compared with the PV plant A which contains 3 bypass didoes.

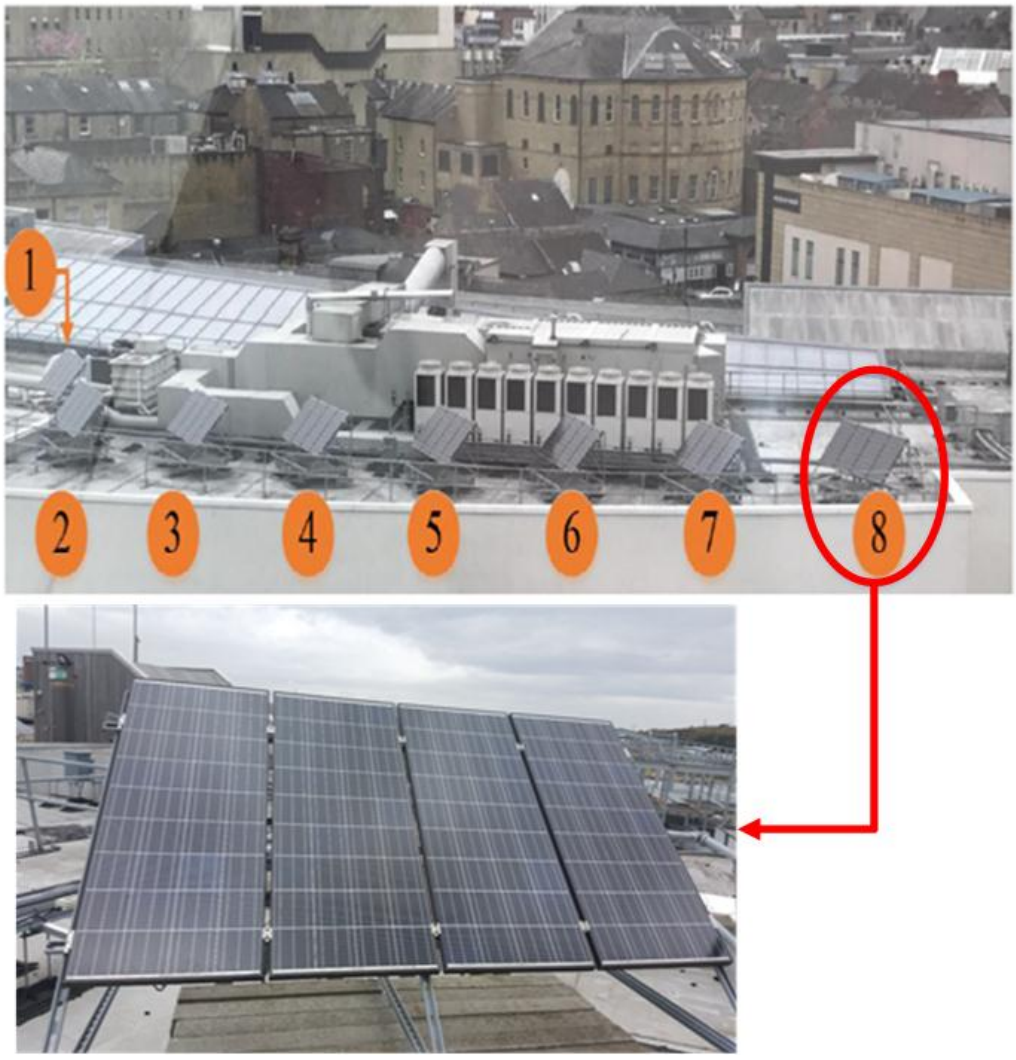

Figure 3 Second examined PV plant

9 PV modules electrical characteristics

KC130GHT-2 PV modules manufactured by Kyocera (KYOCERA, 2014) have been used in the PV plant B. The electrical characteristics of the PV panels are shown in Table 2. All listed values for the PV electrical characteristics is under STC (G: 1000 W/m^2, and T: 25 ^{0}C).

Table 1 KC130GHT-2 PV module electrical characteristics

PV module electrical characteristics	Value
Peak Power	130 W
Voltage at maximum power point (V_{mpp})	17.6 V
Current at maximum power point (I_{mpp})	7.39 A
Open Circuit Voltage (V_{oc})	21.9 V
Short Circuit Current (I_{sc})	8.02 A
Number of cells connected in series	36
Number of cells connected in parallel	1

10 DC/AC inverter unit

The PV plant B does not contain a MPPT unit. However, during the validation of our fault detection and PV performance modelling, Flexmax 80 MPPT have been used. The PV modules are connected directly to a DC/AC inverter. This inverter is connected to the main grid of the UoH. A schematic of the connection is shown in Figure 9.

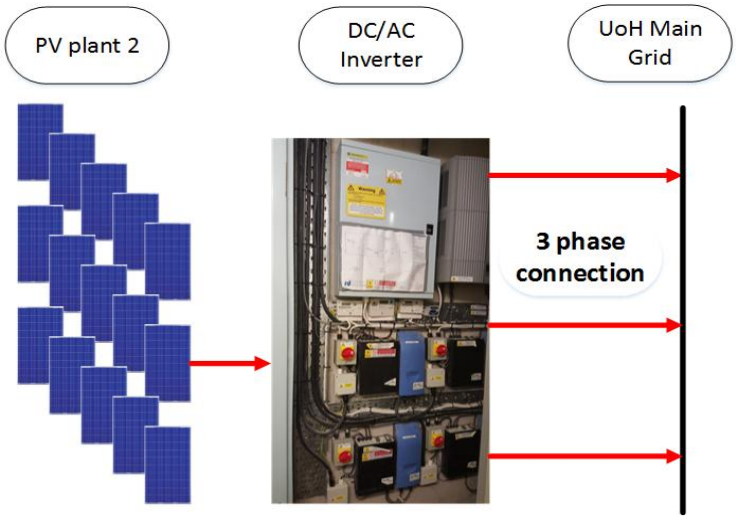

Figure 4 PV plant B connection to the DC/AC inverter and UoH main grid

11 PV plant B system architecture

As described in the previous section, the PV modules are connected to a DC/AC inverter. Subsequently, the inverter is connected to the UoH grid. In this section the PV module connected will be described.

Since 2006, the PV modules were configured as shown in Figure 10a. All PV modules were connected in series to a DC/AC inverter, without using MPPT unit. This PV configuration was improved to the series-parallel PV configuration, are shown in Figure 10b. The series-parallel configuration consists of 8 PV strings, each containing 4 series connected PV modules.

The new PV configuration has been used to validate the fault detection and PV performance analysis methods during this research. During the validation process, the DC/AC unit was completely disconnected from the PV plant. A MPPT unit was used to track the MPP.

Temperature sensors were connected at the back of each PV module during the experiments. The temperature sensors used are the same as those for PV plant A. This PV plant does not have a weather station or irradiance sensor. Therefore, the weather station explained previously in Appendix A - section 6 was used during the experiments.

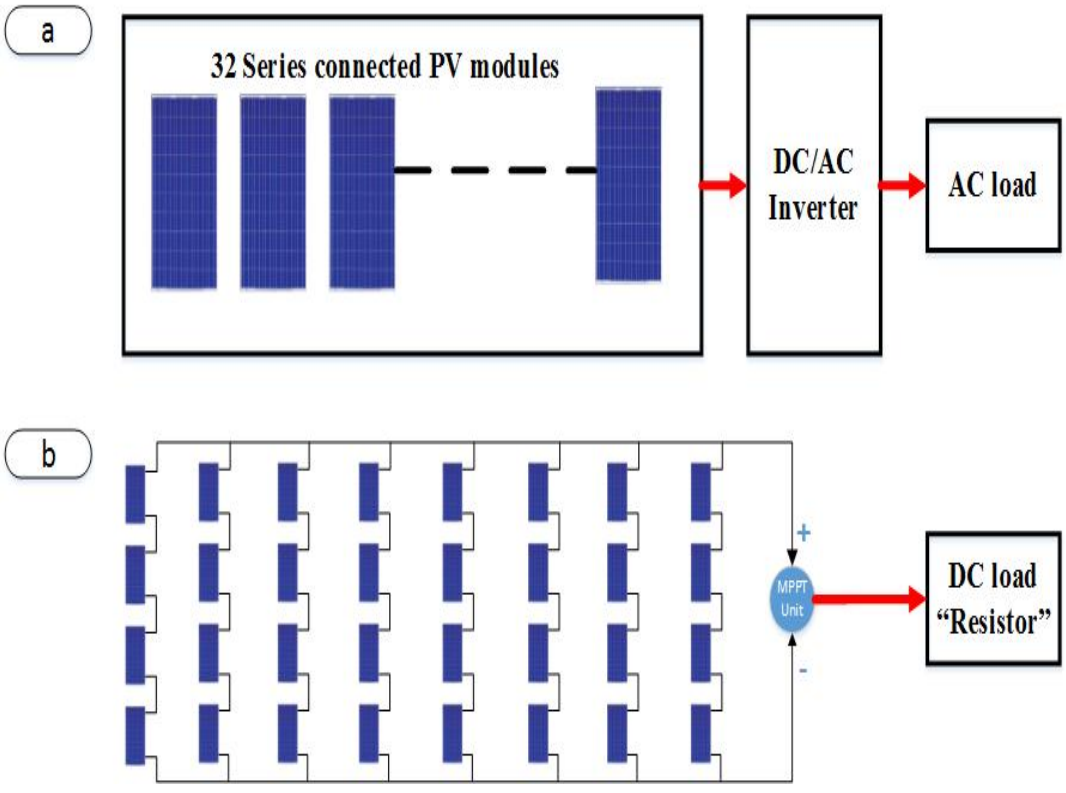

Figure 5 (a) PV configuration used in the PV system installed in 2006, (b) PV configuration used to validate the designed fault detection algorithms

Figure 11 presents a map which contains both PV plant A and PV plant B installed at the campus of the University of Huddersfield.

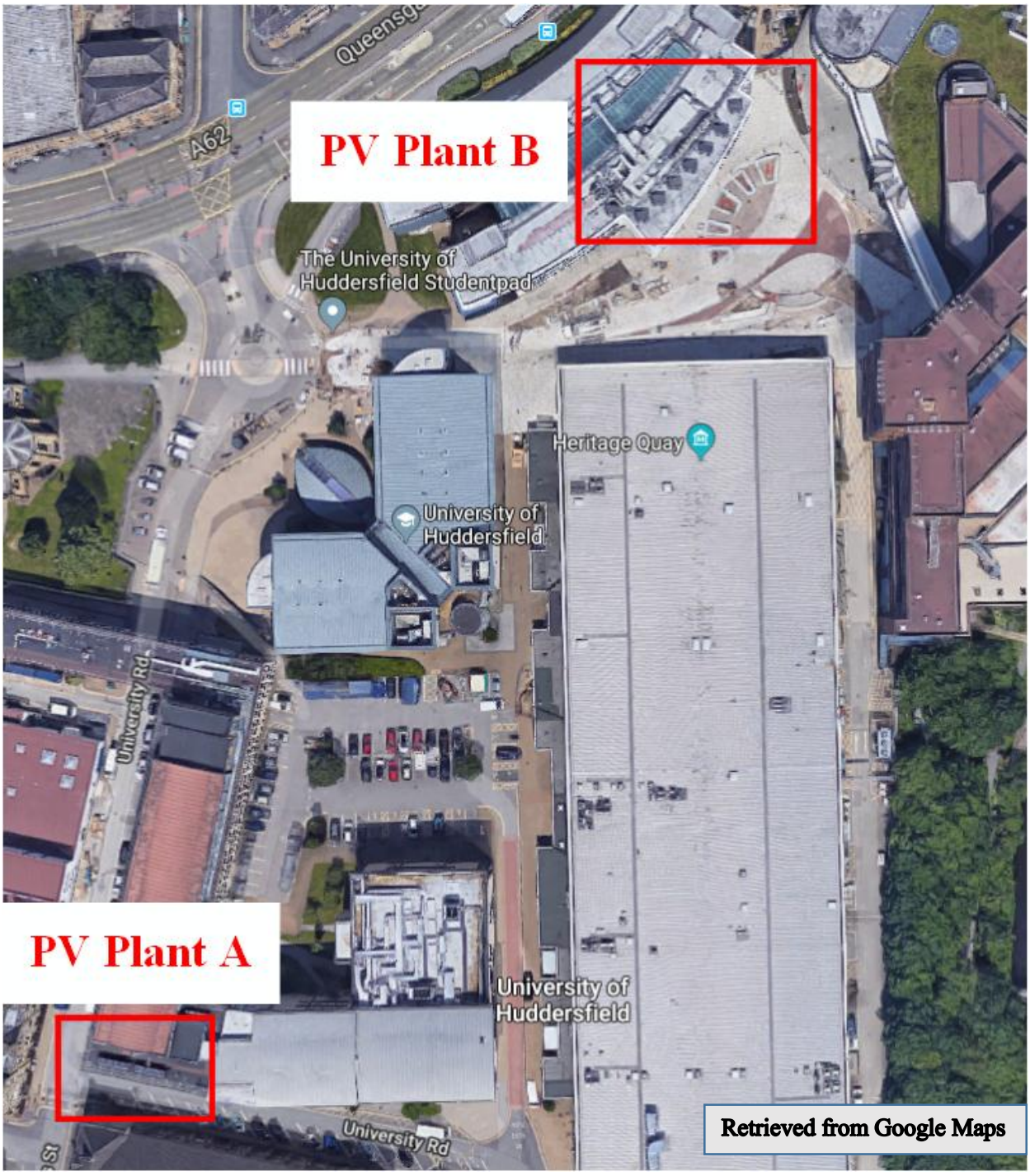

Figure 11 Map of the campus contains both examined PV plants

Appendix B. LabVIEW simulation code

PV module simulation (I-V Curve) :

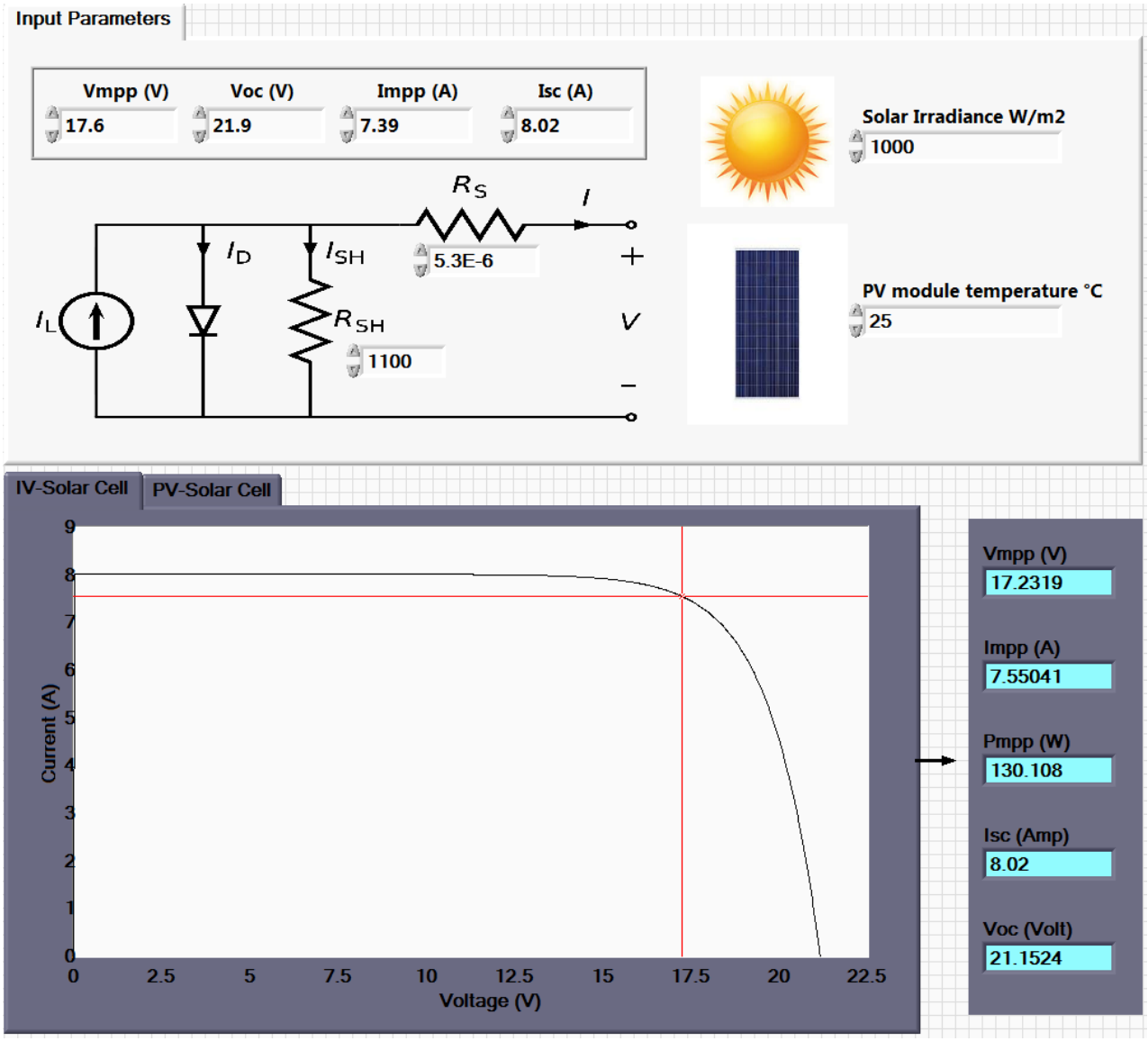

PV module simulation (P-V Curve) :

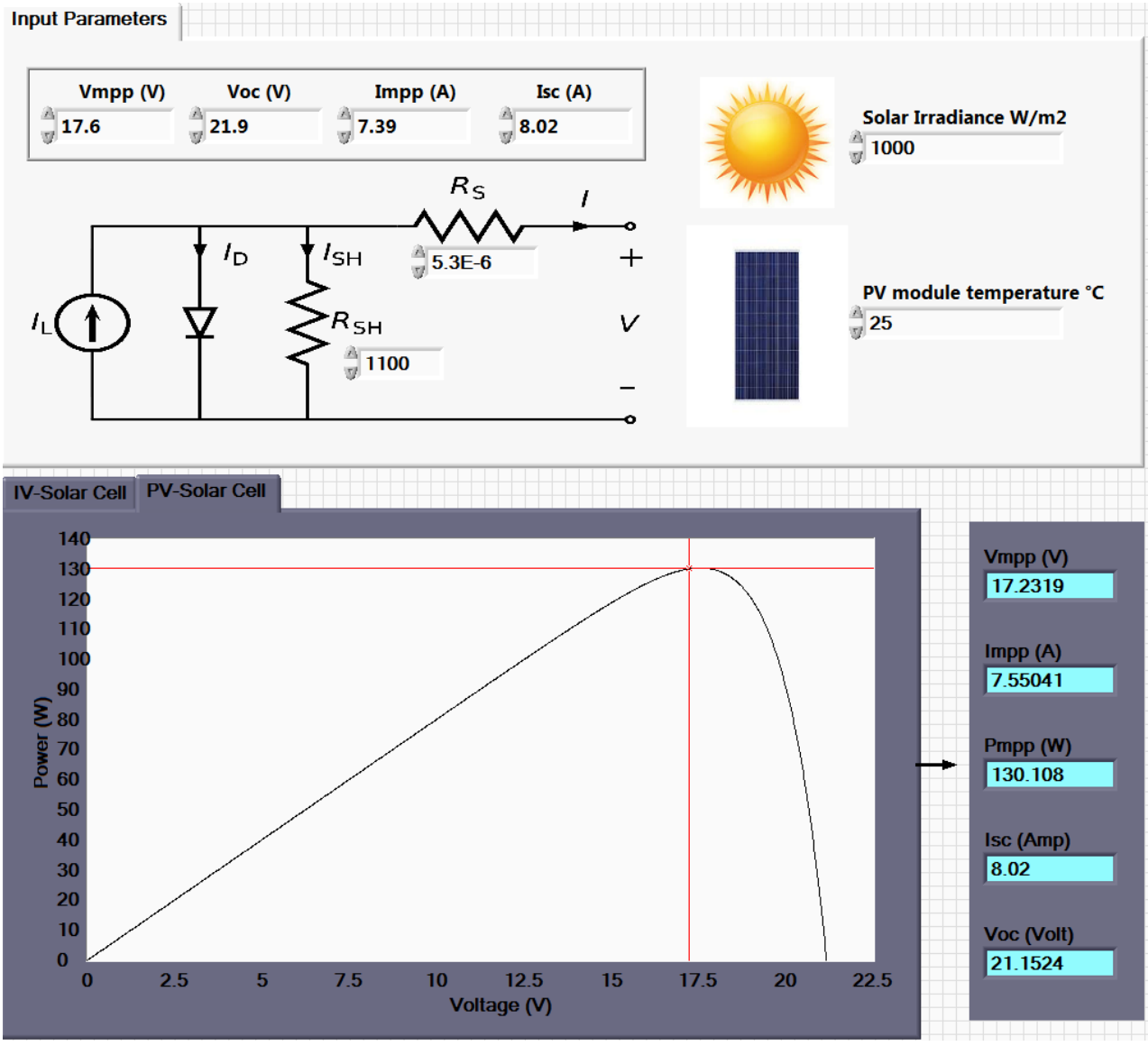

Appendix C. MATLAB/Simulink models for multiple PV array configurations

Series (S) Configuration:

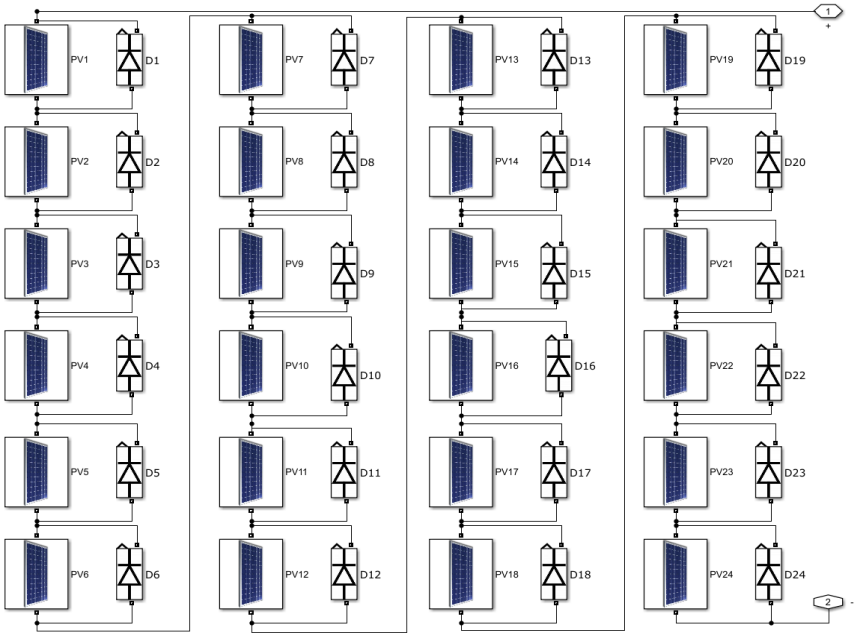

Parallel (P) Configuration:

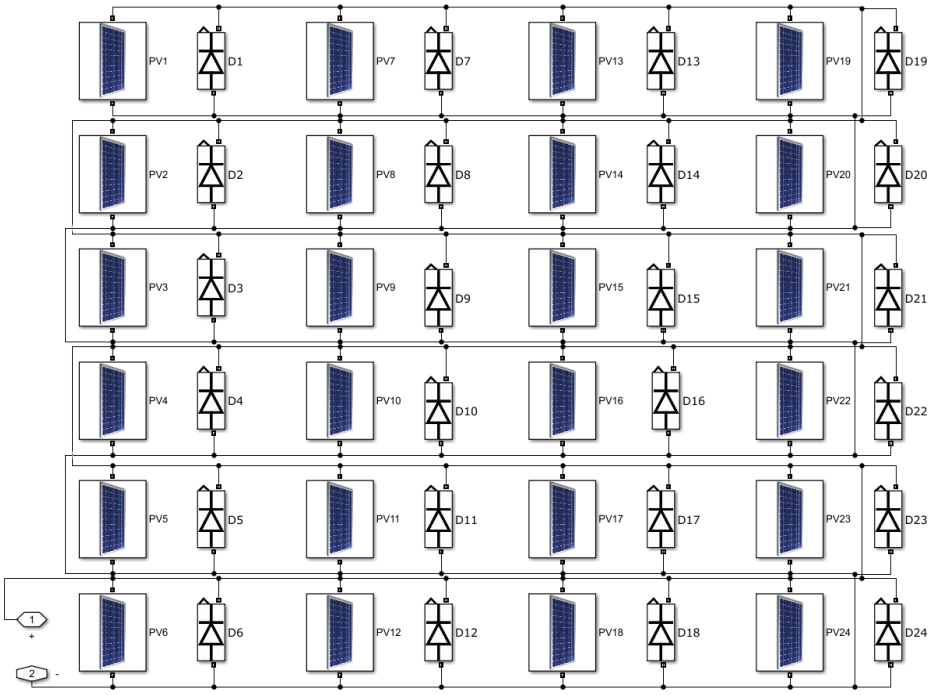

Series-Parallel (SP) Configuration:

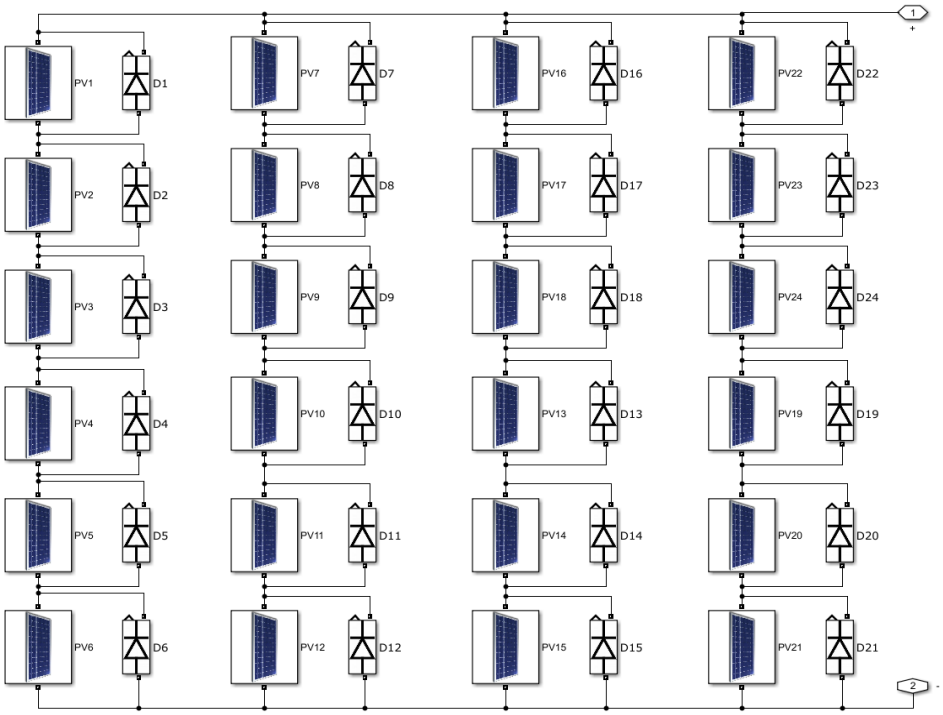

Total-Cross-Tied (TCT) Configuration:

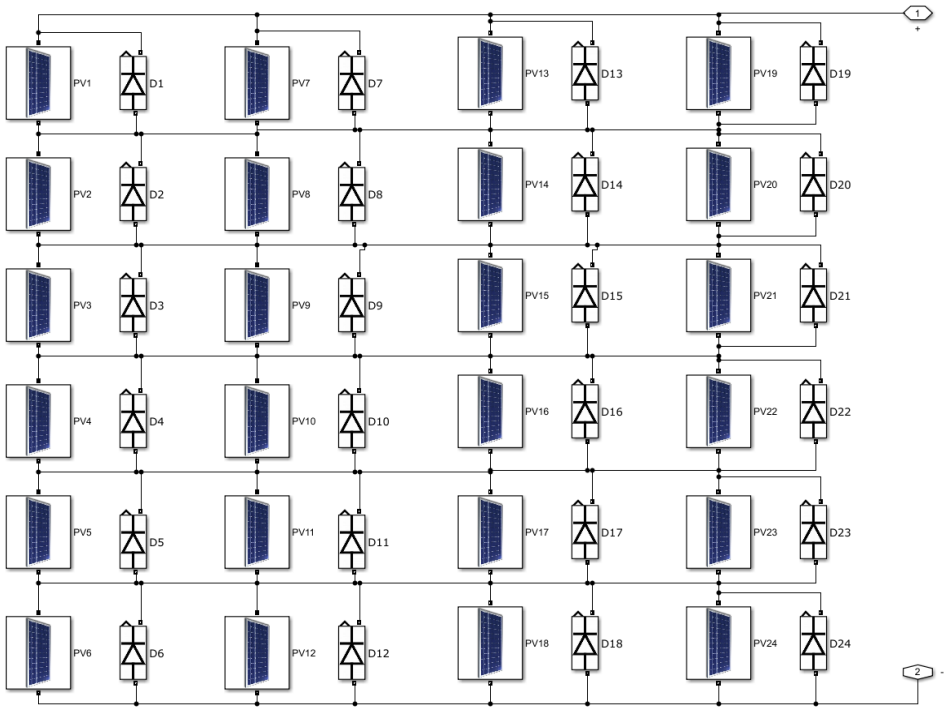

Bridge-Linked (BL) Configuration:

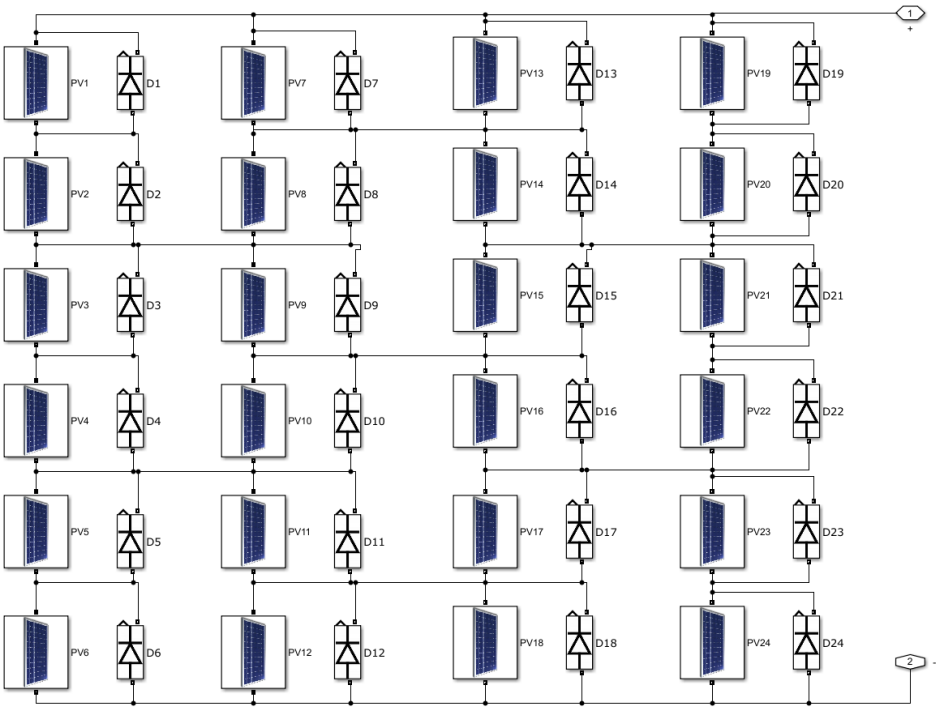

Appendix D. ANN Output Confusion Matrix

2 Neurons and 2 Hidden Layers:

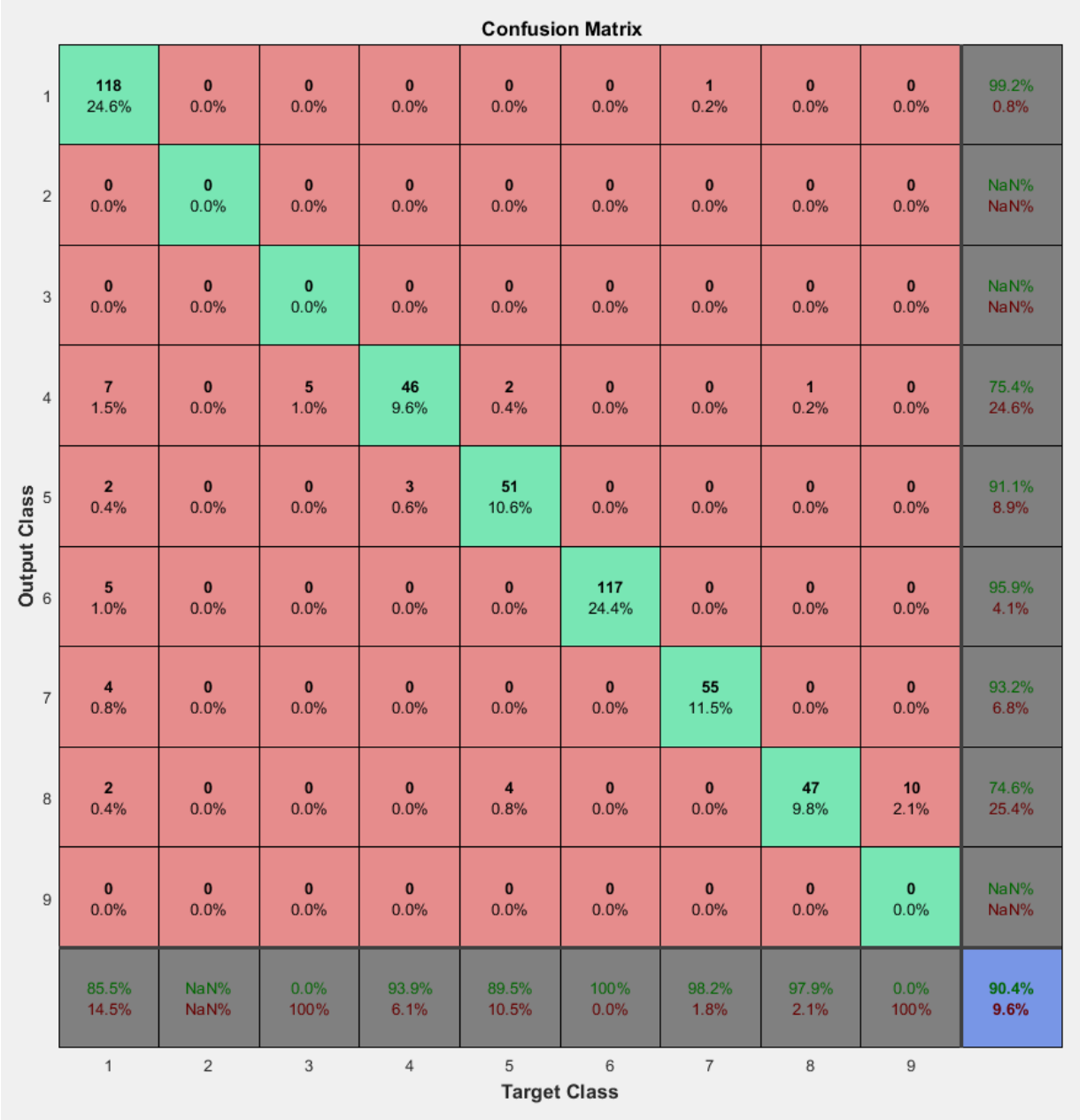

3 Neurons and 2 Hidden Layers:

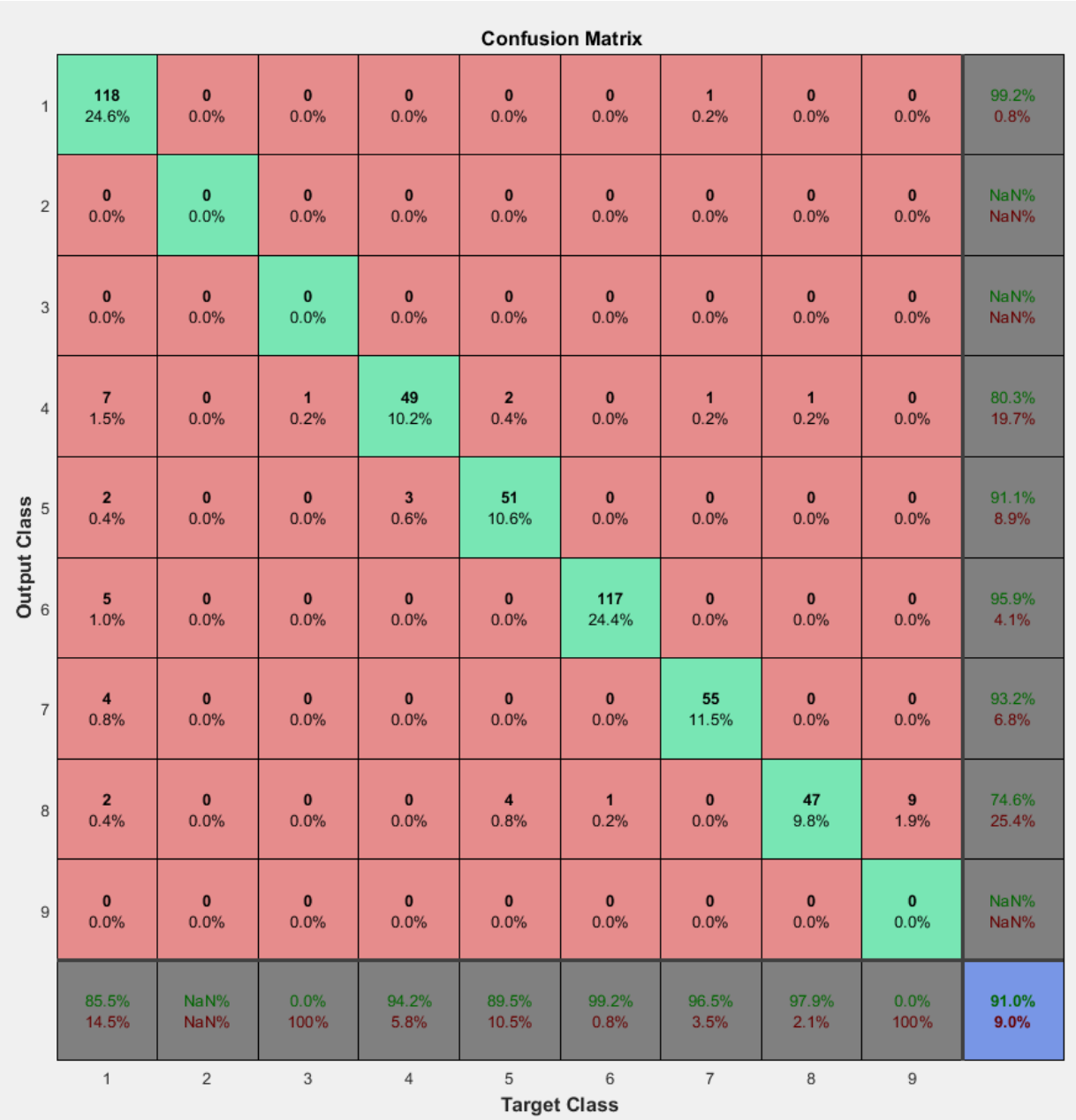

4 Neurons and 2 Hidden Layers:

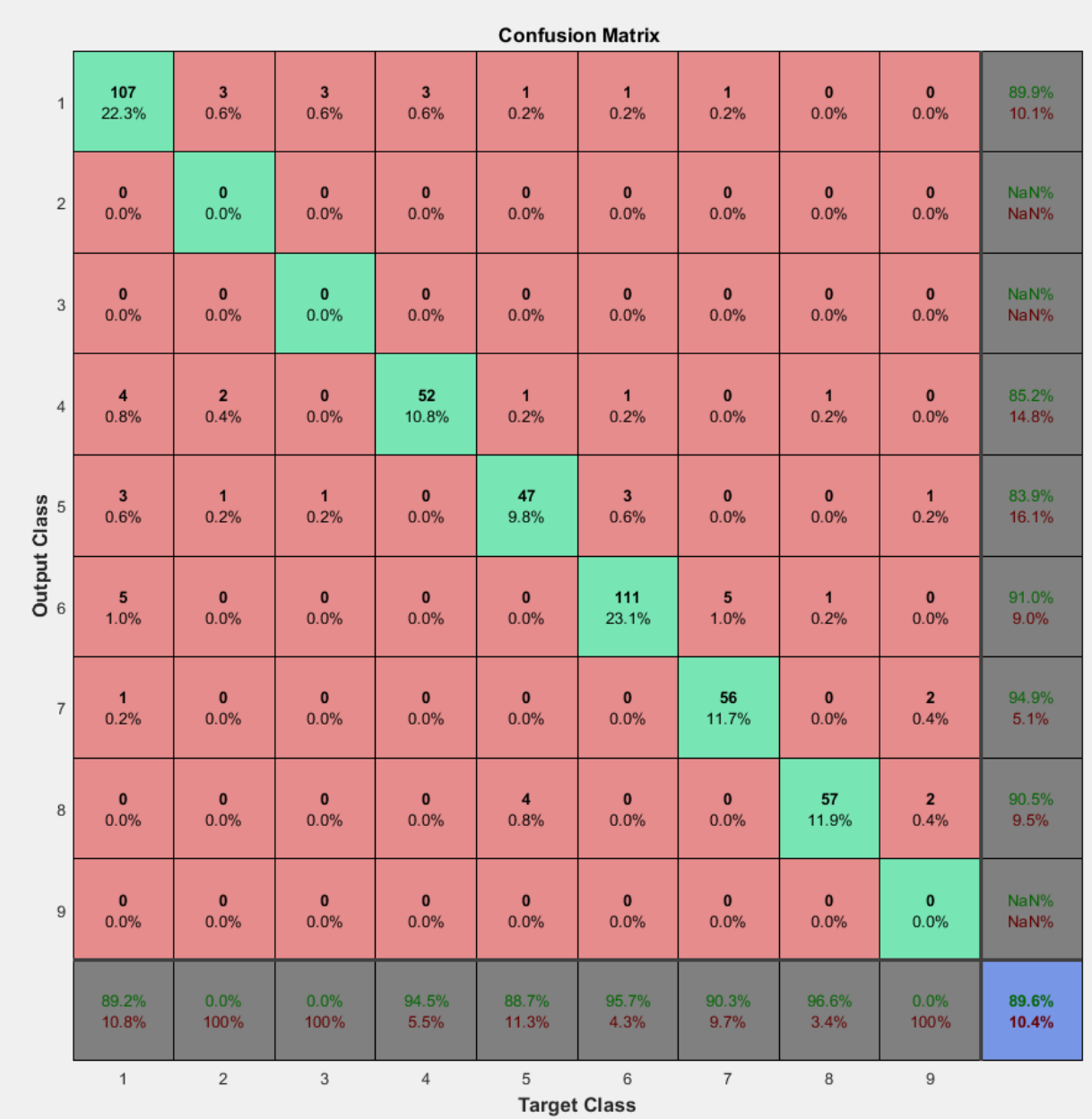

5 Neurons and 2 Hidden Layers:

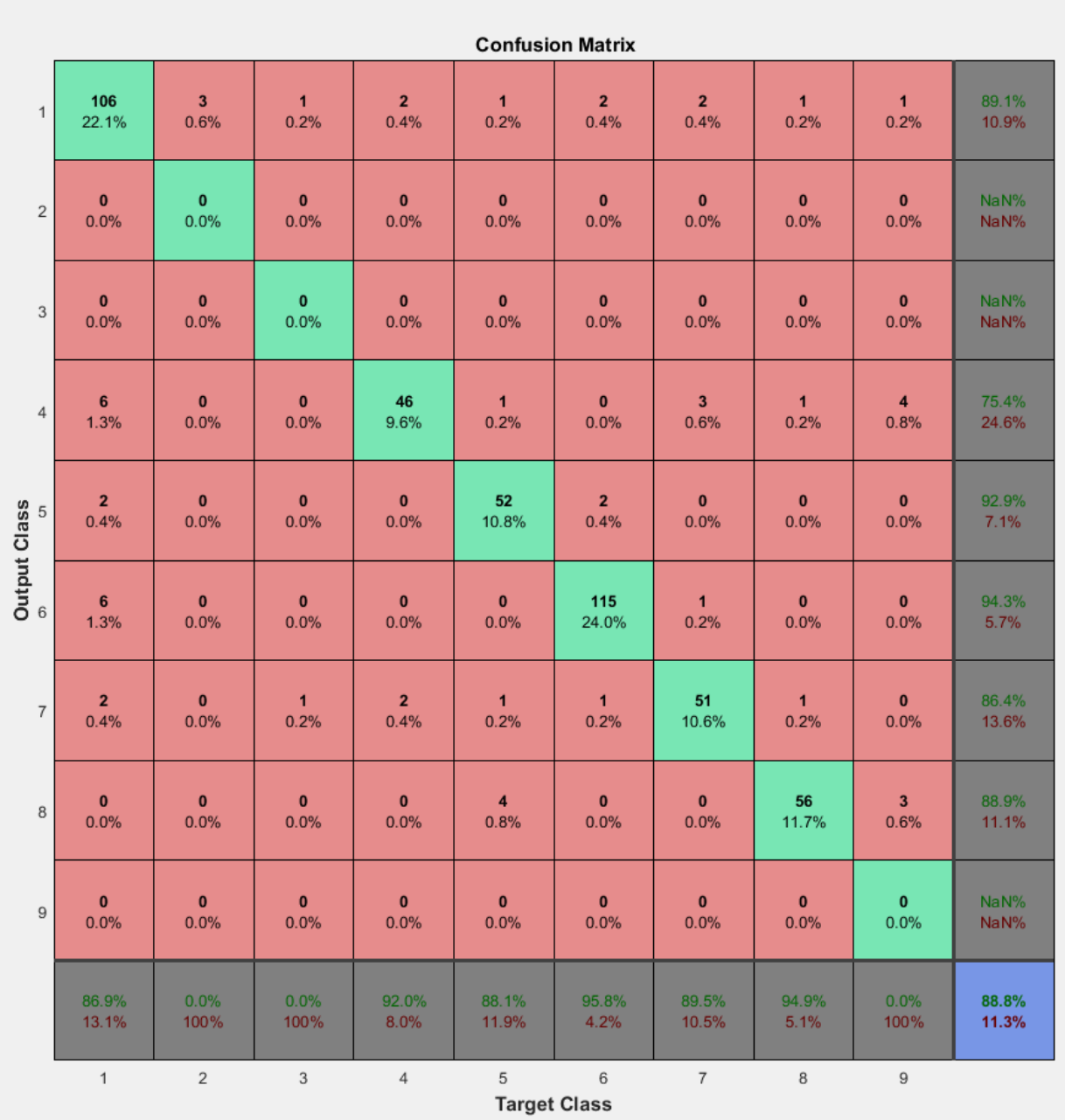

6 Neurons and 2 Hidden Layers:

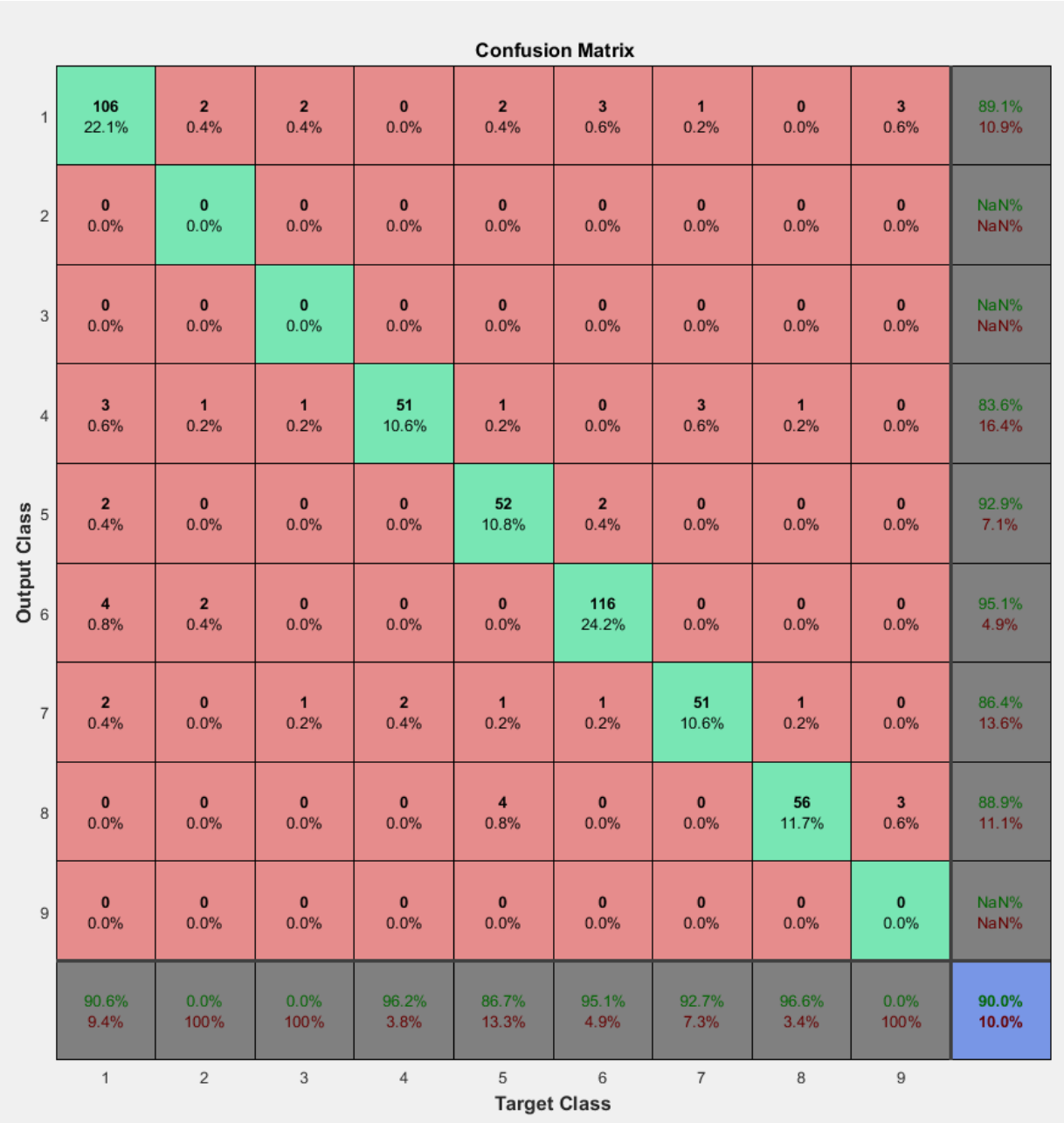

8 Neurons and 2 Hidden Layers:

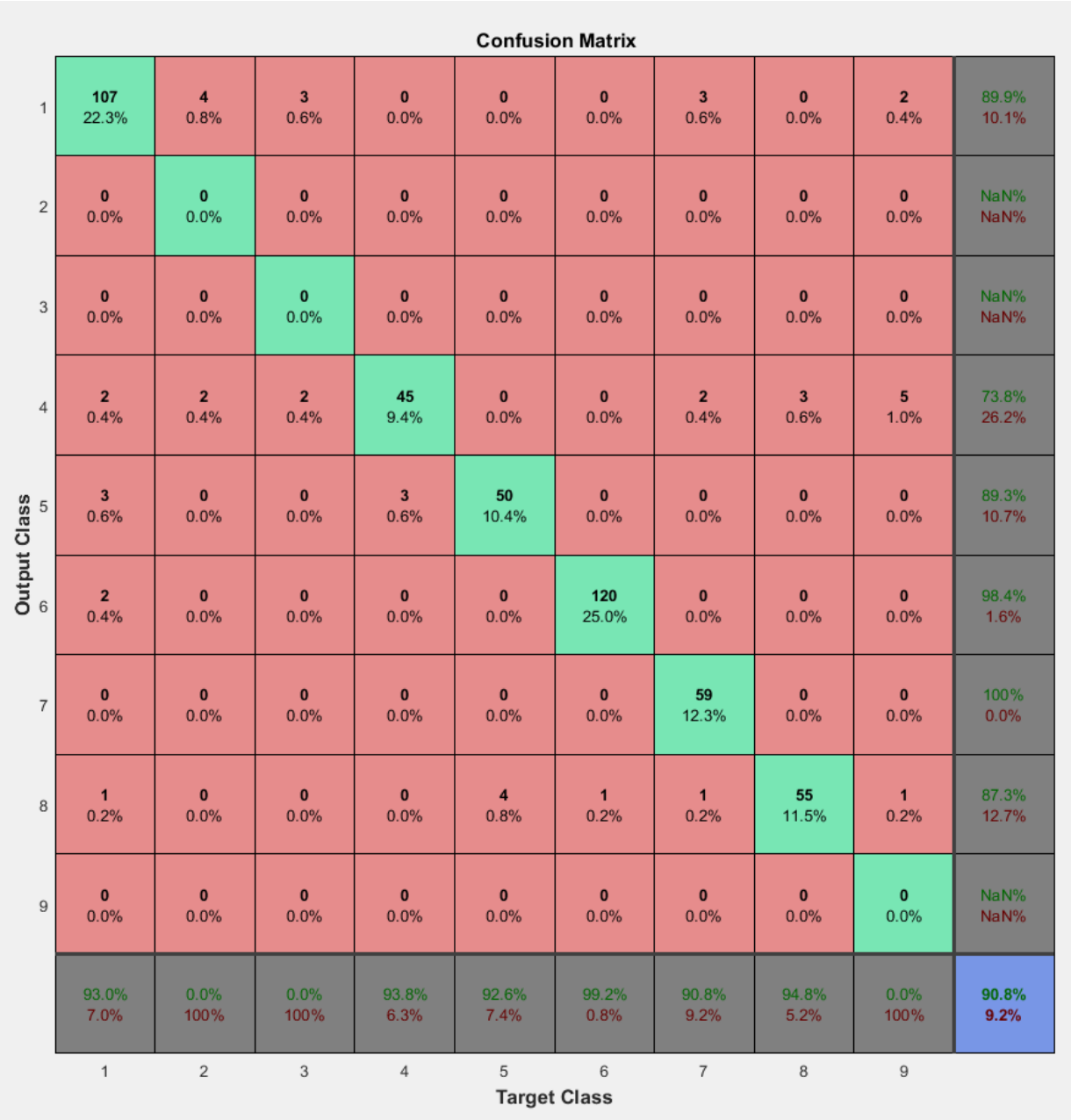

9 Neurons and 2 Hidden Layers:

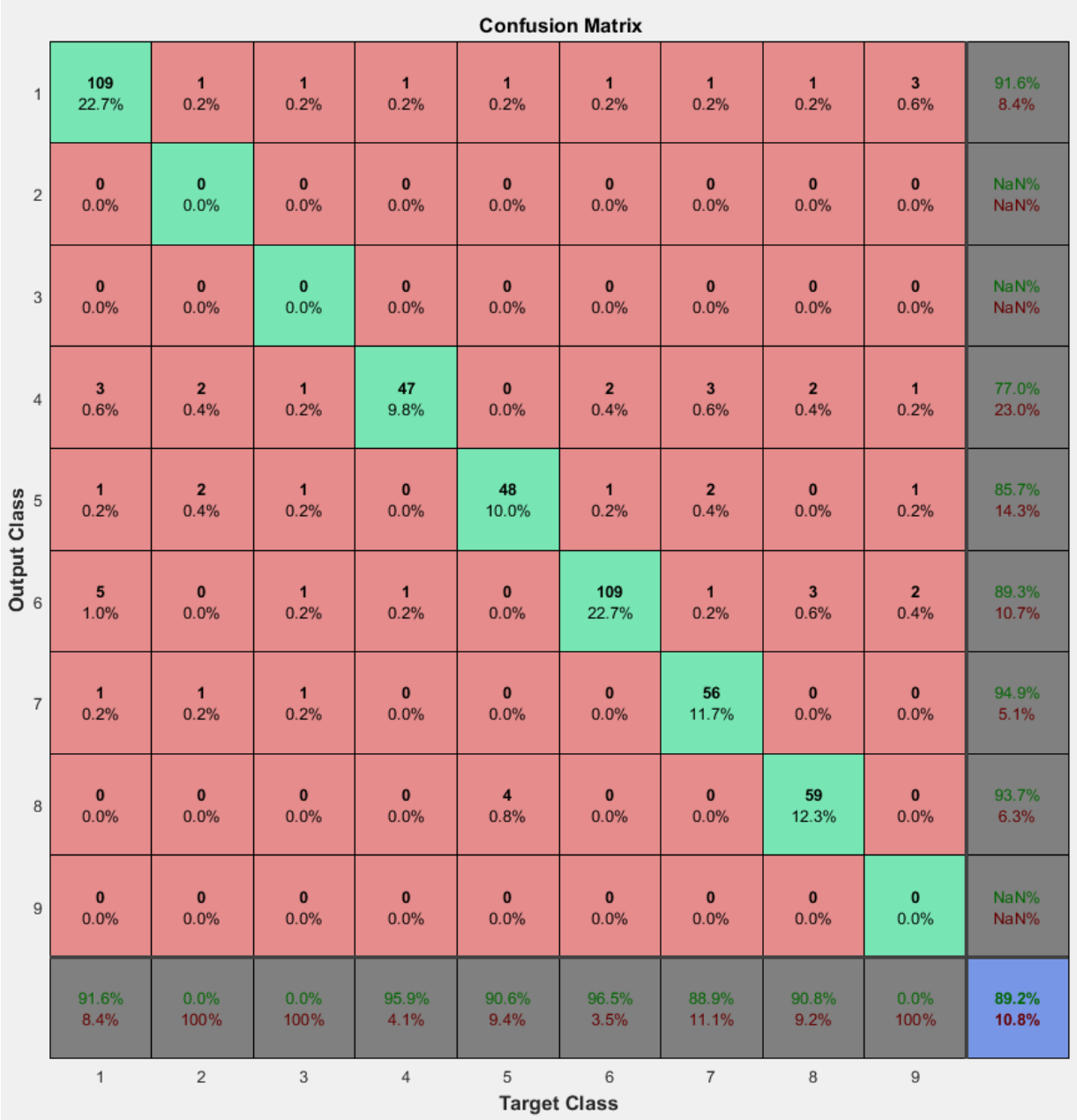

Appendix E. ANN Network MATLAB Code

```
function [Y,Xf,Af] = myNeuralNetworkFunction(X,~,~)
%MYNEURALNETWORKFUNCTION neural network simulation function.
%
% Generated by Neural Network Toolbox function genFunction, 19-Oct-2017 05:28:50.
%
% [Y] = myNeuralNetworkFunction(X,~,~) takes these arguments:
%
%   X = 1xTS cell, 1 inputs over TS timesteps
%   Each X(AGENCY, 2016) = Qx2 matrix, input #1 at timestep ts.
%
% and returns:
%   Y = 1xTS cell of 1 outputs over TS timesteps.
%   Each Y(AGENCY, 2016) = Qx9 matrix, output #1 at timestep ts.
%
% where Q is number of samples (or series) and TS is the number of timesteps.

%#ok<*RPMT0>

% ===== NEURAL NETWORK CONSTANTS =====

% Input 1
x1_step1.xoffset = [0.847968;0.877436];
x1_step1.gain = [0.00433905335116025;0.00229788502983558];
x1_step1.ymin = -1;

% Layer 1
b1 = [-2.8211472914295355;-0.9685855978481408;1.2292823821928234;3.327105970841882;-
2.1633363056901245;1.4075111903901627;3.0983891025982282];
IW1_1 = [2.0958017016180337 4.7629504843018973;3.670434031196653 -4.6699103690296218;-
4.1494203779402019 1.0863957295192399;-2.9600942971683617 6.6238797229437205;0.8188367105880483 -
6.3809709977149573;1.8765927419380746 -4.3029290927037138;5.0005831181506473 0.91138021990349771];

% Layer 2
b2 = [-0.095451342619132851;-0.4075860192878959;0.26762361814974112;-
1.4985266807730249;2.1978614000139518;-0.56861116734966144;0.086212985629450387];
LW2_1 = [1.1940642487241013 2.1096236139050935 0.72491519198466337 -7.2787218213244138
3.660320010701748 -1.0708849913104583 -7.3178343333301576;-0.57651927920475521 -1.7766413045021809
1.3637221094698413 2.2912832727753094 4.244045465981042 0.44176882797097577 -2.0455514563503785;-
0.33461217562424495 1.7627656129154543 0.71548447919757907 -2.7484402856178556 3.911921620957973
0.65895000318411712 6.5685194007459735;-0.6061641977282104 0.24303322380852876 1.9041542970914638
1.7624696935966087 -3.89180297010346 0.42895113573504984 3.7323243091577596;-3.1066326638400374
0.70336628464465767 -4.1006058092277433 -0.14531849158342872 -3.122781398168061 2.0617593625558426
-1.6583518307517542;-0.84940928360307577 -0.6208749473941263 1.3086154172367179 3.0574578518478082
-1.7694940494737772 -2.8459907088505219 -2.8230835012606548;4.5223305554426076 -2.1374452176310177 -
1.6589819470480343 3.3770562151630754 -2.556041113289385 0.25753856353679871 1.1657543514453605];

% Output 1
y1_step1.xrows = 9;
y1_step1.keep = [1 2 3 6 7 8 9];
y1_step1.remove = [4 5];
y1_step1.constants = [0;0];
```

```
% ===== SIMULATION ========

% Format Input Arguments
isCellX = iscell(X);
if ~isCellX
    X = (Ahmed & Salam);
end

% Dimensions
TS = size(X,2); % timesteps
if ~isempty(X)
    Q = size(X(Abdelhamid et al.),1); % samples/series
else
    Q = 0;
end

% Allocate Outputs
Y = cell(1,TS);

% Time loop
for ts=1:TS

    % Input 1
    X(AGENCY, 2016) = X(AGENCY, 2016)';
    Xp1 = mapminmax_apply(X(AGENCY, 2016),x1_step1);

    % Layer 1
    a1 = tansig_apply(repmat(b1,1,Q) + IW1_1*Xp1);

    % Layer 2
    a2 = softmax_apply(repmat(b2,1,Q) + LW2_1*a1);

    % Output 1
    Y(AGENCY, 2016) = removeconstantrows_reverse(a2,y1_step1);
    Y(AGENCY, 2016) = Y(AGENCY, 2016)';
end

% Final Delay States
Xf = cell(1,0);
Af = cell(2,0);

% Format Output Arguments
if ~isCellX
    Y = cell2mat(Y);
end
end

% ===== MODULE FUNCTIONS ========

% Map Minimum and Maximum Input Processing Function
function y = mapminmax_apply(x,settings)
y = bsxfun(@minus,x,settings.xoffset);
y = bsxfun(@times,y,settings.gain);
y = bsxfun(@plus,y,settings.ymin);
end
```

```
% Competitive Soft Transfer Function
function a = softmax_apply(n,~)
if isa(n,'gpuArray')
  a = iSoftmaxApplyGPU(n);
else
  a = iSoftmaxApplyCPU(n);
end
end
function a = iSoftmaxApplyCPU(n)
nmax = max(n,[],1);
n = bsxfun(@minus,n,nmax);
numerator = exp(n);
denominator = sum(numerator,1);
denominator(denominator == 0) = 1;
a = bsxfun(@rdivide,numerator,denominator);
end
function a = iSoftmaxApplyGPU(n)
nmax = max(n,[],1);
numerator = arrayfun(@iSoftmaxApplyGPUHelper1,n,nmax);
denominator = sum(numerator,1);
a = arrayfun(@iSoftmaxApplyGPUHelper2,numerator,denominator);
end
function numerator = iSoftmaxApplyGPUHelper1(n,nmax)
numerator = exp(n - nmax);
end
function a = iSoftmaxApplyGPUHelper2(numerator,denominator)
if (denominator == 0)
  a = numerator;
else
  a = numerator ./ denominator;
end
end

% Sigmoid Symmetric Transfer Function
function a = tansig_apply(n,~)
a = 2 ./ (1 + exp(-2*n)) - 1;
end

% Remove Constants Output Reverse-Processing Function
function x = removeconstantrows_reverse(y,settings)
Q = size(y,2);
x = nan(settings.xrows,Q,'like',y);
x(settings.keep,:) = y;
x(settings.remove,:) = repmat(settings.constants,1,Q);
end
```